AD-A202 021

FRANK J. SEILER RESEARCH LABORATORY

FJSRL-TR-88-0004   September 1988

Workshop II on Unsteady Separated Flow

Proceedings

DTIC
ELECTE
S NOV 2 9 1988 D
E

Project 2307-F1-38

AIR FORCE SYSTEMS COMMAND

UNITED STATES AIR FORCE

88 11 28 220

This document was prepared by the Aerospace Mechanics Division, Directorate of Lasers and Aerospace Mechanics, Frank J. Seiler Research Laboratory, United States Air Force Academy, Colorado Springs, CO. The research was conducted under Project Work Unit Number 2307-F1-38, Unsteady Airfoil Energized Flow. Major John Walker was the Project Scientist in charge of the work.

When U.S. Government drawings, specifications or other data are used for any purpose other than a definitely related government procurement operation, the government thereby incurs no responsibility nor any obligation whatsoever, and the fact that the government may have formulated, furnished or in any way supplied the said drawings, specifications or other data is not to be regarded by implication or otherwise, as in any manner licensing the holder or any other person or corporation or conveying any rights or permission to manufacture, use or sell any patented invention that may in any way be related thereto.

Inquiries concerning the technical content of this document should be addressed to the Frank J. Seiler Research Laboratory (AFSC), FJSRL/NH, USAF Academy, Colorado Springs, CO 80840-6528. Phone (719) 472-3122.

This report has been reviewed by the Commander and released to the National Technical Information Service (NTIS). At NTIS it will be available to the general public, including foreign nations.

This technical report has been reviewed and is approved for publication.

JOHN M. WALKER, Major, USAF
Project Scientist

ROBERT F. REILMAN, JR., Major, USAF
Director, Lasers & Aerospace Mechanics

WILLIAM G. THORPE, Lt Col, USAF
Commander

Copies of this report should not be returned unless return is required by security considerations, contractual obligations, or notice on a specific document.

Printed in the United States of America. Qualified requesters may obtain additional copies from the Defense Documentation Center. All others should apply to: National Technical Information Service
6285 Port Royal Road
Springfield, Virginia 22161

REPORT DOCUMENTATION PAGE

1a. REPORT SECURITY CLASSIFICATION	1b. RESTRICTIVE MARKINGS
UNCLASSIFIED	

2a. SECURITY CLASSIFICATION AUTHORITY	3. DISTRIBUTION/AVAILABILITY OF REPORT
2b. DECLASSIFICATION/DOWNGRADING SCHEDULE	

4. PERFORMING ORGANIZATION REPORT NUMBER(S)	5. MONITORING ORGANIZATION REPORT NUMBER(S)
FJSRL-TR-88-0004	

6a. NAME OF PERFORMING ORGANIZATION	6b. OFFICE SYMBOL (If applicable)	7a. NAME OF MONITORING ORGANIZATION
Frank J. Seiler Research Laboratory	FJSRL/NHM	

6c. ADDRESS (City, State and ZIP Code)	7b. ADDRESS (City, State and ZIP Code)
USAF Academy Colorado Springs CO 80840-6528	

8a. NAME OF FUNDING/SPONSORING ORGANIZATION	8b. OFFICE SYMBOL (If applicable)	9. PROCUREMENT INSTRUMENT IDENTIFICATION NUMBER
Frank J. Seiler Research Laboratory	FJSRL/NHM	

8c. ADDRESS (City, State and ZIP Code)	10. SOURCE OF FUNDING NOS.			
USAF Academy Colorado Springs CO 80840-6528	PROGRAM ELEMENT NO.	PROJECT NO.	TASK NO.	WORK UNIT NO.

11. TITLE (Include Security Classification) Workshop II on Unsteady Separated Flow (Unclassified)	61102F	2307	F1	38

12. PERSONAL AUTHOR(S)

13a. TYPE OF REPORT	13b. TIME COVERED	14. DATE OF REPORT (Yr., Mo., Day)	15. PAGE COUNT
Summary	FROM _____ TO _____	1988 July 28	385

16. SUPPLEMENTARY NOTATION

17. COSATI CODES			18. SUBJECT TERMS (Continue on reverse if necessary and identify by block number)
FIELD	GROUP	SUB. GR.	Unsteady Aerodynamics
0101			Separated Flows,
2004			Dynamic Stall,

19. ABSTRACT (Continue on reverse if necessary and identify by block number)

This document contains the proceedings from the second workshop on unsteady separated flow sponsored jointly by Frank J. Seiler Research Laboratory, Air Force Office of Scientific Research, the University of Colorado and the Department of Aeronautics at the Air Force Academy. The topics of the papers cover several aspects of unsteady flows through experimental, analytical and computational methods. A special emphasis is placed on dynamic stall with several papers covering both two dimensional and three dimensional effects.

20. DISTRIBUTION/AVAILABILITY OF ABSTRACT	21. ABSTRACT SECURITY CLASSIFICATION
UNCLASSIFIED/UNLIMITED ☒ SAME AS RPT. ☐ DTIC USERS ☐	UNCLASSIFIED

22a. NAME OF RESPONSIBLE INDIVIDUAL	22b TELEPHONE NUMBER (Include Area Code)	22c. OFFICE SYMBOL
JOHN M. WALKER	(719) 472-3122	FJSRL/NHM

DD FORM 1473, 83 APR EDITION OF 1 JAN 73 IS OBSOLETE.

AFOSR/FJSRL/DFAN/U. COLORADO

WORKSHOP II ON UNSTEADY SEPARATED FLOWS

ORGANIZERS: Dr. Jim McMichael   Captain Hank Helin, PhD
Program Manager   Program Manager
AFOSR/NA   AFOSR/NA
Bolling AFB DC 20332-6448   Bolling AFB DC 20332-6448

COORDINATION AND
DOCUMENTS: Dr. Marvin W. Luttges   Dr. Michael C. Robinson
Professor   Assistant Professor
Aerospace Engineering Sciences Aerospace Engineering Sciences
Box 429   Box 429
University of Colorado   University of Colorado
Boulder, Colorado 80309   Boulder, Colorado 80309

Major John M. Walker, PhD
Chief, Aerospace Mechanics Division
Frank J. Seiler Research Laboratory
USAF Academy
Colorado Springs, Colorado 80840-6528

COORDINATION AND
ARRANGEMENTS: Lt Col Fred Gilliam, PhD
Associate Professor
Department of Aeronautics
USAFA/DFAN
USAF Academy
Colorado Springs, Colorado 80840-5701

Captain John Wissler
Instructor
Department of Aeronautics
USAFA/DFAN
USAF Academy
Colorado Springs, Colorado 80840-5701

TECHNICAL ASSISTANCE ACKNOWLEDGEMENTS:

Mr. Don Lijana

FINAL PREPARATION:

Captain Eric J. Stephen
Research Associate
Frank J. Seiler Research Laboratory
USAF Academy
Colorado Springs, Colorado 80840-6528

Accession For	
NTIS GRA&I	☒
DTIC TAB	☐
Unannounced	☐
Justification	
By	
Distribution/	
Availability Codes	
Dist	Avail and/or Special
A-1	

Dr. A.A. Abtahi
Advanced Research Organization
Lockheed-Georgia
Detp 72-11, Zone 403
Marietta, Georgia 30063

Dr. Acharya
Department of Aerospace Engineering
Illinois Institute of Technology
Chicago, Illinois 60616

Dr. N.K. Agarwal
Aerospace and Ocean Engineering
Virginia Polytechnic Institute
    and State University
Blacksburg, Virginia 24061

Dr. J. Allburn
SRS Technologies
1500 Wilson
Suite 800
Arlington, Virginia 22209

Major J. Ashworth
Department of Aeronautics
USAF Academy
Colorado Springs, Colorado 80840

Dr. R. Atta
Mechanical Engineering and Mechanics
Lehigh University
Bethlehem, Pennsylvania 18015

Dr. D. Belk
AD/AFATL/FXA
Egland AFB, Florida 32542

Dr. S. Bodapati
NASA-Ames Research Center
Mail Stop 260-1
Moffett Field, California 94035

Dr. A. Bryson
Department of Mechanical Engineering
Stanford University
Stanford, California 94305

Dr. L.W. Carr
NASA-Ames Research Center
Mail Stop 260-1
Moffett Field, California 94035

Dr. F.O. Carta
United Tech Research Center
Silver Lane, Mail Stop 19
East Hartford, Connecticut 06108

Dr. T. Cebeci
Douglas Aircraft Company
3855 Lakewood Boulevard
Long Beach, California 90846

Dr. Gary Chapman
NASA-Ames Research Center
Mail Stop 229-3
Moffett Field, California 94035

Dr. H.K. Cheng
Department of Aerospace Engineering
University of Southern California
Los Angeles, California 90089-1191

Dr. C.Y. Chow
Aerospace Engineering Sciences, Box 429
University of Colorado
Boulder, Colorado 80309

Dr. A. Cunningham
General Dynamics - Fort Worth
Mail Zone 2870
P.O. Box 748
Fort Worth, Texas 76101

Dr. R.G. den Boer
National Aerospace Laboratory
Amsterdam, The Netherlands

Dr. P.E. Dimotakis
Aeronautics and Applied Physics
California Institute of Technology
Pasadena, California 91125

Dr. Doligalski
Army Research Office
Research Triangle Park
Durham, North Carolina 27709

Dr. F.A. Dvorak
Analytic Methods, Inc.
P.O. Box 3786
Redmond, Washington 98009

Dr. J. Eaton
Department of Mechanical Engineering
Stanford University
Stanford, California   94305

Dr. L.E. Ericsson
Lockheed Missiles and Space Company
D/81-10, Bldg 157
Sunnyvale, California   94088

Dr. M. Farshchi
Nielsen Engr and Research Company
510 Clyde Avenue
Mountainview, California   94043-2287

Dr. P. Freymuth
Aerospace Engineering Sciences
University of Colorado, Box 429
Boulder, Colorado   80309-0429

Dr. K-Y Fung
Engineering Experiment Station
College of Engineering
University of Arizona
Tucson, Arizona   85721

Dr. M. Gad-el-Hak
Department of Aero and Mech Engineering
University of Notre Dame
Notre Dame, Indiana   46556

Dr. M. Gharib
Department of Mechanical Engineering
University of California
San Diego, California   92093

Dr. K.N. Ghia
Aerospace Engineering and Engineering
    Mechanics
Mail Location 70
University of Cincinnati
Cincinnati, Ohio   45221-0070

Dr. U. Ghia
Department of Mechanical and
    Industrial Engineering
Mail Location 72
University of Cincinniti
Cincinnati, Ohio   45221-0070

Lt Col F. Gilliam
Department of Aeronautics
USAF Academy
Colorado Springs, Colorado   80840

Dr. G. Graham
Department of Mechanical Engineering
Ohio University
Athens, Ohio   45701-0627

Dr. E.S. Hanff
Unsteady Aerodynamics Laboratory
National Aeronautical Est
Montreal Road
Ottawa, Ontario Canada   K1A OR6

Dr. C. Hefele
Mechanical Engineering and Mechanics
Lehigh University
Bethlehem, Pennsylvania   18015

Captain H.E. Helin
AFOSR/NA
Bolling AFB DC   20332-6448

Mr. R.W. Henk
Department of Mechanical Engineering
Stanford University
Stanford, California   94305

Dr. L. Hesselink
Department of Aeronautics and
    Astronautics
Stanford University
Stanford, California   94305

Dr. C.M. Ho
Department of Aerospace Engineering
University of Southern California
Los Angeles, California   90089-1191

Dr. N.T. Hoang
Department of Engr Science and Mech
Virginia Polytechnic Institute
    and State University
Blacksburg, Virginia   24061

Dr. W.H. Hui
University of Waterloo
Waterloo, Ontario Canada N2L 3G1

Major Bill Humphreys
Department of Aeronautics
USAF Academy
Colorado Springs, Colorado   80840

Dr. N.A. Jarrah
Department of Aero and Astronautics
Durand Room 369
Stanford University
Stanford, California 94305

Dr. J. Jenkins
AFWAL/FIG
Wright-Patterson AFB, Ohio 45433-6553

Dr. Z.X. Jia
Department of Aerospace Engineering
University of Southern California
Los Angeles, California 90089-1191

Lt Col E. Jumper
Air Force Weapons Laboratory
Kirtland AFB, New Mexico 87117

Dr. Kershen
Aerospace and Mechanical Engineering
University of Arizona
Tucson, Arizona 85721

Dr. D.W. Kinsey
AFWAL/FIMM
Wright-Patterson AFB, Ohio 45433

Dr. C.R. Koch
Building 500, Rm 500N2
Department of Mechanical Engineering
Stanford University
Stanford, California 94305

Dr. D.J. Koga
Department of Mechanical Engineering
Stanford University
Stanford, California 94305

Dr. I. Kroo
Department of Aeronautics and
    Astronautics
Stanford University
Stanford, California 94305

Dr. A. Krothapalli
Department of Mechanical Engineering
Florida State University
P.O. Box 2175
Tallahassee, Florida 32306-2175

Dr. C.-H. Kuo
Mechanical Engineering and Mechanics
Lehigh University
Bethlehem, Pennsylvania 18015

Colonel J. Lang
ASD/EN
Wright-Patterson AFB, Ohio 45433-5000

Dr. M. Lee
Department of Aerospace Engineering
University of Southern California
Los Angeles, California 90089-1191

Dr. Lekoudis
Code 1132 F
Office of Naval Research
800 N. Quincey Street
Arlington, Virginia 22217

Dr. A. Leonard
Aeronautics and Applied Physics
California Institute of Technology
Pasadena, California 91125

Dr. P. Lorber
United Tech Research Center
Silver Lane, Mail Stop 19
East Hartford, Connecticut 06108

Dr. Luiz Lourenco
Department of Mechanical Engineering
Florida State University
P.O. Box 2175
Tallahassee, Florida 32306-2175

Dr. M.W. Luttges
Aerospace Engineering Sciences
University of Colorado, Box 429
Boulder, Colorado 80309

Dr. Maskew
Analytic Methods, Inc.
P.O. Box 3786
Redmond, Washington 98009

Dr. D.S. Mathioulakis
41 Agiou Trifonos
Kifisia, Greece

Dr. T. Maxworthy
Department of Mechanical Engineering
University of Southern California
University Park
Los Angeles, California 90089-1191

Dr. P.A. Monkewitz
Mechanical, Aerospace and Nuclear
        Engineering Department
Engineering and Applied Science
Los Angeles, California 90024

Dr. J.E. McCune
Aeronautics and Astronautics
Massachusetts Institute of Technology
Cambridge, Massachusetts 02139

Dr. J. McMichael
AFOSR/NA
Bolling AFB DC 20332-6448

Dr. R. Montividas
Department of Aerospace Engineering
Illinois Institute of Technology
Chicago, Illinois 60616

Dr. D.T. Mook
Engineering Science and Mechanic
Virginia Polytechnic Institute and
    State University
Blacksburg, Virginia 24061

Dr. H.M. Nagib
Department of Aerospace Engineering
Illinois Institute of Technology
Chicago, Illinois 60616

Dr. C.F. Nelson
Department of Mechanical Engineering
Stanford University
Stanford, California 94305

Dr. A.H. Nayfeh
Engineering Science and Mechanic
Virginia Polytechnic Institute and
    State University
Blacksburg, Virginia 24061

Dr. D. Nixon
Nielson Engineering and Research
    Company
510 Clyde Avenue
Mountainview, California 94043-2287

Dr. D. Neuberger
Tel Aviv University
Department of Fluid Mechanics
Ramat Aviv, Israel 69978

Dr. K.J. Orlik-Ruchemann
Unsteady Aerodynamics Laboratory
National Aeronautical Est
Montreal Road
Ottawa, Ontario Canada K1A OR6

Dr. G.A. Osswald
Aerospace Engineering and
    Engineering Mechanics
Mail Location 70
University of Cincinnati
Cincinnati, Ohio 45221-0070

Dr. M. Pladzer
Post Naval Graduate School
Code 67
Monterey, California 93943

Dr. D.R. Poling
Boeing Vertol Company
Philadelphia, Pennsylvania

Dr. J.D. Powell
Building 500, Rm 500N2
Department of Mechanical Engineering
Stanford University
Stanford, California 94305

Dr. M.R. Rai
NASA/Ames Research Center
Moffett Field, California 94035

Dr. H.L. Reed
Department of Mechanical Engineering
Arizona State University
Tempe, Arizona 85287

Major R.F. Reilman, Jr.
FJSRL/NH
USAF Academy
Colorado Springs, Colorado 80840-6528

Dr. Reischman
Code 1131 F
Office of Naval Research
800 N. Quincey Street
Arlington, Virginia 22217

vi

Dr. G.A. Reynolds
Advanced Research Organization
Lockheed-Georgia
Dept 72-11, Zone 43
Marietta, Georgia 30063

Dr. W.C. Reynolds
Department of Mechanical Engineering
Stanford University
Stanford, California 94305

Dr. K. Richey
AFWAL/CA
Wright-Patterson AFB, Ohio 45433-6553

Dr. E. Rignot
Department of Mechanical Engineering
University of Southern California
University Park
Los Angeles, California 90089-1191

Dr. Roberts
Department of Aeronautics and
    Astronautics
Stanford University
Stanford, California 94305

Dr. M.C. Robinson
Department of Aerospace Engineering
    Sciences
Box 429
Boulder, Colorado 80309

Dr. D.O. Rockwell
Mechanical Engineering and Mechanics
Lehigh University
Bethlehem, Pennsylvania 18015

Dr. A. Roshko
Aeronautics and Applied Physics
California Institute of Technology
Pasadena, California 91125

Dr. W. Saric
Department of Mechanical Engineering
Arizona State University
Tempe, Arizona 85287

Dr. J. Shang
AFWAL/FIMM
Wright-Patterson AFB, Ohio 45433-6553

Dr. Q.Y. Sheen
Aerospace Engineering Sciences, Box 429
University of Colorado
Boulder, Colorado 80309

Dr. S.F. Shen
Sibley School of Mechanical
    Engineering
Cornell University
Ithaca, New York 14853

Dr. F. Sherman
Department of Mechanical Engineering
University of California
Berkeley, California 94720

Dr. C. Shih
Department of Aerospace Engineering
University of Southern California
Los Angeles, California 90089-1191

Dr. R.L. Simpson
Aerospace and Ocean Engineering
Virginia Polytechnic Institute
    and State University
Blacksburg, Virginia 24061

Colonel M. Smith
Department of Aeronautics
USAF Academy
Colorado Springs, Colorado 80840

Dr. G. Spedding
OHE 430
Department of Aerospace Engineering
University of Southern California
Los Angeles, California 90089-1191

Dr. K.R. Sreenivasan
Department of Mechanical Engineering
Yale University
New Haven, Connecticut 06520

Captain E. Stephen
FJSRL/NHM
USAF Academy
Colorado Springs, Colorado 80840-6528

Dr. D. Telionis
Department of Engineering Science
    and Mech
Virginia Polytechnic Institute and
    State University
Blacksburg, Virginia 24061

Dr. Murray Tobak
NASA Ames Research Center
Mail Stop 227-3
Moffett Field, California   94035

Dr. M. Visbal
AFWAL/FIMM
Wright-Patterson AFB, Ohio   45433-6553

Major J. Walker
FJSRL/NHM
USAF Academy
Colorado Springs, Colorado   80840-6528

Dr. D. Williams
Department of Aerospace Engineering
Illinois Institute of Technology
Chicago, Illinois   60616

Dr. C.H.K. Williamson
Aeronautics and Applied Physics
California Institute of Technology
Pasadena, California   91125

Dr. J. Wilson
AFOSR/NA
Bolling AFB   DC   20332-6448

Captain J. Wissler
Department of Aeronautics
USAF Academy
Colorado Springs, Colorado   80840

Dr. N. Wood
Department of Mechanical Engineering
Stanford University
Stanford, California   94305

Dr. J.C. Wu
School of Aerospace Engineering
Georgia Institute of technology
Atlanta, Georgia   30332

Dr. Wygnanski
Department of Aerospace and
    Mechanical Engineering
College of Engineering and Mines
University of Arizona
Tucson, Arizona   85721

TABLE OF CONTENTS

MEASUREMENT OF DYNAMIC NON-LINEAR AIRLOADS AT NAE

E.S. Hanff

Unsteady Aerodynamics Laboratory
National Aeronautical Establishment
National Research Council of Canada
Ottawa, Ont.

Abstract

A joint NAE/USAF/DND program has recently been put in place as one of the components of a broad-based USAF supported study of aerodynamics at high incidence with a focus on supermaneuvers. The progr .m is a continuation of NAE's in-house work aimed at developing both a representation of highly non-linear dynamic airloads, as well as a wind-tunnel technique for the measurement of the necessary aerodynamic data.

Some of the background material is briefly reviewed, followed by a description of work in progress under the program. Emphasis is placed on the large-amplitude, high-rate oscillatory roll rig and model that will be used to validate both the technique and the representation. A brief overview of the planned wind-tunnel test program is also presented.

1. Introduction

The maneuverability and agility requirements expected from next generation of aircraft involve flight under extreme conditions, where separated and unsteady flows prevail. Under these conditions the global loads acting on the aircraft can exhibit severe non-linearities which cannot, in general, be adequately represented by a locally linearized aerodynamic model of the type embodied in the stability derivatives representation.

During the last 3-4 years, work has been conducted at NAE to find an effective way to handle aerodynamic non-linearities, thus overcoming the limitations inherent in the above model. The work has two main thrusts, namely, the development of a representation of aerodynamic loads that does not rely on any assumption of linearity and is, therefore, applicable to the flight regime under consideraton, as well as the development of a wind-tunnel technique that generates the data required for the proper utilization of the representation. These two aspects have been described in some detail before (Refs. 1 to 4) and are, therefore, only briefly summarized here for convenience.

The main purpose of this paper is to describe the recent work that has been carried out in this field at NAE as part of an NAE/USAF/DND joint research program instituted to accelerate the progress of the in-house work, while focusing on the aerodynamics associated with supermaneuvers. The program was initiated in early 1987 and is mainly aimed at validating the new representation as a tool for flight mechanics simulations and as a means to attain a better insight of the phenomenology underlying aerodynamic non-linearities. Another important goal of the program is the determination of the approximate domains where the use of the general non-linear representation is mandatory and those where the locally linearized model is adequate for flight mechanics applications.

The wind-tunnel technique as well as the aerodynamic representation will first be implemented for the case of a delta wing model oscillating in roll, for which the necessary hardware, a large-amplitude high-rate oscillatory roll rig and a suitable model, are currently under development.

2. Aerodynamic data representation

The representation is based on the knowledge of the instantaneous values of the airloads acting on a flight vehicle in terms of the corresponding instantaneous values of the pertinent motion variables. This, of course, implies the existence of a well defined (although not necessarily single-valued) relationship between a given aerodynamic reaction and the motion variables, which, in a topological sense, corresponds to an $n+1$ dimensional "reaction hypersurface" that defines the airload in terms of n motion variables. The motion of the aircraft (or model) would, in this case, be described by a trajectory in the n-dimensional phase space of the motion variables. Clearly such an approach does not rely on any assumption of aerodynamic linearity and is, therefore, suitable for the representation of airloads in the non-linear regime.

The assumed existence of a well defined relationship between the airloads and the motion variables implies that the loads - for a given set of values of the motion variables - are independent of the past history of the motion. This is not necessarily so, in fact motion history effects are known to exist under some of the flow conditions of interest (e.g. dynamic lift), in which case these effects are reflected by a "thickening" or "smearing" of the reaction hypersurface, that then would not uniquely define the reaction in terms of the motion parameters. The hypersurface "thickness" naturaly depends on the severity of the motion history effects and can, in principle, be reduced by resolving the motion into more time derivatives of the motion variables. As indicated in Ref. 1, there is a practical limit to this approach, which leads to the conclusion that the proposed representation, in its current form, can only account for "immediate" past history effects. This will likely, however, prove to be adequate for a large number of practical cases where the "long" past history effects are not

overriding. In any case, as indicated in the above reference, the hypersurface representation can deal with aerodynamic non-linearities much more effectively than the linearized force model and constitutes, therefore, a significant contribution to our ability to conduct simulations in the non-linear regime .

As an illustration of the reaction hypersurface concept, an example of a 3-D hypothetical reaction surface corresponding to a single degree-of-freedom motion in roll is shown in Fig. 1. Here the reaction, the rolling moment coefficient, is a function of only two motion variables (ϕ and p), in which case the motion in one degree-of-freedom of the aircraft is described by a trajectory in the ϕ-p phase plane. This surface is representative of a "static" hysteretical process, i.e. one where the values of the threshold levels are independent of the roll rate. Fig. 2 depicts a situation where the threshold values increase with rate, thus representing a "dynamic" hysteretical phenomenon affected by convecting time lags. Both reaction surfaces allow for the transition between the two states if the direction of the motion is reversed (minor loops). The case of a hysteretical relationship which does not exhibit minor loops is given in Ref. 1.

3. Simulations

Probably the most important application of the proposed representation is in flight mechanics simulations. Contrary to the case of the locally linearized aerodynamic model, which invokes various assumptions on the relationship between the reactions and motion variables (Ref. 1), this representation makes it possible to directly utilize the instantaneous value of the reactions (including non-linearities) as the aerodynamic forcing functions at each point of the simulation solution. An example of such a simulation was carried out utilizing the hysteretical relationship shown in Fig.1, which for the single degree-of-freedom under consideration merely involves solving

$$\ddot{\phi} = (q\,S\,b\,/\,I_{xx})\,C_l$$

where arbitrary values for the dynamic pressure q, reference area S, span b and rolling moment of inertia I_{xx} were assumed.

2

The simulation was started near the origin and resulted in a diverging oscillation that reached a limit cycle as shown by the trajectory of the "load point" on the reaction surface in Fig. 3. Another view of the trajectory of the load point on the reaction surface, namely from the p axis (Fig. 4), reveals the energy exchange during the first four cycles of the oscillation, that leads to the establishment of equilibrium at the limit cycle amplitude. The corresponding history of the rolling motion is depicted in Fig. 5. As can be expected, the limit cycle oscillation has an amplitude corresponding to that where the damping derivative C_{lp} would be measured as zero (see Ref. 1 for the definition of derivatives in this representation).

4. Wind-tunnel technique

The purpose of the technique is to establish a data base that defines the instantaneous value of the aerodynamic reactions in terms of the corresponding instantaneous values of the pertinent motion variables. This is accomplished by imparting a well defined periodic motion to the model and measuring the outputs of the balance (details on the technique can be found in Ref. 2). Although typically a sinusoidal motion in one degree-of-freedom (primary DOF) is used, the technique is quite general, permitting the application of arbitrary waveforms in several degrees-of-freedom simultaneously. In the presence of aerodynamic non-linearities, the airloads caused by the model motion contain a number of frequencies harmonically related to the fundamental frequency of the primary motion. Since it is generally desirable to cover a realistic range of motion variables, including rates, the experiments have to be carried out at oscillation frequencies that preclude the direct conversion of balance outputs (deflections) into their causative loads, as this would ignore the significant effects of the model-balance subsystem dynamic response. Instead, the output signals are processed in the frequency domain where they are transformed into their causative loads by means of suitable mechanical transfer functions. This presumes, of course, that the transfer functions are linear, a reasonable assumption if proper care is exercised in the design and construction of the wind-tunnel apparatus.

Inertial effects are subtracted by means of tares and the desired relationship between the reactions and the motion variables are obtained by taking the inverse Fourier Transform of the spectra of these quantities. Even though a large number of harmonics may be required to accurately describe a strong aerodynamic non-linearity, a practical limit is imposed on the number of meaningful harmonics by the model aeroelastic effects, sting vibration modes, etc. This frequency truncation results in a smoothing out of discontinuities and of sharp changes in the measured airloads as well as in the corresponding reaction hypersurfaces. Although this may somewhat complicate the interpretation of the results, as it tends to mask the aerodynamic phenomena leading to the discontinuities, its effect on flight mechanical applications is minimal by virtue of the inherent inertia-caused filtering characteristics of an aircraft

5. High-amplitude roll rig

The technique will be implemented first in conjunction with a large-amplitude high-rate roll rig for the study of non-linearities acting on a 65° delta wing model described below. Inasmuch as one of the most important aspects to be investigated is that of wing rock, the amplitudes and reduced frequencies used in the tests must cover the values expected in real situations. A rig meeting these requirements has been designed and is currently being manufactured. It is inteded to oscillate with an amplitude of up to ±40 ° and a maximum frequency of 20 Hz. Its normal force capability of 2000 lb should allow the testing of the model up to an angle of attack of 70° under maximum dynamic pressure conditions in the AFWAL SARL wind tunnel, where a comprehensive series of tests is planned.

A general assembly of the rig is shown in Fig. 6. The model is mounted on a 5 component balance (no axial force) by means of a tapered polygon capable of transmitting the alternating 3000 in lb needed to overcome the aerodynamic and inertial loads, without backlash. The balance is supported inside the sting by means of suitable bearings. Given the need for very high structural frequencies for the

3

model-balance subsystem, the balance is designed to be very rigid, necessitating the use of semiconductor strain gauges in order to obtain adequate sensitivity. Inertial considerations dictate that a carbon composite driveshaft be used to transfer the torque from the hydraulic rotary actuator, located at the aft end of the rig, to the balance. The angular position of the shaft is measured with an optical encoder mounted on the back of the actuator and is used by a servo-system to control the motion of the model. An arbitrary motion, only limited by the hydraulic system capabilities, can be applied to the model in order to obtain a suitable coverage of the motion variables. As shown in Ref. 2, such arbitrary waveforms are treated by the wind-tunnel technique in the same fashion as pure harmonic motions. Provision is also made to introduce a roll offset angle of up to ±50° about which the oscillation takes place.

In order to extract the balance signals in the presence of the large angular deflections under consideration, the balance leads are carried through a small steel tube between the balance and the aft end of the rig. The tube is anchored at both ends so that the twisting of the leads is distributed over its entire length, and was designed to be capable of withstanding the alternating torsion without fatiguing.

The hydraulic system is fed by a constant-pressure 50 HP power pack that incorporates an elaborate filtering arrangement required to maintain the fluid contamination at a level compatible with the proper operation of the high-speed servo-valve. Suitable safety features are, of course, also incorporated in the servo-system and power pack.

6. 65° sweep delta wing model

The first tests will be carried out on a 2 ft span 65° sweep delta wing model shown in schematic form in Fig. 7. Given the considerable aerodynamic loads that prevail during testing as well as the high angular accelerations that are required to cover a realistic range of the motion variables, the model must be strong and yet very light. Moreover, the model must exhibit high stiffness to raise its structural resonance frequencies and thereby minimize aeroelastic effects. These considerations

dictated the use of a foam-core carbon-composite construction method which, based on preliminary calculations will have adequate strength, stiffness and moment of inertia ($I_{xx} < 0.15$ lb in sec^2). The model is currently in the detailed design phase and, if the original specifications can be met, it will be possible to carry out oscillatory tests with reduced frequencies of up to 0.15 at M=0.6 which, for an oscillation amplitude of ±40°, corresponds to reduced rates in excess of 0.1. Higher reduced frequencies and rates can, of course, be achieved at lower speeds.

7. Wind-tunnel testing

Two test series are currently envisaged. The first one, which will also serve as a shakedown for the overall system, will be carried out at the NAE 6x9 ft. wind tunnel, covering an angle of attack of up to 50° and Mach number of up to 0.3. The second series will be conducted at the AFWAL SARL 7x10 ft. wind tunnel where the angle of attack and Mach number can be increased to 70° and 0.6 respectively. Both series of tests are expected to include extensive forced oscillation tests that will cover the appropriate range of the $\phi, \dot{\phi}$ and $\ddot{\phi}$ motion variables with sufficient redundancy, i.e. using different motions, to permit an evaluation of the importance of the motion history effects. In addition to the forced oscillation tests, a series of free-to-roll experiments will be carried out in order to compare the actual motions with those predicted on the basis of the measured reaction hypersurfaces. It should be pointed out that this comparison helps to "close the loop" in the validation of the non-linear representation as a flight mechanics tool, which, as mentioned before, is one of the goals of the program.

The above tests will be complemented with flow visualization and upper wing surface unsteady pressure measurements, both done while the model is oscillating, to permit their correlation with the measured instantaneous global loads. Such a correlation should facilitate the understanding of the fluid mechanics underlying the global loads.

4

8. References

Hanff E.S. "Dynamic Non-linear Airloads -
Representation and Measurement", AGARD
CP-386, 1985.

Hanff E.S. "Determination of Non-Linear
Loads on Oscillating Models in Wind
Tunnels", ICIASF, 1983.

Hanff E.S. "Non-Linear Representation of
Aerodynamics of Wing Rock of Slender Delta
Wings", AIAA-85-1931.

Hanff E.S. "Instrumentation and Other
Issues in Non-Linear Dynamic Testing in
Wind Tunnels", ICIASF, 1985.
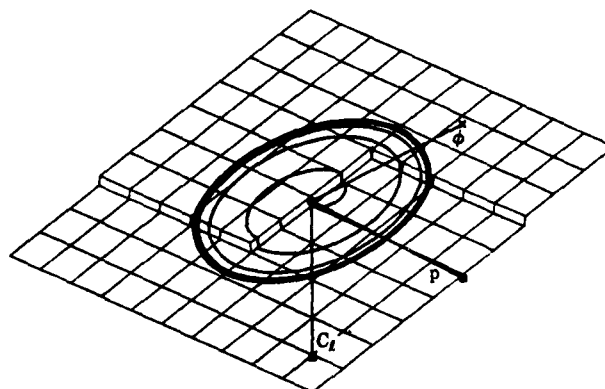
Fig.3 Simulation trajectory of "load point"

9. Figures
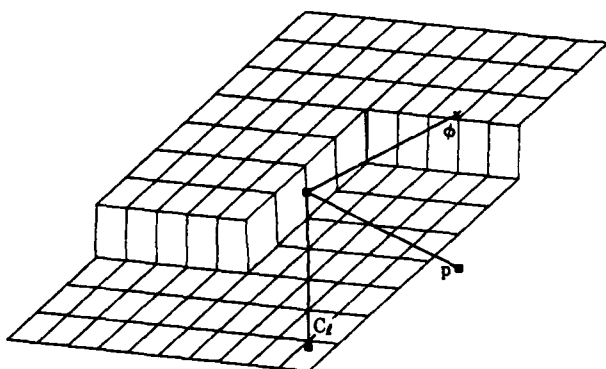
Fig.1 "Static" hysteretical reaction surface

Fig.2 "Dynamic" hysteretical reaction
surface

First cycle ϕ

C_ℓ

Second cycle ϕ

C_ℓ

Third cycle ϕ

C_ℓ

Fourth cycle ϕ

C_ℓ
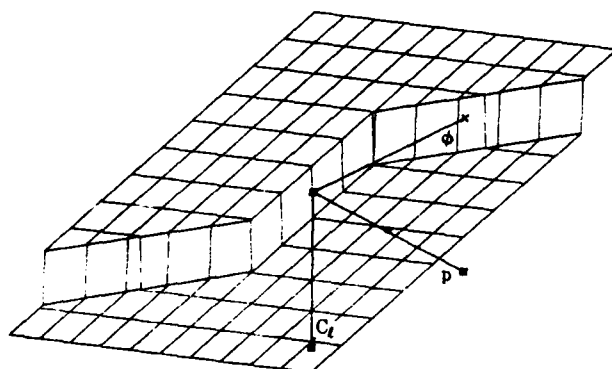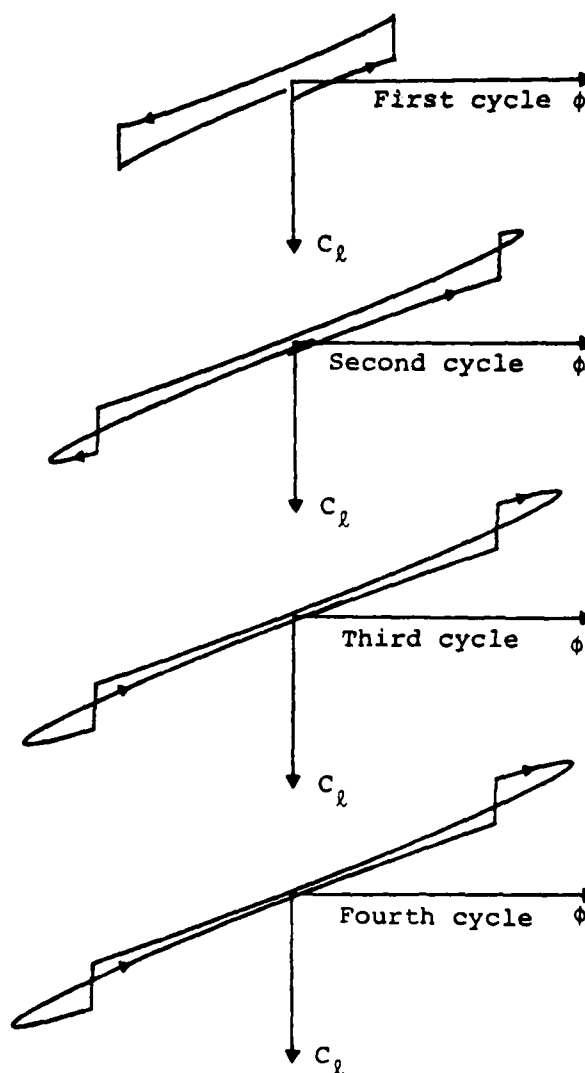
Fig.4 Energy exchange during simulation

5
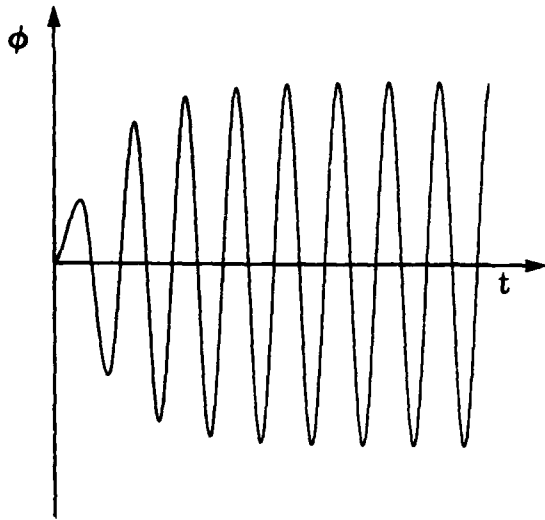
Fig.5 Simulation motion history
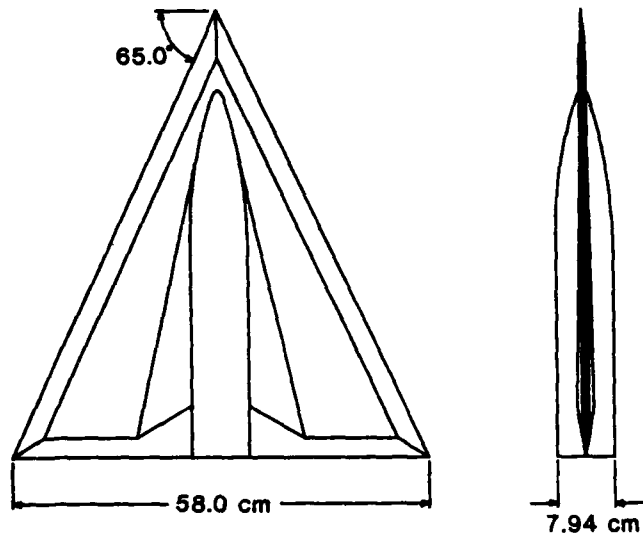
Fig.7 65° sweep delta wing model

65.0°

58.0 cm

7.94 cm
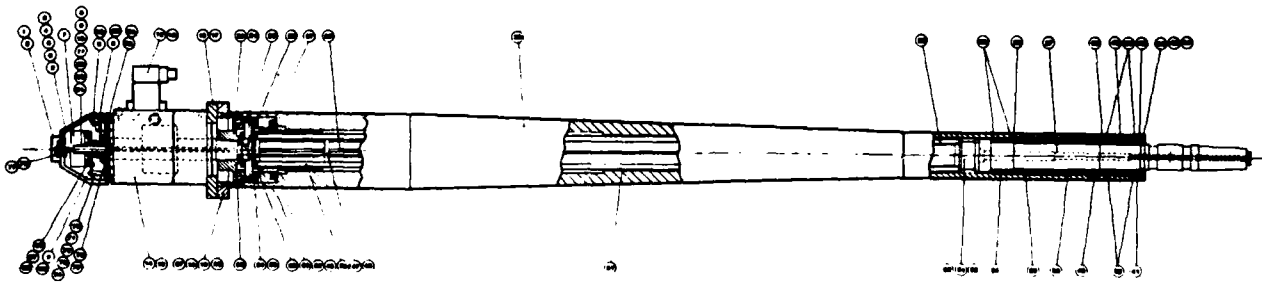
Fig.6 Large-amplitude high-rate roll rig

BIFURCATIONS IN UNSTEADY AERODYNAMICS--IMPLICATIONS FOR TESTING

Gary T. Chapman and Murray Tobak

NASA Ames Research Center
Moffett Field, CA 94035

SUMMARY

The various forms of bifurcations that can occur between steady and unsteady aerodynamic flows are reviewed. Examples are provided to illustrate the various ways in which bifurcations may intervene to influence the outcome of dynamics tests involving unsteady aerodynamics. The presence of bifurcation phenomena in such tests must be taken into consideration to ensure the proper interpretation of results, and some recommendations are made to that end.

INTRODUCTION

An understanding of unsteady aerodynamics is becoming increasingly important in the design of highly maneuverable aircraft. At present, however, unsteady aerodynamic flows are poorly understood, particularly when extensive changes (bifurcations) occur in the flow field. To develop an understanding of unsteady aerodynamics, it is important, first, to understand the various types of aerodynamics that can occur under conditions where the boundary conditions are steady as well as the types of bifurcations that can occur as the parameters representative of the steady boundary conditions, such as angle of attack, are changed. Second, the interaction of the bifurcations in the flow field with unsteady boundary conditions needs to be understood.

The present paper contains a review of the various types of aerodynamics that occur under steady-state boundary conditions and the various types of bifurcations that can occur under these conditions. Next, the roles that these bifurcations can play when the boundary conditions are unsteady are described. Then examples illustrating the impact of bifurcations on testing are introduced. Examples include cases of both forced and free oscillatory motions. Finally, some recommendations are made to assist the consideration of bifurcation phenomena in experiments involving unsteady aerodynamics.

AERODYNAMICS AND BIFURCATIONS WITH STEADY BOUNDARY CONDITIONS

Aerodynamics

Aerodynamic flows with steady boundary conditions can be categorized into five general types. They are: (1) steady-state single-valued, (2) steady-state multi-valued, (3) unsteady periodic, (4) unsteady quasi-periodic, and (5) chaotic. Figure 1(a) shows an example of the first type in which the response in lift coefficient C_L is steady (i.e., time-invariant) and a single-valued function of angle of attack α. An example of the second type is shown in figure 1(b). For a steady-state multi-valued response, there is a range of α within which the aerodynamic response, e.g., the lift coefficient C_L, can have two or more values for the same value of α. This is commonly referred to as static hysteresis. There are at least three different types of aerodynamic flows that are unsteady (i.e., time-varying) even though the boundary conditions are steady. The first of these is periodic unsteadiness. A common example is the periodic shedding of vortices in the wake behind a circular cylinder in cross flow. Vortex-shedding gives rise to a periodic variation of lift and a periodic component of drag. Another example of a periodic aerodynamic flow is illustrated in figure 1(c), showing the lift coefficient for an airfoil. At low α the lift coefficient is steady and is a single-valued function of α. Above some critical value of α, the flow separates from the upper surface of the airfoil. Depending on the Reynolds number, separation can give rise to a periodic lift about some nonzero mean value, as is indicated schematically in figure 1(c). Periodic flows normally first occur with a single frequency. However, in more complex situations, additional frequencies can occur, and if the additional frequencies are integer multiples of each other, we have what are referred to as multiply-periodic flows. On the other hand, flows in which the ratio of frequencies is nonintegral or irrational are referred to as quasi-periodic, because any finite sample of the time series of a coefficient will not contain any periodicity. However, a Fourier analysis or power spectrum will show the relevant frequencies. This case is not illustrated in figure 1.

The final case is that of chaos. Here, the flow or the aerodynamic response is aperiodic and its power spectrum will be very broad. The power spectrum may contain a peak at a frequency of a periodic state but the peak will be very broad and will not drop off to the background noise level indicative of experimental noise. The chaotic type of aerodynamic flow is illustrated in figure 1(d). Here again is shown the lift coefficient versus angle of attack for an airfoil. Again at low values of α, the lift is steady-state and single-valued. Separation will occur above a critical value of α, and, for a certain range of Reynolds numbers, the flow structure and hence the lift will be chaotic. According to the theory of nonlinear dynamical systems, the presence of what is called a strange attractor would be suggested by this type of flow. A more thorough description of chaotic flow properties and strange attractors is given in reference 1.

Bifurcations

In the above discussion, changes in flow have been described and illustrated in figure 1. These changes are often referred to as bifurcations. We have discussed the role of bifurcations in aerodynamics previously in references 1-4. The theoretical basis for our studies can be found in summary form in references 5-8. The following is a brief review.

Bifurcations can occur between any of the states illustrated in figure 1. In addition bifurcations can occur in two ways and hysteresis can occur in still another way. The two types of bifurcation are subcritical and supercritical. These are illustrated in figure 2. In the supercritical case (fig. 2(a)) a perturbation (labeled C) in a coefficient is zero until a critical value of a parameter representative of the steady boundary conditions, here α, is reached. At this point, solutions split into three branches. One branch remains the original solution (i.e., C = 0), but it is unstable and will not occur in practice. The other two branches, shown as symmetric around C = 0, represent stable perturbation solutions that depart from zero. The important point here is that departure from zero is continuous. That is, for a small change in the representative parameter (here, α) beyond the critical value, there is a corresponding small change in the perturbation solution.

In the case of subcritical bifurcation (fig. 2(b)), there is again a branching of solutions as the critical value of the parameter is crossed, but in this case all three solution branches are unstable at the critical point. However, the nonzero initially-unstable branches are multivalued, and they become stable beyond the turning points. As a result, after crossing the critical value of α, the flow field jumps to a new stable configuration, and hence there is a finite change in the perturbation solution for an infinitesimal change in α. This behavior is a source of static hysteresis. With further increases in α beyond the critical value, the perturbation solution continues to move along the stable branch. However, when α diminishes, the perturbation solution remains on the upper branch and returns to the lower branch only after α has diminished sufficiently below its critical value to pass below the value where the upper branch has a turning point.

There is another condition that leads to static hysteresis, namely, the fold. Note that in figures 2(a) and 2(b) both the subcritical and supercritical bifurcations have two branches beyond the critical value of α, reflecting a symmetry in the boundary conditions. Under these conditions, if we fix α at a value above the critical value and change another variable, e.g., the roll angle ϕ, the corresponding response (here the rolling-moment coefficient C_ℓ) will have the form shown in figure 2(c). Hence static hysteresis in the rolling-moment response will be present if the range of the roll-angle variation includes the turning points of the response.

Importance of Bifurcations

The importance of bifurcations for changes in parameters such as the angle of attack is intuitively obvious. It is possible to make this intuition more mathematically precise by illustrating that bifurcation leads to a loss of Fréchet differentiability. Our use of indicial responses allows us to see this by inspection of figure 3. The top left part of this figure shows a plot of the angle of attack as a function of time ξ. At time τ and thereafter, the angle of attack is fixed at a constant value. In the bottom left part is shown the lift coefficient that results from this motion. The top right part of figure 3 again shows an angle-of-attack history. The history prior to time τ is the same as before, but now after time τ, the constant value of the angle of attack is increased by a small amount $\Delta\alpha$. The history of the lift response to this motion is shown at the bottom right of the figure. Now consider the ratio of the increment in lift to the increment in the angle of attack as the measuring time t goes to infinity for two cases. In the first case there is no bifurcation of the equilibrium flow at the given fixed value of $\alpha(\tau)$. In the second case a bifurcation occurs at $\alpha(\tau)$. In the first case we obtain the following relation.

$$\lim_{\Delta\alpha \to 0} \frac{\Delta C_L(t)}{\Delta\alpha} \text{ exists at } t \to \infty$$

The limit in this case exists and is what is referred to as a Fréchet derivative. When a bifurcation occurs at $\alpha(\tau)$, the limit does not exist. This is easy to understand for subcritical bifurcation and for a fold, because in these cases the increment in C_L will be finite for an infinitesimal change in the angle of attack. For supercritical bifurcation, the loss of Fréchet differentiability is not as easy to see. Here we could have a bifurcation from a steady state to a periodic condition. In this case the equilibrium lift changes from a constant value to a mean value plus a time-periodic term. Then the limit may exist but it will be periodic with time, indicating that the form of the solution has to change.

BIFURCATIONS AND UNSTEADY BOUNDARY CONDITIONS

The role of bifurcations in cases where the boundary conditions are unsteady becomes exceedingly diverse and complex. We shall explore this role through examples of two distinct classes of flows having forced and free boundary conditions. In particular, the classes will be represented by examples taken from experiments involving forced and free oscillations.

Forced Oscillations

To fully understand the role of forced unsteady boundary conditions we must examine examples from forced oscillations under two sets of conditions: first, when

the oscillations occur in domains where no bifurcations exist under steady-state boundary conditions; second, when the oscillations occur over a domain within which a bifurcation exists under steady-state boundary conditions. In both of these cases, we will be concerned with low and high reduced frequency.

Forced oscillations in domains without bifurcations are examined for two reasons: first, to establish the traditional background of unsteady aerodynamics; second, to introduce the idea of bifurcations that are induced by the forced-oscillation boundary condition. The first case to be examined is an oscillation at low reduced frequency in a domain where the aerodynamic response to steady boundary conditions is steady and single-valued. This is the traditional case most often encountered in experiments involving unsteady aerodynamics. In this case the effect of the forced oscillation is to introduce a phase shift in the aerodynamic response. The out-of-phase term is the traditional damping term (e.g., $C_{m_q} + C_{m_{\dot{\alpha}}}$). Recent examples of this type of testing can be found in reference 9. For high reduced frequencies, it is possible for the oscillation itself to cause a bifurcation. This topic is being studied in depth for lower-order dynamical systems (e.g., ref. 10). An example in aerodynamics would be an airfoil undergoing pitching oscillations in which the peak angle of attack is just below the angle of attack where separation occurs. Here it is easy to see that if the frequency is high enough, the flow could be forced to separate on the downstroke.

If forced oscillations are performed in a domain where there are no bifurcations but the base flow is periodic, the aerodynamic behavior is analogous to that where the base flow is steady. Here again, for low reduced frequencies there is a phase shift (here, low is relative to the frequency of the periodic base flow). For high reduced frequencies near that of the base flow, the forcing can introduce a bifurcation. In this case, since the base flow is already periodic, the bifurcation will be either to a quasi-periodic or to a chaotic flow. These conditions have been well studied for lower-order dynamical systems (e.g., ref. 10).

The first case to be considered where oscillations occur in a domain that contains a bifurcation involves static hysteresis. The origin of the hysteresis could be either a subcritical bifurcation or a fold. If the oscillation has a low reduced frequency, the effect on the flow again is to cause a phase shift and hence the appearance of a classic damping term. However, care must be exercised in testing to ensure that the hysteresis loop is correctly taken into consideration. The usual method of determining the damping term is to measure the power required to drive the oscillation, in which case the hysteresis will contribute a fictitious damping. The form of this result can be illustrated by considering an example from the open literature (ref. 11). Here roll damping was measured for the forced rolling oscillation of a fighter-type model in a wind-tunnel test. The measured effective damping coefficient is shown plotted in figure 4(a) as a function of the amplitude of the oscillation for several reduced frequencies. Note that there is a very strong effect of the reduced frequency, particularly at the lower values. This is a very good indication that a static hysteresis loop may have been present. These data were reassessed by Schiff and Tobak (ref. 12). They found that if the results were analyzed under the assumption that static hysteresis was present, the results

could be plotted as shown in figure 4(b). When plotted in this manner, the results for the different amplitudes should fall on straight lines that intercept the zero reduced-frequency line at the same point. This intercept point is related to the area of the static hysteresis loop. With the exception of one data point, these data appear to be consistent with existence of the assumed hysteresis loop. Unfortunately, no static aerodynamic data were taken during this experiment which might have confirmed the presence of hysteresis. This omission shows the importance of taking data with steady boundary conditions over the entire domain where forced oscillation testing is to be carried out, and in such a way as to cover all of the possibilities for the existence of hysteresis.

The last forced oscillation case to be considered is that of oscillating over a domain in which there is a bifurcation from a steady state to a periodic state. This is the case in experiments involving dynamic stall. Here, the effect of the oscillation is extreme. Results from a typical set of tests are shown in figure 5 (ref. 13). We see that results even at low reduced frequencies are unexpected. At a low reduced frequency, k, we expect that oscillation might result in a loop surrounding the static data. We see, however, that even at the low reduced frequency of k = 0.004, the lift on the stroke with increasing angle of attack nearly matches the static results, whereas on the stroke with decreasing angle of attack, the lift is much less than static results. These results indicate that the separation which occurs at an angle of attack of 12° has an even more pronounced effect on the downstroke than it does on the static results. The same effect is further indicated at the high reduced frequency of k = 0.25. Here we see that the flow remains essentially attached on the upstroke, reflected by the resemblance of the variation of lift coefficient on the upstroke to that for an unstalled airfoil. Further evidence is provided by the water-tunnel flow visualization shown in figure 5 (ref. 14). Essentially-attached flow is observed on the upstroke, whereas on the downstroke, enhancement of the separation is indicated by both the much lower lift and the extensive region of separated flow shown by the flow visualization. Further discussion of the role of bifurcations in dynamic stall can be found in reference 2.

Free Oscillations

An additional factor must be considered in this case, which is that the body itself is a dynamical system that the aerodynamic system is now forcing and vice versa. If the free oscillations occur in a domain where the aerodynamic response is steady and no bifurcations are induced, there is nothing much of interest that can happen. If the entire system is statically and dynamically stable, a perturbed motion will simply decay to zero.

If the aerodynamic response for the stationary body is periodic, then the possibilities are many. If, for example, the body is supported in a spring-mounted system, the natural frequency of which is less than the frequency of the aerodynamic response, the motion of the body may be quasi-periodic or even chaotic. This in fact is the case for a spring-mounted circular cylinder in crossflow and also the case for a free-to-roll model in a wind-tunnel test.

The case of the circular cylinder in crossflow is well illustrated by the results of Van Atta and Gharib (ref. 15) (an example is shown in fig. 6). The left portion of this figure shows measurements of the velocity in the wake and the motion of the wire (the circular cylinder in this case) for the case of a well-damped motion. Both the time series and the power spectra are shown. For this well-damped case, the wake velocity shows a very pronounced frequency at the Strouhal frequency. However, the wire motion is nearly nonexistent (lower-left-portion plots). The power spectrum is flat and at a level commensurate with experimental noise. The right portion of figure 6 shows the results for the same conditions except that there is no damping. Here the power spectrum for the motion of the wire (lower-right-portion plots) shows a broad peak at a frequency that is near the Strouhal frequency. In addition, and more importantly, the power level is 10 dB higher than the noise level of the experiment (left portion of figure) over a very broad portion of the spectrum. These results show a classic example of chaotic behavior. The peak frequency occurs at the harmonic of the natural frequency of the oscillating wire nearest to the Strouhal frequency. Note that under this condition, the velocity measurements in the wake still show a frequency near the Strouhal frequency but now the signal shows a very broad spectrum. Hence the wake flow may be classified as being even more chaotic than the wire motion itself. This problem is currently under study at NASA Ames. The major thrust of the research is to model the aerodynamics and hence to arrive at a simple predictive model of this type of motion. If successful, this research can lead to a better understanding of the modeling of motions induced by dynamic stall. A simple single-degree-of-freedom motion with a quasi-static modeling of the periodic aerodynamics is described in reference 4. Questions still remain whether modeling at the level of a single degree of freedom can capture the chaotic behavior. A two-degree-of-freedom motion is also under analysis and here it is already clear that chaotic motion occurs with periodic aerodynamics.

Another example of a free oscillation being forced into chaotic-like motion is that of a wind-tunnel model mounted so that it is free to roll. Some results are illustrated in figure 7 (ref. 16), which shows a typical example of the rolling motion. This motion appears to have a well-defined frequency, but the amplitude builds up and decays in bursts. These bursts of motion occur erratically in a manner which is similar to the intermittent bursts of motion that are known to occur in certain simple low-order dynamical systems. The phenomenon is often referred to as intermittent chaos. In this case, the motion is thought to be driven by an oscillatory rolling moment caused by the phasing between oscillatory shock-induced separations on each of the wing panels. The existence of such a periodic aerodynamic driving mechanism creates a dynamic situation in very close analogy to that of the spring-mounted cylinder in crossflow. An appropriate modeling of the aerodynamics for this motion would provide a good candidate for further study of the occurrence of chaotic-like motions in a flight-dynamics setting.

13

CONCLUDING REMARKS

The different types of aerodynamics and bifurcations that can occur under steady-state boundary conditions have been reviewed. Bifurcations were found to involve a loss of Fréchet differentiability. The impact of bifurcations on testing that involves unsteady aerodynamics was reviewed by means of examples of both forced and free oscillatory motions. The following summarizes our main observations.

Body motion can be critical when passing through a bifurcation. Existence of a subcritical bifurcation or a fold can lead to the measurement of a spurious damping if a hysteresis loop is ignored. Body motion combined with bifurcation may cause major changes in the characteristics of the aerodynamics, such as those that occur in dynamic stall. Moreover, bifurcations can lead to changes in the characteristics of the motion itself. We saw that periodic vortex shedding from an elastically-mounted circular cylinder in crossflow may cause the cylinder to undergo a chaotic motion. These observations lead us to the following recommendations concerning the consideration of bifurcation phenomena in experiments involving unsteady aerodynamics. (1) There should be a complete base of testing under static boundary conditions that encompasses all possibilities for the presence of hysteresis. (2) Tests need to be conducted in each domain or type of aerodynamics under consideration and across all bifurcation points. (3) Data analysis must allow for the presence of bifurcations to ensure the proper interpretation of results.

14

REFERENCES

1. Chapman, G. T.; and Tobak, M.: Nonlinear Problems in Flight Dynamics. Proc. Berkeley-Ames Conference on Nonlinear Problems in Control and Fluid Dynamics, Math. Sci. Press, 1985. Also NASA TM-85940, May 1984.

2. Tobak, M.; and Chapman, G. T.: Nonlinear Problems in Flight Dynamics Involving Aerodynamic Bifurcations. AGARD Symposium on Unsteady Aerodynamics-Fundamentals and Applications to Aircraft Dynamics, AGARD CP-386, 1985, pp. 25-1 to 25-15.

3. Tobak, M.; and Ünal, A.: Bifurcations in Unsteady Aerodynamics. NASA TM-88316, June 1986.

4. Tobak, M.; Chapman, G. T.; and Ünal, A.: Modeling Aerodynamic Discontinuities and Onset of Chaos in Flight Dynamical Systems. Ann. Télécommun., tome 42, no. 5-6, mai-juin 1987. Also TM-89420, Dec. 1986.

5. Brooke, Benjamin, T.: Bifurcation Phenomena in Steady Flows of Viscous Fluid. I, Theory. II, Experiments. Proc. Roy. Soc. London, Ser. A, vol. 359, 1978, pp. 1-43.

6. Joseph, D. D.: Stability of Fluid Motions I. Springer-Verlag, New York, 1976.

7. Joseph, D. D.: Hydrodynamic Stability and Bifurcation. Hydrodynamic Instabilities and the Transition to Turbulence: Topics in Applied Physics, Vol. 45. H. L. Swinney and J. P. Gollub, eds., Springer-Verlag, New York, 1981, pp. 27-76.

8. Sattinger, D. H.: Bifurcations and Symmetry Breaking in Applied Mathematics. Bull. (New Series) Amer. Math. Soc., vol. 3, no. 2, 1980, pp. 779-819.

9. Orlik-Rückemann, K., ed.: Unsteady Aerodynamics-Fundamentals and Applications to Aircraft Dynamics. AGARD CP-386, 1985.

10. Guckenheimer, J.; and Holmes, P.: Nonlinear Oscillations, Dynamical Systems, and Bifurcations of Vector Fields. Springer-Verlag, New York, 1983.

11. Grafton, S. B.; and Libbey, C. E.: Dynamic Stability Derivatives of a Twin-Jet Fighter Model at Angles of Attack from 10° to 110°. NASA TN D-6091, Jan. 1971.

12. Schiff, L. B.; and Tobak, M.: Some Applications of Aerodynamic Formulations to Problems in Aircraft Dynamics. AGARD Lecture Series No. 114, Paper 16, March 1978.

13. McAlister, K. W.; Carr, L. W.; and McCroskey, W. J.: Dynamic Stall Experiments on the NACA 0012 Airfoil. NASA TP-1100, Jan. 1978.

14. McAlister, K. W.; and Carr, L. W.: Water-Tunnel Experiments on an Oscillating Airfoil at Re = 21,000. NASA TM-78446, Mar. 1978.

15. Van Atta, C. W.; and Gharib, M.: Ordered and Chaotic Vortex Streets Behind Circular Cylinders at Low Reynolds Numbers. J. Fluid Mechanics, vol. 174, 1987, pp. 113-133.

16. Hwang, C.; and Pi, W. S.: Investigation of Steady and Fluctuating Pressures Associated with the Transonic Buffeting and Wing Rock of a One-Seventh Scale Model of the F-5A Aircraft. NASA CR-3061, 1978.

a) SINGLE VALUED

C_L

α

b) MULTI-VALUED

α

c) PERIODIC

C_L

$f_a = f_{a_0} + A \sin \omega t$

α

HOPF BIFURCATION

d) APERIODIC/CHAOTIC

$f_a = f_{a_0} + f(t)$

α

**ONSET OF A STRANGE
ATTRACTOR**
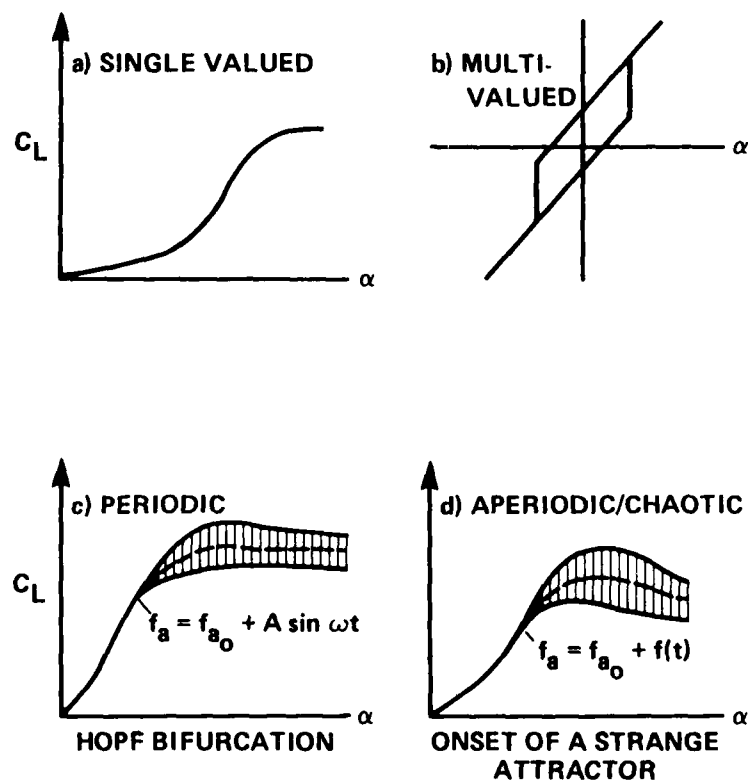
Figure 1.- Types of aerodynamic flows with steady boundary conditions.

a) SUPERCRITICAL   b) SUBCRITICAL

c) FOLD
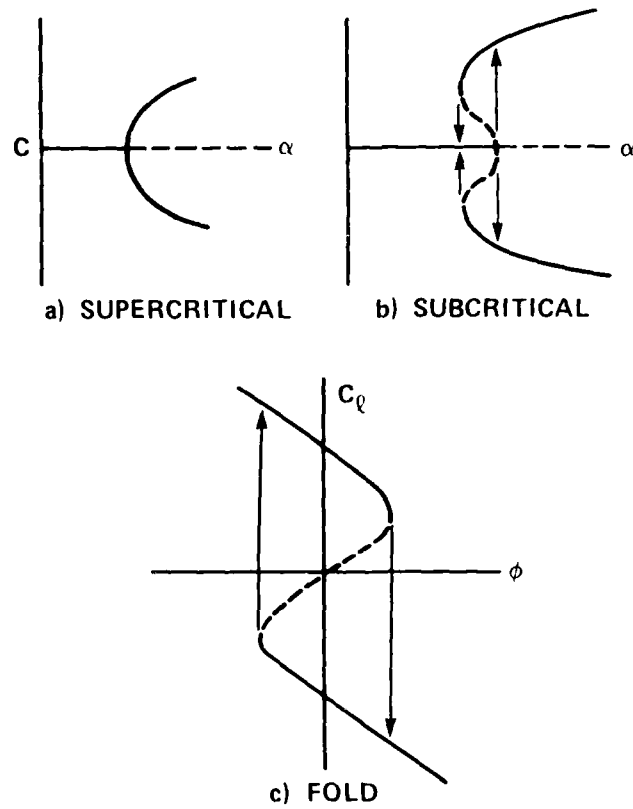
Figure 2.- Bifurcations and fold with steady boundary conditions.

$$\alpha_1(\xi) = \alpha(\xi); \ \xi < \tau$$
$$= \alpha(\tau); \ \xi \geqslant \tau$$

$$\alpha_2(\xi) = \alpha(\xi); \ \xi < \tau$$
$$= \alpha(\tau) + \Delta\alpha; \ \xi \geqslant \tau$$
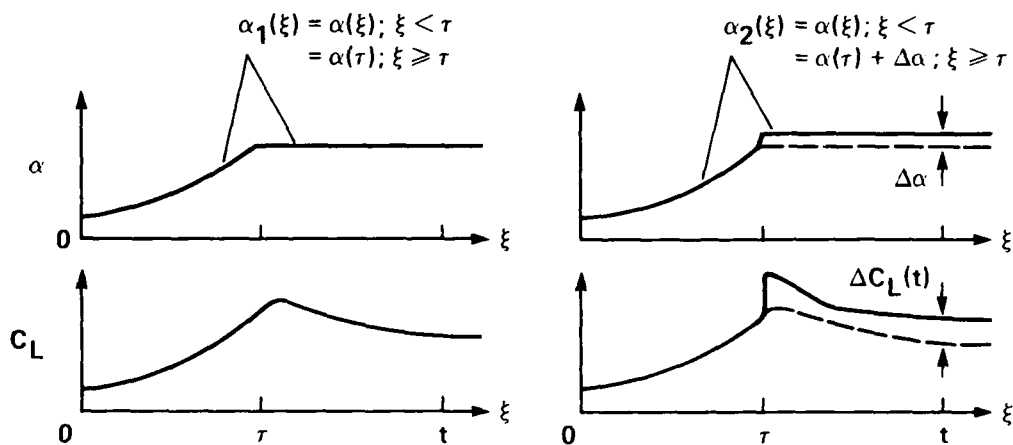
WITHOUT BIFURCATION AT $\alpha(\tau)$

$$\underset{\Delta\alpha \to o}{\text{LIMIT}} \quad \frac{\Delta C_L(t)}{\Delta\alpha} \qquad \textbf{EXISTS AT } t \to \infty$$

WITH BIFURCATION AT $\alpha(\tau)$

$$\underset{\Delta\alpha \to o}{\text{LIMIT}} \quad \frac{\Delta C_L(t)}{\Delta\alpha} \qquad \textbf{DOES NOT EXIST AT } t \to \infty$$

Figure 3.- Importance of bifurcations--indicial response approach.
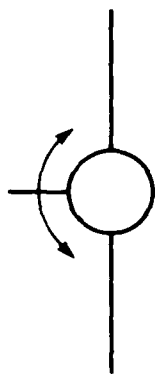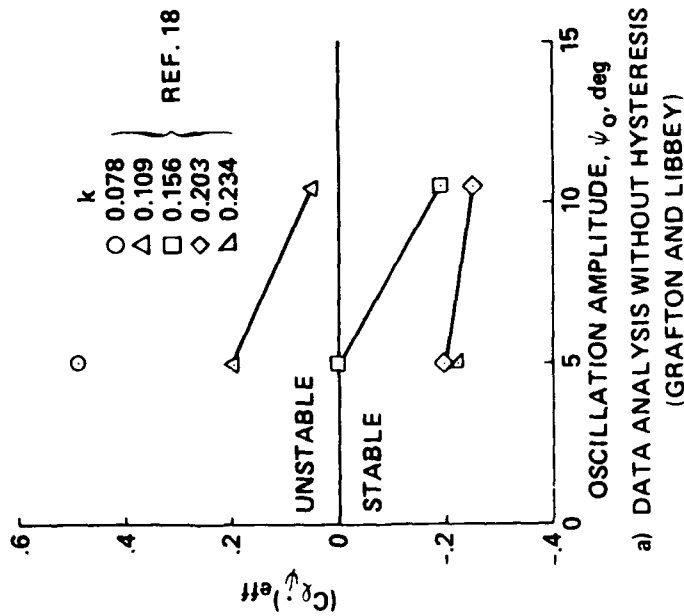
19
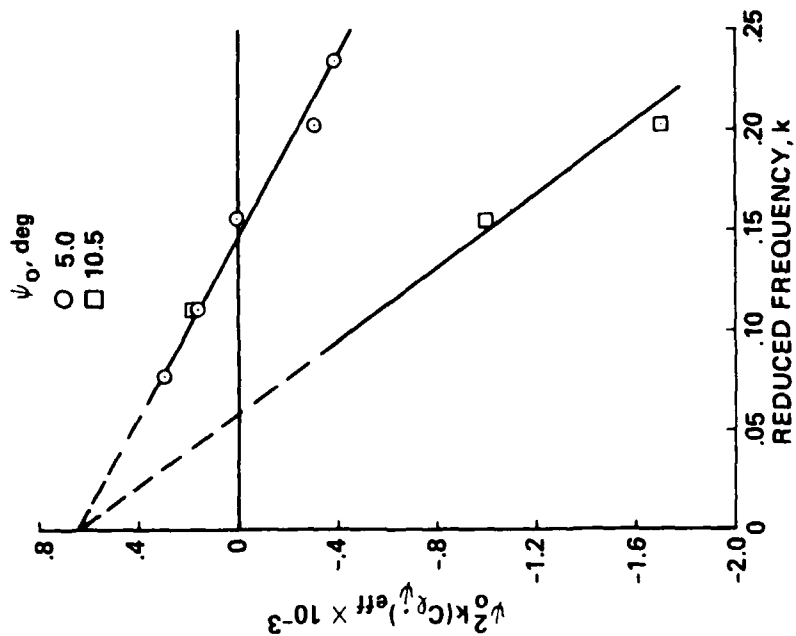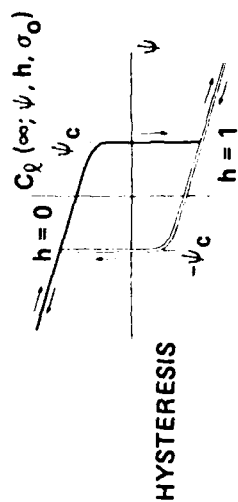
Figure 4.- Forced oscillations in the presence of hysteresis.

$\alpha = 15^\circ, \dot{\alpha} > 0, k = 0.25$

$\alpha = 15^\circ, \dot{\alpha} < 0, k = 0.25$

$\alpha = 10^\circ + 10^\circ \sin \omega t$

a) McALISTER AND CARR
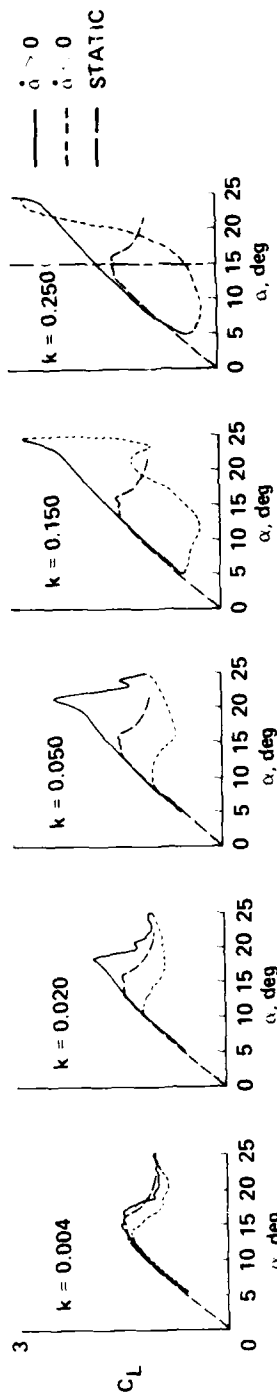
$\alpha = 15^\circ + 10^\circ \sin \omega t$

b) (McALISTER, CARR AND McCROSKEY)

Figure 5.- Dynamic stall.
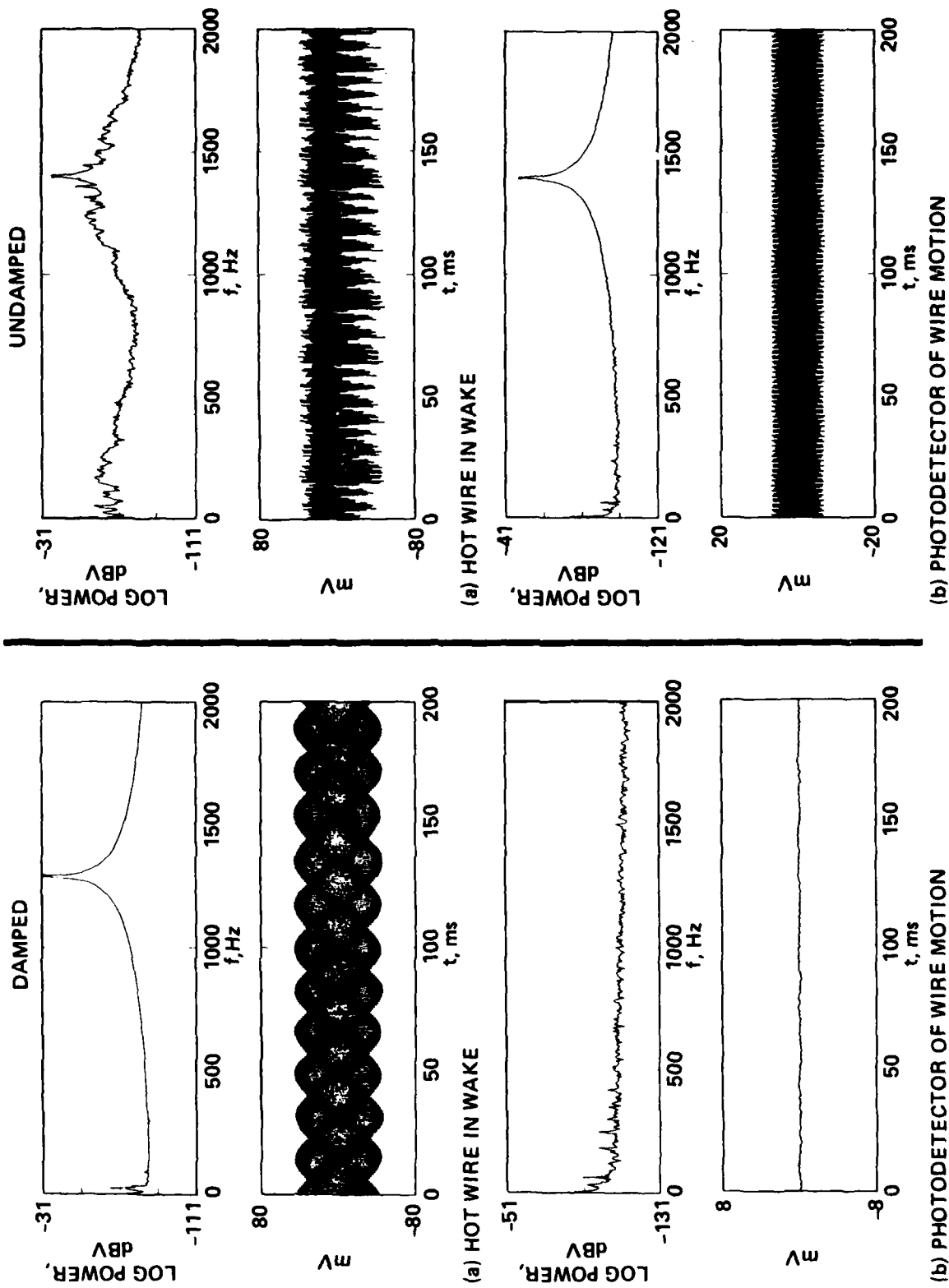
Figure 6.- Dynamics and aerodynamics of a circular cylinder in crossflow (ref. 15).
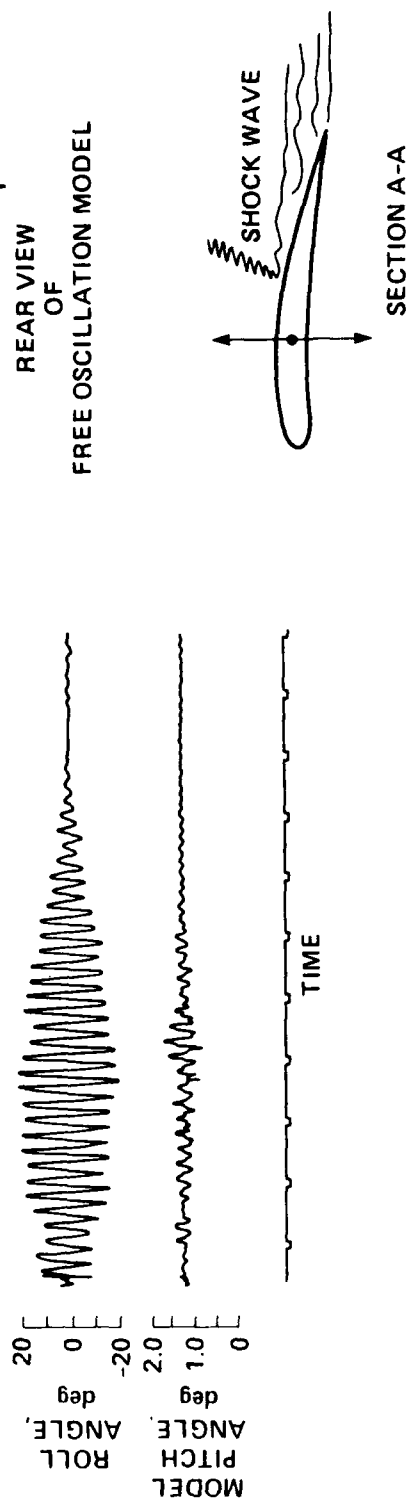
22

Figure 7.- Wing-rock fluctuations caused by shock-induced separation (ref. 16).

CAUSAL NONLINEAR AERODYNAMIC MODELS: TIME DOMAIN, TRANSFORM DOMAIN, AND PHASE SPACE REPRESENTATIONS

Jerry E. Jenkins
Air Force Wright Aeronautical Laboratories
Flight Dynamics Laboratory
AFWAL/FIGC
Wright-Patterson AFB, OH   45433-6553

The study and analysis of rapidly maneuvering aircraft in the high angle-of-attack regime requires the resolution of complex issues involving accurate modeling of the associated aerodynamic responses. At such conditions, the aerodynamic forces and moments exhibit highly nonlinear characteristics that include the effects of motion history, large-scale unsteady flow-separation, and bifurcation of flow states. As a consequence, the aerodynamic reactions often exhibit static and rate-dependant hysteresis.

Analytical models for the aerodynamic reactions have been a powerful tool for the flight dynamicist since Bryan first introduced the linearized stability derivative in 1904. This approach has been used with great success but is clearly inadequate in the nonlinear flow regimes, or in certain cases where the forces are changing rapidly. Etkin, as early as 1956, recognized the limitations of the stability derivative approach (even within the assumption of linearity) and proposed the use of "aerodynamic transfer functions". The advantage of such an approach is that the transfer functions can be used with the Laplace transforms of the linearized equations of motion. Numerical models consisting of large aerodynamic data bases have been used with some success in predicting nonlinear motions. However, this approach does not adequately address control-system synthesis needs, nor does it contribute significantly to a basic understanding of underlying phenomena.

An overview of an AFOSR - AFFDL/NAE initiative in Nonlinear Flight Mechanics is given in this presentation, and key research issues are highlighted. The research focuses on analytical aerodynamic reaction models suitable for use in nonlinear high-rate situations. The model(s) must be causal, i.e., in an input-output form compatible with nonlinear system analysis. They must also be soundly based on the physics of unsteady separated flows. As a result, experimental and computational fluid dynamic issues are being addressed, as are mathematical issues relevant to nonlinear system theory.

The approach draws on three recent developments. Tobak and his co-workers at NASA Ames have developed a nonlinear functional approach to the modeling problem. It is based on step responses in the time domain and the generalized convolution integral. Means for handling discontinuities in the nonlinear step response due to bifurcations in the fluid dynamic states are also suggested. In addition, Hannf at the Canadian NAE has proposed a "phase-space" model which assumes the reactions are functions of the instantaneous states and their time derivatives. This model contains no assumptions of linearity and can handle hysteresis effects. Finally, recent advances in the theory of nonlinear functional expansion lead to a symbolic calculus which generalizes, in a nonlinear setting, many features of the Laplace and Fourier transforms.

CALCULATION OF UNSTEADY FLOW CHARACTERISTICS ON COMPLEX CONFIGURATIONS IN ARBITRARY MOTION*

B. Maskew and F.A. Dvorak
Analytical Methods, Inc.
Redmond, Washington

Abstract

Recent interest in the concept of supermaneuverability has stimulated renewed interest in predicting unsteady flow characteristics of combat aircraft in high angle-of-attack maneuvers. The problem requires treatment of general configurations having separated flows whose extent varies with time and whose downstream development culminates in complex, energetic vortical regions which strongly interact with the aircraft surfaces. It is this interaction which greatly affects the dynamic behavior of the aircraft and which needs to be understood and needs to be predictable if the supermaneuverable concept is to be exploited and integrated into new aircraft designs.

The long'term objectives of the present project are to provide efficient design and analysis tools for investigating vortex flow and separated flow effects on advanced fighter concepts executing arbitrary high-angle maneuvers. The immediate objectives have been to investigate practical ways of calculating these effects.

The above problem strictly requires a solution of the Navier-Stokes equations; however, even though significant advances are being made in both numerical codes and in computer hardware, such a capability has not matured to the point where it is possible to treat the complex geometry of advanced fighter concepts. In order to develop a practical treatment, therefore, the present project examined alternative, simpler approaches to the problem. Emphasis was placed on an accurate representation of the configuration shape. Consequently, the flow equations were simplified to the potential flow panel method formulation. In spite of this, many of the physical aspects of real flow have been restored within the simplified flow model through automated coupling with boundary layer methods and with vortex-wake convection techniques.

The investigations have been carried out based on pilot-code studies in both two- and three-dimensional flows. Both of these codes use the basic Dirichlet formulation of the VSAERO panel code but the solutions are developed in a time-stepping approach. Within each time step, a panel method solution for the instantaneous surface velocity distribution (and its rate of change) are passed to the boundary layer calculation. The wakes are developed by following the motion of points defining the wake surface geometry.

Calculated results for two-dimensional flow of an airfoil in pitch-up motion to high α have compared favorably with experimental measurements. For example, Figure 1 shows the case of a NACA 0012 pitching linearly from 0 to approximately 1 radian at a rate $\dot{\alpha}c/2V_\infty = .089$. Other results from the two-dimensional code-- which is now fully coupled with moving separation points--are included in the paper. The three-dimensional pilot studies have not reached the stage of fully coupled moving separation lines. However, the feasibility of treating complex configurations in arbitrary motion and with fixed separation lines has been demonstrated. A number of cases are included in the paper. For example, Figure 2 shows a delta wing in coning motion. The computed rolling moment as a function of coning rate compares favorably with experimental measurements for three different inclinations to the coning axis, Figure 3. Typical computer times for, say, 30 time steps on a CRAY XMP is of the order of 10 to 15 minutes.

Results from the study are encouraging. Practical, economical solutions to complex problems appear to be feasible. Further effort is required to explore the complete coupling of the moving separation line in the three-dimensional case.

This practical approach could be extended for local treatment of nonlinear effects such as vortex breakdown and compressiblity. In fact, the approach could be regarded as a basic method to which other improvements in modeling techniques could be applied; for example, local zonal treatment by a Navier-Stokes solver for jet plume effects has been investigated.

$\frac{X_{PIV}}{C} = 0.317$

C_l axis, α (RADIANS)
LIFT

○ CALCULATION
— EXPERIMENT
(SEILER LAB)

C_{d_p} axis, α (RADIANS)
PRESSURE DRAG
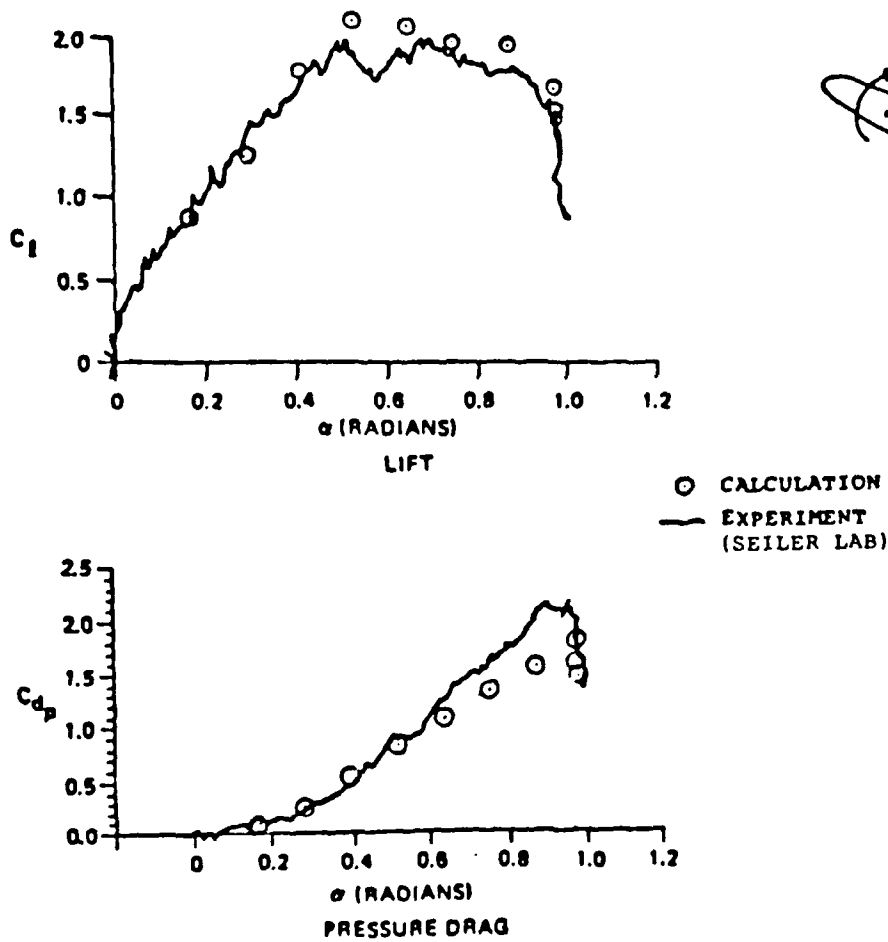
Figure 1. Comparison of Calculated and Experimental Lift and Drag for a Pitching
Airfoil; $\dot{\alpha}c/2V_\infty = 0.089$.
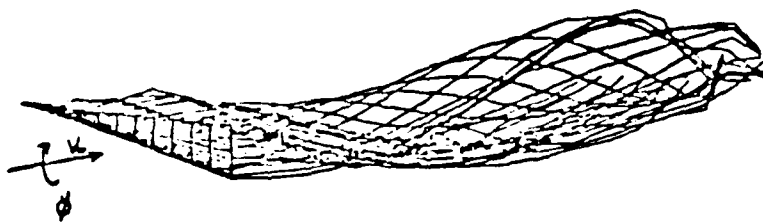
Fig. 2. Calculated Wake for a Delta
Wing on Coning Motion
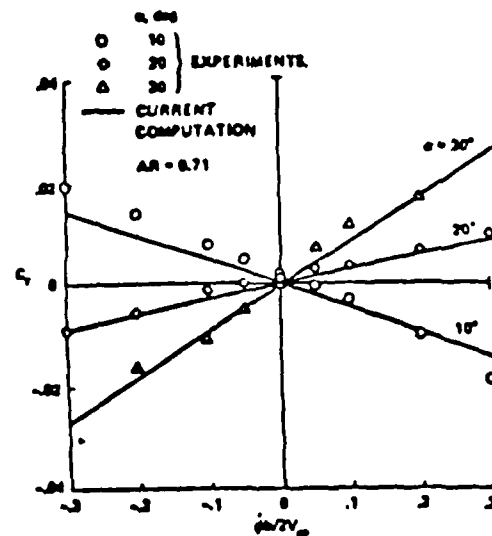
Fig. 3. Rolling Moment Versus Coning Rate
for Delta Wing in Coning Motion.

29

DYNAMIC/AERODYNAMIC INTERACTION
BY
DEAN T. MOOK AND ALI H. NAYFEH

I.   Steady and Unsteady Aerodynamic Interference for Close-Coupled Lifting Surfaces in Vorticity-Dominated Flow Fields

A numerical simulation based on the vortex-lattice concept has been developed for these flowfields. The model can treat arbitrary planforms, at arbitrary angles of attack, executing arbitrary rigid-body motions. The solutions provide the wakes; Figure 1 shows the computed flow past a three-component configuration resembling the X-29.
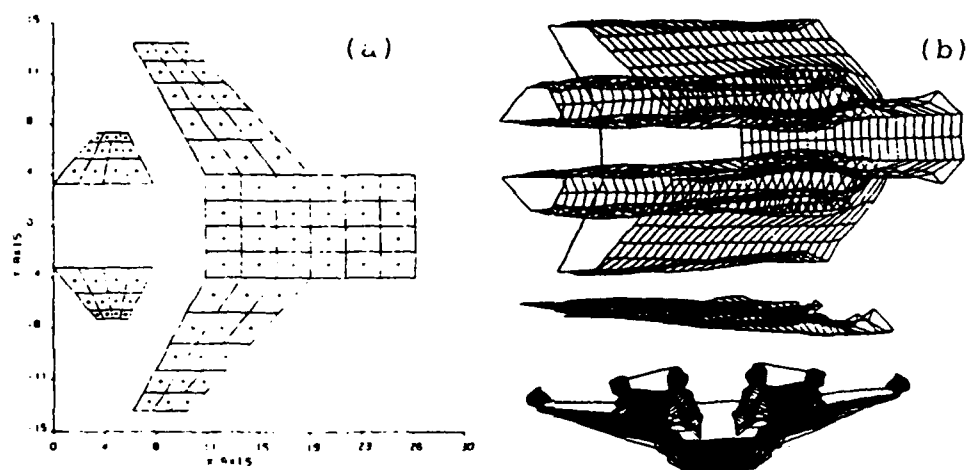
Figure 1. (a) Elements of the vortex lattice representing the three components and (b) elements of the vortex lattice representing the wakes-top, side and front view.
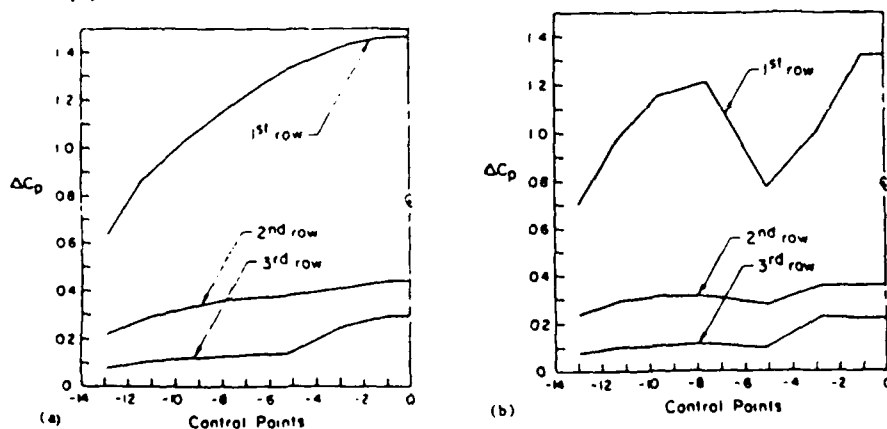
Figure 2. Pressure differences across the main lifting surface: (a) without canards and (b) with canards for steady flow.
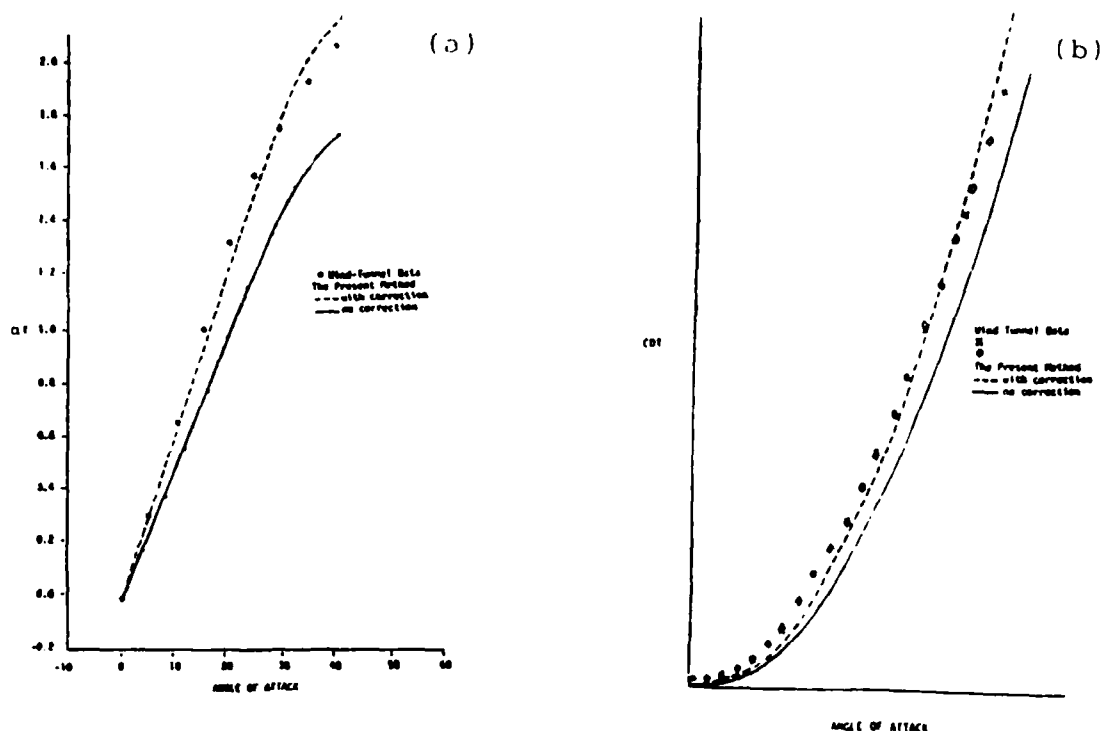
Figure 3. Comparison of predicted and experimental (a) lift and (b) drag as functions of the angle of attack for steady flow.

The pressure distributions across the main wing are strongly influenced by the wakes of the canards as shown in Figure 2. The lift and drag compare well with wind-tunnel data on a model of the X-29 as shown in Figure 3.

The technique can also predict unsteady loads. In Figure 4 lift and moment are plotted as functions of time. The unsteady flowfield was created by giving the canards a simple harmonic oscillation while the main wing remained fixed. Correlations with experiments done by CALSPAN at Tullahoma are still being worked out.
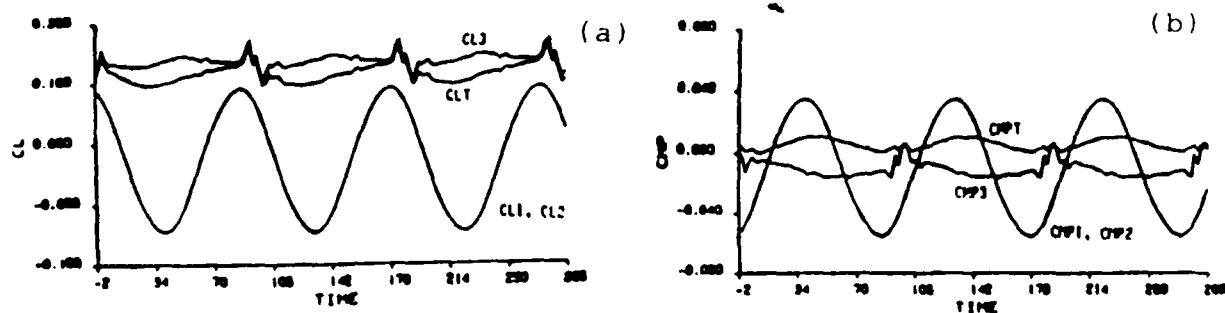
Figure 4. Predicted (a) lift and (b) moment as functions of time: 1 and 2 refers to the canards, 3 to the main wing and T to the complete configuration.

32

II. Subsonic Wing Rock of Slender Delta Wings

A technique to integrate numerically the dynamic equations governing the roll and pitch motions of a delta wing has been developed. With this innovation the flowfield and the motion are computed simultaneously and interactively. A sample of the results is shown in Figure 5.
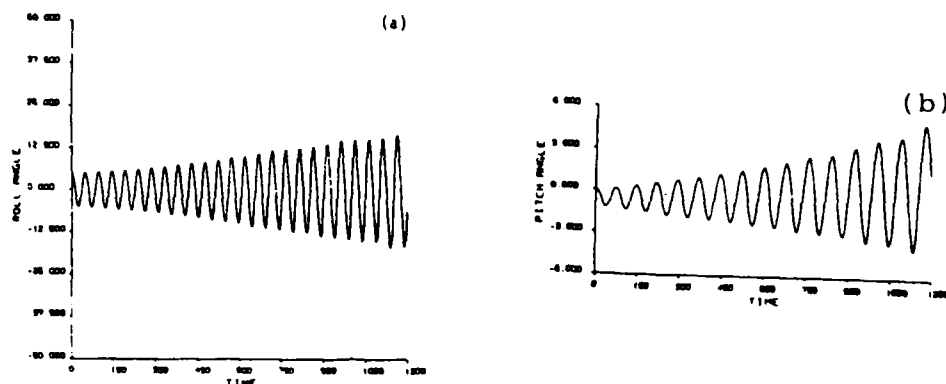
Figure 5. Computed (a) roll and (b) pitch angles as functions of time for $\alpha = 25^\circ$, an unstable case.

The simulation agrees very closely with wind-tunnel data for one degree of freedom. The effect of an additional degree of freedom has not been investigated experimentally.

An analytical study for one degree of freedom has been completed. This study provides a valueable global picture as well as closed-form solutions for periods and amplitudes of the limit cycles when they occur.

III. Additional Efforts

In addition to the major efforts above, effort has been devoted to developing a continuous-vorticity-panel method as an alternative to the vortex-lattice method, predicting the motion of the wing when the motions of the flaps are prescribed, accurately simulating wakes behind airfoils, and numerically modelling massive stall.

33

ON THE UNSTEADY FLOW PAST AN NACA 0012 AIRFOIL UNDERGOING

A LARGE AMPLITUDE INCIDENCE VARIATION

by

A. Krothapalli and L. Lourenco
Department of Mechanical Engineering
The Florida State University
Tallahassee, Florida 32306

Abstract

An experimental investigation is carried out to study the unsteady flow field generated by a two-dimensional NACA 0012 airfoil undergoing large variations in angle of attack. In such cases, the transient aerodynamic characteristics are brought about by phenomena such as a change in air stream around the airfoil due to unsteadiness, development and separation of boundary layer, growth and collapse of vortices. Their interrelationships are very complicated and a clear understanding of these flow fields is not yet available. In the past, it was quite difficult to measure these unsteady vortical flows with conventional measurement techniques, such as LDV or hot-wire anemonetry. However, with recent developments in the whole flow field measuring instruments, such as Particle Image Displacement Velocimetry (PIDV), it is now possible to measure instantaneous velocity fields in unsteady vortical flows.

The problem of interest consists of the understanding of the transient aerodynamic characteristics of an airfoil undergoing a stepwise variation in angle of attack, which is accelerated or decelerated rapidly from one steady velocity to another. To understand the detailed mechanics of this flow, it is necessary

to measure the time evolution of the velocity field. As described below, such an approach is used here.

In the present experiment, a flow visualization and velocity measurement technique known as Particle Image Displacement Velocimetry (PIDV) is used which involves the photographic recording of images of small tracers in a fluid, illuminated by an sheet of pulsed laser light. The resulting image consisting of regularly spaced pairs of particle images is analyzed. The spacing between successive particle images and their orientation are proportional to the local fluid velocity. The analysis of the photograph is carried out using an interferometric method and a digital image processor. The film negatives are locally illuminated with a laser beam generating straight Young's fringes. These fringes are spaced inversely proportional to the particle image displacements and orientated orthogonally in relation to these; and they are acquired by means of a video camera and stored in memory. A fully automated processing algorithm produces the velocity data. In order to obtain the whole velocity field, the film negative is scanned in a pre-determined grid. Following the acquisition of the velocity data, meaningful quantities which further aid in the understanding of flow dynamics, such as vorticity, streamlines and streaklines are produced.

In order to characterize the flow field at a constant angle of attack, the time-space development of the unsteady separated flow generated by a NACA 0012 at different angles of attack $(10° < \alpha < 45°)$, impulsively started from rest is examined. The flow

is created by towing the airfoil in the reduced scale Fluid
Mechanics Research Laboratory towing tank facility. The airfoil
chord is 60mm and is towed with a velocity of 23mm/sec. The
corresponding Reynolds number is 1400.

For the photography, a 35mm camera is used. The flow is
photographed at regular time intervals corresponding to an
equivalent airfoil displacement of $\frac{1}{6}$ of a chord.

The observation of the flow over the airfoil at 10°
incidence showed that the flow is well behaved and attached over
the entire period of observation. However, at larger angles of
attack $\alpha \geq 20°$, the flow separates and generates strong vortices.
The following scenario develops with time: At the start of the
airfoil, a vortex, at the trailing edge, commonly designated as
"starting vortex" is generated and is carried away from the
airfoil. Concomitant with this is the generation of a separation
bubble at the leading edge of the airfoil. At a later time, e.g.
$t^* = U_\infty t/C = 2.58$, the separation bubble grows into an isolated
primary vortex with "secondary vortices" following behind it.
This multiple vortex structure continues to grow together until
t^* reaches a value of about 3.0. At $t^* \simeq 3.0$, because of the close
proximity of the primary vortex, a trailing edge vortex is gene-
rated. At 3.5, the primary vortex abruptly moves away from the
surface of the airfoil leaving behind a "vortex sheet" like
structure. For $t^* \geq 3.75$ this "vortex sheet" rolls up into
distinct vortices and growing in size with time. During this
process the trailing edge vortex also grows and as a result the
whole flow field becomes very complex. (See figure 1a-1d). The

37

detailed time evaluation of the velocity and vorticity fields corresponding to this flow field will be discussed in this paper. Also included in the paper are the preliminary results of the flow field generated by an airfoil undergoing variations in angle of attack.
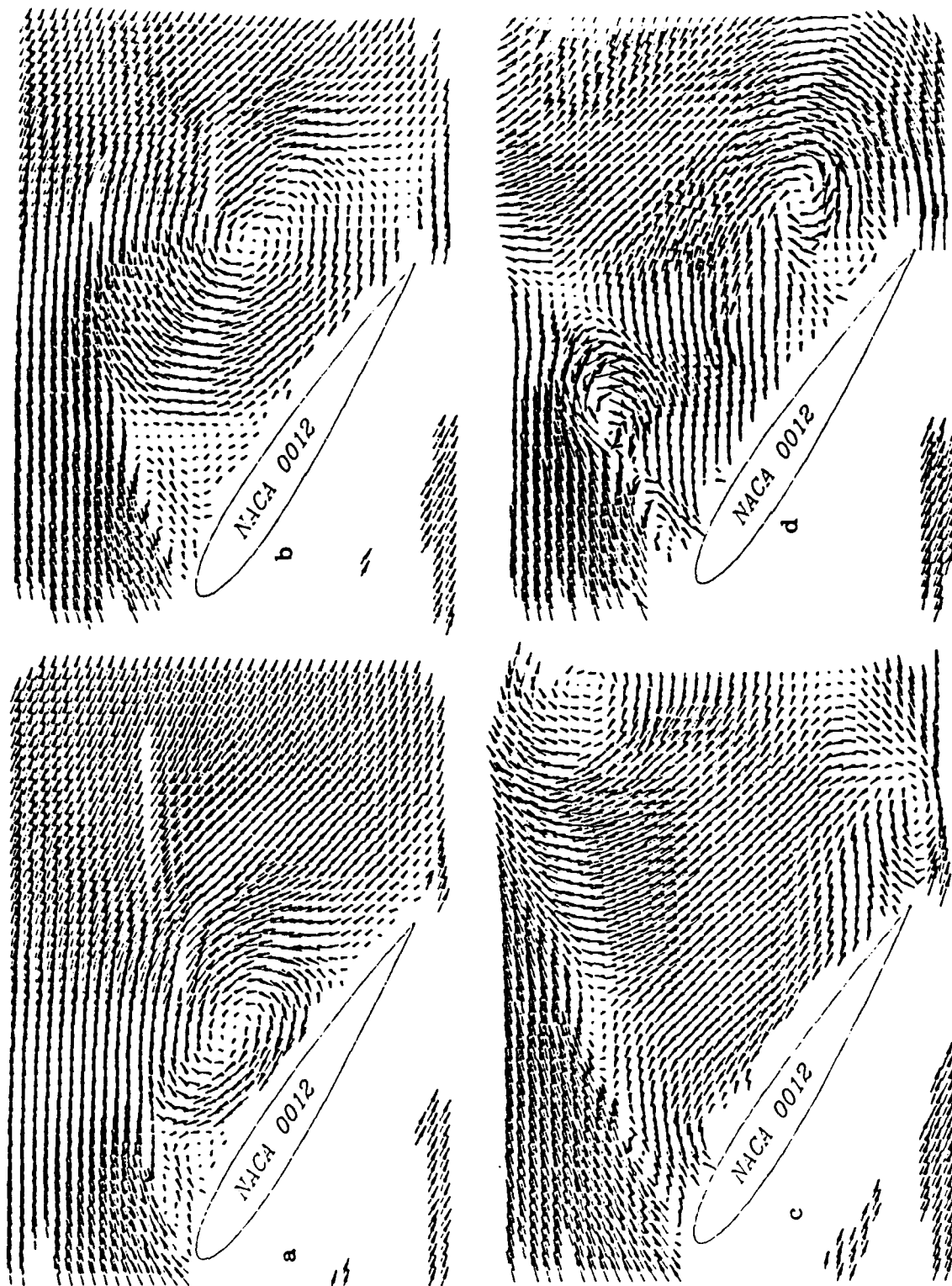

Figure 1. Typical instantaneous velocity fields; a) $t^* = 1.85$, b) $t^* = 2.52$, c) $t^* = 3.52$, d) $t^* = 4.52$, Re = 1410. ($t^* = tU/C$)

39

TOWARD UNSTEADY LIFT AUGMENTATION:
An Assessment of the Role of Competing Phenomena in Dynamic Stall

E. J. Jumper[*]
Professor
Department of Aeronautics and Astronautics
Air Force Institute of Technology
Wright-Patterson AFB, Ohio 45433-6835

and

E. J. Stephen
Research Associate
F. J. Seiler Research Laboratory
United States Air Force Academy, Colorado 80840

Abstract

This paper presents an anatomy of the dynamic-stall event for an airfoil pitching at constant rate in a uniform free stream. The event may be divided into two distinctly different regimes: the first depends solely on the suppression of flow separation from the upper surface of the airfoil by competing "unsteady" phenomena associated with the pitching motion of the airfoil; the second regime is dominated by the dynamics of the formation and convection (over the airfoil) of a large, well-organized leading-edge vortex. Of these two regimes, the dynamic suppression of separation is the largest contributor in the production of additional lift beyond the static maximum lift coefficient. The understanding of the mechanisms involved in dynamic stall is then applied to formulating concepts for using dynamic motions for unsteady sustained lift augmentation.

I. Introduction

In 1978 one of the authors and a friend from the Language Department at the Air Force Academy sat down with a copy of von Max Kramer's paper [Ref. 1] and began a crude translation....."The Increase of $C_{L_{max}}$ of Airfoils with a Sudden Increase in Angle of Attack (Gust Effect)." So began the first published article on dynamic stall, 14 April 1932. We believe that after ten years of study we are ready to state what we think is going on in dynamic stall with the same boldness that Kramer stated his somewhat naive, albeit insightful, explanation more than fifty years ago. But we are not so bold as to assert anything more than that we believe we understand a narrowly-defined, yet useful, corner of a wide range of motions falling under the aegis of "dynamic-stall phenomena." The goal as defined in 1978, and continued to be pursued since 1981 at the Air Force Institute of Technology (AFIT) was to attempt to understand the dynamic-stall event for an airfoil pitching up at constant rate (constant-$\dot{\alpha}$) through its steady-flow stall angle. Even the constant-$\dot{\alpha}$ motions have been limited to "relatively slow" pitch rates. As our and others' studies have clearly indicated, the non-dimensional parameter governing the behavior of a dynamic-stall event is the non-dimensional pitch rate, $\dot{\alpha}_{ND}$, given by

$$\dot{\alpha}_{ND} = \frac{1/2\ c\ \dot{\alpha}}{U_\infty} \qquad (1)$$

where c is the chord, $\dot{\alpha}$ is the pitch rate and U_∞ is the free-stream velocity. For an airfoil pitching about the midchord, this parameter can be interpreted as the speed of the leading edge due to the pitching motion, divided by the free-stream velocity. By "relatively slow," we mean that our attention has been restricted to $\dot{\alpha}_{ND}$'s of less than 0.1, that is to say, motions with leading-edge speeds of less than 10% that of the free stream. This fact should be kept in mind when comparing that which follows to work by others, which in many cases deals with motions that are up to two orders of magnitude faster.

It is appropriate to note that there is both a theoretical and a practical argument for limiting a study of this kind to relatively slow motions. Theoretically speaking, limiting $\dot{\alpha}_{ND}$ to 0.1 means that there are many convective-flow clearings of the airfoil during its pitching motion. This fact

would seem to uncomplicate the understanding of the phenomenon by eliminating the inevitable competition between the physics of the effect of the imposed unsteady boundary conditions and the consequences of delays due solely to the fact that things take times on the order of a clearing time to happen. Further, as will be discussed below, while the effect on separation and stall is far from being able to be classified as a perturbation, an $\dot{\alpha}_{ND}$ of 0.1 or less may be thought of as a perturbation in terms of the inviscid flow. From a practical point of view, a.) even such "slow" motions lead to large changes in both stall angle and maximum lift coefficient, as will be seen; and b.) it is not an inauspicious belief that such "slow" motions could be implemented and even inadvertently or intentionally encountered at actual flight speeds of existing aircraft.

At various stages of our work, this restricted-type motion has been further narrowed to focus on specific aspects of the dynamic-stall event. Because of this dissection of dynamic stall, by now our efforts have become quite extensive and it is difficult to find a presentation format that maintains logical coherence; however, keying on the idea that dynamic stall is an event, the organization of this paper is initially governed by the progress of a constant-$\dot{\alpha}$, dynamic-stall event.

II. The Constant-$\dot{\alpha}$, Dynamic-Stall Event

The constant-$\dot{\alpha}$, dynamic-stall event may be described with the aid of Figures 1 through 4 (details on the collection and reduction of the data presented in Figures 1-3 may be found in Reference 2). Figure 1 is, perhaps, the most useful in gaining an overall perspective of the event. To begin with, we have chosen these data because they graphically demonstrate the notion that the governing non-dimensional parameter, referred to above, is $\dot{\alpha}_{ND}$. The data represent 10 data runs, 5 at a tunnel speed of 26.6 ft/s and 5 at 34.4 ft/s; however, their $\dot{\alpha}$'s are such (~69°/s and 89°/s, respectively) that they have nearly identical α_{ND}'s (~0.023). We note that the scatter up to and beyond dynamic stall is as small for the overlay of the two different dynamic $\dot{\alpha}$-U_∞ cases (5 runs each case, 10 runs total) as for a single dynamic $\dot{\alpha}$-U_∞ case (5 runs). The next thing to note is that relatively slow motions (i.e., the speed of the leading edge here is only 2.3% of the free-stream velocity) have dramatic effects on maximum coefficients of lift, C_{Lmax}, here more than doubling the static C_{Lmax}.

At first glance, the inclination is to infer from the C_L-α curve (Figure 1) that the slope of the dynamic C_L-α curve is the same as slope of the static C_L-α curve, and this approach has been used [Ref. 3]. To do so is useful on the one hand, but misleading on the other. On the useful side, such inference allows one to predict the dynamic C_{Lmax} by using an empirical prediction of the delay in dynamic-stall angle of attack, $(\alpha_s)_{DYN}$, and then using the static C_L-α slope to infer the dynamic C_{Lmax}. On the other hand, to do so can lead to a false confidence about ones understanding of the details of the dynamic-stall event. In order to understand these details it is useful to divide the event into pieces which is the intent of the A through F labels on Figures 1-4. For the purposes of discussion, then, let us divide the event into "fully-attached" (A to B), "separating-but-conforming" (C), "quarter-chord separation" (D), "dynamic stall" (E), and "post stall" (F).

Fully-Attached (A to B). It is a mistake to assume that because this regime occurs so early in the dynamic-stall event, there is little to be learned about the physics of the event in the fully-attached regime. In fact, from the point of view of understanding the physics, this regime is one of the most instructive regarding the external (inviscid), potential flow environment to which the separating boundary layer is subjected.

In the "fully-attached" regime, one can argue that the inviscid flow may be modeled approximately as flow around a Joukowski airfoil pitching at constant rate about approximately the midchord, and this is what we have done. Although the results of our modeling have appeared elsewhere [Refs. 2,4], a complete description of our method is presently available only in a thesis [Ref. 5]. Though differing in details, the method is similar to that of Giesing [Ref. 6], and Chow and Huang [Ref. 7], in that vorticity was allowed to be shed into the wake at the trailing edge as unsteady circulation built on the airfoil, and this shed vorticity was modeled as discrete vortices. In addition to differing in computational details, our approach also differed from those of References 6 and 7 in the particular airfoil motion studied, as well as the method of computing the aerodynamic force coefficients.

The transient nature of the flow was analytically determined by invoking the requirements that the total circulation (bound plus free) remained zero, the free vortices were free to move at the local velocity in the physical plane, the placement of the

42

bound vortices was governed by the circle theorem [Ref. 8] in the circle plane, and the strength of the shed free vortices and bound vortices combined to insure that the Kutta condition was maintained at the trailing edge. The numerical implementation of the above was made by modeling a continuous trailing-vortex-sheet distribution as discrete vortices initially introduced into the external flow after Giesing [Ref. 6] at a distance $U_\infty \cdot \Delta t$ behind the trailing edge at each time step. This process is schematically depicted in Figure 5 for two planes of interest for the Joukowski transformation.

Because the purpose for the analysis was ultimately intended to provide the external boundary conditions for a boundary-layer analysis of separation, a comparison of lift coefficient versus time obtained by integrating the pressure coefficients around the airfoil (i.e., our method) with lift coefficient versus time obtained by the "less direct methods" of Giesing [Ref. 6] and Chow and Huang [Ref. 7] was made for the Wagner problem [Ref. 9] of an impulsively started airfoil at a fixed angle of attack. Figure 6 shows the result of this comparison for a zero-thickness airfoil (flat plate), along with the analytic result by Wagner [Ref. 9]. Figure 7 shows the results of the comparison with Giesing [Ref. 6] for a 25.5% Joukowski airfoil, also superimposed is the Wagner flat plate solution [Ref. 9]. These comparisons indicated that both our analytic treatment and method of computing aerodynamic forces by direct integration of the unsteady pressure field produce consistently good results.

The method was then used to compute the unsteady flow around a Joukowski airfoil initially at some angle of attack in a steady flow, and impulsively set into a constant-$\dot{\alpha}$ pitching motion about approximately the midchord. The gross aerodynamic effects on the $C_L-\alpha$ curve are shown in Figure 8. At onset of rotation (shown in Figure 8 as being at 0°) the airfoil experiences a sudden jump in coefficient of lift, ΔC_L, and a depression of the lift-curve slope. These effects have been shown to be functions of $\dot{\alpha}_{ND}$ as

$$\Delta C_L(\dot{\alpha}_{ND}, t/c) = 3.14 \; \dot{\alpha}_{ND} \; [\; 1 + 2/3(t/c) \;] \quad (2)$$

where t/c is the thickness ratio. The predicted slope depression for a zero thickness airfoil is shown in Figure 9 and may be approximated by

$$C_{L_\alpha} \approx 3.6 \\ + 2.68 \; exp \; (-\dot{\alpha}_{ND} \; X \; 10^3 \; / \; 4.216) \quad (3)$$

Equation (3) is only slightly modified by the inclusion of thickness ratio.

It may be shown that the sudden jump in C_L is identical to that analytically derived using thin-airfoil theory by replacing the requirement in steady flow of the normal component of the velocity being zero at the airfoil surface (camber line in thin-airfoil theory) with the requirement that the normal component be equal to the velocity of the surface at that point normal to itself [Ref. 10], and is referred to as the apparent camber effect in aeroelasticity [Ref. 11]. The slope depression, then, is clearly due to the influence of the unsteady wake, and reflects the notion that the airfoil appears to be experiencing an apparent or time-lagging angle of attack of less than the geometric angle of attack, in much the same way as the "starting vortex" exhibits itself on the airfoil as a "lag time" in the Wagner problem [Ref. 9]. It is interesting to note that such separation of wake effects and apparent curved-body effects was the origin of the motivation that von Karman had for assigning Bill Sears to his Ph.D. thesis work [Ref. 12].

As described in detail in Reference 2, the initial "fully-attached" lift-curve characteristics extracted from wind-tunnel data indicate that the characteristics predicted in Eqs. (2) and (3) and depicted in Figures 8 and 9 do seem to be present in the data. Such indication is shown in Figures 10 and 11, taken from Reference 2. The indication, unfortunately, is not complete, as can be seen by cases of inversions in the reduced curves; the general agreement, however, does appear to be present, and one can point to a number of possible contributors to the few discrepancies. Without doing this, we are satisfied to simply point out that the suggestion that the subtleties predicted by the theory not only probably exist, but may be measured in the wind tunnel.

Separating-but-Conforming (C).
Flow-visualization experiments are instructive in the range of α where the flow closely conforms to the airfoil contours. Such experiments are mentioned in Reference 13, covering our work, but of particular interest are those done at the F. J. Seiler Research Laboratory by Walker et. al. [Ref. 14]. These experiments indicate that, for the type airfoils used in the studies, separation begins at the trailing edge and moves toward the leading edge. In the region from B to at least C, the separation is slight, and the flow closely conforms to the airfoil contours. In fact, the conforming behavior of the flow persists at least until the separation has advanced forward to the quarter chord. This fact, that the flow closely

43

conforms to the airfoil contour even in the presence of regions of separated flow, leads to the conclusion that unsteady inviscid flow calculations obtained assuming the flow follows the airfoil contour (non-interactively) can be useful, when coupled with boundary-layer techniques, in understanding the physics of the unsteady separating flow.

Quarter-Chord Separation (D). From our earliest studies we assumed that understanding the nature of the unsteady separation would be key to understanding the nature of dynamic stall. The rationale went something like this: we intended to use boundary-layer methods for our theoretical treatment, thus precluding the prediction of stall itself; however, knowing that separation and stall are closely related in steady flow, we decided to confine our attention to separation at the quarter chord. We have been asked on a number of occasions, "why the quarter chord?" All we can say is that it was indeed arbitrary, but based on an intuitive notion that when the flow has separated over 75% of the top surface of an airfoil in steady flow, the suction peak is in jeopardy and stall is either achieved or close at hand. In fact, the choice of studying quarter-chord separation in the unsteady case was most fortunate, as we later learned from experiments, because, as mentioned above, up to quarter-chord separation, though the flow is separated ("in the boundary layer"), the external (inviscid) flow conforms closely to the airfoil contour; after quarter-chord separation (either coincident with, or very shortly thereafter [Ref. 2]) the flow catastrophically separates from the airfoil ("snaps free") and a large, well-organized, leading-edge vortex begins to form. We say the choice was fortunate, because: 1) this means that our simple external flow calculations may be used to predict the delay in quarter-chord separation, whereas a choice of say eight-chord separation or anything less than quarter-chord would have required something much more complicated to compute the flow field; and 2) the coincident nature of quarter-chord separation and leading-edge vortex formation means that we chose just the right location for capturing the key to understanding the nature of dynamic stall.

Our first task was to obtain experimental data on quarter-chord separation for the constant-$\dot{\alpha}$ pitching airfoil. This was done using both flow visualization and pressure measurements near the quarter chord. This work is reported in Reference 13, and Figure 12 summarizes our findings for pitch about the midchord. Having obtained a set of data against which theoretical

predictions could be compared, we set about examining the theoretical treatment of quarter-chord separation delay.

Our theoretical method for the investigation of quarter-chord separation solved the unsteady momentum integral [Ref. 15]. The method depended in part on the development of a closure equation for the time rate of change in the displacement thickness, δ_1. As detailed in Reference 15, the closure equation was found to be

$$\frac{\partial \delta_1}{\partial t} \cong -\frac{\delta_1}{2 U_e} \frac{\partial U_e}{\partial t} \qquad (4)$$

where U_e is the velocity of the flow at the edge of the boundary layer. The closure equation, Eq. (4), enabled the construction of modified Polhausen parameters that allowed for step-wise integration of the unsteady momentum-integral equation [Ref. 15].

As in any boundary-layer method, the unsteady, external flow field was needed, and the field was built up in such a way that the contributing effects could be studied individually [Ref. 15]. Using an external flow field built up in this way, the effect of the simple unsteadiness of the flow not including the wake (GUST); the effect of the motion of the airfoil in the direction of the flow, i.e., tangent to the surface, (PITCH); the effect of the Moore-Root-Sears (MRS) separation criteria; the effect of the wake; and the effect of the motion of the airfoil normal to the direction of the flow, i.e., normal to the surface, (MASS) could be studied separately. This last effect mimics "apparent camber" and required the development of a perturbation technique to be able to independently assess only the effect of the motion of the airfoil normal to the flow; the perturbation technique is detailed in Reference 16.

The results of the aforementioned studies are summarized in Figure 13. In matching the theory with experiment, some license was taken in choosing the coefficient for including the wake effect [Refs. 4 and 15], but once chosen for the case of an airfoil pitching about the midchord, the same coefficient was used to predict the effect on quarter-chord separation of changing the pitch location. The predicted effect was in excellent agreement with experimental results from pitch-location-change experiments, as can be seen in Figure 14 [Ref. 4].

It is helpful in interpreting these results to group the contributors into three physically associated effects.

44

First there are the effects due to the fact that the boundary-layer control volume is moving in the direction of the flow; in Figure 13, this would include the contribution to delay labeled "PITCH" and "MRS." As best we can tell, these effects taken together mimic the intuitive physical model suggested by Ericsson and Reding [Ref. 17] referred to as the "leading-edge jet" or "wall jet," shown schematically in Figure 15. For lack of a better place to group it, the "GUST" effect may also be added to the "PITCH" and "MRS" effects. The "GUST" effect is not large; it is due to the effect of the airfoil continuously changing angle of attack which results in the outer boundary condition containing an unsteady term. It should be stressed that this unsteadiness does not contain the unsteadiness due to the vorticity being shed into the wake. The remaining effects are really external or inviscid flow effects, and as we have learned from our study of the "fully-attached" regime (cf. above), they may be further divided into "apparent-camber" effects, and effects due to the wake.

As mentioned above, the apparent-camber effect was modeled using a perturbation technique referred to as "mass ingestion" [Ref. 16] because the pressure gradient due to the apparent curvature can be shown to force/draw or "ingest" fluid into the top of the boundary-layer control volume as long as the surface motion is "into" the fluid, as shown in Figure 16; for an airfoil pitching about the midchord, fluid is "ingested" into the control volume from the leading edge to the midchord. This fluid carries external-flow momentum into the boundary layer ("energizes" the boundary layer) thereby making it more resistant to separation. In this regard, the additional term in the momentum integral shows a one-to-one correlation with a suction term, and may be shown to be as effective in delaying separation [Ref. 16]. Another way of looking at the effect is to think of the motion of the airfoil into the flow as forcing the boundary layer down onto the surface. In a similar way, motion of the wall in the opposite direction, i.e., away from the flow, tends to promote rather than retard separation (all else being equal). Finally, it should be kept in mind that this effect is pitch-location sensitive, and the most beneficial effect is at those points where the surface-normal component of the airfoil motion is greatest. Thus, for a midchord-pitching airfoil, the strongest influence would be near the quarter chord; but, for an airfoil pitching about the quarter chord, this effect would be essentially neutral at the quarter chord.

The remaining effect due to the wake is large, appears to depend only on the time history of the changing angle of attack (cf. above), and may be more-or-less decoupled from pitch location. As best we can determine, this effect most closely mimics Ericsson and Reding's "time-lag effect" [Ref. 17].

Dynamic Stall (E). From the point of quarter-chord separation (D) to dynamic stall (E) the aerodynamic forces appear to be driven by the dynamics of the formation and convection of a large, well-organized, leading-edge vortex. As in the case of quarter-chord separation, data like that in Figure 10.F. can be used to extract delays in the angle at which the airfoil stalls, $(\alpha_s)_{DYN}$; it is again found that such data collapse onto $\dot{\alpha}_{ND}$, as is shown in Figure 17. This figure may be used to confirm the compatibility of the notion that the additional delay in angle of attack between quarter-chord separation and stall is due to the dynamics of the free leading-edge vortex. This may be done with the aid of Figure 18. First, let us assume that the catastrophic detachment of the flow and the formation of the vortex is nearly coincident with quarter-chord separation. Once the vortex has detached it becomes a free vortex, subject to motion based on the local flow velocity. Robinson, et. al. [Ref. 18], have shown that this convection speed is on the order of 0.4 U_∞, and following Chow and Chiu [Ref. 19], the vortex influences the lift spike over a distance of roughly 70% of the chord length, c; so that the convective time of vortex influence is

$$t_C \approx 3.5 \frac{1/2 \ c}{U_\infty} \qquad (5)$$

where the 1/2 is introduced for convenience. In this time the angle of attack will change by

$$\Delta\alpha = \dot{\alpha} \ t_C \approx 200 \ \frac{(1/2 \ c \ \dot{\alpha})}{U_\infty} \qquad (6)$$

where $\dot{\alpha}$ is in radians/s, and the predicted delay is in degrees, so that the difference between the separation angle of attack and the stall angle of attack should scale as

$$\Delta\alpha_S - \Delta\alpha_{SEP} \approx 200 \ \dot{\alpha}_{ND} \qquad (7)$$

Analysis of Figure 17 confirms that this is the correct functional prediction of the difference between separation angle of attack and stall angle of attack. It should be further noted that Eq. (7) is not effected by pitch location [Ref. 4],

implying that quarter-chord separation is really the driving factor in dynamic stall, at least for constant-$\dot{\alpha}$ motions. Finally, chord-normal aerodynamic forces predicted by theoretical inviscid, free point-vortex methods like that of Chow and Chiu [Ref. 19] seem to provide a satisfactory explanation for the magnitude of the additional lift experienced by the airfoil in the presence of the large leading-edge free vortex.

Extent of Leading-Edge Vortex Lift Augmentation (D)-(E).

It is clear from both Figure 1 and 17, that the major portion of the lift overshoot may be attributed to the dynamically-delayed separation of the flow from the upper airfoil surface. This would seem to imply that it is important to understand why such separation delay is present in a dynamic-stall event; yet, if relative number of publications concerned with leading-edge vortex dynamics can be used as a measure of activity, the dynamic-stall community is spending little of its resources on separation. It is understandable from an aesthetic point of view why people are drawn to investigate vortices, especially as large and well organized as leading-edge, dynamic-stall vortices are, but such "VORTEX FIXATION" may be misleading (and, in our case has been misleading, cf. below) in terms of developing schemes for trying to exploit dynamic-stall-like motions for unsteady, sustained lift augmentation. One should always keep Figure 1 in mind, when thinking in terms of lift augmentation, because it is clear, at least in the constant-$\dot{\alpha}$ motion, that almost all of the lift "benefit" in the dynamic-stall event is attributable to the flow remaining attached (i.e., up to quarter-chord separation).

Drag and Moment (C), (D) and (E).

Examination of the pressure-drag and moment curves (Figures 2 and 3, respectively) also gives some insight into the progress of the dynamic stall event. Up to C the drag coefficient is relatively flat indicating that the pressure recovery in the "external flow" continues to stay strong up to angles of attack as high as 20° for this $\dot{\alpha}_{ND}$, reminiscent of "attached" flow over most of the airfoil. As the separation rapidly progresses forward toward the quarter chord, the drag begins to rise. From quarter-chord separation (D) to stall (E) the drag curve rises in a "continuous" fashion, i.e., exhibits no abrupt slope changes; however, the moment curve, Figure 3, shows a "sudden" negative moment spike. From what has been stated above, it may be inferred that this moment spike is caused by/indicates the presence of a leading-edge-vortex-induced low pressure cell

moving over the airfoil as the vortex convects by the airfoil. Though not for the same $\dot{\alpha}_{ND}$, Figure 19 (for $\dot{\alpha}_{ND} = 0.022$) supports this contention [Ref. 2]. The continued reduction in moment (delay in recovery) for a brief time after dynamic stall can also be understood with the aid of Figure 19. We thus go so far as to state that the negative moment spike may be taken as presumptive evidence of the creation and convection of a leading-edge dynamic-stall vortex.

Post-Stall (F).

As several authors have noted (in particular, Ericsson [Ref. 20]), the post-stall aerodynamic forces appear to be driven by Strouhal-type von Karman vortex shedding from the airfoil, similar to such shedding from a plate normal to the flow with the same projected area. Because of the constant-$\dot{\alpha}$ motion, it is possible to show that the periodic-type aerodynamic forces collapse onto $\dot{\alpha}_{ND}$ because this captures the constant Strouhal nondimensionality.

Intuitive Overview of the Dynamic-Stall Event.

At the onset of airfoil rotation in a constant-$\dot{\alpha}$ pitching motion two nearly-equal-in-effect changes in the flow field take place: a.) the airfoil boundary condition changes so that the forward (of pitch location) portion of the top of the airfoil begins to move into the flow, or from an observer-attached-to-the-airfoil's point of view, the boundary layer begins to experience a local stagnation flow; and b.) vorticity begins to shed into the wake as the unsteady circulation builds on the airfoil. These two changes in the flow field persist throughout the motion of the airfoil and act to suppress the progress of the separation as it moves from the trailing to leading edge of the airfoil. The causes for such suppression might be intuitively thought of as, in the first case, the local stagnation flow either forcing the boundary layer down against the airfoil, or causing the "ingestion" of external-flow, momentum-rich fluid into the boundary layer, and thus "energizing" it; and in the second case, the shed-vortex wake mimicking pressure profiles reminiscent of a lower angle of attack, i.e., a lower effective angle of attack. It should be noted that the effect of the motion of the airfoil surface seems to linearly increase with increasing $\dot{\alpha}_{ND}$, while that of the wake seems to saturate after $\dot{\alpha}_{ND}$ becomes larger than about 0.01, at least to the limits of our experience, i.e., $\dot{\alpha}_{ND} \lesssim 0.05$, indicating some "cost-benefit-type" implications. Additionally, though to a lesser extent, the separation delay is aided by the fact that the airfoil surface is moving in the direction of the external flow, which modifies

slightly the separation mechanism, i.e., MRS separation considerations.

As long as the separation remains aft of the quarter chord, the flow more-or-less follows the contour of the airfoil, and the above notions remain valid. Once separation reaches quarter-chord separation, the flow "snaps free" of the airfoil, and the vorticity rolls up into a well-defined leading edge vortex, which remains in the vicinity of the airfoil for a short while. During this while, the dynamic-stall event is dominated by the dynamics of the vortex, and some additional lift is realized.

III. Periodic Motion Experiments

The final portion of this paper deals with our limited excursion into the investigation of periodic motions in an attempt to exploit dynamic-stall-like phenomenon for sustained lift augmentation. Such investigations have been undertaken by others, most notably by McAllister, Carr and McCroskey [Ref. 21]. These investigators explored sinusoidal oscillations of an NACA 0012 airfoil about average angles of attack. While such experiments demonstrated large chord-normal coefficient excursions (C_L's > 3.0), time-averaged C_L's (i.e., sustained lift augmentation) could only be achieved that equaled the static $C_{T_{max}}$. Further, this time-averaged lift was accompanied by large time-averaged pressure drag. Also, leading-edge, dynamic-stall vortices were formed each cycle, as may be inferred from the moment curves. Figure 20 is an example of chord-normal, chord-tangent, and moment coefficients, C_N, C_C, and C_M, respectively, taken from their work [Ref. 21].

Because of the extensive investigations of McAlister, Carr and McCroskey [Ref. 21], we felt that we had little to contribute by way of exploring sinusoidal oscillating motions; however, our background in constant-$\dot{\alpha}$ ramp motions, led us to believe that some new insights into the problem of optimized time-averaged lift augmentation might be gained by an experimental study of saw-tooth motions (i.e., constant-$\dot{\alpha}$ ramp up, constant-$\dot{\alpha}$ ramp down, periodic motions) with the up and down slopes adjusted (and different) based on knowledge available from the constant-$\dot{\alpha}$ (pitch-up-only) studies.

First Notions. Our first thoughts on optimizing the motion went as follows: a.) begin the up ramp in the attached-flow region, i.e., B-C on Figure 1; b.) continue ramp to the α_{ND}-compatible angle for quarter-chord separation, i.e., D on Figure 1; c.) ramp down as rapidly as possible to the attached-flow region; d.) pause (optional) to allow flow to reattach;

e.) repeat. The rationale for step b. and c. was to stop the motion at the point where the leading-edge vortex would begin to form even if the airfoil were to continue its upward pitching motion. The presence of the leading-edge lift-producing vortex in the vicinity of the airfoil would then provide a portion of the time needed for the airfoil to regain its attached-flow position. The plan, then, was to experimentally explore the starting-angle, stopping-angle, and $\dot{\alpha}_{ND}$ surface in search of local optimums.

Experimental Methods. Two wind tunnels were used in this study; the first was located at AFIT, and has been extensively described elsewhere [Refs. 2, 4, and 13]. The second was located at the von Karman Institute of Technology (VKI). The tunnels differed mainly in test-section dimensions; the AFIT tunnel section was 5 ft X 3 ft X 0.25 ft and the VKI section was 3.28 ft X 6.6 ft X 0.92 ft (i.e., 1 m X 2 m X 28 cm). The tunnel speeds were roughly the same ranging from 20 ft/s to 40 ft/s. The VKI tunnel had a somewhat higher turbulence level, details may be found in Reference 22.

The airfoil used was that of References 2, 4 and 13, and consisted of a 1.02 ft-chord NACA 0015 section instrumented with 16 ENDEVCO 8507-2, 2-psi (full range) pressure transducers at the locations indicated in Figure 21; the pitching motions were about the midchord. The same airfoil was used in both tunnels; however, extensions were added to each side the AFIT airfoil configuration to increase its span so that the airfoil also spanned the VKI tunnel.

The motive force for performing the pitch-motion histories was provided in two ways. In the first, the high-torque, constant-speed motor used in previous studies [Refs. 2 and 4] was used. The constant pitch rate and direction (i.e., pitch up or down) was controlled by switching between two independent DC power supplies whose voltages and polarities could be set for the desired rates/directions. The selection of the one or the opposite-polarity power supply was accomplished by relay switches triggered by a spring-steel reed attached to the airfoil rotation shaft. The angles of attack for switching from one to the other power supply could be adjusted by moving the locations of the relay switches relative to the reed in an arc around the airfoil shaft. An adjustable time delay was available and could be used to cause the airfoil to remain stationary for a short period before switching to the other power supply.

47

While this setup allowed for relatively constant-$\dot{\alpha}$ ramps (up and down), it was limited in achievable rates, was not flexible in terms of other motions, and, perhaps more importantly, could not deliver the torque required to drive the larger wing as configured for the VKI tunnel. For these reasons, a second drive system was designed that incorporated a DC servo motor and feed-back control system whose motion could be programmed by interfacing with a portable digital computer (see Ref. 22 for details).

The data-collection system and procedures were identical to those described in References 2 and 4, and the comments regarding accuracy of the results apply equally well to this study. The results shown here, Figures 22-25, indicate the scatter/variance band on the data.

Results. The results of the study are shown in Figures 22-25. Each figure shows counter clockwise, starting in the upper left corner, the angle-of-attack, time history; lift-coefficient, time history; quarter-chord moment-coefficient, time history; and pressure-drag-coefficient, time history.

Based on our first notions, as described above, most of our studies yielded results like those of Figure 22. If the results were replotted as coefficients versus angle of attack, the curves would resemble those of Figure 20. The main difference between figures is that, in the case of Figure 20, the upward motion was still in progress during the convection of the leading-edge vortex over the airfoil; whereas, for Figure 22 the airfoil was pitching down during at least a portion of the vortex convection. In this regard, Figure 22 demonstrates that the airfoil continued to experience some additional lift during the downward motion, as may be seen by the fact that the maximum lift occurs at a later time than the maximum angle of attack. The integrated lift, however, was less than the maximum lift achievable at the steady angle for maximum lift (in fact, it was 0.761 C_{Lmax} static). Though this in part reflects the fact that the minimum angle of attack was small, we were not able to achieve much better results by varying the minimum angle of attack. Our inability to achieve better "performance" may have been due in part to the fact that the lift actually undershot that commensurate with the stopping angle of attack for the steady-flow case; this may be seen by the lift coefficient actually going negative in Figure 22, while the minimum angle of attack remained positive (~1.0°). Though our tests did not include flow visualization, we interpret the undershoot to a stubborn reattachment. Like Reference 21, such motion histories

also yield large drag penalties. Finally, it should be pointed out that the moment curve clearly indicates the presence/formation of a leading-edge, dynamic-stall vortex.

New Insight. Figure 23 represents one of only a handful of cases run almost by accident; the motion history was not what we were trying to obtain. As described in our "first notions," we were attempting to produce motion histories that brought the airfoil to near, or just beyond the angle of attack for separation at the quarter chord. For both Figure 22 and 23, the quarter-chord separation angles were approximately 24°, commensurate with their pitch-up $\dot{\alpha}_{ND}$'s of 0.0322 and 0.0327 respectively (the corresponding dynamic-stall angles of attack, constant-$\dot{\alpha}$, would have been -30°). It is clear, then, that Figure 23 represents stopping short of the quarter-chord separation angle, and Figure 22 represents stopping after the quarter-chord separation angle but before the dynamic-stall angle; in other words, Figure 22 represents the kind of motion history we were after, and Figure 23 does not. Be that as it may, we were fortunate to have run a few cases like that of Figure 23. Although, in this case the time-averaged lift was only slightly improved from that of Figure 22, 0.833 C_{Lmax} static, there are a number of interesting observations. The first thing to notice is that, although the static-stall angle of attack (approximately 15.5°) was exceeded, the lift seemed to follow the motion history, that is, the maximum lift occurred at the maximum angle of attack. Secondly, the lift did not undershoot that commensurate with the lower stopping angle of attack for the steady case (unlike Figure 22). Thirdly, this motion history shows no appreciable drag rise! Finally, the moment curve implies that no leading-edge vortex was formed; it is as if the flow remained attached (or at least airfoil-contour conforming) during the entire motion history. If, as these curves suggest, the flow did not "separate," then one might suppose that had the lower stopping angle of attack been larger, a higher time-averaged lift might have been achieved.

In fact, we did run some cases where the airfoil motion stopped short of the quarter-chord angle of attack, but whose lower stopping angle was not as low as that for Figure 23; two of these cases are shown in Figures 24 and 25. In both these cases the maximum angles of attack were short of the quarter-chord-separation angle of attack (the quarter-chord-separation angles were approximately 21.5° and 22°, respectively). In both cases the airfoil cycled between 11° and 20°. And in both cases the lift seemed to follow the airfoil motion. The time-averaged

48

lift for the cases of Figure 24 and 25 was 1.108 and 1.114 times the maximum achievable in steady flow, respectively. Although there is some drag rise apparent, it is far less than would normally be expected in dynamic stall. And, although the moment curves give some suggestion of something happening, it appears that full-fledged, dynamic-stall vortices did not form. This "something happening" also jibes with the appearance of some drag rise, and suggests that in the case of Figure 23, the absence of moment aberration (i.e., indicating not only the lack of a developing dynamic-stall vortex, but also the lack of "separation") accounts for the absence of a drag rise.

Unfortunately, more cases were not run to explore this new approach to producing time-averaged lift augmentation; but, those few cases that were run auger for some optimism with regard to producing time-averaged lift greater than that achievable in steady flow and without the associated dynamic-stall-type drag. We are left, then, with a new notion for producing time-averaged lift augmentation: pitch up to some angle greater than the static-stall angle but short of the quarter-chord angle commensurate with the $\dot{\alpha}_{ND}$; pitch down to an "attached-flow" angle; and repeat.

Possible Explanation. We have not studied downward pitching motions (from above the static-stall angle of attack) and thus we are not in a position to offer more than a speculative explanation for the cause for the flow apparently remaining attached in the case of Figure 23, and nearly so in the cases of Figures 24 and 25; however, our theoretical work on the constant-$\dot{\alpha}$, pitch-up problem might offer some insight. Without the benefit of flow visualization we cannot say for certain, but let us suppose that, at least in the case of Figure 23, separation had not progressed forward of the midchord. This assumption has a rational basis since the airfoil stopped several degrees short of the quarter-chord separation angle of attack. While pitch-up motion tends to retard separation, as discussed in detail in Section II, it should be noted that at least the apparent-camber effect (cf., above) would also tend to retard/reattach flow separation during a pitch down if the separation had not progressed forward of the midchord. Perhaps such retardation is sufficient to explain why the flow remained contour following. At a minimum we have learned something new; it has always been assumed that once the airfoil has pitched beyond the static-stall angle of attack, stopping, reversing, or even slowing the pitch rate to below the $\dot{\alpha}_{ND}$ required to keep the flow "attached" for the constant-$\dot{\alpha}$ case meant certain catastrophic

detachment of the flow and formation of the dynamic-stall vortex. Here we have seen that motions are possible that do not result in such flow dynamics.

IV. Epilogue

There are some obvious implications from the work offered in this paper. First, it should be restated that the additional lift provided by the leading-edge, dynamic-stall vortex is a relatively minor contributor to the lift overshoot experienced in a dynamic-stall event. This means that the largest portion of the transient "lift augmentation" is due to the flow remaining "attached" (contour following) to the airfoil. Because the dynamic-stall vortex has played such a prominent roll in our thinking ("vortex fixation"), it has colored notions of how to exploit dynamic-stall-like motions for time-averaged lift augmentation. Our study indicates that such dynamic-stall-vortex-inspired notions are not the way to exploit the phenomenon, but rather, the key is to take advantage of the separation retardation and, in fact, suppress the formation of the dynamic-stall vortex. In terms of control, our results also suggest how one might go about sensing when it is appropriate to begin the pitch-down portion of the motion. Figures 24 and 25 seem to imply that at the first hint the development of a pitch-down moment the airfoil should begin its pitch-down motion. The indication that the time has arrived might be sensed by an increase in the current needed to sustain the upward rate when the pitch mechanism is a servo-type system, as was used in our study.

There is a second implication which is not as pleasant as the first, yet is an unavoidable consequence of our understanding of the dynamic-stall event; because the largest portion of the lift augmentation is provided by "attached flow," the phenomenon itself is inherently severely critical-Mach-number limited. This fact has now been independently confirmed experimentally by Lorber and Carta [Ref. 23]. Perhaps these limitations can be somewhat extended by clever airfoil-section design, as has been done for supercritical airfoils in steady flow, but considerations of critical-Mach-number limitations may no longer be ignored in schemes to exploit dynamic stall.

49

References

1. Kramer, M., "Die Zunahume des Maximalauftriesbes von Tragflugeln bei plotzlicher Anstellwinkelvergro Berung (Boeneffekt)," Zeitschrift fur Flugtechnik und Motorluftschiffahrt, 23, 7, 14 April 1932, pp. 1-5.

2. Jumper, E.J., Schreck, S.J. and Dimmick, R.L., "Lift-Curve Characteristics for an Airfoil Pitching at Constant Rate," J. of Aircraft, 24, October 1987, pp. 680-687.

3. Ericsson, L.E., and Reding, J.P., "Unsteady Airfoil Stall, Review and Extension," J. of Aircraft, 8, August 1971, pp. 609-616.

4. Jumper, E.J., Dimmick, R.L. and Allaire, A.J.S., "The Effect of Pitch Location on Dynamic Stall," Forum on Unsteady Flow Separation, FED - Vol. 52, The American Society of Mechanical Engineers, New York, 1987, pp.201-208.

5. Tupper, K.W., "The Effect of Trailing Vortices on the Production of Lift on an Airfoil Undergoing a Constant Rate of Change of Angle of Attack," Thesis, Air Force Institute of Technology, AFIT/GAE/AA/83D-24, December 1983.

6. Giesing, J.P., "Nonlinear Two-Dimensional Unsteady Potential Flow with Lift," J. of Aircraft, 5, 1968, pp. 135.

7. Chow, C.Y., Huang, M.K., "The Initial Lift and Drag of an Impulsively Started Airfoil of Finite Thickness," J. of Fluid Mechanics, 118, May 1982, pp. 393-409.

8. Milne-Thomson, L.M., Theoretical Aerodynamics, 3th ed., MacMillan and Company, Limited, London, 1958.

9. Wagner, H., "Dynamischer Auftrieb von Tragflugeln," Zeitschrift fuer Angewandte Mathematik und Mechanik, 5, February 1925, p. 17.

10. Lamb, H., Hydrodynamics, Cambridge University Press, London, 1932.

11. Bisplinghoff, R.L., and Ashley, H., Principles of Aeroelasticity, Dover, NY, 1975.

12. Kemp, N.H. (editor), Collected Papers of W. R. Sears through 1973, The Sibley School of Mechanical and Aerospace Engineering, Cornell University, Ithaca, NY, 1974.

13. Daley, D.C. and Jumper, E.J., "Experimental Investigation of Dynamic Stall for a Pitching Airfoil," J. of Aircraft, 21, September 1984, pp. 831-832.

14. Walker, J.M., Helin, H.E., and Strickland, J.H., "An Experimental Investigation of an Airfoil Undergoing Large-Amplitude Pitching Motions," AIAA Journal, 23, August 1985, pp. 1141-1142.

15. Jumper, E.J., Hitchcock, J.E., Lawrence, T.S. and Docken, R.G., "Investigating Dynamic Stall Using a Modified Momentum-Integral Method," AIAA Paper Number 87-0431.

16. Jumper, E.J., "Mass Ingestion: A Perturbation Method Useful in Analyzing Some Boundary-Layer Problems," ASME Paper Number 86-WA/FE-10.

17. Ericsson, L.E., and Reding, J.P., "Stall-Flutter Analysis," J. of Aircraft, 10, January 1973, pp. 5-13.

18. Robinson, M., Helin, H., Gilliam, F., Russell, J., and Walker, J., "Visualization of Three-Dimensional Forced Unsteady Separated Flow," AIAA Paper Number 86-1066.

19. Chow, C.Y., and Chiu, C.S., "Unsteady Loading on Airfoil Due to Vortices Released Intermittently from Its Surface," J. of Aircraft, 23, October 1986, pp. 750-755.

20. Ericsson, L.E., "Effect of Karman Vortex Shedding on Stall Flutter," AIAA Paper Number 86-1789-CP.

21. McAllister, K.W., Carr, L.W., and McCroskey, W.J., "Dynamic Stall Experiments on the NACA 0012 Airfoil," NASA Technical Paper 1100.

22. Stephen, E.J., "Investigation of Periodic Pitching Through the Static Stall Angle of Attack," Thesis, Air Force Institute of Technology, AFIT/GAE/AA/87M-4, March 1987.

23. Lorber, P.F., and Carta, F.O., "Airfoil Dynamic Stall at Constant Pitch Rate and High Reynolds Number," AIAA Paper Number 87-1329.
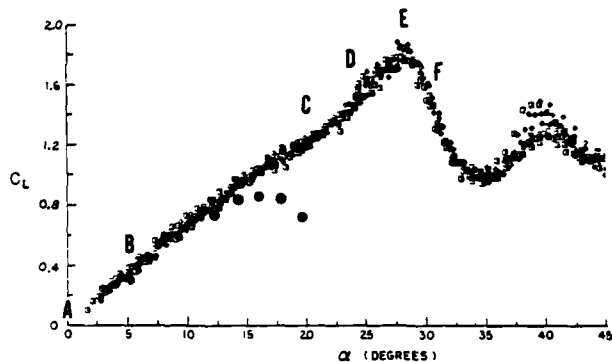
Figure 1. Overlay of coefficient-of-lift versus angle-of-attack data for ten constant-$\dot{\alpha}$, dynamic stall events, five at 69°/s and 26.6 ft/s, and five at 89°/s and 34.4 ft/s; both dynamic combinations have $\dot{\alpha}_{ND}$ = 0.023. The darkened circles indicate the airfoil's static performance. The A - F labels indicate various stages of the dynamic-stall process, see details in text.
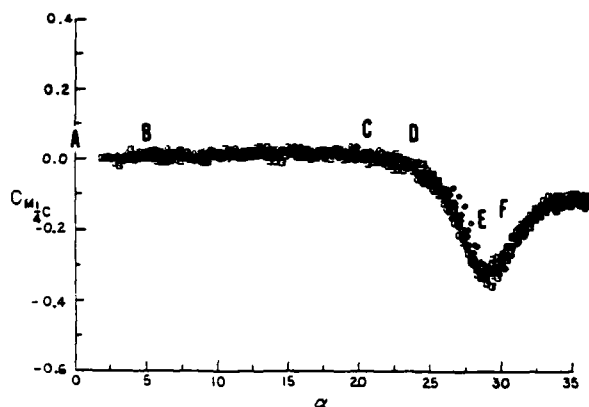
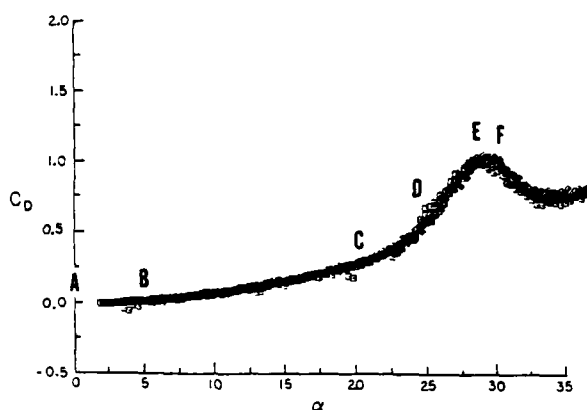**Figure 3.** Same as Figure 1, but for coefficient of moment (at the quarter chord) versus angle of attack.

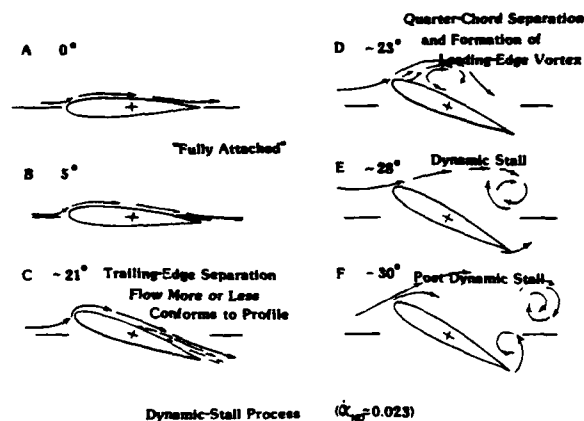**Figure 2.** Same as Figure 1, but for coefficient of pressure drag versus angle of attack.

Figure 4. Schematic representation of the flow at the stages of the dynamic-stall process indicated by the A - F labels in Figures 1 - 3.

A 0° "Fully Attached"

B 5°

C ~21° Trailing-Edge Separation Flow More or Less Conforms to Profile

D ~23° Quarter-Chord Separation and Formation of Leading-Edge Vortex

E ~28° Dynamic Stall

F ~30° Post Dynamic Stall
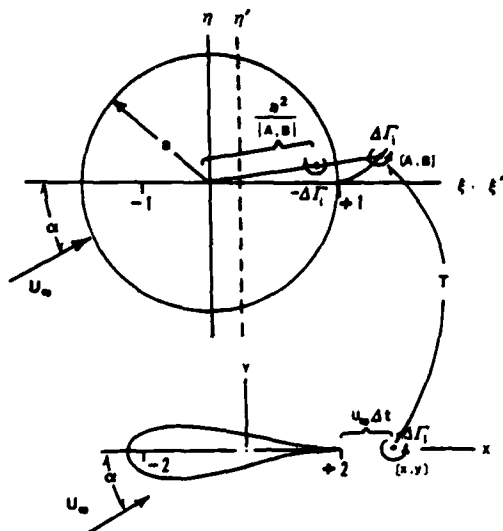
Dynamic-Stall Process $(\dot{\alpha}_{ND}=0.023)$

Figure 5. Circle/intermediate plane and physical plane for a Joukowski airfoil indicating the introduction of the ith discrete free vortex (and its bound partner) into the flow.

Figure 7. Comparison of the present-method predicted unsteady lift on a 25.5% thick symmetric Joukowski airfoil at angle of attack impulsively set into motion, with that of Giesing [Ref. 7]; the Wagner [Ref. 9] flat-plate solution is also shown.
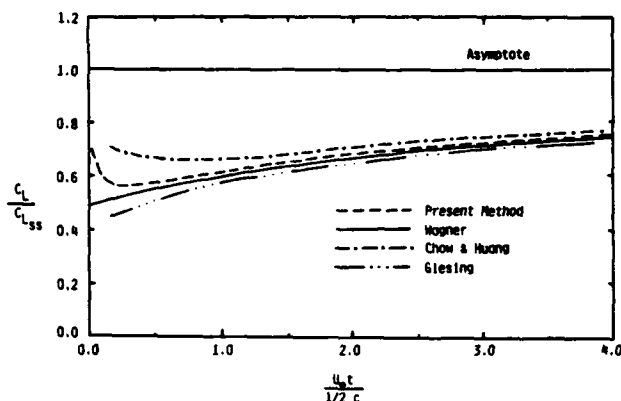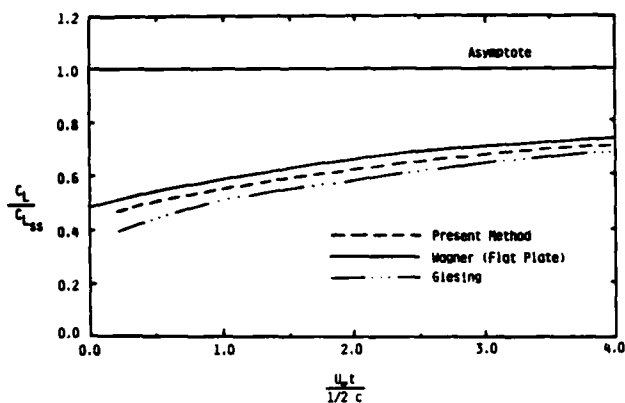

Figure 6. Comparison of the present-method predicted unsteady lift on a flat plate at angle of attack impulsively set into motion, with the analytic solution of Wagner [Ref. 9], and the numerical results of Giesing [Ref. 6], and Chow and Huang [Ref. 7].
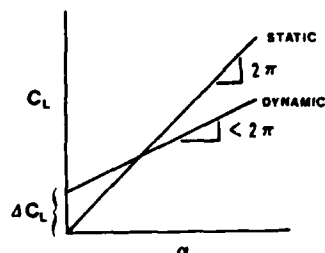
Figure 8. Predicted effect on the coefficient-of-lift versus angle-of-attack curve for a Joukowski airfoil initially at 0° angle of attack in a uniform free stream, suddenly placed into a constant-$\dot{\alpha}$ pitching motion.

$$C_{L_\alpha} \cong 3.6 + 2.68 \exp(-\dot{\alpha}_{ND} \times 10^3 / 4.216)$$

Figure 9. Predicted effect on the slope of the C_L-α curve as a function of $\dot{\alpha}_{ND}$ for a Joukowski airfoil pitching at constant rate.
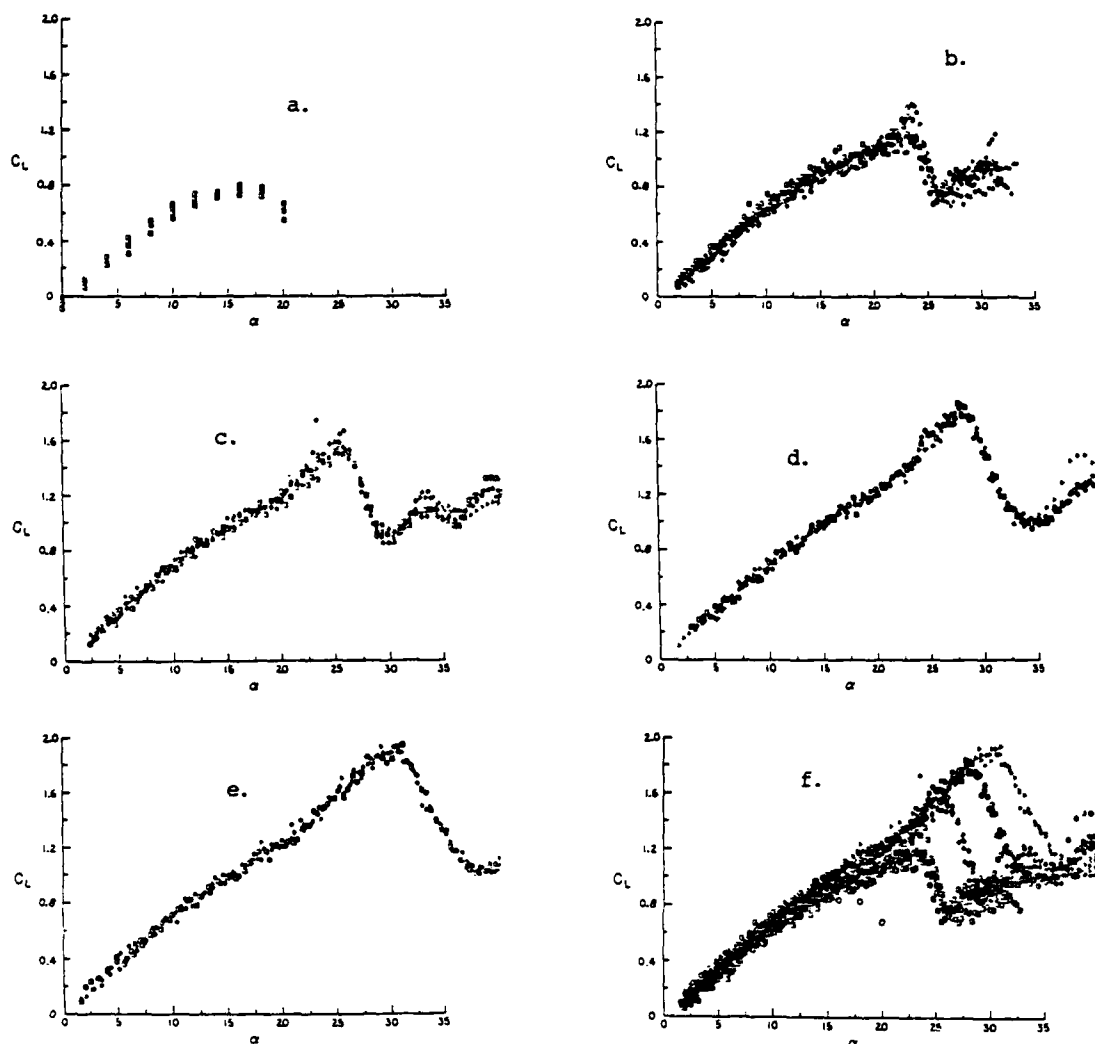
Figure 10. Series of wind-tunnel data of coefficient-of-lift versus
angle of attack for an airfoil at a tunnel speed of 26.6 ft/s,
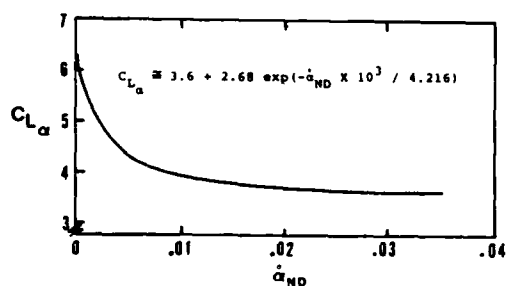including the static data (a.), and four constant-$\dot{\alpha}$ pitching cases with
angular rates of b. 29.34°/s, c. 52.16°/s, d. 69.49°/s, and e. 87.15°/s;
f. is an overlay of a - e. For further explanation see Reference 2.

Figure 11. Straight-line fits of the
linear portions of lift curves, like
those of Figure 10, for five tunnel
speeds. Numbers increase for increasing
$\dot{\alpha}$ at a given tunnel speed, 1 being the
static slope: a. 26.6 ft/s, b. 30.2 ft/s,
c. 34.4 ft/s, d. 39.9 ft/s, e. 47.8 ft/s.
For further explanation see Reference 2.

Figure 12. Experimentally-determined change (from static) in quarter-chord-separation angle of attack versus non-dimensional angular rate [Ref. 13].
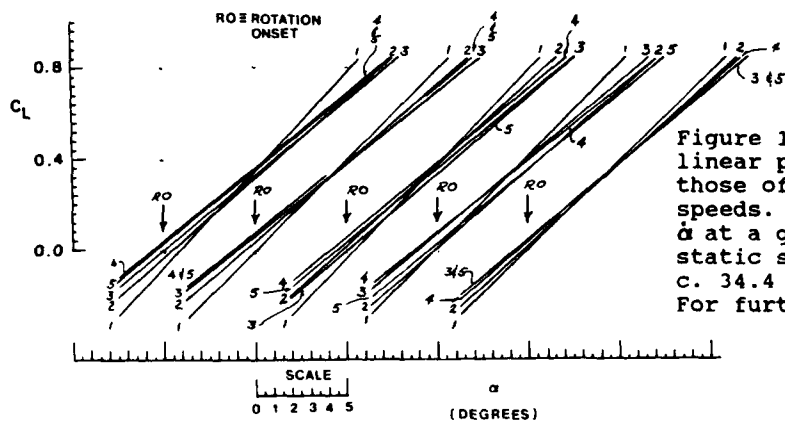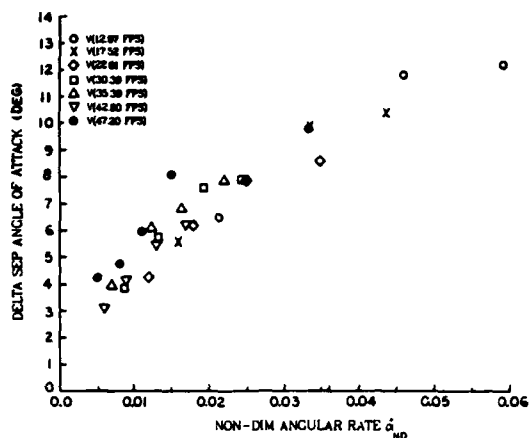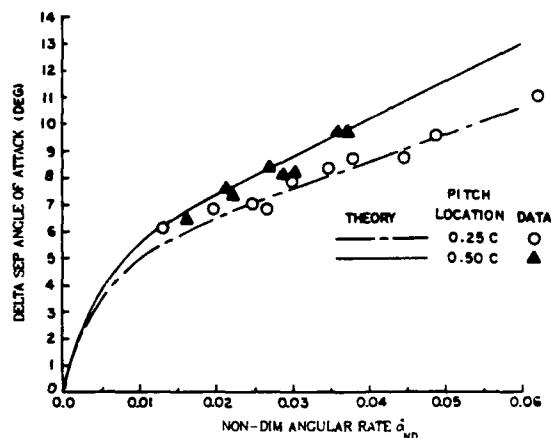

Figure 14. Comparison of the theoretical prediction of the effect of pitch-location change on the delay (from static) in quarter-chord separation, with experimental data [Ref. 4].
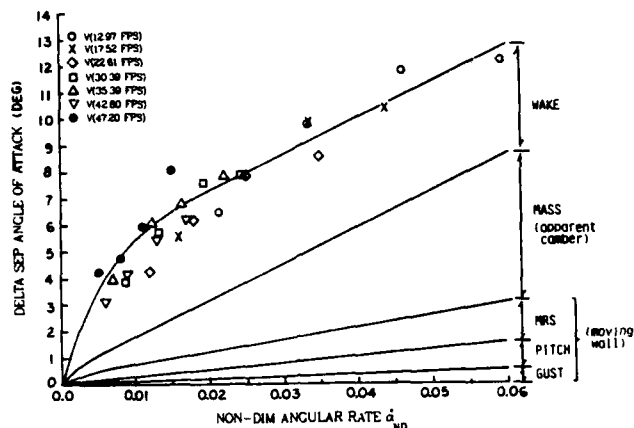
Figure 13. Theoretical predictions for the delay (from static) in quarter-chord-separation angle of attack as a function of non-dimensional angular rate, showing the contribution due to the moving wall (i.e., simple unsteadiness, GUST; motion of the wall in the direction of the flow, PITCH; and the MRS separation criteria), due to the apparent camber, and due to the wake. The wake effect followed the functional form of Eq. (3) with an empirically-determined coefficient [Ref. 4]; the functional form, including the coefficient is $\Delta\alpha_w = 4.125(1.0 - \exp(-\dot{\alpha}_{ND} \times 10^3/4.216)$.
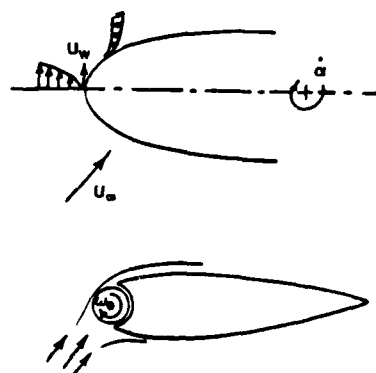
Figure 15. Schematic representation of the "Wall Jet" effect showing the analogy between the motion of the wall in the direction of the flow (i.e., tangent to itself) and a fixed airfoil with a rotating leading edge [Ref. 17]. The theoretical prediction of this effect is shown in Figure 13 by the effects identified as "moving wall."

54
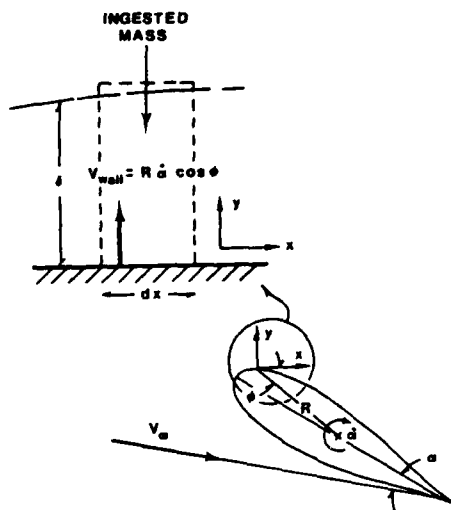
Figure 16. Schematic representation of the effect of the motion of the airfoil surface (wall) moving into the flow (i.e., normal to itself) [Ref. 16].
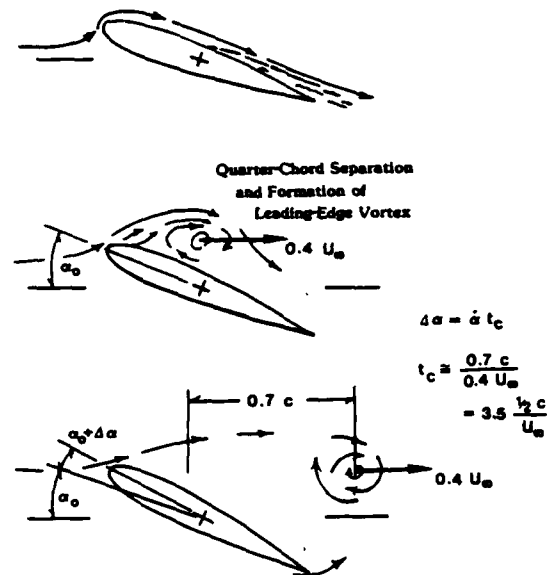
Figure 18. Schematic representation of the change in the airfoils angle of attack during the time the leading-edge vortex continues to cause an increase in lift.
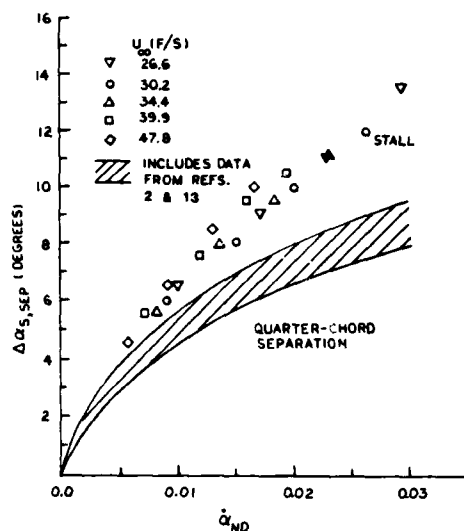
Figure 17. Dynamic delay from static conditions in the angle of attack for quarter-chord separation, and stall as functions of non-dimensional pitch rate [Ref. 2].
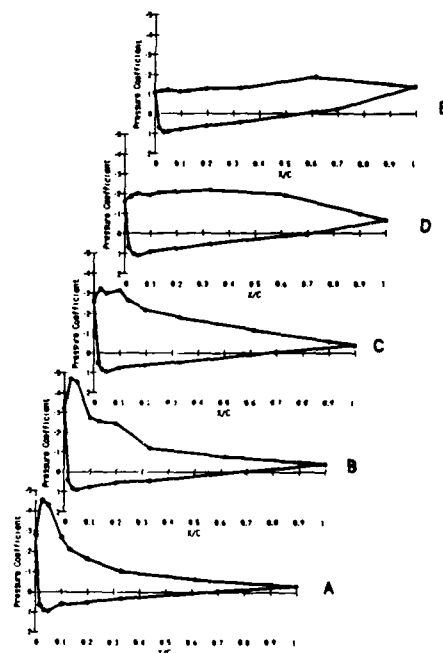
Figure 19. Series of C_p distributions for $\dot{\alpha}_{ND}$ = 0.022, where quarter-chord separation was at approximately $23°$ and dynamic stall at approximately $27°$; the angles of attack presented are: a. $20.2°$, b. $22.3°$, c. $24.3°$, d. $26.4°$ and e. $29.4°$. [Ref. 2].
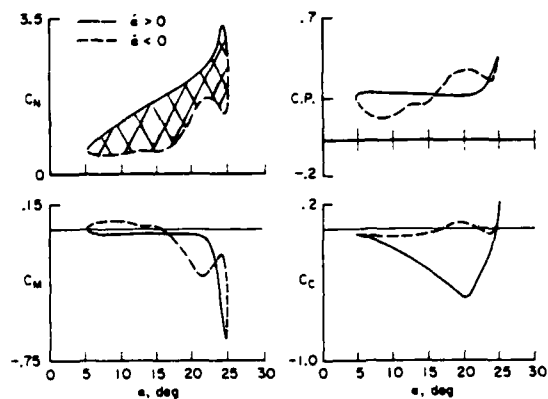
Figure 20. Results from McAllister, Carr and McCrosky for the sinusoidal motion $\alpha(t) = 15° + 10° \sin(\omega t)$, at a reduced frequency of 0.15 [Ref. 21].

Figure 22. Angle-of-attack, coefficient-of-lift, coefficient-of-pressure-drag, and quarter-chord-coefficient-of-moment time histories for $(\dot{\alpha}_{ND})_{up} = 0.0322$, $(\dot{\alpha}_{ND})_{down} = 0.08$; time-averaged lift is 0.761 $(C_{Lmax})_{static}$.

Figure 21. Pressure transducer locations.
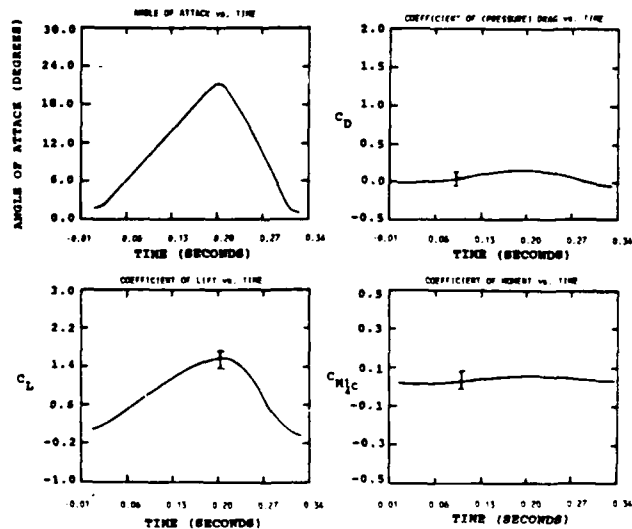
Figure 23. Same as Figure 22, but for $(\dot{\alpha}_{ND})_{up} = 0.0327$, $(\dot{\alpha}_{ND})_{down} = 0.0725$; time-averaged lift is 0.833 $(C_{Lmax})_{static}$.
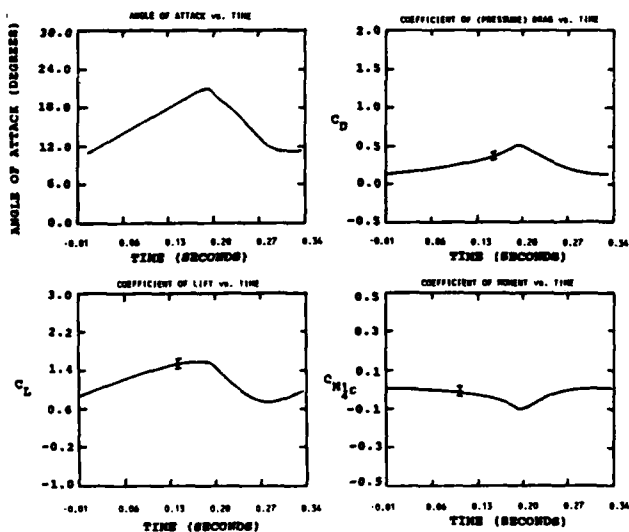
Figure 24. Same as Figure 22, but for
$(\dot{\alpha}_{ND})_{up} = 0.0119$, $(\dot{\alpha}_{ND})_{down} = 0.0208$;

time-averaged lift is 1.108 $(C_{Lmax})_{static}$.
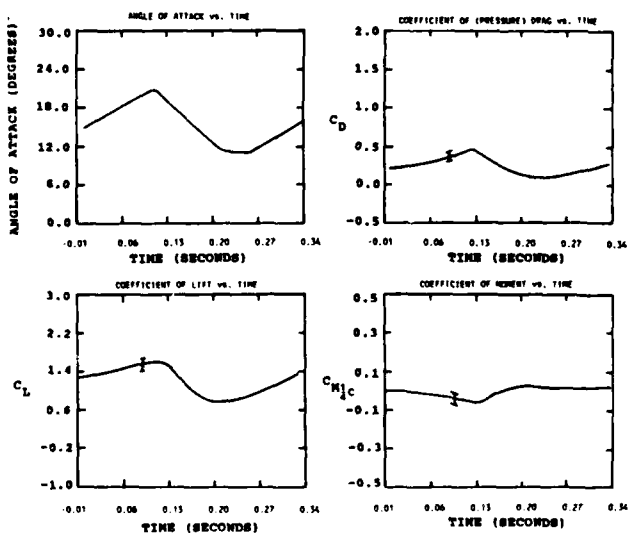
Figure 25. Same as Figure 22, but for
$(\dot{\alpha}_{ND})_{up} = 0.0142$, $(\dot{\alpha}_{ND})_{down} = 0.025$;

time-averaged lift is 1.114 $(C_{Lmax})_{static}$.

Airfoil Dynamic Stall at Constant Pitch Rate and High Reynolds Number

Peter F. Lorber[*] and Franklin O. Carta[**]
United Technologies Research Center
East Hartford, CT 06108

Abstract

An experiment has been performed to study the aerodynamics of dynamic stall penetration at constant pitch rate and high Reynolds' number, in an attempt to more accurately model conditions during aircraft post-stall maneuvers and during helicopter high speed forward flight. An airfoil was oscillated at pitch rates, $A = \dot{\alpha} c/2U$, between 0.001 and 0.020, Mach numbers between 0.2 and 0.4, and Reynolds numbers between 2×10^6 and 4×10^6. Surface pressures were measured using 72 miniature transducers, and the locations of transition and separation were determined using 8 surface hot film gages. The results demonstrate the influence of the leading edge stall vortex on the unsteady aerodynamic response during and after stall. The vortex is strengthened by increasing the pitch rate, and is weakened by increasing the Mach number and by starting the motion close to the steady-state stall angle. A periodic pressure oscillation occurred after stall at high pitch angle and moderate Reynolds number; the oscillation frequency was close to that predicted for a von Karman vortex street. A small supersonic zone near the leading edge at $M = 0.4$ was found to significantly reduce the peak suction pressures and the unsteady increments to the airloads. These results provide the first known data base of constant pitch rate data at realistic combinations of Reynolds and Mach number.

Nomenclature

A pitch rate, $\dot{\alpha} c/2U$, rad/sec
c airfoil chord, m
C_D section pressure drag coefficient, D/Qc
C_L section lift coefficient, L/Qc
C_M section pitching moment coefficient about $x/c = 0.25$, M/Qc^2
C_p pressure coefficient, $(P-P_{static})/Q$
k reduced frequency of sinusoidal motion, $\omega c/2 U$
Q freestream dynamic pressure, $0.5 \rho U^2$, Pa
t time from start of data acquisition, sec
T data acquisition period, sec
Re Reynolds number, $c U/\nu$
U freestream velocity, m/sec
x distance from airfoil leading edge, m
α geometric pitch angle, deg
ν kinematic viscosity, m^2/sec
ρ air density, kg/m^3
τ nondimensional time, t/T
ω frequency of sinusoidal oscillation, $2\pi f$

Introduction

The aerodynamic effect of rapidly pitching an airfoil beyond its steady-state stall angle has been studied by numerous investigators. An extensive period of experimentation occurred between the early 1960's and the mid 1970's. This work emphasized application to the retreating blade stall of a helicopter rotor that occurs in high speed forward flight. Consequently, measurements were typically made of the unsteady airloads during sinusoidal pitching oscillations in the range of 0 to 20 deg, and at Mach and Reynolds numbers characteristic of the retreating blade of a helicopter ($M < 0.4$, $Re < 5 \times 10^6$). Representative efforts were reported in Refs. 1-4.

A more recent interest has developed in using the lift and drag augmentations that occur during dynamic stall to improve combat aircraft maneuverability (Refs. 5-6). Such maneuvers typically involve a rapid controlled pitching of the aircraft to very high angle of attack at low to moderate Mach numbers. Several experiments have been performed to study constant pitch rate dynamic stall. The early work of Ham and Garelick (Ref. 7) measured the surface pressures on a NACA 0012 airfoil that was pitched up to 20 to 30 deg at roughly constant nondimensional rates, $A = \dot{\alpha} c/2U$, between 0.005 and 0.02 and at the moderate Reynolds number of 3.4×10^5. Additional constant pitch rate experiments have been reported in Refs. 8-12. These studies have concentrated on obtaining airload and flow visualization results for large amplitude motions (up to $\alpha = 90$ deg) at high pitch rates (up to $A = 1.0$). However, this work was conducted at Mach numbers less than 0.1 and Reynolds numbers between 4×10^4 and 3×10^5, values substantially below those of a typical fighter wing during low-speed maneuvers ($10^6 < Re < 10^8$). Steady-state measurements for $Re < 5 \times 10^5$ indicate that stall frequently occurs when the laminar upper surface flow separates near the leading edge (Ref. 13). This process leads to large steady-state stall hysteresis. A turbulent boundary layer separation is more common at higher Reynolds number. It is likely that the unsteady stall characteristics also differ with Reynolds number.

The current experiment was designed to provide detailed aerodynamic information at a more representative scale. Earlier dynamic stall

[*]Associate Research Engineer. Member AIAA.
[**]Supervisor, Aerodynamics Group. Associate Fellow AIAA.

studies at the United Technologies Research Center (UTRC) used a tunnel-spanning-wing system to oscillate an airfoil in a sinusoidal motion (Ref. 14-15). A new version of this apparatus has been built that incorporates a high response hydraulic drive system capable of producing arbitrary airfoil pitching motions. The first use of this system was to measure surface pressures and flow conditions for a series of constant pitch rate ramps and sinusoidal oscillations at Mach numbers between 0.2 and 0.4, Reynolds numbers between 2 and 4×10^6, and pitch rates between A = 0.001 and 0.02.

Experiment

The model wing consists of a set of fiberglass panels mounted on a steel spar that spans the 8 ft (2.44 m) test section of the UTRC Large Subsonic Wind Tunnel (Fig. 1). A Sikorsky SSC-A09 airfoil with a 17.3 in (43.9 cm) chord was used (Fig. 2). This is a 9% thick supercritical section designed for low drag at high subsonic Mach numbers. The pitch angle of the model is set by hydraulic actuators that are attached to each end of the spar and controlled using a dual channel closed-loop system. A digital waveform synthesizer provides the sinusoidal or ramp input to the hydraulic controller and triggers the data acquisition system. This allows 1024 samples of each data channel to be acquired at identical positions during each cycle of the wing motion.
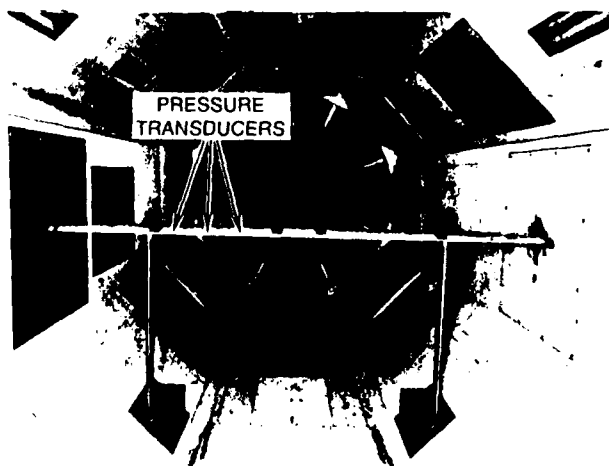

Fig. 1   Tunnel-spanning wing model in the 8 ft (2.4m) test section of the UTRC wind tunnel.

Fig. 2   SSC-A09 airfoil section.

The wing-mounted instrumentation consists of 72 miniature pressure transducers and 8 surface hot film gages. The pressure transducers are mounted inside the fiberglass skin and are connected to the surface by short pipettes. This technique provides a point measurement on a smooth surface contour and retains a frequency response that is flat within 5% out to at least 5 kHz. Each group of eight pressure transducers is connected to an electronic power distribution and switching circuit located inside the model. An ensemble average based upon 20 cycles of the motion is digitized, converted to pressure coefficient, and stored on magnetic tape.

The primary chordwise pressure transducers are located in arrays of 18 on each surface, 0.5 chord-lengths from the tunnel centerline, and 2.3 chord-lengths from the side wall. The transducers are arranged in a segmented Gaussian array from x/c = 0.005 to x/c = 0.99 to minimize the integration error in computing the sectional airloads. The other 36 transducers are located in additional arrays located 1.8 and 1.4 chord-lengths from the wall, and are primarily intended for use in future swept wing and finite tip experiments. During this experiment the additional arrays were used to verify the two-dimensionality of the flow. With the exception of an apparent irregularity in the formation of the leading edge vortex at x/c = 0.010 at the stations furthest from the centerline, the data show only a small amount of spanwise variation. The pressure transducers are calibrated by placing the instrumented section of the wing inside an environmental chamber, and recording the output voltages over the full expected range of pressures and temperatures. The data system is then able to correct for any thermal changes in each transducer's sensitivity and offset voltage. This technique, in combination with the acquisition of frequent wind-off transducer zeros, allows both mean and unsteady pressures to be determined to within ±1% of the calibration range. The data reported here do not include any corrections for wind tunnel interference. The hot film gages are located along an array parallel to the primary pressure array. The gage closest to the leading edge is at x/c = 0.026, and that closest to the trailing edge is at x/c = 0.880. No calibration was performed since the hot films are intended to provide only qualitative information on the location of transition, separation, and reattachment. Additional information on the experimental apparatus is given in Ref. 16.

Unsteady data were acquired for 36 constant pitch rate ramps and 9 sinusoidal oscillations, as shown in Table 1. The maximum pitch rate of 360 deg/sec occurred at A = 0.02 and M = 0.2, and the minimum of 18 deg/sec at A = 0.001. The maximum rate is lower than the maximum reached in many smaller scale experiments (Refs. 8-12), but is larger than that for both the 'typical' (A = 0.0010) and 'minimum time' (A = 0.0044) maneuvers described in Ref. 5. The wing angle-of-attack was limited by the support system to a maximum of 30

Table I   Test Conditions Studied

a) Ramps

| M	α range	Pitch Rate 0.0010	0.0025	0.0050	0.0100	0.0200
0.2	0-10 deg	x	x	x	x	
	0-20	x	x	x	x	
	0-30	x	x	x	x	x
	10-20	x	x	x	x	
	12-22	x		x		
	14-24				x	
	20-30	x	x			
	20-10	x			x	
	30-0	x		x		
0.3	0-20			x		
	0-30				x	
0.4	0-10	x		x		
	0-20	x	x	x	x	
	20-0				x	

b) Sinusoids

M	α	Reduced Frequency, k 0.025	0.050	0.100
0.2	6- 6cos ωt	x		
	10-10cos ωt	x	x	x
	20-20cos ωt	x	x	x
0.3	9- 8cos ωt		x	
	12- 8cos ωt			x

deg, again less than the maximum obtained in the smaller scale tests, but sufficient to include all of the primary stall-related events at the pitch rates used. The airfoil motion for a ramp consists of an initial delay of several seconds at the minimum angle, a constant rate increase to the maximum angle, a second delay at the maximum angle, and a return to the initial condition. Data are acquired only during a small portion, T, of this cycle. Time histories of the pitch angle during the data acquisition period are shown in Fig. 3 for several 0 to 30 deg ramps at M = 0.2. The ramp begins at a nondimensional time, $\tau = t/T$, of 0.125 and ends at $\tau = 0.625$. The pitch increase is quite linear with time and has sharp corners for A < 0.0050. At higher pitch rates the damping of the hydraulic system rounds the corners, but still maintains a nearly linear pitch rate near stall.

Steady-state Results

Steady pressure data were acquired at M = 0.2 and 0.4. As shown in Fig. 4, the SSC-A09 airfoil has conventional stall characteristics at these Mach numbers. At M = 0.2 the maximum C_L of 1.4 is reached at α = 14 deg, and is followed by a rapid drop to a C_L of 0.9 at α = 17 deg. Increasing the Mach number to 0.4 reduces the maximum C_L to 1.2 and flattens the stall. The pressure distributions include a very strong leading edge suction peak prior to stall. The maximum suction occurs at α = 13 deg, and reaches values of C_p = -8.2 at M = 0.2 and C_p = -5.2 at M = 0.4, as shown in Fig. 5. Since the sonic pressure coefficient at M = 0.4 is -3.7, a small supersonic zone exists at the leading edge, terminated in a shock near x/c = 0.03. The compressibility effects associated with this zone create the lift curve differences seen in Fig. 4. Between α = 15 and 17 deg, the flow is separated over the rear of the airfoil at both Mach numbers, but maintains a pressure gradient near the leading edge. At higher angles of

Fig. 3 Time histories of the pitch angle for 0 to 30 deg ramps at M = 0.2.
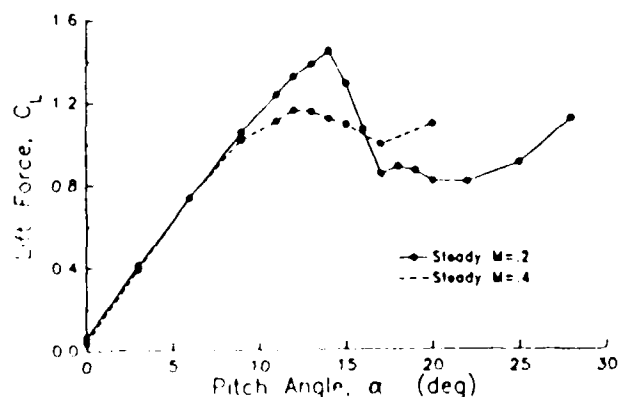
Fig. 4 Steady state lift at M = 0.2 and M = 0.4.
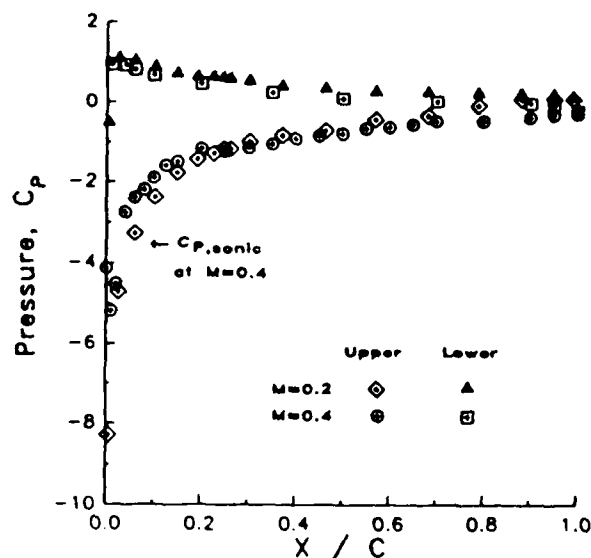
Fig. 5 Steady state pressures at $\alpha = 13$ deg for $M = 0.2$ and 0.4.

Fig. 6 Upper surface pressure coefficient time histories for a 0 to 30 deg ramp at $M = 0.2$ and $A = 0.005$.

attack, the region of attached flow disappears at $M = 0.2$ and is greatly reduced at $M = 0.4$. These steady characteristics indicate that stall is caused by massive separation of a turbulent boundary layer rather than by the bursting of a laminar leading edge bubble.

Results for an $A = 0.005$, $M = 0.2$ Ramp

The characteristics of constant pitch rate motion at $M = 0.2$ will be discussed using the example of a 0 to 30 deg ramp at $A = 0.0050$. The ensemble averaged upper surface pressure time histories for 11 of the 18 chordwise locations are shown in Fig. 6. The ordinate scale on the lower left refers absolutely to the curve for $x/c = 0.005$. For clarity, each additional curve is offset vertically by $\Delta C_p = 1.0$, and each curve is referenced to its own origin, as indicated by the upper left scale. The pressure responds smoothly to the imposed pitch angle until maximum suction is reached at $\tau = 0.40$ ($\alpha = 15.5$ deg). This is identified as letter A in Fig. 6. At this time the peak suction pressure at $x/c = 0.005$ is $C_p = -12.5$, which corresponds to a local Mach number of 0.84. The rapid local increase in pressure associated with passage of the vortex (letter B) is only observed for $x/c > 0.1$, implying that the vortex forms ahead of this position and travels downstream after its release. This disturbance propagates along the airfoil chord at 0.16U, and reaches the trailing edge at $\tau = 0.45$. For $\tau > 0.50$ the upper surface separation is massive and the pressures vary little in either time or position along the chord (letter C). All of the stall-related events are completed well before the airfoil motion stops at $\tau = 0.625$
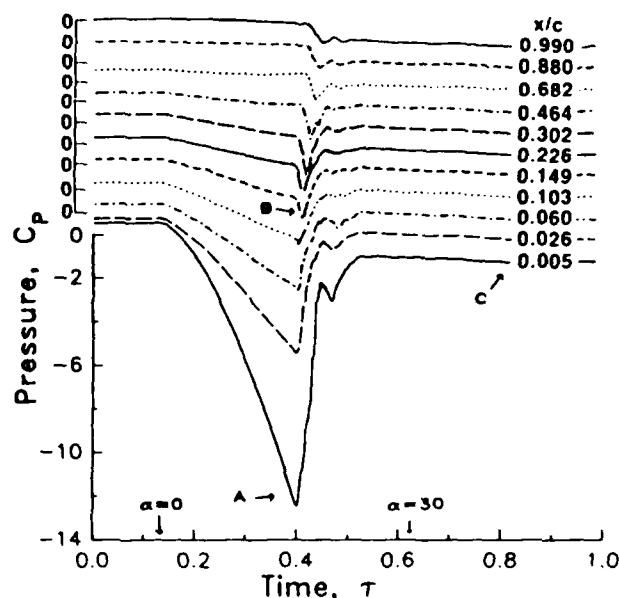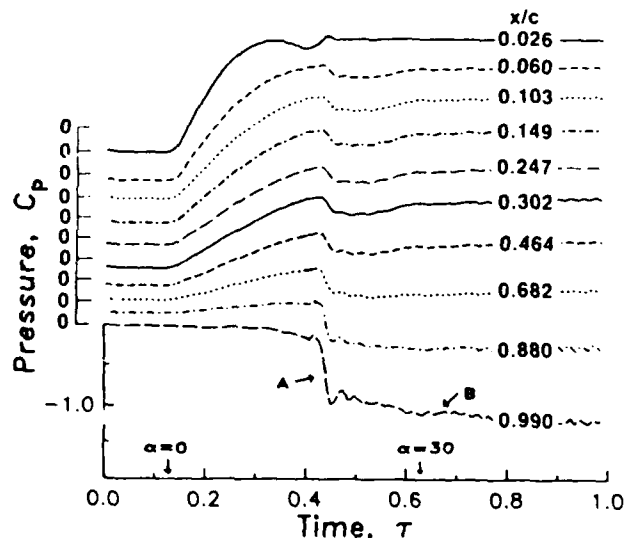
Fig. 7 Lower surface pressure coefficient time histories for a 0 to 30 deg ramp at $M = 0.2$ and $A = 0.005$.

The lower surface does not separate and therefore has pressure time histories that are quite different, as shown in Fig. 7. There is a vertical shift of the successive curves in this figure of $\Delta C_p = 0.25$. The pressures near the leading edge are influenced by the aft motion of the stagnation point to $x/c = 0.060$ at $\tau = 0.40$, and then forward to $x/c = 0.026$ following stall. Downstream of stagnation the pressures generally respond smoothly to the changes in pitch. An exception is a rapid change when the upper surface separates at $\tau = 0.40$ (letter A in Fig. 7). The largest change at this time occurs near the trailing edge, where the pressure is required to match that on the upper surface. A periodic

62

oscillation in the ensemble averaged pressures is also present at the rear of the lower surface (letter B). The oscillation frequency of 62 Hz is very close to the 65 Hz frequency calculated for the von Karman vortex street shed by a circular cylinder having a diameter, D, equal to the vertical projection of the airfoil chord, c sinal. As discussed in Ref. 17, a cylinder will generate a vortex street at a Strouhal number, fD/U, of 0.21 for Reynolds numbers less than 10^6 and at $fD/U = 0.27$ for $Re > 3 \times 10^6$. No regular vortex street is formed when the Reynolds number is between these limits. The Reynolds number of the cylinder equivalent to this airfoil at $M = 0.2$ and $\alpha = 30$ deg is 10^6, a value near the boundary where periodic oscillations should cease.

A larger post-stall oscillation amplitude is found for individual records of the motion than for the ensemble average. The top time history in Fig. 8 represents the ensemble averaged lower surface pressure at $x/c = 0.99$, while the lower five curves represent individual records. Each curve is offset vertically by $C_p = 0.5$. The oscillations have the same frequency and a similar maximum amplitude during each record, but they are not very well correlated in phase. The resulting cancellation greatly reduces the ensemble-averaged amplitude. A separate oscillation at a lower frequency is frequently present immediately following the passage of the stall vortex at $\tau = 0.45$ (letter A in Fig. 8), and may result from secondary stall vortices.

A quantitative measure of the degree of randomness is provided by the root-mean-square variation of the individual records about the ensemble average. Figure 9 shows time histories of the rms pressure coefficient on the upper surface. The curves are offset vertically and each begins at a value of approximately 0. The rms is greatest during separation ($0.4 < \tau < 0.5$) and near the
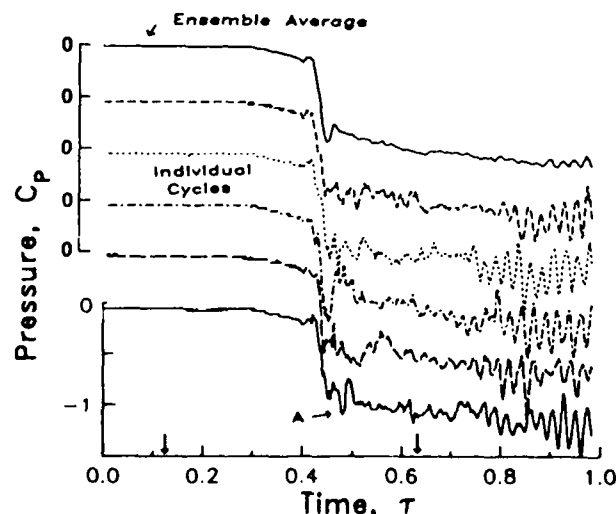
Fig. 8 Pressure coefficient time histories on the lower surface at $x/c = 0.99$ - ensemble averaged and individual cycle results for a 0 to 30 deg ramp at $M = 0.2$ and $A = 0.005$.
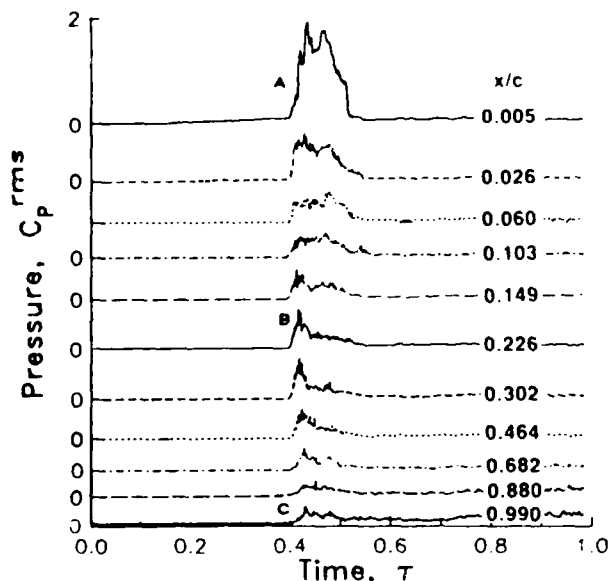
Fig. 9 Time histories of the root-mean-square upper surface pressure coefficient for a 0 to 30 deg ramp at $M = 0.2$ and $A = 0.005$.

leading edge (letter A). Aft of the stall vortex release point ($x/c = 0.1$) the rms has a peak that corresponds to the passing vortex (letter B). Near the trailing edge this peak is preceded by a region of more gradual increase in the rms (letter C), implying that irregular pressure disturbances caused by stall reach the downstream stations ahead of the vortex. The rms at the rear of the airfoil also has an overall increase after stall caused by the non-synchronous oscillations induced by the vortex street. The concentration of this post-stall oscillation near the trailing edge implies that it results from vorticity shed from the trailing edge rather than from the separation point near the leading edge.

Hot Film Gage Results

Further information on the surface flow conditions is provided by the hot film gages. Ensemble averaged time histories of the hot film output at six stations are shown in Fig. 10. The data are self-scaled so that the difference between the maximum and minimum values is one unit. The boundary layer is initially laminar at $x/c = 0.026$ and 0.060 and is turbulent for $x/c > 0.1$ (the gage at $x/c = 0.103$ was not functioning during this run, but indicated turbulent flow at similar conditions during other runs). The transition point, as indicated by a rapid rise in heat transfer, moves forward past $x/c = 0.060$ at $\tau = 0.241$ ($\alpha = 7.0$ deg) and past $x/c = 0.026$ at $\tau = 0.254$ ($\alpha = 7.7$ deg). Transition occurs ahead of $x/c = 0.026$ for the remainder of the cycle. (Appendix A describes a new method that has been developed to determine the transition point from the rms pressures. This technique may allow this information to be obtained much more easily in complex unsteady or three-dimensional flows, in particular when pressure transducers are the primary instrumentation.)

63

Fig. 10   Skin friction gage time histories for a 0 to 30 deg ramp at M = 0.2 and A = 0.005.

Fig. 11   Upper surface pressure time histories at pitch rates for a 0 to 30 deg ramp at M = 0.2 and A = 0.020.

Fig. 12   Location of the stall vortex for 0 to 30 deg ramps at M = 0.2, as determined by the times of minimum pressure.

Ahead of the stall vortex release point ($x/c = 0.1$) the heat transfer drops when the boundary layer separates at $\tau = 0.40$. Downstream of the release point the heat transfer drops slightly at separation but then rises rapidly as the high velocities induced by the stall vortex pass each gage. There is excellent agreement between the times of separation as measured by the hot film gages and by the adjacent pressure transducers.
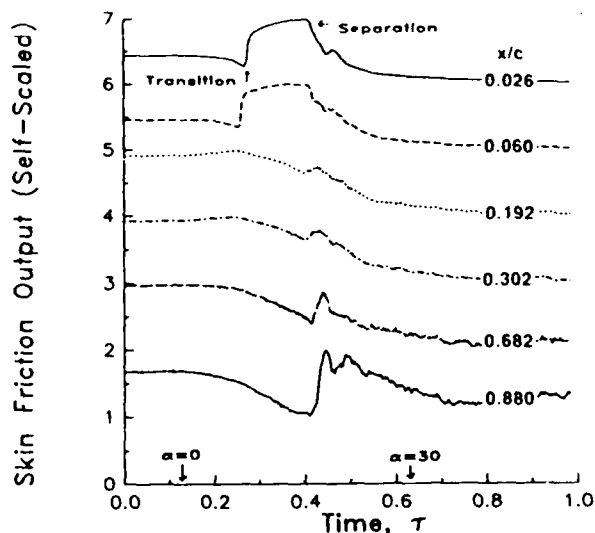
The location of transition in unsteady flow at high Reynolds number is primarily influenced by changes in the pitch rate. The forward motion of the transition point is delayed by increasing the pitch rate. As indicated by the hot film results of Ref. 16, transition passes the gages at a pitch angle about 2 deg higher at A = 0.020 than at A = 0.001. Doubling the freestream velocity to produce M = 0.4 and Re = 4×10^6 causes only minor changes in the motion of the transition point. At the same nondimensional pitch rate, transition moves forward at pitch angles only 0.2 to 0.3 deg lower than at Re = 2×10^6 (Ref. 16).

The Effect of Pitch Rate

Detailed pressure and hot film data for five 0 to 30 deg ramps at M = 0.2 are presented in Ref. 16. Only the A = 0.02 upper surface pressure results are presented here (Fig. 11). Qualitative similarity exists before stall; the primary differences occur during and after stall. The unsteady increments to the airloads are strongly influenced by the strength of the stall vortex. This strength may be estimated by measuring the change in C_p induced at $x/c = 0.302$. This increment increases from $\Delta C_p = 1.0$ at A = 0.001 to $\Delta C_p = 1.5$ at A = 0.005 and to $\Delta C_p = 2.5$ at A = 0.020. The speed with which the vortex travels

downstream may be estimated using the times of minimum pressure at each transducer. Figure 12 shows these times at five pitch rates. The region of constant vortex speed generally begins near $x/c = 0.10$ and ends between $x/c = 0.80$ and 0.90. The speed in this region increases approximately linearly with pitch rate, from 0.13U at A = 0.001 to 0.33U at A = 0.020. Both the location of the constant speed region and the variation with pitch rate are consistent with the results of Ref. 15 for a sinusoidally oscillating NACA 0012 airfoil at similar values of M and Re.

The post-stall pressure oscillations noted earlier change character at pitch rates above A = 0.010. At all lower pitch rates the persistent oscillations have frequencies between 59 and 62 Hz and do not occur with the same phase during each

individual record. By A = 0.020 the oscillations have shifted frequency to 51 Hz and have synchronized with the imposed airfoil motion and with the stall vortex, producing the large pressure response indicated by letter A in Fig. 11. Large oscillations are also observed in the integrated force and pitching moment results shown in Fig. 13. Previous studies of sinusoidal motions of several airfoil sections at Re = 3-4x10^{6} produced similar large post-stall oscillations for some, but not all, of the sections (Ref. 18). Jumper (Ref. 9) also observed large oscillations in the lift response during constant rate ramps of a NACA 0015 airfoil at pitch rates similar to the current experiment but at smaller scale (1.5 x 10^{5} < Re < 2.8 x 10^{5} and M < 0.05). Other studies at apparently similar conditions (Ref. 11 and 12) did not show such large oscillations. The differences among the results at lower Reynolds number may result from differences in airfoil shape or from differences in the wind tunnel turbulence level and mounting technique. These have been shown to cause significant differences between steady-state results at low Reynolds numbers (Ref. 13). It is therefore not clear what, besides high pitch rate, is required to produce strong and synchronized post-stall oscillations.

The integrated lift, pressure drag, and pitching moment (Fig. 13) show the anticipated qualitative trends with increasing pitch rate: 1) Before the stall vortex is formed, increasing the pitch rate decreases the lift slope, decreases the pitching moment, and increases the drag. The lift slope effect agrees with the results of Ref. 9 at lower Reynolds number. 2) There is a rapid build-up of lift (Fig. 13a) as the leading edge vortex forms. The unsteady increment added to the quasi-steady lift increases from $\Delta C_L = 0.4$ at A = 0.001 to $\Delta C_L = 1.1$ at A = 0.020. 3) The pressure drag (Fig. 13b) increases smoothly before stall, rises and falls rapidly as the stall vortex travels over the chord, and then increases slowly as the pitching of the airfoil rotates the aerodynamic force vector. 4) The pitching moment (Fig. 13c) in attached flow becomes more negative at higher pitch rate, following the prediction of thin airfoil theory (Appendix B). 5) The peak negative C_M after stall increases with pitch rate, from CM = -0.22 at A = 0.001 to C_M = -0.52 at A = 0.020.

The sequence of the stall events as a function of pitch rate is shown in Fig. 14. The process begins when the stall vortex forms and C_L and C_D start to rise. Moment stall occurs when the vortex is released. The maximum C_L occurs as the vortex travels downstream along the chord, and when the vortex reaches the trailing edge the minimum C_M and maximum C_D are obtained. At these pitch rates the angle when moment stall occurs increases approximately linearly with A, in agreement with earlier results for a sinusoid at similar peak pitch rates (Ref. 15). This linear dependence at low pitch rate does not agree with the square root of pitch rate correlation postulated by Gormont (Ref. 19).

Fig. 13 Lift, moment, and drag time histories for 0 to 30 deg ramps at M = 0.2.

65

Fig. 14 Sequence of stall events as a function of pitch rate for 0 to 30 deg ramps at M = 0.2.

Fig. 15 Upper surface pressure time histories for a 0 to 20 deg ramp at A = 0.005 and M = 0.4.

Results at Higher Mach Number

The influence of the leading edge supersonic zone at M = 0.4 on the unsteady upper surface pressures is illustrated in Fig. 15. The time histories for this 0 to 20 deg ramp at A = 0.005 are not shifted vertically: the same scale applies to all of the curves. At x/c = 0.005 the flow becomes supersonic at τ = 0.34 (α = 7.6 deg), and reaches a peak local Mach number of 1.3 at τ = 0.45 (α = 10.6 deg). The sharp rise and fall of the pressure at x/c = 0.026 (letter A in Fig. 15) is caused by the movement of the shock downstream past this station at τ = 0.40 and back upstream at τ = 0.46. A distinct stall vortex is released at τ = 0.46 and x/c = 0.060, just downstream of the shock (letter B). Several of the vortex characteristics differ from those at M = 0.2: 1) the release point is at x/c = 0.060 instead of x/c = 0.10; 2) the vortex speed is approximately 10% less than the speed at M = 0.2; 3) the strength of the vortex is reduced by approximately 50%; and 4) the pressure signature of the vortex is not observed downstream of x/c = 0.57. In addition, no clearly defined oscillations are present after stall at M = 0.4. The Reynolds number of the equivalent bluff body is 1.4×10^6 for this case, above the maximum of 1×10^6 for a stable vortex street (Ref. 17).

Figure 16 shows the time histories of C_L and C_M at M = 0.4 for 0 to 20 deg ramps at A = 0.001, 0.005, and 0.010. The vortex-induced peak in C_L (Fig. 16a) is greatly reduced from the values at M = 0.2, especially at low pitch rate. For pitch rates below A = 0.005 the increment to C_L is less than 0.10 and the delay in the angle of maximum C_L is less than 1.5 deg. This suggests that compressibility prevents the development of the extremely strong suction peak seen at M = 0.2, and therefore reduces the strength of the stall vortex. The peak negative pitching moment (Fig. 16b) 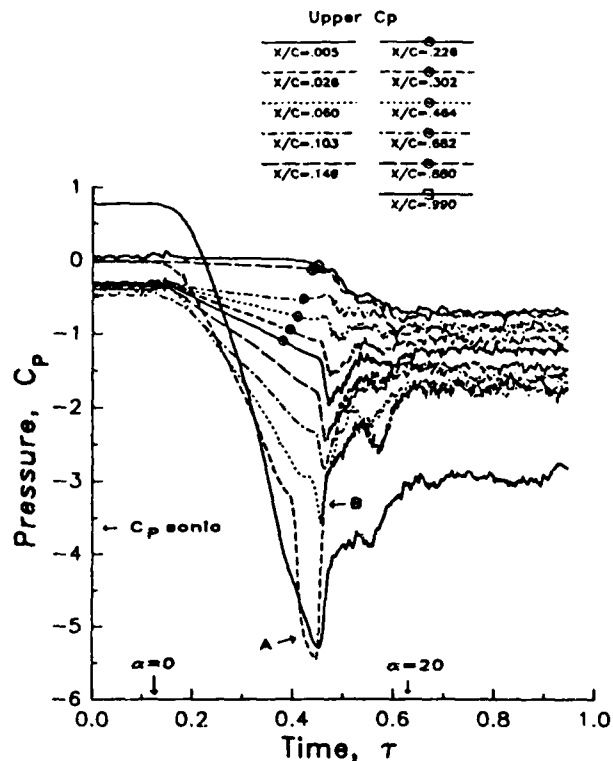is similarly reduced. After stall the absence of strong vortex shedding at the trailing edge allows C_L and C_M to approach relatively constant values that are approximately the same at all pitch rates studied.

The Effect of Starting and Ending Angle

Changing the pitch angles at which the airfoil motion begins and ends may have a significant effect on both the stall and post-stall characteristics. The largest changes occur if the combination of pitch rate and final pitch angle is such that the stall vortex has not reached the trailing edge when the motion ends. In such a case the peak airloads are reduced, and a distinct stopping vortex is released near the leading edge. Figure 17 illustrates the effect of pitch range on lift for constant pitch rate ramps at A = 0.010 and M = 0.2. The premature termination of the stall process when the motion stops causes a rapid drop in C_L when the final angle is 20 or 22 deg. As shown by the times of minimum pressure for the 10 to 20 deg ramp in Fig. 18, the stall vortex appears to pause for $\Delta\tau$ = 0.034, and then resumes traveling downstream. The propagation speed is the same (0.28U) both before and after the pause, and is also the same for all three pitch ranges at A = 0.010. The pressure time histories for these cases (Ref. 16) show the signature of the stopping vortex only near the leading edge, implying that this vortex merges with the stall vortex during the pause. Flow visualization would be useful in verifying this explanation.
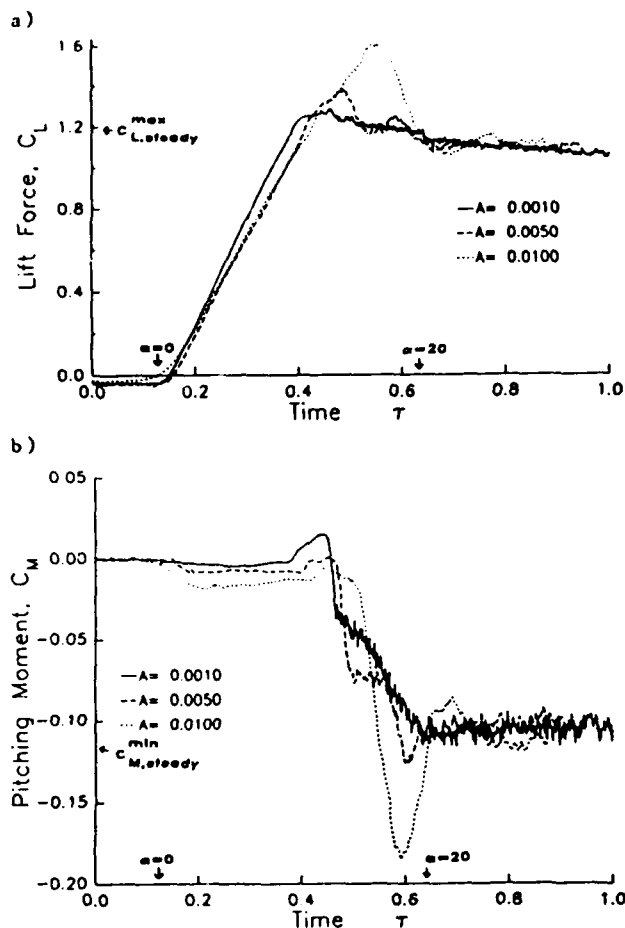
66

a)

Fig. 17 Effect of pitch angle range on unsteady
lift for ramps at A = 0.001 and M = 0.2.

b)

Fig. 16 Lift and moment time histories for 0 to 20
deg ramps at M = 0.4.
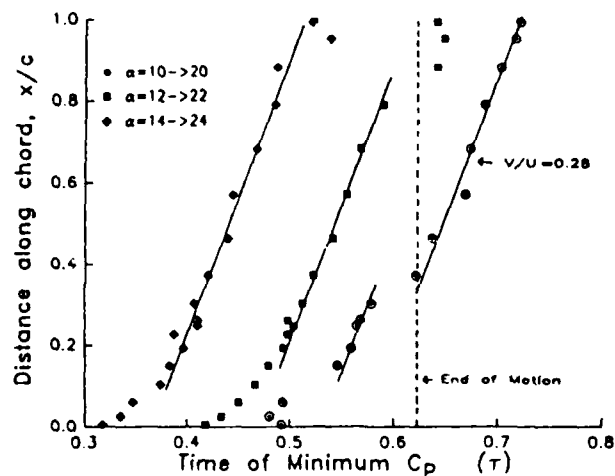
Fig. 18 Effect of pitch angle range on the stall
vortex propagation at A = 0.001 and
M = 0.2.

Figure 17 also shows how the initial angle of
the motion affects the lift. For initial angles
below the steady-state stall angle the differences
are small, but if the initial steady flow is
already partially stalled the maximum lift is
significantly reduced. This occurs for the 14
to 24 deg ramp, where the maximum C_L is only 1.6,
much less than the value of C_L = 2.3 for the base
(0 to 30 deg) case. The stall vortex strength, as
measured by the change in pressure at x/c = 0.30,
is also reduced (by 30%).

Results for Sinusoidal Oscillations

Sinusoidal motion differs from ramp motion in
two important respects: in a sinusoid the airfoil
does not start from a steady-state condition and
the pitch rate is constantly changing.
Nonetheless, there are many qualitative
similarities between the responses to the two
motions. Upper surface pressure time histories for
$\alpha = 20-10\cos\omega t$ at M = 0.2 and k = 0.025 are shown
in Fig. 19. The motion begins at $\tau = 0.0$, reaches
maximum pitch angle at $\tau = 0.50$, and returns to the
minimum value at $\tau = 1.0$. Each time history in the
illustration is offset vertically by $\Delta C_p = 1.0$.
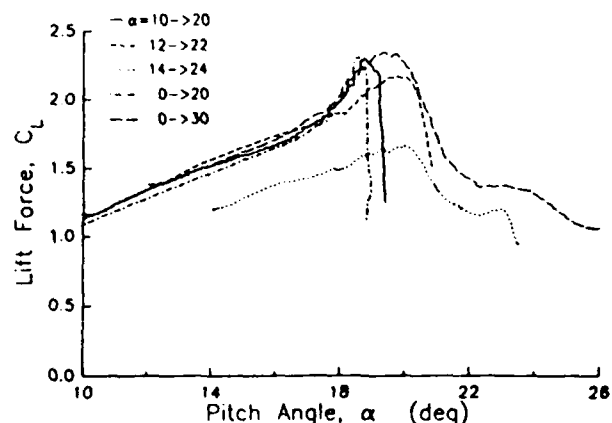The characteristics are similar to the constant

Fig. 19 Upper surface pressure time histories for
sinusoidal motion, $\alpha = 20 - 10\cos\omega t$, at
k = 0.025 at M = 0.2.

67

pitch rate results at A = 0.005 (Fig. 6). This is reasonable because the instantaneous pitch rate at stall is similar, A = 0.0042. The stall vortex is released somewhat further upstream during the sinusoid (x/c = 0.06 instead of 0.10), it is somewhat weaker (ΔC_p = 1.3 instead of 1.6), and propagates more rapidly (0.25U instead of 0.16U). The post stall pressures for the sinusoid show a uniformity in space and time that is similar to the massive stall observed at constant pitch rate.

Conclusions

The primary results of this experimental investigation of dynamic stall at large Reynolds number and moderate Mach number include:

1) For constant pitch rate ramps the unsteady aerodynamic response near stall is strongly dependent on the characteristics of the leading edge stall vortex. The vortex is released from about x/c = 0.10 during stall, and propagates downstream at a velocity that increases with pitch rate. The vortex strength also increases with A, as do the unsteady increments to C_L, C_M, and C_D.

2) A periodic oscillation of the surface pressures occurs at high angle of attack when the equivalent bluff body Reynolds number, $Uc\sin\alpha/\nu$, is less than 10^6. At higher pitch rates, above A = 0.01, the oscillations synchronize with the motion of the airfoil and of the stall vortex, and increase in amplitude.
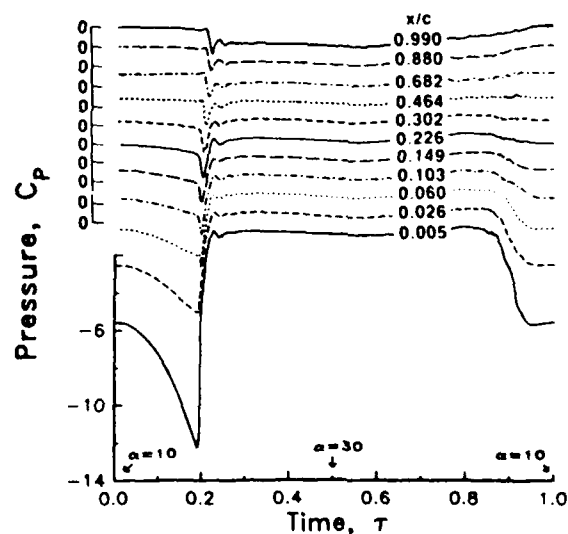
3) The location of boundary layer transition to turbulence moves forward along the airfoil chord as the pitch angle increases. This shift is delayed at higher pitch rate, but is only slightly advanced by doubling the Reynolds number to 4×10^6.

4) A supersonic zone is formed near the leading edge at M = 0.4. This zone reduces the peak suction pressures and airloads and reduces the strength of the stall vortex.

5) Stopping the airfoil pitching motion before the stall vortex has passed the trailing edge generates a stopping vortex near the airfoil leading edge. This vortex may combine with the stall vortex and, after a pause, continue propagating downstream at a speed equal to that of the original stall vortex.

6) Starting the airfoil pitching motion at an angle above that at which the stall vortex would have begun to form weakens the vortex and reduces the unsteady increments to the airloads.

7) Results for sinusoidal oscillations are qualitatively similar to ramp motions having the same values of M, Re, and A at stall, but contain quantitative differences in the stall vortex strength and propagation speed.

Appendix A - Determination of Transition from the RMS Pressure

Accurate determination of the point of boundary layer transition is critical to many numerical computations. Surface heat transfer gages are usually required to determine the unsteady motion of the transition point. These gages are frequently cumbersome to install and each

requires an individual active anemometer circuit to operate. Examination of the time history results for this experiment has shown that it may be possible to locate the transition point using the increased rms pressures measured by an unsteady pressure transducer in a turbulent boundary layer. An example of the correlation between the hot film and pressure transducer results is shown in Fig. 20. All results are at x/c = 0.026 for a 0 to 30 deg ramp at A = 0.050 and M = 0.20. The increase in pressure rms corresponds with the increase in ensemble averaged heat transfer and with the spike in rms heat transfer. No change at transition is apparent in the ensemble averaged pressure. If these promising early results are confirmed by additional correlations, this method may make it much easier to locate transition in complex three-dimensional and unsteady flows.
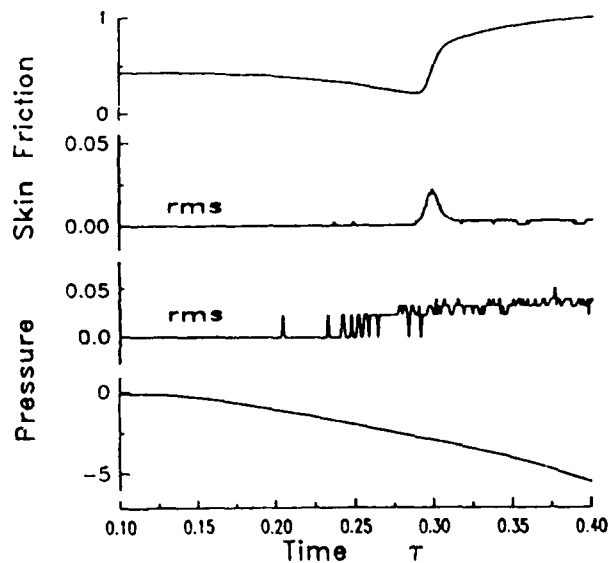
Fig. 20 Determination of transition from rms pressure time histories for a 0 to 30 deg ramp at A = 0.02 and M = 0.2.

Appendix B - Pitching Moment Offset in Attached Flow

In attached flow at moderate angles of attack, the section force and moment coefficients may often be accurately estimated using unsteady thin airfoil theory. For a constant rate pitching motion about the quarter-chord of the section, the expression for the pitching moment (Eqn. 4-171 in Ref. 20) is reduced to a single term:

$$M = -\tfrac{1}{8} \pi \rho c^3 U \dot{\alpha}$$

or, in terms of the nondimensional parameters,

$$C_M = -\tfrac{1}{2} \pi A.$$

68

The results for the 0 to 30 deg ramps at M = 0.2 presented in Fig. 13c are summarized below:

ň	C_M theory	C_M expt.
0.0010	0.0016	0.0020
0.0025	0.0040	0.0045
0.0050	0.0079	0.0080
0.0100	0.0157	0.0160
0.0200	0.0314	0.0300

Acknowledgement

References

1. Liiva, J. and Davenport, F.J., "Dynamic Stall of Airfoil Sections for High-Speed Rotors," Journal of the American Helicopter Society, Vol. 13, Apr. 1968, pp. 49-55.

2. Carta, F.O., and Niebanck, C.F., "Prediction of Rotor Instability at High Forward Flight Speeds, Volume III. Stall Flutter," USAAVLABS Tech. Rept. 68-18C, U.S. Army Aviation Material Laboratories, Ft. Eustis, VA, Feb. 1969.

3. McCroskey, W.J., McAlister, K.W., and Carr, L.W., "Dynamic Stall Experiments on Oscillating Airfoils," AIAA Journal, Vol. 14, Jan. 1976, pp. 57-63.

4. Dadone, L.U., "Two-Dimensional Wind Tunnel Test of an Oscillating Rotor Airfoil," NASA CR-2914, Dec. 1977.

5. Herbst, W.B., "Supermaneuverability," Proceedings of the AFOSR-FJSRL-University of Colorado Workshop on Unsteady Separated Flows, U.S. Air Force Academy, Colorado Springs, Aug. 1983.

6. Lang, J.D., " Unsteady Aerodynamics and Dynamic Aircraft Maneuverability," AGARD CP-386, Unsteady Aerodynamics - Fundamentals and Application to Aircraft Dynamics, Nov. 1985.

7. Ham, N.D. and Garelick, M.S., "Dynamic Stall Considerations in Helicopter Rotors," Journal of the American Helicopter Society, Vol. 13, Apr. 1968, pp. 49-55.

8. Daley, D.C. and Jumper, E.J., "Experimental Investigation of Dynamic stall for a Pitching Airfoil," Journal of Aircraft, Vol. 21, Oct. 1984, pp. 831-832.

9. Jumper, E.J., Schreck, S.J., and Dimmick, R.L., "Lift-Curve Characteristics for an Airfoil Pitching at Constant Rate," AIAA Paper 86-0117, Jan. 1986.

10. Walker, J.M., Helin, H.E., and Strickland, J.H., "An Experimental Investigation of an Airfoil Undergoing Large Amplitude Pitching Motions," AIAA Journal, Vol. 23, Aug. 1985, pp. 1141-1142.

11. Francis, M.S. and Keese, J.E., "Airfoil Dynamic Stall Performance with Large Amplitude Motions," AIAA Journal, Vol. 23, Nov. 1985, pp. 1653-1659.

12. Strickland, J.H. and Graham, G.M., "Force Coefficients for a NACA-0015 Airfoil Undergoing Constant Pitch Rate Motions," AIAA Journal, Vol. 25, April 1987, pp. 622-624.

13. Marchman, J.F., "Aerodynamic Testing at Low Reynolds Numbers," J. Aircraft, Vol. 24, Feb. 1987, pp. 107-114.

14. St. Hilaire, A.O., Carta, F.O., Fink, M.R., and Jepson, W.D., "The Influence of Sweep on the Aerodynamic Loading of an Oscillating NACA 0012 Airfoil. Volume 1 - Technical Report," NASA CR-3092, May 1979.

15. St. Hilaire, A.O. and Carta, F.O., "Analysis of Unswept and Swept Wing Chordwise Pressure Data from an Oscillating NACA 0012 Airfoil Experiment. Volume 1 - Technical Report," NASA CR-3567, March 1983.

16. Lorber, P.F. and Carta, F.O., "Unsteady Stall Penetration Experiments at High Reynolds Number," United Technologies Research Center Report R87-956939-3, April 1987 (to be released as a technical report by the U.S. Air Force Office of Scientific Research).

17. Schlichting, H., "Boundary Layer Theory," McGraw-Hill, New York, 1979, pp. 31-32.

18. McAlister, K.W., Pucci, S.L., McCroskey, W.J., and Carr, L.W., "An Experimental Study of Dynamic Stall of Advanced Airfoil Sections, Volume II - Pressure and Force Data," NASA TM-84245, Sept. 1982.

19. Gormont, R.E., "A Mathematical Model of Unsteady Aerodynamics and Radial Flow for Application to Helicopter Rotors," USAAMRDL Technical Report 72-67, May 1973.

20. Bisplinghoff, R.L. and Ashley, H., "Principles of Aeroelasticity," John Wiley and Sons, New York, 1962, pp. 120.

COMPRESSIBILITY EFFECTS ON THE DYNAMIC STALL OF AIRFOILS
UNDERGOING RAMP-TYPE MOTION
by
Satya Bodapati
Naval Postgraduate school, Monterey
and
### Lawrence W. Carr
NASA Ames Research Center, Moffett Field

Much of the expected improvement in maneuvering that is sought in the Maneuverability Intiative that was introduced by AFOSR at Boulder, in March 1985, will depend on the attainment of high lift, especially through use of unsteady aerodynamics effects. However, it has been observed that the dynamic stall phenomenon, which is the primary source of this high unsteady lift, is significantly affected by compressibility effects. Very little work has been done in documenting the influence of compressibility on dynamic stall characteristics of aircraft wings. Our proposed program will supply the basic qualitative and quantitative information about this developing compressible flow field which is needed to understand the basic phenomena and permit rational development of techniques to allow application of concepts developed at low speeds to the compressible flow environment. A cooperative program supported by Army Research Office is also in progress, directed toward quantitative determination of the effects of compressibility on the dynamic stall of airfoils in pitch. The object of the present investigation is to qualitatively and quantitatively determine the effects of unsteady compressible flow on dynamic stall vortices, transition, seperation, reattachment, type of stall, and stall development as the Mach number is increased progressively from 0.2 to 0.5. The primary emphasis is to visualize and measure the unsteady flow fields. This program will operate in conjunction with the program being carried out for ARO , making use of certain common facilities, instrumentation, and experimental terchniques.

A 25 X 35cm wind tunnel test section and sinusoidally oscillating mechanism has been designed and is in the final stages of fabrication for the ARO investigation (Figure 1). A model is attached between a pair of schlieren quality windows and the windows are rotated; the view of the flow near the surface of the airfoil will be completely unobstructed. The schlieren windows were loaded statically under simulated dynamic loading conditions to test the quality of the schlieren pictures; the loading did not effect the schlieren quality. A mechanism to rotate the model in a ramp-type motion is being designed and various schemes are being investigated. One such scheme is shown in figure 2. This rig will be built after carefully studying the problems involved in the operation of the sinusoidally oscillating mechanism in the solid wall test section. However the proposed experiments for AFOSR will be carried

out in a new ventilated wall transonic test section.

While the actual experimental apparatus is being fabricated, some exploratory tests are being carried out using the existing 25cm X 11cm test section with an oscillating airfoil model to develop the flow visualization and LDV data acquisition and analysis techniques which will be required for tests in the new facility. Typical stroboscopic schlieren pictures are shown in figure 3. The schlieren photographs corresponding to two free stream Mach numbers (0.2 and 0.5) at an angle of attack of approx 25 deg. Note that the oscillating mechanism blocked the front portion of the flow field (this problem will be eliminated in the new facility). Simulated experiments are being carried out to visualize the instantaneous flow field in the Mach number range of interest. Heated wires on the surface of the airfoil are being investigated to visualize the flow at low Mach numbers, where the density gradients are low.

Fig. 1 25 cm × 35 cm TEST SECTION
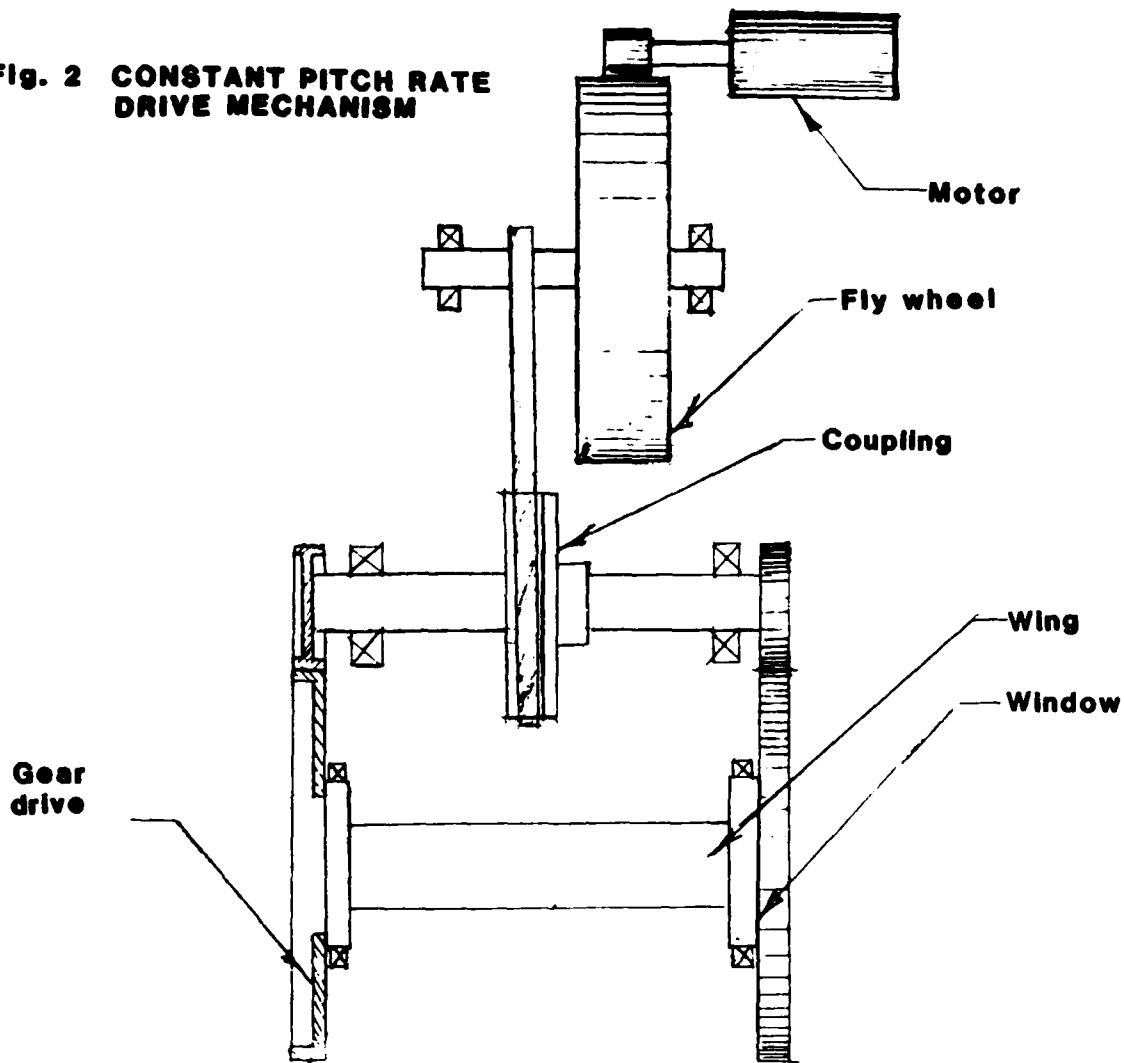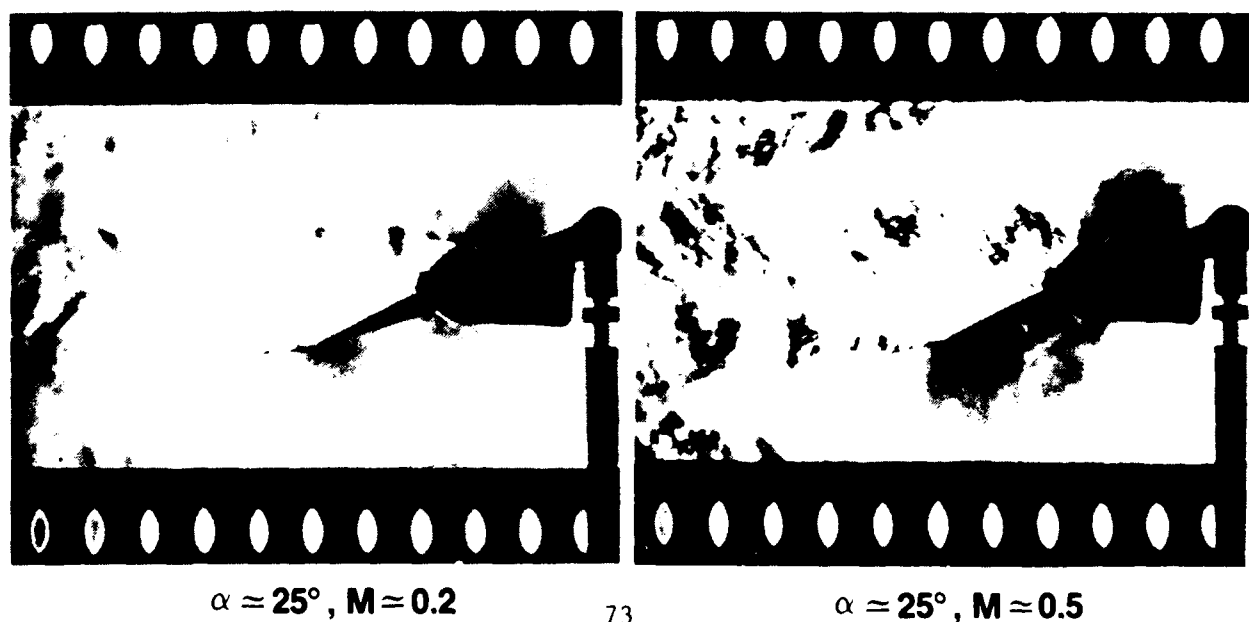WITH OSCILLATING AIRFOIL
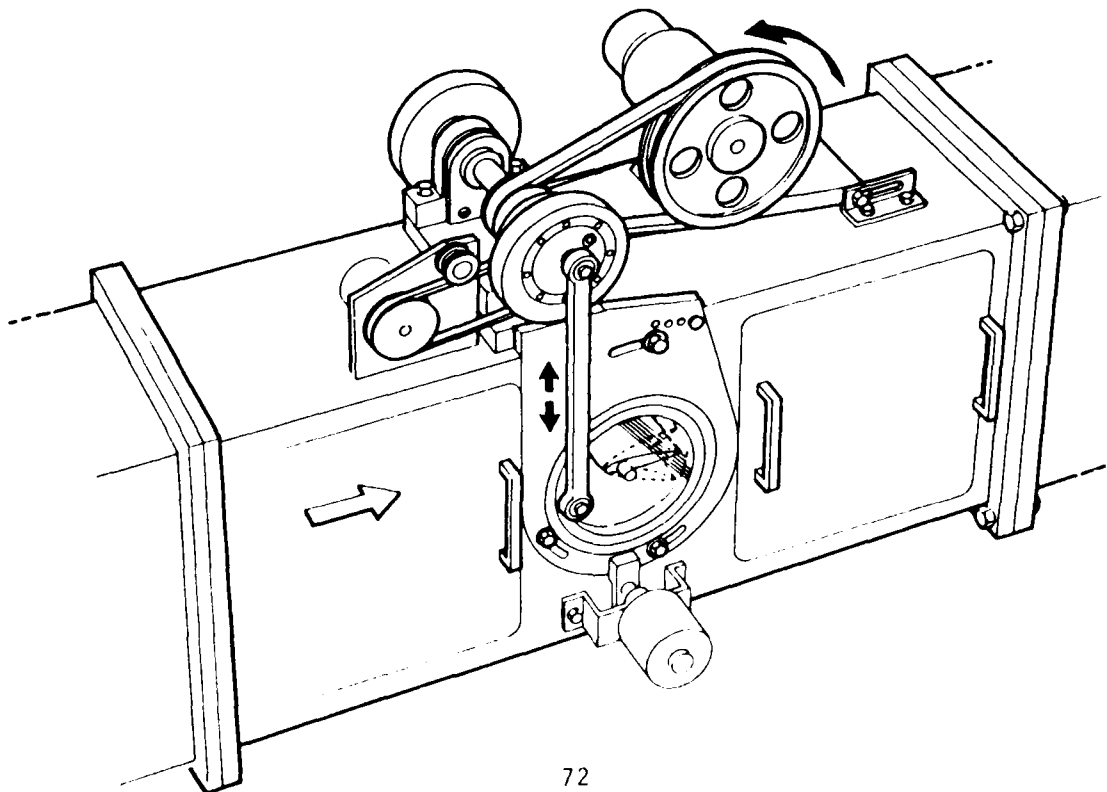
Fig. 2 CONSTANT PITCH RATE
DRIVE MECHANISM

Motor

Fly wheel

Coupling

Wing

Window

Gear
drive

Fig. 3 STROBOSCOPIC SCHLIEREN PHOTOGRAPHS

$\alpha \simeq 25°$, $M \simeq 0.2$ 73 $\alpha \simeq 25°$, $M \simeq 0.5$

AN ANALYTICAL STUDY OF COMPRESSIBILITY EFFECTS ON DYNAMIC STALL

K.-Y. Fung*
Department of Aerospace and Mechanical Engineering
University of Arizona, Tucson, Arizona

and

L. W. Carr**
Fluid Dynamics Research Branch and U.S. Army Aeroflightdynamics Directorate
NASA-Ames Research Center, Moffett Field, California

Abstract

In this paper, typical computational pre-dictions and experimental measurements of com-pressible flow past an airfoil at dynamic stall conditions are studied and compared to identify the compressibility effects on dynamic stall. The dependency of the critical Mach number on airfoil leading edge curvature, camber, and angle of attack is investigated. It is shown that the flow past an air'oil at high angles of attack can easily become supercritical. The shock that terminates the local sonic bubble and the vorticity it gener-ates grow rapidly and become very unstable as the angle of attack further increases beyond the value at which the maximum local flow speed first exceeds the speed of sound. It is suggested that these compressibility effects and the dynamic viscous effects in the boundary layer are compet-ing factors in the determination of the onset of separation of the unsteady boundary layer.

Introduction

Historically, researchers have investigated problems of dynamic stall that have been of low free stream Mach number. The idea of supersonic flow at three-tenths of the free stream Mach number or lower has not been a familiar one to most aerodynamicists until the recent interests in post-stall maneuvers of combat aircraft and the availability of a considerable amount of experi-mental data on dynamic stall. There is little doubt that free stream Mach number is an important parameter in dynamic stall, and the effects of changing it have been observed in many experi-mental studies. The role compressibility plays in dynamic stall, however, has not been well under-stood. McCroskey et al.[1] showed that a local supersonic region exists in many of the cases they studied, but they found no evidence of a shock that normally terminates the supersonic zone. Ericsson and Reding[2] argued that a strong shock would soon appear if the Mach number in the experiment were further increased, even though it has not been observed in experiments to date. They went ahead with their analysis, assuming shock-induced stall, and were quite successful in predicting global aerodynamic charateristics. Katary[3] confirmed the existence of a local supersonic zone for pitching motions that exceed certain critical pitch angle and frequency. Carr[4] observed that, for low Mach numbers, the flow reversal first starts at the trailing edge and moves upstream; for higher Mach numbers, it starts at the leading edge as well, suggesting different types of flow separation for different ranges of free stream Mach number. The difficulty of analyzing the dynamic stall phenom-ena is to discern their dependency on the many parameters thought to be important. In his comprehensive review paper, Carr discussed the effects of the pitch-rate, pitch-axis, mean pitching angle, pitching amplitude, frequency, free stream Mach number, Reynolds number, etc., on dynamic stall. It seems that all the parameters are important for certain phenomena or certain parts of the flow, but none can be isolated from the others without introducing uncertainties about its effects on the events in dynamic stall.

The focus of this paper is to study how compressibility may affect the dynamic stall process. For the sake of our discussion here, we divide the flow of an airfoil undergoing oscilla-tory motions about the static stall angle into three regimes: the attached flow regime, where viscous effects are confined in the boundary layer and the outer flow can be considered inviscid; the separated flow regime, where a breakdown of the boundary layer has occurred, forming large eddies that are the dominating features of the flow; and, the reattachment regime, a transient period, after most of the vortices are downstream of the trail-ing edge, when the flow recovers to a status close to the static counterpart at the same incidence and free stream. Our studies here mainly concern the attached flow regime. It is believed that the flow in this regime is describable in terms of classical aerodynamics up to the point where a breakdown occurs and the separated flow regime begins.

Three sets of pressure history for three different free stream Mach numbers, extracted from the work of McCroskey et al.,[5] will be discussed to exemplify typical effects of the reduced fre-quency on the flow in the attached flow regime. It will be shown that the effects of frequency on the stall onset are distinctively different, depending on whether the flow has locally exceeded sonic conditions during part of the cycle of oscillation. A review of classical theories on compressible aerodynamics is presented, which provides a basis for predicting the conditions under which a flow becomes Mach-critical, i.e., the maximum flow speed exceeds the local speed of sound. It is shown that flow around an airfoil at high angles of attack can reach Mach-critical conditions, even at very low free stream Mach numbers, as long as the flow remains attached. A subsequent study based on numerical computations confirms the validity of the classical theories for the predition of Mach-critical flow and also reveals the possibility that the outer flow may become unstable because of vorticity generated by the shock as the flow exceeds the critical conditions. The conditions for which the numerical calculations indicate instability coincide with the experimental conditions at which the onsets of

*Associate Professor
**Research Scientist

flow separation over a wide range of oscillatory motions of the NACA-0012 airfoil were observed.

Based on these studies, a new mechanism for flow separation is proposed and discussed. This mechanism, coupled with the theories on unsteady boundary layer, can be used to provide convincing explanations for a wide range of dynamic stall phenomena.

Compressibility Versus Frequencies

To set the stage for the discussion from here on, three sets of unsteady pressure distributions of an NACA-0012 airfoil pitching about the static stall angle were chosen from McCroskey et al.[5] to represent typical dynamic stall processes. The first set is shown in Fig. 1, where the pressure distribution over the upper surface of the airfoil is plotted at intervals marked by the corresponding instantaneous angles of attack for two different reduced frequencies (defined as $k = \omega C/2U$, where ω is the circular frequency of oscillation, C is the chord, and U is the free stream speed). The effects of unsteadiness on the onset of stall is discussed in the following. Starting from a low angle of attack where the flow is attached, one sees that the suction peak rises as the angle of attack increases, the instantaneous pressure distributions resemble their corresponding steady ones, and the static stall angle is passed without the breakdown of the pressure distributions associated with stall. Then, a sudden drop of the pressure peak occurs, the boundary layer has broken away, and the flow has separated. Up to the point where the flow separates, the pressure distributions for the two frequencies differ only slightly from each other for the same angle of attack. Note, however, that lower suction peaks occur for the higher frequency at each angle,

which is related to a well-known phenomenon in unsteady aerodynamics--that it takes the flow a finite time to respond to a change in angle of attack. The separation angle was delayed from 16 to 18 degrees due to increased unsteadiness (faster upward pitching), which suppresses the breakaway tendency of the boundary layer beyond the static stall angle. The second set, Fig. 2, shows similar effects of frequency for a higher free stream Mach number. The flow detaches before the airfoil reaches the maximum angle of attack for the lower reduced frequency, but remains attached throughout the cycle for the higher reduced frequency; measurement for an intermediate frequency shows a delayed, milder separation. For this free stream Mach number, the flow remains subsonic everywhere. It is interesting to note that the pressure distributions in the second set are smoother than those in the first set, possibly due to thinning of the boundary layers at higher Reynolds numbers.

The last set of pressure distributions, Fig. 3, contains the same type of information, but for a Mach number of 0.3. The static stall angle was 13.5 degrees, and the maximum suction peak before stall was above the Mach-critical value. For the lower reduced frequency, the flow was attached throughout the cycle, since the maximum pitch angle was above the static stall angle by only half a degree. It would be expected by a simple extrapolation of the trend observed in the previous sets that if the frequency is increased, the flow should stay attached throughout the cycle. On the contrary, it had separated before reaching the maximum angle. The corresponding maximum suction peaks before separation (Fig. 4), which is related to the maximum attainable C_ℓ, were all about -9.0, a value considerably below those attainable in the lower Mach number cases. In the context of boundary layer theory, there is no reason to
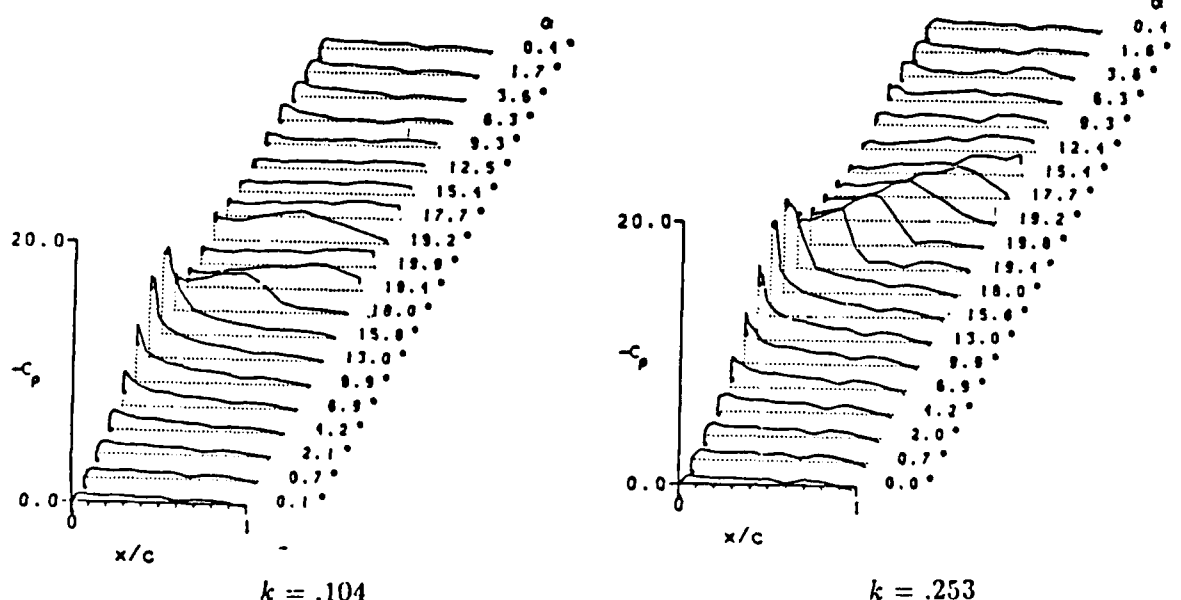

$k = .104$

$k = .253$

Fig. 1   Dynamic data from McCroskey et al.[5] for two frequencies and M = 0.035 for the NACA-0012 airfoil.
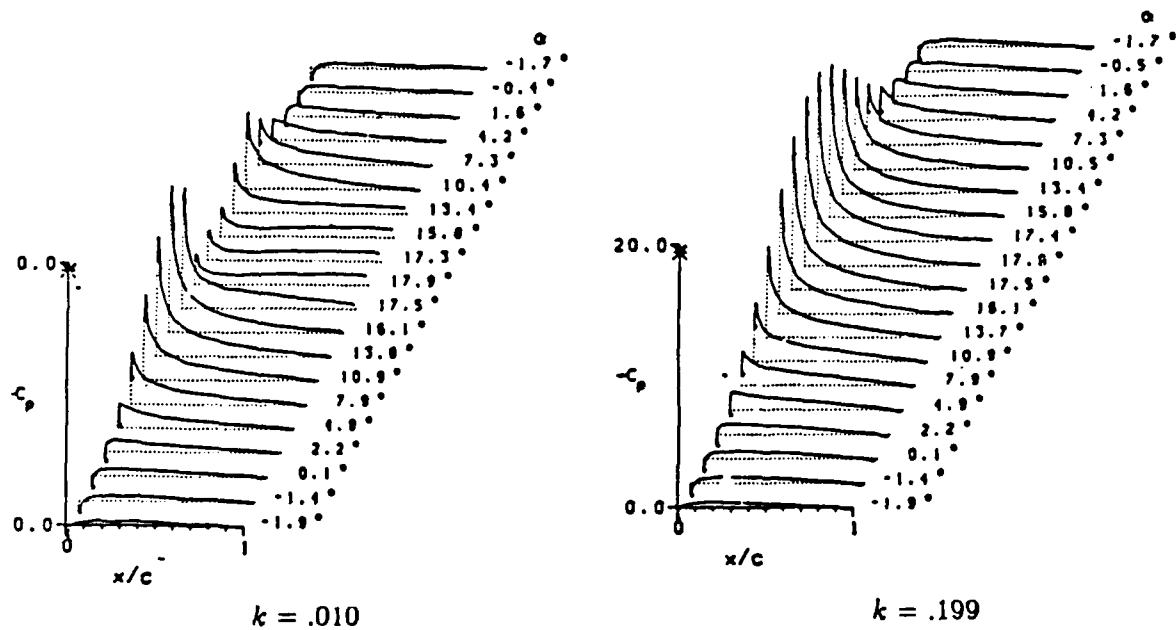
Fig. 2   Dynamic data for two frequencies and M = 0.184 for the NACA-0012 airfoil.
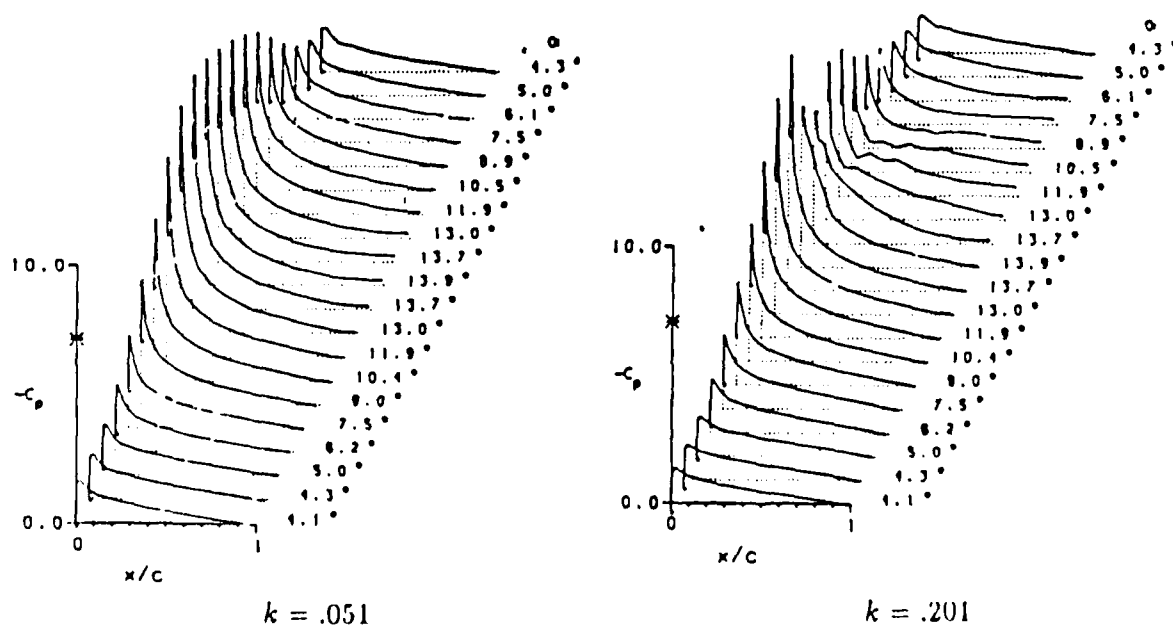

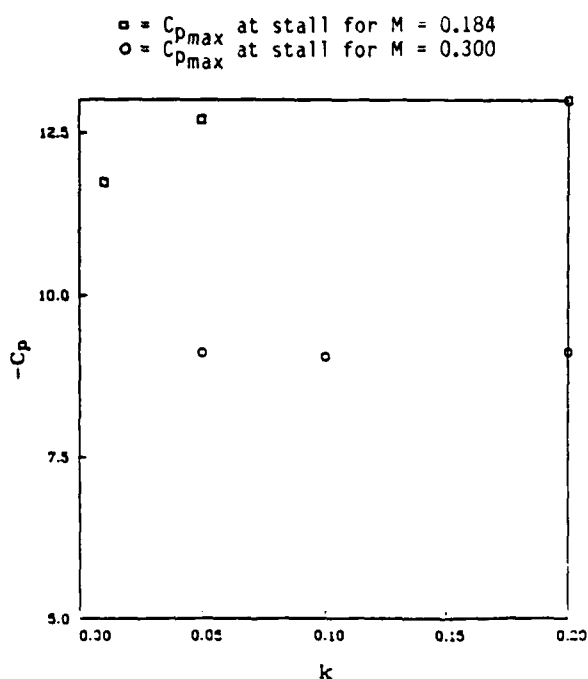Fig. 3   Dynamic data for two frequencies and M = 0.299 for the NACA-0012 airfoil.

Fig. 4   Effects of frequency on suction peak
          $(C_{p_{max}})$ at stall.

Fig. 5   Critical C_p and free stream Mach number
          (Karman-Tsien tangent gas formula).

expect that the thinner boundary layer associated with this higher speed case will be more suscepti- ble to the milder pressure gradients and lower peak values than that in the second set. Furthermore, according to inviscid unsteady aero- dynamics, the pressure peaks should again be lower for higher frequencies, thus implying milder, more favorable pressure gradients, which would help keep the boundary layer attached. All these suggest that the physics of separation of the third set is fundamentally different from that of the first two sets. A strong candidate for the explanation of this unusual behavior of the boundary layer will be shown to be a shock-related instability of the flow, as it has become locally Mach-supercritical.

Supercritical Flow of High Incidence

A flow becomes critical when the maximum local flow speed equals the local sound speed. The C_p at this critical point is a function of the free stream Mach number and the ratio of specific heats (see Liepmann and Roshko[6]). The variation of C_p with the free stream Mach number is shown by the light, solid line in Fig. 5 for the specific heats of air. Up to this critical point, the flow is subsonic everywhere. This flow can be related to the flow of an incompressible fluid over the same body by a Rayleigh-Janzen expansion. Von Karman[7] approximated this relation with the Karman-Tsien tangent gas assumption and gave a formula which relates the critical C_p, the free stream Mach number, and the corresponding C_p of an incompressible fluid. The bold line in Fig. 5 shows this relation. Notice that the pressure of an incompressible fluid differs very little in magnitude from that of a compressible flow. These curves can be used to study and predict critical flow conditions if the corresponding incompressible flow is known.
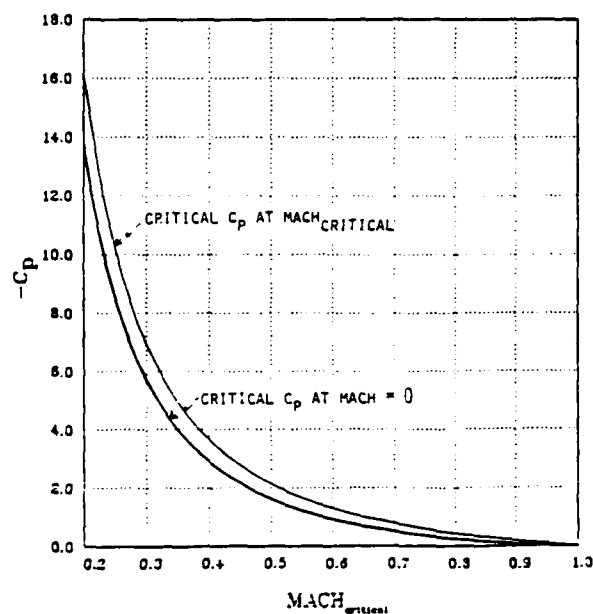
Figure 6 shows the suction peaks of six Joukowsky airfoils of different thicknesses at M = 0 as a function of angle of attack. (Similar results showed that the peaks are relatively insensitive to airfoil camber at high angles.) The peaks increase rapidly with alpha and are very sensitive to thickness or, rather, the radius of curvature of the leading edge at high angles of attack. From the bold curve in Fig. 5, the corresponding incompressible C_p is about -6.0 for a free stream of M = 0.3. A 12% Joukowsky airfoil will be critical at alpha = 9 degrees. All the airfoils shown will be supercritical for angles of 12 degrees or higher. It is an unusual situation to consider compressibility effects for free streams of Mach numbers lower than 0.3. However, the curves in Fig. 7 show how easy it is for an airfoil to reach critical conditions at high angles of attack. For example, an airfoil of 10% thickness will reach critical conditions at alpha = 13 degrees and M = 0.2. Similar, presumably more accurate results could have been obtained, at much higher costs, by solving the full potential equation for a compressible fluid rather than the exact solutions for an incompressible fluid used here. However, we found no reason to suspect that the parametric dependency of the suction peak borne out by the simpler approach would be qualitatively different from that of a more realistic approach.

Beyond the critical conditions, any increases in Mach number or angle of attack will result in the development of a local supersonic zone and a shock. Shock-free flows are unlikely according to the Morawetz theorems,[8-10] which state that shock- free flows are isolated and it is impossible to find shock-free flows for a continuous range of angles of attack. The local time scale for disturbances to propagate is the local length scale divided by the local sound speed and is proportional to the free stream Mach number, the local length scale, and the reduced frequency, i.e.,
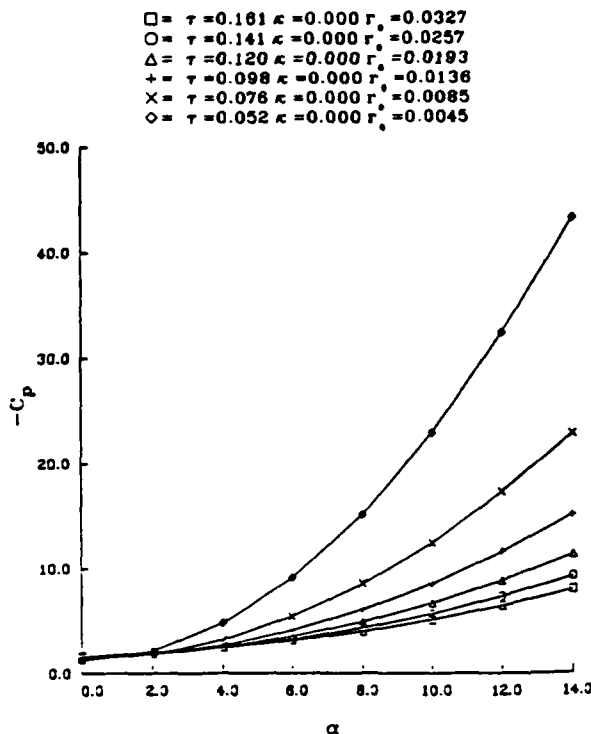
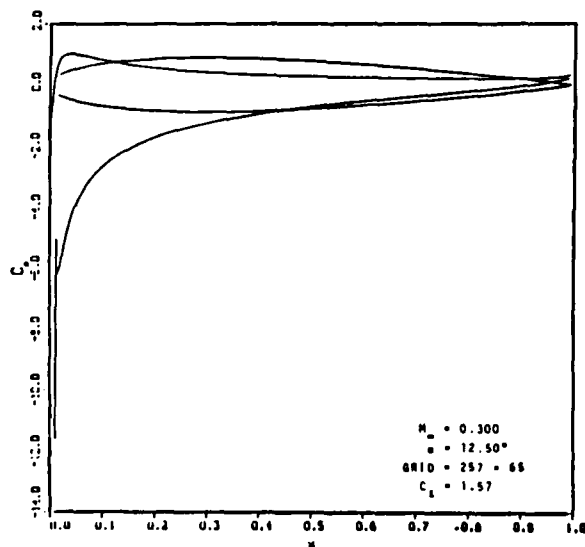Fig. 6   Suction peak versus angle of attack for six Joukowsky airfoils.

Fig. 7   Computed C_p distribution for the NACA-0012 airfoil at M = 0.300.

$$\frac{d}{a} = \frac{d}{C} * \frac{C\omega}{U} * \frac{U}{a} * \frac{1}{\omega} \sim \frac{d}{C} * k * M * \frac{1}{\omega} , \quad (1)$$

where d is the local length scale, C is the chord, ω is the frequency of oscillation, U is the free stream speed, and a is the speed of sound. For the range of reduced frequencies and Mach numbers considered in dynamic stall, the local flow field

can be considered frozen, as far as formation of shock is concerned, since the local time scale is at least four orders of magnitude smaller than the frequency of oscillation.

To study the flow after the critical angle is exceeded, we computed the steady flow over a NACA-0012 airfoil at a free stream Mach number of 0.3 and for a range of angles of attack using ARC2D, an Euler code of Steger[11] and Pulliam et al.[12] The critical angle for which the maximum local flow speed equals the sound speed was 10 degrees, a mere difference of 1 degree from the prediction of Fig. 5 for the 12% Joukowsky airfoil which could be attributed to the difference in leading edge curvature. Computation indicates that further increases in angle of attack will result in the formation of a shock at the leading edge, provided the computational grid distribution near the shock is fine enough to have it resolved. For a 12.5-degree angle of attack and a grid with a minimum spacing of 0.0007 chord at 0.03 chord downstream of the leading edge and on the suction side of the airfoil, a shock was found at 0.013 chord downstream of the leading edge. The local Mach number just before the shock was 1.6. Further attempts to compute the flow for higher angles of attack failed to yield a steady flow field, even for fixed airfoil incidence. Barton and Pulliam,[13] using the same code, found that the flow over the same airfoil at M = 0.301 and alpha = 13.5 degrees was unsteady and that a kind of self-induced oscillation was repeated at the reduced frequency (based on a half chord) of 0.036. The computed lift history, shown in Fig. 8 as a function of iteration, varies dramatically over the cycle. The events in a cycle include the development of a shock at the leading edge, formation of a recirculation region at the trailing edge, and building up and shedding of vortices. After having verified that their results were independent of the grid and other numerical factors, they concluded that the unsteady flow was a result of the vorticity produced by the strong, but short shock occurring at the leading edge. We propose that this phenomenon may be the cause of the dramatic change in dynamic stall character that was observed in experiments as the free stream Mach number was increased.

Shock-Induced Separation

These numerical results suggest that the inviscid flow is no longer stable beyond a certain angle of attack. The reason for the instability is not the shock, since there was no boundary layer in the numerical solution for it to impact on, but the vorticity generated by the shock. Ordinarily, at high free stream Mach numbers and low angles of attack, the shock sits on the flat part of the airfoil where the radius of curvature equals roughly the inverse of the thickness of the airfoil; the vorticity generated by it is proportional to the gradient of entropy, which is a third-order quantity of the pressure jump across the shock and is expected to be small and, hence, negligible. The situation here is different. The shock, as a result of the rapid expansion at the leading edge, occurs at a location near the leading edge where the radius of curvature is very small. According to Fung,[14] who studied the flow at the foot of a shock on a body of radius R, the vorticity ζ behind a shock at the foot is given by Eq. (2),
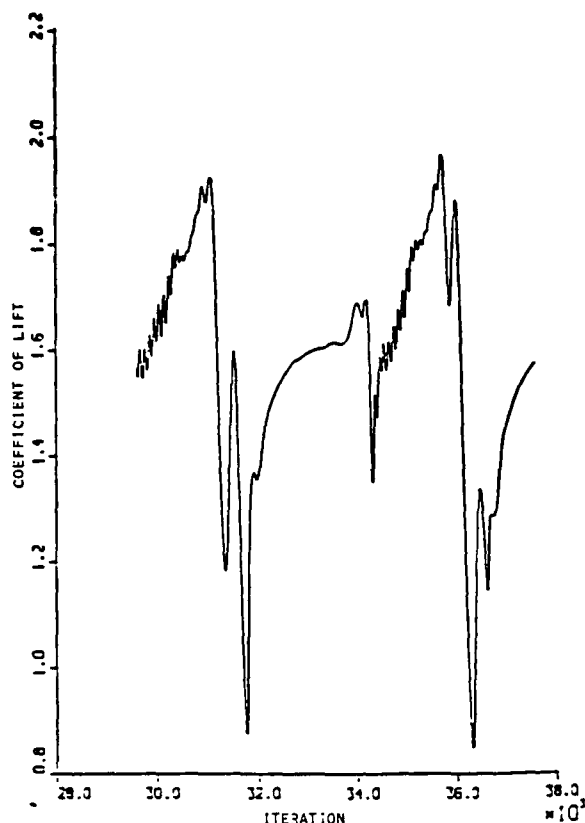
Fig. 8 Lift coefficient history for the NACA-0012 airfoil at M = 0.300 and α = 13.5.

$$\zeta = (1 - \epsilon) * \frac{V}{R} * (1 - M^2) \qquad (2)$$

(where ϵ is the density before divided by the density after, M is the local Mach number before, V is the velocity before the shock, and R is the radius of curvature of the body where the shock is), and can be very high simply because of the small radius of curvature. The gradient of vorticity is also high, since there is no vorticity generation beyond the supersonic region, and the extent of the supersonic region into the flow is small because of the low free stream Mach number. The vorticity subsequently follows the fluid downstream, creating a favorable situation for roll-up, pairing, and shedding of inviscid vortices to occur, as evidenced by the drops and rises of the multiple time-scaled C_ℓ history in Fig. 7. The reaction of the boundary layer to an outer flow which is no longer quasi-steady and favorable for the confinement of the boundary layer of high vortical intensity had been ignored in the computations of Barton and Pulliam[13] due to the mathematical model used. In reality, the shock reacting with the boundary may change the growth rate or the slope of the boundary layer which will, in return, weaken the shock. It may also separate the boundary layer, causing the shedding of high intensity vortices into the free stream. Our knowledge of shock-boundary layer interaction is limited, particularly for cases with shock at the leading edge. The boundary layer may become

unstable and break up simply because the outer flow is no longer stable enough to confine it. Without sufficient experimental data, it would be difficult to ascertain the actual process of separation for this case. It is unlikely that the results of Barton and Pulliam alone can represent the process of dynamic stall once a strong shock has developed and the flow has separated, but it surely suggests a new kind of separation onset mechanism, which may explain the unusual reaction of the boundary layer to increased unsteadiness found in data at M = 0.3. Surprisingly, the C_ℓ values that corresponded to the maximum suction peaks found in this data set were only 1/4 of 1 percent lower than the computed C_ℓ value of 1.57 for the NACA-0012 at an angle of attack of 12.5 degrees, for which a steady flow was still possible. Table 1 lists the case number, the angle of attack, the maximum suction peak, the corresponing C_ℓ value, the reduced frequency k, and the free stream Mach number M of the first 14 tests where flow separation had occurred in part of the pitching cycle reported by McCroskey et al.[5] for the NACA-0012 airfoil. There is a significant consistency of the conditions immediately preceding separation in these cases. The maximum suction peaks were all around -9.0, the corresponding C_ℓ values around 1.5, and the angle of attack around 14 degrees, regardless of the differences in frequency, mean angle, and amplitude of oscillation. Taking into account all the uncertainties in the experiments and the discrete nature of data recording, one cannot help but arrive at the conclusion that separation is being caused by a new phenomenon not seen at low Mach number; shock-related instabilities are a very strong contender.

Table 1 Maximum suction peaks, corresponding α, and C_ℓ found in McCroskey et al.[5] for the NACA-0012 airfoil stalling over a range of reduced frequencies, mean angles, and amplitudes of oscillation.

Case	α	C_pm	C_ℓ	k	M
7021	13.7	-9.06	1.47	0.100	0.299
7023	13.6	-9.13	1.53	0.201	0.299
7101	13.8	-9.23	1.51	0.150	0.301
7112	13.8	-9.03	1.41	0.025	0.301
7113	13.8	-9.10	1.51	0.099	0.301
7114	13.8	-9.08	1.56	0.199	0.301
7117	14.0	-8.98	1.41	0.025	0.301
7118	13.9	-9.01	1.47	0.050	0.301
7119	13.9	-9.05	1.52	0.099	0.301
7120	14.1	-9.08	1.54	0.149	0.301
7121	14.1	-8.99	1.57	0.198	0.301
7200	14.0	-8.97	1.40	0.025	0.301
7205	14.0	-9.07	1.52	0.099	0.302
7207	14.4	-9.01	1.59	0.198	0.302

Conclusions

From the observed behaviors of the flow before separation, it may be said that the outer flow is quasi-steady until separation. We have shown that the parametric dependency of separation for supercritical flows is different from that for subcritical flows. For subcritical flows, increas-

ing the reduced frequency delays separation of the boundary layer and, hence, allows the airfoil to attain higher lift values at higher angles of attack. However, as the airfoil assumes lift values higher than the value at static stall, the flow around it can easily reach supercritical conditions. The formation of a local supersonic region and the associated shock can occur at a location close to the leading edge where the radius of curvature is small. The vortical content of the flow is intensified by the rapid expansion after the shock and the high entropy gradient due to the relatively short extension of the local supersonic region. The outer flow itself, which has been keeping the boundary layer from detaching, is no longer stable. The numerically predicted conditions under which the outer flow is unstable are surprisingly close to those found in a wide range of dynamic stall experiments on the NACA-0012 airfoil at 0.3 free stream Mach number. Hence, **compressibility effects severely limit lift enhancement by increased unsteadiness.**

Our studies here suggest that a new mechanism which can be related to the shock-generated vorticity is responsible for the onset of separation for supercritical flows. Hence, **compressibility effects must be considered in all studies of dynamic stall.**

Our studies have been based on experiments on the NACA-0012 airfoil, and we are in the process of applying the same analysis to other airfoils for which experimental data are available in order to consolidate the theories proposed here.

Acknowledgments

References

1. McCroskey, W. J., McAlister, K. W., Carr, L. W., Pucci, S. L., Lambert, O., and Indergrand, R. F., "Dynamic Stall on Advanced Airfoil Sections." J. Am. Helicopter Soc., July 1981, pp. 40-50.

2. Ericsson, L. E. and Reding, J. P., "Shock-Induced Dynamic Stall," J. Aircraft, May 1984, pp. 316-321.

3. Katary, M., "An Experimental Study of the Development of an Airfoil Oscillation in Subsonic Flow," AIAA Paper 83-2133.

4. Carr, L. W., "Progress in Analysis and Prediction of Dynamic Stall," accepted for publication in J. Aircraft.

5. McCroskey, W. J., McAlister, K. W., Carr, L. W., and Pucci, S. L., "An Experimental Study of Dynamic Stall on Advanced Airfoil Sections," NASA TM 84245.

6. Liepmann, H. W. and Roshko A., Elements of Gasdynamics, Wiley 1957, pp. 398.

7. von Karman, T., "Compressibility Effects in Aerodynamics," J. Aeronautical Sciences, Vol. 8, No. 9, July 1941, pp. 337-356.

8. Morawetz, C., "On The Non-Existence of Continuous Transonic Flow Past Profiles, I," Comm. Pure Appl. Math., Vol. 9, 1956, pp. 45-68.

9. Morawetz, C., "On The Non-Existence of Continuous Transonic Flow Past Profiles, II," Comm. Pure Appl. Math., Vol. 10, 1957, pp. 107-131.

10. Morawetz, C., "On The Non-Existence of Continuous Transonic Flow Past Profiles, III," Comm. Pure Appl. Math., Vol. 11, 1958, pp. 129-144.

11. Steger, J. L., "Implicit Finite-Difference Simulation of Flow About Arbitrary Two-Dimensional Geometries," J. Comp. Phys., Vol. 16, 1978, pp. 679-686.

12. Pulliam, T. H., Jespersen, D. C., and Childs, R. E., "An Enhanced Version of an Implicit Code for the Euler Equations," AIAA Paper 83-0344, Jan. 1983.

13. Barton, J. T. and Pulliam, T. H., "Airfoil Computation at High Angles of Attack, Inviscid and Viscous, Phenomena," AIAA J., Vol. 24, No. 5, May 1986, pp. 705-712.

14. Fung, K.-Y., "Vorticity at the Shock Foot in Inviscid Flow," AIAA J., Vol. 21, No. 6, pp. 915-916.

UNSTEADY VORTICAL FLOWS AROUND AN AIRFOIL

Quen-Yaw Sheen* and Chuen-Yen Chow

Department of Aerospace Engineering Sciences
University of Colorado
Boulder, Colorado 80309

Abstract

The method of discrete vortices is used in combination with the conformal mapping technique to simulate unsteady vortical flows around a symmetric airfoil in an inviscid and incompressible fluid. Numerical results indicate that a free vortex, while passing an oscillating airfoil, may temporarily increase the lift of the airfoil, and with a suitable arrangement such a vortex may become trapped above the oscillating airfoil to cause lift augmentation for a much longer period. In the study of accelerating flows past a flat-plate airfoil at high angle of attack, the computed vortex patterns agree well with those observed in the laboratory.

Introduction

Vortices are generated in the wake of an airfoil when the airfoil either changes its translational velocity or performs an angular motion, or when the airfoil moves toward an already existing free vortex in the fluid. While moving relative to the airfoil, these vortices change the pressure distribution around the body and thus modify the airfoil performance. On the other hand, the flow distortion caused by the presence of the airfoil alters the trajectory of all free vortices in the vicinity. With a proper maneuver of the airfoil, vortices in its neighborhood may be effectively utilized to produce a thrust or an additional lift on the airfoil.

A general analysis is presented for studying unsteady vortical flows about an airfoil in two-dimensional configuration. The fluid is considered to be inviscid and incompressible so that the potential flow theory can be applied. To facilitate flow computations, the vortex sheet shed continuously from the airfoil is approximated by a large number of discrete vortices. Each free vortex in the flow is assumed to be carried about by the local fluid velocity. Thus a numerical scheme can be constructed by which the flow field as well as forces on the airfoil are computed by marching in small time steps until a desirable time level is reached.

In the study of interaction between a free vortex and an oscillating airfoil, it is found that the lift may be enhanced when the vortex passes the airfoil. If the frequency of the airfoil oscillation is right, the free vortex may become trapped by the airfoil in the sense

*Present address: Computational Fluid Dynamics Branch, Aeronautical Research Laboratory, Taichung, Taiwan.

that it moves within a small confined region above the airfoil. As a result the lift is increased. Another class of solved problems deals with accelerating flows past an airfoil at high angle of attack, with the airfoil replaced by a flat plate with two sharp edges to simulate vortex shedding from both leading and trailing edges of the airfoil. Excellent agreements have been obtained between computed and photographed vortex patterns.

Analysis

The unsteady two-dimensional flow field caused by the arbitrary planar motion of a symmetric Joukowski airfoil through an inviscid and incompressible fluid is analyzed. All variables shown in this analysis are nondimensionalized using half of the chord as the reference length and a speed that travels one reference length per unit time as the reference speed. The unbounded fluid is at rest at infinity and at a certain instant the airfoil is performing a translational motion of velocity $-\vec{V}_0$ at angle of attack α and a pitching motion of angular velocity Ω about the point $(x_0, 0)$ as shown in Fig. 1. The total circulation in the flow is $-\Gamma_0$ initially, and will remain at the same value at all times in an inviscid fluid. The discrete vortices in the flow, of total number n at that instant, are symbolically displayed by a single representative vortex of circulation $-k_j$. In this analysis a counterclockwise circulation is considered positive.

In a coordinate system moving with the airfoil at the same translational velocity, the airfoil in the physical $z(=x+iy)$ plane is mapped into a circle of radius a in the $z_2(=x_2+iy_2)$ plane, as sketched in Fig. 1, through the Joukowski transformation

$$z = \frac{1}{2}\left(z_2 + \frac{1}{z_2}\right) \quad \text{where} \quad z_2 = z_1 - a + 1 \quad (1)$$

The complex potential of the flow is conveniently expressed in the transformed circle plane as

$$w = \frac{V_0}{2}\left(\frac{a^2}{z_2 z_2} e^{i\alpha} - \frac{i}{z_2} e^{-i\alpha}\right) - \frac{i\Gamma_0}{2\pi}\ln z_1$$

$$- \frac{\Omega}{4}\left[\frac{a^2}{z_1 z_2} - (a-1)\left(\frac{a^2}{z_1} + \frac{1}{z_2}\right)\right.$$

$$\left. + \frac{1}{2}\left[a^2 - (a-1)\left(z_2 + \frac{1}{z_1}\right)\right]^{-1} - 2x_0\left(\frac{a^2}{z_1} + \frac{1}{z_2}\right)\right]$$

$$- \sum_{j=1}^{n}\frac{k_j}{2\pi}\left[\ln(z_1 - z_{1j}) - \ln\left(z_1 - \frac{a^2}{\bar{z}_{1j}}\right)\right]$$

$$- \frac{k_s}{2\pi}\left[2\ln(z_1 - z_{1s}) - \ln z_1\right] \quad (2)$$

where M is the strength of a point sink placed on the circle at z_{1s}, which is used to simulate a suction applied on the surface of the airfoil.

The complex fluid velocity in the physical plane is obtained by differentiating Eq.(2),

$$u - iv = \frac{dW}{dz} = \frac{dW}{dz_1} / \frac{dz}{dz_1} \qquad (3)$$

However, to compute the motion of the jth free vortex Eq.(3) has to be modified by taking proper limits in the following expression:

$$(u - iv)_{z_j} = (\frac{dW}{dz} - \frac{k_j}{2\pi} \frac{1}{z - z_j}) z_1 + z_{1j} \qquad (4)$$

The displacement of the vortex in a small time interval is then computed using a two-step predictor – corrector procedure.

To satisfy the Kutta condition, it is required that the velocity at the point in the circle plane that maps into the trailing edge be vanishing, so that

$$\frac{dW}{dz_1} = 0 \quad at \quad z_1 = a \qquad (5)$$

The flow velocity relative to the moving trailing edge is

$$(u + iv)_{te} = (\overline{\frac{dW}{dz}})_{z=1} + V_o e^{i\alpha} - i\Omega(1 - x_o) \qquad (6)$$

After substituting W from Eq. (2), the right-hand side of Eq. (6) turns out to be real as is expected for a symmetric airfoil.

During a short time interval Δt, a vortex sheet of constant circulation density γ is assumed to be shed on the x axis from the trailing edge, whose length Δx is equal approximately to the product of Δt and u_{te} obtained from Eq. (6). The numerical value of γ is determined by requiring that the Kutta condition (5) be satisfied in the presence of such a vortex sheet. This short vortex sheet is then replaced by a discrete vortex of circulation $\gamma\Delta x$ situated on the x axis, whose location is computed from the requirement that the Kutta condition is still satisfied.

After the instantaneous flow field is computed, the lift, drag and moment acting on the airfoil can be obtained by using the Blasius theorem for unsteady flows. Details of the analysis described here are referred to Ref. 1.

Results

This general analytical-numerical computation scheme is first employed to study the problem of flow around an oscillating airfoil that has analytical solution after linearization, results of which are used to test the accuracy of this method. The computed wake patterns show the rolling up of the trailing vortex sheet to form vortex clusters of alternating circulations, in agreement with the phenomenon observed behind an oscillating airfoil in the laboratory. A comparison with analytical results reveals that the linearized theory with thickness effects ignored can predict very well the lift even on a 17% thick airfoil in a sinusoidal pitching motion.

Presented in the following are results computed for several unstea y vortical flow problems. In all cases a 17% thick airfoil is chosen for numerical computations, which is generated by letting a = 1.15 in Eq. (1). Such an aifoil has a dimensionless chord of 2.035 in the physical plane.

(I) Influence of a Passing Free Vortex on an Oscillating Airfoil

The interaction between a free vortex and an airfoil traveling with a constant velocity and at a fixed angle of attack was studied in Ref. 2. We now examine the effect when the airfoil is given an oscillatory pitching motion.

In the numerical example presented here, the airfoil is assumed to oscillate about the origin of the coordinate system with an angular motion $\alpha = 0^{\circ} + 5^{\circ} \sin \omega t$ where the dimensionless angular speed ω is set to be 10. For $V_o = 1$, a vortex of counterclockwise circulation $k = 3$ is released at the point z = -2+i at t=0. As time increases the trajectory of the vortex and the airfoil lift coefficient are plotted in Figs. 2 and 3, respectively. The lift coefficient of the oscillating airfoil in the absence of the free vortex is also plotted in Fig. 3 for comparison. It shows that lift is augmented when the vortex is approaching or above the airfoil; the effect is diminishing after the vortex leaves the trailing edge at about t = 4.5.

On the other hand, if the vortex is replaced by one of clockwise circulation with k = -3 while keeping all other conditions the same, the computed results plotted in Figs. 4 and 5 show that the motion of the free vortex is slowed down in the presence of the oscillating airfoil, and the vortex causes a decrease in lift on the airfoil.

(II) Trapping of Free Vortex by an Oscillating Airfoil

It has been known that a free vortex may be trapped above an airfoil for lift augmentation (Refs. 3,4). However, the analysis in Ref. 2 shows that the trapped vortex is always unstable since it will move away from its equilibrium position after being disturbed with a sufficiently large displacement. Attempts have been made to stabilize the vortex, for example by using a surface suction (Ref. 5). Examined here is an alternative method in which the airfoil is given a sinusoidal pitching motion.

Computations are performed based on $V_0 = 1$ and for $\alpha = 0° + 5° \sin \omega t$. After a vortex of circulation $k = -3$ is released initially at $z = 0.55 + 0.25i$, the subsequent vortex trajectory is found to be confined within a small region above the airfoil oscillating with $\omega = 10$ and seemingly will stay there for a long time as shown in Fig. 6. The variation of lift coefficient with time is plotted in Fig. 7, which shows that a time-averaged lift coefficient of 1.31 is generated by the vortex on the oscillating airfoil, whose average lift would be zero in the absence of the vortex. Note that if a circulation equal to that of the free vortex were applied around the same airfoil without oscillation, the steady lift coefficient would be 1.5.

The vortex-trapping ability of the oscillating airfoil is enhanced by surface suction according to the numerical solution. For example, when a sink of strength $M = 0.2$ is placed on the upper surface of the airfoil at $x = -0.55$, the same vortex as described in Fig. 6 will move in a tighter path as shown in Fig. 8, resulting in a higher average lift coefficient of 1.41. On the other hand, surface blowing is found to have a destabilizing effect on the trapped free vortex. When the sink in Fig. 8 is replaced by a source of the same strength, the vortex starts to move downstream according to the result plotted in Fig. 9, and the average lift drops back to zero soon after the vortex leaves the trailing edge.

(III) Simulation of Unsteady Flows Past an Airfoil at High Angles of Attack

In addition to the trailing edge, vortices are shedding also from the leading edge of an airfoil flying at a high angle of attack as a result of boundary layer separation there. The interaction of these two groups of vortices can be observed at an extended distance in the wake.

To simulate such a flow using the present method, the airfoil is approximated by a flat plate having two sharp edges. Within a small time duration, short vortex sheets are shed respectively from both leading and trailing edges. They are replaced by two concentrated discrete vortices whose strengths and positions are determined from the requirement that the Kutta condition be satisfied simultaneously at both ends.

Several experiments with an airfoil in either impulsively started or accelerating motions have been successfully simulated as reported in Refs. 1 and 6. To show as a representative example, the photographed and computed flow patterns around an accelerating airfoil at progressive time steps are compared in Figs. 10(a) and 10(b). The NACA 0015 airfoil of 5.1 cm chord, started from rest, is in a constant acceleration of 1.7 m/sec^2 at an angle of attack of 50°. A direct comparison of the two patterns at the same time levels is not possible, because of the fact that the laboratory flow has a strong viscous effect during the starting period. That effect becomes less important after the shed vortices have moved out of the boundary layer. For the comparison shown in Fig. 10(a), a first frame in the computed flow sequence is selected that closely resembles the first frame of the photographed series, and the subsequent frames are then displayed at the same time intervals of 1/32 seconds for both physical and numerical experiments. They show the rolling of the vortex sheets shed respectively from leading and trailing edges. Both the roll-up speed and the size of the vortex sheet at the leading edge are greater than those at the trailing edge.

Further comparisons are continued in Fig. 10(b), whith the first frames started at 3/32 seconds later from the last frames of Fig. 10(a). While the initial cluster of vortices is moving away from the trailing edge, a second cluster starts to form there which grows and interacts with the leading edge vortex sheet to cause a large distortion in the latter. Remarkable agreements can be observed between computed and visualized flow patterns. However, the development of the leading-edge secondary vortices initiated in the photographs of Fig. 10(a) and their evolution into complex vortical structures as revealed in the pictures of Fig. 10(b) are presumably boundary layer related phenomena and therefore cannot be observed in the computed results based on an inviscid formulation.

Conclusion

Various unsteady vortical flows around an airfoil have been simulated using the method of discrete vortices. Computations show that the lift on an oscillating airfoil may be enhanced while interacting with a passing free vortex or with a vortex trapped temporarily above the airfoil. Oscillation of the wing is probably a method used by some tandem-winged insects such as the dragonfly to generate additional lift on the rear wing that maneuvers in the wake of the fore wing.

The fair comparison between computation and flow visualization in Figs. 10(a) and 10(b) demonstrates the feasibility of using the method of discrete vortices to simulate unsteady vortical flows in the region where viscous effects are not important.

References

[1]Sheen, Q.-Y.,"Potential Flow Analysis of Unsteady Joukowski Airfoil in the Presence of Discrete Vortices," Ph.D. Thesis, University of Colorado at Boulder, 1986.

[2]Chow, C.-Y., Huang, M.-K., and Yan, C.-Z., "Unsteady Flow About a Joukowski Airfoil in the Presence of Moving Vortices," AIAA Journal, Vol. 21, No. 5, May 1985, pp. 657-658.

[3]Saffman, P.G. and Sheffield, J.S., "Flow Over a Wing with an Attached Free Vortex," Studies in Applied Mathematics, Vol. 57, 1977, pp. 107-117.

[4]Huang, M.-K. and Chow, C.-Y., "Trapping of a Free Vortex by Joukowski Airfoils," AIAA Journal, Vol. 20, No. 3, March 1982, pp. 292-298.

[5]Chow, C.-Y., Chen, C.-L., and Huang, M.-K., "Trapping of a Free Vortex by Airfoils with Surface Suction," AIAA Journal, Vol. 24, No. 8, Aug. 1986, pp. 1217-1218.

[6]Finaish, F., "Experimental Study of Two-Dimensional Vortex Patterns for Impulsively Started Bodies in Comparison with Other Configurations," Ph.D. Thesis, University of Colorado at Boulder, 1987.
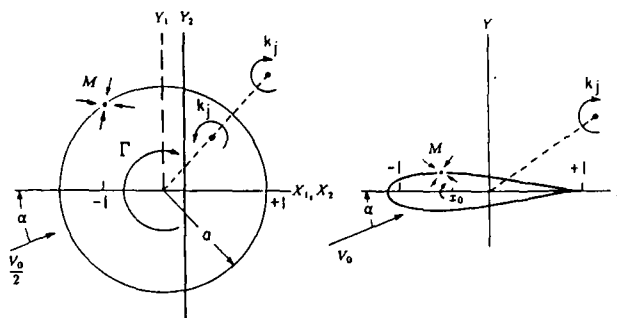
Fig. 1   Mapping between physical and transformed planes.
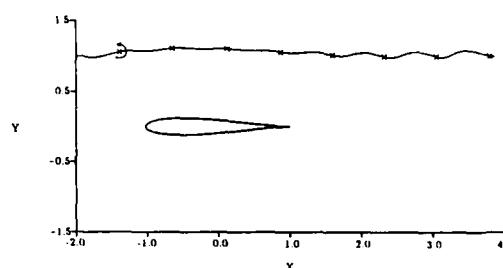
Fig. 2   Trajectory of a free vortex of counterclockwise circulation approaching an oscillating airfoil.
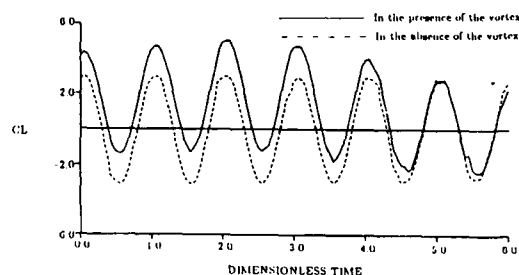
Fig. 3   Effect of moving vortex on the lift of the oscillating airfoil described in Fig. 2.
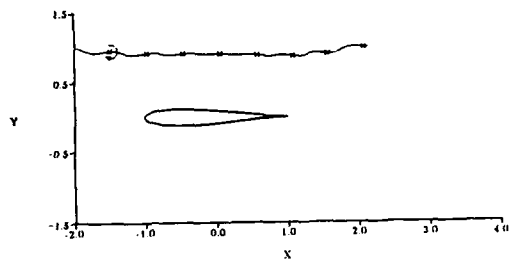
Fig. 4   Trajectory of a free vortex of clockwise circulation approaching an oscillating airfoil.
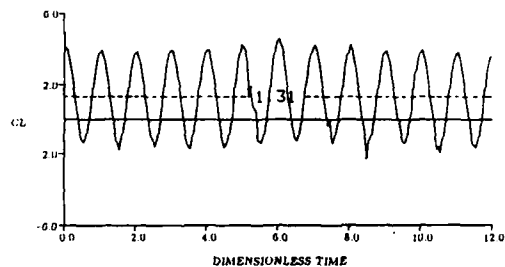
Fig. 7   Augmented lift on the oscillating airfoil described in Fig. 6 with a vortex trapped above.
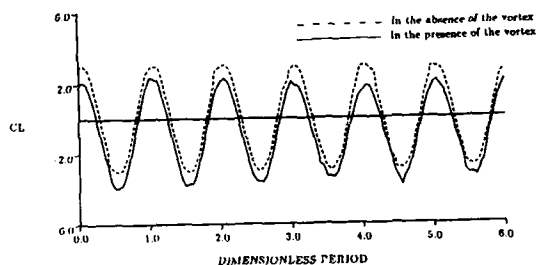
Fig. 5   Effect of moving vortex on the lift of the oscillating airfoil described in Fig. 4.
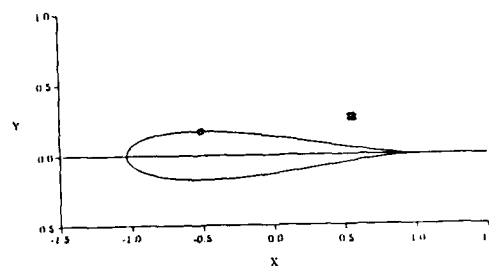
Fig. 8   Tighter vortex trajectory when a sink is placed on the upper surface of the oscillating airfoil described in Fig. 6.
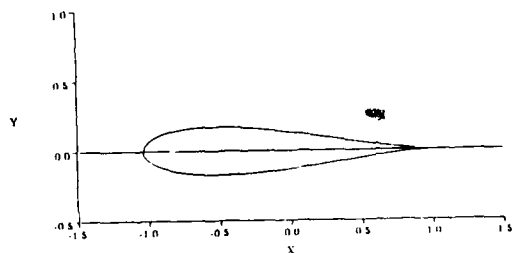
Fig. 6   Trajectory of a vortex trapped above an oscillating airfoil.
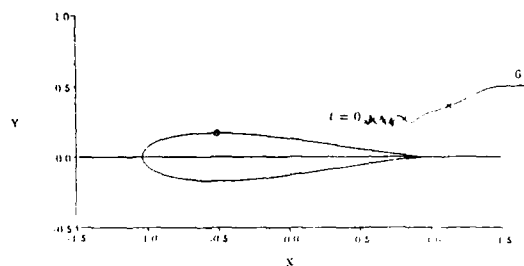
Fig. 9   Vortex trajectory after the sink in Fig. 8 is replaced by a source.

87
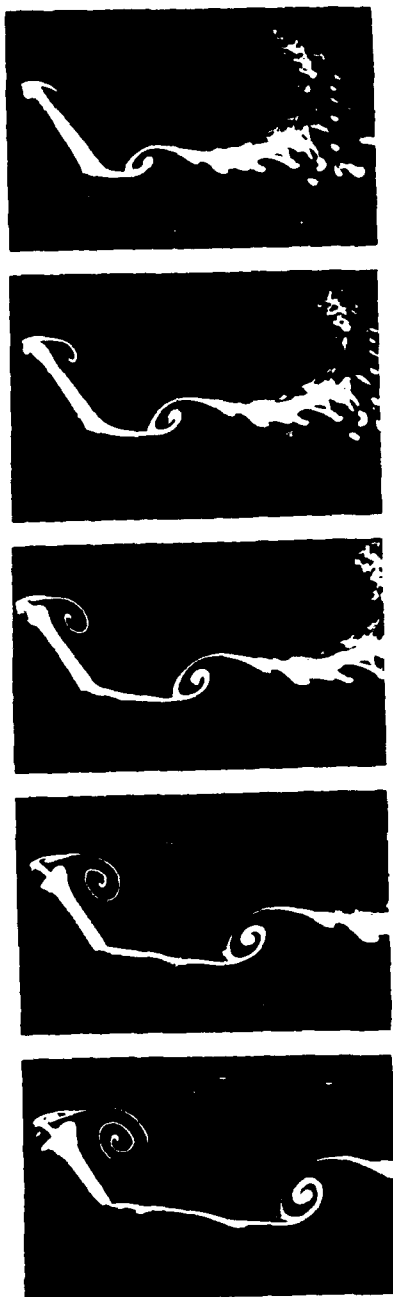
Fig. 10(a) Comparison between computed and photographed vortical patterns around a NACA 0015 airfoil at a 50° angle of attack. The airfoil of 5.1 cm chord is in a constant acceleration of 1.7 m/sec² starting from rest. Interval between consecutive frames is 1/32 seconds.
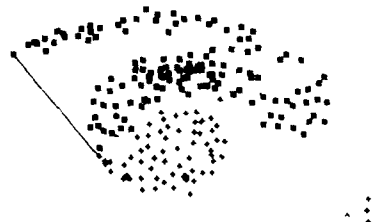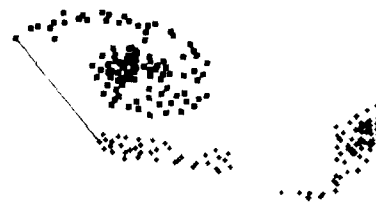
Fig. 10(b)   Continuation of Fig. 10(a) at 3/32
seconds later.

89

NUMERICAL INVESTIGATION OF THE FLOW STRUCTURE
AROUND A RAPIDLY PITCHING AIRFOIL

Miguel R. Visbal[*] and Joseph J. S. Shang[**]

Air Force Wright Aeronautical Laboratories
Wright-Patterson Air Force Base, Ohio 45433-6553

Abstract

A numerical study is presented for unsteady laminar flow past a NACA 0015 airfoil which is pitched, at a nominally constant rate, from zero incidence to a very high angle of attack. The flow field simulation is obtained by solving the full two-dimensional compressible Navier-Stokes equations on a moving grid employing an implicit approximate-factorization algorithm. An assessment of the accuracy of the computed solutions is presented, and the numerical results are shown to be of sufficient quality to merit physical interpretation. The highly unsteady flow field structure is described and is found to be in qualitative agreement with available experimental observations. A discussion is provided for the effects of pitch rate and pitch axis location on the induced vortical structures and on the airfoil aerodynamic forces.

Nomenclature

|	
c	airfoil chord
C_L, C_D	lift and drag coefficients
C_N, C_A	normal and axial force coefficients
C_M	quarter-chord moment coefficient
C_p	pressure coefficient, $2(p-p_\infty)/\rho_\infty U_\infty^2$
M_∞	freestream Mach number, $U_\infty / \sqrt{\gamma R T_\infty}$
n	indicates direction normal to airfoil surface
Re_c	chord Reynolds number, $\rho_\infty U_\infty c / \mu_\infty$
u, v	Cartesian velocity components in inertial frame of reference
U_∞	freestream velocity
x, y, t	Cartesian coordinates in inertial frame of reference and time
X, Y	coordinate system attached to airfoil (Fig. 1)
$X_\bullet$	pitch axis location
α	geometric angle of attack
α_{eff}	effective angle of attack at airfoil leading edge
ξ, η, τ	transformed coordinates
ν	kinematic viscosity
Ω	airfoil pitch rate, rad/sec
Ω^+	non-dimensional pitch rate, $\Omega c / U_\infty$
ω	vorticity, $\frac{\partial v}{\partial x} - \frac{\partial u}{\partial y}$
ω_F	net vorticity flux at airfoil surface, $-\oint \nu \vec{\nabla} \omega \cdot \vec{n}\, ds$
ω_F^+	positive (counter-clockwise) vorticity flux at airfoil surface
ω_F^-	negative (clockwise) vorticity flux at airfoil surface

---

[*] Aerospace Engineer, Member, AIAA

[**] Technical Manager, Associate Fellow, AIAA

I. Introduction

The understanding and potential utilization of unsteady separated flows constitute a challenging area of fluid mechanics. Within this broad flow category, one encounters the phenomenon of dynamic stall, a term loosely used to describe the complex physical events induced by large amplitude motion of aerodynamic bodies or lifting surfaces. Dynamic stall is of importance in various aerodynamic applications including aircraft maneuverability, helicopter rotors and wind turbines. As the extensive reviews of McCroskey[1] and Carr[2] indicate, the majority of the research on dynamic stall has been devoted to the case of airfoils performing harmonic motions of moderate amplitude in a uniform incoming stream. For the cases when the airfoil reaches very high angles of attack, the generated flow fields are characterized by massive, unsteady separation, and by large scale vortical structures. Since such complex flow fields are not amenable to analysis using classical aerodynamic tools, both computational and experimental studies must be conducted to elucidate their structure. As pointed out in Refs. 1 and 2, progress in this problem area is also complicated by the need to account for many flow parameters. In addition to the usual flow field dependence on Mach number, Reynolds number and airfoil shape, the effects of the form, the rate and the amplitude of the forcing motion must be considered. Furthermore, difficulties are compounded by the interrelated effects of various parameters. For instance, compressibility effects are not only a function of freestream Mach number, but also of the product of Mach number with the non-dimensional rate of motion. Due to the complexity of these highly unsteady separated flows, the need for systematic computational and experimental studies is apparent. This current need constitutes the motivation for the present numerical investigation.

This paper presents a computational study of the unsteady laminar flow past an airfoil which is pitched at a constant rate to very high angles of attack. The simple constant pitch rate motion represents the first logical step in a building block approach, before more complex types of motion are considered. The constant pitch up case should also permit the study of relevant dynamic stall phenomena, without introducing further complications associated with motion history effects. In addition, the large amplitude constant pitch rate case is of potential importance in future aircraft maneuverability.[3] Current interest in the present problem area is evidenced by the recent experimental investigations of Refs. 4-9, and the preliminary computational (viscous) studies of Visbal[10] and Wu et. al.[11] The present work constitutes a more extensive and systematic study than those of Refs. 10 and 11.

Although the simulation of high Reynolds number (turbulent) flows is ultimately desired, the present computational results are limited to the case of low Reynolds number laminar flow. This constraint is imposed due to the following main reasons:

(1) Suitable modeling of transition and turbulence is not currently available for such a complex unsteady flow as the one under investigation.

(2) Although simple eddy viscosity models[12] can be tailored for the prediction of steady separated[13] or vortical[14] flows, this approach is impractical in the present application where vortices move in an arbitrary manner and even impinge against the airfoil surface.

(3) The use and validation (tuning) of a more complex turbulence model must await detailed flow field measurements, not presently available for this rapid pitch-up problem.

In the meantime, the present laminar results complement ongoing experimental efforts by providing clarification of important dynamic stall features and trends. This is particularly true in the high pitch rate regime for which the violent forcing motion is expected to overwhelm some transition and turbulence effects. The favorable agreement found between predicted and experimental primary flow features confirms the previous hypothesis. Finally, two dimensional results are of relevance since experimental flow visualizations[9] for a straight wing reveal a nearly two-dimensional flow structure (away from the wing tip) during the pitch up motion.

The specific flow configuration considered is shown in Fig. 1. A NACA 0015 airfoil is pitched about a fixed axis at a constant rate from zero incidence to a maximum angle of attack of approximately sixty degrees. The particular airfoil section selected has been used in the majority of pitch up experimental studies.[5-9] The freestream Mach number and chord Reynolds number are 0.2 and 10^4, respectively. For the case of pure rotation, the similarity parameter associated with the airfoil motion is the non-dimensional pitch rate $\Omega' = \dot{\Omega} c / U_\infty$. This parameter arises in the non-dimensionalization of the velocity boundary conditions on the airfoil surface, and it is simply the inverse of the Rossby number. In the present study, Ω' varies over the range 0.1-0.6, and

different pitch axis locations are
employed (ranging from the airfoil leading
edge to the 75%-chord station). Numerical
results are obtained by solving the full
compressible Navier-Stokes equations on a
moving grid using an implicit approximate-
factorization algorithm.[15] The main
objectives of this study are summarized as
follows:

(1) Description of the basic flow
field structure for the rapidly pitched
airfoil.

(2) Parametric investigation of the
effects of pitch-rate and pivot axis
location on the flow structure and
aerodynamic loads.

(3) Qualitative comparison of
computed and experimental primary flow
features.

II. Governing Equations and Boundary Conditions

For the case of external flow past a
body in arbitrary motion, the governing
equations can be formulated using two
different approaches. In the first
approach, the flow equations are written
in a non-inertial frame of reference
attached to the body. While this avoids
the introduction of a moving grid, it
requires the inclusion of fictitious
acceleration terms in the governing
equations. In the second approach,
selected in this research, the velocity
is defined in the inertial system, and
motion of the body is provided for by
means of a general time-dependent
coordinate transformation. Introducing
such a transformation $[\xi = \xi(x,y,t),$
$\eta = \eta(x,y,t), \tau = t]$, the full two-dimensional
compressible Navier-Stokes equations may
be expressed in the following strong-
conservation form:[16]

$$\partial_\tau q + \partial_\xi E_1 + \partial_\eta E_2 = \partial_\xi (V_1 + V_2) +$$

$$\partial_\eta (W_1 + W_2) \tag{1}$$

where

$$q = J^{-1} [\rho, \rho u, \rho v, \rho e]$$

$$E_1 = \frac{1}{J} \begin{vmatrix} \rho U \\ \rho u U + \xi_x p \\ \rho v U + \xi_y p \\ (p + \rho e) U - \xi_t p \end{vmatrix}$$

$$E_2 = \frac{1}{J} \begin{vmatrix} \rho V \\ \rho u V + \eta_x p \\ \rho v V + \eta_y p \\ (p + \rho e) V - \eta_t p \end{vmatrix}$$

$$V_1 = \frac{1}{J} \begin{vmatrix} 0 \\ b_1 u_\xi + b_2 v_\xi \\ b_2 u_\xi + b_3 v_\xi \\ b_1 u u_\xi + b_2 (vu_\xi + uv_\xi) + b_3 vv_\xi + b_4 T_\xi \end{vmatrix}$$

$$V_2 = \frac{1}{J} \begin{vmatrix} 0 \\ c_1 u_\eta + c_2 v_\eta \\ c_3 u_\eta + c_4 v_\eta \\ c_1 u u_\eta + c_2 uv_\eta + c_3 vu_\eta + c_4 vv_\eta + c_5 T_\eta \end{vmatrix}$$

$$W_1 = \frac{1}{J} \begin{vmatrix} 0 \\ c_1 u_\xi + c_3 v_\xi \\ c_2 u_\xi + c_4 v_\xi \\ c_1 u u_\xi + c_2 vu_\xi + c_3 uv_\xi + c_4 vv_\xi + c_5 T_\xi \end{vmatrix}$$

$$W_2 = \frac{1}{J} \begin{vmatrix} 0 \\ d_1 u_\eta + d_2 v_\eta \\ d_2 u_\eta + d_3 v_\eta \\ d_1 u u_\eta + d_2 (vu_\eta + uv_\eta) + d_3 vv_\eta + d_4 T_\eta \end{vmatrix}$$

U and V denote the contravariant velocity
components

$$U = \xi_t + \xi_x u + \xi_y v$$
$$V = \eta_t + \eta_x u + \eta_y v \tag{2}$$

b_i, c_i, d_i are viscous coefficients,[20] and

$$\xi_x = y_\eta J, \qquad \xi_y = -x_\eta J,$$
$$\xi_t = -(x_\tau y_\eta - y_\tau x_\eta) J$$

$$\eta_x = -y_\xi J, \qquad \eta_y = -x_\xi J,$$
$$\eta_t = (x_\tau y_\xi - y_\tau x_\xi) J \tag{3}$$

$$J = 1/(x_\xi y_\eta - x_\eta y_\xi)$$

are the transformation metrics. Closure
of this system of equations is provided by
the perfect gas law, Sutherland's
viscosity formula and the assumption of a
constant Prandtl number.

In reference to the pitching airfoil
configuration shown in Fig. 1, the
boundary conditions are prescribed as
follows. Along the inflow portion of the
farfield boundary, freestream conditions
are given. First order extrapolation
$(\partial[\ ]/\partial x = 0)$ is used on the outflow
boundary for all flow variables. In the
azimuthal direction, periodicity is
imposed by means of a five station grid
overlap. On the airfoil surface, the
following isothermal, no slip condition is
applied:

93

$$\vec{U} = \vec{U}_B$$

$$T_w = T_\infty \qquad (4)$$

$$\frac{\partial p}{\partial n} = - \rho \vec{a}_B \cdot \vec{n}$$

where $\vec{U}_B$ and $\vec{a}_B$ denote respectively the velocity and acceleration on the airfoil surface given by

$$\vec{U}_B = \vec{\Omega} \times (\vec{r}_B - \vec{r}_0) \qquad (5a)$$

$$\vec{a}_B = \frac{d\vec{\Omega}}{dt} \times (\vec{r}_B - \vec{r}_0) - \Omega^2 (\vec{r}_B - \vec{r}_0) \qquad (5b)$$

for the case of rotation about a fixed axis (Fig. 1). For the nominally constant pitch-up motion considered in this paper, the following temporal variation, which avoids an infinite angular acceleration, is prescribed for Ω:

$$\Omega(t) = \Omega_\bullet (1 - e^{-4.6t/t_\bullet}), \quad t \geq 0 \qquad (6)$$

where $t_\bullet$ denotes the time taken by the airfoil to reach 99% of its final pitch rate $(\Omega_\bullet)$. The influence of $t_\bullet$ on the computed flow field had been previously investigated[10] and found to be limited to the early stages of the airfoil motion.

Finally, the formulation of the problem is completed by imposing as an initial condition the computed flow at zero-degree angle of attack.

III.   Numerical Procedure

The time-dependent coordinate transformation (i.e. moving grid) required in the present flow simulation may be implemented in two different fashions. One approach employs a deformable grid with a fixed farfield boundary, as described for instance in Ref. 17. An alternative method, more suitable for the case of a single, non-deformable body in an unbounded domain, consists of using a 'rigid' grid attached to the airfoil.[16] The latter approach is employed in this work since it eliminates the need for multiple grid generation. Once an initial grid is constructed, the physical coordinates (x,y) and grid speeds (x_τ, y_τ) can be easily computed as a function of the airfoil angle of attack $[\alpha(t)]$ and angular velocity $[\Omega(t)]$.

Nearly-orthogonal boundary-fitted grids are generated about the airfoil employing the elliptic technique of Ref. 18. A typical grid for the NACA 0015

section is shown in Fig. 2. In order to facilitate the use of an O topology, the airfoil trailing edge is rounded (Fig. 2) with a circular arc of radius $r/c = 0.002$. Three different grid sizes are considered (113x51, 203x101, and 304x123). The medium grid, selected for the majority of the calculations, extends approximately 30 chords away from the airfoil and has minimum spacings of 0.00075c and 0.00005c in the ξ and η directions respectively.

The governing equations are numerically solved employing the implicit approximate-factorization algorithm of Beam and Warming.[15] This scheme is formulated using three-point backward time-differencing and second-order centered approximations for all spatial derivatives. In order to control numerical stability, both explicit and implicit smoothing terms are added to the basic algorithm. A fully vectorized Navier-Stokes solver which employs the above scheme has been developed and successfully validated for a variety of both steady and unsteady flow problems.[10,13,19] Further details of the numerical procedure can be found in Refs. 10 and 20.

IV.   Results and Discussion

Calculations were performed for the flow field configuration depicted in Fig. 1. A NACA 0015 airfoil was pitched about a fixed axis from zero incidence to a maximum angle of attack of approximately sixty degrees with an angular velocity of the form given by Eq. (6). The freestream Mach number and chord Reynolds number were 0.2 and 10^4 respectively. The non-dimensional pitch rate $\Omega_\bullet^{\prime}$ was varied from 0.1 to 0.6, while the pivot axis location ranged from the airfoil leading edge to the 75%-chord station. A summary of all cases computed is provided in Table 1.

The discussion of the present results is divided into the following major areas: (1) Evaluation of the accuracy of the computed results, (2) description of the basic flow field structure, and (3) parametric effects of pitch rate and pivot axis location.

Evaluation of the Accuracy of the Computed Solutions

Before proceeding to make any observations pertaining to the physical aspects of the flow, estimates of the accuracy of the computed solutions must be provided. Despite the obvious importance of such accuracy evaluations, they are not common in the literature, a fact which renders many computationally derived observations inconclusive, at best.

94

In the present calculations, numerical uncertainties were mainly associated with (1) time-discretization (i.e. time step value), (2) spatial resolution, and (3) numerical damping terms. Other sources of error (e.g. farfield boundary location and implementation of implicit boundary conditions) were previously investigated[10] for an unsteady separated flow, and found to be of less significance.

The effect of the time step value on the computed pitching airfoil flow was documented in Ref. 10 for the case of $\Omega_\bullet^+ = 0.2$ (case 4, Table 1). It was concluded in that study that a numerical solution effectively independent of time step was achieved if $\Delta t^+ \leq 0.001$, where Δt^+ denotes the non-dimensional time step $(\Delta t U_\infty/c)$. Therefore, the time step value $\Delta t^+ = 0.001$ was specified in all the present calculations. For the medium (203x101) grid size used, the corresponding Courant number was approximately 100, which indicates that the scheme is very efficient compared to an explicit algorithm.

The sensitivity of the computed flow field to spatial resolution was evaluated for the case when $\Omega_\bullet^+ = 0.6$ (case 11, Table 1). Calculations were performed using the three different grid systems, previously discussed in Section III. Although further grid refinements are desirable, the finest (304 x 123) grid employed was the largest one possible given the available computer resources (CRAY XMP/12). The effect of grid size on the predicted lift and drag coefficients is shown in Fig. 3. The maximum difference in C_L between the fine and the medium grid was approximately 3.5%. A clearer estimation of spatial resolution effects can be obtained by examining the vorticity field in the vicinity of the airfoil. Vorticity is the variable which best describes the physics of these unsteady separated flows and also is a good indicator of the fidelity of numerical simulations to the physics. Figure 4 is a plot of iso-vorticity contours obtained with the three different grid systems, at two instants during the airfoil pitching motion. It can be observed that the first grid refinement produced significant changes in the computed solution. However, after the second mesh refinement, the discrepancies were considerably reduced and did not alter the primary vortical structures in the vicinity of the airfoil. The medium grid was considered suitable for the present study since it adequately resolved all the primary features of the flow.

To conclude this accuracy evaluation, the sensitivity of the solution to numerical smoothing was evaluated for the selected (203x101) grid. As shown in Fig. 5, increasing both the explicit and the implicit damping coefficients by a factor of two produced only small changes in the computed vorticity field without altering its primary structure.

The present limited accuracy study seems to indicate that the computed results are of sufficient quality to merit further physical analysis. However, two important observations must be kept in mind. First, the level of accuracy is in general a function of the specific flow parameters (i.e. $\Omega_\bullet^+$, $X_\bullet/c$). Secondly, the numerical uncertainties become more significant at higher angles of attack (Figs. 3 and 4). This is a consequence of the cummulative effects of dissipation errors, and of the increased flow field complexity with time.

Basic Flow Field Structure

This section presents a description of the most important unsteady features of the flow past a pitching airfoil. This is done in order to set the stage for the subsequent discussion of parametric effects. The flow field evolution for the case when $\Omega_\bullet^+ = 0.2$ (case 4, Table 1) is provided by means of iso-vorticity contours (Fig. 6) and surface pressure distributions (Fig. 7). From these figures as well as from a computer generated color movie, the following sequence of flow events is observed.

At zero incidence, the flow is symmetric and displays a small trailing edge separation region. As the pitching motion begins, the flow becomes fully attached along the airfoil lower surface, while on the upper surface the separation point moves upstream (Fig. 6a). The near-wake experiences significant curvature and after a short time reorganizes itself into a series of discrete vortices (Fig. 6a). Counter clockwise (positive) vorticity is shed into the wake, while negative vorticity accumulates and remains close to the airfoil. Both of these features contribute to an increase in clockwise circulation and lift. With the continuous increase in airfoil incidence, the upper surface separation region eventually reaches the leading edge area. Subsequently, the separated shear layer reattaches dividing the upper surface flow into two distinguishable vortical structures denoted as the leading edge or dynamic stall vortex and the shear layer vortex (Fig. 6b). The latter is in itself composed of two sub structures which rotate about each other and later amalgamate to form a single vortex (Fig. 6c). In addition to these primary vortical features, secondary vortical structures are also observed. The leading edge vortex grows in size and its center

95

is displaced downstream (Figs. 6b,c,d), as also evidenced by the pressure distribution (Fig. 7). The leading edge vortex detaches when its center is approximately at the mid-chord location. By this time, a well-defined and rapidly growing counter-clockwise vortex is observed to remain attached to the trailing edge (Fig. 6e). The shear layer vortex, which had begun to be convected downstream (Fig. 6d), is brought back and impinges on the airfoil surface due to the combined influence of the leading and trailing edge vortices (Fig. 6e). In a very complex interaction, which involves dramatic rotational effects, the first and second leading edge vortices as well as the shear layer vortex combine to form a larger vortical structure (Fig. 6f). This structure is then convected along a path nearly normal to the airfoil chord due to the blockage effect of the trailing edge vortex. As it will be seen later in this paper, many of the above basic flow features are retained over a wide range of pitch rates and pivot axis locations.

The basic flow structure previously described is in qualitative agreement with experimental flow visualizations[6,21] obtained for higher Reynolds numbers $(Re_c > 4.5 \times 10^4)$. In order to permit a more direct comparison with the experiments, the case when $\Omega_o^+ = 0.2$ and $X_o/c = 0.25$ (case 4, Table 1) was recomputed using a chord Reynolds number of 45,000, while still retaining the assumption of laminar flow. For this higher Reynolds number, the computed flowfield at zero incidence was unsteady with periodic shedding of vortices at the trailing edge. This behavior is in agreement with experimental flow visualizations.[6,21] A comparison of the computed and experimental[7] lift coefficient histories is shown in Fig. 8. The agreement is reasonable despite the assumption of laminar flow employed in the calculation. In particular, the maximum lift value and the angle of attack at which it occurs are in close agreement.

A comparison of the computed streaklines with the experimental smoke visualization is presented in Fig. 9 for selected angles of attack. Both the computed and the experimental flow visualizations are primarily characterized by a large region of recirculating streaklines on the airfoil leeward side. The correlation of this recirculation region of streaklines with the dynamic stall vortex is shown in Fig. 10 at an angle of attack of 40 degrees. Comparison of the computed and experimental flow visualizations (Fig. 9) also indicates reasonable agreement regarding the size and location of the dynamic stall vortex. The agreement between experimental and computed vortex location is also illustrated in Fig. 11 which shows the displacement,

along the airfoil upper surface, of the vortex-induced suction peak.

The previous favorable comparison between the experimental and the computed laminar results has the following important implication: For high values of Ω_o^+, the strong large-amplitude forced motion overwhelms transition and turbulence effects in so far as the primary flow features are concerned. In this regard, the prediction of static stall or of dynamic stall for values of $\Omega_o^+ << 1$ would constitute a more difficult problem.

Effects of Pitch Rate and Pitch Axis Location

The dependence of the flow field structure on the pitch rate and the pivot location was investigated. As Table 1 indicates, the non-dimensional pitch rate was varied over the range 0.1-0.6, and four different axis locations were considered $(X_o/c = 0., 0.25, 0.5,$ and 0.75). The influence of pitch rate and axis location on the flow is discussed in terms of how these parameters affect the observed vortical structure and the airfoil aerodynamic loads.

Figures 12-14 show the vorticity field at three angles of attack for different pitch rates and pitch axis locations. Based on these figures and many others,[22] the following observations can be drawn pertaining to the qualitative aspects of the vortical structure:

(1) Over the range of Ω_o^+ and X_o/c considered, the flow was qualitatively characterized by the same primary features. These features include: upstream propagation of the trailing edge separation region, shedding of counter-clockwise vortices into the wake, formation of a leading edge vortex and a shear layer vortex, as well as their complex interaction. However, the quantitative characterization of these basic features (e.g. timing, vortex strength, etc) showed a strong dependence on the pitch rate and the axis location. In addition, some of the flow events observed for $\Omega_o^+ = 0.2$ (Fig. 12) had not yet occurred for higher values of Ω_o^+ (Figs. 13 and 14) by the time α_{max} was reached. For instance, for $\Omega_o^+ = 0.6$ and $X_o/c = 0.75$ (Fig. 14b), the leading edge vortex was just beginning to form when the airfoil was near its maximum incidence.

(2) For a fixed pitch axis location downstream of the leading edge $(\frac{X_o}{c} > 0)$, increasing the pitch rate resulted in the

96

formation of the leading edge vortex at a higher angle of attack (Figs. 12-14). Similarly, for a given value of Ω_o^+, displacing the pivot axis downstream delayed the appearance of the leading edge vortex. This behavior, which agrees with experimental observations,[6] can be partially explained by the following reasonings:

(a) Formation of the leading edge vortex involves a substantial flux of clockwise vorticity into the fluid by diffusion at the airfoil surface due to the high favorable streamwise pressure gradient present in the leading edge region. It also depends on the convection of this vorticity around the airfoil leading edge, and on the rolling up of the detached shear layer. Since this process requires a finite time, the airfoil, therefore, attains a higher angle of attack for a higher value of Ω_o^+, before the leading edge vortex is observed.

(b) The flow field evolution in the immediate vicinity of the leading edge is expected to be related to an 'effective' angle of attack (α_{eff}), defined[22] in terms of the relative velocity at the leading edge. In order to illustrate this point, the vorticity field in the neighborhood of the leading edge is shown in Fig. 15 for several Ω_o^+ and X_o/c values at the same effective incidence of $30°$. It can be seen that for a given pitch rate, the delay in the formation of the leading edge vortex due to the increase in X_o/c correlates reasonably well with the effective angle of attack. Since the non-dimensional leading edge speed is

$$\Omega_o^+ \left(\frac{X_o}{c}\right),$$

the retardation of the vortex evolution associated with the downstream displacement of the axis becomes quite pronounced at high values Ω_o^+. For $\Omega_o^+ = 0.6$ and $X_o/c = 0.75$, the induced negative values of α_{eff} are sufficient to produce temporary boundary layer separation on the airfoil lower surface.[22]

(3) Examination of the leading edge vortex at the time of shedding indicated that increasing Ω_o^+ resulted in a more coherent vortex whose center was located closer to the airfoil leading edge. On the other hand, variation of the pitch axis did not significantly affect the vortex size and location at the time of shedding. These characteristics had been also observed experimentally.[4,6]

(4) Examination of iso-vorticity contours in the forward stagnation region revealed dramatic displacement of the stagnation point along the airfoil surface. For the case of $\Omega_o^+ = 0.6$ and $X_o/c = 0.75$, the stagnation point moved from its initial location at the leading edge to the $X/c = 0.02$ station on the airfoil upper surface then backwards to the $X/c = 0.54$ station on the lower surface. In addition, as Fig. 16 indicates, the structure of the stagnation region differed considerably from the locally-symmetric structure encountered for stationary airfoils. The assumption of $\omega = o$ at the stagnation station, as done for instance in the marching technique of Ref. 11, obviously does not hold for high pitch rates.

After the above remarks on the qualitative features of the vorticity field, we now discuss a few of its quantitative aspects. Figure 17 shows the minimum surface pressure levels induced by the leading edge vortex for different pitch rates and pitch axis locations. If these high suction values are interpreted as an approximate measure of vortex strength, the following observations can be made: (1) the vortex strength is a function of both pitch rate and pivot location, (2) increasing Ω_o^+ or displacing the axis upstream produce a more energetic leading edge vortex, and (3) the effects of axis location on the vortex strength become less significant with decreasing Ω_o^+.

Since the vorticity present in the flow field is introduced at the airfoil surface by diffusion, it is of interest to document how the net vorticity flux at the wall varies as a function of pitch rate and axis position. As Fig. 18a indicates, the net flux of vorticity (ω_F) is only significant during the period of angular acceleration and becomes negligible as a constant pitch rate is reached. The net vorticity flux increases with Ω_o^+ but is independent of the pitch axis location. This behavior of ω_F is consistent with the law of vorticity conservation as explained in Ref. 23 for the case of incompressible flow. Since the same net vorticity flux can be satisfied by different combinations of a positive vorticity flux (ω_F^+) and a negative vorticity flux (ω_F^-), it is of more value to examine ω_F^+ and ω_F^- separately. As shown in Fig. 18b, the fluxes of clockwise or counter-clockwise vorticity are a function of both pitch rate and axis position. For instance, increasing Ω_o^+ (with $X_o/c = 0.0, 0.25$) or displacing the axis upstream (with fixed

97

$\Omega_\bullet^+$) results in larger amounts of positive and negative vorticity being introduced in the flow. This observed variation of ω_F^+ and ω_F^- as a function of $\Omega_\bullet^+$ and $X_\bullet/c$ correlates with the leading edge vortex strength previously discussed (Fig. 17). In addition, since aerodynamic forces are linked to the time rate of change of the first moment of vorticity,[23] it is reasonable to expect that the maximum forces experienced by the airfoil will show a dependence on $\Omega_\bullet^+$ and $X_\bullet/c$ similar to that displayed by ω_F^+ and ω_F^-. The behavior of the airfoil aerodynamic loads is discussed in the remainder of this section.

Complete results of the airfoil aerodynamic coefficient histories are given in Ref. 22. As a representative example, the evolution of the aerodynamic loads is shown in Fig. 19 for the case of $\Omega_\bullet^+ = 0.4$ and $X_\bullet/c = 0.0$. The dynamic effect of the pitch-up motion on the magnitude of the aerodynamic coefficients is striking. In this particular case, the normal force coefficient (C_N) attains a maximum value of approximately 5.5 (at $\alpha = 52°$) before it begins to decline. Figure 19b indicates that a large nose-down quarter-chord moment coefficient is also obtained. More surprising however, is the fact that the axial force coefficient (C_A) assumes a large negative value (Fig. 19b) which denotes thrust. The thrust on the airfoil becomes more significant with increasing pitch rate.[22] During the onset of rotation, the normal force is seen to vary at a rapid rate due to the effects of impulsive forces (which include apparent mass effects). These forces, shown in Fig. 20, are dependent on the magnitude of the maximum angular acceleration ($\dot{\Omega}^+$) and on the location of the pivot axis. For the cases when $X_\bullet/c = 0.75$, these impulsive forces are directed downwards (negative) since most of the airfoil section is moving in the opposite direction.

The variation of maximum lift coefficient ($C_{L_{max}}$) as a function of pitch rate and pivot axis location is shown in Fig. 21 as an example of the effect of these parameters on the aerodynamic loads. Some experimental results from Refs. 7, 8, and 24 are also included for comparison. The maximum lift is dependent on both pitch rate and axis position. However, the influence of pivot location becomes less significant with decreasing $\Omega_\bullet^+$. In all cases it is found that for a fixed $\Omega_\bullet^+$,

the upstream displacement of the pitch axis results in an increase in lift. For a given value of $X_\bullet/c$, however, the variation of $C_{L_{max}}$ with $\Omega_\bullet^+$ cannot be so easily described. For instance, the slope $\dfrac{\partial C_{L_{max}}}{\partial \Omega_\bullet^+}$, can be either positive or negative depending on the pivot location. For $X_\bullet/c = 0.$ and $X_\bullet/c = 0.25$, the maximum lift coefficient is approximately proportional to $\sqrt{\Omega_\bullet^+}$ over the range of pitch rates considered. For $X_\bullet/c = 0.75$, $C_{L_{max}}$ increases for small pitch rates ($\Omega_\bullet^+ \lesssim 0.2$), remains nearly constant over a wide range ($0.2 \lesssim \Omega_\bullet^+ \lesssim 0.4$) and then actually begins to decrease ($\Omega_\bullet^+ \gtrsim 0.4$).

A precise explanation of the large aerodynamic loads experienced by the airfoil and of their dependence on the pitch rate and axis location constitutes a difficult problem. This difficulty arises in part due to the fact that aerodynamic forces are the integrated effect of various complex flow processes which simultaneously take place in the vicinity of the airfoil. Several comments, however, can be made which, despite being of a qualitative nature, provide some insight into the observed flow behavior. In the theoretical work of Wu,[23] it is shown that the force exerted by the fluid on the airfoil is the result of two contributing terms. The first term is proportional to the time rate of change of the total first moment of vorticity while the second term is an inertia force associated with the mass of fluid displaced by the airfoil. For the case of constant rotation rate about a fixed axis, the second term is proportional to $(\Omega_\bullet^+)^2 (A/c^2)(r_c/c)$ where r_c/c denotes the distance from the pitch axis to the centroid of the airfoil area A. This contribution, which has the form of a centrifugal force, is not significant for the pitch rates and pitch axis locations considered in the present investigation ($\Omega_\bullet^+ < 1$, $A/c^2 < 1$, $r_c/c < 1$). The large aerodynamic loads observed are therefore the result of the time rate of change of the first moment of vorticity. In principle, this term could be computed, and the contribution to the aerodynamic forces due to the different physical processes could be identified. However, this approach is only practical if the vorticity may be assumed to be contained within thin regions (vortex sheets) or concentrated in point vortices (see, for

example, Refs. 25 and 26). Nevertheless, on a qualitative basis, vorticity-moment arguments suggest that large transient aerodynamic forces are the result of substantial amounts of counter-clockwise vorticity being shed from the lower surface boundary layer into the wake, while the corresponding clockwise vorticity (which must be present according to vorticity conservation) temporarily remains in the vicinity of the airfoil due to the formation of the leading edge vortex. This behavior is the key feature observed in the present computations as well as in experimental flow visualizations.[6,21]

To conclude this section, a few remarks are included regarding the role of the pitch axis location. The position of the pitch axis determines how much of the airfoil is moving against the incoming flow. For pivot locations upstream of the leading edge $(X_o/c \leq 0)$, the airfoil is moving as a whole against the incoming flow. On the other hand, for $X_o/c \geq 1.0$ the airfoil is retreating. In addition, for a fixed value of Ω_o^+, the pitch axis position determines the relative velocities at the airfoil leading- and trailing-edge. Displacing the pivot axis upstream therefore results in (1) higher pressures on the airfoil lower surface (Fig. 22) and in (2) larger relative velocities at the leading and trailing edge areas. Both of these features result in higher pressure gradients along the airfoil surface, and consequently, in an increase in the vorticity fluxes (Fig. 18b) and the aerodynamic forces (Fig. 21) (since also more counter-clockwise vorticity can be shed at the trailing edge from the lower surface boundary layer into the wake). A comment should also be made regarding the relation between lift and the delay in the leading edge vortex formation. It is incorrect to assume that larger aerodynamic forces will be induced as a result of further delays in the leading edge vortex development. As the present calculations indicate, for a given Ω_o^+, displacing the pitch axis downstream delays the appearance of the leading edge vortex (Figs. 12-14) but results in smaller values of lift (Fig. 21).

Finally, the location of the pitch axis determines whether the airfoil actually imparts or extracts energy from the incoming flow. This is illustrated in Fig. 23 which shows the moment coefficient about the pivot axis (i.e. torque) required to maintain the prescribed constant pitch rate motion. It can be seen that for the cases when $X_o/c = 0.5$ and $X_o/c = 0.75$ the torque exerted by the fluid on the airfoil is in the direction of rotation, and consequently, the airfoil extracts energy from the surrounding stream.

V. Concluding Remarks

A numerical study was conducted for the case of laminar flow around a NACA 0015 airfoil which pitches at a constant rate to a very high angle of attack. The sensitivity of the computed solutions to grid resolution and numerical damping was investigated, and the results were shown to be of sufficient quality to merit examination of the primary features of the flow.

The highly unsteady flow structure was found to be characterized by (1) upstream propagation of separation from the trailing edge, (2) shedding of counter-clockwise vortices into the wake, (3) the formation of a leading edge vortex and a shear layer vortex on the airfoil leeward side and (4) the complex interaction of these vortices as they are being shed. The basic flow field structure for high pitch rates was shown to be in qualitative agreement with experimental observations, in spite of the assumption of laminar flow.

The dependence of the flowfield on the pitch rate and the pivot axis location was investigated. Over the range of Ω_o^+ and X_o/c considered, the flow displayed the same primary features or flow events. However, the quantitative characterization of these features showed a strong dependence on both the pitch rate and the axis position. For a given pitch rate, the downstream displacement of the pivot axis resulted in a delay in the dynamic stall vortex formation and in a reduction of the aerodynamic force experienced by the airfoil. For a given axis location downstream of the leading edge, increasing the pitch rate caused the dynamic stall vortex to form at a higher incidence. The behavior of the aerodynamic force coefficients with pitch rate was strongly dependent on the axis position. The maximum lift may either increase or decrease with increasing pitch rate, depending upon the axis placement.

References

1. McCroskey, W. J., "Unsteady Airfoils," Ann. Rev. Fluid Mech., Vol. 14, 1982, pp. 285-311.

2. Carr, L. W., "Dynamic Stall Progress in Analyses and Prediction," AIAA Paper 85-1769CP, 1985.

3. Lang, J. D. and Frances, M. S., "Unsteady Aerodynamics and Dynamic Aircraft Maneuverability," AGARD Symposium on Unsteady Aerodynamics-Fundamentals and Applications to Aircraft Dynamics, Gottingen, Germany, May 1985.

4. Francis, M. S. and Keesee, J. E., "Airfoil Dynamic Stall Performance with Large-Amplitude Motions," AIAA Journal, Vol. 23, No. 11, November 1985, pp. 1653-1659.

5. Jumper, E. J., Shreck, S. J., and Dimmick, R. L., "Lift-Curve Characteristics for an Airfoil Pitching at Constant Rate," AIAA Paper 86-0117, 1986.

6. Helin, H. E. and Walker, J. M., "Interrelated Effects of Pitch Rate and Pivot Point on Airfoil Dynamic Stall," AIAA Paper 85-0130, 1985.

7. Walker, J., Helin, H., and Chou, D., "Unsteady Surface Pressure Measurements on a Pitching Airfoil," AIAA Paper 85-0532, 1985.

8. Strickland, J. H. and Graham, G. M., "Force Coefficients for a NACA 0015 Airfoil Undergoing Constant Pitch Rate Motions," AIAA Journal, Vol. 25, No. 4, April 1987, pp. 622-624.

9. Robinson, M. et al, "Visualization of Three Dimensional Forced Unsteady Separated Flow," AIAA Paper 86-1066, 1986.

10. Visbal, M. R., "Evaluation of An Implicit Navier-Stokes Solver for Some Unsteady Separated Flows," AIAA Paper 86-1053, 1986.

11. Wu, J. C., Wang, C. M., and Tuncer, I. H., "Unsteady Aerodynamics of Rapidly Pitched Airfoils," AIAA Paper 86-1105, 1985.

12. Baldwin, B. and Lomax, H., "Thin Layer Approximation and Algebraic Model and Separated Turbulent Flows," AIAA Paper 78-257, 1978.

13. Visbal, M. and Knight, D., "The Baldwin-Lomax Turbulent Model for Two-Dimensional Shock Wave/Boundary Layer Interactions," AIAA Journal, Vol. 22, No. 7, July 1984, pp. 921-928.

14. Degani, D. and Schiff, L. B., "Computation of Supersonic Viscous Flows Around Pointed Bodies at Large Incidence," AIAA Paper 83-0034, 1983.

15. Beam, R. and Warming, R., "An Implicit Factored Scheme for the Compressible Navier-Stokes Equations," AIAA Journal, Vol. 16, No. 4, April 1978, pp. 393-402.

16. Steger, J., "Implicit Finite Difference Simulation of Flow About Arbitrary Two-Dimensional Geometries," AIAA Journal, Vol. 16, No. 7, July 1978, pp. 679-686.

17. Chyu, W. J., Davis, S. S., and Chang, K. S., "Calculation of Unsteady Transonic Flow Over an Airfoil," AIAA Journal, Vol. 19, No. 6, June 1981, pp. 684-690.

18. Visbal, M. and Knight, D., "Generation of Orthogonal and Nearly Orthogonal Coordinates with Grid Control Near Boundaries," AIAA Journal, Vol. 20, No. 3, March 1982, pp. 305-306.

19. Visbal, M. R. and Shang, J. S., "Comparative Study Between Two Navier-Stokes Algorithms for Transonic Airfoils," AIAA Journal, Vol. 24, No. 4, April 1986, pp. 599-606.

20. Visbal, M. R., "Calculation of Viscous Transonic Flows About a Supercritical Airfoil," AFWAL-TR-86-3013, 1986.

21. Walker, J. M., Helin, H. E., and Strickland, J. H., "An Experimental Investigation of an Airfoil Undergoing Large Amplitude Pitching Motions," AIAA Journal, Vol. 23, No. 8, August 1985, pp. 1141-1142 (see also AIAA Paper 85-0039, 1985).

22. Visbal, M. R., "Dynamic Stall of a Rapidly Pitched Airfoil A Numerical Study," Technical Report, Air Force Wright Aeronautical Laboratory (to be published).

23. Wu, J. C., "Theory for Aerodynamic Force and Moment in Viscous Flows," AIAA Journal, Vol. 19, No. 4, April 1981, pp. 432-441.

24. Dimmick, R. L., "Pitch Location Effects on Dynamic Stall," M.S. Thesis AFIT/GAE/AA-85-D-4, December 1985.

25. Wu, J. C., Sankar, N. L., and Hsu, T. M., "Some Applications of Generalized Aerodynamic Forces and Moments Theory," AIAA Paper 83-0543, 1983.

26. Wu, J. C. and Hu-Chen, H., "Unsteady Aerodynamics of Articulate Lifting Bodies," AIAA Paper 84-2184, 1984.

Table 1. Summary of Pitching Airfoil Computations

(NACA 0015 Airfoil, $M_\infty = 0.2$, $Re_c = 10^4$)

Case	Ω^*	t^*	X_*/c
1	0.1	0.5	0.25
2	0.1	0.5	0.75
3	0.2	0.5	0.0
4	0.2	0.5	0.25
5	0.2	0.5	0.75
6	0.4	1.0	0.0
7	0.4	1.0	0.25
8	0.4	1.0	0.5
9	0.4	1.0	0.75
10	0.6	1.0	0.0
11	0.6	1.0	0.25
12	0.6	1.0	0.75

Ω^*: Non Dimensional Pitch Rate, $\Omega.c/U_\infty$

t^*: Non Dimensional Acceleration Time, $t.U_\infty/c$ (Eq. (6))

X_*/c: Pivot Axis Location Measured from Airfoil Leading Edge
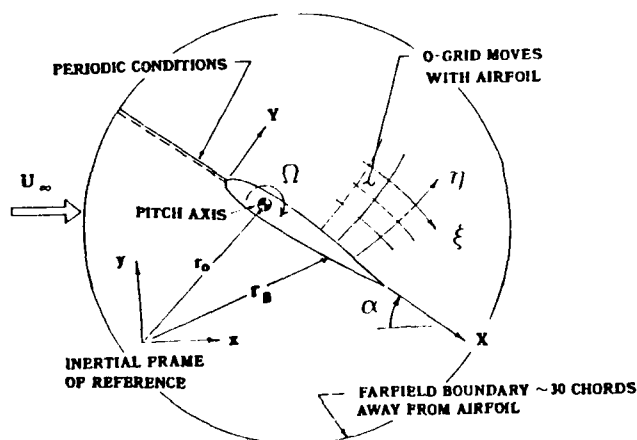
Figure 1. Pitching Airfoil Configuration
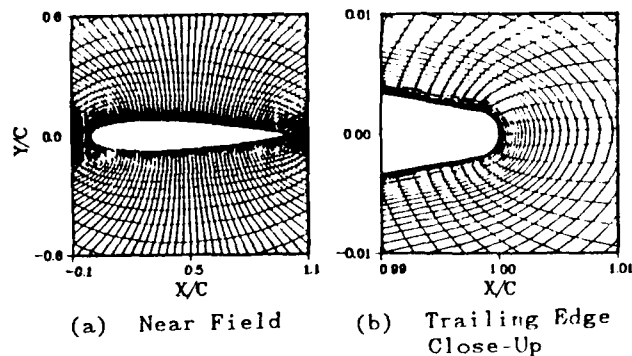

(a) Near Field   (b) Trailing Edge Close-Up

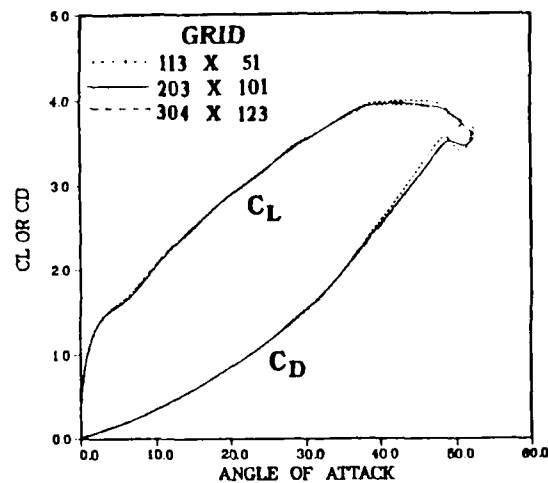Figure 2. Body Fitted Grid for NACA 0015 Airfoil

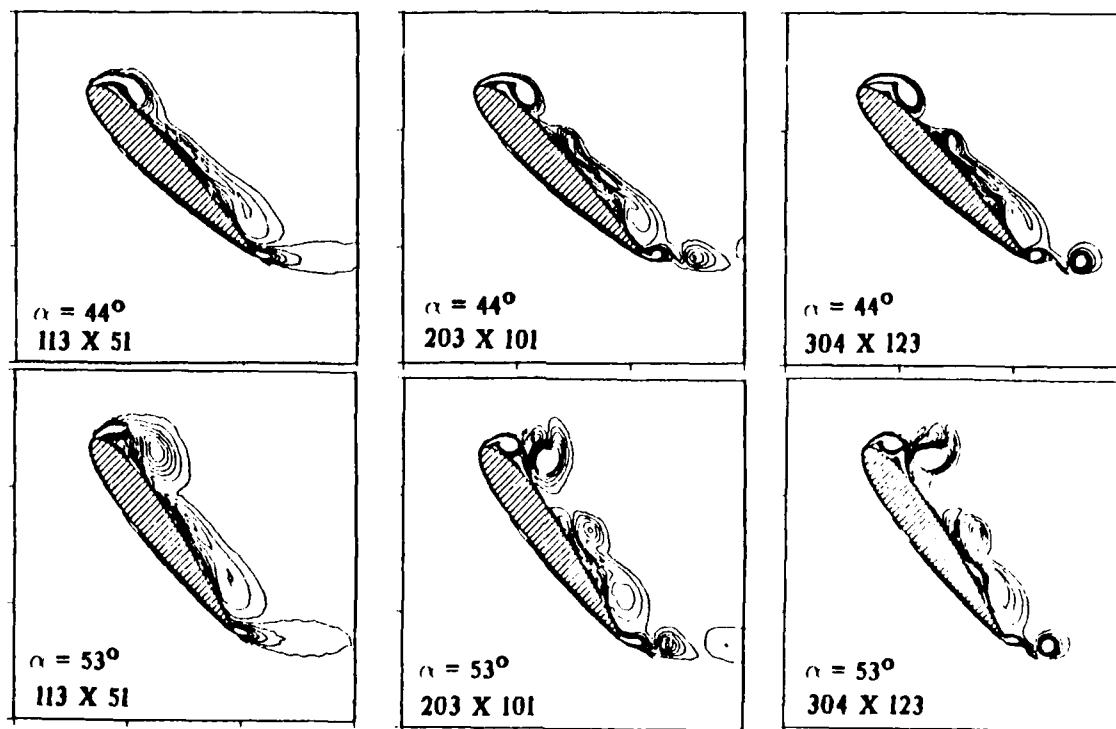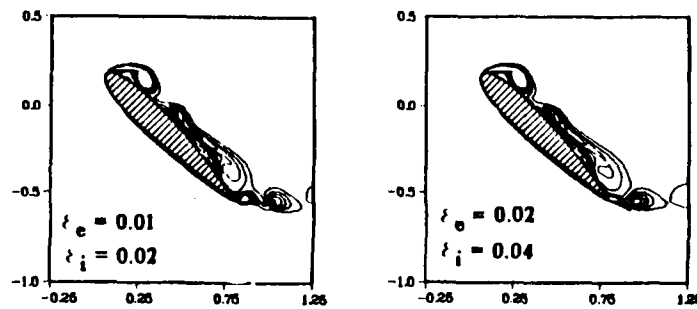Figure 3. Effect of Spatial Resolution on Computed Lift and Drag Coefficients (case 11)

Figure 4. Effect of Spatial Resolution on Vorticity Field (case 11)

101

ℓ_e = EXPLICIT DAMPING COEFFICIENT

ℓ_i = IMPLICIT DAMPING COEFFICIENT

Figure 5.   Effect of Damping Coefficients
on Vorticity Field (case 11,
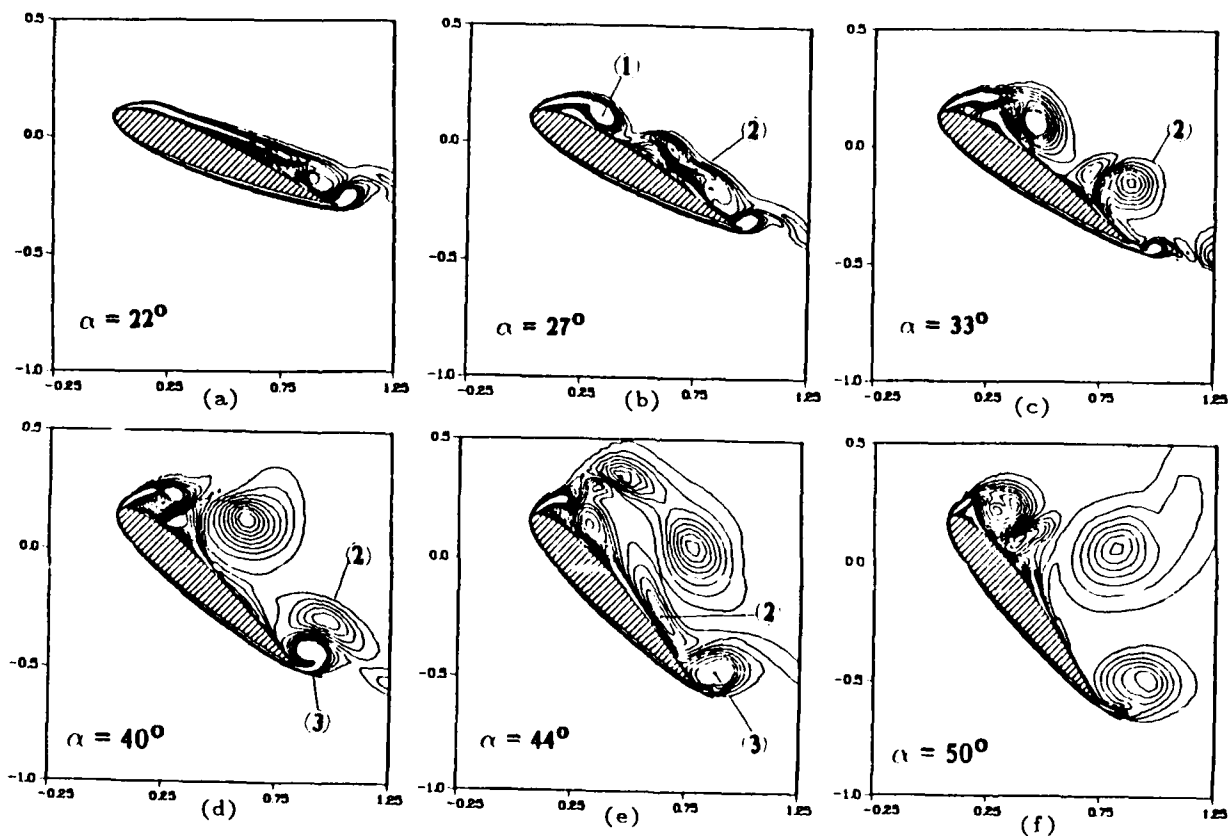$\alpha = 44^{\circ}$, Grid: 203 x 101)

Figure 6.   Evolution of Vorticity Field
(case 4)

① Leading Edge Vortex

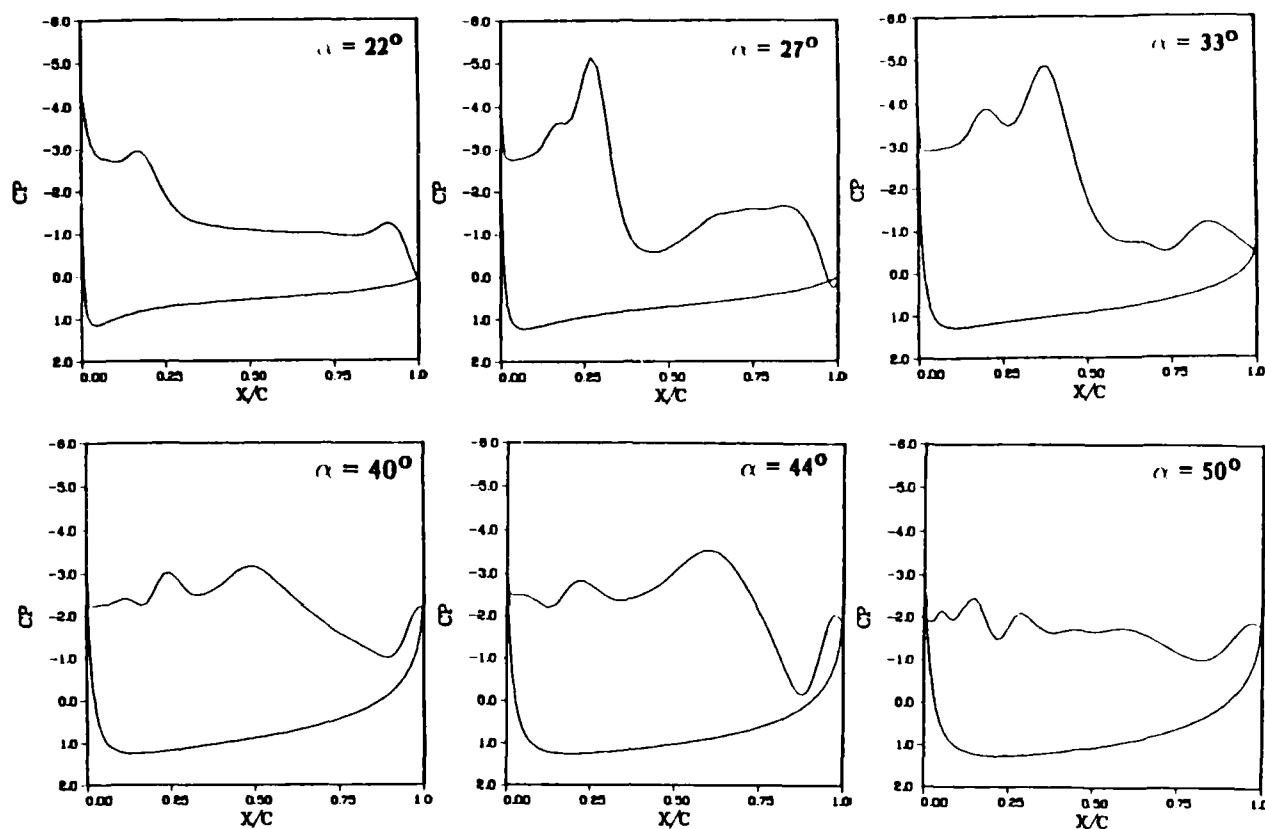② Shear Layer Vortex

③ Trailing Edge Vortex

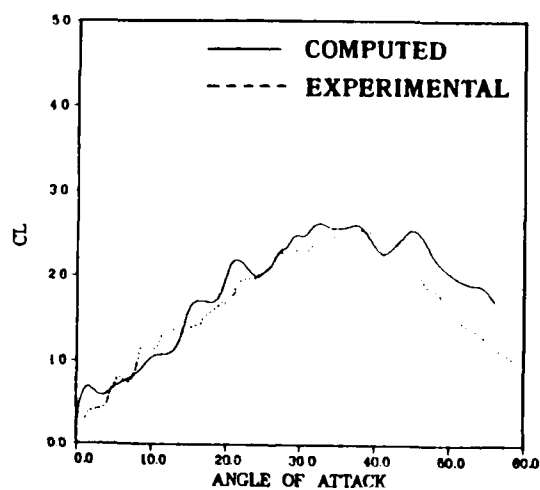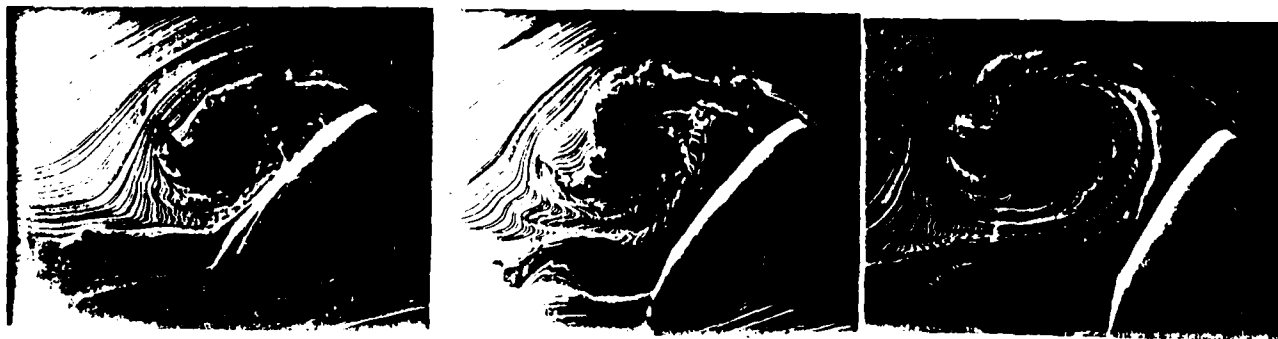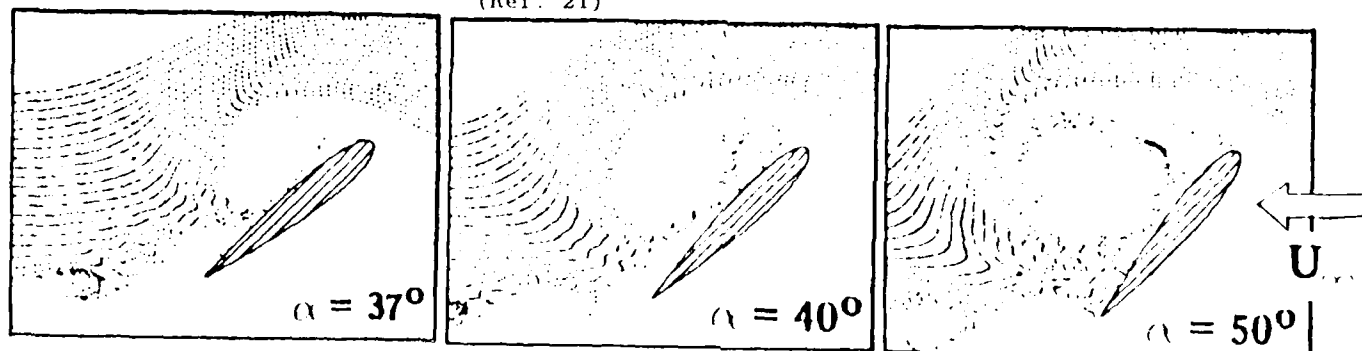Figure 7. Computed Airfoil Surface
Pressure Distributions (case 4)

Figure 8. Comparison of Computed and
Experimental Lift Coefficients
($\Omega_\bullet^+ = 0.2$, $X_\bullet/c = 0.25$,
$Re_c = 45,000$)

103

(a) Experimental Smoke Visualization
(Ref. 21)

$\alpha = 37^{\circ}$ $\alpha = 40^{\circ}$ $\alpha = 50^{\circ}$ U_∞

(b) Computed Streaklines

Figure 9.   Comparison of Computed and
Experimental Flow Visualiza
tions ($\Omega_o^+ - 0.2$, $X_o/c - 0.25$,
Re_c 45,000)
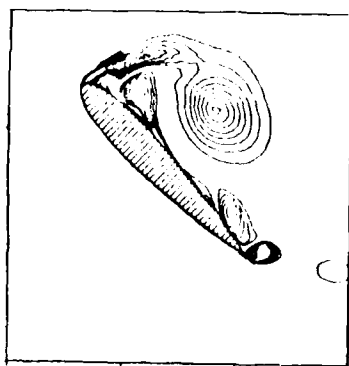
(a)   Iso Vorticity Contours

$\alpha = 40^{\circ}$
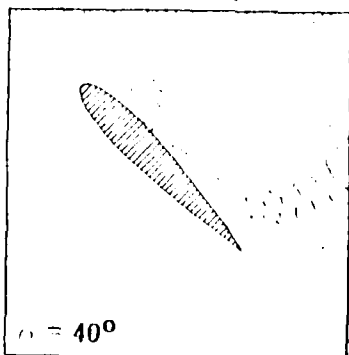
(b)   Streaklines

Figure 10.   Correlation of Computed
Dynamic Stall Vortex with
Streakline Recirculation
Region (Ω_o^+ 0.2, X_o/c 0.25,
Re_c 45,000)
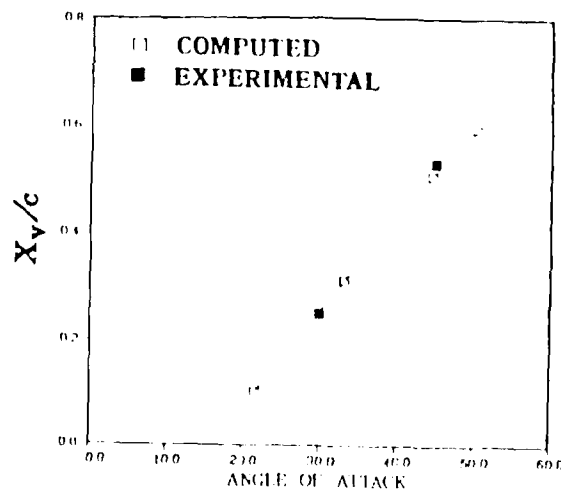
Figure 11.   Comparison of Computed and
Experimental Locations of the
Vortex Induced Suction Peak
(Ω_o^+ 0.2, X_o/c 0.25,
Re_c 45,000)

104

(a) $\Omega_e^+ = 0.2$, $X_e/c = 0.25$
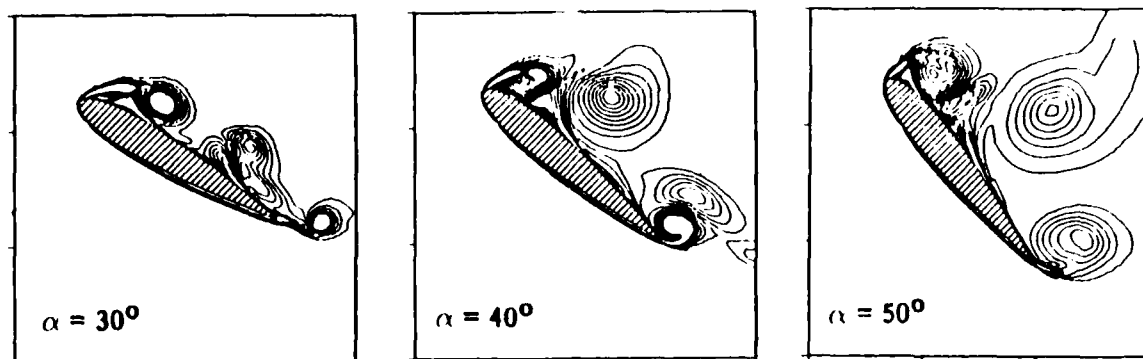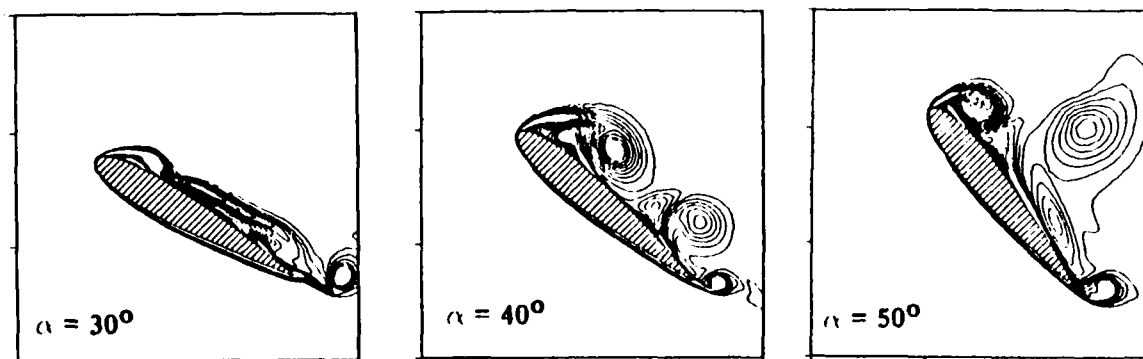
(b) $\Omega_e^+ = 0.2$, $X_e/c = 0.75$

Figure 12.   Evolution of Vorticity Field
for cases 4 and 5.

(a) $\Omega_e^+ = 0.4$, $X_e/c = 0.25$
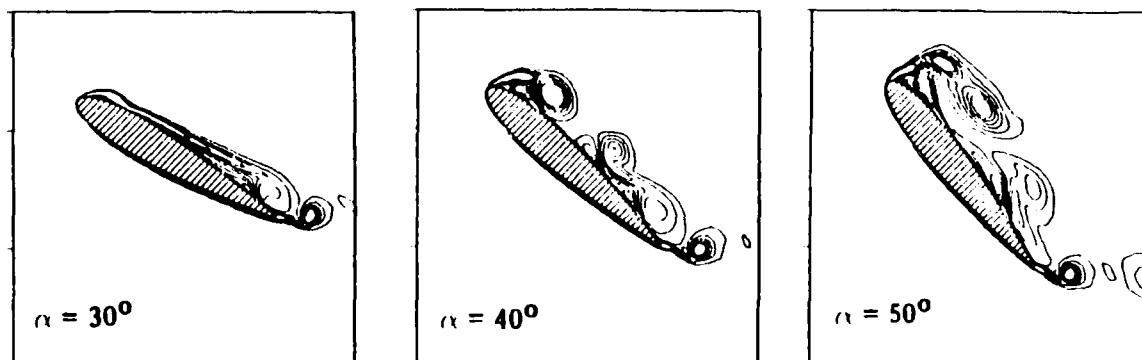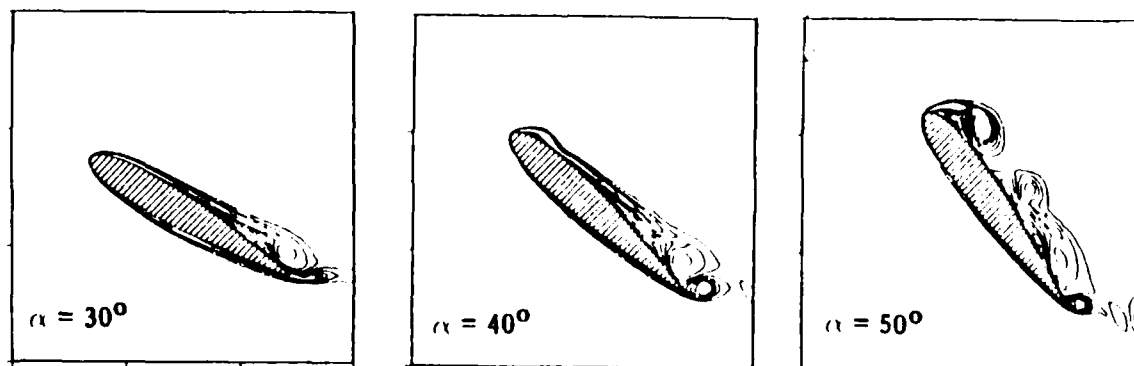
(b) $\Omega_e^+ = 0.4$, $X_e/c = 0.75$

Figure 13.   Evolution of Vorticity Field
for cases 7 and 9

105

(a) $\Omega_\bullet^+ = 0.6$, $X_\bullet/c = 0.25$

(b) $\Omega_\bullet^+ = 0.6$, $X_\bullet/c = 0.75$
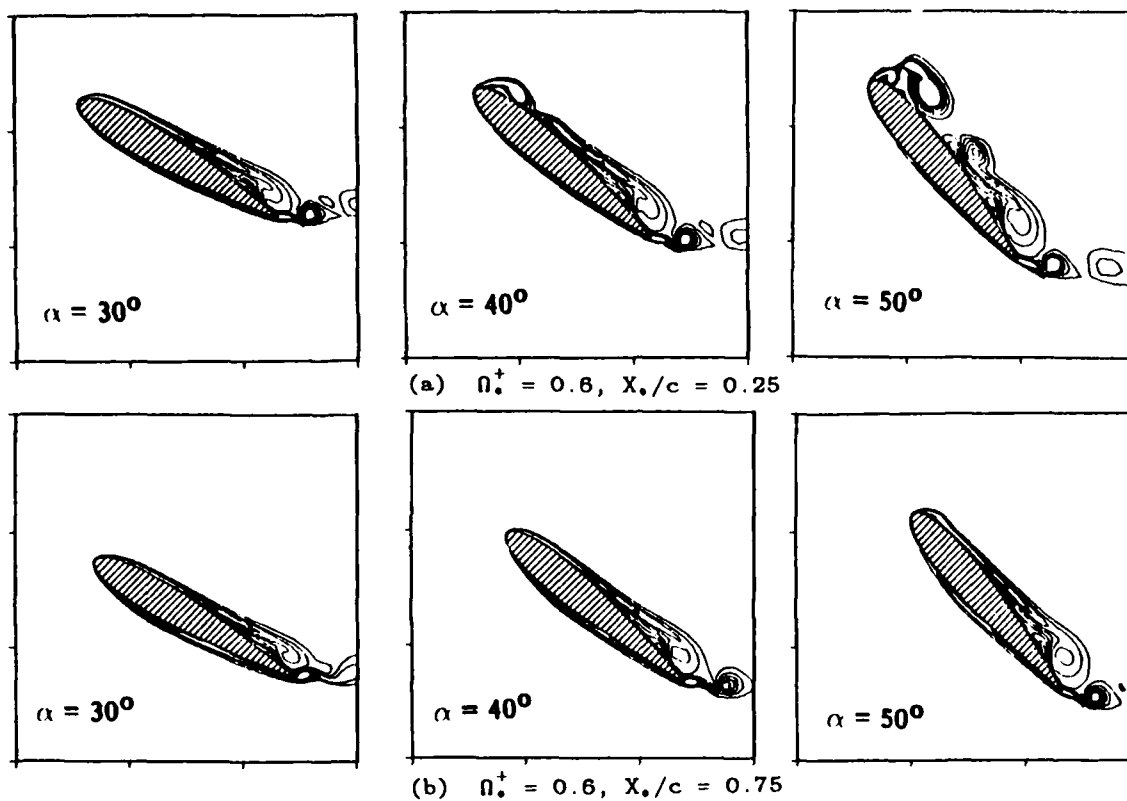
Figure 14.   Evolution of Vorticity Field
for cases 11 and 12

(a) $\Omega_\bullet^+ = 0.4$

(b) $\Omega_\bullet^+ = 0.6$
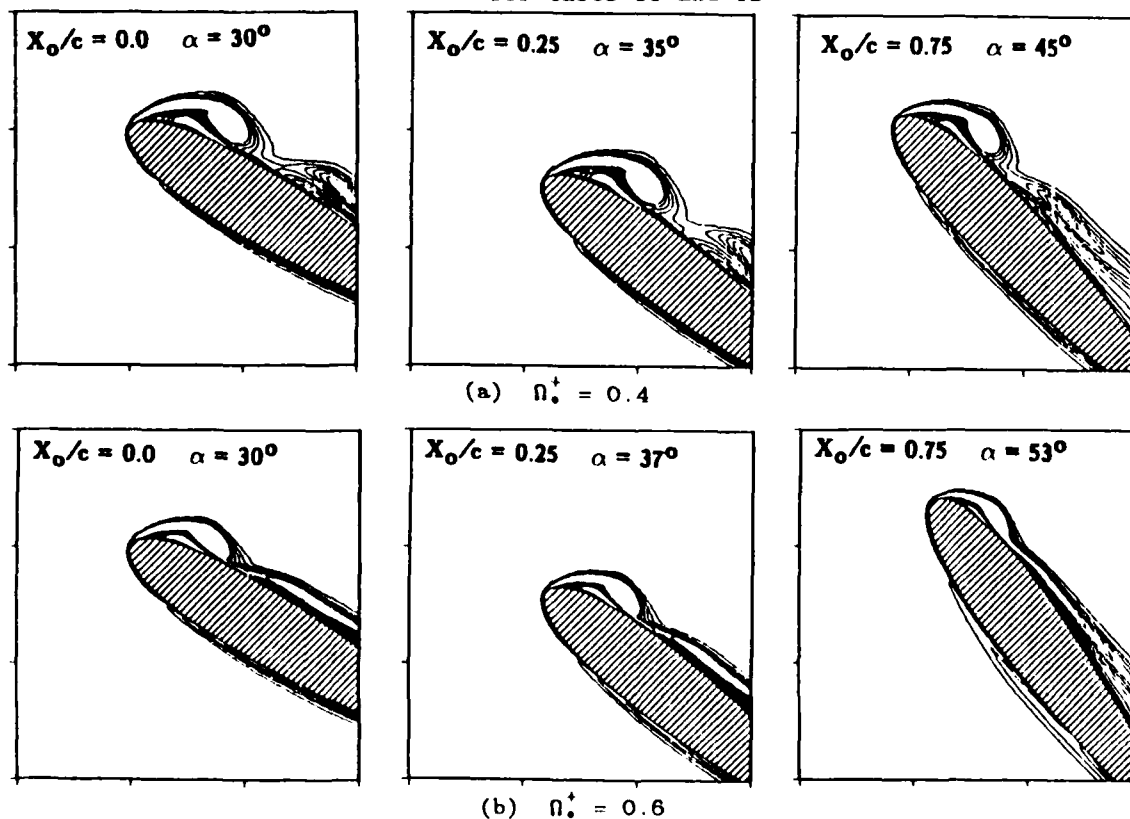
Figure 15.   Correlation of the Leading-
Edge Vortex Formation with the
Effective Angle of Attack

$(\alpha_{eff} = 30^\bullet)$

106
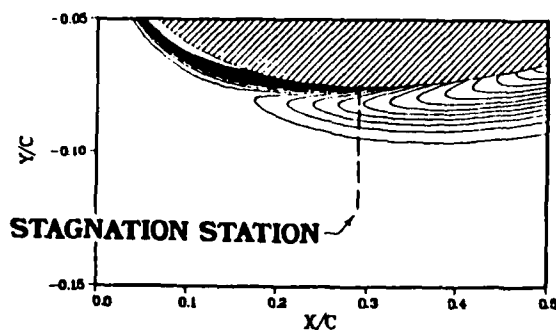
Figure 16.   Iso-Vorticity Contours Near
Stagnation Region ($\Omega_{\circ}^{+} = 0.6$,
$X_{\circ}/c = 0.25$)

Figure 17.   Effect of $\Omega_{\circ}^{+}$ and $X_{\circ}/c$ on the
Vortex-Induced Suction Peak

Ω_{o}^{+}	X_{o}/c
- - - - 0.6	0.0
△ 0.6	0.25
—— 0.4	0.0
○ 0.4	0.25
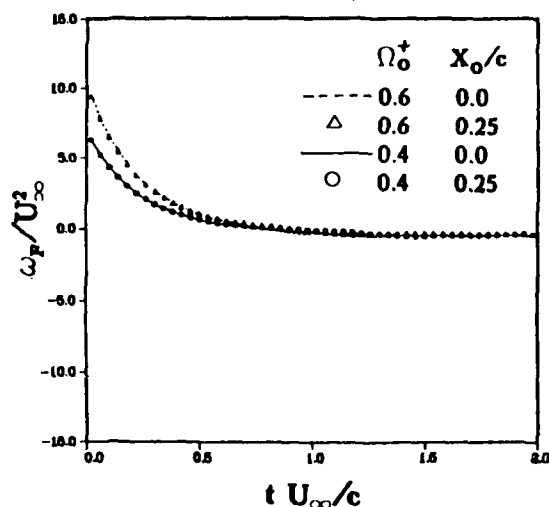
(a)   Net Vorticity Flux (ω_F)
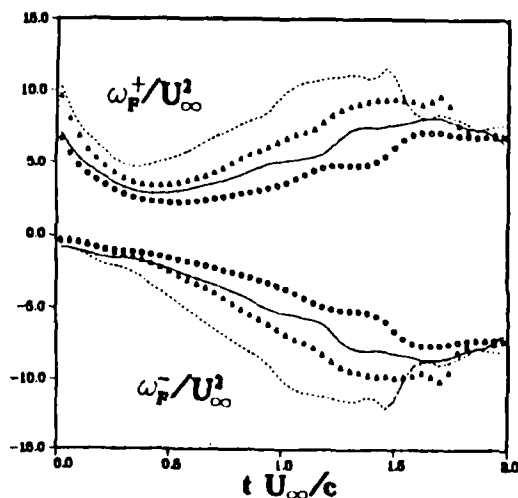
(a) C_L, C_N, and C_D

(b)   Positive (ω_F^{+}) and Negative

(ω_F^{-}) Vorticity Fluxes

Figure 18.   Effect of $\Omega_{\circ}^{+}$ and $X_{\circ}/c$ on the
Vorticity Flux at Airfoil
Surface
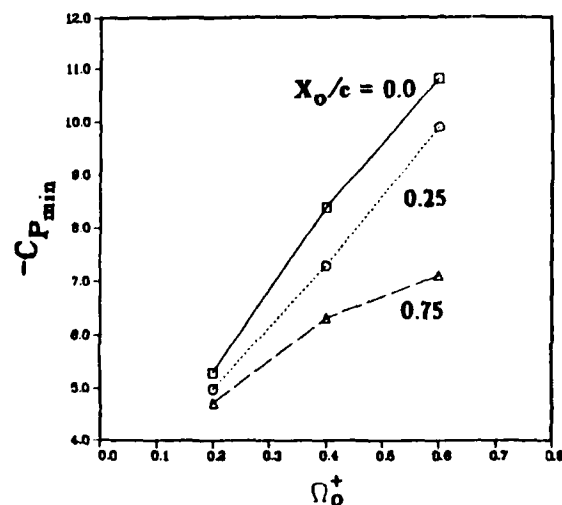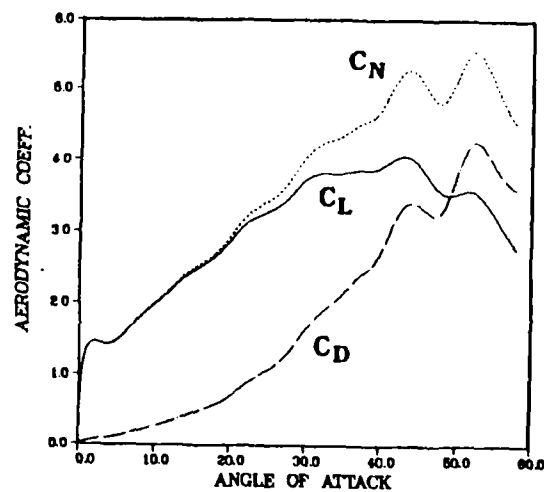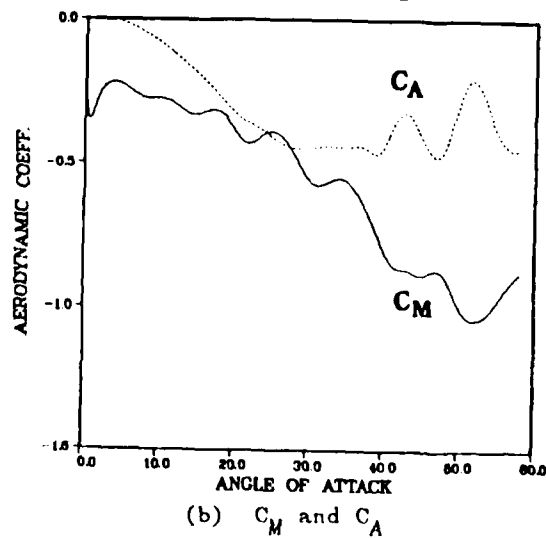
(b) C_M and C_A

Figure 19.   History of Airfoil Aerodynamic
Coefficients (case 6)

107
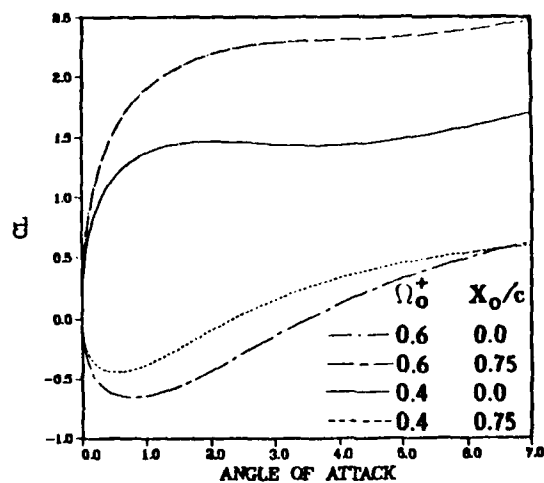
Figure 20. Effect of Ω_o^+ and X_o/c on the Impulsive Force at the Onset of Rotation
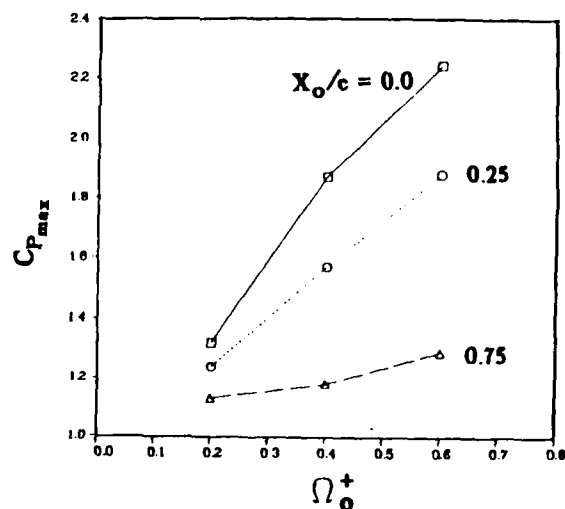
Figure 22. Effect of Ω_o^+ and X_o/c on the Maximum Lower Surface Pressure Coefficient

X_o/c		Re_c
Computed		
0.0		10^4
0.25		"
0.50		"
0.75		"
X 0.25		4.5×10^4
Experimental		
■ 0.25		4.5×10^4 (Ref. 7)
⊞ 0.25		10^5 (Ref. 8)
● 0.08 ~ 0.61		$1.5 \times 10^4 - 2.7 \times 10^4$ (Ref. 24)
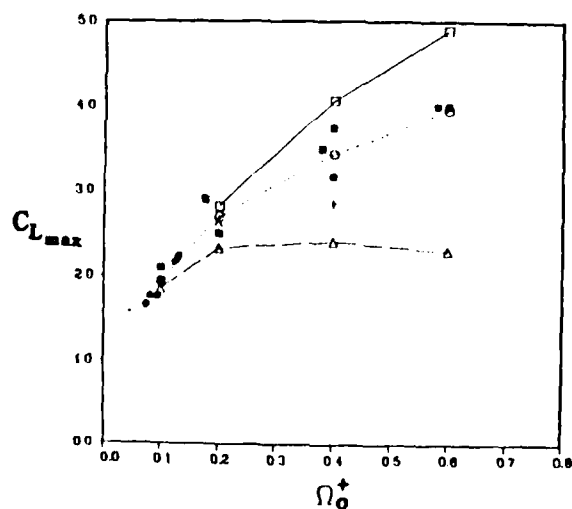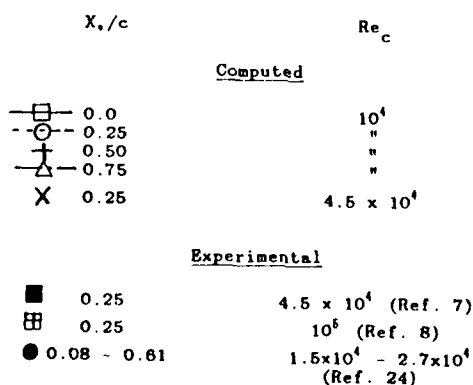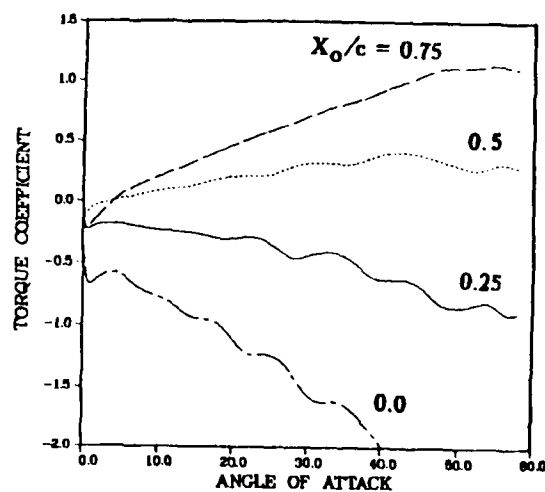
Figure 23. Effect of Pivot Location on the Torque Coefficient ($\Omega_o^+ = 0.4$)

Figure 21. Effect of Ω_o^+ and X_o/c on the Maximum Lift Coefficient

108

STUDY OF UNSTEADY SEPARATED VISCOUS FLOWS AND THEIR CONTROL

by

K.N. Ghia*, U. Ghia** and G.A. Osswald*
*Department of Aerospace Engineering and Engineering Mechanics
**Department of Mechanical and Industrial Engineering

Abstract

To provide a better understanding of the physics of massively separated viscous flows and their control, the present investigators are developing computational fluid dynamics (CFD) analyses for complex interacting viscous flows, using the unsteady Navier-Stokes (NS) equations. Three specific unsteady analyses, developed by the authors, partly under AFOSR sponsorship, are of particular interest and will be discussed here. Two of these analyses have been successfully applied to low-speed viscous flow problems to obtain their detailed flow structure and further insight into these flows.

1. Two-Dimensional Unsteady Flow in Near-Stall and Post-Stall Regimes

This study is undertaken to quantify the self-excited large-scale vortex-dominated unsteady separation associated with symmetric and cambered Joukowski airfoils at high incidence and extends the authors' earlier studies; Refs. 5, 6 and 9. The conservation form of the incompressible NS equations is formulated, using vorticity and stream function (ω, ψ) in generalized orthogonal curvilinear coordinates. A clustered conformal grid is generated. The clustering is controlled by appropriate 1-D stretching transformations. An attempt is made to resolve many of the dominant scales of an unsteady flow with massive separation, while maintaining the transformation metrics to be smooth and continuous in the entire flow field.

The self-excited large-scale vortex-dominated unsteady separation associated with airfoils at incidence has been shown to represent time-asymptotic attractor solutions of the unsteady Navier-Stokes equations. Limit-cycle (i.e., one-dimensional attractor geometries) and 2-torus (i.e. two-dimensional attractor geometries) solutions have been observed at Re=1,000 with both symmetric and cambered 12% thick Joukowski airfoils at incidence angles ranging from 15° to 53°. To date, no strange attractor has been simulated; however, the 2-torus solution for a symmetric Joukowski airfoil at 53° angle of attack has a low power broadband spectral tail, suggestive of the onset of chaotic flow or strange-attractor behavior.

First, results for the symmetric 12% thick Joukowski airfoil at 30° angle of attack are presented. Figure 1 displays an instantaneous picture of the streamlines and vorticity field for this flow. Instantaneous large-scale coherent vortex structure is clearly visible in Fig. 1b. The aerodynamic lift and drag coefficients as well as and L/D histories are presented in Fig.2. The airfoil was started impulsively from rest and the flow evolution is monitored until the initial transient has decayed and the time-asymptotic

persistently unsteady attractor solution is computed for a number of cycles.

Figure 3 is an attempt to visualize the attractor itself through the use of a pseudo phase-space portrait and Poincaré .sections. This attractor is a period-doubled limit cycle as demonstrated by its Fourier signature given in Fig. 4, which shows that the maximum power tone occurs at the shedding frequency of the large scale O(1) coherent vortex structures associated with the shear layers of the leading edge and the trailing edge. Here, the shedding occurs at a Strouhal number of 0.16769 in good agreement with experiment. In addition, the next most powerful tone occurs at the first subharmonic or a Strouhal number of 0.08384, with all other major tones occurring at integer multiples of this subharmonic. Since only a single harmonic series appears, the attractor is a limit-cycle or one-dimensional attractor. However, since a subharmonic of the physical shedding frequency occurs, the attractor has period-doubled, but has not yet bifurcated to become a two-dimensional attractor.

Once the underlying attractor has been established, its mean properties can be established with statistical confidence. Figure 5 presents the mean flow quantities, namely, the mean stream-function and mean vorticity fields. The tracks of the individual shed eddies are clearly revealed within the mean vorticity field of Fig. 5b. More importantly, Fig. 6 shows the Reynolds stress distributions within the highly unsteady wake regions computed from first principles. For these predictions, a turbulence model is neither employed nor required. These calculations are done strictly using unsteady Navier-Stokes analysis with sufficient resolution to resolve the dominant length scales of engineering significance.

Figures 7-10 present similar results for the Göttingen 580 airfoil, i.e., an 11.8% thick cambered Joukowski airfoil with a zero-lift angle of attack $\alpha_0 = -5.711°$. Again a period-doubled limit-cycle attractor evolves for the flow at 30° angle of attack.

2. Unsteady Flow Control Using 2-D Backstep Channel

Background

The present authors had previously studied in Refs. 4 and 8, the flow in a backstep channel and had observed persistently unsteady flow. This problem is reconsidered now for the purpose of controlling this flow via the oscillating-flap mechanism. This mechanism has been experimentally shown to provide effective control. In Refs. 7 and 11, Nagib and his colleagues demonstrated this in their experiments with the backstep channel.

Similar control should be possible for other internal-flow configurations, as well as for control of blunt-base wakes and airfoil wakes. The goal of active flow control is to employ forced unsteadiness to reduce reattachment length (or to close wakes), even if only momentarily, for achieving high lift and maneuverability.

For all of these flow-control configurations (Fig. 11), the boundary geometry changes with time. In order to study flows with temporally changing boundaries, it is necessary to develop an adaptive grid that continually aligns itself with the deforming boundary. Repeated at every time instant of the numerical simulation of the problem, this becomes computationally very time-consuming. Therefore, the first step in the present study consisted of developing a highly efficient second-order accurate grid-generation method for geometries with arbitrary boundaries. The method of Davis (1979) provides an excellent starting point to achieve this. The method is based on conformal mapping. The use of a conformal-mapping based grid-generation method is particularly important for temporally deforming boundaries. This is explained as follows.

A time-accurate solution of the unsteady flow field is needed. For this to be achieved using a vorticity-stream function formulation, the stream-function field ψ is best obtained by a direct-solution method based on block-Gaussian elimination (BGE), for every time-step advance of the vorticity field ω. With temporally deforming grids, even the linear differential equation for ψ takes on time-varying coefficients. Therefore, additional computational time is required not only for the evaluation of these coefficients but also for the solution of the corresponding partial differential equation by direct inversion. By contrast, for efficiency of the BGE procedure, the differential operator for ψ must remain time-invariant. Conformal mapping allows this to be achieved even in the presence of temporally deforming grids, as described next.

In Cartesian coordinates, the stream-function equation has the form

$$\psi_{xx} + \psi_{yy} = -\omega \tag{1}$$

where the source function is the vorticity ω which is a function of x, y and t, i.e., $\omega = \omega(x,y,t)$. In conformal coordinates (ξ,n), this equation can be represented as

$$\psi_{\xi\xi} + \psi_{nn} = -\frac{\omega}{h^2} \tag{2}$$

where $h = h_1 = h_2$ is the scale factor of the conformal mapping

$$\xi + in = f(x+iy) \quad . \tag{3}$$

In terms of complex variables, the conformal mapping and its scale factor become

$$\zeta = f(z) \quad , \qquad h = \left|\frac{df}{dz}\right| = \frac{d\zeta}{dz} \tag{4a,b}$$

where

$$\zeta = \xi + in \quad \text{and} \quad z = x + iy \quad . \tag{5a,b}$$

For a temporally deforming boundary-aligned conformal coordinate system, the scale factor h varies with time, in addition to being spatially varying. However, by virtue of the special form of the stream-function equation (2) that results with a conformal mapping, this time-varying h can be absorbed in the source function of this equation, leading simply to the equation

$$\psi_{\xi\xi} + \psi_{nn} = S(\xi,n,t) \tag{6a}$$

where

$$S(\xi,n,t) \overset{\Delta}{=} -\omega/h^2 \quad . \tag{6b}$$

This leaves the stream-function equation with time-invariant coefficients. It is important to note that any clustering transformations, introduced in Eq. (6a) for the purpose of resolving the length scales of the problem, must be time-independent in order for the final form of the equation to possess time-independent coefficients. The clustering transformations used in the present work are of the form $\xi = \xi(S)$, $n = n(N)$ where (S,N) are the final computational coordinates.

The Basic Schwarz-Christoffel Transformation

The original form of the Schwarz-Christoffel transformation for polygons (Fig. 12) is given by

$$\frac{dz}{d\zeta} = f(\zeta) = M \prod_{i=1}^{n} (\zeta-a_i)^{\alpha_i/\pi} \quad . \tag{7}$$

Integration of Eq. (7) yields

$$z = M \int_{\zeta_0}^{\zeta} \prod_{i=1}^{n} (\zeta'-a_i)^{\alpha_i/\pi} d\zeta' + z_0 \tag{8}$$

which maps the upper half of the ζ-plane onto the interior (or exterior) of the polygon in the z-plane (see Fig. 12b for the case of exterior). In Eq. (8), z_0, ζ_0 and M are complex constants. All the a_i's are located on the ξ-axis (i.e., the real axis) and, hence, are real. For a given geometry, α_i's are the angles shown in Fig. 12, measured in radians, and taken to be positive for clockwise rotation. The complex constants z_0 and ζ_0 can be chosen as any complex numbers, two of the a_i's can be chosen arbitrarily, and all the rest are determined by the shape of the geometry. The coefficient M is determined by the size and the orientation of the geometry; it is also related to the a_i's when $\sum_{i=1}^{n} \alpha_i = -\pi$. But, in practice,

$\sum_{i=1}^{n} \alpha_i = -\pi$ is used most often for internal flows. Therefore, M is determined solely by the size and the orientation of the geometry in most cases.

Treatment of Curved Boundaries

In order to extend the applicability of the Schwarz-Christoffel transformation to geometries with curved boundaries, following Davis [1979], Eq. (7) is re-written as

110

$$\frac{dz}{d\zeta} = M \exp\left\{ \frac{1}{\pi} \sum_{i=1}^{n} \alpha_i \ln(\zeta - a_i) \right\} \qquad . \qquad (9)$$

The boundary curve is considered to be made up of an infinite number of infinitesimally small straight-line segments. Therefore, as the number n approaches infinity, the α_i's are replaced by $d\beta$, a_i's by b and the summation is replaced by integration. The reason that β and b are used instead of α and a is that they need to be discretized for numerical integration and their discretized values α_i's and a_i's need to be distinguished from their values for corners. Then, Eq. (9) becomes

$$\frac{dz}{d\zeta} = M \exp\left\{ \frac{1}{\pi} \int_{\beta_1}^{\beta_2} \ln(\zeta - b) \, d\beta \right\} \qquad (10)$$

where β is the angle from the real axis to the curved element in the physical plane and is positive if the angle is clockwise. Integration of Eq. (10) with respect to ζ yields

$$z = M \int_{\zeta_0}^{\zeta} \exp\left\{ \frac{1}{\pi} \int_{\beta_1}^{\beta_2} \ln(\zeta' - b) \, d\beta \right\} d\zeta' + z_0 \qquad . $$
$$(11)$$

Equations (10) and (11) can be considered as general forms which include corners, with the understanding that β could be a step function of b so that, at a corner of angle α_i, the integration in Eq. (10) around the corner yields

$$\int_{\beta_i^-}^{\beta_i^+} \ln(\zeta - b) d\beta = (\beta_i^+ - \beta_i^-) \ln(\zeta - b) = \alpha_i \ln(\zeta - a_i)$$
$$(12)$$

where β_i^- and β_i^+ represent the angles on the two sides of the corner. It should be noted that, while β changes from β_i^- to β_i^+, b actually remains the same.

With the use of Eq. (12) for integration at corners, Eq. (10) can be written as

$$\frac{dz}{d\zeta} = M \exp\left\{ \frac{1}{\pi} \sum \ln(\zeta - a_i) \alpha_i + \frac{1}{\pi} \int \ln(\zeta - b) \, d\beta \right\}$$
$$(13)$$

where the summation term corresponds to integration around corners.

Generalization of Transformation Formulae to Include Internal Geometries

The channel transformation relations developed by Davis (1979) are quite different from and much more complicated than those for external geometries. In the present study, an important concept, namely, generalization of internal and external transformation formulae, is developed. Because of this generalization, the transformation for channels becomes very similar to that for external geometries and, therefore, the resulting

formulae are much simpler than those presently available.

An arbitrary channel can always be mapped into the upper half of the ζ-plane by using the Schwarz-Christoffel transformation described above, and then mapped into a straight channel by using another Schwarz-Christoffel transformation

$$\frac{d\zeta}{dT} = \frac{1}{m} (\zeta - a) \qquad (14a)$$

which has the following inverse:

$$\frac{dT}{d\zeta} = m (\zeta - a)^{-1} \qquad . \qquad (14b)$$

The parameters m and 'a' have the same meaning as M and the a_i's in Eq. (7). Therefore, the parameter 'a' can be chosen arbitrarily, and m depends on only the size and the orientation of the straight channel, since $\sum_{i=1}^{n} \alpha_i = -\pi$ in the case of a straight channel. Integration of Eq. (14b) yields

$$T = T_0 + m \ln(\zeta - a) \qquad (15a)$$

or

$$\zeta = a + e^{(T - T_0)/m} \qquad . \qquad (15b)$$

If the parameters a and T_0 are set to zero and m is set to $1/\pi$, then Eqs. (15a) and (15b) become

$$T = \frac{1}{\pi} \ln(\zeta) \qquad (16a)$$

and

$$\zeta = e^{\pi T} \qquad , \qquad (16b)$$

respectively. The condition $|m| = 1/\pi$ yields a channel of unit height; however, m can be set to any non-zero value.

In order to transform upstream infinity of the straight channel to upstream infinity of the channel in the physical plane, the following compatibility requirement must be satisfied:

$$a = a_j \qquad (17)$$

where j corresponds to the corner at upstream infinity. Otherwise, distortion and possibly singularities may develop in the transformation. With the above compatibility requirement, the corresponding Schwarz-Christoffel transformation for mapping an arbitrary channel to a half-plane becomes

$$\frac{dz}{d\zeta} = (\zeta - a)^{\alpha/\pi} f^*(\zeta) = M (\zeta - a)^{\alpha/\pi} \prod_{i=1}^{n} (\zeta - a_i)^{\alpha_i/\pi}$$
$$(18)$$

where $\alpha = \alpha_j = -(\pi + \delta)$ is the angle of the corner at the left end of the channel, the a_j corresponding to α is set to be the parameter 'a' so as to satisfy the compatibility requirement, and $f^*(\zeta)$ has the same form as $f(\zeta)$, except that the number n

now excludes the corners at infinity. Substituting $\alpha = -(\pi+\delta)$ into Eq. (18) and letting parameter 'a' be zero (since two of the a_i's can be chosen arbitrarily), leads to

$$\frac{dz}{d\zeta} = M\ \zeta^{-(\pi+\delta)/\pi}\ \prod_{i=1}^{n}\ (\zeta-a_i)^{\alpha_i/\pi} \quad . \qquad (19)$$

It should be kept in mind that only one parameter in the above equation is arbitrary. For curved boundaries, Eq. (19) becomes

$$\frac{dz}{d\zeta} = M\ \zeta^{-(\pi+\delta)/\pi}\ \exp\{\frac{1}{\pi}\ \int_{\substack{\text{upper \&}\\ \text{lower wall}}}\ \ln\ (\zeta-b)\ d\beta\}$$

$$(20)$$

It should be noted that Eqs. (19) and (20) are only special forms of the Schwarz-Christoffel transformation for channel mapping and can be rearranged to resemble Eqs. (7) and (10), respectively.

Substitution of $\alpha = -(\pi+\delta)$ into Eq. (18) yields

$$\frac{dz}{d\zeta} = (\zeta-a)^{-(\pi+\delta)/\pi}\ f^*(\zeta) \qquad . \qquad (21)$$

The combined transformation that maps an arbitrary channel to a straight channel can then be obtained using the following equation:

$$\frac{dz}{dT} = \frac{dz}{d\zeta}\ \frac{d\zeta}{dT} \quad . \qquad (22)$$

Substitution of Eq. (16b) and Eq. (21) into the above equation leads to

$$\frac{dz}{dT} = \frac{1}{m}\ (\zeta-a)^{-\delta/\pi}\ f^*(\zeta)\Big|_{\zeta=e^{\pi T}} \quad . \qquad (23)$$

Letting $a=0$ and $m=1/\pi$, Eq. (23) becomes

$$\frac{dz}{dT} = \pi\ \zeta^{-\delta/\pi}\ f^*(\zeta)\Big|_{\zeta=e^{\pi T}}$$

$$= \pi\ M\ \zeta^{-\delta/\pi}\ \prod_{i=1}^{n}\ (\zeta-a_i)^{\alpha_i/\pi}\Big|_{\zeta=e^{\pi T}} \quad . \qquad (24)$$

Since M is only a constant, π can be absorbed into M and the above equation can be written as

$$\frac{dz}{dT} = M\ \zeta^{-\delta/\pi}\ \prod_{i=1}^{n}\ (\zeta-a_i)^{\alpha_i/\pi}\Big|_{\zeta=e^{\pi T}} \quad . \qquad (25)$$

In most practical cases, δ is equal to zero and Eq. (25) simplifies to the following:

$$\frac{dz}{dT} = M\ \prod_{i=1}^{n}\ (\zeta-a_i)^{\alpha_i/\pi}\Big|_{\zeta=e^{\pi T}} \quad . \qquad (26)$$

It is significant that Eq. (26) and Eq. (7) have exactly the same form; only the interpretation of ζ is different. Therefore, it can be easily seen that the derivation and the resulting formulae for the channel transformation will resemble those for

external geometries. Hence, the generalization of internal and external mapping has been achieved. This generalization will make the numerical transformation for channels much simpler than the existing methods. Even when δ is not zero, the method will still be more efficient than existing methods since the only modification needed is to multiply the equation corresponding to $\delta=0$ by the expression $\zeta^{-\delta/\pi}$ and the numerical solution procedure does not change significantly. Further consideration of the channel transformation formulae is not necessary since it will resemble that for the external transformation. The transformation formula for general internal curved boundaries is very similar to that for external geometries and has the following form

$$\frac{dz}{d\zeta} = M\ \zeta^{-\delta/\pi}\exp\{\frac{1}{\pi}\ \sum\ \ln(\zeta-a_i)\alpha_i\ +\ \frac{1}{\pi}\ \int\ \ln(\zeta-b)d\beta\}$$

$$= M\ \exp\{-\frac{1}{\pi}\ \ln(\zeta)\delta\ +\ \frac{1}{\pi}\ \sum\ \ln(\zeta-a_i)\ \alpha_i$$

$$+\ \frac{1}{\pi}\ \int\ \ln(\zeta-b)\ d\beta\} \qquad (27)$$

For $\delta=0$, the above equation becomes

$$\frac{dz}{d\zeta} = M\ \exp\ \{\frac{1}{\pi}\ \sum\ \ln(\zeta-a_i)\ \alpha_i\ +\ \frac{1}{\pi}\ \int\ \ln(\zeta-b)\ d\beta\}.$$

$$(28)$$

It should be kept in mind that infinity is not a corner in the above discussion and the difference between internal and external transformation is reflected in the evaluation of ζ and by the appearance of the additional exponential function $\zeta^{-\delta/\pi}$ when $\delta\ne0$. The basic transformation is now complete. The next section describes a numerical grid-generation procedure based on conformal mapping.

Grid Generation Based on Schwarz-Christoffel Theorem

Numerical grid generation based on the Schwarz-Christoffel mapping involves the following main steps:

1) Iteration to get the unknown parameters in the transformation; for this, integration along (part of) the boundary must be done for every iteration;

2) Integration to generate the grids;

3) Calculation of the components of the covariant metric tensor of the transformation.

The first step determines the unknown parameters in the transformation and, therefore, the final form of the transformation. The second step provides the physical coordinates of the grid points. It can also be utilized to calculate the covariant metric tensor, but it leads to greater error and is more time-consuming than step three, which is specifically used for calculating the covariant metric tensor needed ... .. flow analysis.

In the case of adaptive grids with small grid speed, it is more efficient to calculate the

112

covariant metric tensor from $\frac{dz}{d\zeta}$, since the coordinates are needed for displaying the grids at only a few time levels. In the case of fixed grids, it is more efficient to determine the metric coefficient tensor by using the grids obtained from the integration, since the integration must be carried out to display the grids.

It should be noted that the most time-consuming part of the iteration (step 1) is the integration along the boundary. Therefore, the efficiency of integration is important even for generating adaptive grids with small grid speed where integration to get the grid points is not necessary at every time-level.

Figure 13 shows typical grids obtained, using this analysis, for the backstep channel with an oscillating flap. Two representative positions of the flap are shown. The grid clustering occurring on the left of the flap is unnecessary for these positions of the flap. However, it is retained because the grid-clustering transformations are time-invariant and the clustering shown will be needed when the flap rotates to occupy a position in the second quadrant with reference to the axis of the flap motion. This is a small price to pay for the important advantage that the stream-function equation retains time-invariant coefficients and can continue to be solved efficiently by the BGE direct method.

Enhancement of Efficiency for Evaluation of Transformation

Since the transformation needs to be re-evaluated for every incremental change in orientation of the flap, considerable effort was focused on enhancing the efficiency of determination of the transformation. The results of this effort are summarized in Table 1. Prior to commenting on these results, it is important to note the following. The Schwarz-Christoffel transformation directly provides the complex derivative $dz/d\zeta$ or dz/dT and, hence, the scale factor h of this conformal mapping. The flow equations contain only h and its derivatives. Strictly, the equations also contain the grid-speed terms x_τ, y_τ; however, it appears possible to circumvent their presence. Therefore, integration of $dz/d\zeta$ itself is needed only when it is desired to view the grid. This may not be necessary at each and every time step of the flow simulation; only h needs to be evaluated at every computational time level.

For channels, the transformation possesses a simple asymptotic form as $Re(\zeta) \to \pm \infty$. The transformation equations approach this asymptotic form in an exponential manner, so that the simplified form constitutes an accurate representation of the actual transformation beyond relatively small distances away from the last deviation from the straight-channel configuration. As shown in Table 1, implementation of this asymptotic form (Item A) resulted in 66-80 percent saving of CPU time for the computation of h^2, while the CPU time saved in the grid calculation was almost 80-95 percent when the grid is obtained by integrating dz/dT in the T-plane, i.e., in the straight-channel plane. If the integration is done in the computational plane of the clustered coordinates (S,N), the CPU time saved is not nearly as large, but the grid clustering obtained in the physical plane is better.

In Table 1, item B refers to the actual coding employed for evaluating the multi-exponential terms appearing in Eq. (7). After examining the manner in which such terms are actually evaluated in the computer, the coding was modified to reflect this manner of evaluation. This resulted in an additional 50 percent saving in the CPU time required to evaluate h^2. Hence, the implementation of both items A and B resulted in a total CPU time saving of almost 90 percent. · It is believed that this level of efficiency is acceptable for proceeding on with the flow-control study.

3. Three-Dimensional Unsteady Flow Analysis

This analysis provides a direct simulation technique for studying 3-D unsteady flows. It is anticipated that this analysis will aid in examining nonlinear instabilities, using model flow problems. The direct solution of the 3-D unsteady NS equations for genral geometries is now becoming feasible on current-generation supercomputers. Direct-solution methodology, developed by the authors for the solution of the 2-D unsteady NS equations, has proved to be both robust and efficient; hence, a corresponding 3-D analysis is developed also based on this methodology. This direct implicit analysis is constructed using the 3-D unsteady NS equations, formulated in terms of velocity and vorticity $(\bar{V}, \bar{\omega})$ in generalized orthogonal coordinates, e.g., Osswald, K. Ghia and U. Ghia (1987). The choice of this formulation was made after carefully examining this formulation as well as other vector-potential vorticity $(\bar{A}, \bar{\omega})$ formulations and the primitive-variable $(\bar{V}, p)$ formulation. Appropriate references on the various formulations have been cited earlier by the authors in Ref. 10. The $(\bar{V}, \bar{\omega})$ formulation was selected for use because of some of its desirable properties. First of all, the vorticity is a linear function of the velocity. The boundary conditions are physical, direct and simple to apply. Furthermore, the governing equations in this formulation separate, in a natural manner, the spin dynamics of a fluid particle (vorticity-transport problem) from the translational kinematics of the fluid particle (elliptic velocity problem).

Since the velocity-vorticity $(\bar{V}, \bar{\omega})$ formulation involves six unknowns, it may appear that considerably greater computational effort is associated with this formulation than with the primitive-variable $(\bar{V}, p)$ formulation, which involves only four unknowns. However, in the $(\bar{V}, \bar{\omega})$ formulation, as presently set up, a sparse matrix problem with repetitive block structure results. Furthermore, the computational effort equivalent to that associated with determining one implicit unknown can be effectively eliminated from the velocity problem. A similar amount of computational effort can also be eliminated from the vorticity-transport problem. Hence, the computational effort associated with the present

113

$(\bar{V}, \bar{\omega})$ analysis approximates that needed for four implicit unknowns. The analysis also employs generalized orthogonal coordinates so as to permit consideration of complex flow geometries and attempts to resolve the dominant multiple length scales prevailing in the flow problem.

A stable and efficient direct inversion procedure is developed in Ref. 10 for the computationally intensive divergence-curl elliptic velocity problem. The over-determined partial-differential operator is first formulated as a uniquely determined, non-singular matrix-vector problem; this aspect of the procedure is a unique feature of the present analysis. The vorticity-transport equations are solved by a modified approximate factorization technique which completely eliminates the need for any block-matrix inversions and only scalar tridiagonal matrices need to be inverted. The development of the vorticity transport algorithm is presented next.

The vorticity transport equations are solved using a modification of the Douglas-Gunn (1964) version of the alternating-direction implicit (ADI) technique. A part of this modification is the use of a three-level "forward" implicit time integration scheme which provides second-order temporal accuracy without requiring any iteration upon the wall vorticity boundary values or upon the nonlinear vorticity convection terms. Even more important is the current manner of distributing the partial derivatives in the convection and diffusion terms amongst the various directional sweeps. The present analysis permits direct implicit treatment of the mixed partial derivative terms which occur in the generalized coordinate diffusion operator, in contrast to the procedure of Beam and Warming (1977). The present analysis reduces the entire 3-D vorticity transport inversion to a sequence of 1-D scalar tridiagonal inversions swept through the 3-D domain. No block-tridiagonal inversions are required whatsoever.

The Vorticity Transport Algorithm

The unsteady 3-D vorticity transport equation, written in conservation law form, is

$$\frac{\partial \bar{\omega}}{\partial t} + \nabla \times (\bar{\omega} \times \bar{V}) + \frac{1}{Re} \nabla \times (\nabla \times \bar{\omega}) = 0 . \quad (29)$$

Here, Re is a Reynolds number defined as $Re = (U_R L_R)/\nu$, with U_R a reference speed, L_R a reference length, and ν the constant kinematic viscosity of the incompressible fluid. The governing equations are nondimensionalized using U_R, (L_R/U_R) and (U_R/L_R) as the characteristic units of velocity, time and vorticity, respectively. Use is made of generalized orthogonal coordinates to facilitate the treatment of complex flow geometries and permit the resolution of the often disparate length scales of unsteady viscous flows. Using covariant velocity and vorticity components, the ω_1 vorticity transport equation can be written as

$$(\frac{\partial \omega_1}{\partial t}) + \frac{g_{11}}{\sqrt{g}} [\frac{\partial}{\partial \xi^2} \{\frac{g_{33}}{\sqrt{g}} (\omega_1 V_2 - \omega_2 V_1)$$

$$- \frac{1}{Re} \frac{g_{33}}{\sqrt{g}} (\frac{\partial \omega_1}{\partial \xi^2} - \frac{\partial \omega_2}{\partial \xi^1})\} + \frac{\partial}{\partial \xi^3} \{\frac{g_{22}}{\sqrt{g}} (\omega_1 V_3$$

$$- \omega_3 V_1) - \frac{1}{Re} \frac{g_{22}}{\sqrt{g}} (\frac{\partial \omega_1}{\partial \xi^3} - \frac{\partial \omega_3}{\partial \xi^1})\}] = 0 \quad (30)$$

Here, g_{ij} are the elements of the covariant metric tensor

$$g_{ij} = \sum_{k=1}^{3} (\frac{\partial x^k}{\partial \xi^i}) (\frac{\partial x^k}{\partial \xi^j})$$

and g is its determinant. Similar equations result for the ω_2 and ω_3 vorticity components.

Notice that the only mixed partial derivative terms occurring in the ω_1-transport equation are associated with the ω_2 and ω_3 components. This fact permits the implicit treatment of these terms within a Douglas-Gunn (1964) ADI scheme without disrupting the scalar tridiagonal structure of any directional sweep. This contrasts the structure of the 3-D linear momentum equations for which mixed partials of V_1 occur within the V_1-transport equation, thus complicating the Beam and Warming (1977) procedure.

Currently, Eq. (30) is discretized using the two-level central-time central-space Crank-Nicholson technique, with the velocity field extrapolated in time to the $(n+1/2)$ time level from known velocities at the current (n) and previous $(n-1)$ time levels, thus forming a three-level forward implicit technique. Delta form is introduced where

$$(\delta W1)^{n+1} \triangleq W1^{n+1} - W1^n \quad \text{and} \quad W1^n \triangleq (\omega_1)^n_{ijk}$$

and the discrete analogue of Eq. (30) is approximately factored. In finite-difference operator notation, this result can be written as

$$[I][I + (\frac{\Delta t}{2}) A_{12}][I + (\frac{\Delta t}{2}) A_{13}](\delta W1)^{n+1}$$

$$- (\frac{\Delta t}{2})[B_{12}](\delta W2)^{*2*} - (\frac{\Delta t}{2})[B_{13}](\delta W3)^{n+1}$$

$$+ (\Delta t)\{[A_{12} + A_{13}](W1)^n - [B_{12}](W2)^n$$

$$- [B_{13}](W3)^n\} = 0 \quad (31)$$

where (Δt) is the discrete time step,

$$[I](\delta W1)^{n+1} \triangleq (\delta W1)^{n+1}_{ijk}$$

and

$$[A_{12}](W1)^n \triangleq GW1_{ijk}[G33_{ijk}\{\frac{(V2^{n+1/2}_{ij+1k} + V2^{n+1/2}_{ij+1k-1})}{2}$$

$$-\frac{1}{Re}\}(W1^n_{ij+1k}) + [G33_{ijk}\{\frac{(V2^{n+1/2}_{ijk}+V2^{n+1/2}_{ijk-1})}{2}$$

$$+\frac{1}{Re}\} - G33_{ij-1k}\{\frac{(V2^{n+1/2}_{ijk}+V2^{n+1/2}_{ijk-1})}{2}$$

$$-\frac{1}{Re}\}](W1^n_{ijk}) - G22_{ij-1k}\{\frac{(V2^{n+1/2}_{ij-1k} + V2^{n+1/2}_{ij-1k-1})}{2}$$

$$+\frac{1}{Re}\} (W1^n_{ij-1k})] \quad .$$

Similar forms can be obtained for the operators A_{13}, B_{12}, and B_{13}. Also, $(\delta W2)^{*2*}$ represents the second intermediate estimate of $(\delta W2)^{n+1}$ that occurs as a part of the (ADI) solution methodology. Similarly, the ω_2 and ω_3 vorticity transport equaitons can be discretized as follows:

$$[I + (\frac{\Delta t}{2})A_{21}] [I] [I+(\frac{\Delta t}{2})A_{23}] (\delta W2)^{n+1}$$

$$- (\frac{\Delta t}{2})[B_{21}](\delta W1)^{*1*}$$

$$- (\frac{\Delta t}{2})[B_{23}](\delta W3)^{n+1} + (\Delta t) \{[A_{21}+A_{23}](W2)^n$$

$$- [B_{21}](W1)^n - [B_{23}](W3)^n\} = 0 \qquad (32)$$

and

$$[I + (\frac{\Delta t}{2})A_{31}][I + (\frac{\Delta t}{2})A_{32}] [I] (\delta W3)^{n+1}$$

$$- (\frac{\Delta t}{2})[B_{31}](\delta W1)^{*1*} - (\frac{\Delta t}{2})[B_{32}](\delta W2)^{*2*}$$

$$+ (\Delta t) \{[A_{31}+A_{32}](W3)^n - [B_{31}](W1)^n$$

$$- [B_{32}](W2)^n\} = 0 \quad . \qquad (33)$$

The direct implicit solution of Eqs. (31)-(33) proceeds as follows:

(1-Sweep of ω_1-Equation)

$$[I](\delta W1)^{*1*} = (\Delta t) \{[B_{12}](W2)^n + [B_{13}[(W3)^n$$

$$- [A_{12}+A_{13}](W1)^n\} \qquad (34a)$$

(1-Sweep of ω_2-Equation)

$$[I + (\frac{\Delta t}{2})A_{21}](\delta W2)^{*1*} = (\Delta t) \{[B_{21}](W1)^n$$

$$+ [B_{23}](W3)^n - [A_{21}+A_{23}](W2)^n\}$$

$$+ (\frac{\Delta t}{2}) [B_{21}](\delta W1)^{*1*} \qquad (34b)$$

(1-Sweep of ω_3-Equation)

$$[I + (\frac{\Delta t}{2})A_{31}](\delta W3)^{*1*} = (\Delta t) \{[B_{31}](W1)^n$$

$$+ [B_{32}](W2)^n - [A_{31}+A_{32}](W3)^n\}$$

$$+ (\frac{\Delta t}{2}) [B_{31}](\delta W1)^{*1*} \qquad (34c)$$

(2-Sweep of ω_2-Equation)

$$[I](\delta W2)^{*2*} = (\delta W2)^{*1*} \qquad (35a)$$

(2-Sweep of ω_1-Equation)

$$[I + (\frac{\Delta t}{2}) A_{12}] (\delta W1)^{*2*} = (\delta W1)^{*1*}$$

$$+ (\frac{\Delta t}{2}) [B_{12}](\delta W2)^{*2*} \qquad (35b)$$

(2-Sweep of ω_3-Equation)

$$[I + (\frac{\Delta t}{2}) A_{32}] (\delta W3)^{*2*} = (\delta W3)^{*1*}$$

$$+ (\frac{\Delta t}{2})[B_{32}](\delta W2)^{*2*} \qquad (35c)$$

(3-Sweep of ω_3-Equation)

$$[I](\delta W3)^{n+1} = (\delta W3)^{*2*} \qquad (36a)$$

(3-Sweep of ω_1-Equation)

$$[I + (\frac{\Delta t}{2}) A_{13}](\delta W1)^{n+1} = (\delta W1)^{*2*}$$

$$+ (\frac{\Delta t}{2})[B_{13}](\Delta W3)^{n+1} \qquad (36b)$$

(3-Sweep of ω_2-Equation)

$$[I + (\frac{\Delta t}{2}) A_{23}](\delta W2)^{n+1} = (\delta W2)^{*2*}$$

$$+ (\frac{\Delta t}{2})[B_{23}](\delta W3)^{n+1} \quad . \qquad (36c)$$

Finally,

$$(W1)^{n+1} = (W1)^n + (\delta W1)^{n+1} \qquad (37a)$$

$$(W2)^{n+1} = (W2)^n + (\delta W2)^{n+1} \qquad (37b)$$

$$(W3)^{n+1} = (W3)^n + (\delta W3)^{n+1} \quad . \qquad (37c)$$

The above development shows that three of the nine sweeps described above do NOT require any matrix inversions whatsoever, and that the remaining six sweeps require the inversion of only scalar (as opposed to block) tridiagonal matrices. Consequently, the vorticity algorithm is a very efficient 3-D transport procedure, with the computational intensity which more closely reflects

the cost of solving for two, rather than three, unknowns.

Results for Shear-Driven Cubical Box

The method is applied to the model problem of the 3-D flow within a shear-driven cubical box. The boundary conditions for solid walls on all six faces of the box in terms of $\bar{V}$ and $\bar{\omega}$ are discussed in detail in the authors' earlier work in Ref. 10. The results obtained so far using a Concurrent 3250 computer system on a (17x17x17) grid are strictly for demonstration purpose. Typical results in Figure 14a provide the steady-state velocity vectors for the x^2=0.71875 plane (top view), x^3=0.71875 plane (front view), and x^1=0.71875 plane (side view). These views place the observer just below the vortex center (top view) and just to the right of the vortex center (side view). Figure 14b presents the corresponding contours of normal vorticity. Coherent structures of vorticity in the streamwise direction are seen to appear in both the top and side views in Fig. 14b. These structures are associated with the rapidly descending fluid just ahead of the dominant spanwise vortex (top view) and the return flow near the front and back walls just below the dominant spanwise vortex (side view). Additional results obtained are given in Ref. 10.

Since then, the code has been fully vectorized for the CYBER 205 computer, resulting in efficient direct numerical simulation capabilities for highly unsteady 3-D viscous flows. Memory management considerations are currently being investigated using a two-pronged approach. Results of this memory management exercise as well as fine-grid flow results for the driven cavity and 3-D backstep channel geometries will be presented at the ICNMFD '86 Conference in June 1988 at Williamsburg, Virginia. The flow inside a backstep channel with finite spanwise extent will be examined next. For this geometry, careful laser-Doppler velocimetry results are available for the entire range of flow, i.e., for laminar, transition and turbulent flows.

References

1. Beam, R.M. and Warming, R.F. (1977), "An Implicit Factored Scheme for the Compressible Navier-Stokes Equations," AIAA Paper 77-645.

2. Davis, R.T., (1979), "Numerical Methods for Coordinate Generation Based on Schwarz-Christoffel Transformations," AIAA Paper 79-1463.

3. Douglas, J. and Gunn, J.E., (1964), "A General Formulation of Alternating Direction Methods. Part I. Parabolic and Hyperbolic Problems," Numerische Mathematik, Vol. 6, pp. 428-453.

4. Ghia, K.N., Osswald, G.A. and Ghia, U. (1983), "A Direct Method for the Solution of Unsteady Two-Dimensional Incompressible Navier-Stokes Equations," Proceedings of Second Symposium on Numerical and Physical Aspects of Aerodynamic Flows, Long Beach, California, January 1983.

5. Ghia, K.N., Osswald, G.A. and Ghia, U. (1986a), "Analysis of Two-Dimensional Incompressible Flow Past Airfoils Using Unsteady Navier-Stokes Equations," Chapter in Numerical and Physical Aspects of Aerodynamic Flows: Vol. III, Editor: T. Cebeci, Springer-Verlag, New York, pp. 318-340.

6. Ghia, K.N., Osswald, G.A. and Ghia, U. (1986b), "Simulation of Self-Induced Motion in the Near-Wake of a Joukowski Airfoil," Lecture Notes in Engineering, Edited by K. Kuwahara, R. Mendez and S.A. Orszag, Springer-Verlag, New York, Vol. 24, pp. 18-132.

7. Nagib, H.M., Reisenthal, P.H. and Koga, D.J., (1985), "On the Dynamical Scaling of Forced Unsteady Separated Flows," AIAA Paper 85-0553.

8. Osswald, G.A., Ghia, K.N. and Ghia, U. (1983), "Study of Incompressible Separated Flow Using an Implicit Time-Dependent Technique," AIAA CP 834, pp. 686-696.

9. Osswald, G.A., Ghia, K.N. and Ghia, U. (1986), "Simulation of Buffeting Stall for a Cambered Joukowski Airfoil Using a Fully Implicit Method," Lecture Notes in Physics, Editors: F.G. Zhuang and Y.L. Zhu, Springer-Verlag, New York, Vol. 264, pp. 516-522.

10. Osswald, G.A., Ghia, K.N. and Ghia, U., (1987), "A Direct Algorithm for Solution of Incompressible Three-Dimensional Unsteady Navier-Stokes Equations," AIAA CP 874, pp. 408-421.

11. Reisenthal, P.H., Nagib, H.M. and Koga, D.J., (1985), "Control of Separated Flows Using Forced Unsteadiness," AIAA Paper 85-0556.

TABLE 1. ENHANCEMENT OF EFFICIENCY OF GRID GENERATION.

BY IMPLEMENTING	PERCENTAGE OF COMPUTATIONAL TIME SAVED	
	h^2 CALCULATION	GRID CALCULATION
ITEM 'A'	66 - 80	80 - 95* (66 - 80)•
ITEM 'B'	50	0
ITEMS 'A'+'B'	83 - 90	80 - 95* (66 - 80)•

'A' : ASYMPTOTIC FORM FOR CHANNEL MAPPING.

'B' : TIME-SAVING TECHNIQUE FOR EVALUATING MULTI-EXPONENTIAL TERMS.

NOTE: CURVED BOUNDARIES ARE ALSO TREATED WITH COMPARABLE EFFICIENCY.

* INTEGRATION DONE IN CHANNEL PLANE (T).

• INTEGRATION DONE IN COMPUTATIONAL PLANE (S,N)

Fig. 1. Instantaneous Contours of Stream Function and Vorticity for Symmetric Joukowski Airfoil at Re = 1,000, t = 100. (a) Stream Function, (b) Vorticity.
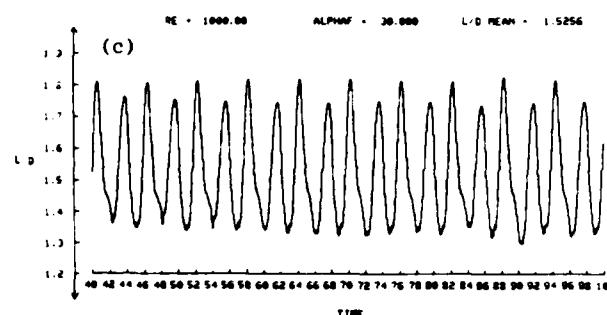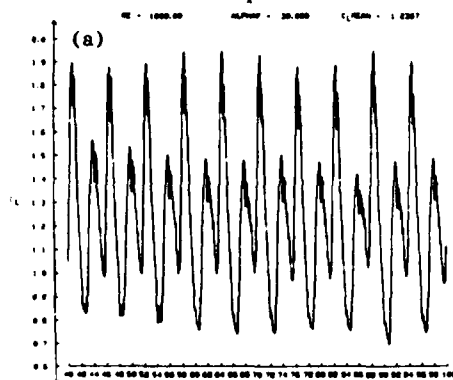
Fig. 2. Instantaneous Aerodynamic Coefficients for Symmetric 12% Joukowski Airfoil at Re = 1,000, $x_f = 30°$. (a) Lift C_L, (b) Drag C_D, (c) L/D.
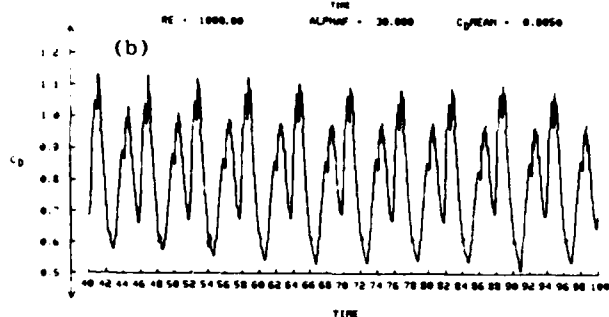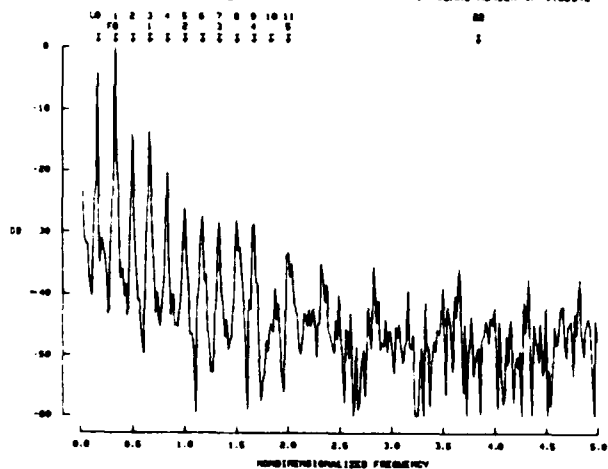
Fig. 3. Phase-Space Portrait and Poincaré Section for Symmetric Joukowski Airfoil at Re = 1,000, $x_f = 30°$. (a) C_L, (b) C_D.

Fig. 4. Normalized Power-Density Spectrum of C_L at Re = 1,000, $x_f = 30°$.

116
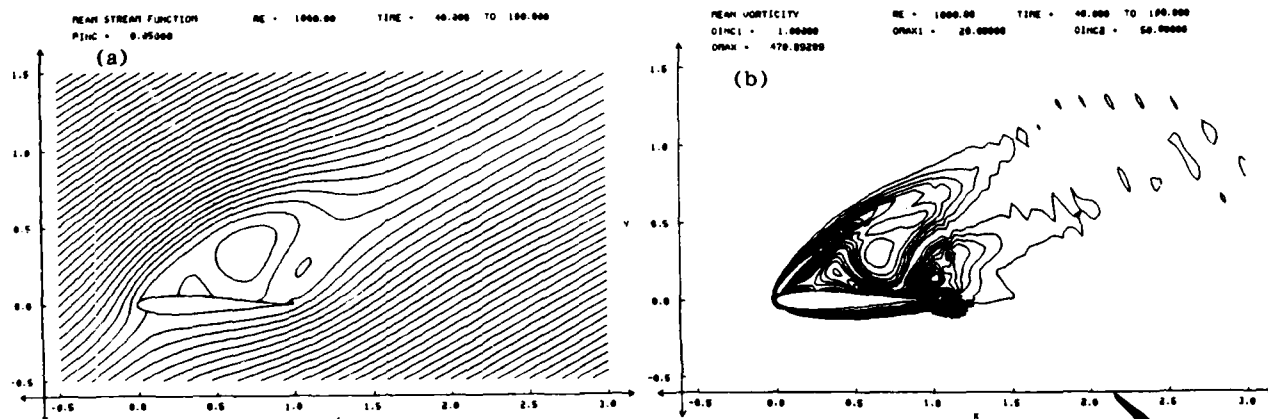
Fig. 5. Time-Averaged Stream-Function and Vorticity Contours for $40 \leq t \leq 100$; Re = 1,000, $\alpha_f = 30°$.
(a) Stream Function, (b) Vorticity.
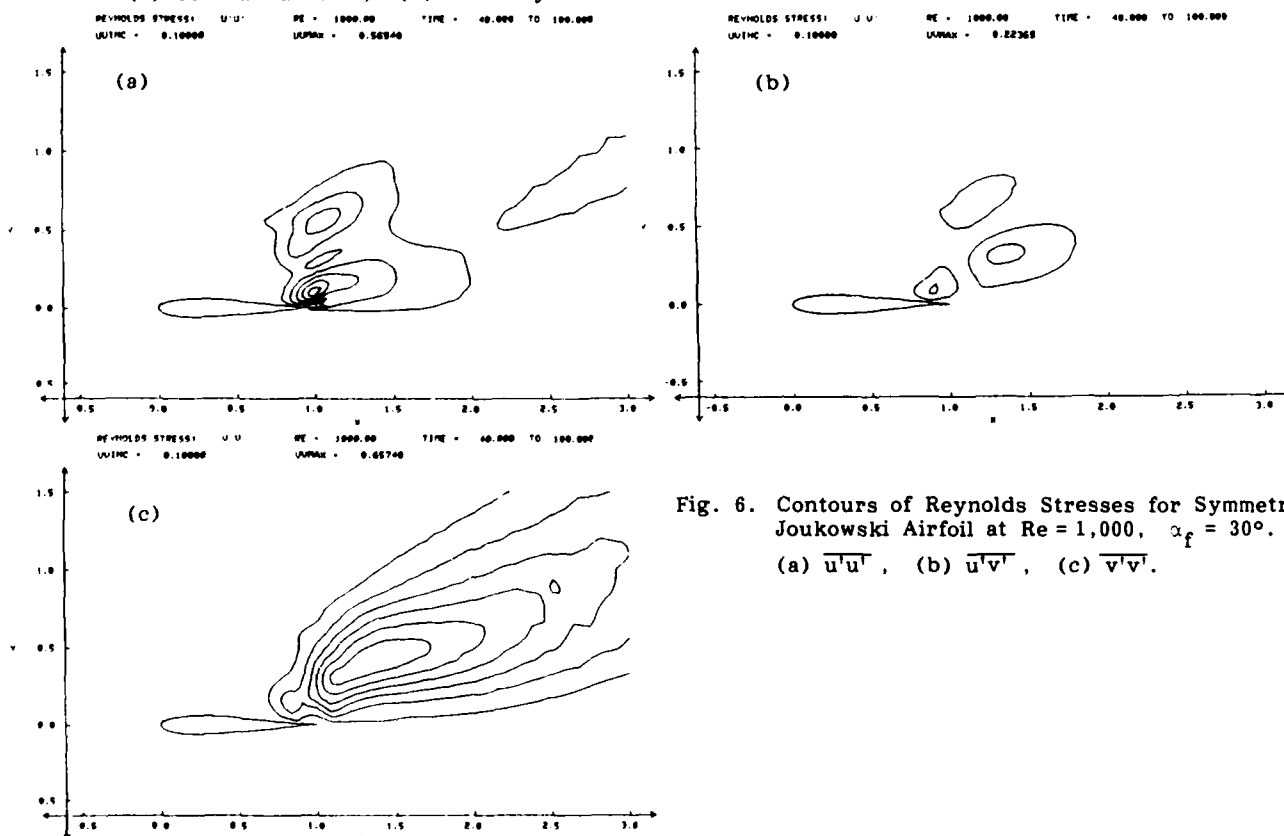
Fig. 6. Contours of Reynolds Stresses for Symmetric
Joukowski Airfoil at Re = 1,000, $\alpha_f = 30°$.

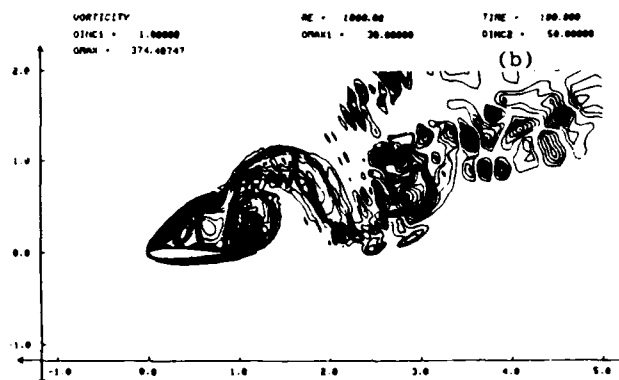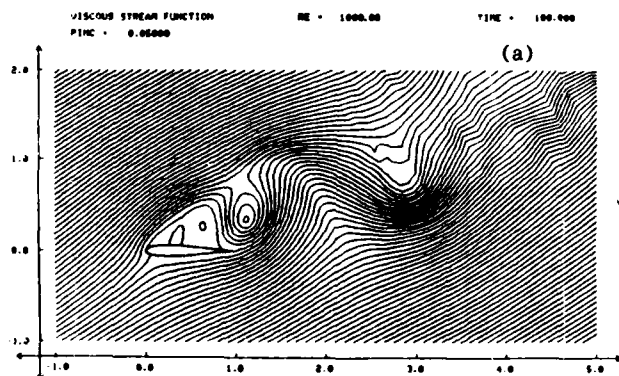(a) $\overline{u'u'}$, (b) $\overline{u'v'}$, (c) $\overline{v'v'}$.
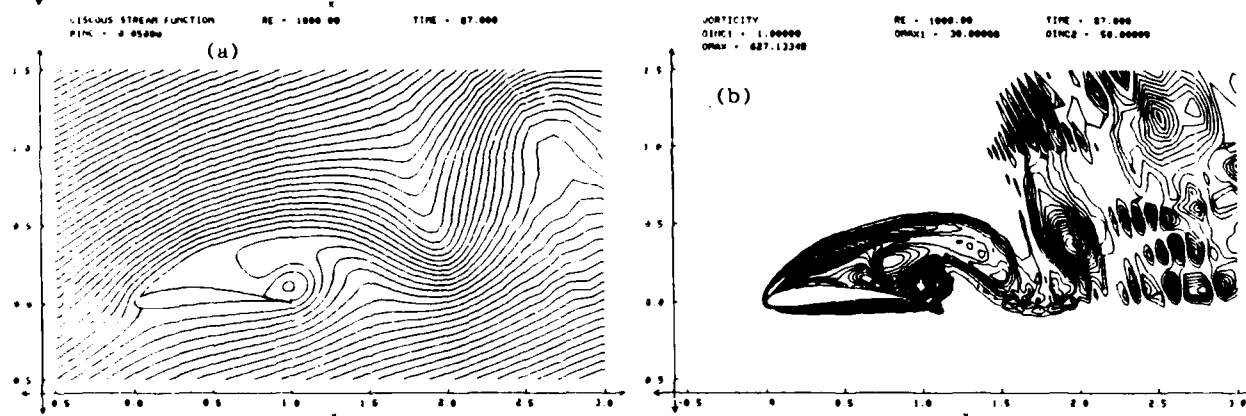
Fig. 7. Instantaneous Contours of Stream Function and Vorticity for Cambered Joukowski Airfoil at
Re = 1,000, $\iota_e = 30°$. (a) Stream Function, (b) Vorticity.
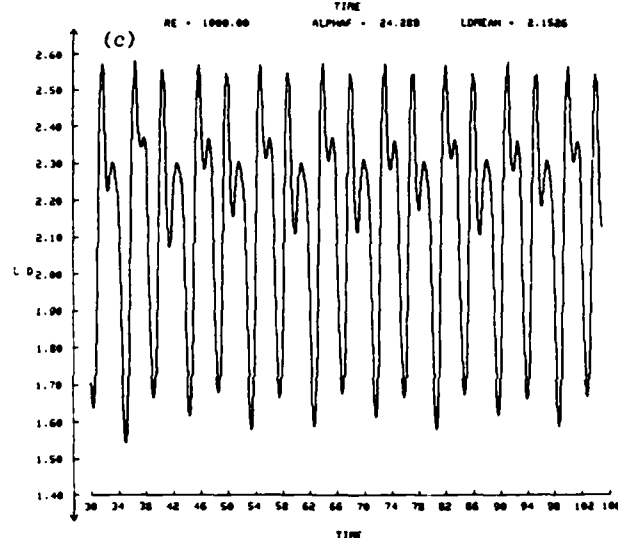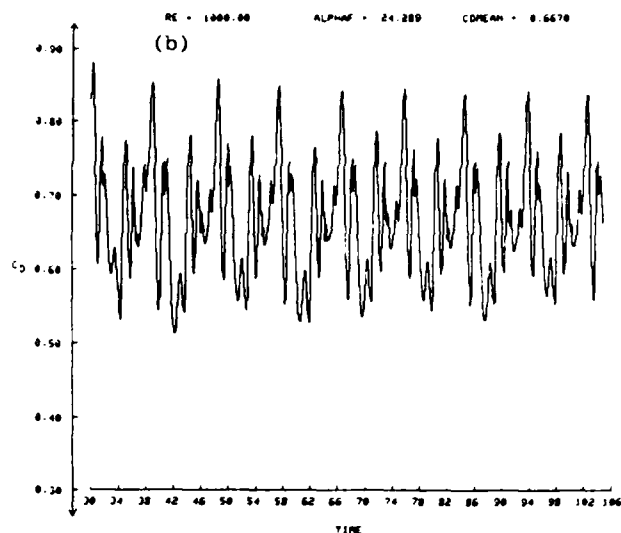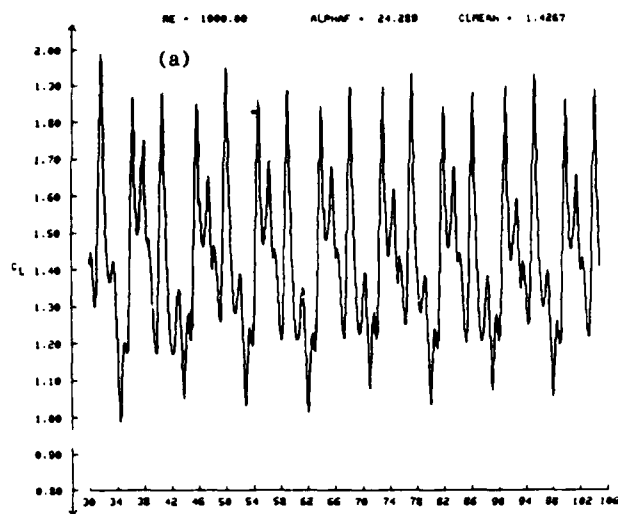
Fig. 8. Instantaneous Aerodynamic Coefficients for 12% Cambered Joukowski Airfoil at Re = 1,000, $\alpha_e = 30°$. (a) Lift C_L, (b) Drag C_D, (c) L/D.

Fig. 9. Phase-Space Portrait and Poincare Section for Cambered Joukowski Airfoil at Re = 1,000, $\alpha_e = 30°$.
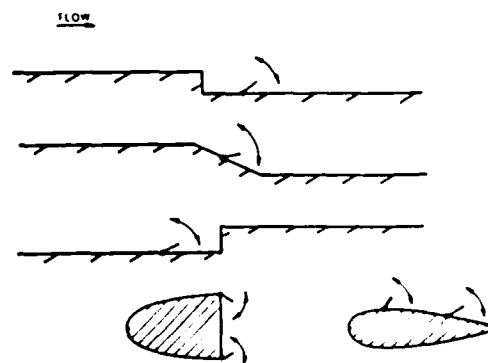
Fig. 11. Prospective Geometries for Unsteady Flow-Field Separation Control (After Nagib and Co-Workers).

Fig. 10. Normalized Power-Density Spectrum of C_L at Re = 1,000, $\iota_e = 30°$.

118
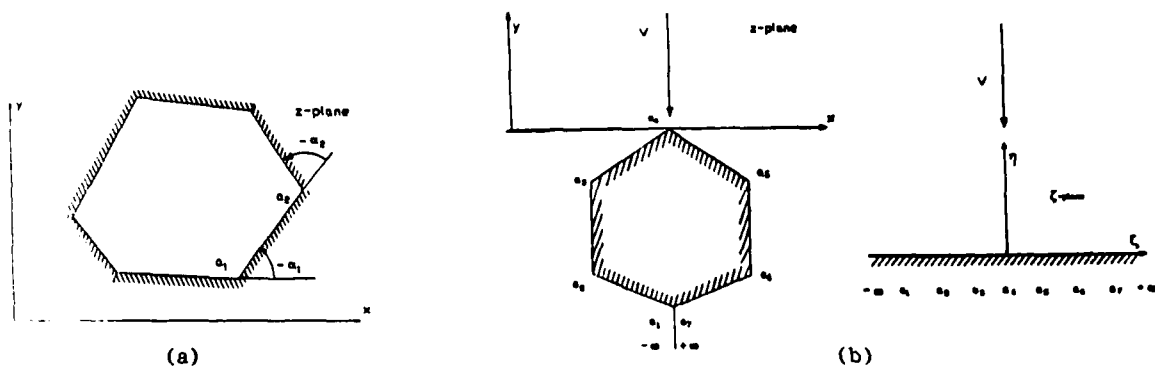
Fig. 12. Basic Schwarz-Christoffel Transformation - Upper-Half ζ-Plane to (a) Interior of Polygon, (b) Exterior of Polygon, in z-Plane.
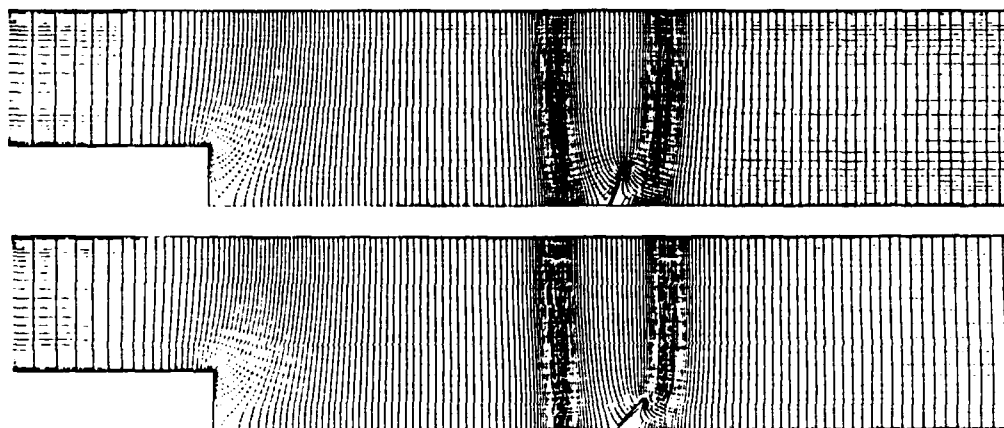
Fig. 13. Clustered Conformal Boundary-Aligned Grid for Backstep Channel with Oscillating Flap in Two Different Positions.
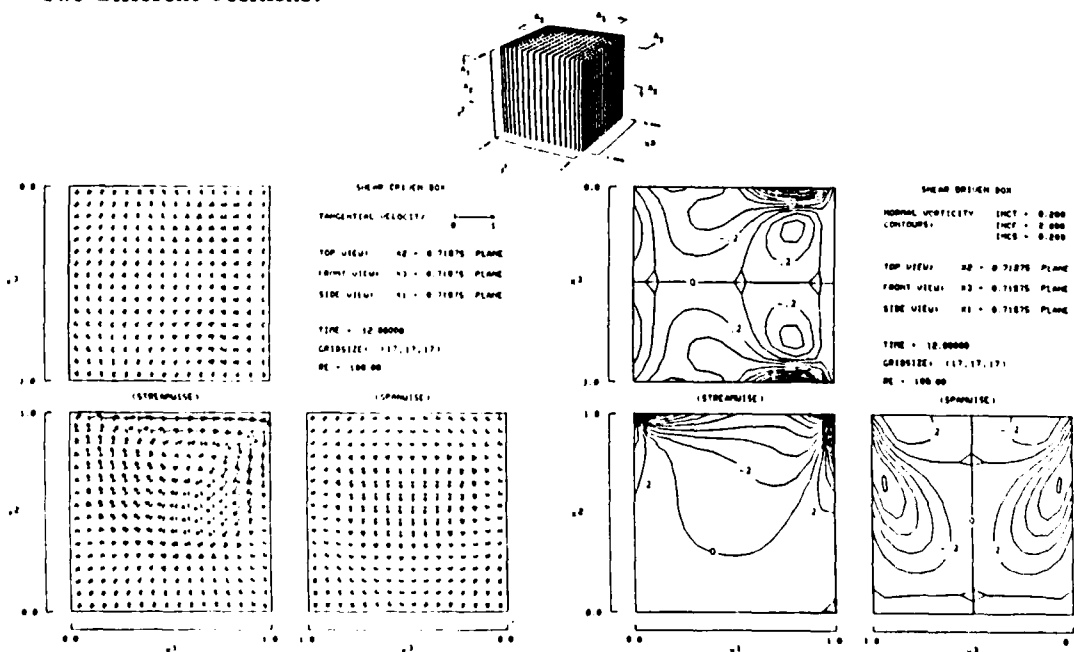
Fig. 14. Tangential Velocity Vectors and Contours of Normal Vorticity at Re = 100; Steady-State Solution at Off-Center Planes of Cubical Box.

119

WHAT DID WE LEARN SINCE THE LAST WORKSHOP?[*]

Mohamed Gad-el-Hak[**]
University of Notre Dame
Notre Dame, IN 46556

ABSTRACT

One of the objectives for conducting the present (1987) Workshop on Unsteady Separated Flows is to "assess the current content of the AFOSR unsteady aerodynamics research program." Towards this end, the present article attempts to answer the question posed in its title albeit from a highly personal point of view. Highlights of progress in the field since the last workshop held in 1983 are presented. It is shown that, although much research has been carried out, overall theoretical understanding of the phenomenon of unsteady separation is still lacking. In the absence of new, tradition-shattering paradigm, progress in the field could be readily classified as "normal science."

1. INTRODUCTION

The last workshop on Unsteady Separated Flows was held on 10-11 August 1983. The opening talk by W.B. Herbst was entitled "Supermaneuverability" and set the tone for the rest of the meeting. Motivated by the recent advances in short-range infrared guided missiles, Herbst[1,2] indicated the needed changes in close air combat characteristics and the desirability of achieving very fast maneuverability of fighter aircraft, including previously unattained regions of the maneuver envelope such as post-stall flight maneuver and side slipping. In support of these goals, several researchers have since been involved in experimental, numerical and theoretical studies aimed at understanding the dynamic stall on two-and three-dimensional lifting surfaces and the behavior of attached and separated unsteady shear layers affected by time-dependent boundary conditions. Attempts were also made to exploit the unsteady flow characteristics to improve aerodynamic efficiency and enhance performance. This article is intended to review several such investigations, albeit from a highly personal point of view.

A major part of the present knowledge of the flow around two-dimensional airfoils undergoing large-amplitude harmonic oscillations in pitch and the phenomenon of dynamic stall is due to the work conducted at the U.S. Army's Aeromechanics Laboratory during the decade preceding the 1983 Workshop.[3-6] During the past five years, the two-dimensional work has been extended to include three-dimensional lifting surfaces. Experiments using low-aspect-ratio rectangular wings, swept wings, delta wings and bodies of revolution have been conducted primarily at the University of Colorado[7-14] and at Flow Research.[15-19] The results of such experiments have inspired the formulation of a heuristic model to explain the complex, time-dependent flowfield around the different three-dimensional lifting surfaces. In this model, the mutual induction between the leading-edge separation vortex and the trailing-edge shedding vortex could explain the effects of the reduced frequency, the leading edge shape, the lifting surface planform and the aspect ratio on the observed flow patterns.[17]

A second area of active research is aimed at identifying the mechanism involved in unsteady separation. The experiments of Ho and his colleagues[20-22] have indicated a plausible mechanism for time-dependent separation. They investigated the laminar boundary layer produced by an axisymmetric jet impinging normally onto a flat plate. By forcing the air jet, primary ring vortices were periodically generated in the jet shear layer. These vortices produced a fast moving stream while approaching the wall, causing a negative wall pressure in the low-pressure region downstream from the jet axis. Further downstream, pressure recovery resulted in an unsteady adverse pressure gradient which retarded the flow in the viscous layer. Hence, a strong shear layer was generated at the viscous-inviscid interface. The instability of this shear layer led to the rollup of the vortex sheet and the formation of a secondary vortex. Didden and Ho[21] have shown that the ejection of this secondary vortex is associated with the onset of unsteady separation. Thus, time-dependent separation has been shown to be linked to the instability of a spatially developing local shear layer. This interesting association may allow researchers in the field of unsteady separation to borrow from the extensive knowledge available in free shear layer studies.[23-27] The present author has reviewed available knowledge of unsteady spearation on two-and three-dimensional lifting surfaces.[28-29] Available experimental data were interpreted in light of the idea advanced by Didden and Ho[21] and summarized above.

A third area of active research deals with the attempts to exploit the unsteady flow characteristics to improve aerodynamic efficiency and enhance performance. According to Somps and Luttges,[30] the dragonfly has probably exemplified some of the highest achievement in insect flight for more than 250 million years. It appears to control and use unsteady separated flow to support flight. Reynolds and Carr[31] reviewed the main features of unsteady, driven, separated flows from the viewpoint of a vorticity framework. They asserted that a good understanding of vorticity production and transport mechanisms is very useful in understanding these flows and in designing effective mechanisms for separation control. In here, we simply mention few of the recent attempts to actively or passively control separated flows.[32-38]

With all the activities currently taking place in the field of unsteady aerodynamics, a legitimate question is: "What did we learn?" A straightforward, objective answer is clearly difficult without the benefit of hindsight,

---

particularly since major discoveries are often not recognizable as such by contemporary scientists. At present, however, a philosophical discussion is perhaps more appropriate in order to enable us to assess the pertinent developments in the current research program. To set the theme for such discussion, we start by developing a tool that will help us to measure our progress in the field. This tool requires a search for order or pattern in scientific achievement. Such a search is a major occupation among philosophers of science, and a very brief review of an accepted structure is provided in the next section.

2. STRUCTURE OF SCIENTIFIC ACHIEVEMENTS

In this section we very briefly illustrate an accepted model for the structure of scientific advances. Such a model will help us in judging our progress in the field of unsteady separated flows. The logical empiricist view of science as an objective progression toward the truth or the steady, cumulative acquisition of knowledge has more or less been shattered by the pioneering and well accepted work of Thomas S. Kuhn.[39] He asserts that science is instead a series of peaceful interludes punctuated by (intellectually) violent revolutions, where in each revolution one conceptual world view is replaced by another. Kuhn terms an accepted model or pattern in a scientific endeavor a paradigm. In the absence of such a paradigm (pre-paradigm period), early fact-gathering is nearly random, since a reason for seeking some particular of more concealed information is clearly absent. Scientific research without a paradigm will most probably produce a morass. On the other hand, a universally recognized scientific achievement (a paradigm) would provide, for a time, model problems and solutions to a community of practitioners. This tradition-shattering activity must seem better than its competitors and will suggest what further experimental or theoretical research to be conducted.

A period of tradition-bound activity follows the acceptance of a paradigm. This "normal science" is highly focused and directed and is firmly based upon one or more past scientific achievements. The normal science is highly cumulative and eminently successful in its aim, the steady extension of the scope and precision of scientific knowledge.

Normal science is committed to certain rules and standards. As a result, it often suppresses fundamental novelties. Normal science does not seek new theory, rather it is directed to the articulation of those phenomena and theories supplied by the accepted paradigm. This articulation may take the form of a theoretical activity, which uses existing theory to predict factual information, or a fact-gathering activity to determine the value of a constant or a property with greater precision or in a larger variety of situations. According to Kuhn's view, the paradigm assures the importance of a particular quantity to be measured. Normal science as defined above obviously fits the most usual image of scientific endeavor.

Kuhn[39] reiterates that normal science may have as its objective one or more of the following classes of problems: the determination of significant fact; matching facts with theory; or articulation of theory. Extraordinary problems

emerge only on special occasions prepared by the advance of normal research. The resolution of such unusual problems may well be what makes the scientific enterprise as a whole so particularly worthwhile. However, Kuhn asserts that the overwhelming majority of the problems undertaken by even the very best scientists must fall under the classification of normal science.

How does a new paradigm emerge from normal science? According to Kuhn, external conditions and technological advances often yield to an awareness of one or more anomaly; in other words, to the recognition that nature has somehow violated the paradigm-induced expectations. A new discovery begins with this awareness and ends only with the adjustment of the old paradigm so that the anomalous has become the expected. The particular field of science will then have a new paradigm. Kuhn maintains that all new discoveries are characterized by three stages:

I. Previous awareness of anomaly.

II. An extended exploration of the area of anomaly, where observational and conceptual recognition are gradually and simultaneously emerge.

III. Consequent change of paradigm categories and procedures, often accompanied by resistance.

The schema for the process of scientific discovery is described in Kuhn's words as follows: "In science, ..., novelty emerges only with difficulty, manifested by resistance, against a background provided by expectation. Initially, only the anticipated and usual are experienced even under circumstances where anomaly is later to be observed. Further acquaintance, however, does result in awareness of something wrong or does relate the effect to something that has gone wrong before. That awareness of anomaly opens a period in which conceptual categories are adjusted until the initially anomalous has become the anticipated. At this point the discovery has been completed."

In summary, anomalies appearing during the conduct of the tradition-bound normal science lead to the new, tradition-shattering paradigm. This new paradigm rarely coexists peacefully with its predecessor and provides, for a time, model problems and solutions to a community of practitioners in the specific field of research.

The above discussion provides a model for the structure of scientific advances. In the next section, we will apply these ideas to the subfield of unsteady separation in an effort to judge the recent progress in the particular area of research.

3. STEADY AND UNSTEADY SEPARATION

Separation of a steady, two-dimensional boundary layer was explained first by Ludwig Prandtl[40] in his milestone presentation "Fluid Motion with Very Small Friction," in which he introduced the boundary-layer theory. Fluid particles near the surface are retarded by the friction of the wall and by any adverse pressure gradient present in the freestream. If the near-wall fluid has insufficient momentum for it to continue its motion, it will be brought to rest at

the separation point(line). Further downstream, the adverse pressure forces will cause reverse flow. Since the velocity at the wall is always zero, the gradient $\partial U/\partial y|_{y=0}$ must be positive upstream of separation, zero at the point of separation, and negative in the reverse flow region. In Prandtl's view, the separation point is entirely determined by external conditions. Boundary-layer separation is accompanied by a thickening of the rotational flow region and ejection of vorticity. Downstream of the separation point the original boundary layer either passes over the region of recirculating fluid and reattaches to the surface or forms a wake and never reattaches to the body. In the latter case, the characteristic dimension of the recirculating region is quite large and is of the order of the body diameter.

Analytically, the solution of the steady, two-dimensional, laminar boundary-layer equations with a prescribed external-pressure (or external-velocity) distribution breaks down at the point of separation, and this is commonly known as the Goldstein singularity,[41] in honor of Sydney Goldstein who first noted the singular behavior of the solution near a point of zero skin friction. The singularity of the boundary-layer equations at separation is obviously not a physical property of the flow and can be mathematically overcome by prescribing either the displacement thickness or the wall shear distribution instead of the external pressure. This kind of analysis is termed inverse calculation.

For axially symmetric flow, the line of separation becomes a circle and the point of vanishing shear still coincides with the point of separation. On the other hand, for two-dimensional flow over moving walls, two-dimensional unsteady flows, and three-dimensional steady flows, the point (line) of vanishing wall shear does not coincide with separation, and this greatly complicates the problem. This was first observed by Rott[42] while analyzing the unsteady flow in the vicinity of a stagnation point. He observed that, while the wall shear vanished with an accompanying reverse flow, there was no singularity or breakdown in the boundary-layer assumptions. In seeking a generalized model for separation, Sears[43] postulated that the unsteady separation point is characterized by the simultaneous vanishing of the shear and the velocity at a point within the boundary layer as seen by an observer moving with the separation velocity.

Moore[44] while investigating a steady flow over a moving wall, arrived at the same model for unsteady separation. Based on an intuitive relationship between steady flow over a moving wall and unsteady flow over a fixed wall, Moore was able to sketch the expected velocity profiles for both cases. He considered the possibility that a Goldstein-type singularity occurs at the location where the velocity profile has simultaneously zero velocity and shear at a point above the moving wall. Equivalently, for unsteady separation on a fixed wall, the separation point is the location at which both the shear and velocity vanish in a singular fashion in a frame of reference moving with the separation point. The main drawback of this model in the fixed wall case is that the speed of the separation point is not known a priori, making it difficult to locate this point and forcing researchers to rely on more qualitative measures for unsteady separation.

Because of the above difficulty, early attempts to verify this important Moore-Rott-Sears model of unsteady separation considered the more tractable problem of steady separation over moving walls. References 45 and 46 investigated experimentally a shrouded rotating cylinder in steady flow. As expected, separation was delayed (moved downstream) for downstream moving wall and was advanced (moved upstream) when the wall moved opposite the main flow. The measured velocity profiles corresponded to those hypothesized by Moore.[44] References 47 and 48 presented an analytical verification of the separation model for the case of a downstream moving wall.

Until the work of Williams and Johnson,[49] the relationship between unsteady boundary-layer separation over fixed walls and steady separation over moving walls has been an intuitive one. Their work established a rigorous analytical link between the two problems for the special case in which the external velocity distribution is a function of a linear combination of the streamwise coordinate and time and where the wall moves downstream with the speed of the unsteady separation point.

Despard and Miller[50] provided the first experimental evidence of the Moore-Rott-Sears model for a moving separation point for the case where the imposed pressure gradient is adverse but oscillating in magnitude. They used an array of 10 hot-wire probes to measure the instantaneous velocity profiles in a boundary-layer flow produced by a freestream having large-scale oscillations in velocity. Despard and Miller concluded that the presence of an oscillating velocity component, superimposed on the mean flow, and a time-dependent adverse pressure gradient cause the separation point to move upstream during part of the cycle and downstream during the rest of the cycle. Because of the difficulty of determining the speed of the separation point, Despard and Miller provided a practical definition of unsteady separation as the farthest upstream point at which there is zero velocity or reverse flow at some point in the velocity profile throughout the entire oscillation cycle. The first indication of detachment or wake formation was observed at the separation point as defined above. Thus, Despard and Miller's results provided the first experimental evidence that a thin layer of reversed flow can be embedded at the bottom of an attached boundary layer.

Shortly after this important experiment, Sears and Telionis[51] provided a review of the numerical evidence of the validity of the Moore-Rott-Sears model. Numerical integrations of unsteady laminar and turbulent boundary layers showed no evidence of the Goldstein (separation) singularity, even in a region of partially reversed flow and through the point of zero skin friction.

Some controversy still exists over the precise definition of unsteady separation. Telionis[52] reiterates that separation means the location on the solid boundary where the flow stops creeping over the skin of the body and breaks away from the wall, thus generating a turbulent wake. In Reference 53, Sears and Telionis argue that abrupt changes of boundary-layer properties in the first-order boundary-layer equations may signal the approach of the point of separation, or of the Goldstein singularity. Despard and Miller,[50] on the other hand, define separation as the farthest upstream

station at which the shear fluctuates between zero and some negative value throughout an entire cycle of freestream oscillation. Tsahalis and Telionis[54] numerically studied the unsteady separation in an oscillating flow and found that Despard and Miller's criterion could be verified under certain but not all situations.

Recently, Ho and his colleagues[20-22] have conducted well controlled experiments that indicated a plausible mechanism for time-dependent separation. They investigated the laminar boundary layer produced by an axisymmetric jet impinging normally onto a flat plate. By forcing the air jet, primary ring vortices were periodically generated in the jet shear layer. These vortices produced a fast moving stream while approaching the wall, causing a negative wall pressure in the low-pressure region downstream from the jet axis. Further downstream, pressure recovery resulted in an unsteady adverse pressure gradient which retarded the flow in the viscous layer. Hence, a strong shear layer was generated at the viscous-inviscid interface. The instability of this shear layer led to the rollup of the vortex sheet and the formation of a secondary vortex. Didden and Ho[21] have shown that the ejection of this secondary vortex is associated with the onset of unsteady separation. Thus, time-dependent separation has been shown to be linked to the instability of a spatially developing local shear layer. This interesting association may allow researchers in the field of unsteady separation to borrow from the extensive knowledge available in free shear layer studies.[23-27] The present author has reviewed available knowledge of unsteady separation on two-and three-dimensional lifting surfaces.[28,29] Available experimental data were interpreted in light of the idea advanced by Didden and Ho[21] and summarized above.

Only a brief recap has been given above on the subject of steady and unsteady separation. The complexity of the problem is evident from the numerous articles written on the subject, and the reader is referred to the many excellent review articles available, each with a list of references that provide a wealth of information.[29]

According to the criteria presented in Section 2, in the subfield of unsteady separated flows, the Moore-Rott-Sears's paradigm replaces Prandtl's paradigm as a criterion for unsteady separation.* In fact, the Prandtl's model for steady separation is included as a special case in the more general Moore-Rott-Sears's model for a moving separation point. Research in the field since 1958 could be readily classified as normal science according to the Kuhnian view.[39]

The tradition-shattering paradigm of Moor-Rott-Sears suggested what further experimental or theoretical research to be conducted. It only resulted after the observation of an anomaly; namely, the observation that, in the unsteady flow in the vicinity of a stagnation point, no

*Of course, the much more general paradigm of boundary layer theory still stands today as one of the major achievements in the physical sciences. Some will even say that, of any fluid dynamicist in history, Ludwig Prandtl came closest to deserving a Nobel prize for introducing the concept of a boundary layer.

singularity or breakdown in the boundary-layer assumptions existed while the wall shear stress vanished with an accompanying reverse flow. The tradition-bound activities that followed the Moore-Rott-Sears paradigm continue to this date. The complexity of the problem has thus far precluded overall theoretical understanding. New approaches are being attempted, however, and the work on bifurcation theory by Murrary Tobak and Gary T. Chapman (presented in these proceedings) is one such attempt that has the potential for becoming the new paradigm in the field. Such predictions are of course risky and I underline the word "potential."

4. TWO- AND THREE-DIMENSIONAL LIFTING SURFACES

A major part of the present knowledge of the flow around two-dimensional airfoils undergoing large-amplitude harmonic oscillations in pitch and the phenomenon of dynamic stall is due to the work conducted at the U.S. Army's Aeromechanics Laboratory during the decade preceding the 1983 Workshop.[3-6] During the past five years, the two-dimensional work has been extended to include three-dimensional lifting surfaces. Experiments using low-aspect-ratio rectangular wings, swept wings, delta wings and bodies of revolution have been conducted primarily at the University of Colorado[7-14] and at Flow Research.[15-19]

In here, we briefly recap results of the work conducted by the present author.[15-19] The unsteady separated flow around three-dimensional lifting surfaces undergoing harmonic pitching motion has been shown to be dominated by large-scale vortices, about a chord length in size. Several features observed at different operating parameter ranges can be understood through the mutual induction among the leading-edge separation vortex and the vortices shed as a result of the vertical motion of the trailing edge.

The wake pattern of the rectangular wing varies significantly with the reduced frequency and is determined by the phase angle of the leading-edge vortex's arrival at the trailing edge. At a reduced frequency of $K = 1.0$, the wake consists of a vortex pair above the chord line and a single clockwise vortex below the chord line. The clockwise vortex induces an upward motion that results in a thick separation zone on the chord. At $K = 3.0$, the wake has a vortex pair below the chord line. The induction of the counterclockwise trailing-edge vortex suppresses the upward motion of the leading-edge vortex; hence, the separation zone on the chord is much thinner than that at $K = 1.0$.

A secondary counter-rotating vortex is clearly identified on a sharp leading-edge rectangular wing. The mutual induction between the vortex pair lifts the vortices from the wall and results in a large intrusion into the inviscid region. The separation zone is about twice as thick as that on a blunt leading-edge wing. Gad-el-Hak and Ho[17] speculated that the counter-rotating vortex could have an important role in the generation of unsteady lift.

On a rectangular wing, the leading-edge separation vortex convects downstream, while it is stationary during part of the cycle on a swept wing. On a delta wing, the leading-edge vortex does not convect, rather it experiences a growth-decay cycle as the angle of attack changes.

Additional end and side views of the sharp leading-edge rectangular wing used by Gad-el-Hak and Ho[17] revealed the existence of three distinct regions similar to those observed by Adler and Luttges[7] on a NACA 0015 wing: the tip vortex, which undergoes a growth-decay cycle; the leading-edge separation vortex, which convects downstream and seems to be triggered by the upstream-propagating separation near the wing tip; and the intermediate zone, where the tip vortex and the leading-edge vortex interact. The strong three-dimensional effects demonstrated in the experiments of Gad-el-Hak and Ho[17] and Adler and Luttges[7] make it clear that any attempt to model the unsteady flow around finite-aspect-ratio wings using a two-dimensional approximation is bound to fail.

In a related experiment,[18] the complex flow patterns on a pitching slender body were visualized by using fluorescent dye techniques. The slender body was an ogive cylinder that was towed in an 18m water channel and was undergoing a large-amplitude, harmonic pitching motion about the midbody at $x/L = 0.5$. It was found that the unsteady separation phenomenon was significantly different from the separation around the body in steady flight. Two separation vortex pairs were identified as the slender body underwent a complete pitching cycle. Gad-el-Hak and Ho[18] termed these pairs "forebody and aftbody separation vortices." During the upstroke, the unsteady separation started near the base of the body and propagated upstream as the angle of attack increased. During the downstroke, the separated zone moved downstream and a secondary separation seemed to be triggered by the primary separation near the nose of the body. Both separation regions were in the form of counter-rotating vortex pairs that underwent a growth/decay cycle.

The size, circulation, and degree of symmetry of the leeward vortices changed dramatically with changes in the pitching parameters. On the other hand, at moderate-to-large reduced frequencies, the Reynolds number effects were negligible. The unsteady effects dominated the viscous effects and were mainly responsible for the variations of the aerodynamic properties.

The above investigation provided a closer look at the unsteady motion around a body of revolution undergoing a pitching motion. Other modes of unsteadiness should also be studied, such as plunging or time-dependent ambient velocity. References 55 and 56 indicated that the mode of the unsteady motion can significantly affect the hystersis loops and the aerodynamic properties of a lifting surface.[57] The results of the visualization experiments should be used to design fast-response probe experiments to measure the velocity field and to correlate the visualization events with the unsteady forces and moments experienced by the slender body.

Once more, although much research has been carried out since the last workshop to study the time-dependent flow over three-dimensional lifting surfaces at high incidence, the complexity of the problem precludes overall theoretical understanding. The recent activities are all tradition-bound normal science and no new tradition-shattering paradigm has been developed in the last five years.

5. CONCLUDING REMARKS

Prior to the 1983 Workshop on Unsteady Separated Flows, aerodynamic research for time-dependent viscous flows at high incidence has centered primarily on the flow over two-dimensional airfoils. These data can play an essential role in applications having high aspect ratios where the local flow behaves, in a sense, two-dimensionally. The classic lifting line theory for an unswept wing or its extension to include wings with sweep is of little value for low-aspect-ratio wings of fighter/attack aircraft because the local airfoil section, particularly for the higher incidence angles, cannot be divorced from the wing as an entirety. Therefore, two-dimensional data play a less significant role in the design of low-aspect-ratio wings.

As evidenced from the number of presentations in the present workshop that deal directly with three-dimensional effects, considerable research has been conducted since the last workshop to study the time-dependent flow over three-dimensional lifting surfaces at high incidence. This research is mainly motivated by the need to establish a detailed understanding of the physics of three-dimensional, time-dependent flows coupled with the need to establish a data base to assess and to improve prediction methods.

More experimental validation of the Moore-Rott-Sears criterion for unsteady separation has appeared in the open literature since the last workshop. The experiments of Ho and his colleagues[20-22] have indicated a plausible mechanism for time-dependent separation. A downstream-moving separation has been shown to be linked to the instability of a spatially developing shear layer.

Considering the Kuhnian views[39] summarized in Section 2 and stating that science is a series of peaceful interludes (normal science) punctuated by violent revolutions (paradigms), the subfield of unsteady separation has not enjoyed a new paradigm since the pioneering work of Moore, Rott and Sears.[42-44] The considerable amount of work since the middle 1950's could be readily classified as tradition-bound normal science. Although normal science is not directed to novelties and even tends at first to suppress them, it is nevertheless so effective in causing eventually new ideas to arise leading to new paradigm. New approaches to the problem such as bifurcation theory, vorticity framework, etc. are all potential tools towards the eventual goal of understanding the complex problem of unsteady separated flows.

REFERENCES

1. Herbst, W.B. (1983) "Dynamics of Air Combat," J. Aircraft 20, p. 594.

2. Herbst, W.B. (1984) "Supermaneuverability," in Unsteady Separated Flows, eds. M.S. Francis and M.W. Luttges, University of Colorado, Boulder, p.1.

3. Carr, L.W., McAlister, K.W., and McCroskey, W.J. (1977) "Analysis of the Development of Dynamic Stall Based on Oscillating Airfoil Experiments," NASA TN D-8382.

4. McCroskey, W.J. (1977) "Some Current Research in Unsteady Fluid Dynamics," J. Fluids Eng. 99, p. 8.

5. McAlister, K.W., and Carr, L.W. (1978) "Water Tunnel Visualization of Dynamic Stall," in Nonsteady Fluid Dynamics, eds. D.E. Crow and J.A. Miller, ASME, New York, p. 103.

6. McCroskey, W.J. (1982) "Unsteady Airfoils," Ann. Rev. Fluid Mech. 14, p. 285.

7. Adler, J.N., and Luttges, M.W. (1985) "Three-Dimensionality in Unsteady Flow About a Wing," AIAA Paper No. 85-0132.

8. Freymuth, P. (1985) "The Vortex Patterns of Dynamic Separation: A Parameteric and Comparitive Study," Prog. Aerospace Sci. 22, p. 161.

9. Freymuth, P., Finaish, F., and Bank, W. (1986) "Visualization of Wing Tip Vortices in Unsteady and Steady Wind," AIAA Paper No. 86-1096.

10. Ashworth, J., Waltrip, M., and Luttges, M.W. (1986) "Three-Dimensional Unsteady Flow Fields Elicited by a Pitching Forward Swept Wing," AIAA Paper No. 86-1104.

11. Robinson, M., Helin, H., Gilliam, F., Russel, J., and Walker, J. (1986) "Visualization of Three-Dimensional Forced Unsteady Flow," AIAA Paper No. 86-1066.

12. Ashworth, J., and Luttges, M. (1986) "Comparison in Three-Dimensionality in the Unsteady Flows Elicited by Straight and Swept Wings," AIAA Paper No. 86-2280-CP.

13. Saharon, D., and Luttges, M. (1987) "Three-Dimensional Flow Produced by a Pitching-Plunging Model Dragonfly Wing," AIAA Paper No. 87-0121.

14. Gilliam, F., Wissler, J., Robinson, M., and Walker, J. (1987) "Visualization of Unsteady Separated Flow About a Pitching Delta Wing," AIAA Paper No. 87-0240.

15. Gad-el-Hak, M., and Blackwelder, R.F. (1985) "The Discrete Vortices from a Delta Wing," AIAA J. 23, p. 961.

16. Gad-el-Hak, M., and Ho, C.-M. (1985) "The Pitching Delta Wing," AIAA J. 23, p. 1660.

17. Gad-el-Hak, M., and Ho, C.-M. (1986) "Unsteady Vortical Flow Around Three-Dimensional Lifting Surfaces," AIAA J. 24, p. 713.

18. Gad-el-Hak, M., and Ho, C.-M. (1986) "Unsteady Flow Around an Ogive-Cylinder," J. Aircraft 23, p. 520.

19. Gad-el-Hak, M. (1986) "The Use of the Dye-Layer Technique for Unsteady Flow Visualization," J. Fluids Eng. 108, p. 34.

20. Ho, C.-M. (1983) "Genesis of Unsteady Separation," in Unsteady Separated Flows, eds. M.S. Francis and M.W. Luttges, University of Colorado, Boulder, p. 165.

21. Didden, N., and Ho, C.-M. (1985) "Unsteady Separation in a Boundary Layer Produced by an Impinging Jet," J. Fluid Mech 160, p. 235.

22. Ho, C.-M. (1986) "An Alternative Look at the Unsteady Separation Phenomenon," in Recent Advances in Aerodynamics, eds. A. Krothappalli and C.A. Smith, Springer-Verlag, New York, p. 165.

23. Winant, C.D., and Browand, F.K. (1974) "Vortex Pairing: The Mechanism of Turbulent Mixing-Layer Growth at Moderate Reynolds Number," J. Fluid Mech. 63, p. 237.

24. Brown, G.L., and Roshko, A. (1974) "On Density Effects and Large Structure in Turbulent Mixing Layers," J. Fluid Mech. 64, p. 775.

25. Roshko, A. (1976) "Structure of Turbulent Shear Flows: A New Look," AIAA J. 14, p. 1349.

26. Ho, C.-M., and Huang, L.-S. (1982) "Subharmo.ics and Vortex Merging in Mixing Layers," J. Fluid Mech. 119, p. 443.

27. Ho, C.-M., and Huerre, P. (1984) "Perturbed Free Shear Layers," Ann. Rev. Fluid Mech. 16, p. 365.

28. Gad-el-Hak, M. (1987) "Unsteady Separation on Two-and Three-Dimensional Lifting Surfaces," Proc. 10th U.S. National Congress of Applied Mech., ed. J.P. Lamb, ASME, New York, p. 515.

29. Gad-el-Hak, M. (1987) "Unsteady Separation on Lifting Surfaces," App. Mech. Rev. 40, p. 441.

30. Somps, C., and Luttges, M. (1985) "Dragon Flight: Novel Uses of Unsteady Separated Flows," Science 228, p. 1326.

31. Reynolds, W.C., and Carr, L.W. (1985) "Review of Unsteady, Driven, Separated Flows," AIAA Paper No. 85-0527.

32. Koga, D.J. (1983) "Control of Separated Flowfields Using Forced Unsteadiness," Ph.D. Thesis, Illinois Institute of Technology, Chicago.

33. Reisenthel, P.H. (1984) "Reattachment Control Behind a Rearward Facing Step Using Forced Unsteadiness," M.S. Thesis, Illinois Institute of Technology, Chicago.

34. Nagib, H.M., Reisenthel, P.H., and Koga, D.J. (1985) "On the Dynamical Scaling of Forced Unsteady Separated Flows," AIAA Paper No. 85-0553.

35. Reisenthel, P.H., Koga, D.J., and Nagib, H.M. (1985) "Control of Separated Flows Using Forced Unsteadiness," AIAA Paper No. 85-0556.

36. Luttges, M.W., and Robinson, M.C. (1985) "Control of Unsteady Separated Flow Structures on Airfoils," AIAA Paper No. 85-0531.

37. Robinson, M.C., and Luttges, M.W. (1986) "Vortices Produced by Air Pulse Injection from the Surface of an Oscillating Airfoil," AIAA Paper No. 86-0118.

38. Shih, C., Lee, M., and Ho, C.-M. (1987) "Control of Separated Flow on Symmetric Airfoil," to be published.

39. Kuhn, T.S. (1970) "The Structure of Scientific Revolutions," second edition, the University of Chicago Press, Chicago.

40. Prandtl,L. (1904) Über Flussigkeitsbewegung bei sehr kleiner Reibung," Proc. Third Int. Math. Congr., Heidelberg, Germany, p. 484.

41. Goldstein, S. (1948) "On Laminar Boundary Layer Flow Near a Position of Separation," Q.J. Mech. Appl. Math., 1, p. 43.

42. Rott, N. (1956) "Unsteady Viscous Flow in the Vicinity of a Stagnation Point," Q. Appl. Math. 13, p. 444.

43. Sears, W.R. (1956) "Some Recent Developments in Airfoil Theory," J. Aeronaut. Sci. 23, p. 490.

44. Moore, F.K. (1958) On the separation of the Unsteady Laminar Boundary Layer, in Boundary-Layer Research, ed. H.G. Gortler, Springer-Verlag, Berlin, p. 296.

45. Vidal, R.J. (1959) "Research on Rotating Stall in Axial-Flow Compressors; Part· III---Experiments on Laminar Separation from a Moving Wall," Wright Air Dev. Cent. Tech. Report No. 59-75, Wright-Patterson Air Force Base, OH.

46. Ludwig, G.R. (1964) "An Experimental Investigation of Laminar Separation from a Moving Wall," AIAA Paper No 64-6.

47. Telionis, D.P., and Werle M.J. (1973) "Boundary-Layer Separation from Downstream Moving Boundaries, J. Appl. Mech. 40, p. 369.

48. Tsahalis, D. Th., and Telionis, D.P. (1973) "The Effect of Blowing on Laminar Separation," J. Appl. Mech. 40, p. 1133.

49. Williams, J.C., III, and Johnson, W.D. (1974) "Note on Unsteady Boundary-Layer Separation," AIAA J. 12, p. 1427.

50. Despard, R.A., and Miller, J.A. (1971) "Separation in Oscillating Laminar Boundary-Layer Flows," J. Fluid Mech. 47, p. 21.

51. Sears, W.R., and Telionis, D.P. (1971) "Boundary-Layer Separation in Unsteady Flow," J. Appl. Math. 28, p. 215.

52. Telionis, D.P. (1979) "Review--Unsteady Boundary Layers, Separated and Attached." J. Fluids Eng. 101, p. 29.

53. Sears, W.R., and Telionis D.P. (1971) "Unsteady Boundary-Layer Separation," in Recent Research of Unsteady Boundary Layers, ed. E.A. Eichelbrenner, Vol. 1, p. 404.

54. Tsahalis, D. Th., and Telionis, D.P. (1974) Oscillating Laminar Boundary Layers and Unsteady Separation," AIAA J. 12, p. 1469.

55. Carta, F.O. (1979) "A Comparison of the Pitching and Plunging Response of an Oscillating Airfoil," NASA CR-3172.

56. Chen, S.-H., and Ho, C.-M. (1985) "Unsteady Aerodynamics of a Plunging Airfoil," Bul. Am. Phys. Soc. 30, p. 1701.

57. Ericsson, L.E., and Reding, J.P. (1983) "The Difference Between the Effects of Pitch and Plunge on Dynamic Stall," Ninth European Rotorcraft Forum, Stresa, Italy, Paper No. 8.

Unsteady Separation over Two- and Three-Dimensional Airfoils

Chiang Shih, Mario Lee and Chih-Ming Ho
Aerospace Engineering Department
University of Southern California
Los Angeles, California 90089-1191

Abstract

The responses of a NACA 0012 airfoil and a delta wing have been studied in a vertical water channel with the freestream velocity undergoing a periodic variation with time. Unsteady lift measurements and flow visualization results showed that vortex dynamics is important in understanding separated flows. It was found that a delicate balance between the production and the convection of the vorticity on the suction surface dictated the unsteady performance of the two-dimensional wing. In the case of the delta wing, the two streamwise vortices were insensitive to the imposed unsteadiness of the freestream.

Nomenclature

AR	aspect ratio
c_{Lo}	static lift coefficient
c_L	phase averaged lift coefficient
t	time
T	oscillation period
U	average freestream velocity
ΔU	max-min phase averaged freestream velocity
α	angle of attack
β	sweepback angle of delta wing
ρ	density

Introduction

Unsteady airfoils have received significant attention recently due to the interest in developing fast maneuvering aircrafts[1]. Although notable progress has been made in this area, some important aspects of the flow received insufficient attention. For instance, the study of unsteady aerodynamics from the fundamental fluid mechanics point of view had been lacking.

Also, very little is understood about three dimensional separation although most practical problems are three dimensional in nature to some extent[2]. Likewise, most of the past studies focused on the behavior of oscillating airfoils during pitching and plunging motions while neglecting the equally important unsteady effects produced by a time-dependent freestream over a stationary wing[3,4]. It is imperative that all types of unsteady flow be considered to yield a better understanding of the controlling mechanisms of flow separation[5,6,7].

In a model proposed by Reynolds and Carr[8], the development of separated driven flows was viewed as a balance between vorticity generation and convection by the freestream. The local pressure gradient on the boundary was identified as the dominating source of vorticity besides moving surfaces and transpiration through the wall. Consequently, separation control would be effective by applying boundary layer control techniques to separated flows.

In order to extend our understanding of unsteady separated flows, a series of experiments were performed using a NACA 0012 airfoil and a delta wing in an unsteady freestream. First a brief account of the vorticity balance concept is provided for later analysis. Second, the unsteady behavior of the two and three-dimensional wings will be discussed. Finally, some preliminary results of controlling the two-dimensional separation using a movable flap is presented.

Experimental Facility

The vertical water channel, as shown in Fig. 1, consisted of a constant head settling chamber, a test section and a downstream collection reservoir. Inside the chamber, several layers of foam, honeycomb and fine mesh screens made up the turbulence reduction section. Immediately before the straight section was a 7.7:1 contraction with a fifth order polynomial profile. The test section had a 23x23 cm cross-section and a length of 2 m. The maximum time-averaged freestream velocity was 23 cm/sec. The freestream turbulence level was less than 0.5% which was the resolution of the Laser Doppler Anemometer.

The unsteady freestream velocity was controlled by a gate downstream of the test section. The gate was made up of three elements. The top two pieces had the same opening patterns and were allowed to slide linearly over each other to determine the mean flow rate of the channel. The third element was a rotating gear with a different opening pattern. When the gear was driven by a stepping motor, the opening area of the gate varied with time. This produced the unsteady freestream velocity throughout the channel. By incorporating the stepping motor with a pre-programmed BCC-52 microprocessor, a wide range of freestream oscillation patterns could be achieved. Examples of two typical waveforms are shown in Fig. 2. The maximum peak-to-peak velocity variation could be 80% of the time mean velocity. The corresponding wave

pattern and magnitude were found to be independent of the oscillation frequency. The maximum frequency was limited by the available torque of the stepping motor.

For the two-dimensional experiments, an airfoil with NACA 0012 profile was used. The airfoil was made out of Hysol from an epoxy casting with a chord of 7.5 cm. A delta wing with an aspect ratio of 2, or a 63.4° sweep angle, was used to study three-dimensional separation. The wing had a 10 cm chord and a thickness of 1 mm with square edges.

Instrumentation

The freestream velocity in the channel was measured using a two components Laser Doppler Anemometer (Dantec 55x system). Counter-type processors were used to process the Doppler signal into digital velocity data which were then collected by a PDP 11-73 computer. Ensemble averaging was made possible by a phasing circuit connected to the PDP 11-73 and the BCC-52 computers.

The lift of the wings was measured by a pair of waterproof load cells manufactured by Sensotec (model 31). The load cells were mounted with their sensitive axes in the horizontal direction in two enclosed boxes filled with water next to the channel. The boxes were connected to the channel through flexible tubes and independently supported to avoid vibration. Each load cell was supporting one leg of the wing's mounting rod on opposite side of the channel. Signal from the load cells were amplified and lowpass filtered before being sampled by the computer. The total lift on the wing was determined by adding the outputs from both load cells. The lift measurements were calibrated with a combined uncertainty of 0.02 N.

Flow Visualizations

Different flow visualization techniques were employed for the two-dimensional and delta wing. In the case of the two-dimensional wing, a half watt Argon-ion laser with an optical scanning mirror system (General Scanning Inc. Model G-0612) was used to generate a thin laser sheet. This laser sheet was then directed to shine along the mid-span on the upper surface of the airfoil. Air bubbles suspended in the water were used as light reflectors. Drops of dishwashing detergent were added into the channel to maintain the appropriate concentration of air bubbles. Phase-triggered photographs were taken by a Nikon F-2 35 mm camera. A RCA motion video camera at 30 frames/sec was also used to document the flow.

For the delta wing, flow visualization was achieved by injecting diluted food coloring at the apex through a 1.5 mm diameter tube placed along the pressure side of airfoil. The pressure difference across the wing brought the dye to the suction surface. Eventually, the dye was entrained into the core of the vortex marking its development. Only video recording was taken for the delta wing study.

The Convection and Diffusion of Vorticity

The vorticity balance concept that we will use to analyze the results is based on the observation that large vortices dominate both two and three-dimensional separation during part or all of the unsteady freestream cycle. On the boundary of the airfoil, vorticity is generated on the surface and diffuses into the boundary layer. Away from the surface, the vorticity is transported by the velocity potential of the freestream. The balance between vorticity generation on the surface and vorticity transport in the freestream dictates the growth or decay of the large vortices.

To get a better understanding of the mechanisms affecting vorticity generation, we can rewrite the streamwise momentum equation as

$$\nu\left(-\frac{\partial^2 u}{\partial x^2} + \frac{\partial \Omega_z}{\partial y} - \frac{\partial \Omega_y}{\partial z}\right) = -\frac{1}{\rho}\frac{\partial p}{\partial x} - u\frac{\partial u}{\partial x} + v\Omega_z - w\Omega_y - \frac{\partial u}{\partial t} \quad [1]$$

where

$$\Omega_z = -\frac{\partial u}{\partial y} \quad [2]$$

and

$$\Omega_y = \frac{\partial u}{\partial z} \quad [3]$$

On the surface of the airfoil, the equation reduces to

$$\nu\frac{\partial \Omega_z}{\partial y} = -\frac{1}{\rho}\frac{\partial p}{\partial x} - V\Omega_z - \frac{\partial u}{\partial t} \quad [4]$$

We find that the diffusion of vorticity away from the boundary is governed by the local pressure gradient, transpiration through the surface and motion of the surface.

The variation of the freestream velocity is equivalent to change the streamwise pressure gradient. This global change of the pressure gradient affects the local pressure distribution on the wing and hence modifies the vorticity flux.

2-D Unsteady Aerodynamics

The NACA 0012 airfoil profile was chosen for the two-dimensional wing study and the data discussed here were taken with the freestream velocity varying in a sinusoidal pattern. A wide range of oscillation frequencies, from .08 to 1 Hz, were used while the wing was set at the static stall angle of 12°.

The response of the wing to the unsteady flow is indicated by the phase-averaged lift coefficient, C_L, as shown in Fig. 3. Depending on whether the freestream oscillation period is

short or long, C_L can either increase or decrease during deceleration. This migration of the lift pattern between different oscillation periods developes in a gradual fashion and can be best understood through the vorticity balance concept.

As the freestream slowed down, the vorticity generated around the leading edge experienced a diminishing downstream convection and started to accumulate to form a discrete vortex. The strength of the vortex was determined by the amount of vorticity contained. For long oscillation periods, the roll-up time for the vortex and the convection time from the leading to the trailing edge were a small portion of the period. The vortex rolled up during the initial phase of deceleration as the freestream velocity was still high. Therefore large portion of the vorticity was convected downstream. As a result, a weak vortex was generated and contributed little to the total lift. In Figure 3, this unsteady effect is represented by the plateau in the curve at the beginning of the deceleration period for several of the low frequency cases. Eventually the downstream moving vortex took off from the trailing edge and triggered the airfoil into deep stall with a drop in the lift. As the flow started to accelerate again, the vorticity generated at the leading edge encountered an increasing downstream convection. This produced two effects. First, the convection was strong enough to wash the vorticity away and the flow remained attached along the suction side of the airfoil. Second, according to equation [4], favorable pressure gradient induced by the accelerating freestream produced a large flux of clockwise vorticity around the airfoil thereby increasing the circulation and lift. After the flow attached to the surface, the lift for all different periods collapsed onto a single curve. In other words, the rate of lift increment scaled exactly with the frequency of the freestream oscillation in this region (Fig. 3). At the end of acceleration, C_L reached a value about 15% higher than the steady lift coefficent which was 0.77.

For shorter oscillation periods, the time for the vorticity to roll up into vortex occupied a larger portion of the entire deceleration cycle. Therefore, the freestream velocity dropped significantly during this rolling-up process. Consequently, the convection of the vorticity was much reduced and a strong leading edge vortex was formed. This vortex induced a significant suction on the upper surface and dominated the airfoil behavior during deceleration. A 90% increase of the unsteady lift during deceleration can be seen at the highest frequency case (Fig. 3). Due to this high vorticity accumulation during deceleration and the generation of high level of vorticity produced by the pressure gradient in the acceleration period, large amount of upper surface vorticity was collected at the beginning of the acceleration. Hence, a higher convection speed was necessary to wash this vorticity downstream in order to form an attached flow during acceleration. Therefore, the flow became attached at a later phase compared with that of longer oscillation periods.

The sequence of photographs in Figs. 4a-d shows the correlation between the upper surface flow behavior and the unsteady lift at a short oscillation period (T=2 sec.). Fig. 4b reveals the existence of a leading edge vortex, while the lift coefficient starts to go up (Fig. 4a). This vortex increases its size and rolls down to mid-chord as the lift reached its maximum value (Figs. 4a & 4c). At this moment, a clear reattachment can be seen near the trailing edge. When the flow starts to accelerate, the vortical flow convects downstream and eventually the upper surface flow becomes reattached again(Fig. 4d).

As shown in equation [4], the surface vorticity flux can be manipulated by a moving surface. A preliminary experiment indicated that the unsteady separated airfoil was greatly modified by using a control flap. The short flap (6% chord in length), which alternated between a flush and vertical position on the upper surface, was placed at 15% chord from the leading edge. By driving the flap at the same frequency as the freestream and through appropriate adjustment of the phase, the size of the separation zone was successfully reduced (Fig. 5). The relative phase of the flap movement with respect to the freestream variation was found to be important. Ineffective or even unfavorable effects on the separation control had been observed by using different phase angles. Based on equation [4], the moving flap can either inject or remove vorticity from the flow. Thus, it is clear that a timely-activating flap can drastically change the vortex dynamics, and hence the aerodynamic properties, on the wing. Therefore, it is possible to find the optimum configuration of controlling the unsteady separated airfoil by properly arranging all the governing parameters of the flap, e.g. phase, amplitude, location and frequency.

Delta Wing

The delta wing at angles of attack from 25° to 45°, was subjected to a near-sinusoidal periodic acceleration and deceleration of the freestream. The period of oscillation varied from 1, 1.5, 3 to 6 seconds.

From the dye-injection pictures (Fig. 6), the vortices on the delta wing were not very much affected by the imposed unsteady freestream. During the acceleration part of the cycle, the vortex broke down earlier and during the deceleration part, the breakdown was delayed as shown in Figs. 6a and 6b. The variation of the vortex breakdown location was less than 10% of the chord for all oscillation periods investigated. The vortex appeared to spiral in a tighter fashion during acceleration and uncoil during deceleration. This behavior of the vortices is consistent with the observations made by Lambourne and Bryer[9].

A plausible explanation for the small influence of the unsteady freestream on the vortices is as follow. From the momentum equation [1], a variation of the pressure gradient in the freestream direction affects only the vorticity

131

components in the other two directions. At a given angle of attack, the major component of the vorticity on the delta wing lies in the streamwise direction. Therefore, the effect of the unsteady streamwise pressure gradient on the structure of the vortices is small.

One of the most interesting findings as a consequence of the robustness of the vortices is that the difference between the phase averaged lift coefficient and the static lift coefficient follows the time derivative of the freestream velocity without any phase lag (Fig. 7). This is true for all the oscillation periods but the difference is much less in the large oscillation period cases. There are two implications in this finding; first, the unsteady lift is produced by the phase averaged velocity component normal to the wing $U_0 \sin\beta$. This suggests that the unsteady lift is generated by the inertial of the incoming flow. The phenomenon is similar to an object placed in an oscillating freestream with the force exerted on the body being partially contributed by the time derivative of the incoming velocity (Sarpkaya and Garrison[10]). Second, the time averaged lift, which is mainly caused by the leading edge vortices is not strongly influenced by the unsteady pressure gradient. This result is also supported by the flow visualization, i.e., the vortices do not change significantly in the unsteady freestream.

Conclusions

In the present study, the magnitude of the free stream velocity can be easily varied with time by a uniquely designed water channel. In essence, we can impose many different types of spatial pressure gradients on the wings and hence control the vorticity flux from the surface as well as the streamwise convection of the vortex. With this versatile tool, we are able to understand the unsteady aerodynamics of two- and three-dimensional airfoils through the underlying fluid mechanics of the flow.

Based upon the results from flow visualizations and the lift measurements, a delicate balance of the upper surface vorticity dominates the unsteady performance of the two-dimensional airfoil. At high frequency, a strong vortex forms because of a slow convection of vorticity during deceleration and the lift coefficient increases with the bluiding up of the vortex. The vorticity accumulated during deceleration and the high level vorticity generation from the surface (eq. [2]) require high convection speed to wash away the vortical flow during acceleration. Therefore, the upper surface flow reattaches at a later phase. At low frequencies, the low level diffusion of vorticity into the surface and the fast convection of vorticity in the streamwise direction causes the flow to fully separate during the deceleration perid. Hence the lift coefficient decreases with time.

The two separated vortices on top of the delta wing are insensitive to the unsteady freestream, because the streamwise pressure gradient produced by the unsteady stream does not generate streamwise vorticity. Lift measurements show that the difference between the phase averaged and static lift coefficient scales with the time derivative of the incoming velocity. This suggests that the unsteady lift on a delta wing is generated by the inertia of the flow.

References

1. "Unsteady Separated Flows", Proceeding of the workshop I on unsteady separated flow, eds. M.S. Francis and M.W. Luttges, University of Colorado. 1983.

2. McCroskey, W.J., "Unsteady Airfoils," Ann. Rev. Fluid Mech. 14, 1982, p. 285.

3. Gad-el-Hak, M., and Ho, C.M., "The pitching Delta Wing," AIAA J. 23, 1985, p. 1660.

4. Chen, S.H., and Ho, C.M., "Near Wake of an Unsteady Symmetric Airfoil," J. of Fluids and Structures 1, 1987, p. 151.

5. Shih, C., Lee, M. and Ho, C.M., "Control of Separated Flow on a Symmetric Airfoil", Proceeding of IUTAM Symp. on Turbulence Mangemente and Relaminarization, Bangalore, India, Jan 1987.

6. Lee, M., Shih, C. and Ho, C.M., "Response of a Delta Wing in Steady and Unsteady Flow", Proceeding of Forum on Unsteady Flow Separation, 1987 ASME App. Mech, Bioeng. and Fluid Mech. Conf., Cincinnati, Ohio.

7. Maresca, C. Favier, D. and Rebont, J., "Experiments on an Aerofoil at High Angle of Incidence in Longitudinal Oscillations", J. of Fluid Mech. Vol. 92, part 4, 1979, p.671.

8. Reynolds, W.C., and Carr, L.W., "Review of Unsteady, Driven, Separated Flows," AIAA Paper No. 85-0527, 1985.

9. Lambourne, N.C., and Bryer, D.W., "The Bursting of Leading-Edge Vortices - Some Observations and Discussion of the Phenomenon," Aeronautical Research Council Reports and Memoranda. No. 3282, 1962.

10. Sarpkaya, T., and Garrison, C.J., "Vortex Formation and Resistance in Unstady Flow," J. of Applied Mechanics. Vol. 30, Series E. No. 1, 1963, p. 16.
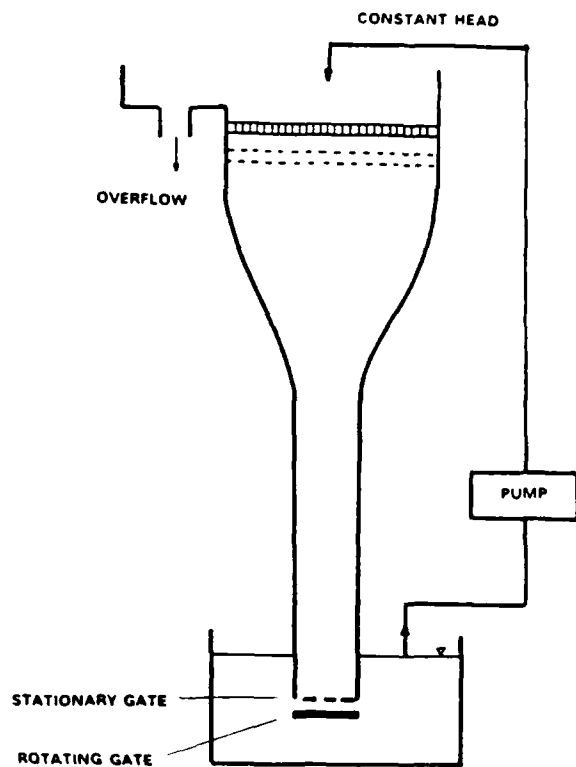
Fig. 1   Unsteady water channel facility.
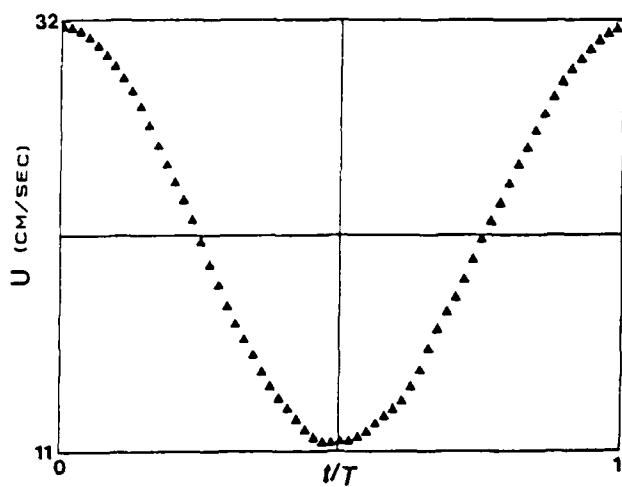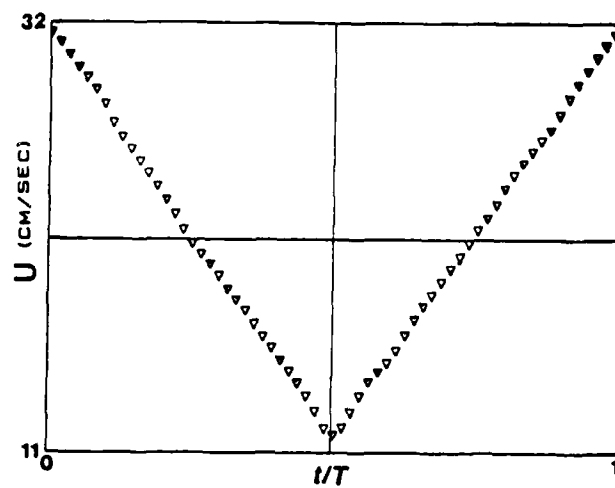
b) triangular

Fig. 2   Freestream velocity profiles.

a) sinusoidal
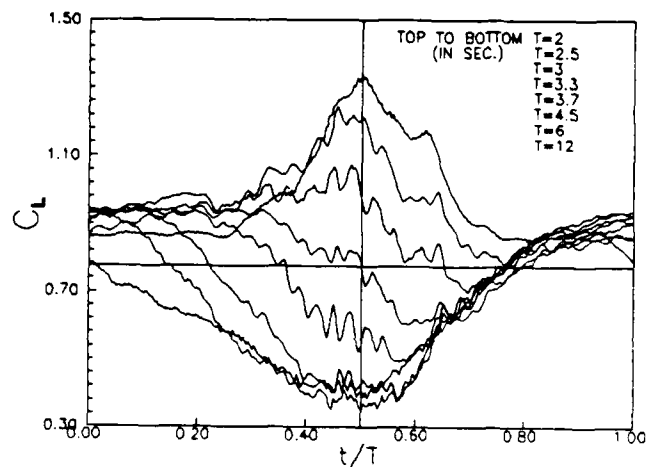
Fig. 3   Unsteady lift coefficient of NACA 0012 airfoil at different periods of oscillation and $\alpha=12°$.

(a) Lift
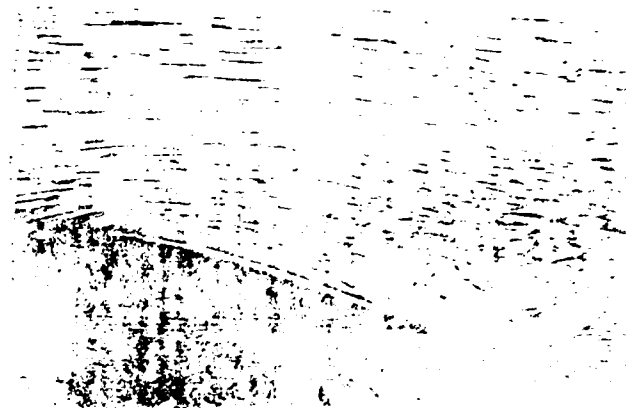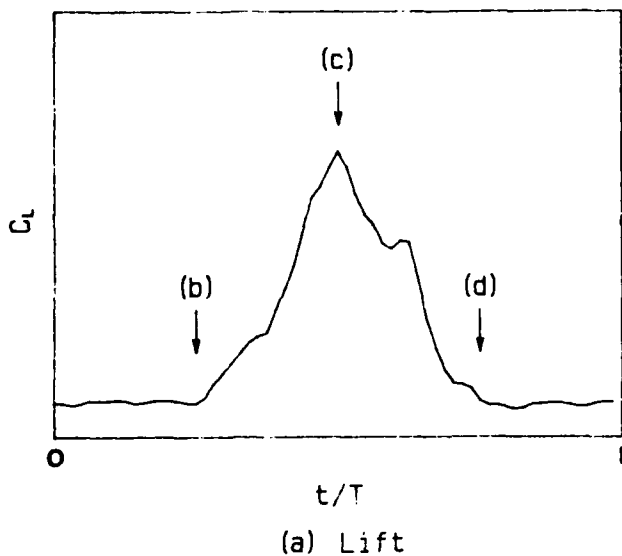
b) t/T=0.25

c) t/T=0.50

d) t/T=0.75

Fig. 4   Flow visualization of NACA 0012 airfoil at T=2 sec and α=12°.
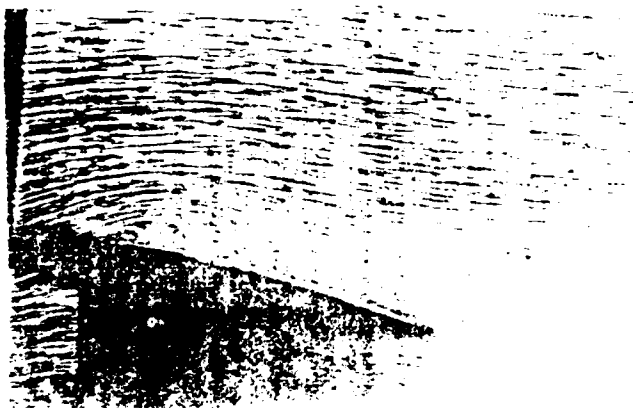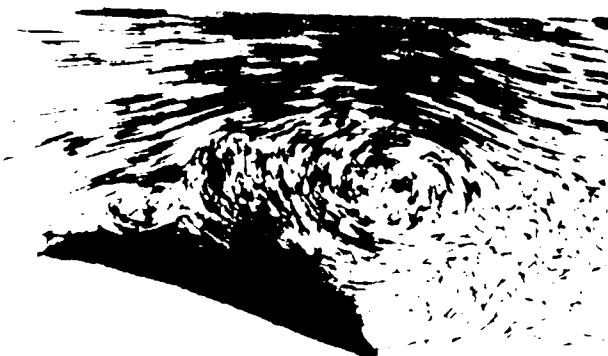
a) noncontrolled
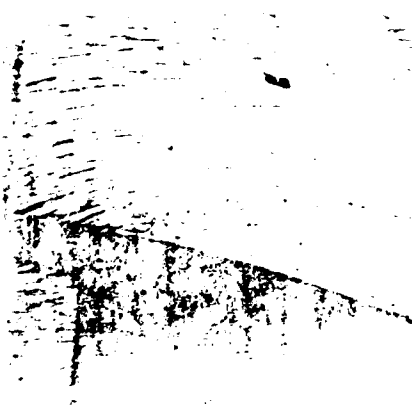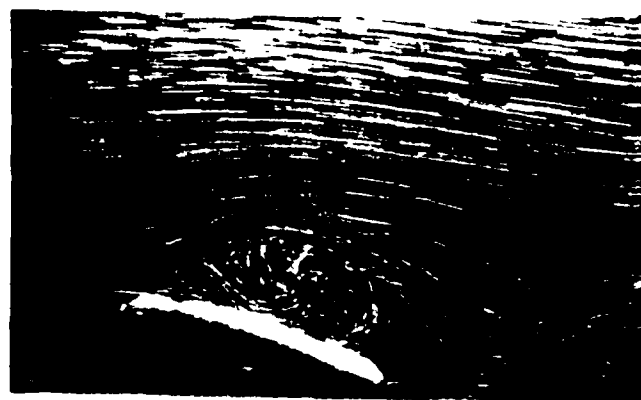
b) with flap control

Fig. 5   Flow visualization of NACA 0012 airfoil at T=6 sec
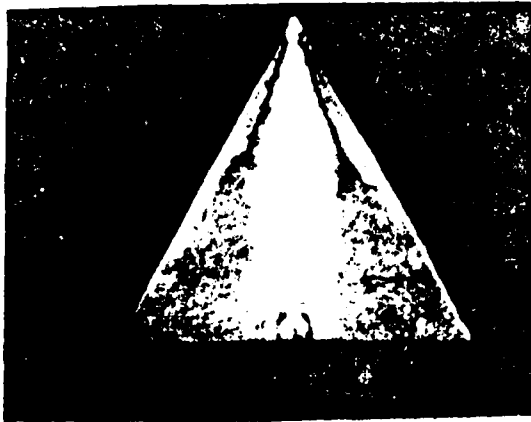
a) acceleration
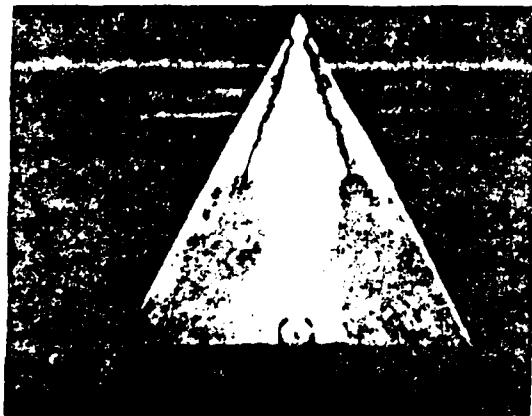
b) deceleration

Fig. 6   Flow visualization of delta wing with
         AR=2, α=30° and T=1 sec.
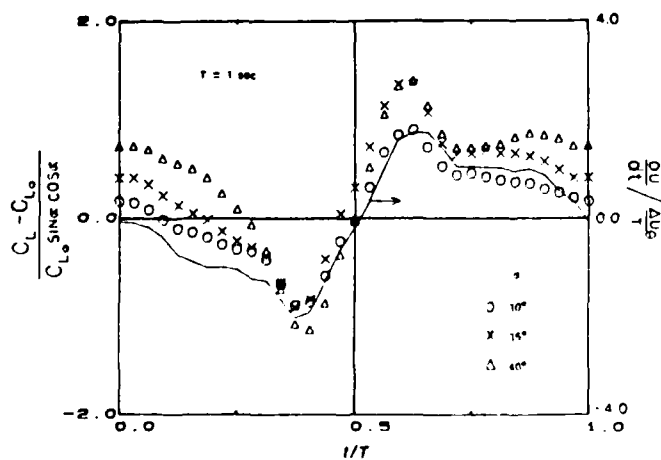
Fig. 7   comparison between unsteady lift of
         delta wing and freestream acceleration
         for T=1 sec at α=30°.

OSCILLATING AIRFOILS - ACHIEVEMENTS AND CONJECTURES[†]

by
Tuncer Cebeci
Aerodynamics Research and Technology
Douglas Aircraft Company, Long Beach, CA

Abstract

Recent developments and applications of an inter-active boundary-layer procedure for unsteady flows are reviewed. The emphasis is on a model problem corresponding to an oscillating thin airfoil in laminar flows and results are reported for differ-ent amplitudes and frequencies of oscillation. The use of the characteristic box scheme, with its sta-bility criterion, are shown to allow the accurate calculation of reverse flows and the interaction procedure removes the singularity to allow calcula-tion through regions of separated flow. Although the current focus of the interactive boundary-layer procedure has been on the leading-edge region, it has general applicability and, together with models for transition and turbulent flows, it can provide the basis for a method to deal with oscillating airfoils and wings and the rapid movement of fixed-wing arrangements at angles of attack up to and beyond those of dynamic stall.

Calculations at high angles of attack indicate that the behavior of the unsteady separated leading-edge flow has similarities to steady flows downstream of surface corrugations. The use of linear stability theory in the latter case shows that the location of the onset of transition moves upstream with severity of corrugation and can move inside the separation bubble. In practice this means that the bubbles will be shortened and analogy with unsteady flows suggests that transition may play an important role and preclude the existence of the long separa-tion bubbles determined by the laminar-flow calculations.

1.0 Introduction

The experimental investigations of McCroskey, McAlister and Carr[1], Carr, McAlister and McCroskey[2], Dadone[3], Francis, Keese and Retille[4], Daley and Jumper[5], Francis and Keese[6], Lorber and Covert[7] and Lorber and Carta[8] were prompted by the need to pro-vide better understanding of the flow characterist-ics of oscillating airfoils. It is important, for example, that the rotor blades of helicopters do not experience dynamic stall and the experiments have demonstrated that stall is preceded by a near-surface vortex associated with separation of the unsteady boundary layer. It is likely that the vor-tex stems from a laminar separation bubble which, with increasing angle of attack, grows until it be-comes unstable and bursts to form a vortex which rolls and grows. These experiments have been comp-lemented by a number of computational investigations which involve the solution of the Navier-Stokes equations[9], and of the boundary-layer equations sometimes coupled to inviscid flow equations as, for example, by Cebeci and Carr[10-12]. As yet, calculation methods have not been successful in representing the measurements and a procedure to provide accurate representation of oscillating air-foil flows for a wide range of flow conditions in-cluding dynamic stall remains to be developed. A useful review covering all aspects of the subject has been provided by Lang[13] and important appli-cations considered by Herbst[14].

The calculation of flow over an oscillating airfoil by an interactive boundary-layer scheme makes use of inviscid and viscous flow methods and couples them by a special procedure. The success and accu-racy of this method depends on the accuracy of each component including the procedure used to link the inviscid and viscous flow methods. In general the inviscid flow methods are based on panel methods, such as those of Geissler[15], Maskew and Dvorak[16] and Teng[17], and their accuracy and ability to solve flow problems of great complexity are well known. The viscous-flow methods, on the other hand, are not so well developed and their application to time-dependent flows has not received the same interest as to steady flows. The calculation of unsteady flows with large regions of flow reversal has been confined mostly to model problems involving flows such as the laminar flow over a circular cylinder impulsively started from rest. The emphasis has been on the solution of the boundary-layer equations for a prescribed pressure distribution and explora-tion of the relationship between flow singularity and separation. In spite of the apparent simplicity of this model problem, many difficulties were en-countered and some remain to be solved.

The calculation of boundary layers on an oscillating airfoil poses some problems that are different than those considered in other unsteady boundary-layer flows. Perhaps the most important of these is the calculation of the upstream boundary conditions in the (t,y) plane at some $x = x_0$ which are needed in the solution procedure. Contrary to steady flows where the streamwise velocity u is identically zero across the shear layer at the stagnation point, this is not the case in time-dependent flows; flow reversals occur due to the movement of the stagna-tion point and cause the locus of zero u-velocity to vary with space requiring the use of a special numerical method. It should be emphasized that the problem of the upstream boundary conditions has a physical counterpart and is not solely numerical. The evolution of an unsteady flow at high angles of attack can involve the formation of a vortex in the region close to the leading edge and is associated with the onset of dynamic stall. Thus it is imper-ative that calculations of the flow in the upstream region be accurate.

The difficulties in the solution of the time-dependent boundary-layer equations depend on whether or not there is flow reversal across the boundary layer. In its absence, there are several numerical methods that can be used to solve the equations including those of Crank-Nicholson[18] and Keller[19]. In the presence of flow reversal, however, it is necessary to use a scheme like the characteristic box method which is based on the solution of time-dependent boundary-layer equations along the local streamlines as described by Keller[20] and Cebeci[21].

This scheme allows the step sizes in the time and streamwise directions to be automatically adjusted to ensure that the region of backflow, as determined by the local streamlines, does not violate a stability condition like that of Courant, Friedrichs and Lewy (CFL). Although the zig-zag scheme of Krause et al.[22] can also be used for this purpose, it can be inaccurate in regions of large flow reversal since the orientation of numerical mesh is chosen a priori, as discussed by Cebeci[21] and Cebeci, Khattab and Schimke[23].

The coupling between inviscid and viscous flow methods has attracted even less attention than the above and most work has again been directed to the development of methods for steady flows. Two coupling procedures have been proposed and that suggested by Veldman[24] offers greater flexibility than that of LeBalleur[25] and Carter[26] and has been developed for two-dimensional airfoils by Cebeci and his associates[27]. It has also been extended to three-dimensional flows, albeit with strip theory and quasi-three-dimensional approximations, including flow over swept wings[28] and leading-edge separation bubbles on thin wings[29].

The flow singularity in steady flows corresponds to the vanishing of the wall shear and the boundary-layer equations can be solved routinely with a prescribed pressure distribution up to this point; there are no questions regarding the accuracy of the solutions. The u-velocity does not exhibit flow reversals across the layer and the inaccuracies resulting from the rapid variation of flow conditions near the separation location can be accounted for by taking small steps in the streamwise direction. It is also known that with interaction, that is computing the external velocity as part of the solution, this singularity can be removed and separated flows can be calculated for both laminar and turbulent flows. Time-dependent flows follow a similar pattern and concentration on the "proper" definition of flow singularity or separation, ensures that any singularity can be removed by interaction. This requires that the singularity is identified and that the region of reverse flow, which usually precedes the singularity at separation of an unsteady flow, be calculated accurately. Inaccuracy in the calculation of the reverse flows can lead to breakdown of the solution procedure and the erroneous assumption that it is caused by a singularity. An interactive boundary-layer method may not remedy this situation since its success depends on the accuracy of the solutions of the boundary-layer equations. We shall discuss this point further in this paper.

2.0 Model Problem

This paper reviews some of the results which have been obtained with a numerical procedure designed to overcome the problems outlined above. Thus, with support from the Air Force Office of Scientific Research, AFOSR, we have addressed fundamental aspects of the problem including the determination of upstream boundary conditions, the relationship between singularity and separation, and the development of an interactive procedure. To overcome the corresponding difficulties, we have developed a novel method to deal with the leading-edge region (Section 3.1), an accurate numerical method for the region of reverse flow (Section 3.2) and an interactive procedure which, together with a numerical

stability requirement, have allowed us to study the nature of the singularity and to provide fundamental understanding of the mechanisms of the region of recirculating flow near to the leading edge of an oscillating airfoil (Section 3.3). We have also made use of the linear stability theory and analogy between unsteady flow at high angle of attack and steady flow over a surface with corrugation to conjecture that long separation bubbles obtained for laminar flows may not exist in practice. It appears likely that transition will occur within these bubbles with consequent reduction in their length. This is discussed in Section 4.

To accomplish these objectives, we have considered the model problem of laminar flow over a thin airfoil with a thickness ratio of γ ($\equiv b/a$) at a reduced angle of attack ξ_0. The external velocity for a steady flow in this case can be deduced from inviscid flow to be

$$\bar{u}_e(\xi) = \frac{u_e}{u_\infty(1 + \gamma)} = \frac{\xi + \xi_0}{\sqrt{1 + \xi^2}} \qquad (1)$$

where the parameter ξ is related to the surface distance s by

$$s = a\gamma^2 \int_{\xi_0}^{\xi} (1 + \xi^2)^{1/2} d\xi \qquad (2)$$

Equation (2) is extended to unsteady flows by introducing time dependence in the form

$$\bar{u}_e(\xi,t) = \frac{\xi + \xi_{eff}}{\sqrt{(1 + \xi^2)}} \qquad (3)$$

where

$$\xi_{eff} = \xi_0(1 + A \sin\omega t)$$

The resulting flow contains the essential ingredients of the leading-edge region of an oscillating airfoil including the moving stagnation point with consequent reverse flows, the possibility of boundary-layer separation and reattachment and their dependence upon the amplitude of oscillation, A, the frequency ω and distance from the leading edge, s. It also permits comparison with the equivalent steady flows for which calculations have been reported by, for example, Cebeci, Stewartson and Williams[30].

The coupling between the inviscid and viscous flows is accomplished by writing the edge boundary condition in the boundary-layer equations as the sum of the inviscid velocity $u_e^0(\xi,t)$ and a perturbation velocity $\delta u_e(\xi,t)$, that is,

$$\text{at } y = \delta \quad u_e(\xi,t) = u_e^0(\xi,t) + \delta u_e(\xi,t) \qquad (4)$$

and $\delta u_e(\xi,t)$ is obtained from the Hilbert integral given by

$$\delta u_e(\xi,t) = \frac{1}{\pi} \int_{s_a}^{s_b} \frac{d}{ds} (u_e\delta^*) \frac{d\sigma}{s - \sigma} \qquad (5)$$

with the interaction region confined between s_a and s_b and with $u_e^0(\xi,t)$ given by Eq. (3). Further details can be found in Ref. 30.

The emphasis of the present work has been on the leading-edge region and makes use of an expression for the freestream boundary condition which has been obtained by solution of the inviscid-flow equations. The interactive boundary-layer method is, however, general so that it can involve any solutions to inviscid-flow equations and an entire airfoil with laminar, transitional and turbulent flow.

3.0 Achievements

The following three subsections highlight results obtained, respectively, with the special procedure to deal with the stagnation point, to show the importance of numerical accuracy in regions of reverse flow and to report and discuss the effects of unsteadiness on recirculation bubbles.

3.1 Moving Stagnation-Point Problem

The numerical difficulties associated with the moving stagnation point exist in a number of flows including those associated with turbomachinery, as discussed by Cebeci, Simoneau and Platzer[31]. Thus the wakes generated by moving rotor blades lead to movement of the stagnation points on the downstream of stator blades. An accurate numerical scheme has been developed to solve this problem and, as described by Cebeci et al.[31], makes use of the characteristic box scheme in an iterative manner to deal with the flow reversals.

Figures 1 and 2 show calculated results for the model problem with two circular frequencies, $\omega = \pi/30$, $\pi/3$, and $\xi_0 = 1$, $A = -0.5$. They allow examination of the effect of frequency on the calculated velocity profiles in the vicinity of the stagnation point. Figure 1 shows that the locus of the u-velocity on time lines $t = \pi/2$ and π is essentially the same as in the steady case and as a result there are no flow reversals in the velocity profiles. However, as can be seen from Figure 2, flow reversals begin to occur around the stagnation point with increase in the frequency to $\pi/3$ and become more prolonged as time increases to $\omega t = 3\pi/2$. At $\omega t = 2\pi$, the region of flow reversal is reduced but is not zero as it was at $\omega t = 0$.

3.2 Large Flow Reversals and the Need for Numerical Accuracy

Our calculations for the model problem were arranged to parallel those reported by Cebeci[21] for the flow
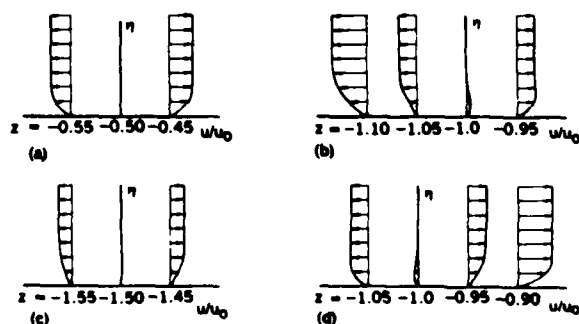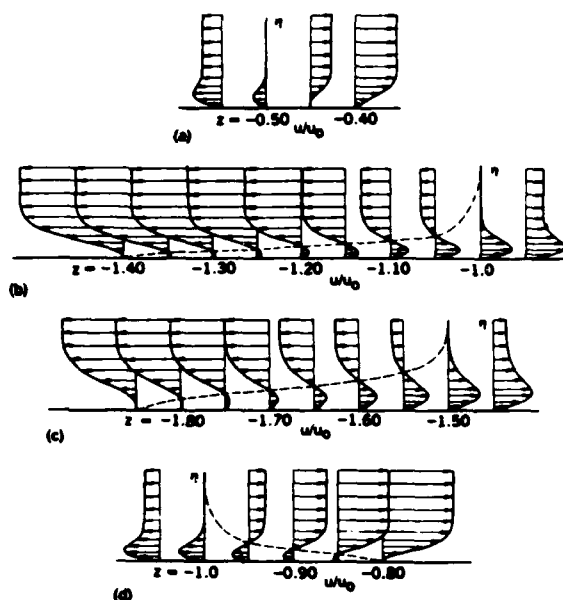

Fig. 2. Variation of the velocity profiles for $\omega = \pi/3$ near the stagnation region for different values of ωt, (a) 90, (b) 180, (c) 270, (d) 360. The dashed line indicates the locus of zero u-velocity.

over a circular cylinder. Thus the zig-zag and the characteristic box schemes were used with time and distance steps chosen arbitrarily and the calculations repeated with values in agreement with a stability criterion. The results of Fig. 3 for $\omega = 0.10$ were obtained with the zig-zag box scheme by Cebeci, Khattab and Schimke[32] for a $\Delta\xi$-spacing specified such that $\Delta\xi_1 = 0.01$ up to $\xi = 1.7$, $\Delta\xi_1 = 0.005$ for $1.7 < \xi < 4$ and $\Delta\xi_1 = 0.01$ for $4 < \xi < 8$; the time steps Δt_n were 10 degrees for $0 < \omega t < 260°$, 5 degrees for $260° < \omega t < 295°$, and 1.25 degrees for $295° < \omega t < 360°$. The calculations broke down at $\omega t = 310°$, suggesting flow separation at this location.

Fig. 3 shows that the variation of the dimensionless displacement thickness δ^* is generally smooth except in the neighborhood of $\xi = 2.12$ and for $\omega t = 308.75°$. Here R is Reynolds number based on nose radius and is defined by $(2au_\infty/\nu)$. The first sign of irregularity is the steepening of the slope of δ^* when $\omega t = 300°$ and a local maximum of δ^* occurs at $\xi = 2.12$ when $\omega t = 308.75°$. When the same results were plotted for a displacement velocity, $(d/d\xi)(u_e\delta^*)$, we observed steepening of the displacement velocity as the peak move from $\xi = 2.125$ to 2.08 with ωt changing from 300 to 308.75 degrees.

The calculations which led to Fig. 3 were repeated with the characteristic box scheme using the same coarse variations of Δt_n and $\Delta\xi_1$ and the results were identical to those obtained with the zig-zag scheme up to $\omega t = 280°$. At $\omega t = 282.5°$, the solutions of the zig-zag scheme were smooth and free of wiggles but those of the characteristic box scheme exhibited oscillations in f_w'' which led to their breakdown. The solutions with the zig-zag scheme, however, continued without numerical difficulties until $\omega t = 310°$, where oscillations appeared and led to the breakdown of the solutions at the next time step.

Fig. 1. Variation of the velocity profiles for $\omega = \pi/30$ near the stagnation region for different values of ωt, (a) 90, (b) 180, (c) 270, (d) 360.
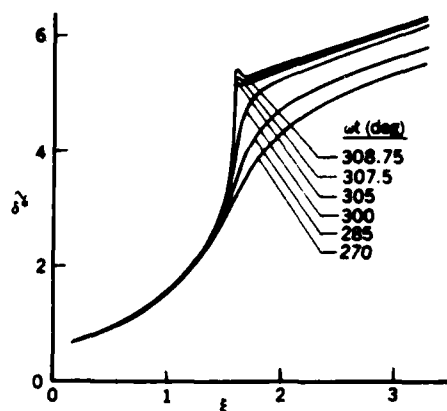
Fig. 3. Variation of: displacement thickness, $\tilde{\delta}^*$ with ξ for the oscillating airfoil, $A = 1$, $\omega = 0.1$, obtained with the zig-zag scheme.

The characteristic box was used subsequently with values of $\Delta\xi_i$ fixed as before and with values of Δt_n determined in accord with the stability requirement as discussed by Cebeci et al.[23]. This procedure avoided the breakdown of the solutions and, as can be seen from Fig. 4, the maximum value of the stability parameter β increases considerably with ωt so that the solutions required correspondingly smaller values of the time step. It is interesting to note that the wall-shear distributions of Fig. 5 are uninfluenced by the mesh at $\omega t = 280°$ and $310°$ but, for $\omega t > 310°$, the coarse mesh leads to large values of β and breakdown of the solutions.

Figure 6a shows the distributions of displacement thickness for values of ωt from 260° up to 360° and completes the cycle. The results up to 300° were identical with those of Fig. 3 with rapid increase of the displacement thickness corresponding to the increasing extent of flow reversal, as shown by the wall-shear distributions of Fig. 6b.

It can also be seen from this figure that the maximum displacement thickness and minimum wall shear move upstream with increasing ωt for values of
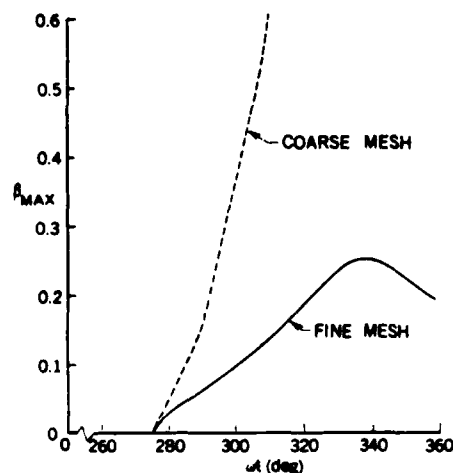
Fig. 4. Effect of the coarse and fine meshes on the variation of the stability parameter β with ωt.

(a)   (b)
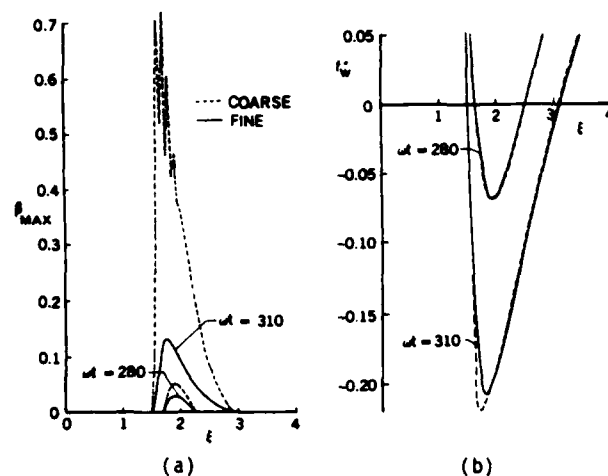
Fig. 5. Effect of the coarse and fine meshes on the variation of the (a) stability parameter β, and (b) wall shear f_w'' with ξ.

(a)   (b)
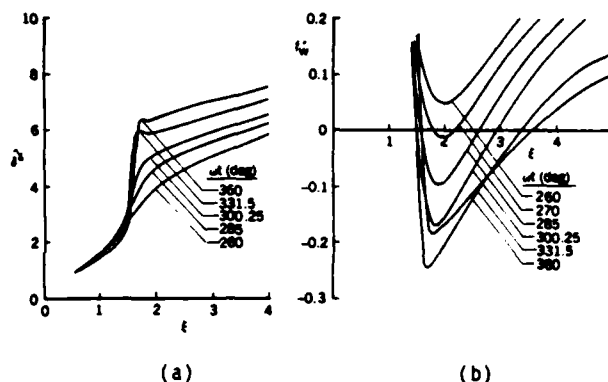
Fig. 6. Results obtained with the characteristic box scheme for $\omega = 0.1$. Variation of (a) displacement thickness $\tilde{\delta}^*$ and (b) wall shear f_w'' with ξ.

ωt up to 324.5°; this feature was also observed in the calculations performed for the circular cylinder[21]. The results obtained with the zig-zag scheme and values of Δt_n determined by the characteristic scheme for the oscillating airfoil were identical to those discussed above, and similar correspondence was obtained with the calculations performed for the circular cylinder.

3.3 Effects of Unsteadiness and Interaction on Separated Flows

Figure 7 shows distributions of wall shear for frequencies $\omega = 0.01$ and 0.001. As expected, the critical value of the reduced angle which corresponds to separation, is smaller than that for the higher frequency of Section 3.2 and closer to that of the steady state, $\xi = 1.16$. For $\omega = 0.01$, the breakdown of the solutions occurs at $\omega t = 226°$, which corresponds to an effective reduced angle of $\xi_{eff} = 1.360$; for $\omega = 0.001$, the corresponding values are $\omega t = 204°$ and 1.203. We also note from Figs. 7a and 7b that the flow is a little unsteady even at these frequencies, and the solutions do not break down with the appearance of flow reversal,

140
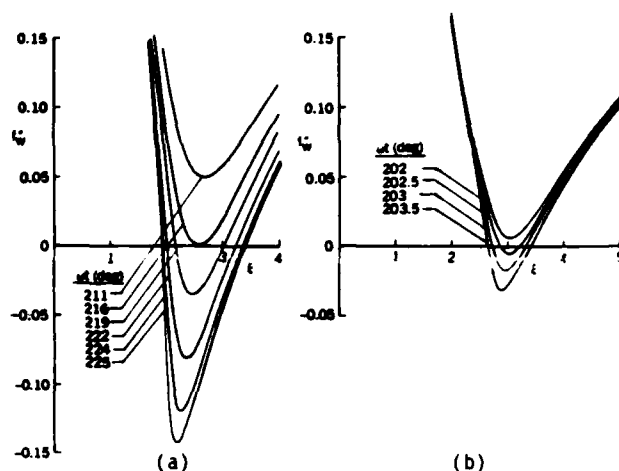
Fig. 7. Variation of wall shear f_w'' with ξ for (a) $\omega = 0.01$, (b) $\omega = 0.001$.

which increases in extent as ω changes from 0.001 and 0.01.

The above results, and those of the previous subsection, were obtained without interaction between the solutions of inviscid-flow and boundary-layer equations. In contrast, the results of Fig. 8 were obtained with interaction and were performed in the following way. For all values of time with ωt ranging from 0° to 360°, the standard method and the leading-edge region procedure discussed in Section 3.1 were used to generate upstream boundary conditions at a short distance from the leading edge, $\xi = 0.5$. With these conditions and for each value of ωt, the inverse method was used to calculate the unsteady flow from $\xi = 0.5$ to 10, for the specified value of Reynolds number and thickness ratio of $\gamma = 0.1$. Since the system of equations is now elliptic, sweeps in the ξ-direction were necessary to achieve a converged solution; around three sweeps were required where flow reversal was encountered and a single sweep sufficed where it did not. It is to be expected that the value of R will influence the number of sweeps and, since it is linked to physical parameters, will affect the singularity and the size of the bubble.
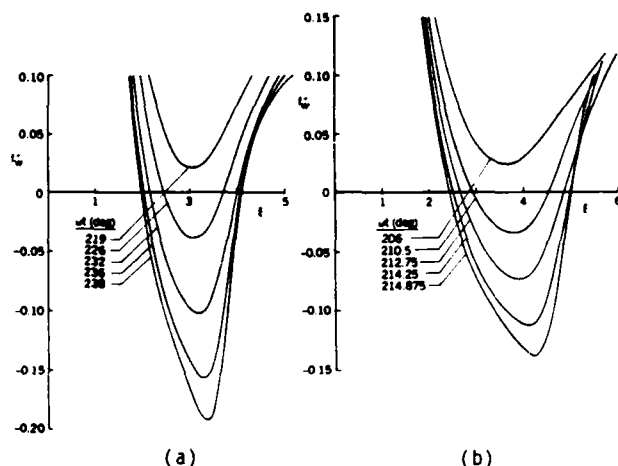

Fig. 8. Effect of interaction on the variation of wall shear f_w'' with ξ for (a) $\omega = 0.01$, (b) $\omega = 0.001$. $R = 10^4$.

Figure 8 shows the results for $\omega = 0.01$ and 0.001 with $R = 10^4$. They are nearly the same as those obtained by the standard method as shown in Fig. 7 prior to flow reversal where the influence of the Reynolds number is small and increase after flow reversal. In the case of $\omega = 0.001$, for example, the standard method predicts flow reversal around $\xi_{eff} = 1.19$ (see Fig. 7) and with interaction (Fig. 8) this effective angle is between 1.219 and 1.254. The maximum negative value of the wall-shear parameter f_w obtained with the standard method is around -0.03 at $\xi_{eff} = 1.199$ and may be compared with the maximum value of f_w'' of -0.14 at $\xi_{eff} = 1.286$ obtained with interaction. As expected, the interaction allows the calculations to be performed at higher angles of attack than those achieved with the standard method. For $\omega = 0.001$, the maximum α_{eff} for which calculations can be performed with the standard method is 1.199 with breakdown occurring at $\xi_{eff} = 1.209$; the corresponding values with interaction are 1.286 and 1.287. Comparison of wall-shear results with both procedures and $\omega = 0.001$ indicates that the extent of the recirculation region $\Delta\xi$ is around 0.5 for the standard case, and around 2.5 for the interactive case. The solutions do not have a singularity in the former case but do contain flow reversals and this suggests that time-dependent flows can be calculated without using an inverse procedure. As the angle of attack exceeds $\xi_{eff} = 1.199$ for $\omega = 0.001$, a singularity develops and requires an inverse procedure as in two-dimensional steady flows. This procedure allows the calculation of larger regions of reverse flow where the flow is now separated.

We see a similar picture with the greater unsteadiness corresponding to $\omega = 0.01$, for which the standard method allows calculations up to an effective angle of attack of 1.354 (Fig. 7a), a value considerably higher than 1.199 obtained at $\omega = 0.001$. The first flow reversal occurs shortly after $\xi_{eff} = 1.294$ and breakdown occurs at $\xi_{eff} = 1.360$ with maximum negative wall shear values of -0.14 at $\xi_{eff} = 1.354$ and -0.035 at $\xi_{eff} = 1.315$. The extent of the maximum reverse-flow region is now 1.5, considerably larger than for $\omega = 0.001$, and indicates that the more unsteady nature of the flow produces a bigger region of reverse flow free from singularities. For this value of ω, the interactive scheme increases the value of ξ_{eff} for which solutions can be obtained to 1.424 with breakdown occurring shortly after this value at 1.428 (see Fig. 8b). The first flow reversal occurs after $\xi_{eff} = 1.315$ with maximum negative wall shear equal to -0.19 at $\xi_{eff} = 1.424$, and the extent of the recirculation region has now increased by about 30%. Comparison of maximum wall shear values, f_w'', at a similar value of ξ_{eff} indicates that those computed with the interactive scheme are lower than those with the standard scheme so that, for example, the interactive scheme gives $(f_w'')_{max} = -0.04$ at $\xi_{eff} = 1.36$ compared to -0.14 at $\xi_{eff} = 1.354$ with the standard method (Fig. 7a).

Since the calculations began at $\omega t = 0$ with solutions obtained by solving steady-state equations, it was necessary to confirm the extent of their influence. As a consequence, calculations were performed for a second cycle and gave results at $\omega t = 720°$ which were identical to those at $\omega t = 360°$, confirming that the flow is cyclic. Examination of the results showed that the influence of the initial conditions die out rapidly and have no influence on the solutions presented here.

The results obtained with $\omega = 0.001$ can usefully be compared with the steady-state results of Cebeci et al.[30] shown in Fig. 9. We might expect that the small unsteadiness associated with this frequency will lead to results very similar to those of steady state. Inspection of Figs. 7b and 9 shows that although this is correct in general terms, the answers are quantitatively different. As can be seen, the maximum effective angle at which solutions can be obtained is greater in the unsteady case by some 1%. There are differences in the two calculation procedures but it is unlikely that they are responsible for this difference. On the other hand, it is possible that the difference in the negative wall shear values may have been influenced by the use of the FLARE approximation in the steady-state solutions. Nevertheless, the unsteady nature of the flow with $\omega = 0.001$ is clear, in spite of this very low reduced frequency.
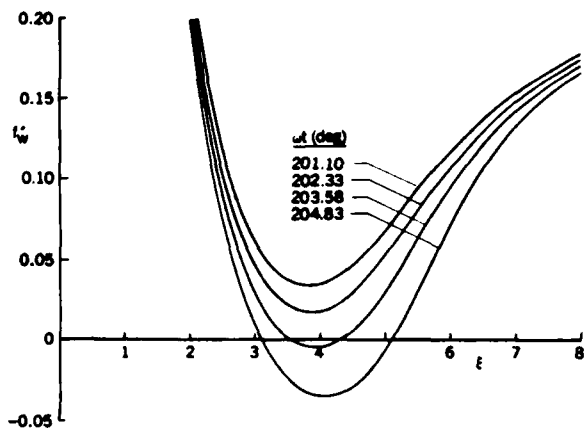

Fig. 9.   Effect of interaction on the variation of wall shear parameter f_w'' for a steady flow at $R = 10^4$.

4.0   Conjectures; Separation Bubbles and Transition

An important conclusion from the results of Section 3.3 is that the problem of the singularity, discussed in several papers including that of Cebeci et al.[32], has been overcome by the combined use of an interactive boundary-layer method and a novel numerical scheme with its stability requirements fulfilled. This combination had allowed calculations to be performed but there remains a concern about the physical realism of the long regions of reverse flow predicted in some circumstances. Experiments suggest that leading-edge regions of reverse flow tend to be small with transition to turbulent flow making difficult the existence of long bubbles. This concern is examined by Cebeci[33] in the context of steady flows. It is briefly described in the following paragraphs and the implications of the results for unsteady-flow calculations considered.

As a steady-flow counterpart of the above flows, calculations were performed for the thin airfoil as a function of angle of attack and for the same thickness ratio γ ($\equiv 0.1$) and were reported by Cebeci et al.[30] and Cebeci[33] for Reynolds numbers of 10^6 and 10^5, respectively. The corresponding distributions of f_w'' are shown on Fig. 10 and
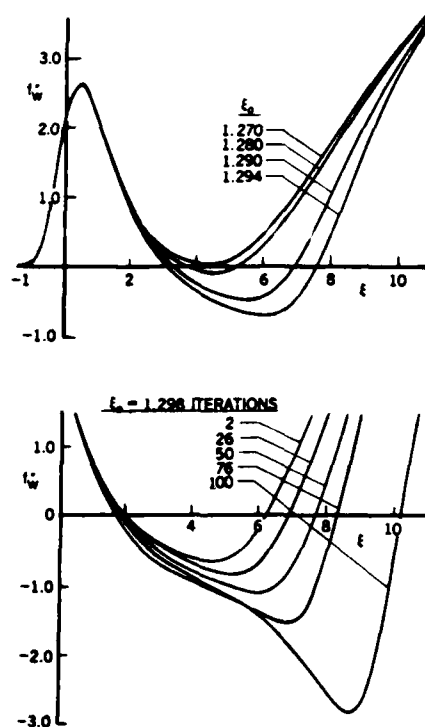
Fig. 10.   Separation bubbles and their breakdown - explanation from steady flow (i.e. $\omega = 0$), $R = 10^5$.

have the same form as those presented for the oscillating airfoil. At the highest angle, the separation bubble tends to grow with the number of numerical iterations and suggests that the bubble is unstable.

The large separation bubbles calculated for steady flow seem unrealistic and, at least for the 10^5 Reynolds number where transition is certain to occur downstream of the bubble, there is the possibility that the real flow cannot remain laminar in the region of interest and that this may affect the bubble length. There are, however, no experimental data for airfoils with which to test the possibility and recourse has been made to a different flow for which information of transition is available and which has close similarities to the leading-edge flow.

The experiments of Fage[34] were performed with a series of bumps on a plate and provide information of the location of transition downstream of a region of separated flow caused by the bump and the consequent adverse pressure gradient. Figure 11 shows the bump and a series of distributions of f_w'' calculated with the interactive procedure: more extensive results have been reported by Cebeci and Egan[35]. The shapes of the f_w'' distributions are similar in form to those of Figs. 8 and 9, downstream from the beginning of the favorable pressure gradient and lend support to the idea that conclusions based on the bump flows can be extrapolated to those on steady and unsteady thin airfoils.

The calculations which led to the results of Fig. 17 provided velocity profiles and those, in turn, were used in the e^n-method of Smith and Gamberoni[36]

142

Fig. 11. Accuracy of stability approach to transi-
tion. Steady flow over bumps, data of
Fage[34].

and of Van Ingen[37] to calculate the location of
transition shown on the figure. This method solves
the Orr-Sommerfeld equation for given velocity pro-
files and computes the amplification rates to deter-
mine the location of the onset of transition. As
can be seen from Fig. 11, the calculated values of
the location of transition agree well with measured
values and indicate a clear trend for transition to
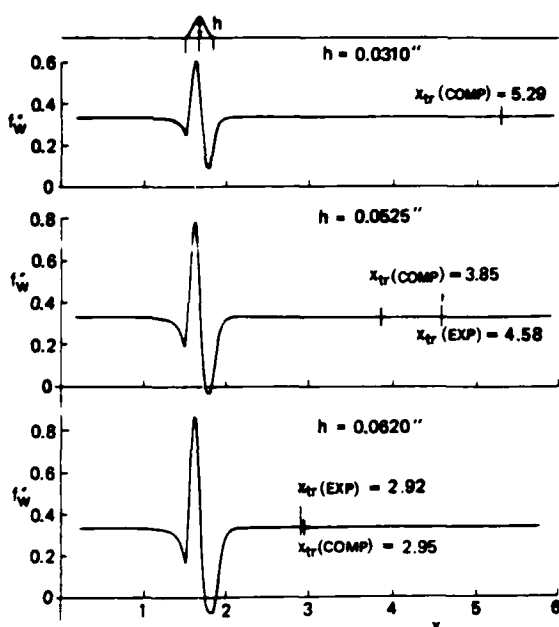move upstream with increase in the height of the
bump and, therefore, with the strength of the ad-
verse pressure gradient and length of the region of
separation. In the case of the largest bump shown,
the transition location is inside the bubble and,
if the interactive boundary-layer calculations were
to be repeated with transition specified at this
location, the bubble would be correspondingly
reduced in length.

It can be conjectured that the separation bubble
would be further shortened as the adverse pressure
gradient is increased in strength and transition
moves further upstream. This result can be extrap-
olated to the steady thin-airfoil flows discussed
above and their unsteady counterpart. Thus, it
seems likely that the long separation bubbles calc-
ulated above are unrealistic and in practice would
be shortened by transition from laminar to turbulent
flow.

5.0 Concluding Remarks

A series of contributions have been made to the
understanding of the flow characteristics of the
leading-edge region of an oscillating airfoil. They
required the development and use of a calculation
method which involves the accurate solution of time-
dependent boundary-layer equations and their inter-
action with solutions to inviscid-flow equations.
The need for accurate calculations of regions of
reverse flow, including those associated with the
moving stagnation point, demanded the use of the
characteristic box scheme and the fulfillment of an

associated stability requirement. Although those
formulated investigations have been made in relation
to the model problem of laminar flow in the leading-
edge region of a thin airfoil, the calculation
method is general and can readily be extended to
permit the calculation of the flow around an oscil-
lating airfoil.

Among the specific conclusions which can be drawn
are the following:

1. The accuracy of the results obtained from the
solution of the boundary-layer equations has been
examined with emphasis on regions of flow reversal
and separation where the characteristic box scheme
is used. Attempts to improve accuracy by ad hoc
changes to the finite-difference mesh failed and
revealed the need for a procedure which would auto-
matically guarantee accuracy by the selection of an
appropriate mesh. This was achieved through a sta-
bility criterion, similar to that of Courant,
Friedrichs and Lewy[38]. The combination of this
requirement and the characteristic box scheme led
to accurate solutions and showed that the mesh
requirements were extremely severe in the region of
large flow reversals.

2. Calculations performed for a range of reduced
frequencies from 0 to 0.1 show that increased un-
steadiness allows results to be obtained at higher
angles of attack before the solutions break down and
that, in the case of the highest frequency, there
was no breakdown. The calculations with the stand-
ard method led to regions of flow reversal which
were limited in their extent by the singularity
except at the highest frequency. The interactive
procedure removed this singularity and resulted in
larger regions of flow reversal which involved sep-
aration at higher angles of attack.

3. The unsteady nature of the flow at the highest
frequency allowed the calculation of large regions
of flow reversal and it is expected that yet higher
frequencies will lead to even larger regions of flow
reversal. This in turn will permit calculations to
be performed at larger angles of attack where the
occurrence of the singularity will require the use
of the interactive procedure. The gains in angles
of attack are again likely to be limited by the
ability of the laminar flow to sustain separation
bubbles and results obtained from the application
of linear stability theory suggest that the location
of the onset of transition moves upstream with in-
creasing angle of attack and extent of the separa-
tion bubble so that it can occur within the bubble.
In practice, this would lead to the curtailment of
the region of separated flow and the development of
a turbulent boundary layer. Support for the accu-
racy of the calculations of the onset of transition
is afforded by comparison of calculated results with
measurements in the steady flow over bumps which
give rise to distributions of the wall-shear param-
eter similar to those of airfoil flows.

The research which led to the preceding conclusion
is fundamental in nature but has practical implica-
tions which should be emphasized. The calculation
method has been applied to a model problem and shown
to be able to represent unsteady laminar flows with
regions of flow reversal and separation. It can
equally be applied to calculate the flow over
complete airfoils subjected to cyclic or other
time-dependent boundary conditions. The additional
features to allow these extensions already exist so

143

that, for example, turbulence models have been embodied in a steady-state version of the method and have been shown to represent boundary-layer and wake flows with accuracy close to that of the test measurements; steady-state calculations of transitional flows, including those with flow separation, have been examined and shown to be calculable; and a foundation has been laid for the calculation of flows around components of aircraft. With this catalogue of achievements, it is recommended that work be carried out to develop the method further and to apply it to problems including those associated with helicopter blades and the maneuverability of aircraft such as the X-31 so that the merits of different designs can be assessed. It is particularly appropriate that it be used to study flows associated with angles of attack close to those of static and dynamic stall.

6.0 References

1. McCroskey, W.J., McAlister, K.W., and Carr, L.W., "Dynamic Stall Experiments on Oscillating Airfoils," AIAA Journal, Vol. 14, Jan. 1976, pp. 57-63.

2. Carr, L.W., McAlister, K.W. and McCroskey, W.J., "Analysis of the Development of Dynamic Stall Based on Oscillating Airfoil Experiments," NASA TN D-8382, 1977.

3. Dadone, L.U., "Two-Dimensional Wind Tunnel Test of an Oscillating Rotor Airfoil," NASA CR-2914, Dec. 1977.

4. Francis, M.S., Keese, J.E. and Retelle, J.P., Jr., "An Investigation of Airfoil Dynamic Stall with Large Amplitude Motions," FJSRL-TR-83-0010, F.J. Seiler Research Labs, Air Force Academy, Colorado Springs, 1983.

5. Daley, D.C. and Jumper, E.J., "Experimental Investigation of Dynamic Stall for a Pitching Airfoil," Journal of Aircraft, Vol. 21, Oct. 1984, pp. 831-832.

6. Francis, M.S. and Keese, J.E., "Airfoil Dynamic Stall Performance with Large Amplitude Motions," AIAA Journal, Vol. 23, Nov. 1985, pp. 1653-1659.

7. Lorber, P.F. and Covert, E.E., "Unsteady Airfoil Boundary Layers - Experiment and Computation," in Numerical and Physical Aspects of Aerodynamic Flows III (T. Cebeci ed.), Springer-Verlag, N.Y., 1986, pp. 235-251.

8. Lorber, P.F. and Carta, F.O., "Unsteady Stall Penetration Experiments at High Reynolds Number," United Technologies Research Center Report R87-956939-3, Apr. 1987 (to be released as a technical report by the U.S. Air Force Office of Scientific Research).

9. Shamroth, S.J., "A Turbulent-Flow Navier-Stokes Analysis for an Airfoil Oscillating in Pitch," in Unsteady Turbulent Shear Flows (R. Michel, J. Cousteix and R. Houdeville, eds.), Springer-Verlag, 1981, pp. 185-196.

10. Cebeci, T. and Carr L.W., "Prediction of Boundary-Layer Characteristics of an Oscillating Airfoil," in Unsteady Turbulent Shear Flows (R. Michel, J. Cousteix and R. Houdeville, eds.), Springer-Verlag, 1981, pp. 145-158.

11. Cebeci, T. and Carr, L.W., "Calculation of Boundary Layers Near the Stagnation Point of an Oscillating Airfoil," NASA TM 84305, 1983.

12. Cebeci, T. and Carr, L.W., "An Interactive Boundary-Layer Method for Oscillating Airfoils: Status and Prognosis," NASA Report in preparation.

13. Lang J.D. "Unsteady Aerodynamics and Dynamic Aircraft Maneuverability," AGARD CP-386, Unsteady Aerodynamics - Fundamentals and Application to Aircraft Dynamics, Nov. 1985.

14. Herbst, W.B., "Supermaneuverability," Proceedings of the AFOSR-FJSRL-University of Colorado Workshop on Unsteady Separated Flows, U.S. Air Force Academy, Colorado Springs, Aug. 1983.

15. Geissler, W., "Unsteady Boundary-Layer Separation on Airfoils Performing Large Amplitude Oscillations - Dynamic Stall," AGARD Symposium on Unsteady Aerodynamics, Fundamentals and Applications to Aircraft Dynamics, Gottingen, Germany, 1985.

16. Maskew, B. and Dvorak, F.A., "Prediction of Dynamic Separation Characteristics Using a Time-Stepping Viscid/Inviscid Approach," in Numerical and Physical Aspects of Aerodynamic Flows III (T. Cebeci, ed.) Springer-Verlag, N.Y., 1986, pp. 380-396.

17. Teng, N.G., "The Development of a Computer Code (U2DIIF) for the Numerical Solution of Unsteady, Inviscid and Incompressible Flow Over an Airfoil," M.S. Thesis, Department of Aeronautics, Naval Postgraduate School, Monterey, CA, 1987.

18. Crank, J. and Nicolson, P., "A Practical Method of Numerical Evaluation of Solutions of Partial-Differential Equations of the Heat-Conduction Type," Proceedings of Cambridge Philosophical Society, Vol. 43, 1947, p. 50.

19. Keller, H.B., "Accurate Difference Methods for Two-Point Boundary-Value Problems," SIAM Journal of Numerical Analysis, Vol. 11, 1974, pp. 305-320.

20. Keller, H.B., "Numerical Methods in Boundary-Layer Theory," Annual Review of Fluid Mechanics, Vol. 10, 1978, pp. 417-433.

21. Cebeci, T., "Unsteady Boundary Layers with an Intelligent Numerical Scheme," Journal of Fluid Mechanics, Vol. 163, 1986, p. 129.

22. Krause, E., Hirschel, E.H. and Bothman, Th., "Die Numerische Integration der Bewegungs-gleichungen Dreidimensionaler Laminarer Kompressibler Grenzschichten," Bond 3, Fachtagung Aerodynamic, Berlin; D6LR-Fachlinchreike, 1968.

23. Cebeci, T., Khattab, A.A. and Schimke, S.M., "Separation and Reattachment Near the Leading Edge of a Thin Oscillating Airfoil," to be published in Journal of Fluid Mechanics, 1988.

24. Veldman, A.E.P., "New Quasi-Simultaneous Method to Calculate Interacting Boundary Layers," AIAA Journal, Vol. 19, 1981, p. 769.

25. LeBalleur, J.C., "Couplage visqueux-nonvisquex: Methode Numerique et Applications Aux Ecoulements Bidimensionnels Transoniques et Supersoniques," Le Recherche Aerospatiale No. 1978-2, 1978, p. 65.

26. Carter, J.E., "A New Boundary-Layer Inviscid Interaction Technique for Separated Flow," AIAA Paper 79-1450, 1979.

27. Cebeci, T., Clark, R.W., Chang, K.C., Halsey, N.D. and Lee, K., "Airfoils with Separation and the Resulting Wakes," Journal of Fluid Mechanics, Vol. 163, 1986, p. 323.

28. Cebeci, T., Sedlock, D., Chang, K.C. and Clark, R.W., "Applications of Two- and Three-Dimensional Interactive Boundary-Layer Theory to Finite Wings with Flow Separation," AIAA Paper No. 87-0590, 1987.

29. Cebeci, T., Kaups, K. and Khattab, A.A., "Separation and Reattachment Near the Leading Edge of a Thin Wing," IUTAM Proceedings, London, Aug. 1986.

30. Cebeci, T., Stewartson, K. and Williams, P.G., "Separation and Reattachment Near the Leading Edge of a Thin Airfoil at Incidence," AGARD CP-291, Paper 20, 1981.

31. Cebeci, T., Simoneau, R.J. and Platzer, M.F., "A General Method for Unsteady Heat Transfer on Turbine Blades," NASA CR in preparation.

32. Cebeci, T., Khattab, A.A. and Schimke, S.M., "Can the Singularity be Removed in Time-Dependent Flows?," in Workshop on Unsteady Separated Flow (M.S. Francis and M.W. Luttges, eds.), Colorado Springs, 1984.

33. Cebeci, T., "Instability of Laminar Separation Bubbles: Causes and Effects," paper in review.

34. Fage, A., "The Smallest Size of Spanwise Surface Corrugation which Affects Boundary-Layer Transition on an Airfoil," R&M No. 2120, Brit. A.R.C., 1943.

35. Cebeci, T. and Egan, D., "The Effect of Wave-Like Roughness on Transition," paper in preparation.

36. Smith, A.M.O. and Gamberoni, N., "Transition, Pressure Gradient and Stability Theory," Proc. IX Intl. Congress Applied Mechanics, Brussels, 1956.

37. Van Ingen, J.L., "A Suggested Semi-Empirical Method for the Calculation of the Boundary-Layer Transition Region," Report No. VTH71, VTH74, Delft, Holland, 1956.

38. Isaacson, E. and Keller, H.B., Analysis of Numerical Methods, John Wiley, N.Y., 1966.

EXPERIMENTAL MEASUREMENTS OF THE STRUCTURE OF A LARGE
AMPLITUDE UNSTEADY SEPARATING TURBULENT BOUNDARY LAYER

N.K. Agarwal[*] and R.L. Simpson[+]
Virginia Polytechnic Institute and State University
Blacksburg, Virginia 24061

Abstract

Hot-wire anemometer and directionally-sensitive laser anemometer measurements of $\hat{U}$, $\hat{u^2}$, $\hat{v^2}$ and $-\hat{uv}$ on a large amplitude waveform flow (amplitude to mean velocity ratio of 0.7 at a reduced frequency based on the length of the converging-diverging test channel of $k = \omega c/2\bar{U}_{ei} = 1.33$) are reported. This type of flow shows measurable unsteady effects on the turbulence structure in the presence of flow reversal, especially during phases when the washout of reversed flow occurs. During the phases that the flow is accelerating or near the maximum free-stream velocity, intermittent backflow occurs only near the wall in the diverging portion of the test channel. The turbulent boundary layer during these phases appears to behave like a normal steady attached turbulent boundary layer. During strongly decelerating and minimum free-stream velocity phases, backflow occurs in the diffuser section and even near the wall in the converging section. This appears to be due to the strong oscillatory pressure gradient that opposes the slow near-wall flow to produce backflow.

In the absence of flow reversal, as in the moderate amplitude flows, the flow is quasi-steady. During phases when the flow is detaching, it also appears to be quasi-steady. Downstream of detachment the oscillation waveform and amplitude appears to govern the flow behavior which has large hysteresis, especially during phases when detached flow is washed downstream.

1. Introduction

Unsteady turbulent boundary layers are of considerable interest because of unsteady aerodynamic phenomena associated with blades in compressors and turbines, helicopter rotors in translating motion, high pressure recovery diffusers, and aeroelastic flutter and buffet of airfoils. They are particularly important during high loading conditions when separation may be present during a portion of the oscillation cycle. Under such conditions there is significant interaction between the thick turbulent shear layer and the inviscid flow. Thus, experimental information on the structure of separating unsteady turbulent shear layers is necessary for the proper understanding and calculation of the physical behavior of these practical flows.

---

[*]Research Associate, Dept. of Aerospace and Ocean Engineering

[+]Professor, Dept. of Aerospace and Ocean Engineering

In spite of its importance, relatively little fundamental work has been done towards describing the behavior of unsteady turbulent shear flows near separation and downstream. Simpson and Shivaprasad[1] and Simpson, Shivaprasad and Chew[2] have reported the measurements showing the effect of frequency on moderate amplitude (amplitude to mean velocity ratio of 0.33) sinusoidal unsteadiness of the free-stream velocity on a separating boundary layer at reduced frequencies $k = \omega c/2\bar{U}_{ei}$ of 0.61 and 0.90, where $\bar{U}_{ei}$ is the test section entrance time-averaged free-stream velocity; $c = 4.9$ m, length of the converging-diverging test section shown in Figure 1; and $\omega = 2\pi f$, where f is 0.596 Hz, the frequency of oscillation. Agarwal and Simpson[3] have reported the measurements on a large amplitude (amplitude to mean velocity ratio of 0.8) flow at $k = 0.61$. They also presented[4] some upstream attached flow results for the $k = 1.33$ flow discussed here. It is clear from these earlier results that substantial hysteresis of the turbulence structure occurs for unsteady separating flows and the oscillation waveform and amplitude strongly affect the backflow behavior.

The unsteady flow terminology used here is the same as documented by Simpson et al.[2]. For periodic unsteady turbulent flow, the ensemble-averaged velocity $\hat{U}$ for a specific phase $2\pi t/T$ of the flow oscillation is given by

$$\hat{U} = \lim_{N \to \infty} \frac{1}{N} \sum_{n=1}^{N} U(t + nT) \qquad (1)$$

where T is the period of oscillation and N is the number of cycles that are averaged. The instantaneous velocity U can also be represented as

$$U = \bar{U} + \tilde{U} + u \qquad (2)$$

where $\bar{U}$ is the time-averaged or mean value, $\tilde{U}$ is the periodic oscillation and u is the turbulent fluctuation. $\hat{U}$ can also be written as

$$\hat{U} = \bar{U} + \tilde{U} \qquad (3)$$

The ensemble-averaged variance for the turbulent fluctuations, e.g., $\hat{u^2}$ (and $-\hat{uv}$ and $\hat{v^2}$) are given by

$$\hat{u^2} = \lim_{N \to \infty} \frac{1}{N} \sum_{n=1}^{N} (U - \hat{U})^2, \qquad (4)$$

and $\hat{u^2} = \bar{u^2} + \tilde{u^2}$. $\qquad (5)$

2. Experimental Equipment

The wind tunnel with boundary layer control, the programmable-rotating-blade damper for producing the unsteadiness, and the hot-wire and laser anemometers used in measurements have been previously discussed in Ref. 1-6 and will not be discussed here in much detail. Figure 1 is a

sideview schematic of the 8 m long, 0.91 m wide wind tunnel test section. The damper is about 8 m upstream of the test section.

All events during an oscillation cycle were synchronised with respect to a 'reference' square wave voltage signal (0.954 Hz) at the oscillation frequency that is generated by the quartz clock in the damper control electronics. A 'clock' square-wave voltage signal with a frequency of 96 times the reference signal is also generated in the control electronics to aid data acquisition. Data were acquired at the beginning of each of these 96 phase bins of an oscillation cycle. Data were ensemble-averaged over 200 cycles. In all the measurements, signals from a hot wire located at the throat (1.63 m) were recorded simultaneously to verify the phase repeatability of the free-stream velocity data.

The variation in the period of each flow cycle, or the 'jitter' follows a Gaussian distribution. Simpson et al.[2] have estimated that this jitter has no effect on ensemble-averaged velocity values and only a very small effect on turbulent fluctuation measurements near the free-stream where the turbulence is low.

3. Test Flow and Experimental Results

The ensembled-averaged free-stream velocity $\hat{U}_e$ outside the boundary layer can be expressed in terms of its Fourier component $\bar{U}_{ne}$ as

$$\hat{U}_e = \bar{U}_e \left\{ 1 + \sum_{n=1} \left[\frac{\bar{U}_{ne}}{\bar{U}_e} \cos(\omega nt - \phi_{ne}) \right] \right\}. \quad (6)$$

Figure 2 shows the mean free-stream velocity along the tunnel centerline obtained using the single wire probe. Upstream of 2.8 m the first harmonic ratio $\frac{\bar{U}_{1e}}{\bar{U}_e}$ is slightly over 0.7 while the phase ϕ_{1e} increased only by less than 3.75° (Figure 4), which corresponds to one phase bin. Second and third harmonics have amplitudes that are 15 ~ 20% and 3 ~ 7% of the mean velocity, respectively. The flow temperature was 77 ± 1° F for all measurements.

Using this streamwise distribution the free-stream streamwise pressure gradient was calculated from the mean and first ten harmonics using Euler's equation. The mean and first harmonic are given by

$$\frac{1}{\rho} \frac{d\bar{P}}{dx} = - [\bar{U}_e \bar{U}_e' + \frac{1}{2} \bar{U}_{1e} \bar{U}_{1e}'] + [(\bar{U}_e \bar{U}_{1e}' + \bar{U}_{1e} \bar{U}_e')^2$$
$$+ \bar{U}_{1e}^2 (\bar{U}_e \phi_{1e}' - \omega)^2] \cos(\omega t - \phi_{1e} - 180° - \gamma_{1e}),$$
$$(7)$$

where

$$\gamma_{1e} = \arctan \frac{\bar{U}_{1e}(\bar{U}_e \phi_{1e}' - \omega)}{\bar{U}_e \bar{U}_{1e}' + \bar{U}_{1e} \bar{U}_e'}. \quad (8)$$

Here primes denote streamwise derivatives. These derivatives are evaluated at a given streamwise location by differentiating the least-squares curve fit of a quadratic model of the five data points nearest to that location.

Figure 3 shows the non-dimensional mean, maximum and minimum pressure gradient $\frac{dC_p}{dx}$ along the centerline of the test wall. Here $C_p = 2(P - P_i)/\rho\bar{U}_{ei}^2$, where i denotes the nominal mean free-stream entrance condition. Unlike the moderate amplitude flows of Simpson et al.[1,2] in the diverging section a small favorable pressure gradient exists during the high velocity phases.

Figure 4 shows the phase angle of the first harmonics of the free-stream velocity ϕ_{1e} and the pressure gradient $\gamma_{1e} + \phi_{1e} + 180$ and shows that the first harmonic pressure gradient strongly lags the local free-stream velocity in the converging section of the tunnel upstream of 2 m. The lag is considerably lower in the diverging section. After detachment the oscillatory pressure gradient only slightly leads the velocity oscillation with the onset of pressure gradient relaxation, as observed by Simpson et al.[1,2] in moderate amplitude experiments and also in other high amplitude flow by Agarwal and Simpson.[3]

Study of the velocity and pressure gradient oscillations shows that upstream of the throat, where the maximum velocity increases as the tunnel area decreases there are some phases where an adverse pressure gradient exists as shown in Figure 5. In the diverging section of the tunnel, where large back flow exists, an adverse pressure gradient is present for most of the phases of the cycle (Figure 6).

Free-stream velocity distribution along the tunnel length shows a disturbance travelling downstream with a phase shift of about $\pi/3$ from X = 0.61 to 4.27 m. These discontinuities in free stream velocities are confirmed by x-wire and normal wire profile measurements. A similar but weaker effect was observed with the other large amplitude flow studied by Agarwal and Simpson[3], but not with moderate amplitude flows.

Ensemble-averaged velocity profiles were obtained using cross-wire and laser anemometers. In regions where both the laser and hot-wire anemometers produce valid data the results agreed within experimental uncertainties. Estimated uncertainties for the hot-wire are $\Delta\hat{U} = \pm 3.2\%$, Δv^2 and $\Delta u^2 = \pm 10\%$, $\Delta(-\hat{uv}) = \pm 20\%$ and for the laser anemometer are $\Delta\hat{U}$ and $\Delta\hat{V} = \pm 0.25$ m/s, Δu^2 and $\Delta v^2 = \pm 4\%$ of the maximum profile value, and $\Delta(-\hat{uv}) = \pm 20\%$ for all phases.

Ensemble-averaged data for various phases at X = 0.53 m are shown in Figure 7. The shape of the profiles at high free-stream velocity phases is essentially the same as reported by Simpson et al.[1,2] for the steady and moderate amplitude unsteady flows and high amplitude flow of Agarwal and Simpson[3], without flow reversal. A semi-logarithmic region in the ensemble-averaged velocity profiles is clearly evident. There is agreement between the cross wire and laser anemometer data except at high velocity phases at

148

larger values of y because of low smoke concentration and at very low velocity phases.

At low velocity phases close to the wall, intermittent backflow exists upstream of the throat of the test section, the fraction of time that there is downstream flow $\hat{\gamma}_{pu}$ is less than unity.[4]

$\sqrt{\overline{\hat{u}^2}}/\hat{U}_e$ and $\sqrt{\overline{\hat{v}^2}}/\hat{U}_e$ vs. y/δ profiles collapse on top of one another for the accelerating and high velocity phases at $X = 0.53$ m. This supports the observation that the ensemble-averaged flow at high velocity attached flow phases looks the same at a given streamwise location.

Other recent papers[3,4] have concentrated on the attached phases of these unsteady flows. Detailed $\hat{U}$, $\hat{V}$, $\hat{u}^2$, $\hat{v}^2$, and $-\hat{uv}$ measurements have been made all along this flow. Here we wish to discuss the results at only a couple locations with detached flow. Figure 8 shows ensemble-averaged velocity profiles at 4.27 m for the 'reattaching' flow phases of a cycle while Figure 9 shows results for 'detaching' phases. During detaching phases $\partial\hat{U}/\partial t < 0$ while $\partial\hat{U}/\partial t > 0$ for reattaching phases. Figures 10 and 11 show smoothed Reynolds shear stress results for the same conditions, respectively, while Figures 12 and 13 show the shear stress correlation coefficient. The meaning of these results is discussed in the next section.

5. Discussion and Conclusions

Experimental data for a $k = 1.33$, large amplitude unsteady flow have been presented. This flow has nearly similar streamwise oscillating and mean pressure gradient distributions as that for the $k = 0.61$ large amplitude flow earlier studied by Agarwal and Simpson.[3]

Ensemble-averaged velocity profiles at $X = 0.53$ and 1.53 m, i.e. upstream of the throat for the phases without flow reversal, i.e. $\omega t = 90°$ – $270°$ are quite similar and show a distinct semi-logarithmic region and are similar to that for low Reynolds number attached turbulent boundary layers. The ensemble-averaged velocity profiles at $\omega t = 45°$, where the flow is strongly accelerating are quite different from that of other phases, resembling that of laminarescent turbulent flow. These velocity profiles are very similar to the sink flow studied by Simpson and Wallace.[8] The acceleration parameter

$$\hat{K} = \frac{\nu}{\hat{U}_e^3}\left[\frac{\partial \hat{U}_e}{\partial t} + \hat{U}_e\frac{\partial \hat{U}_e}{\partial x}\right]$$

values for $\omega t = 45°$ at these two locations are large values. Similar velocity profiles at $\omega t = 45°$ were observed with the other high amplitude flow studied by Agarwal and Simpson.[3]

Simpson and Wallace observed that for a steady flow with a $K > 3.6 \times 10^{-6}$ at low momentum Reynolds numbers, relaminarization of an initially turbulent boundary layer could occur. For the $k = 0.61$ flow,

$\hat{K} > 3.6 \times 10^{-6}$ over 20° of the cycle during rapid acceleration from the minimum velocity phases. For the same phases in the $k = 1.33$ flow, $\hat{K}$ is over 10 times greater. In both flows nearly zero correlation coefficients $-\hat{uv}/\hat{uv}$ were observed at these phases. These large $\hat{K}$ values are sufficient to produce laminarescent ensemble-averaged profiles during a short portion of the cycle, but are not imposed long enough to produce true relaminarization. Velocity profiles at this location for $\omega t = 360°$ where the flow is highly decelerating are similar to typically high adverse pressure gradient flows, Simpson et al.[5]

Upstream of detachment the ensemble-averaged velocity profiles exhibit a negligible phase angle variation through the boundary layer. Simpson et al.[1] showed that the phase angle variation of the ensemble-averaged oscillation is zero within a semi-logarithmic region. The turbulence in the absence of flow reversal also behaves in a manner as the steady flow, (i.e., the ensemble-averaged turbulence profiles are similar to those of the comparable steady flow and $\hat{u}^2$ and $\hat{v}^2$ are in phase with $\hat{U}$). This is in agreement with the moderate amplitude flows and a large amplitude flow previously investigated at these low reduced frequencies.

In the phases where there is no flow reversal, skin-friction coefficients were calculated at each phase from the semi-logarithmic region and also agree with the Ludwieg-Tillmann equation at the valid phases within the experimental uncertainties.

In the detached and reattaching flow, ensemble-averaged velocity profiles away from the wall show the hysteresis that occurs in detaching and reattaching flows (Simpson[7]) and non-quasi-steady behavior. Simpson et al.[1,2] also noted such hysteresis for their moderate amplitude flows. Outer region results for the ensemble-averaged mean velocity profile near detachment at $X = 2.2$ m and 2.95 m at the phases without flow reversal follow the universal velocity defect law proposed by Schofield.[9]

For the detaching phases such as shown at $X = 4.27$ m in Figure 9, the increasing backflow becomes as great as the freestream velocity in magnitude. During such large backflows, significant turbulence production occurs near the wall and all terms of the Reynolds-averaged momentum equation

$$\frac{\partial \hat{U}}{\partial t} + \hat{U}\frac{\partial \hat{U}}{\partial x} + \hat{V}\frac{\partial \hat{U}}{\partial y} = -\frac{1}{\rho}\frac{\partial \hat{p}}{\partial x} + \frac{\partial(-\hat{uv})}{\partial y}$$

are important. Figure 13 shows that decreasing correlation coefficients of -0.5 or so are produced near the wall during these large backflow phases. Typically large correlation coefficients of 0.5 are in the outer region where most of the turbulence energy production and the maximum shear stress occur (Figure 11).

During the reattaching or 'washout' of detached flow phases, the backflow velocities decrease and the near wall shearing stresses and correlation coefficients (Figures 10 and 12) increase to attached flow. Figure 8 shows distinct

semi-logarithmic velocity profiles as soon as there is no mean backflow. Values of wall shear stresses deduced from the attached flow logarithmic 'law-of-the-wall' velocity profile are within experimental uncertainty of the measured Reynolds shear stresses in the semi-log region. This reattachment of the flow is apparently due to the increasing rate-of-strain $\partial \hat{U}/\partial y$, outer region shear stress for the thinning shear layer, and the convection of upstream flow. Figure 6 shows only a small pressure gradient in the freestream during the washout phases. Note that the semi-log region velocities remain almost independent of time for $105° < \omega t < 165°$.

Figure 14 shows the behavior of the normalized maximum backflow velocity $\hat{U}_N/\hat{U}_e$ as a function of $\hat{Y}_{pu}$. As shown by Simpson and Shivaprasad when $\partial Y_{pu}/\partial t$ or $\partial Y_{pu}/\partial x$ is negative, all steady and unsteady velocity profiles fall along the same path in this plot and in a $\hat{U}_N/\hat{U}_e$ vs. $1/\hat{H}$ plot. This is because under these conditions the flow at a given location is increasingly separated and the flow structure is governed by the local turbulence and velocity profile structure.

Also as shown by Simpson and Shivaprasad, for phases of a cycle when $\partial \hat{Y}_{pu}/\partial t$ is positive hysteresis loops occur on these plots, indicating a different velocity profile and turbulence structure from increasingly separated phases. Simpson and Shivaprasad presented data for two flows with nearly sinusoidal freestream unsteadiness with an amplitude to mean velocity ratio of about 0.33. None of the hysteresis loops coincide for these four unsteady separated flows.

This behavior when $\partial \hat{Y}_{pu}/\partial t > 0$ is due to the different flow structure during phases when the 'washout' of backflow occurs. Only during 'washout' is the turbulence and flow structure significantly different from steady freestream separated flows and therefore non-quasi-steady.

References

1. Simpson, R.L., Shivaprasad, B.G. 1983a The structure of a separating turbulent boundary layer: Part 5. Frequency effects on periodic unsteady free stream flows. J. of Fluid Mech. 121, 319.

2. Simpson, R.L., Shivaprasad, B.G. and Chew, Y-T. 1983b The structure of a separating turbulent boundary layer: Part 4. Effects of periodic free stream unsteadiness. J. of Fluid Mech. 127, 219.

3. Agarwal, N.K. and Simpson, R.L. 1986 LDV measurements of large amplitude unsteady separated turbulent boundary layers. International Symposium of Applications of Laser Anemometry to Fluid-Mechanics, Lisbon.

4. Agarwal, N.K. and Simpson, R.L. The structure of large amplitude unsteady separating turbulent boundary layers. AIAA-87-0191, AIAA 25th Aerospace Sciences Meeting, January 12-15, 1987, Reno, NV.

5. Simpson, R.L., Chew, Y-T. and Shivaprasad, B.G. 1981a The structure of a separating turbulent boundary layer: Part 1. Mean flow and Reynolds stresses. J. of Fluid Mech. 113, 23.

6. Simpson, R.L., Sallas, J.J. and Nasburg, R.E. 1978 Tailoring the waveform of a periodic flow with a programmable damper. J. of Fluids Engrg. 100, 287.

7. Simpson, R.L. 1985 Two-dimensional turbulent separated flow. AGARDograph No. 287, Vol. 1.

8. Simpson, R.L. and Wallace, D.B. 1975 Laminariscent turbulent boundary layers: Experiments on sink flows. Project SQUID Rept. SMU-1-PU.

9. Schofield, W.H. 1980 Turbulent boundary layers in strong adverse pressure gradient. Australian Defense Sci. and Tech. Org. Aero. Res. Lab. Mech. Engrg. Rep. 157 (AR-002-218).
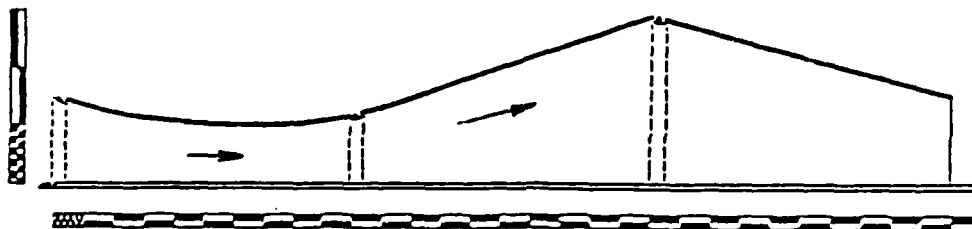
Figure 1. Sideview of the Test Section. Major Dimension on Scale is 25 mm. Note Baffle Plate Upstream of Blunt Leading Edge on Bottom Test Wall and Side, and Upper Wall Jet Boundary Layer Control.
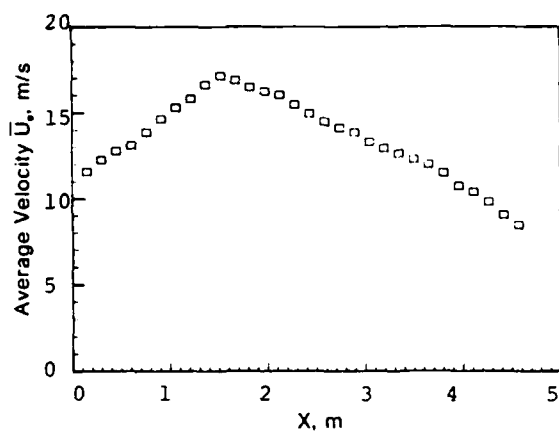
150

Figure 2. Free-stream Mean Velocity, $\overline{U}_e$.
($k = 1.33$, $\overline{U}_{e_o} = 11$ m/s)
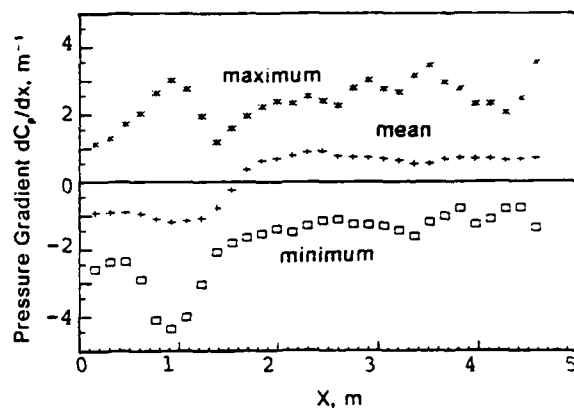
Figure 3. Mean Pressure Gradient Distribution along the Tunnel Centerline and limits of the unsteady pressure gradient. $C_p = 2(P - P_r)/\rho \overline{U}_{e_o}^2$.
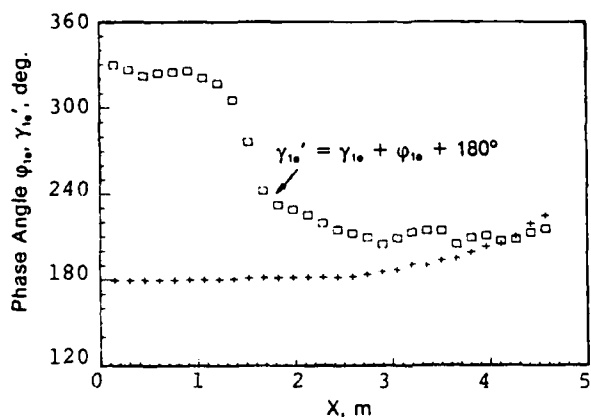
Figure 4. Phase Angles of the First Harmonic.
($+$, φ_{1e}, Free-stream Velocity; $\square$, γ_{1e}', Pressure Gradient)

Figure 5. Free-stream Velocity and Pressure Gradient at $X = 0.61$ m. ($\square$, Free-stream Velocity; $\ast$, Pressure Gradient)

Figure 6. Free-stream Velocity and Pressure Gradient at $X = 4.27$ m. ($\square$, Free-stream Velocity; $\ast$, Pressure Gradient)

151
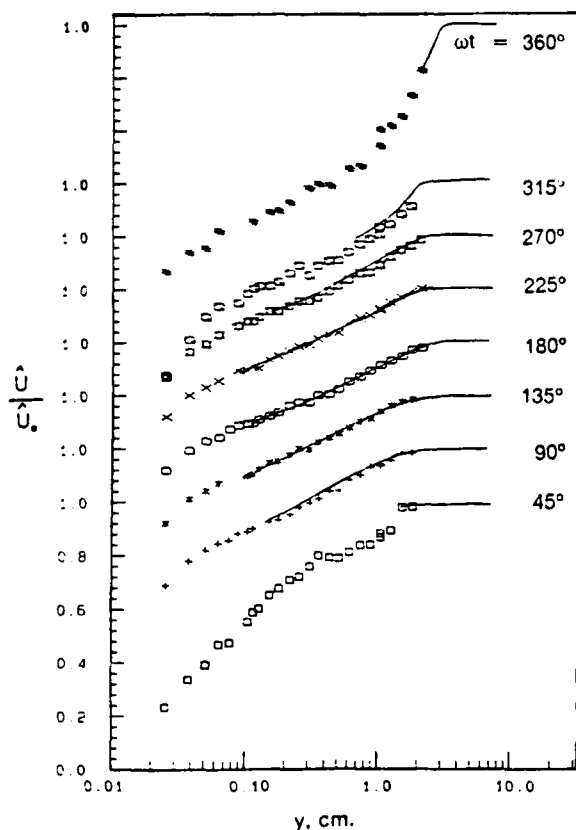
Figure 7. Ensemble-averaged Velocity Profiles, $\hat{U}/\hat{U}_*$, at X = 0.53 m. (Solid Lines: Cross-Wire Measurements)
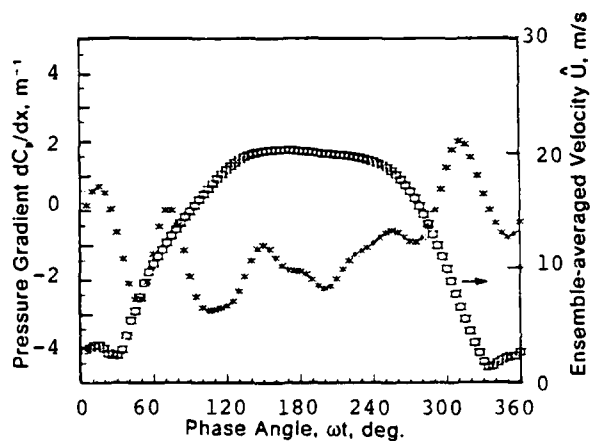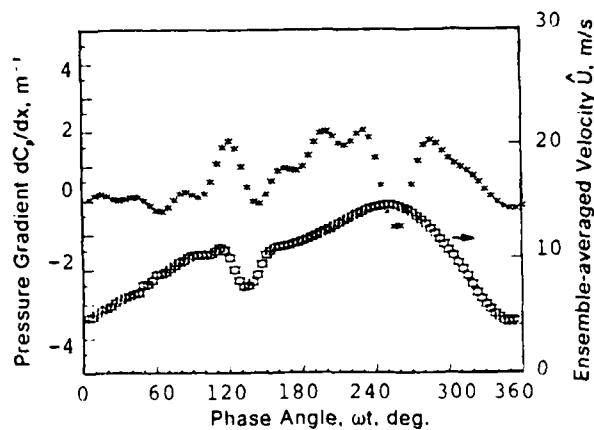

Figure 8. Ensemble-averaged Velocity Profiles, $\hat{U}$, at X = 4.27 m for 'Reattaching' Phases 345 ° ≤ ωt ≤ 180°. Lines for vidual aid only. (□ = 15°; △ = 30°; ◇ = 45° ; ▽ = 60°; ○ = 75° ; ◘ = 90°; ⬡ = 105° ; ⬓ = 120°; ▲ = 135° ; ◈ = 150°; ▼ = 165° ; ● = 180°; ◦ = 345° ; ∅ = 360°); Open Symbols: Laser Anemometer and Solid Symbols: Cross-Wire Measurements.

Figure 9. Ensemble-averaged Velocity Profiles, $\hat{U}/\hat{U}_*$, Vs. log(y/δ), at X = 4.27 m for 'Detaching' Phases 195° ≤ ωt ≤ 330°. Lines for vidual aid only. (□ = 195°; △ = 210°; ◇ = 225° ; ▽ = 240°; ○ = 255° ; ◘ = 270°; ⬡ = 285° ; ⬓ = 300°; ▲ = 315° ; ◈ = 330°); Open Symbols: Laser Anemometer and Solid Symbols: Cross-Wire Measurements.
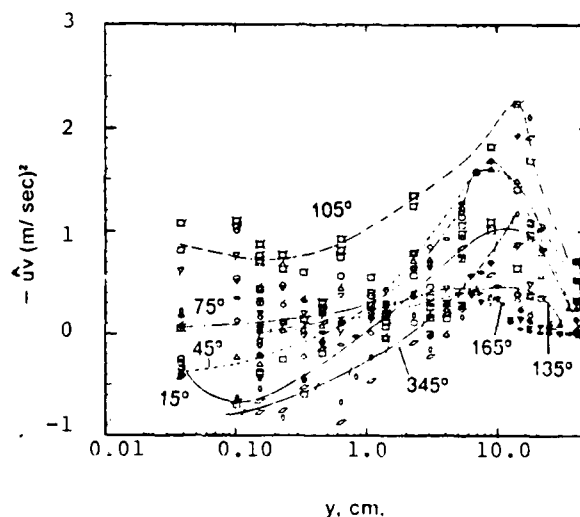
Figure 10. Ensemble-averaged Reynolds' Shearing Stress $-\hat{uv}$ Profiles at X = 4.27 m for 'Reattaching' Phases 345° ≤ ωt ≤ 180°. Lines for vidual aid only. Legend same as for Figure 8.

152

Figure 11. Ensemble-averaged Reynolds' Shearing Stress $-\hat{uv}/U_\bullet^2$ Vs. log (y/δ) Profiles at $X = 4.27$ m for 'detaching ' Phases $195^\circ \leq \omega t \leq 330^\circ$. Lines for vidual aid only. Legend same as for Figure 9.
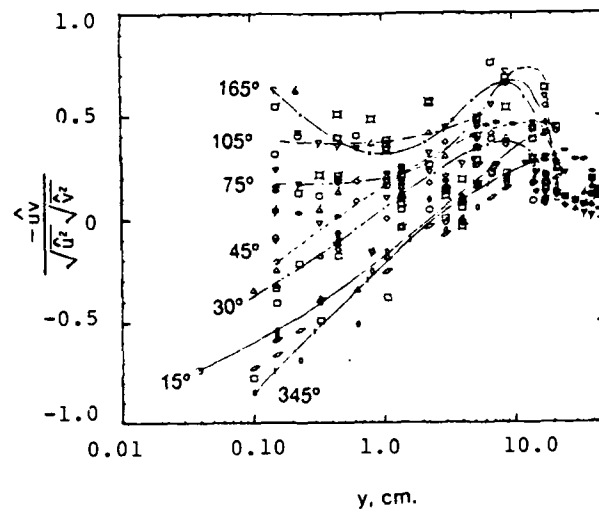
Figure 12. Ensemble-averaged Shear Stress Correlation Coefficient Profiles at $X = 4.27$ m for 'Reattaching ' Phases $345^\circ \leq \omega t \leq 180^\circ$. Lines for vidual aid only. Legend same as for Figure 8.
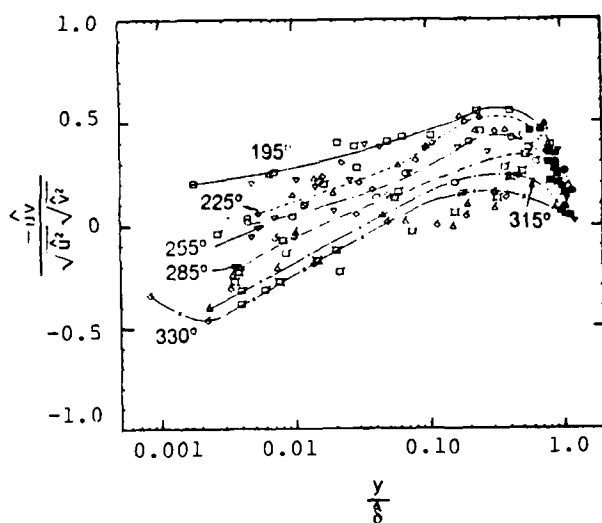
Figure 13. Ensemble-averaged Shear Stress Correlation Coefficient Profiles at $X = 4.27$ m for 'detaching ' Phases $195^\circ \leq \omega t \leq 330^\circ$. Lines for vidual aid only. Legend same as for Figure 9.
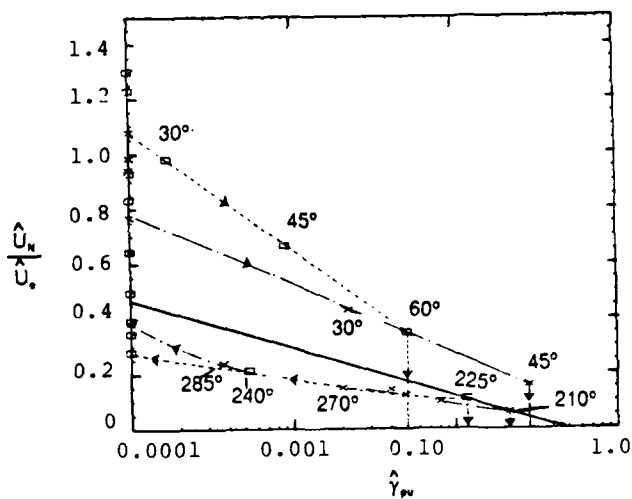
Figure 14. Normalized Maximum Mean Backflow Velocity $\hat{U}_N/\hat{U}_\bullet$ Vs. $\hat{\gamma}_{pu}$ at $X = 3.5$ m and 4.27 m. Dashed Lines for vidual aid only. Solid line: Steady Flow Results of Simpson et al.[ ] ($\times$, 3.5 m; $\square$. 4.27m)

153

Impulsively-started Laminar Flow
Around a Sharp Edge

Frederick S. Sherman
Department of Mechanical Engineering
University of California
Berkeley, CA, 94720

Abstract

A theoretical model of viscous flow around the edge of a flat plate is constructed. The velocity field is composed of (1) the inviscid potential flow obtained by conformal transformation of a uniform stream in the upper half plane; (2) a moving and intensifying line vortex, which is a zeroth approximation to the self-similar vortex spiral which grows from the edge of the plate; and (3) laminar boundary layers on the windwar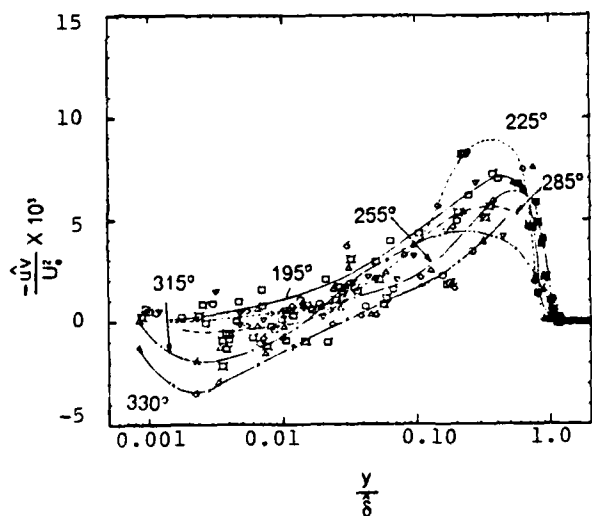d and leeward sides of the plate. When flow (1) is started impulsively at time zero, the vortex starts to move away from the edge, along a line normal to the plate. Its distance from the edge is proportional to $t^{2/3}$; its strength, as required to impose a Kutta condition at the edge, grows in proportion to $t^{1/3}$

The boundary layer on the windward side develops uneventfully, under a consistently favorable pressure gradient. That on the leeward side develops under a potential flow with a moving stagnation point. The flow in the leeward boundary layer is correspondingly complicated, but most of it is easily computed by marching forward in a similarity variable proportional to $t^{1/3}/x^{1/2}$, where x is distance from the edge. This computation reveals, for any given time, one region in which the tangential flow in the boundary layer is everywhere directed away from the edge, one region in which it is everywhere toward the edge, and two regions of bidirectional tangential flow. There is no sign of separation associated with the outermost region of bidirectional flow, which is completely described by the calculation. The calculation only penetrates a small distance into the outer edge of the second region of bidirectional flow, when it is terminated by failure to satisfy the CFL condition. The point at which it does so is also the point at which the MRS criterion for separation of an unsteady boundary layer is satisfied The domain that is inaccessible to calculation covers only about 3 % of the distance from the edge to the stagnation point of the potential flow

Spatial distributions of skin friction, normal velocity at the edge of the boundary layer, and a newly-defined boundary-layer thickness are presented for a non-dimensional time of unity

Introduction

The motivation for study of this model problem arose from a desire to understand the changes which would occur in the boundary layer of a two-dimensional wing, during a very sudden change of angle of attack. In his very useful monograph, D.P.Telionis (1981) sets forth ideas largely due to W.R.Sears, which make it clear that it is necessary to understand the history of the external inviscid flow during the maneuver. The discussion, however, seems to focus on external potential flows, which leaves open the question of how one might proceed if the body of interest has a sharp edge. At such an edge, vorticity may be convected away from the body at a rate much higher than the rate of diffusive transport, and it seems likely that an appropriate inviscid flow calculation, even for a very sudden maneuver, must contain some model of this shed vorticity.

This line of reasoning leads back to the work of Prandtl, who drew attention, in 1922, to the possibility of an inviscid, self-similar flow pattern in which a growing vortex sheet, coiled into a spiral of infinitely many turns, develops at the edge of a semi-infinite thin plate which is suddenly moved normal to itself. By 1939, Anton had developed a clever scheme of successive approximation, by means of which the requirements of self-similarity of the spiral, and of finite velocity at the edge of the plate, could be translated into a computation of the configuration of the spiral, and the distribution of circulation along the sheet. Anton's work was subsequently refined by Wedemeyer in 1961, and was greatly extended by Blendermann in 1969. Wedemeyer's paper presents a fine review, and a very clear description of the method, insofar as it is needed here. An alternative numerical method, which gives results nearly indistinguishable from those of Wedemeyer or Blendermann, was presented by Pullin in 1978, with excellent references. The present paper picks up the thread of this old work, to see what may be learned about laminar boundary-layer growth on the two faces of the plate, during the growth and motion of the inviscid vortex spiral

For a preliminary investigation, it seemed reasonable to approximate the inviscid flow, so as to obtain a closed-form expression for the velocity along the surfaces of the plate. The zeroth approximation in the calculations of Anton and Wedemeyer seemed very suitable. It represents the sheet by a single vortex. When a potential flow around the edge is started impulsively at time zero, this vortex is born and starts to move away from the edge, along a line normal to the plate. Its distance from the edge is proportional to $t^{2/3}$, its strength grows in

proportion to $t^{1/3}$. The imaginary situation at a given time is shown in Figure 1, first in a transformed plane in which the flow occupies only the upper half plane, and then in the physical plane.
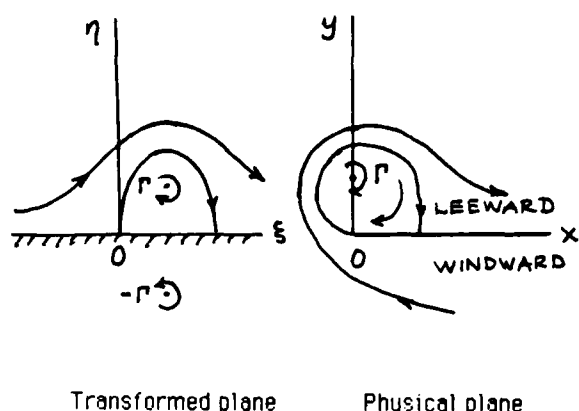

Transformed plane   Physical plane

Figure 1

The flow field is characterized in the transformed plane by a uniform flow of speed U_0, and by a scale of distance, H. The position of the vortex is constrained by the consideration that it should approximate the shape-preserving spiral vortex sheet, and is given by $\zeta = H\tau^{1/3}(1+i)$, where τ is the non-dimensional time, $\tau = U_0 t/H$. The strength of the vortex, which must combine with its image and the uniform stream to produce a stagnation point at $\zeta = 0$, is thus $\Gamma = 2\pi U_0 H \tau^{1/3}$.

When this flow is carried over to the physical plane by the transformation $z/H = (\zeta/H)^2$, the resulting velocity along the upper (leeward) surface of the plate is

$$U(x,t)/U_0 = (2H/x)^{1/2}(1-\chi)/(1+(1-\chi)^2) \qquad (1)$$

in which

$$\chi = \tau^{1/3}(2H/x)^{1/2}. \qquad (2)$$

The stagnation point corresponds to $\chi = 1$, the edge to $\chi = \infty$, and the point at infinity to $\chi = 0$. It can be shown, from (1), that $\partial U/\partial x > 0$ in the range $2-\sqrt{2} < \chi < 2+\sqrt{2}$, so that the potential flow will, at least here, encourage the boundary layer to stay close to the wall. It is assumed that the corresponding velocity, which would appear if the vortex spiral were more accurately represented, would be very much like this, although not given by a convenient closed-form expression.

The lack of a physically defined reference length, which led Prandtl to the idea that the vortex spiral should be governed by a similarity law, may be used again for the boundary-layer analysis. As will be shown in the next section, a successful Ansatz for the streamfunction in the boundary layer is

$$\Psi = U_0 (vtH/x)^{1/2} f(\chi,\eta) \qquad (3)$$

in which

$$\eta = y/(vt)^{1/2}. \qquad (4)$$

The details of the analysis follow in Section 3, the results in Section 4.

3. Analysis

The velocity components derived from the streamfunction (3) are

$$u = \partial\Psi/\partial y = U_0 (H/x)^{1/2} f'(\chi,\eta),$$

and

$$v = -\partial\Psi/\partial x = U_0 (vtH/4x^3)^{1/2} \partial\{\chi f(\chi,\eta)\}/\partial\chi.$$

The equation for streamwise momentum in the boundary-layer,

$$\partial u/\partial t + u\partial u/\partial x + v\partial u/\partial y - (\partial U/t + U\partial U/\partial x) = u\,\partial^2 u/\partial y^2, \qquad (5)$$

now appears as

$$f''' + (\eta/2 - \gamma f)f'' + \gamma f'^2 + \delta = \phi\,\partial f'/\partial\chi + \psi(f'\partial f'/\partial\chi - f''\partial f/\partial\chi). \qquad (6)$$

The primes denote partial differentiation with respect to η, and the coefficients are all functions only of χ, to wit:

$$\gamma = (\sqrt{2}/8)\chi^3, \qquad \phi = \chi/3, \qquad \psi = -(\sqrt{2}/8)\chi^4,$$

and

$$\delta = -(\sqrt{2}/12)(\chi^2/D^3)(3\chi^4 - 11\chi^3 + 2\chi^2 + 18\chi - 16),$$

in which

$$D = 1 + (1-\chi)^2$$

The boundary conditions are

$$f'(\chi,0) = 0 \text{ (no slip)},$$

$$f(\chi,0) = 0 \text{ (impervious wall)},$$

and

$$f'(\chi,\infty) = \sqrt{2}(1-\chi)/D,$$
$$\text{(matching with potential flow)}$$

The initial condition is

$$f'(0,\eta) = (1/\sqrt{2})\,\text{erf}(\eta/2), \qquad (7)$$

156

which is simply the solution of (5) at $\chi = 0$. This corresponds to the fact that diffusion always dominates the initial development of an impulsively-started boundary layer.

Equation (6) can be solved numerically by marching forward in the variable χ, from the initial condition (7), providing that the coefficient of $\partial f'/\partial \chi$ remains everywhere positive. This requirement is the Courant-Friedrichs-Lewy (CFL) condition, that the domain of dependence of the finite-difference scheme should include the corresponding domain for the differential equation. If the coefficient becomes negative, the marching calculation becomes analogous to an effort to solve the heat equation with negative time increments, and blows up. In the present case, the coefficient equals $\phi + f'\psi$, which is positive if $\chi^3 f' < \sqrt{(32/9)}$. As the solution develops, the maximum value of $\chi^3 f'$ remains very small and positive while $\chi < 1$; then it is negative until $\chi = 5.44732$, when positive values of f' reappear near the wall. The critical value of $\chi^3 f'$ is reached at $\chi \approx 5.7049$, after which the marching procedure quickly blows up.

It is interesting to note that the point at which the marching scheme fails is also the point at which the Moore-Rott-Sears (MRS) criterion for separation of an unsteady boundary layer is met. In the present context, the MRS criterion associates separation with a moving x-t station at which there is, within the boundary layer, a local velocity extremum, equal to the velocity of the station itself. For the case of interest here, the shape of the boundary-layer velocity profile depends only on the value of χ. Therefore, the x-t trajectory of the station at which the profile exhibits any distinctive feature, such as a reversal of skin friction direction or a singular eruption of flow away from the wall, is a locus of constant χ. The slope, dx/dt, of that locus gives the velocity of that distinguished station.

The MRS criterion thus states, in the present case. that the $\xi-\tau$ trajectory of the fluid particle that is at a local extremum of the u-profile at the value of χ for which the boundary layer separates is instantaneously tangent to the curve $\xi = 2\tau^{2/3}\chi^{-2}$. From this we can calculate that, at a separation station, we should find a local maximum of f', given by $\chi^3 f'_{max} = \sqrt{(32/9)}$. This is exactly the critical condition for violation of the CFL condition, just as it is for a simple downstream-marching calculation of a steady boundary layer which approaches separation. Figure 2 illustrates this situation, and simultaneously illustrates the local domains of dependence for the finite-difference scheme and the differential equation.
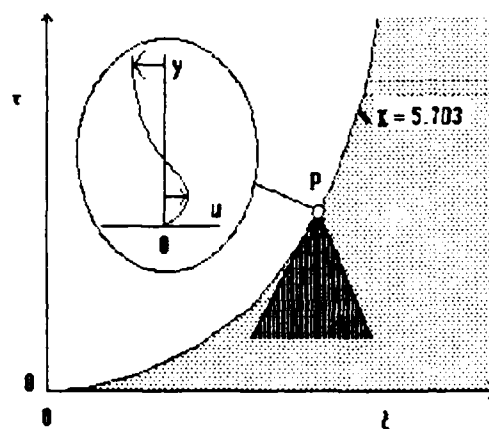
Figure 2   Exaggerated view of domains of dependence

For point P, the domain of dependence of the marching calculation is the dotted region. That of the differential equation is, locally, the darkly shaded wedge, bounded by rays of slope u_{max} and u_{min}. The CFL condition requires that none of these rays should approach P from the unshaded side of the curve χ = constant. When the CFL condition is first violated, the ray that does so represents the extreme velocity referred to in the MRS criterion for separation.

It probably makes little sense to worry too much about the details of the flow so near the edge of the plate, because they might change substantially if the present zeroth approximation to the inviscid vortex spiral were to be replaced by a more accurate approximation. However, similar matters have attracted much attention in the past, as is shown well in Chapter 7 of Telionis' monograph, because of the difficulty of an unambiguous identification of separation in unsteady flow. A few more comments will be given, when the results of the computation are discussed.

Figure 3 shows an overall view of the ξ-t plane, as a guide to important features of the inviscid flow along the wall. The 3/2 - power parabolas issuing from the origin are loci of constant χ, which bound regions in which the flow shows some special feature. The curve AB is the path followed by a particle of the potential flow that lies at x = H when the flow is started. It starts moving away from the edge, but is soon overtaken by the effect of the vortex, which arrests it and moves it eventually back to the edge. The acceleration of the particle is toward the edge, until $\chi = 2.9634$, where the quantity δ, which is proportional to the pressure gradient, changes sign. Where $\chi < 2.9634$, the vorticity continuously added at the wall has the opposite sign from that in the boundary layer when $\chi = 0^+$. We might expect this to lead eventually to

157

flow reversal near the wall. The vorticity added at the wall changes sign again after $\chi = 2.9634$, so that we might expect a second flow reversal near the wall.

Within the dotted region $\partial U/\partial x > 0$, so that the potential flow tends to keep the boundary layer thin.
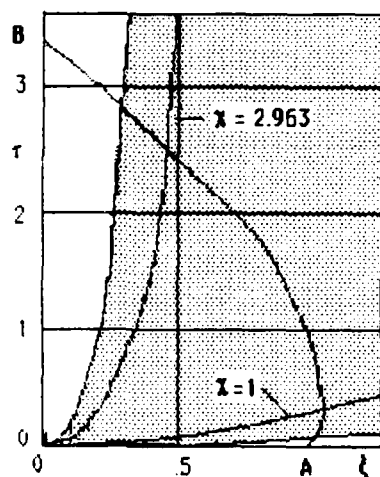

Figure 3 Inviscid Flow Domains

To calculate the boundary layer on the windward side of the plate, we replace Equation (1) with

$$U(x,t)/U_0 = (2H/r)^{1/2}(1+\chi)/(1+(1+\chi)^2),$$

in which r, the distance upstream of the edge, also replaces x in the definition of χ. This causes some small changes in the formulas for the χ-dependent coefficients. The marching procedure is the same as before, but the solution is much less eventful, since the vorticity added at the wall after t=0 has the same sign as that in the initial vortex sheet. There is consequently no separation, and no difficulty with the CFL condition.

Computational parameters

A conventional implicit finite- difference procedure, employing centered three-point differences with uniform step size in η, and trailing three-point differences with uniform step size in χ, was used. The nonlinearity of the resulting algebraic equations is handled with a few cycles of Newton-Raphson iteration at each step forward in χ. The steps in η and χ were reduced; the number of iterations was increased, and the maximum value of η, at which the outer boundary condition was imposed, was increased; until all computed quantities became independent of further numerical refinements, to

five-decimal accuracy. The most refined computation involved 2283 values of χ, and 161 values of η. It took about 18 seconds on an IBM 3090; and cost about $3.50.

4. Results

Boundary layer on the leeward side

Figure 4 shows computed distributions of the scaled skin friction, $f''(\chi,0)$, and a scaled vorticity thickness, δ_Ω, as functions of χ. The vorticity thickness is defined by an unconventional formula,

$$\delta_\Omega = \int_0^\infty \eta|\Omega|d\eta \ / \ \int_0^\infty |\Omega|d\eta, \qquad (7)$$

which yields the conventional scaled displacement thickness if there is no bi-directional flow in the boundary layer.

The first reversal of skin friction occurs where $\chi = 0.76705$; the second where $\chi = 5.44732$. There is no hint of singular behavior of the skin friction at either of these points.

The scale factor, by which δ_Ω is multiplied to get a physical thickness, is simply $(\upsilon t)^{1/2}$, so the spatial variation of boundary-layer thickness at any given time is surprisingly small. The fairly sudden decrease between $\chi = 1$ and $\chi = 1.5$ is the result of cancellation of the original charge of vorticity by the outward diffusion of vorticity of the opposite sign.
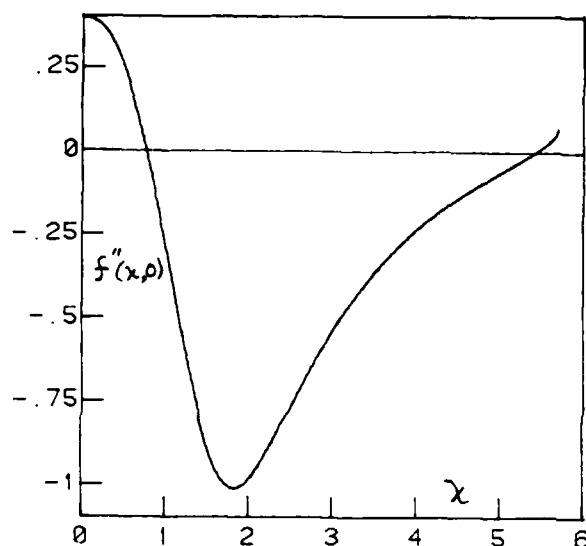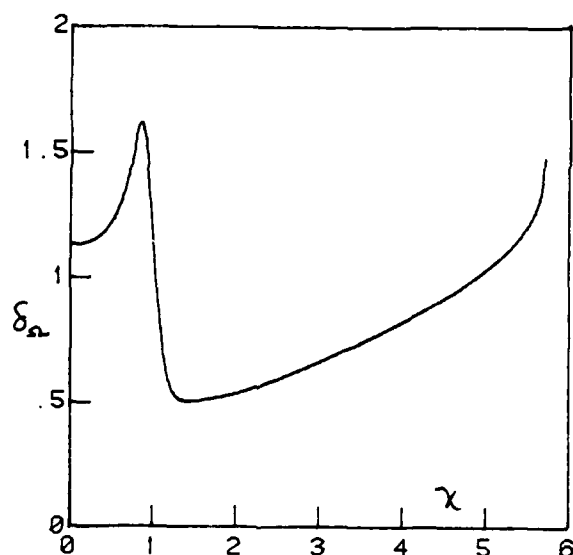

Figure 4a. Scaled wallshear, versus χ.

158

Figure 4b. Scaled boundary-layer thickness, versus χ.

Figure 5a. Spatial distribution of wall shear, $\tau = 1$.

Figure 5 shows spatial distributions, at non-dimensional time $\tau = 1$, of skin friction, and of the y-component of velocity, evaluated at $\eta = 6$, just outside the boundary layer. The shape of the latter distribution differs little from that of $-\partial U/\partial x$, except as $\chi \to 5.7049$, the value at which the MRS criterion for separation is met, and at which the calculation ends.   It is difficult to draw definite conclusions about the possibility of a singularity in the distribution of velocity normal to the wall, but the present numerical data are quite well fit, in the range $5.68 \leq \chi \leq 5.7049$, by the formula

$$Re^{1/2}\, v(\chi,6)/U_0 \;=\; 4.783\,(5.7049 - \chi)^{-1},$$

which certainly implies a singularity. There is no evidence of a corresponding singularity for the skin friction.

Figure 6 is a pictorial guide to the flow in the boundary layer at dimensionless time $\tau = 1$.

Boundary layer on the windward side

The one thing which adds interest to the calculation for the windward side is the possibility of comparing the solution, with and without the shed vortex as a component of the potential flow. A comparison of skin-friction distributions , for time $\tau = 1$, is shown in Figure 7   As expected, the vortex reduces the acceleration of the inviscid flow as it approaches the edge of the plate, consequently reducing the skin friction.   Note that in this comparison, the skin friction is referred to the same, constant, dynamic pressure in both cases.

Figure 5b. Spatial distribution of normal velocity, $\tau = 1$.

Without the vortex, the inviscid flow is steady after its impulsive start. The corresponding boundary layer on the windward side eventually becomes steady, developing a self-similar velocity profile which is a close cousin to the Falkner-Skan profiles The profile shape is very nearly independent of time, for $\chi \geq 10$ Of course, the boundary layer under the inviscid flow with vortex never becomes steady
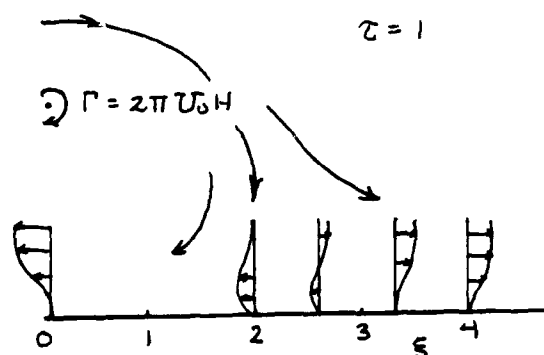
Figure 6. Pictorial sketch of leeward boundary layer, $\tau = 1$.
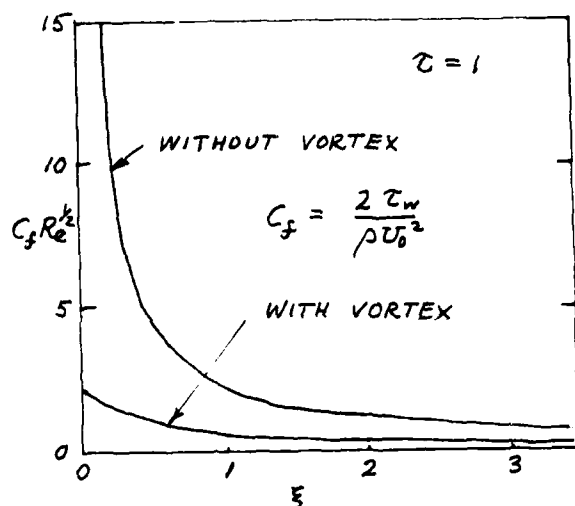
Figure 7. Effect of vortex on wall shear on windward side

Conclusion

A tolerably self-consistent theoretical model of impulsively-started laminar flow over the sharp edge of a semi-infinite plate has been demonstrated. It incorporates laminar boundary layers which flow toward the edge of the plate on both windward and leeward sides, feeding their vorticity into a spiral sheet which is approximated by a single point vortex of growing strength and separation.

There are some obvious inconsistencies in the model, which are now listed and discussed.

(1) The zeroth approximation to the inviscid flow is conceptually not self-consistent, in that it provides no channel into which the vorticity of the boundary layers can pass, in order to enhance the

circulation of the shed vortex. There is no vortex sheet which might be imagined to be a continuation of the boundary layers. In principle, the boundary layer calculation would be no more difficult, if a more exact model of the inviscid vortex spiral were to be used. One would simply have to substitute a numerically-determined function of χ for the rational fraction which appears in Equation (1). The coefficients, γ, S, ψ and ϕ in Equation (6) would then be known only numerically. This would be a nuisance for programming, but now that satisfactory levels of discretization are known, it should not be too difficult to prepare the necessary input data files.

(2) There is a small region, near the edge of the plate on the leeward side, where the present calculation gives no picture of the flow. Further, there is no obvious way to fill this gap, without surrendering the desire to use nothing more than boundary-layer theory and a predetermined inviscid flow. The failure of the CFL condition can be evaded by adoption of a different differencing scheme, but any such scheme will require boundary values along a line normal to the wall at the edge of the plate, and there is no ready way to get these values. Our best hope may be that the second reversal of skin friction, near the edge of the plate, will go away when a more accurate description of the vortex spiral is used.

(3) There is of course a conceptual difficulty with the inviscid, self-similar, model of the vortex spiral at very early times. Such a spiral, as an object standing free and clear of a growing viscous boundary layer, can only be imagined if the distance to the center of the spiral is much greater than the boundary-layer thickness. This requires that

$$\nu t/H^2 \ll (U_0 t/H)^{4/3},$$

or, equivalently, that $\tau \gg Re^{-3}$, where $Re = U_0 H/\nu$.

To evaluate Re, we need to recognize that this analysis provides a local approximation to flow near the edge of a large finite plate, moving with a definite speed, so that U_0 and H can be assigned numerical values. Assuming that the resulting value of $Re \gg 1$, we conclude that the picture of a clearly separate vortex spiral need be surrendered only for very tiny values of τ.

References

D. P. Tellonis, *Unsteady Viscous Flow*, Springer Verlag, 1981

E. Wedemeyer (1961) *Ausbildung eines Wirbelpaares and den Kanten einer Platte*, Ing.-Arch. **30**, 187-200

D.T. Pullin (1978) *Unsteady self-similar rolled-up vortex sheets*, J. Fluid Mech. **88**, 401-430.

INTERACTIVE AERODYNAMICS OF WINGS IN SEVERE MANEUVER*†

J.E. McCUNE

Massachusetts Institute of Technology, Cambridge, Massachusetts

ABSTRACT

This paper describes an interactive technique for the study and analysis of the aerodynamics of wings in severe maneuver. Both the 2D airfoil case and the cross-flow properties for slender 3D wings are addressed. To begin the study, the non-linear interaction of a 2D airfoil undergoing large-amplitude unsteady motion with its wake of shed vorticity was studied interactively on the computer using quick and efficient codes. The user can now input a "maneuver" and study and observe on-line the non-linear wake evolution and airfoil response. The allowable maneuvers for the airfoil presently include any combination of pitching and plunging, suddenly imposed. Also, airfoil response to sudden large-amplitude gusts of any shape and relative passage speed can be observed and analyzed. A detailed review of progress and results from this part of our work is provided by Scott.[1] In the present report we emphasize application of related techniques to 3D slender wings. We also provide information on improved methods of calculating lift and moment via wake integrals, emphasizing conservation of impulse, for the 2D as well as the 3D case.

1 Introduction

One important use of the non-linear 2D airfoil study is to provide a test of the exact wake evolution method, applied at low amplitudes, against classical linearized airfoil theory. This tests the accuracy and efficiency of the present approach, at least in the classical limit. But, in addition, the 2D work has set the stage for significant advances in the study of the 3D non-linear aerodynamic response of low-to-moderate $A\!\!R$ wings (delta and other) to severe imposed maneuvers.

It has long been recognized that at large but finite Reynolds Nrs. the cross-flow at any chordwise station of a slender wing must include two "wakes" (actually, wake traces) representing concentrated vorticity, often partially rolled into "cores," convecting above the wing surface. The

role of this vorticity, emanating via "leading-edge separation," is to maintain acceptably smooth flow at the wing edges. At sufficiently large Reynolds numbers, this smooth flow requirement is often called, even in this context, a "Kutta condition."

The present paper emphasizes recent progress in the development of a new method for studying on-line the dynamical effects of these two cross-flow wakes for the 3D wing. The method proceeds in analogy with, but also extends, techniques used in the 2D airfoil case. Additional ideas and theoretical framework needed for the 3D case are outlined. It is shown that the wake structures above a delta can be determined in a manner similar to the 2D airfoil problem, and that these structures have a history unique to any given maneuver.

As discussed in the body of the paper, the model of the wake structure used is somewhat idealized, in that the development during wake roll-up of vortex "cores" at finite Reynolds Numbers, with attendant regions of distributed total pressure loss, is not addressed. Similarly, the related occurrence of vortex breakup is not included in the present model. Our recent efforts to deal with these matters, as an elaboration of the technique described here, will be reported elsewhere.

2 Non-Linear Unsteady Wake Convection

2.1 2D Case

Any free vorticity associated with unsteady plane 2D fluid motion in the incompressible limit obeys the Helmholtz relation

$$\frac{D\Omega_z}{Dt} \equiv \frac{\partial \Omega_z}{\partial t} + \underset{\sim}{V} \cdot \nabla\Omega_z = 0 \qquad (2.1)$$

where $\underset{\sim}{V}$ is the planar fluid veloctiy, $\underset{\sim}{V} = (u,v,0)$, and $\underset{\sim}{\Omega} = \text{curl } \underset{\sim}{V} = (0,0,\Omega_z(x,y,t))$. Formally, therefore, if $A^{(1)} = \lambda(x,y,t)$ and $A^{(2)} = \eta(x,y,t)$ are two independent characteristic solutions of

$$\frac{DA^{(n)}}{Dt} = 0, \qquad (2.2)$$

161

with appropriate boundary (/ initial) conditions, then $\Omega_z = \Omega_z(\eta, \lambda)$. Boundary conditions can be specified such that one of these characteristic variables, "η," say, is constant on streaklines drawn at fixed t. The remaining variable, λ, can be chosen to be

$$\lambda \equiv t - \tau \tag{2.3}$$

where

$$\frac{D\tau}{Dt} = 1. \tag{2.4}$$

"τ" is then the Eulerian "drift time" with the usual simple physical interpretation [2]. But if the velocity field is discontinuous as in the classical model of concentrated vortex sheets representing the wakes behind wings and airfoils, this formulation may not be convenient.

It turns out, however, that when a concentrated vortex sheet is embedded in the flow the variable η can be conveniently replaced by a continuous function, η_c, say, which instead of (2.2) satisfies

$$\left. \begin{array}{c} \frac{\overline{D}\eta_c}{Dt} \equiv \frac{\partial \eta_c}{\partial t} + < \underset{\sim}{V} > \cdot \nabla \eta_c = 0 \\[2mm] \Delta \underset{\sim}{V} \cdot \nabla \eta_c = 0 \end{array} \right\} \tag{2.5}$$

and

i.e., η_c is constant on the sheet, and the sheet is a streak surface (streakline in 2D), whose deformation is controlled by convection at the <u>mean</u> velocity, $< \underset{\sim}{V} >$:

$$< \underset{\sim}{V} > \equiv \frac{1}{2} \left(\underset{\sim}{V}^+ + \underset{\sim}{V}^- \right) \tag{2.6}$$

As with a vortex sheet,

$$\Delta \underset{\sim}{V} \equiv \underset{\sim}{V}^+ - \underset{\sim}{V}^- \tag{2.7}$$

has no component perpendicular to the sheet at any time, as stated in (2.5(b)).

In a distance ds along the sheet at any fixed t the elemental change in circulation, $d\Gamma$, is determined by the local jump across the sheet of the velocity potential $\phi(x, y, t)$ such that

$$-d\Gamma = ds\Delta\frac{\partial \phi}{\partial s} = ds\frac{\partial}{\partial s}\Delta\phi = d\Delta\phi \qquad \text{(fixed } t\text{)}$$

In the 2D unsteady case the strength of this potential jump, $\Delta\phi$, occurring at the sheet specified by $\eta_c = $ constant, is a function of both x and t which must be determined. But application of the Bernoulli equation on either side of the sheet, together with the requirement that there be no jump in static pressure across the sheet, yields the restriction

$$\frac{\partial \Delta\phi}{\partial t} + < \underset{\sim}{V} > \cdot \nabla \Delta\phi = 0. \tag{2.8}$$

Thus, in the 2D case we can write $\Delta\phi = \Delta\phi(\bar{\lambda})$, and $d\Gamma = d\Gamma(\bar{\lambda}) = -\frac{d\Delta\phi}{d\bar{\lambda}}d\bar{\lambda} \equiv \Gamma'(\bar{\lambda})d\bar{\lambda}$ where

$$\bar{\lambda} \equiv t - \bar{\tau} \tag{2.9}$$

and

$$\frac{\overline{D}\bar{\tau}}{Dt} = \frac{\partial \bar{\tau}}{\partial t} + < \underset{\sim}{V} > \cdot \nabla \bar{\tau} = 1 \tag{2.10}$$

Here, $\bar{\tau}$ is the "mean" drift time of fluid elements within the vortex sheet.

The variable η_c can be expressed in the form $\eta_c = y - Y_c(\bar{\tau}, t)$ where $\frac{\overline{D}Y_c}{Dt} = v$. With $\eta_c = $const. on the streakline, we have $y = $ const.$+ Y_c(\bar{\tau}, t)$ on that line. When $\bar{\tau}$ is expressed in terms of x at any t we define a space curve, $y = y(x; t)$, giving the usual instantaneous picture of an airfoil wake. (See Figures 1 and 2.)

As noted above, condition (2.8) was derived by requiring that there be no net force anywhere on the free vortex sheet. For systems of conserved global circulation, this corresponds to guaranteeing conservation of impulse for the airfoil-plus-wake.

In the linear case, in which the wake is assumed simply to lie along the x-axis extending from the trailing edge with the vorticity within it convected at free-stream speed U_∞, the above exact results reduce to

$$\bar{\lambda} \rightarrow t - \frac{x - x_0}{U_\infty}$$

$$\frac{d\bar{\lambda}}{dx} \rightarrow -\frac{1}{U_\infty}$$

so that, if $\gamma(x, t)$ is the wake vorticity in that limit,

$$d\Gamma(\bar{\lambda})^{(\text{linear})} \rightarrow \gamma(x, t)dx$$

and

$$\frac{d\Gamma^{(\text{lin})}}{d\bar{\lambda}}\frac{d\bar{\lambda}}{dx} \rightarrow -\frac{1}{U_\infty}\frac{d}{dt}\left(\Gamma^{(\text{lin})}\left(t - \frac{x - x_0}{U_\infty}\right)\right) = \gamma\left(t - \frac{x - x_0}{U_\infty}\right)$$

reproducing the classical result in the linear limit.

In the actual non-linear situation $\bar{\lambda}$ replaces x as the useful parameter along the vortex sheet representing the wake, whether the wake is distorting and rolling-up or not. Thus, for example, the total wake circulation at any given time t is

$$\Gamma_{\text{wake}}(t) = \int_0^t d\bar{\lambda}\Gamma'(\bar{\lambda}). \tag{2.11}$$

Further, the (plane, 2D) velocity induced by the wake can be written in complex-variable notation as

$$u_{\text{wake}}(x,y,t) - iv_{\text{wake}}(x,y,t) \equiv w_{\text{wake}}(z,t)$$

$$= \frac{1}{2\pi i} \int_0^t d\bar{\lambda} \Gamma'(\bar{\lambda}) \frac{1}{z - z_v(\bar{\lambda},t)}. \qquad (2.12)$$

Here, $z \equiv x + iy$, and $z_v = x_v + iy_v$ is the complex location at t of the vortex element having circulation $d\Gamma(\bar{\lambda})$.

This formulation provides a powerful tool for writing down exactly all the various non-linear effects related to the wake in a manner which conveniently follows the contortions of the wake, including roll-up, as it evolves. Since $\bar{\lambda}$ is conserved during the history of each fluid element in the wake, it provides a convenient label for each such element. In the present example $\bar{\lambda}$ is the (earlier) time at which a given element entered the wake at the airfoil trailing edge. Figure 1 illustrates a portion of the evolution of a streakline constituting a vortex sheet, and Figure 2 shows a typical example of a computer-generated version of the wake behind an oscillating airfoil.

On the computer, of course, the above continuous vortex sheet model is replaced by an approximate discretized version. Individual discreet vortices of strength $\delta\Gamma(\bar{\lambda})$ replace the line elements of the sheet. Details of how to do this properly so as to maximize the effectiveness of the approximation have been discussed by Mook, et. al. [3] and more recently by Scott [1].

The computer screen provides an almost ideal tool for depicting and understanding wake evolution in this framework. At each time step each fluid element (and free circulation element) is advanced to its new location in x and y, moving in the field of all its neighbors. Since $\bar{\lambda}$ is constant for any fluid element and t is known, then $\bar{\tau}$ is determined at each new location at each t. In effect, the computer automatically maps the drift time field. When all the fluid elements in a given wake are shown in their new positions at each new time, t, for example, the line through them and the trailing edge at that moment is a streakline which depicts the momentary shape and location of the vortical wake. We discuss in Section 3 how the individual strengths, $d\Gamma$, of the circulation elements are determined (the Wagner equation).

2.2   3D Case

The classical picture of the 3D vortex-wake pattern above a delta wing in steady flow at large Reynolds Nr. and modest angle of attack is shown in Figures 3 and 4. At any chordwise station the trace of the double wake (somewhat idealized) is as illustrated in the inset of Figure 3. The necessity for a wake pattern resembling this structure, in order to provide acceptably smooth flow at the wing edges at large Re, has been recognized by many authors [4], [5], [6], [7], [8]. Even though the vorticity may roll up partially into two strong "cores," the strength of these cores must vary in the chordwise direction, which requires the existence of the joining umbilical vortical sheets from the edges to the cores, as illustrated.

Although this model is certainly oversimplified because of such effects as separation of the return boundary layers on the wing upper surface (leading to "secondary" and "tertiary" vortices [9], [10]), it offers an important improvement for real flows over the completely inviscid classical theory ($Re \equiv \infty$) with its singular flow at the edges [11]. This postulated wake pattern is often referred to as the result of "leading-edge separation" in the present context. The strength of the vorticity is presumed to be determined so as to provide Kutta conditions (smooth flow) at both wing edges. (Section 3.)

At higher angles of attack, even in steady flow, the model pattern in Figure 3 has a further defect. Vortex breakup [12], [13], [14] can be expected to occur at some conditions of interest with a consequent sudden and intense change at some chordwise location of the vorticity pattern above the wing. This paper does not attempt to deal with vortex breakup phenomena.

In the unsteady case, especially for 3D wings in severe maneuver, the classical wake pattern also has other defects. Clearly, for example, a pilot could well be able to roll or pitch so rapidly as to catch and move through his own wake pattern. Understanding wing response to that sort of condition will require improved understanding of the vorticity distribution within the cores themselves and any associated total head loss within the wake system. [15], [16] For that matter, the same improved understanding of the cores and total pressure defects appears to be required to interpret vortex breakup [12]. In the following discussions we largely ignore such defects, leaving their treatment for future elaborations of the technique we wish to describe here.

The evolution of the free 3D wake pattern over the wing proceeds in a manner analogous to the 2D case, complicated only by the need for an additional characteristic variable in the chordwise direction. To maintain zero net force on the free wake system each circulation element, $-\Delta\phi(x,z,t)$, once it enters the wake pattern at a wing edge location, is convected unchanged at the speed determined by the mean velocity at the sheet, including the motion "induced" by all its neighboring vortex elements. Thus, again,

$$\frac{\partial \Delta\phi}{\partial t} + <\underset{\sim}{V}> \cdot \nabla \Delta\phi = 0 \qquad (2.13)$$

where $\underset{\sim}{V} = (u,v,w)$ and

$$<\underset{\sim}{V}> \equiv \frac{1}{2}(\underset{\sim}{V}^+ + \underset{\sim}{V}^-) \qquad (2.14)$$

Once more we define the mean drift time, $\bar{\tau}$, now in the 3D field, such that

$$\frac{\partial \bar{\tau}}{\partial t} + <\underset{\sim}{V}> \cdot \nabla \bar{\tau} = 1 \qquad (2.15)$$

and reintroduce the characteristic variable (now 3D)

$$\bar{\lambda} \equiv t - \bar{\tau} \qquad (2.16)$$

163

which is constant, as before, for each fluid element moving in the vortex wake system.

What emerges is the description of the overall 3D wake pattern, however contorted, made up of twisted streaklines of vorticity extending at any instant from the plane of observation at a given chordwise location to the upstream wing edge location at which the corresponding vortex elements have entered or are entering the wake system. To describe the shape and location of these streaklines we again need the characteristic, η_c, as defined in (2.5), and one additional characteristic

$$\varsigma_c \equiv z - Z_c(x, y, z, t) \qquad (2.17)$$

where

$$\frac{\overline{D}Z_c}{Dt} \equiv \frac{\partial Z_c}{\partial t} + < \underset{\sim}{V} > \cdot \nabla Z_c = w. \qquad (2.18)$$

For the latter we can choose the boundary condition $Z_c = 0$ at or along any wing edge so that Z_c is just the chordwise distance at any t and z a given element of the wake has travelled since entering the system at the upstream chordwise location ς_c, and at a corresponding earlier time $\overline{\lambda}$. Thus, $\varsigma_c = 0$ for any wake element entering the pattern at the wing vertex, and $\varsigma_c = z$ for any element just entering at the plane of observation at z. The η_c and ς_c variables define instantaneous surfaces in the 3D case, and their intersections are the streaklines making up the wake pattern at any given moment.

In analogy with the 2D case one can express the variables η_c and ς_c in the forms

$$\eta_c = y - Y_c(\overline{\tau}, \varsigma_c, t)$$
$$\varsigma_c = z - Z_c(\overline{\tau}, \eta_c, t)$$

$\overline{\tau}$, in turn, is a function at each z and t of z, the height of the wake element above the wing surface. For example, in the linear model of a wake, with wake elements convected on straight lines at speed U_∞ as depicted in Figure 4(b), we have

$$\overline{\tau} = \frac{h}{U_\infty \sin \overline{\alpha}} ; \ \varsigma_c = Z_{edge} ; \ \eta_c = Y_{edge}$$
$$y = Y_{edge}(Z_{edge}) + f U_\infty \overline{\tau} \cos \overline{\alpha}$$
$$z = Z_{edge} + U_\infty \cos \overline{\alpha} \ \overline{\tau}$$

so that the simple surfaces

$$z - Z_{edge} = \frac{h}{\tan \overline{\alpha}}$$
$$y - Y_{edge} = \frac{fh}{\tan \overline{\alpha}}$$

are formed. The more realistic non-linear case follows similar rules and is depicted in Figure 4(a).

When observed at a given chordwise location, z, in the corresponding cross-flow plane including the wing trace, the vortex pattern over the wing creates a trace (actually, a pair of traces) of the wake as it passes through the observation

plane. In the unsteady case, these traces will deform, contort, and appear to roll-up, much as if we were observing a 2D airfoil with two wakes rather than one.

In Figure 5 we illustrate the sort of wake surfaces, and their traces, to be expected above a delta wing undergoing yaw and roll. Simultaneous observation of the wake trace behavior at several cross-flow planes can provide significant insight as to the interactive aerodynamics associated with violent maneuvers. On-line use of computer graphics, including split screen capabilities, promises to be very helpful in understanding the large-scale unsteady behavior of the wing and its wake.

On taking account of the right hand rule in the definition of circulation, each circulation element in each trace at fixed z and t can now be described in terms of the above variables as

$$\begin{aligned} d\Gamma^{STBD} &= -d\Delta\phi(\varsigma_c, \overline{\lambda})^{STBD} \\ d\Gamma^{PORT} &= +d\Delta\phi(\varsigma_c, \overline{\lambda})^{PORT} \end{aligned} \qquad (2.19)$$

in view of (2.13). (In the steady case, with nothing changing in time at a given z, only the first variable need appear and $d\Gamma = d\Gamma(z - Z_c(x, y, z)) = \Gamma'(\varsigma_c)d\varsigma_c$ in each wake.

The drift time $\overline{\tau}$ observed at z and t for any element in either of the two wake traces is related to ς_c, so that we can find $\overline{\lambda}(\varsigma_c, z, x, t)$, and/or the inverse. Then, the total circulation at fixed z and t in either trace (starboard or port) can be written

$$\begin{aligned} \Gamma^{STBD,PORT}_{wake}(z,t) &= \int_{(fixed\,x,t)} d\Gamma(\varsigma_c, \overline{\lambda})(\varsigma_c) \\ &\qquad (STBD,PORT) \\ &= \int_0^z d\varsigma_x \frac{d\Gamma^{STBD,PORT}}{d\varsigma_c} \\ &= \mp \int_z^0 d\varsigma_c \left(\frac{\partial \Delta\phi}{\partial z} + \frac{\partial \Delta\phi}{\partial t}\frac{d\overline{\lambda}}{d\varsigma_c}\right)^{STBD,PORT} \end{aligned} \qquad (2.20)$$

Note that in the linear case or for slender wings at mean angle of attack $\overline{\alpha}$, $\frac{d\overline{\lambda}}{d\varsigma_c} = \frac{1}{(U_\infty \cos \overline{\alpha})}$.

As discussed in Section 3.2, the incremental circulation associated with each vortex element is determined just as it enters the wake pattern so as to always maintain the postulated smooth flow at the edges. After that, each element is simply convected, at fixed elemental circulation, to new locations in the wake pattern.

3 Determining the Vortex Strength Distribution in the Wakes

3.1 2D Airfoil Case

In our treatment of this case we assume the Kutta condition to hold at the airfoil trailing edge at any instant. The airfoil itself is assumed to be a flat plate[1] in arbitrary

---

[1] A general 2D airfoil profile can be treated in the same manner, with only a minor elaboration of the technique used here.

plunging and/or pitching motion.

As already discussed, the unsteady airfoil motion requires the existence of a wake such as illustrated in Figure 2, so that the net circulation of the wake-plus-airfoil is constant. No linearizations of the airfoil motion of wake contortions are admitted in the present treatment.

The airfoil circulation can be described conveniently in two parts. The first, $\Gamma_0(t)$, is the "quasi-steady" Kutta value associated with the airfoil motion itself and calculated as if no wake were present. Thus, $\Gamma_0(t)$ is known for any specified airfoil motion. The general expression is

$$\Gamma_0 = -\pi c U_\infty \sin \alpha(t) + 2 \int_{-\frac{c}{2}}^{\frac{c}{2}} d\hat{x}\, \theta_0(\hat{x}, t) \sqrt{\frac{\frac{c}{2} + \hat{x}}{\frac{c}{2} - \hat{x}}} \quad (3.1)$$

where "c" is the airfoil chord, $\alpha(t)$ is the angle of attack, $\hat{x}$ is the instantaneous chordwise coordinate along the airfoil, and $\theta_0(\hat{x}, t)$ is the <u>actual</u> normal component of fluid velocity at the oscillating and plunging plate necessary to accommodate its unsteady motion. (See Figure 6). Then, without approximation, (see Ref. [1] for more details)

$$\theta_0 = \dot{h} \cos \alpha(t) - \hat{x} \dot{\alpha} \quad (3.2)$$

and

$$\Gamma_0(t) = -\pi c \left(U_\infty \sin \alpha - \dot{h} \cos \alpha \right) - \frac{\pi c^2}{4} \dot{\alpha}. \quad (3.3)$$

The bound vorticity associated with Γ_0 and θ_0 is called $\gamma_0(\hat{x}, t)$ and

$$\Gamma_0(t) = \int_{-\frac{c}{2}}^{\frac{c}{2}} \gamma_0(\hat{x}, t) d\hat{x}. \quad (3.4)$$

Defining the angle variable β such that $\hat{x} \equiv \frac{c}{2} \cos \beta$, we can write

$$\gamma_0(\hat{x}, t) = -2 \left(U_\infty \sin \alpha - \dot{h} \cos \alpha \right) \frac{1 - \cos \beta}{\sin \beta}$$
$$- c \dot{\alpha} \sin \beta \quad (3.5)$$

This "quasi-steady" bound vorticity would be all that is present if it weren't for the wake. But, as illustrated in Figure 6, and calculated in Eq. (2.12), the wake causes an apparent upwash at the airfoil which must be cancelled out by the action of additional bound vorticity on the airfoil, $\gamma_1(\hat{x}, t)$. The amount needed is given by the theory of conjugate functions in the form

$$\gamma_1(\hat{x}, t) = \frac{1 - \cos \beta}{\pi \sin \beta} \fint_0^\pi \frac{d\tau \left(-2\theta_{\text{wake}} \right) (1 + \cos \tau)}{\cos \tau - \cos \beta} \quad (3.6)$$

where, as in (3.5), the Kutta condition has been applied at the trailing edge. Correspondingly, the additional circulation on the airfoil, $\Gamma_1(t)$, is given by

$$\Gamma_1(t) \equiv \int_{-\frac{c}{2}}^{\frac{c}{2}} \gamma_1(\hat{x}, t) d\hat{x}$$
$$= 2 \int_{-\frac{c}{2}}^{\frac{c}{2}} d\hat{x} \left(-\theta_{\text{wake}}(\hat{x}, t) \right) \sqrt{\frac{\frac{c}{2} + \hat{x}}{\frac{c}{2} - \hat{x}}} \quad (3.7)$$

The quantity $\theta_{\text{wake}}(\hat{x}, t)$ can be obtained readily from (2.12). Using a system $\hat{z} \equiv e^{-i\alpha(t)}(z - ih(t)) = \hat{x} + i\hat{y}$ rotating and plunging with the airfoil, the normal component of the apparent wake velocity at the airfoil is determined. Inserting the result in (3.7) yields an expression for $\Gamma_1(t)$ in terms of an integral over the wake vorticity. Details of this calculation are available in Ref. [1].

The next step is to apply the Kelvin Theorem in the form

$$\Gamma_{\text{airfoil}}(t) + \Gamma_{\text{wake}}(t) = \text{constant} = \Gamma(0) \quad (3.8)$$

where $\Gamma(0)$ is any existing initial or steady-state airfoil circulation. For example, if the airfoil maneuver begins from steady flight at angle of attack α_0,

$$\Gamma(0) = -\pi c \sin \alpha_0.$$

But we have

$$\Gamma_{\text{airfoil}} = \Gamma_0(t) + \Gamma_1(t)$$

and $\Gamma_{\text{wake}}(t)$ is written out in Eq. (2.11), also in terms of an integral over the wake circulation elements. Cancellations occur, and the final result is, in complex-variable notation,

$$\Gamma_0(t) - \Gamma(0) = \text{Re} \int_0^t d\bar{\lambda}\, \Gamma'(\bar{\lambda}) \sqrt{\frac{\hat{z}_v(\bar{\lambda}, t) + \frac{c}{2}}{\hat{z}_v(\bar{\lambda}, t) - \frac{c}{2}}} \quad (3.9)$$

where "Re" means real part implied and

$$\hat{z}_v \equiv e^{i\alpha} \left(z_v - ih(t) \right)$$

with z_v as defined below (2.12).

Equation (3.9) was first derived by Wagner [17], in the linearized limit, and used by many authors to understand airfoil response to sudden starts, sudden (but small) changes in angle of attack, and flying through gusts. [18], [19] It seems remarkable that the non-linear version (3.9) of Wagner's equation is essentially the same as his original except that $\hat{z}_v(\bar{\lambda}, t)$ is complex, reflecting the distortion and roll-up of the wake. The principal mathematical nicety in the non-linear case is the need to determine the correct branch of the complex square root occurring in the integral.

The left-hand side of (3.9) is known as a function of t for any given imposed airfoil motion (see Eqn. (3.3), for example), so Eqn. (3.9) is an integral equation for the strengths, $d\Gamma(\bar{\lambda})$, of the circulation elements in the wake.

Operationally, on the computer, use of Eqn. (3.9) to determine the wake vorticity is relatively straightforward, except for finding the initial incremental vortex element at the very start of a maneuver. Difficulties arise there because the kernel on the *rhs* of (3.9) is singular. An effective method for treating this crucial first moment of the "starting problem" is described in Ref. [1]. After the procedure has been properly started, however, it runs easily because once the strength of a vortex element has been determined by (3.9), at the instant it enters the wake, that strength, as measured by *its* incremental circulation, remains unchanged as the element convects to its subsequent positions in the wake.

3.2 3-D Case. Smooth Flow at Both Edges

From Kelvin's theorem we know the net circulation in each cross-flow plane is zero:

$$\Gamma_{STBD} + \Gamma_{PORT} + \Gamma_{TRACE} = 0 \qquad (3.10)$$

We treat the 3D case in this paper in the slender-wing (low $\mathcal{R}$) limit, determining the velocity and potential field in each cross-flow plane on a quasi-two-dimensional basis in the spirit of Ref. [11]. In that limit we must determine the 2D potential solution in each observation plane corresponding to the concentrated vorticity on the wing trace and in the traces of the two wakes (Figure 7).[2]

In order to treat a general large-amplitude maneuver and still maintain an inertial frame "almost" moving with the wing, we specify a system moving with the mean or initial steady flight condition, as sketched in the figure. This initial or mean forward speed is U_∞, with angle of attack $\bar{\alpha}$. A cross-flow observation plane at any fixed z (analogous to the computer screen) is oriented normal to the wing surface in its initial or mean configuration. The observer in this plane sees an incoming steady free stream of speed U_∞ at angle $\bar{\alpha}$ to the z axis. Additional pitch, yaw, or roll of the wing, as well as plunging or sideslip of the wing vertex, are perceived in each observation plane as vertical or sideways displacements, $X_0(z,t)$ and $Y_0(z,t)$. Acceleration or deceleration of the vertex in the z-direction is seen as a

[2] For 3D wings and their wakes during sudden and violent maneuver the "slenderness direction" becomes somewhat ambiguous. Near and on the low $\mathcal{R}$ wing, for example, quantities may vary slowly in space only in the instantaneous chordwise direction, whereas this is generally misaligned with the original z-axis of Figure 7. The main wake structure, on the other hand, may still tend to be "slender" with respect to the original flight alignments. Ultimately, of course, use of the full 3D relations is required. We are suggesting here, however, that this be done after fully exploiting the additional insights to be gained in the Jones-Munk tradition.

growth or shrinking of the wing trace at any z. For maneuvers with very rapid forward acceleration or complete changes in flight direction, a frame fixed in the atmosphere may be preferable, with the wing flying "through" the observation plane or planes. Of course, one could also choose an observation system fixed in the wing, with attendant complications associated with non-inertial frames of reference. For our present purposes, we adopt the scheme shown in Figure 7.

In complex-variable notation the quasi-2D cross-flow velocity field associated with the wakes is, with $Z = X + iY$,

$$U_{\text{wake}} - iV_{\text{wake}} = W_{\text{wake}}(Z)$$

$$= \frac{1}{2\pi i} \left\{ \int_0^z d\varsigma_c \frac{d\Gamma^{STBD}(\varsigma_c, \bar{\lambda})}{d\varsigma_c} \frac{1}{Z - Z_v^{STBD}} \qquad (3.11) \right.$$

$$\left. + \int_0^z d\varsigma_c \frac{d\Gamma^{PORT}(\varsigma_c, \bar{\lambda})}{d\varsigma_c} \frac{1}{Z - Z_v^{PORT}} \right\}$$

in analogy with (2.12). Here, we have used (2.19) and $Z_v^{STBD}(\varsigma_c, t, z)$ and $Z_v^{PORT}(\varsigma_c, t, z)$ are the instantaneous complex locations in any given cross-flow plane (x, y) of the vorticity elements in the starboard and port wake traces respectively. In the following we also have use for

$$\hat{W}_{\text{wake}}(z) \equiv e^{-iK} W_{\text{wake}}$$

$$= \hat{U}_{\text{wake}} - i\hat{V}_{\text{wake}}.$$

The boundary condition at the wing trace as viewed in each cross-flow plane can be written in a form somewhat similar to that in (3.2) for the 2D airfoil. Using the coordinates suggested in Figure 7 the actual component of velocity in the (x, y) plane normal to the instantaneous wing trace can be written

$$\hat{U}_0(\hat{y}, z, t) = \frac{D_z X_0(z,t)}{Dt} \cos K + \frac{D_z Y_0(z,t)}{Dt} \sin K$$

$$-\hat{y} \frac{D_z K(z,t)}{Dt} \qquad (3.12)$$

where $\frac{D_z}{Dt} \equiv \frac{\partial}{\partial t} + \overline{W} \frac{\partial}{\partial z}$. For a low $\mathcal{R}$ wing in steady forward flight without pitch or yaw, for example, $\overline{W} = U_\infty \cos \bar{\alpha}$, since the additional fluid speed in the chordwise direction is negligible because of the wing slenderness. During pitch and yaw, however, $\overline{W}$ requires adjustment to allow for the instantaneous flight angles and the fact that the chordwise (or "slenderness") direction is then misaligned with the z-axis chosen in Figure 7.

Starting from the mean or initial steady flight condition described above, an observer on the wing sees an effective cross-flow from below of $U_\infty \sin \bar{\alpha}$, the normal component of which is $U_\infty \sin \bar{\alpha} \cos K$. Eqn. (3.12) then allows for any additional unsteady wing motion, including any acceleration of the wing vertex as well as pitch, yaw and roll about specified axes. Any built-in camber of the wing can also be included in the form (3.12). The angle "K" is an apparent

"roll" angle, observed at fixed z, which is actually a composite of the usual Euler angles. For this reason X_0, Y_0 and K can depend on z as well as t. For simplicity we assume the wing trace to be flat, although the method used here can be generalized to include any moderately thin cross section as well as control surface deflections. Note that $\hat{y}$, in this case, is the instantaneous spanwise coordinate as shown in Figure 7, and $\frac{\hat{b}}{2}$ is the effective semispan at that instant at the specified z. Thus, $X_0(z, t)$, $Y_0(z, t)$ give the instantaneous position of the mid-effective span which is not on the wing center line during yaw.

If there were no wake the discontinuous part of the velocity at the wing trace, $\Delta \hat{V}_0$, would be

$$\Delta \hat{V}_0|_{\text{trace}} =$$
$$-\frac{2\hat{y}}{\sqrt{\frac{\hat{b}^2}{4} - \hat{y}^2}} \left[\left(U_\infty \sin \overline{\alpha} - \frac{DX_0}{Dt} \right) \cos K - \sin K \frac{D_s Y_0}{Dt} \right]$$
$$+ 2 \frac{D_s K}{Dt} \left(\sqrt{\frac{\hat{b}^2}{4} - \hat{y}^2} - \frac{\left(\frac{\hat{b}^2}{8}\right)}{\sqrt{\frac{\hat{b}^2}{4} - \hat{y}^2}} \right) \quad (3.13)$$

since in that case, according to (3.10), we would have $\Gamma_{TRACE} = 0$. For example, in the limit of steady motion at small $\overline{\alpha}$ and with no yaw, pitch or roll, (3.13) reduces to

$$\Delta \hat{V}_0|_{\text{trace}} = -\frac{2y}{\sqrt{\frac{\hat{b}^2}{4} - y^2}} U_\infty \overline{\alpha} \quad (3.13a)$$

corresponding to Jones' classical result {11}. Note that in either (3.13) or (3.13a) the flow predicted in this way (without vortical wakes above the wing) is singular at the wing edges. The next step is to add the wakes and to determine their vorticity distributions so as to "smooth" the flow at the edges.

In a manner similar to that used for the 2D airfoil, we introduce an "angle variable" such that

$$\hat{y} = \frac{\hat{b}}{2} \sin \beta \quad (3.14)$$

and use the theory of conjugate functions to write down the additional vorticity (or jump in $\hat{V}$) required at the wing trace in order to continue to satisfy the boundary condition (3.12) despite the velocity field (3.11) induced by the wakes. The result is

$$\Delta \hat{V}|_{\text{trace}} \equiv \Delta \hat{V}_0|_{\text{trace}} + \Delta \hat{V}_1|_{\text{trace}}$$

where

$$\Delta \hat{V}_1|_{\text{trace}} = +\frac{2\Gamma_{TRACE}(z,t)}{\pi \hat{b} \cos \beta}$$
$$+ \frac{2 \tan \beta}{\pi} \int_{-\frac{\pi}{2}}^{\frac{\pi}{2}} \frac{d\tau \left(-\hat{U}_{\text{wake}} \cos \tau \right)}{\cos \tau - \cos \beta} \quad (3.15)$$

The wing-edge singularities in these additional "wake-induced" terms must exactly cancel the singularities in

$\Delta \hat{V}_0|_{\text{trace}}$ at both edges of the wing if our Kutta-condition postulate is to be satisfied. Note that at this point we can no longer simply assume $\Gamma_{TRACE} = 0$, but must apply (3.10) in order to try to determine it.

In Eqn. (3.15) $\hat{U}_{\text{wake}}(\hat{y}, t)$ can be written down in terms of the wake integrals in (3.11). Cancellation of the singularities at both wing edges then requires

for $\hat{y} = +\frac{\hat{b}}{2}$:

$$2 \left[\left(U_\infty \sin \overline{\alpha} - \frac{DX_0}{Dt} \right) \cos K - \sin K \frac{D_s Y_0}{Dt} \right] + \hat{b} \frac{D_s K}{Dt}$$
$$= \frac{2\Gamma_{TRACE}(z,t)}{\pi \hat{b}}$$
$$+ Re \frac{i}{\pi} \int_0^z d\varsigma_c \left\{ \frac{\frac{d\Gamma^{PORT}}{d\varsigma_c}}{\sqrt{\left(\hat{Z}_v^{PORT}\right)^2 + \frac{\hat{b}^2}{4}}} + \frac{\frac{d\Gamma^{STBD}}{d\varsigma_c}}{\sqrt{\left(\hat{Z}_v^{STBD}\right)^2 + \frac{\hat{b}^2}{4}}} \right\}$$

for $\hat{y} = -\frac{\hat{b}}{2}$:

$$2 \left[\left(U_\infty \sin \overline{\alpha} - \frac{DX_0}{Dt} \right) \cos K - \sin K \frac{D_s Y_0}{Dt} \right] - \hat{b} \frac{D_s K}{Dt}$$
$$= -\frac{2\Gamma_{TRACE}(z,t)}{\pi \hat{b}}$$
$$+ Re \frac{i}{\pi} \int_0^z d\varsigma_c \left\{ \frac{\frac{d\Gamma^{PORT}}{d\varsigma_c}}{\sqrt{\left(\hat{Z}_v^{PORT}\right)^2 + \frac{\hat{b}^2}{4}}} + \frac{\frac{d\Gamma^{STBD}}{d\varsigma_c}}{\sqrt{\left(\hat{Z}_v^{STBD}\right)^2 + \frac{\hat{b}^2}{4}}} \right\}$$

In the above relations

$$\hat{Z}_v^{PORT} \equiv e^{-iK(z,t)} \left(Z_v^{PORT}(\varsigma_c, t, z) - (X_0 + iY_0) \right)$$

and

$$\hat{Z}_v^{STBD} \equiv e^{-iK(z,t)} \left(Z_v^{STBD}(\varsigma_c, t, z) - (X_0 + iY_0) \right)$$

with the Z_v as defined below (3.11).

Taking the difference of the two equations involving Γ_{TRACE} yields $\Gamma_{TRACE} = \left(\frac{\pi \hat{b}^2}{2} \right) \frac{D_s K}{Dt}$, so that we obtain the constraint

$$\Gamma_{PORT}(z,t) + \Gamma_{STBD}(z,t) = -\frac{\pi \hat{b}^2}{2} \frac{D_s K}{Dt} \quad (3.16)$$

The sum of the two relations then yields an equation for the vorticity strengths (circulation elements) in the wake traces which is analogous to the Wagner integral equation (3.9). The result is

$$\left(U_\infty \sin \overline{\alpha} - \frac{DX_0}{Dt} \right) \cos K - \sin K \frac{D_s Y_0}{Dt}$$
$$= Re \frac{i}{2\pi} \int_0^z d\varsigma_c \left\{ \frac{\frac{d\Gamma^{PORT}(\varsigma_c, \overline{\lambda})}{d\varsigma_c}}{\sqrt{\left(\hat{Z}_v^{PORT}\right)^2 + \frac{\hat{b}^2}{4}}} + \frac{\frac{d\Gamma^{STBD}(\varsigma_c, \overline{\lambda})}{d\varsigma_c}}{\sqrt{\left(\hat{Z}_v^{STBD}\right)^2 + \frac{\hat{b}^2}{4}}} \right\}$$
$$(3.17)$$

The left-hand-side of (3.17) is known at each z and t for any given imposed wing motion. Thus, (3.17), together with (3.16) and (2.20), determines the circulation elements throughout the wake system within the present model. Solution proceeds in a manner mathematically quite similar to the 2D airfoil case.

4 Loads, Forces and Moments

4.1 2D Airfoil Case. Large-Amplitude Unsteady Response

In Ref. [1] the forces and moments occurring on 2D airfoils in large-amplitude unsteady motion were calculated using the pressures over the airfoil surface as predicted by the Bernoulli equation for unsteady potential flow. In reckoning the lift, a "leading-edge force" was included in the classical manner, except that no linearizations were admitted. This procedure was built into the "NLWAKE" code reported in [1].

More recently, we have reformulated the lift and moment expressions by taking advantage of the possibility of expressing all or most wake-related terms (without linearizing) in terms of the corresponding "wake integrals" - integrals over the (known) wake vorticity. This step mimics classical procedures in the linear theory [18] and establishes the equivalence of the original formulation in Ref. [1] with the application of the principle of conservation of impulse. Most importantly, the reformulation greatly improves the numerical accuracy achievable in the codes. The reason is that several large contributing terms in C_ℓ and C_{m_0} in NLWAKE almost exactly cancel, leaving crucial small differences which can be difficult to calculate with sufficient accuracy. In the extension of NLWAKE to include the new formulation, these partial cancellations are explicit and the remainders are written in a manner more suited to precise numerical evaluation.

The (non-linear) expressions for lift and moment including the appropriate wake integrals in this way are written out here both for completeness and for comparison with their classical linear versions. For the lift coefficient, using the notation of Eqn. (2.11), (3.3) and (3.5), we find

$$C_\ell(t) = -\frac{2\Gamma_0}{U_\infty c}\left(\frac{\overline{U}}{U_\infty}\right) + \frac{2c}{U_\infty \cos\alpha}\frac{d}{dt}\int_{-\frac{c}{2}}^{\frac{c}{2}} \frac{d\hat{x}\,\hat{x}\,\gamma_0(\hat{x},t)}{c^2 U_\infty}$$

$$- \frac{2}{c\cos\alpha}Re\int_0^t \frac{d\lambda\Gamma'(\lambda)}{U_\infty^2}\left(\frac{c}{2}\frac{da}{dt}\right)\frac{1}{\sqrt{a^2-1}} \qquad (4.1)$$

$$+ \frac{2}{c\cos\alpha}Re\int_0^t \frac{d\lambda\Gamma'(\lambda)}{U_\infty^2}\left[\left(\frac{c}{2}\frac{da}{dt}\right) - \overline{U}\cos\alpha\right]\left\{\sqrt{\frac{a+1}{a-1}} - 1\right\}$$

$$+ C_{\ell\text{wake}}(t)$$

where $a \equiv 2\hat{x}_v/c$ with $\hat{x}_v$ defined as below (3.9), and $\overline{U} \equiv U_\infty + \dot{h}\tan\alpha$. The small non-linear term $\tilde{C}_{\ell\,\text{wake}}(t)$ is

$$\tilde{C}_{\ell\,\text{wake}}(t) \equiv$$

$$-\frac{2}{cU_\infty^2\cos\alpha}\int_{-\frac{c}{2}}^{\frac{c}{2}} d\hat{x}\,\hat{u}_\text{wake}\,(\hat{x},t)\,(\gamma_0(\hat{x},t) + \gamma_1(x,t)),$$

$$(4.1a)$$

and can also be written out in terms of wake integrals. The resulting expression is cumbersome, however. It is perhaps

more useful here simply to note that $\tilde{C}_{\ell\,\text{wake}}$ vanishes identically in the linear limits of a wake extending straight behind the airfoil since it involves $\hat{u}_\text{wake}$. Also, we have not yet encountered a case, even in the non-linear treatment, for which $\tilde{C}_{\ell\,\text{wake}}$ has been important, even though it clearly can be significant or even crucial, for a maneuver in which the airfoil flies "through," or just above or below, its own wake.

The fourth term on the *rhs* of (4.1) also vanishes in the linear limit, since in that case both $\frac{c}{2}\left(\frac{da}{dt}\right)$ and $\overline{U}\cos\alpha$ approach U_∞. This term in fact illustrates the numerical advantage of the wake-integral formulation, since it represents explicitly the partial cancellation between two otherwise quite large terms.

The first three terms on the *rhs* of (4.1), on the other hand, approach their classical linear counterparts exactly in the limit of small amplitude motion. The 2nd term is often called the "apparent mass" term, and the 3rd the "wake effect." Thus, on using (4.1), we know that the non-linear theory appropriately reproduces the linear version, and includes it.

The corresponding moment coefficient, C_{m_0}, about midchord is given in similar fahsion by

$$C_{m_0}(t) = -2\frac{\overline{U}\cos\alpha}{U_\infty}\int_{-\frac{c}{2}}^{\frac{c}{2}}\frac{d\hat{x}\,\hat{x}\,\gamma_0(\hat{x},t)}{c^2 U_\infty}$$

$$+ \frac{c}{U_\infty}\frac{d}{dt}\int_{-\frac{c}{2}}^{\frac{c}{2}}\frac{d\hat{x}\,\gamma_0\,(\hat{x},t)\left(\hat{x}^2 - \frac{c^2}{8}\right)}{c^3 U_\infty} \qquad (4.2)$$

$$+ \frac{1}{2c}Re\int_0^t \frac{d\lambda\Gamma'(\lambda)}{U_\infty^2}\left(\frac{c}{2}\frac{da}{dt}\right)\frac{1}{\sqrt{a^2-1}}$$

$$+ \frac{1}{c}Re\int_0^t \frac{d\lambda\Gamma'(\lambda)}{U_\infty^2}\left[\left(\frac{c}{2}\frac{da}{dt}\right) - \overline{U}\cos\alpha\right]\left\{\sqrt{a^2-1} - a\right\}$$

$$+ \tilde{C}_{m\,\text{wake}}(t)$$

where

$$\tilde{C}_{m\,\text{wake}}(t) \equiv$$

$$\frac{-2}{c^2U_\infty^2}\int_{-\frac{c}{2}}^{\frac{c}{2}}\hat{x}d\hat{x}\,\hat{u}_\text{wake}(\hat{x},t)\,(\gamma_0(\hat{x},t) + \gamma_1(\hat{x},t)). \qquad (4.2a)$$

Once again, the final two terms on the *rhs* of (4.2) vanish at small amplitudes, and the first three terms reduce precisely to their classical counterparts in the linear limit.

Computer-generated results corresponding to Eqns. (4.1) and (4.2) are illustrated in Section 5 in terms of 2D airfoil response to large-amplitude imposed motions.

4.2 3D Case. Loads and Normal-Force Distribution on Slender Wings

The pressure difference, or loading, across the wing for the 3D case can again be calculated using the Bernoulli equation for unsteady potential flow on either side of the

wing. As before, the wake-related terms are two-fold. First, the associated velocity field of the wake, as given by Eqn. (3.11), contributes directly to the pressure variations. Secondly, the apparent upwash caused by the wake must be *cancelled out by the effects of an addition wing-trace vorticity*, $\Delta V_1(\hat{y}, t)$, as given in (3.15), thus implying an additional jump in the $\frac{\partial \phi}{\partial t}$ term in the Bernoulli relation. In calculating the latter we take advantage of the possibility of writing $\phi(x, y, t)$ on the wing on either side $(+, -)$ as

$$\phi^{\pm}(x, y, z, t) \equiv \Phi(z, t; \hat{y}, \hat{x} = 0^{\pm})$$

where the coordinates $(\hat{x}, \hat{y})$ are as illustrated in Figure 7. We find, for slender wings, with $\underset{\sim}{V} = (\hat{u}, \hat{v}, \hat{w})$

$$-\frac{1}{\rho_\infty}\Delta p \equiv \frac{1}{\rho}p\Big]_{\text{bottom}}^{\text{top}} \equiv p^-(z, t; \hat{y}, 0^-) - p^+(z, t; \hat{y}, 0^+)$$

$$= <\underset{\sim}{V}> \cdot \Delta\underset{\sim}{V} + \Delta\left(\frac{\partial \phi}{\partial t} + w\frac{\partial \phi}{\partial z}\right) \qquad (4.3)$$

$$\cong <\hat{V}> \Delta\hat{V}$$

$$+ \frac{D_z}{Dt}\Delta\Phi(z, t; \hat{y}) + \Delta\hat{V}\left(\frac{D_z X_0}{Dt}\sin K - \frac{D_z Y_0}{Dt}\cos K\right)$$

where $\frac{D_z}{Dt} \equiv \frac{\partial}{\partial t} + \overline{W}\frac{\partial}{\partial z}$ as before. In writing (4.3) we have also used the notation defined in (2.6) and (2.7) and below (3.12), as well as in Figure 7.

As mentioned in Section (3.2) proper use of the slender-wing concept allows us to repace $\hat{W}$ with $\overline{W}$, provided we recall that the low $\mathcal{R}$ wing is "slender" along the chordwise direction and not necessarily along the z-direction during violent pitch and yaw.

The $\Delta\Phi$ occurring in (4.3) can be written

$$\Delta\Phi(\hat{y}, z, t) = \Gamma_{STBD}(z, t)$$

$$+ \int_{-\frac{\hat{b}}{2}}^{\hat{y}} d\hat{y}\, \Delta\hat{V}(\hat{y}, z, t) \qquad (4.4)$$

where $\Delta\hat{V}$ is given in (3.13) and (3.15). Further, $<\hat{V}> = -U_\infty \sin\overline{\alpha}\sin K + \hat{V}_{\text{wake}}$.

Expression (4.3), with (4.4), lends itself to relatively straightforward calculation of the normal force distribution $C_n(z, t)$. Spanwise integration with respect to $\hat{y}$ proceeds in a manner mathematically the same as for the 2D airfoil case, except that in the present model no edge forces are included. The lift and drag and also the roll, pitch, and yaw moments of a given wing can be reckoned in a similar manner, on including subsequent weighted integrations over z. We find

$$C_n(z, t) \equiv \frac{2}{\rho U_\infty^2 \hat{b}(z, t)}\int_{-\frac{\hat{b}}{2}}^{\frac{\hat{b}}{2}} d\hat{y}\ p]\,(\hat{y}, z, t)$$

$$= \frac{1}{U_\infty^2}\frac{D_z}{Dt}\left\{\frac{\pi\hat{b}}{2}U_\infty \sin\overline{\alpha}\cos K\right.$$

$$\left. -\frac{\pi\hat{b}}{2}\left(\frac{D_z X_0}{Dt}\cos K + \frac{D_t Y_0}{Dt}\sin K\right)\right\}$$

$$- \left(\frac{\pi\hat{b}}{U_\infty^2}\frac{D_z K}{Dt}\right)\left\{U_\infty \sin\overline{\alpha}\sin K\right.$$

$$\left. -\frac{D_z X_0}{Dt}\sin K + \frac{D_z Y_0}{Dt}\cos K\right\} \qquad (4.5)$$

$$+ C_{n_{\text{wake}}} + \tilde{C}_n$$

where

$$C_{n_{\text{wake}}}(z, t) \equiv \frac{1}{U_\infty^2}\frac{D_z}{Dt}\left\{\hat{b}\int_{-\frac{\hat{b}}{2}}^{\frac{\hat{b}}{2}} d\beta\,(\cos^2\beta)\,\hat{U}_{\text{wake}}\right.$$

$$\left. +\frac{\Gamma^{STBD} - \Gamma^{PORT}}{2}\right\} \qquad (4.5a)$$

and

$$\tilde{C}_n(z, t) \equiv \frac{1}{U_\infty^2}\int_{-\frac{\hat{b}}{2}}^{\frac{\hat{b}}{2}} d\beta\cos\beta\hat{V}_{\text{wake}}\left(\Delta\hat{V}_0 + \Delta\hat{V}_1\right) \qquad (4.5b)$$

Using (3.11) we can express $C_{n_{\text{wake}}}(z, t)$ in terms of a wake integral analogous to the 2D airfoil case. The result is

$$C_{n_{\text{wake}}}(z, t)$$

$$= \frac{1}{U_\infty^2}\frac{D_z}{Dt}Re\int_0^z d\zeta_c\left\{\frac{d\Gamma^{STBD}}{d\zeta_c}\left(\frac{1}{2} - ia_s - i\sqrt{a_s^2 + 1}\right)\right.$$

$$\left. +\frac{d\Gamma^{PORT}}{d\zeta_c}\left(-\frac{1}{2} - ia_p - i\sqrt{a_p^2 + 1}\right)\right\} \qquad (4.6)$$

where

$$a_s \equiv 2Z_v^{STBD}/\hat{b}\ ;\quad a_p \equiv 2Z_v^{PORT}/\hat{b}$$

and we note $a_s = -i$ at the starboard edge and $a_p = +i$ at the port edge.

In the interactive method for the slender wing case this latter "wake-integral" is easy to calculate on the computer, since the necessary information becomes available automatically at the same time the wake structure itself is being generated using the method described in Section (3).

The $\tilde{C}_n(z, t)$ term can also be calculated in terms of wake integrals, and that approach appears to be the most convenient and numerically accurate method to determine its value. We note here only that $\tilde{C}_n$ has no linear counterpart (and vanishes by symmetry in certain simple flight configurations), yet its effect appears to be potentially of great importance in certain maneuvers involving intimate interaction between the wing and its wakes.

The first term on the *rhs* of (4.5) corresponds for small $\overline{\alpha}$ to the linear theory result of Ref. [11]. In fact, for pointed slender wings in steady flight at small $\overline{\alpha}$, this term integrates chordwise to yield

$$C_L \doteq \frac{\pi\mathcal{R}}{2}\overline{\alpha}, \qquad (4.7)$$

the classical Jones result. The additional terms in the corresponding curly brackets represent the local, instantaneous

normal-force effects of plunge, pitch, etc., that would arise if there were no wakes.

The wake-integral terms, $C_{n_{wake}}(z,t)$ and $\bar{C}_n(z,t)$, represent "history effects" in the relationship between wing motion and wing loading or response. As we have seen, the various vorticity elements in each wake reflect conditions imposed at upstream wing edges, each at an earlier time. Thus, for example, in the event of a sudden maneuver of short duration, the outer parts of the wake affecting $C_n(z,t)$ will often represent wing attitude and other conditions in effect before the maneuver began. Conversely, after a given maneuver is "over", many outer wake elements will still reflect the actions taken during the maneuver, so that wing loading will take time to adjust and/or return to "normal." Naturally, any occurrence of vortex breakup can have a drastic effect on this history-related part of the wing response, although it may not always be unfavorable. Of course, before we can regard wing response as "deterministic" we must learn how to predict both the occurrence and specific nature of such vortex bursting. [12]-[14]

5 Typical On-Line Results: Non-Linear 2D Airfoil Response

A critical part of studying the behavior of wings in maneuver is the understanding of the wing's aerodynamic response to new conditions suddenly imposed. Representative of such response are, for the 2D case, the results of the classical Wagner problem, illustrated for the low-amplitude (linear) case in Figure 8(a). The net bound circulation on the airfoil, $\Gamma_0 + \Gamma_1$, adjusts only gradually to the suddenly imposed change in angle-of-attack as represented by the jump in Γ_0. The lift coefficient jumps to $\frac{1}{2}$ its eventual value and gradually adjusts. Note that the relaxation to the quasi-steady result, is very slow. On the Figures, time is normalized to $\left(\frac{1}{4}\right)(c/U_\infty)$.

The corresponding nonlinear (large-amplitude) case is illustrated in Figure 9(a). Note that the response is very similar to the linearized result, despite the relatively severe deformation of the wake as illustrated in Figure 9(b). This appears to be a result of the fact that the wing in each case is adjusting to shed vorticity which is rather strongly concentrated toward the far reaches of the wake, ultimately several chord lengths downstream.

Illustration of the airfoil's aerodynamic response to a rudimentary but severe maneuver is illustrated in Figure 10. There, a sudden single-cycle sinusoidal angle of attack variation of large amplitude is imposed and just as suddenly stopped. The wake vorticity coagulates and begins roll-up without significant net displacement from the plane of the airfoil (Figure 10(a)). The lift jumps quickly, and then leads the quasi-steady value into the negative lift region (Figure 10(b)). It then overshoots the recovery, plunges again, and only very slowly recovers to the state before the maneuvers, illustrating a "history effect" for the 2D case suggestive of the phenomena discussed at the end of Section 4. During the maneuver, from start to finish, the airfoil advances 5 chord lengths in this example. Both "apparent mass" effects and upwash associated with the developing wake play vital roles in the net result.

The pitching moment for this example, though large in amplitude, is essentially classical in response, except for the relatively pronounced history effect after the maneuver is complete (Figure 10(c)).

A number of additional examples of airfoil response to imposed large-amplitude motions of various types are reported in Ref. [1]. It is especially instructive, in addition to the figures, to actually run the codes of [1] on-line, taking advantage of the almost instantaneous wake displays to develop a sense of airfoil response and the reasons for it. Several of these "flight" sessions have been taped recently. In the 3D case one can carry out similar on-line runs with split-screen displays of the wing configuration, wake deformations at various locations, and wing loading response.
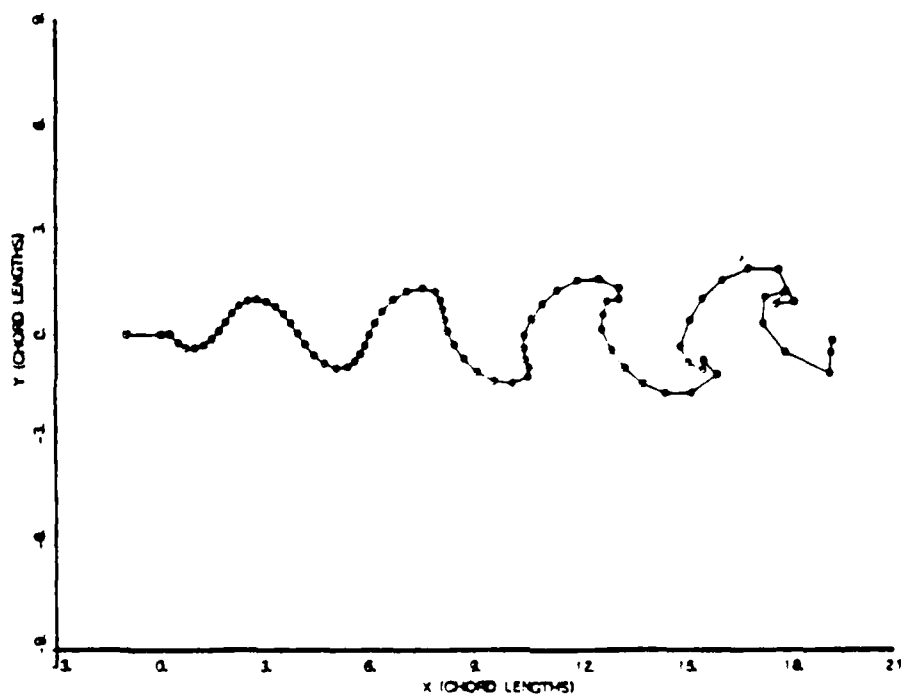
References

1. Scott, Matthew T., "Nonlinear Airfoil-Wake Interactions in Large Amplitude Unsteady Flow," M.I.T. Master's Thesis, June, 1987. See also: Scott, M. and McCune, J.E. AIAA paper Nr. 88-0129, AIAA 26th Aerospace Science Meeting, Reno NV, Jan., 1988.

2. Lamb, Sir Horace, *Hydrodynamics*, 6th edition, Dover Publ., N.Y., 1945.

3. Mook, D.T., et.al., "On the Numerical Simulation of the Unsteady Wake Behind an Airfoil," AIAA-87-0190, Jan., 1987.

4. Adams, Mac, "Leading Edge Separation from Delta Wings at Supersonic Speeds," J. Aeron. Sci., 21, Readers Forum, June, 1953.

5. Edwards, R.H., "Leading Edge Separation from Delta Wings," J. Aeron. Sci., 21, Readers Forum, Nov., 1953.

6. Cheng, H.K., "Remarks on Non-Linear Lift and Vortex Separation," J. Aeron. Sci., 21, Readers Forum, Dec., 1953.

7. Brown, C.E., and Michael, W.H., Jr., "Effects of Leading Edge Separation on the Lift of a Delta Wing," J. Aeron. Sci., 22, 1954.

8. Mangler, K.W., and Smith, J.H.B., "A Theory of the Flow Past a Slender Delta Wing with Leading Edge Separation," Proc-Roy Soc. 251, 200-217, 1959.

9. Powell, Kenneth G., "Vortical Solutions of the Conical Euler Equations," M.I.T. Ph.D. Thesis, June, 1987.

10. Müller, Berndhard, and Rizzi, Arthur, "Navier-Stokes Computation of Transonic Vortices Over a Round Leading Edge Delta Wing," AIAA Paper Nr. 87-1227, AIAA 19th Fluid Dyn., Plas. Dyn., and Laser Conf., Honolulu, June, 1987.

11. Jones, R.T., "Properties of Low-Aspect-Ratio Pointed Wings at Speeds Below and Above the Speed of Sound," NACA TR 835, 1946.

12. Hall, M.G., "Vortex Breakdown," Annual Review of Fluid Mechanics, Vol. 4, 1972, pp. 195-218.

13. Lambourne, N.C. and Bryer, D.W., "The Bursting of Leading Edge Vortices; Some Observation and Discussion of the Phenomenon," Aeronautical Research Council, R and M 3282, 1961.

14. Reynolds, G.A. and Abtahi, Ali, "Vortex Dynamics for Transient Flight Conditions," Lockheed-Georgia Company, Presented at AFOSR Workshop on Unsteady Separated Flows, Air Force Academy, 28-30, July, 1987.

15. Murman, E.M., Powell, K.G., Goodsell, A.M., and Landahl, M.T., "Leading Edge Vortex Solutions with Large Total Pressure Losses," AIAA Paper Nr. 87-0039, AIAA 25th Aerospace Sciences Meeting, Reno, NV, Jan., 1987.

16. McCune, J.E., Tavares, T. Sean, Lee, Norman, and Weissbein, David, "Slender Wing Theory Including Regions of Embedded Total Pressure Loss," AIAA Paper Nr. 88-0320, AIAA 26th Aerospace Sciences Meeting, Reno, NV, Jan. 1988.

17. Wagner, H., "Dynamischer Auftrieb von Tragflügeln," Zeitschr. f. Angew. Math. u. Mech. (ZAMN), 5, 17, 1925.

18. von Karman, T., and Sears, W.R., "Airfoil Theory for Non-Uniform Motion," J. Aeron. Sci., 5, 10, 1935.

19. Küssner, H.G., "Zusammenfassender Bericht über den instationären Auftrieb von Flügeln," Luftfahrtforschung, Bd. 13, page 410, 1936.

20. Ashley, H. and Landahl, M., *Aerodynamics of Wings and Bodies*, Dover edition, Dover Publ., N.Y., 1985.
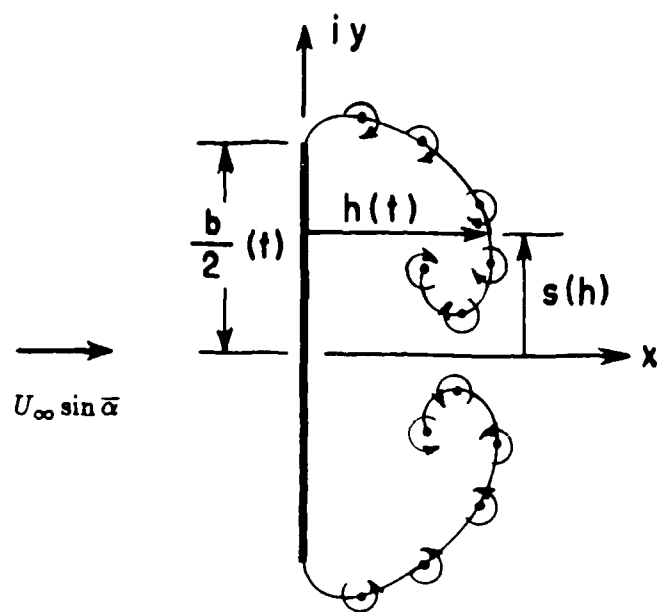
Airfoil Trailing Edge · Particle Path Lines · Streakline
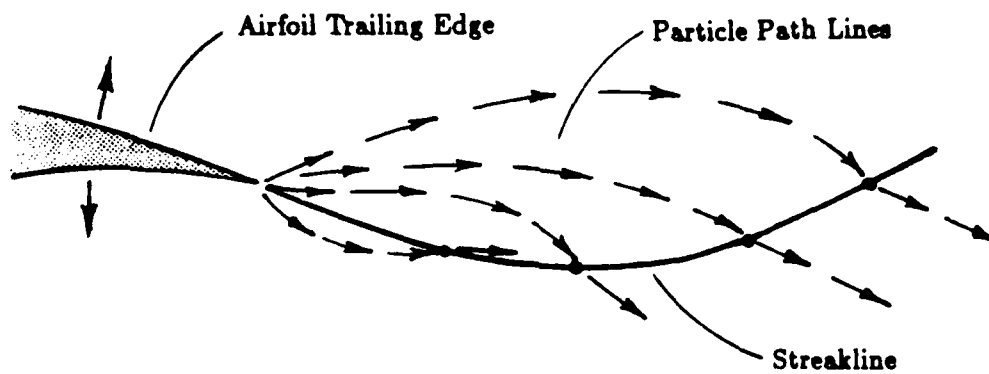
1. Particle Paths vs. Streakline. Formation of a Vortex Sheet.

2. Wake Behind an Oscillating Airfoil.

172

Non-Linear Case (fr. Ref. [20])
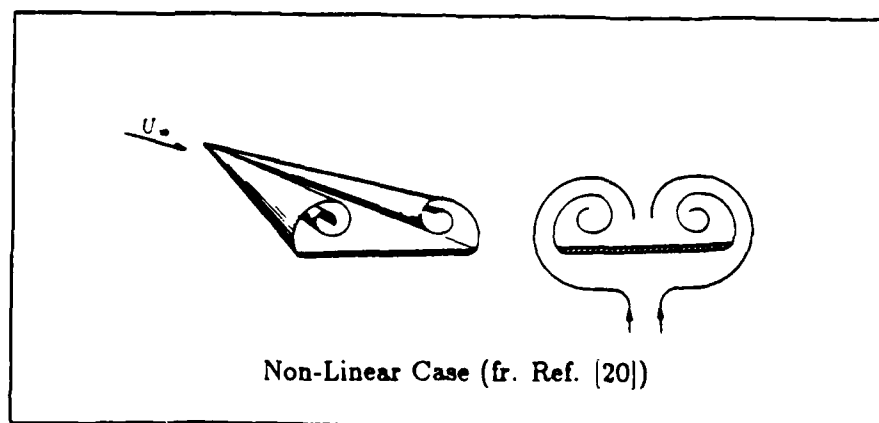
3. Sketch of Wakes from a Delta Wing.
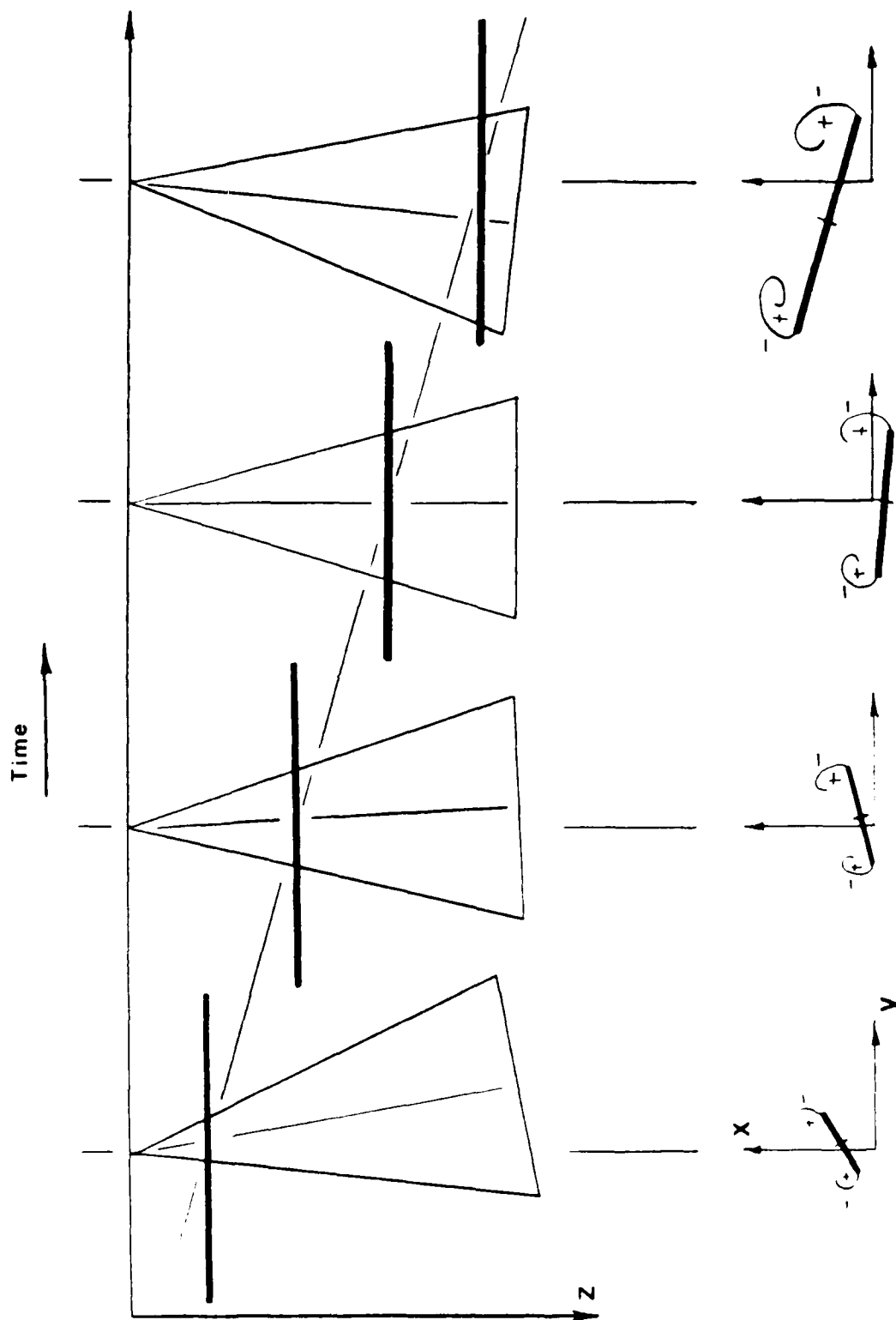
a)

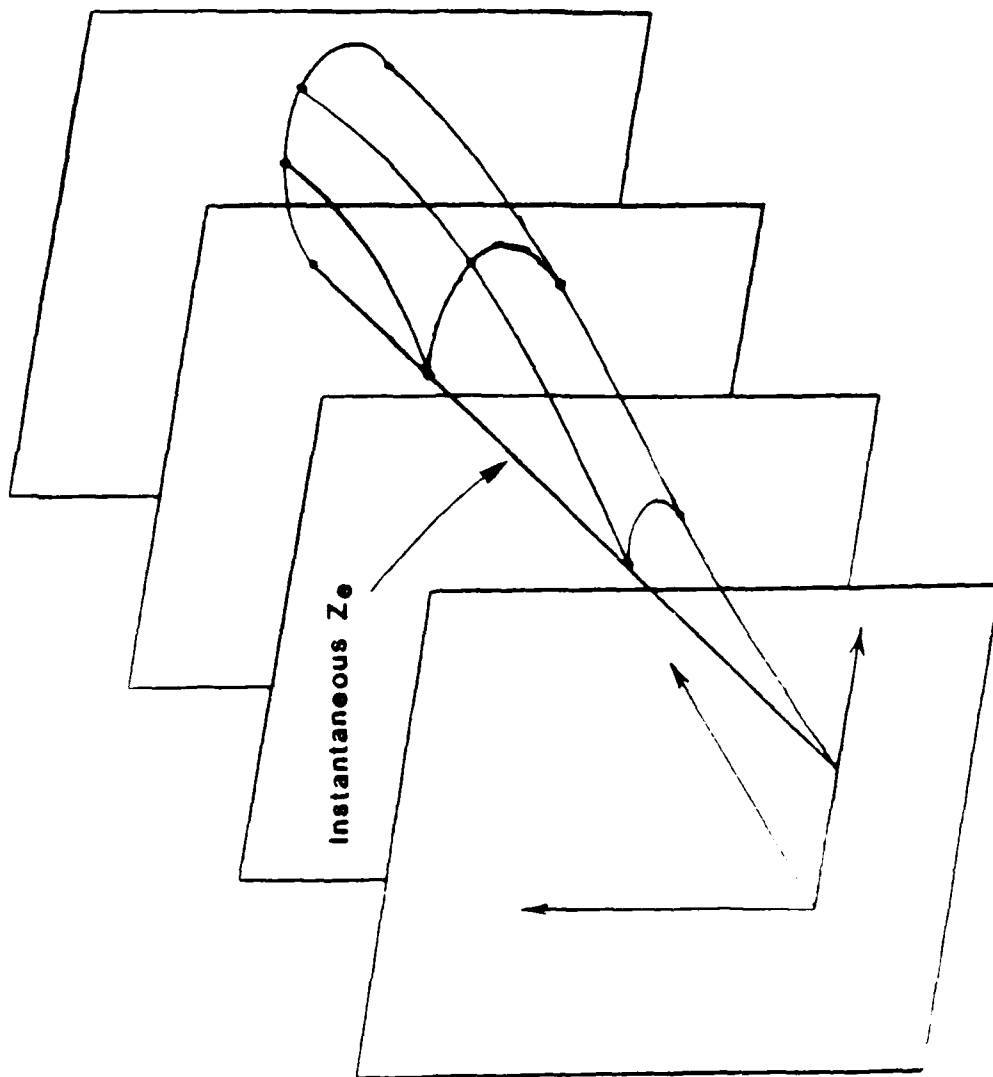Top View

Side View

View In Cross-Flow Plane
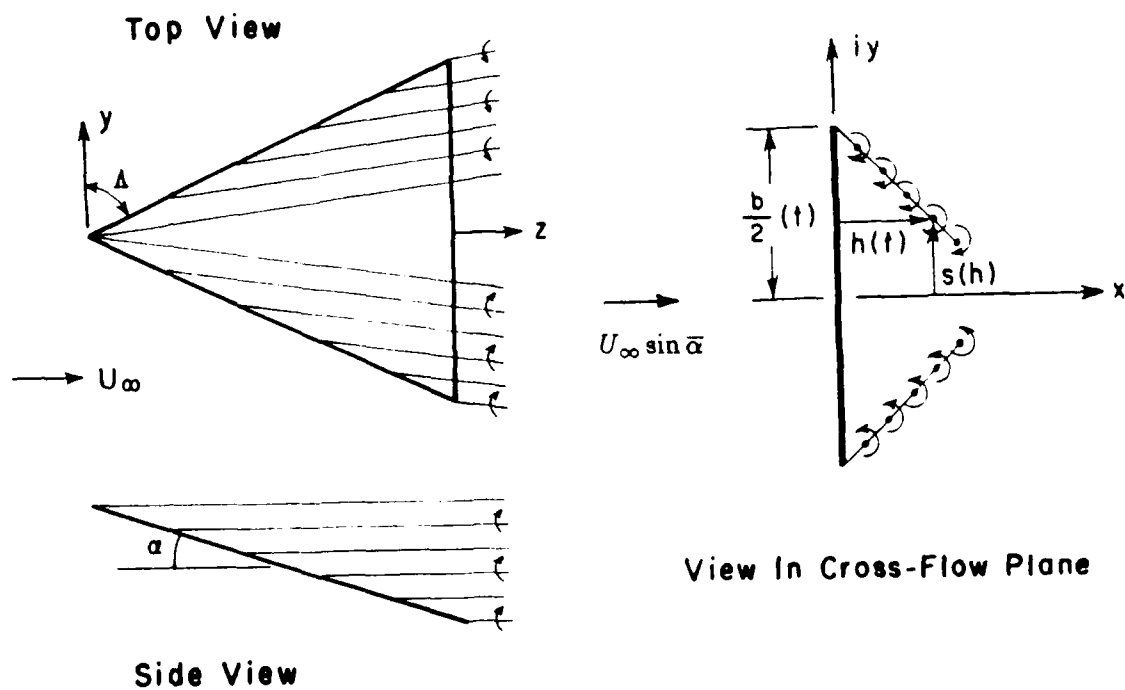
b)
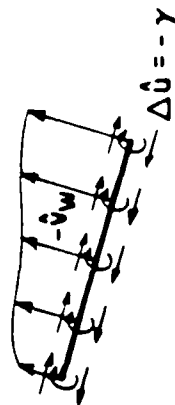
4. Typical Wake Traces. a) Non-Linear. b) Linear, Idealized

5. Wing in Maneuver. a) Wing and Wake Traces at Various Chordwise Locations.

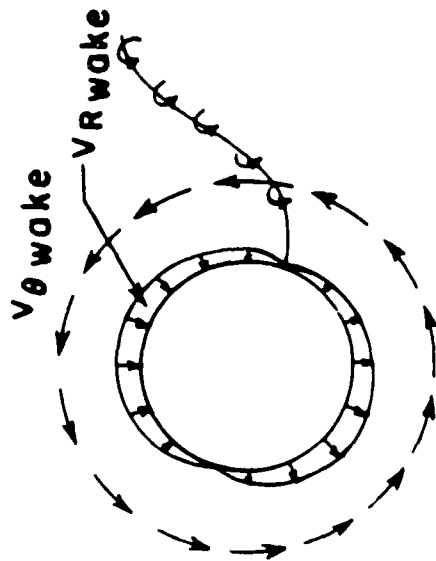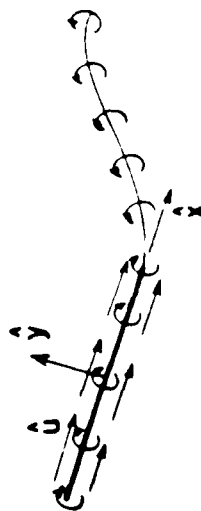**Streak Surface**

Instantaneous Z_θ

b) A Streak Surface, Starboard Side, for given t.

176

$V_{R_{wake}}$

$V_{\theta_{wake}}$

Radial And Tangential Components Of Wake Induced Velocity As Viewed In The Circle Plane

Apparent Wake Induced Velocity

$\hat{u}_w$

$\hat{u}_w$

$+$

Velocity Due To Additional Bound Vorticity

$\Delta\hat{u} = -\gamma$

$-\hat{u}_w$

$=$

Net Flow With Normal Velocity Cancelled At Airfoil Surface

$\hat{y}$

$\hat{x}$

$\hat{u}$

6. Superposition Algorithm for Determining Bound Vorticity Necessary to Cancel Upwash at the Plate.

177

Observation Cross Plane at Fixed z

$U_\infty \cos \bar{\alpha}$

U_∞

$U_\infty \sin \bar{\alpha}$

$\bar{\alpha}$

Mean Location of Projection of Wing Trace in (x, z) Plane

Observation Cross Plane at Fixed z

$\overline{W}$

Relative Vertex
Displacement Vector

U_∞
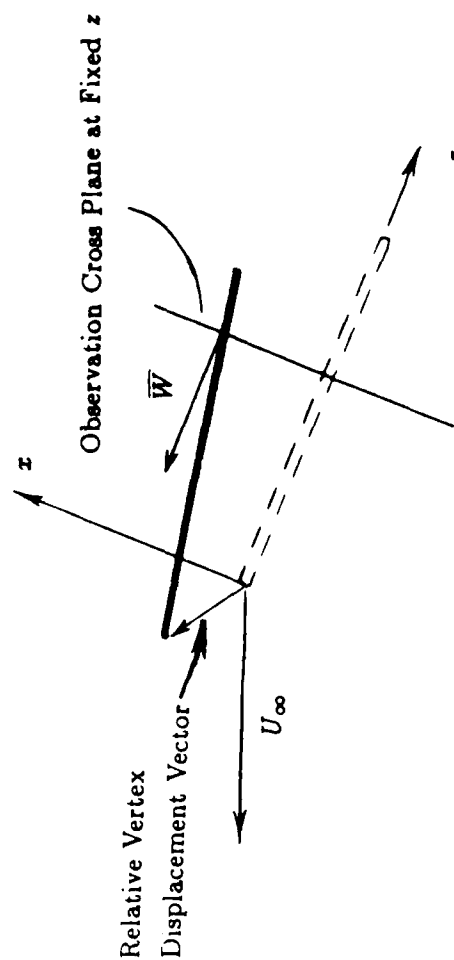
Instantaneous Projection of Wing Trace in (x, z) Plane

7. Choice of Cross-Flow Observation Planes. a) $x - z$ Projection.

Γ_{STBD}

Γ_{PORT}

$\bar{\alpha}$

U_∞

Wing in Steady Motion at Constant Angle of Attack

178

Projection of Wing Trace in (x, y) Plane
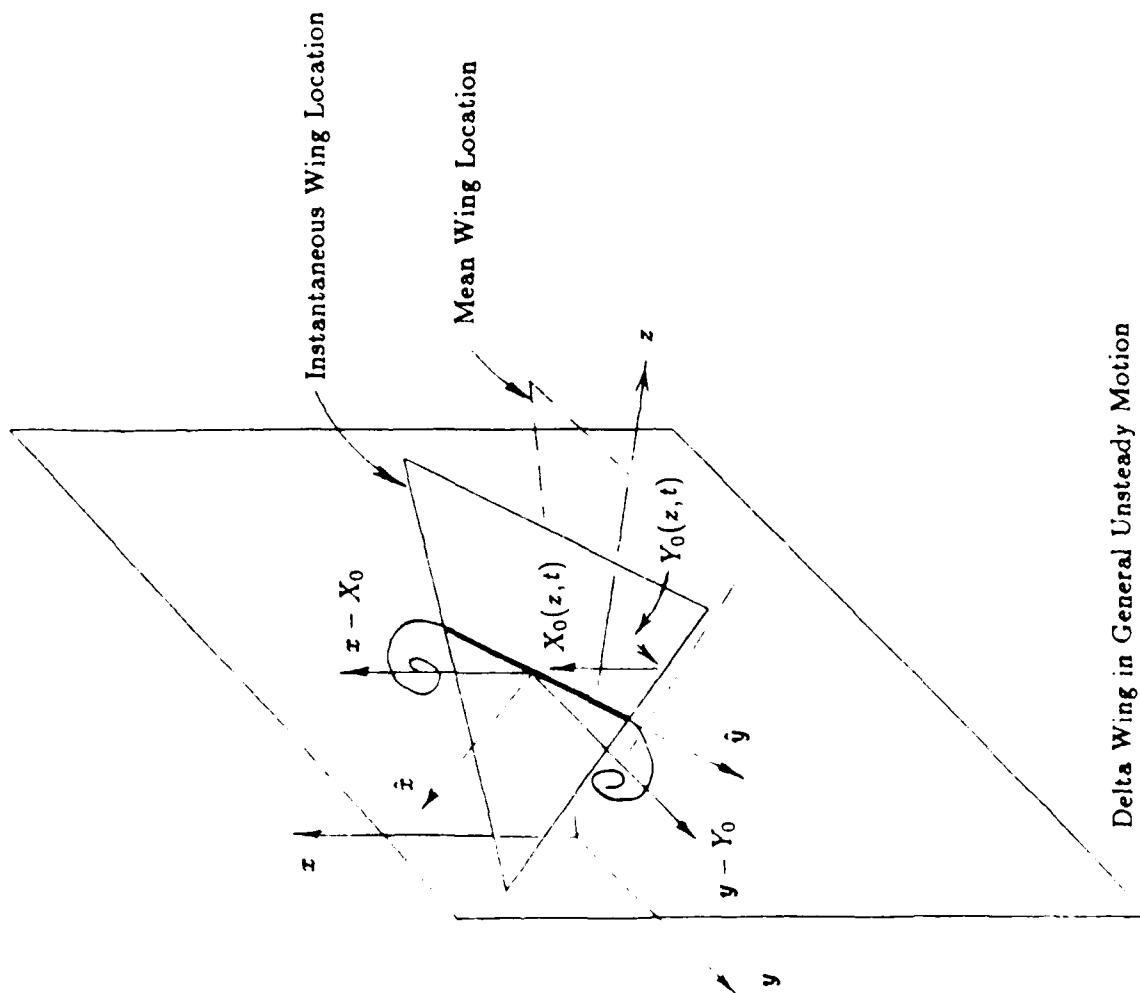
Delta Wing in General Unsteady Motion

b) $x - y$ Projections and "Roll".

179

M SCOTT-- LIFT AND BOUND CIRCULATION VS INPUT MOTION
G 0. TOTAL CL AND TOTAL CM

GAMMA-0

GAMMA-0 + GAMMA-1

COEFFICIENT OF LIFT AND ASYMPTOTE

DPHI/DT TERMS

GAMMA-1

M SCOTT -- WAKE DISPLAY
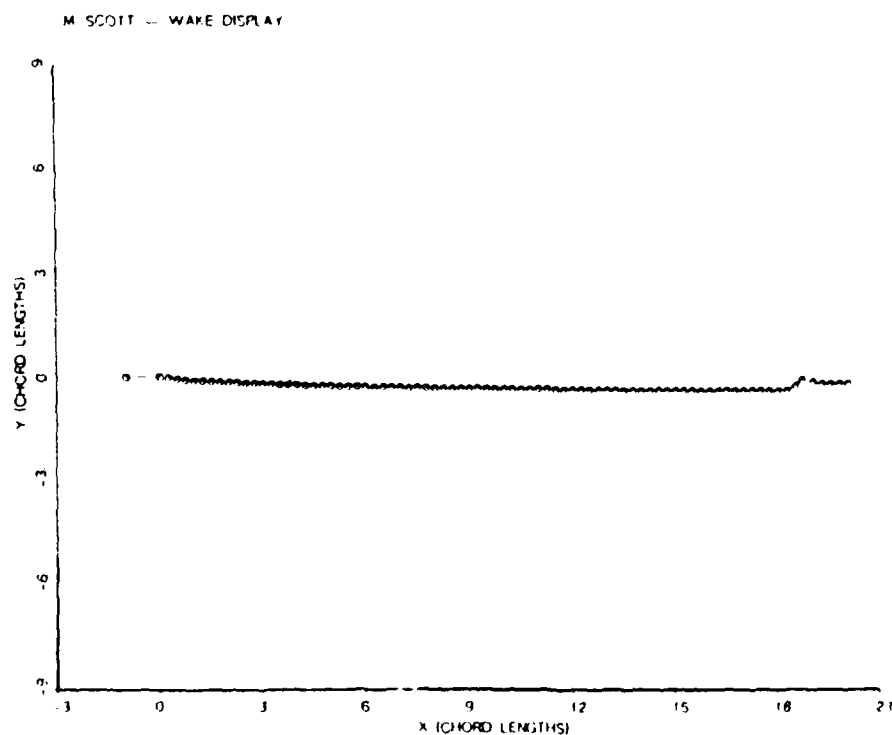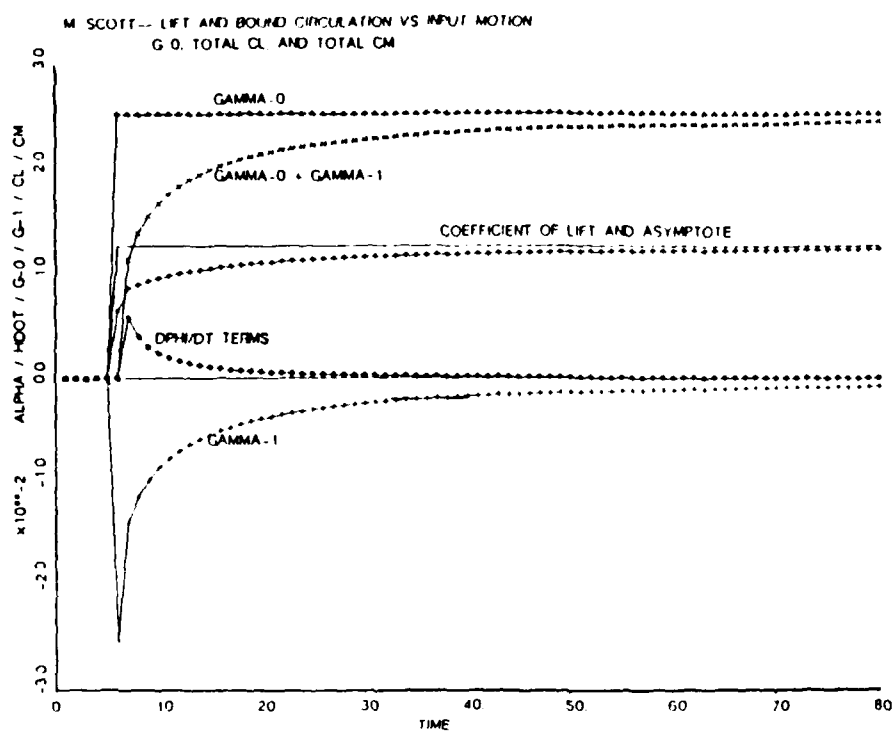
8. *Airfoil Response to Low-amplitude Step Change in Attitude.* a) Circulation and C_l vs. Time. b) Wake Display.

M. SCOTT— LIFT AND BOUND CIRCULATION VS INPUT MOTION
G-0, TOTAL CL, AND TOTAL CM

M. SCOTT — WAKE DISPLAY
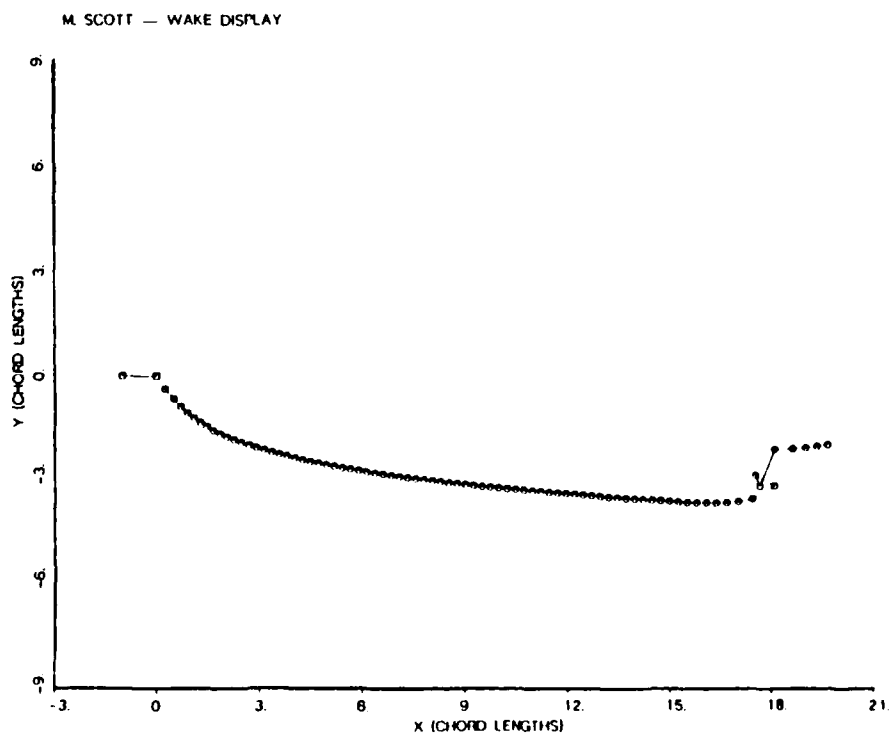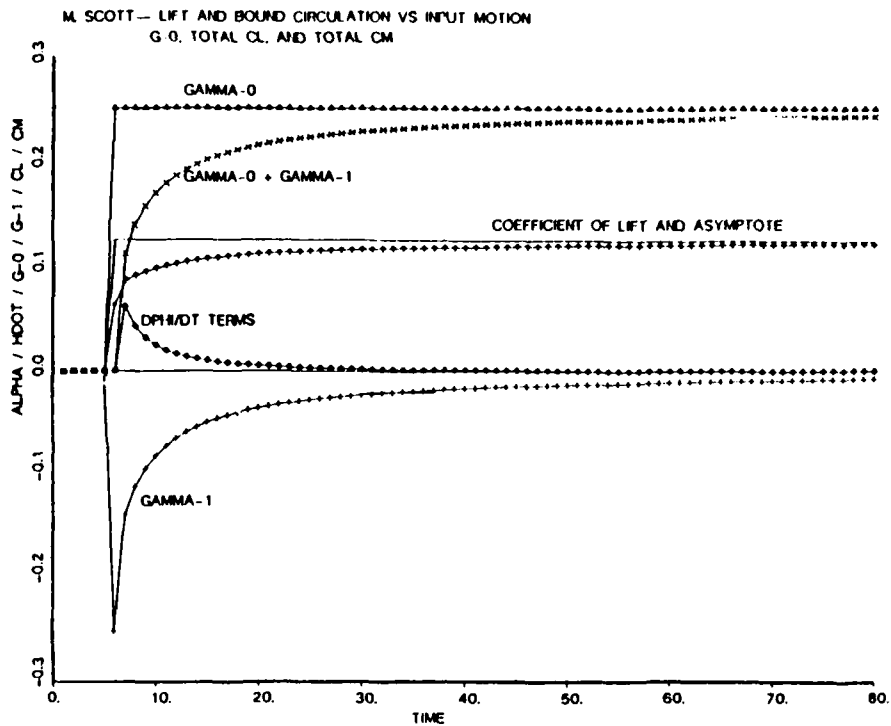
9. Airfoil Response to Large Amplitude Step Change in Attitude. a) Circulation and C_ℓ vs. Time. b) Wake Display.

181
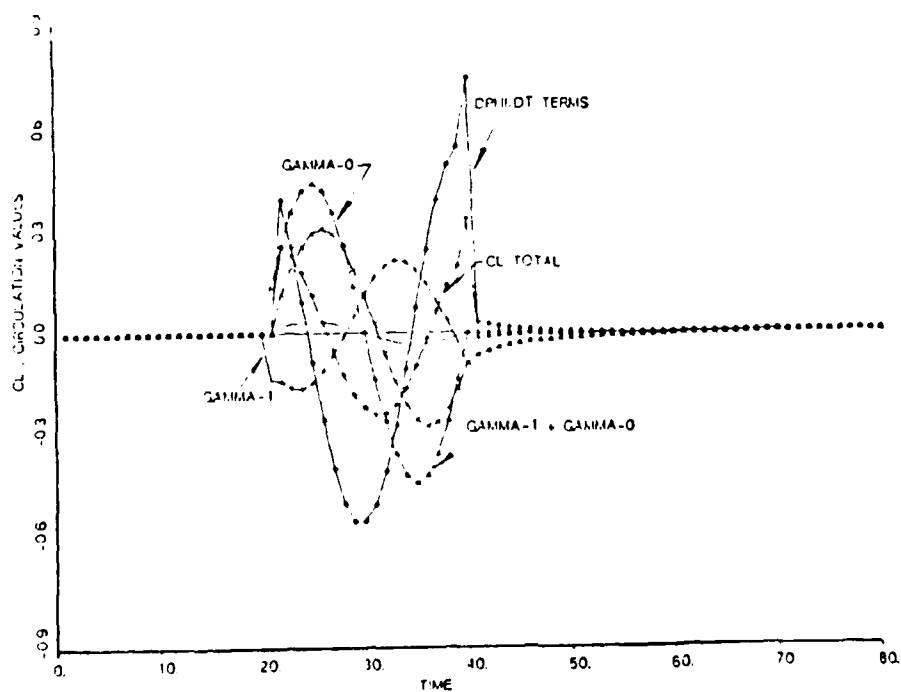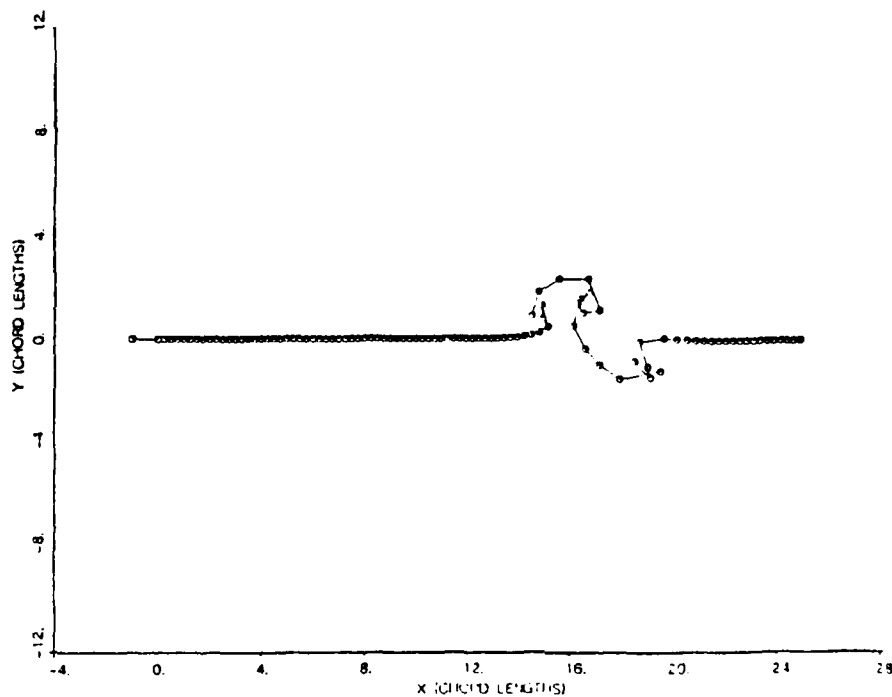
10. Airfoil Response to a Single Full-cycle Completed Imposed Oscillation. a) Wake Display. b) Lift and Circulation vs. Quasi-steady Values.

182

c) Moment Coefficient, with History Effect.

AN UNIFIED THEORETICAL-COMPUTATIONAL APPROACH
FOR NON-LINEAR UNSTEADY AERODYNAMICS

J. C. Wu, Professor
Georgia Institute of Technology
Atlanta, Georgia 30332

Abstract

This paper describes a unified theoretical-computation approach for unsteady aerodynamics in the non-linear domain, where viscous separation and strong unsteady effects are such that the linearization of flow equations are not justified. A number of focal problems in non-linear a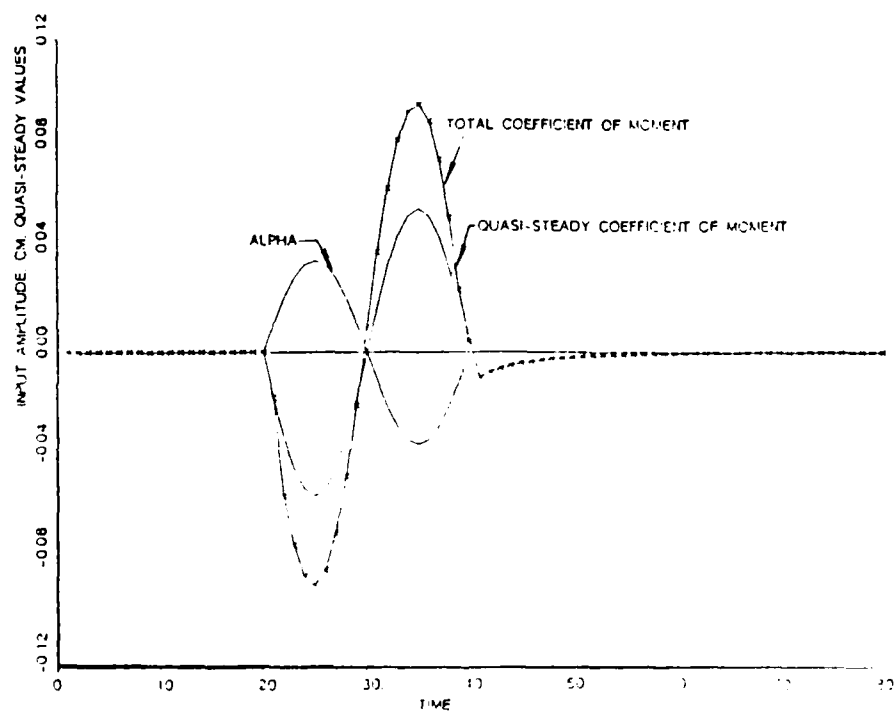erodynamics have been solved recently using this unified approach. In the present paper, unique attributes of this unified approach are described. Selected results obtained recently for these focal problems are presented to demonstrate the application of the unified approach.

A lifting body undergoing unsteady motion and experiencing non-linear unsteady airload is in general surrounded and trailed by a region in which the vorticity content of the fluid is significant. This vortical region is composed of distinctive attached and detached flow zones, i.e., the boundary layers, the recirculating flows or separation vortices, the wakes and the starting vortex assemblies. The domains of these vortical zones are time-dependent. For flows at high Reynolds number, the thickness of the attached boundary layer is, in general, drastically smaller than the length scales of the detached vortical zones. The well-known boundary layer simplifications are justifiable in the boundary layer zone. In contrast, the full Navier-Stokes equations provide the proper mathematical description of the flow. Surrounding these vortical zones is a potential flow zone where the vorticity contents of the fluid, and hence viscous effects, are negligibly small. The physical and mathematical characteristics of the various flow zones that co-exist in an unsteady flow are greatly different from one another. The simultaneous presence of the drastically diverse length scales, physical and mathematical characteristics has led to serious theoretical and computational difficulties in studies of non-linear unsteady aerodynamics. The unified approach resolves these difficulties by confining aerodynamic analyses to the vortical zones and by treating the vortical zones separately.

The theoretical basis of the unified approach is a general viscous theory of aerodynamics developed earlier by the present author. This theory is derived mathematically rigorously from the full Navier-Stokes equations. No simplifying assumptions are introduced other than those contained in the Navier-Stokes equations. This theory is valid for flows in either the linear or the non-linear domain. The aerodynamic load acting on a lifting body, rigid or articulate, is related by the theory to integrals of moments of vorticity. Since these integrals vanish outside the vortical zone, aerodynamic analyses using the theory can be confined to the vortical zones. The vorticity moment integrals are expressible as sums of zonal integrals, each zonal integral is an integration of a moment of vorticity over a specific vortical zone.

The individual contribution of each flow zone to the total aerodynamic load is directly related to a zonal integral. This contribution is readily identified and determined once the time-dependent vorticity distribution in the zone is known.

Under certain circumstances, the general viscous theory of aerodynamics permits the unsteady aerodynamic load to be determined approximately without a detailed computation of the unsteady flowfield. Closed-form analytical expressions are obtainable under special circumstances. Under general circumstances, the time-dependent distributions of vorticity in the vortical zones need to be determined through detailed computations. With the coordinated theoretical-computational approach, the vorticity distributions are computed using a zonal method.

The zonal method for the computation of time-dependent vorticity distributions utilizes an integral formulation of the full viscous flow equations. The integral formulation is derived mathematically rigorously using the concept of fundamental solutions. In aerodynamic studies, the integral formulation permits the computation field to be confined to the vortical zones. It further permits each of the vortical zones to be computed individually. The unsteady boundary layers are computed separately from the detached vortical zones without iteratively matching the different zones. Thus, the zonal method is totally compatible with the general viscous theory of aerodynamics.

The unified approach has been developed to a stage of maturity for nonlinear unsteady aerodynamic problems involving two spatial dimensions. Efforts are in progress to apply this approach to non-linear unsteady aerodynamic problems involving three spatial dimensions. Applications ranging from the Weis-Fogh problem to the dynamic stall of rapidly pitched airfoils have been studied using the present approach. In Figure 1 are shown lift hysteresis loops for an airfoil oscillating sinusoidally in pitch at a reduced frequency of 0.15 and a Reynolds number of 1,000,000. The excellent qualitative and quantitative agreement between the present results and the experimental data exhibited in Figure 1 is typical of all problems studied as a part of the present research program. The interplay between the theoretical and the computational components of the present approach brings about improved physical insight and enables the establishment of simplified and yet realistic flow models. In Figure 2 are shown unsteady aerodynamic forces experienced by an airfoil encountering a free vortex passing nearby. The solid curve in Figure 2 shows the result obtained using a flow model based on the present approach. The computational effort required to obtain this result is negligibly small. The dashed curve shows the computed results based on the full Navier-Stokes equations. The agreement between the two sets of results shows the effectiveness of the present approach in the development of simplified models of non-linear unsteady aerodynamics.
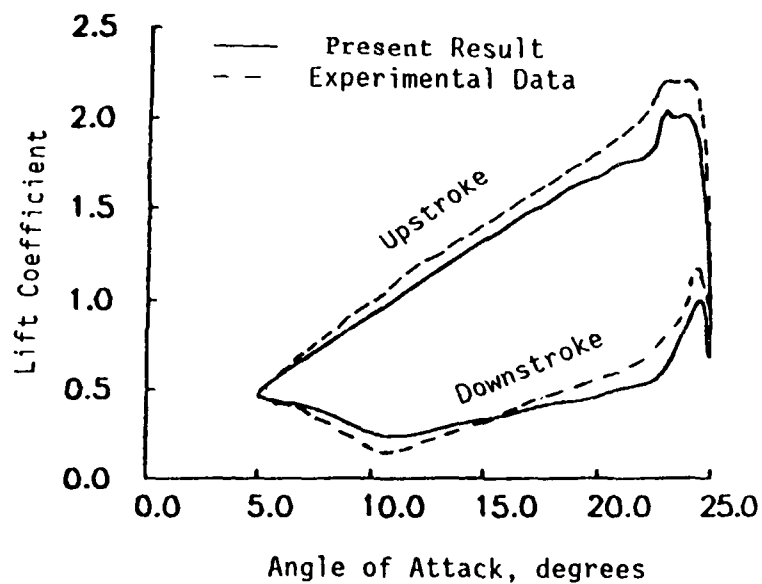
186

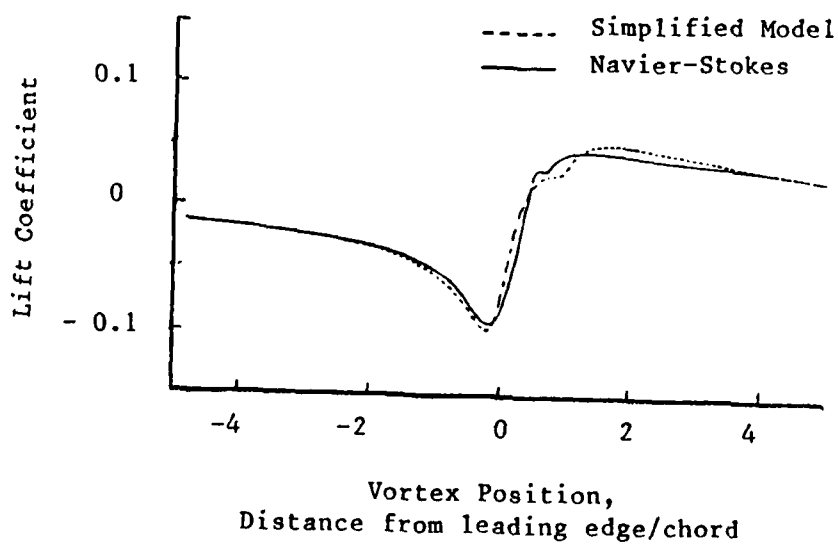Figure 1   Lift Hysteresis Loop

Figure 2.   Vortex-Airfoil Interaction

TRANSITION EFFECTS ON AIRFOIL DYNAMICS AND ASSOCIATED SCALING PROBLEMS

L. E. Ericsson
Lockheed Missiles & Space Company, Inc.
Sunnyvale, California

ABSTRACT

Boundary layer transition is found to have a dramatic impact on unsteady airfoil aerodynamics. On a stalling airfoil this effect is complicated further by strong compressibility effects. Thus, dynamic simulation of full scale airfoil aerodynamics requires that both Reynolds number and Mach number are simulated everywhere on the airfoil surface in physical experiments; and that the coupling between transition and airfoil motion is correctly simulated in numerical experiments.

PITCH OSCILLATIONS

Greidanus et al[1], performing a thorough experimental check of airfoil theory for small amplitude oscillations at $\alpha = 0$, obtained results that illustrate the dynamic effect of the strong coupling existing between the airfoil motion and boundary layer transition (Fig. 1). Their 7.3% thick symmetric airfoil had natural transition occurring near the trailing edge (when no tripping was used), causing dramatic variations from the expected theoretical results, the latter being in agreement with the trip-on experimental results. Figure 2 explains what happens[2]. The reduced frequency, $\bar{\omega} = \omega c/U_\infty$, was changed by changing the (incompressible) flow velocity (U_∞), while keeping the frequency ($\omega = 2\pi f$) constant. Thus, the velocity, and hence the Reynolds number, increases with decreasing reduced frequency ($\bar{\omega}$). As a consequence, transition moves forward from the trailing edge with decreasing reduced frequency ($\bar{\omega}$).

At angle of attack the boundary-layer transition occurs more forward on the leeward side, mainly due to the increased adverse pressure gradient. The differential transition on top and bottom surfaces causes a force couple (Fig. 2, insets) similar to what is the result of leeward side trailing-edge separation. When the Reynolds number is increased (decreasing $\bar{\omega}$), the transition moves forward. Thus, the forward force component loses lever arm and becomes less and less effective, causing the overall static effect of boundary-layer
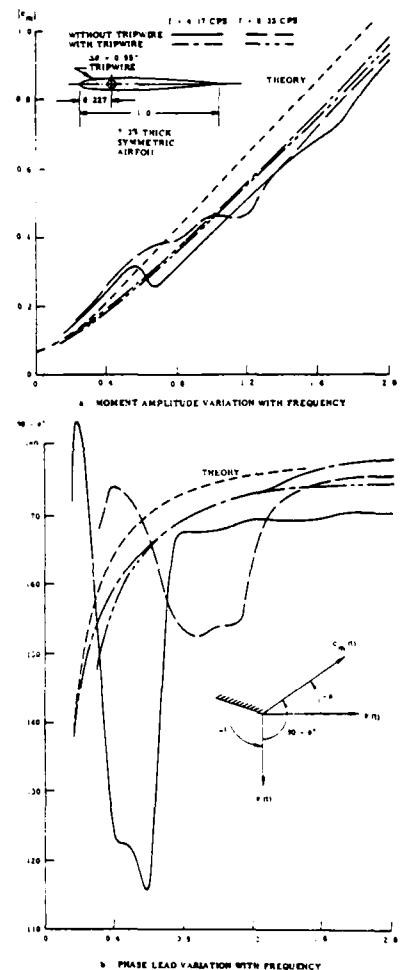

Fig. 1 Effect of tripwire on Dynamic Airfoil Characteristics (Ref. 1)

transition to change from destabilizing to stabilizing. With this in mind, one can illustrate the effects using vector diagrams, as shown in Fig. 2.
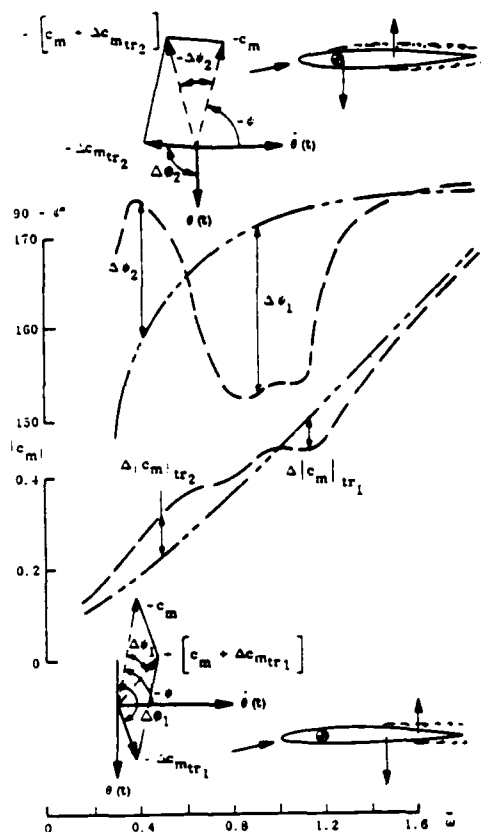
Fig. 2   Effect of transition-induced loads on
unsteady aerodynamic characteristics
(Ref. 2)

In the frequency range $0.8 < \omega < 1.2$, the transition takes place near the trailing edge, causing a moment increment of magnitude $\Delta_1 c_{m}'|_{tr_1}$. Note that the stabilizing moment ($-c_m$) is used in the vector diagram in sign agreement with the way the experimental results were presented in Ref. 1. Without transition effects, the moment vector leads the velocity vector by $-\psi \approx 80°$ (due to the high apparent mass effects at these high reduced frequencies). Without any motion-induced lag effects, the instantaneous transition-induced moment would lead the angle of attack vector, $\alpha(t)$, by $180°$, as it is destabilizing.

Using the effective time lags discussed in Refs. 3 and 4 for dynamic stall, the time lag effects will be estimated using the transition/turbulent stall similarity pointed out by Kline[5]. That is, Eq. (7) in Ref. 4 is used with $\alpha_o = \alpha_s = 0$. For the frequency range of interest, $\Delta A < 0.02$ for the oscilla-

tion amplitude $\Delta\theta < 1°$ used in the experiment[1] (Fig. 1). Thus, Eq. (7) in Ref. 4 applies.

$$(\omega t)_{Lt} = 2\tan^{-1}\left\{\left[\frac{\cos(\varphi_w + \varphi_s)}{K\,\bar\omega + \sin(\varphi_w + \varphi_s)}\right]\right.$$

$$\times\left.\left\{\sqrt{1 + \left[\frac{K\,\bar\omega + \sin(\varphi_w + \varphi_s)}{\cos(\varphi_w + \varphi_s)}\right]^2} - 1\right\}\right\} \quad (1)$$

When transition occurs near the leading edge, $(\omega t)_{tr} = (\omega t)_{LE}$ is obtained directly from Eq. (1) with $\varphi_w = 14°$, the attached flow value for $\bar\omega > 0.16$, and $\varphi_s = 0.75\bar\omega$, the turbulent value[4,5]. When transition occurs near the trailing edge, $(\omega t)_{tr}$ is obtained as

$$(\omega t)_{tr} = (\omega t)_{LE} + \varphi_c \quad (2)$$

$(\omega t)_{LE}$ is obtained from Eq. (1) with $\varphi_s = 0$. From Ref. 3 one obtains $\varphi_c = 1.25^S \xi_{tr}\bar\omega$, and $K = 2.91$ for $\xi_o = 0.227$.

The transition effects illustrated in Fig. 2 are explained in detail in Ref. 6, using Eqs. (1) and (2).

PLUNGING OSCILLATIONS

Recent experimental[7] results for a high performance airfoil[7] (Fig. 3) demonstrate the strong coupling existing between airfoil plunging and boundary layer transition. In an aeroelastic test at $\alpha = 0$ of a 25 deg. swept wing, violent oscillations in the first bending mode occurred if the transition location was not fixed by a tripping device. The oscillations were of the limit cycle type, the typical result of negative aerodynamic damping (Fig. 3). Similar results have been obtained by others[8] when transition is not fixed. As earlier for the pitching airfoil (Figs. 1 and 2), the effects of transition are associated with time lag. However, in the present case the time lag effect can not influence the aerodynamic damping. The transition-induced load is proportional to $\dot z(t-\Delta t)/U_\infty$,# which for small amplitude/low frequency oscillations, such as the ones observed in Ref. 7, can be Taylor-expanded as $\dot z(t)/U_\infty - \Delta t\,\ddot z(t)/U_\infty$.

That is, the time lag in the transition response to a change of the effective angle of attack, $\dot z/U_\infty$, can not affect the damping; it only affects the inertia term. The corresponding dilemma in regard to the plunging response of shock/boundary layer interaction is discussed in Refs. 9 and 10.

#For the pitching airfoil the effective angle of attack is $\alpha(t-\Delta t) = \alpha(t) - \Delta t\,\dot\alpha(t)$; i.e. the time lag affects the damping.
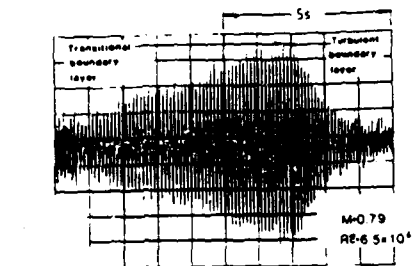
Fig. 3 Wing-root rms strain response to bending
oscillation (Ref. 7)

Fig. 4 Magnus lift characteristics for initially
subcritical flow conditions

The moving wall effect is of significant magnitude only in the region near the stagnation point, where the boundary layer is thin and, therefore, very sensitive to this wall-jet-like action. A similar moving wall effect on boundary layer transition has been observed on airfoils. Figure 5 illustrates how the plunging and pitching

The effect of $\dot{z}(t)/U_\infty$ on the airfoil with its positive lift slope, $c_{l\alpha} > 0$, is, of course, damping. The effect on the damping via transition, through $\dot{z}(t)/U_\infty$, occurs mainly through the so called moving wall effect[11]. The Magnus lift reversal, observed on a circular cylinder[12], illustrates this (Fig. 4). The positive Magnus lift, at $U_w/U_\infty < 0.3$, is caused by the wall-jet-like downstream moving wall effect on the top side, which fills out the boundary layer velocity profile, thereby delaying flow separation. A similar lift-contribution is obtained from the upstream moving wall effect on the bottom side, which promotes separation. At $U_w/U_\infty > 0.3$, so called Magnus lift reversal occurs. This is caused by the upstream moving wall effect on the bottom side, which, when the critical U_w/U_∞ - Reynolds number combination is approached, will cause boundary layer transition to occur upstream of flow separation, thereby changing the separation from the subcritical towards the supercritical type. This results in a more or less discontinuous loss of lift.
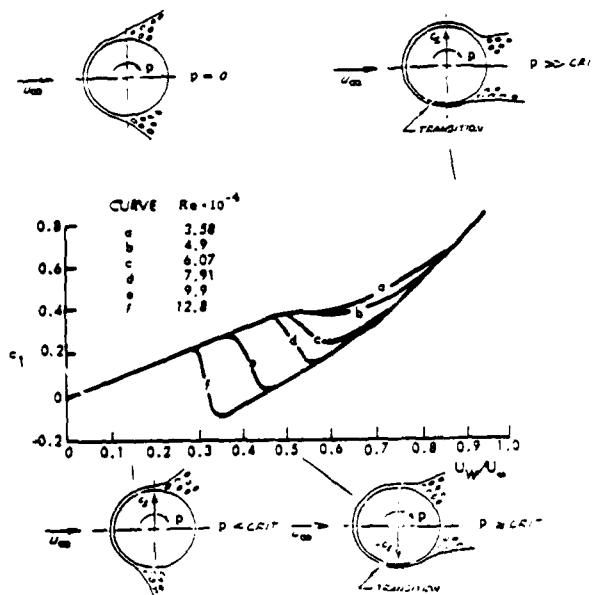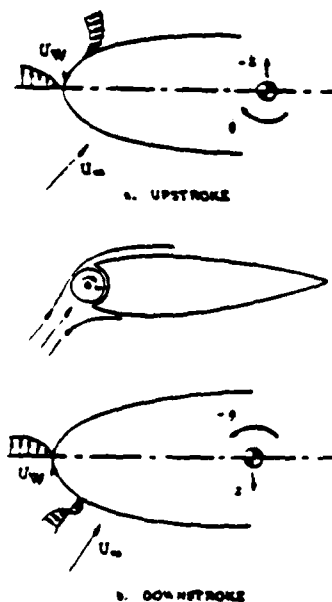

Fig. 5 Leading-edge-jet effect

airfoils will have opposite moving wall effects for increasing effective angle of attack, $\dot{z}/U$ and θ, respectively. Carta's hot film response data[13] (Fig. 6)* show how the adverse (upstream) moving wall effect $\dot{z}(t)$ promotes leeside transition and causes the plunging airfoil to have a longer run of attached turbulent flow prior to stall. As a result, the flow stays attached past 7.5% chord, whereas flow separation occurs forward of 5% chord on the pitching airfoil, which has a shorter turbulent run before stall due to the opposite, transition-delaying, moving wall effect.

Thus, the plunging airfoil section for the bending wing[1] (Fig. 3) will experience a transition-promoting moving wall effect on the top side during the "down stroke" of the bending oscillation. On the bottom side, the moving wall effect is opposite, delaying transition. As a result, a negative lift component is generated, which drives the oscillation (Fig. 7a). How this coupling of transition to the bending oscillation via the moving wall effect can generate the observed divergent bending oscillation[7] (Fig. 3) is described in Ref. 6.

Figure 7b illustrates how the plunging-induced moving wall effect would generate a negative force component in the case of laminar separation, similar to that induced through transition (Fig. 7a), and one would expect the wing to have bending oscillations also in this case. If the Reynolds number is increased, the situation sketched in Fig. 7c results. In this case of transitional separation, the moving wall effect promotes transition and thereby delays leeside flow separation, as was demonstrated by Carta's results[13] (Fig. 6). Thus, the combined effect of transition and flow separation is in this case to damp the plunging oscillation, and one would not see any wing bending oscillations. If the Reynolds number is increased further, until transition moves far forward of the flow separation, the situation becomes similar to that illustrated in Fig. 7b for laminar flow separation. However, transition still has an effect. In this case, it amplifies the dynamic effect of the

a. Plunging

b. Pitching

Fig. 6 Hot film response for plunging and pitching oscillations of a NACA-0012 airfoil (Ref. 13)

a. Transition

b. Laminar Separation

c. Transitional Separation
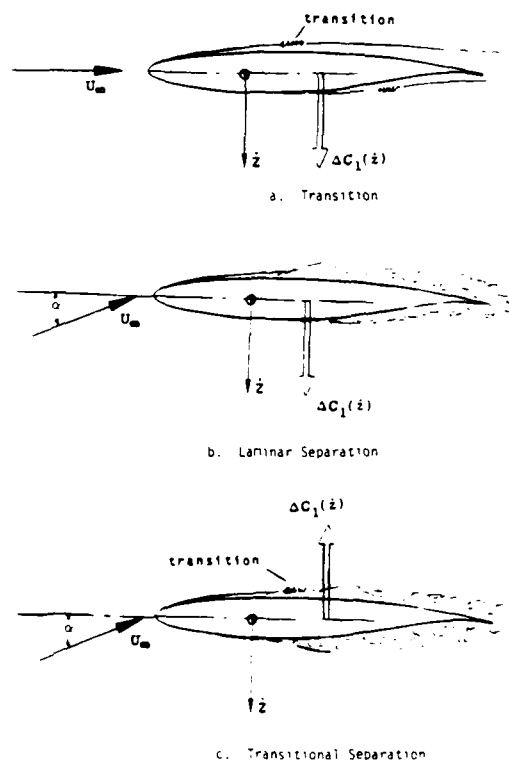
Fig. 7 Loads induced by viscous flow effects

----

*The amplitudes of $\dot{z}(t)/U_\infty$ and $\theta(t)$ are of the same magnitude.

turbulent flow separation, as the moving wall effect promotes transition and thereby increases the leeside flow separation extent.

The implication of the possible flow situations sketched in Fig. 7 is that in subscale tests one can obtain dangerously misleading results. For example, in full scale flight the flow separation is likely to be turbulent, and the transition-coupling with the bending wing will amplify the negative damping, resulting in an increase of the oscillation amplitude. If the subscale test is performed at laminar flow conditions, the wing will at least respond in a similar manner as in full scale flight, exhibiting divergent bending oscillations until the limit cycle amplitude is reached (where the attached flow lift damping together with the structural damping balances the separation-induced negative damping.) It is not unlikely, however, that in his desire to get as close to the full scale Reynolds number as he can the test engineer ends up with the situation sketched in Fig. 7b, in which case he will never become aware of the fact that the full scale wing will experience possibly unacceptable bending oscillations.

In the case of pitch oscillations, the coupling between the airfoil motion and transition and/or flow separation has the opposite effect of what it has for plunging oscillations, as was demonstrated by Carta's data[13] (Fig. 6) - it should be emphasized that the effect of the upstream pressure gradient time history[14] is the same for the plunging and pitching airfoil data shown in Fig. 6. Thus, the results in Fig. 6 demonstrate that the moving wall effect dominates over the pressure gradient effect, permitting the coupling to be described satisfactorily using only the moving wall effect - . That is, the moving wall effect on an airfoil in pitch-up motion delays transition. Whether the effect is to drive or damp the pitch oscillation depends upon the transition location relative to the pitch axes, as was demonstrated in Figs. 1 and 2. However, the combined effect of transition and separation in the case of transitional separation (Fig. 7b) is the same in the sense that the effect of pure separation is reversed. With that in mind, one is inclined to interpret the results[15] in Fig. 8 as follows. The periodic flow separation oscillation, established in the Mach number range $0.82 < M_\infty < 0.86$, is likely to be of the self-induced type. That is, in that M-region the frequency and time lag associated with the circulation change and the motion of the shock-induced flow separation are such that a coupling, similar to that between translation and Karman vortex shedding for a circular cylinder in crossflow[16], can be esta-
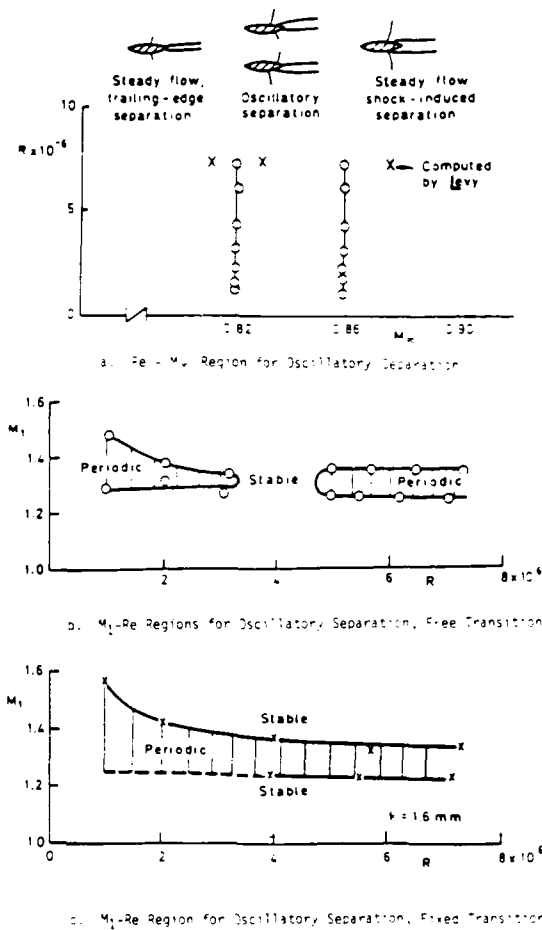
Fig. 8 Mach number - Reynolds number boundaries for periodic separated flow (Ref. 15)

blished. As in the cases discussed earlier, when the separation becomes transitional in nature, the separation-induced effect is reversed, e.g. in the present case it would change from negative to positive damping, as was discussed in connection with Fig. 7b, (M_1 is the local Mach number ahead of the shock.)

COMPRESSIBILITY EFFECTS

It was shown in Ref. 17 that incompressible dynamic stall is largely a fictitious flow phenomenon. Already at a free stream Mach number of $M_\infty > 0.2$ the locl peak velocity on the stalling airfoil will exceed sonic speed. In view of the transition effects discussed earlier, the results[18] in Fig. 9 give cause for concern. With M_1 being the local Mach number on the airfoil surface, the free stream Mach number will be low subsonic for $M_1 < 2$. Thus, the wind tunnel noise problem present at supersonic tunnel speeds[19] will be absent and Mack's linear stability analysis[18] (Fig. 9) should apply. It shows# that when the local Mach number

----

#In an approximate sense, as no pressure gradient effects are included.

193

Fig. 9 Theoretical calculations of the effect
of Mach number on boundary layer
transition (Ref. 18)

on the airfoil surface goes from $M_1 \approx 0.6$
to $M_1 \approx 1.3$, the transition Reynolds
number increases by a factor of 4 or
more. Thus, in the planned tests of
compressibility effects on dynamic stall
described by Bodapati[20], one can expect
the appearance of all of the transition-
separation combinations described
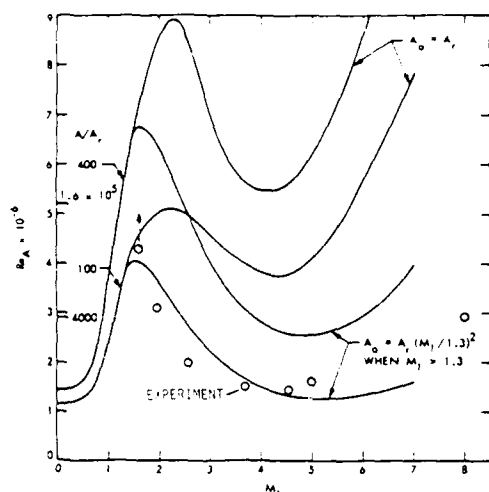earlier. From everything discussed so
far one would draw the conclusion that
very small increments in M_∞ and Re_∞ are
needed in order to catch the various
flow situations that have been described
in this paper.

CONCLUSIONS

Analysis of existing experimental
airfoil data reveals the following:

o   A strong coupling exists between
    airfoil motion and boundary layer
    transition, which even in the case
    of attached flow can have signifi-
    cant consequences, causing
    intolerable bending oscillations of
    a slightly swept wing in one docu-
    mented case.

o   When transition and flow separation
    occur simultaneously, both of which
    are strongly coupled to the airfoil
    motion, the unsteady aerodynamic
    characteristics can vary drastic-
    ally with Reynolds number, a small
    Re-change leading to either the
    cancelation or occurrence of flow
    oscillations.

o   When considering compressibility
    effects, the scaling problem
    indicated by the above paragraphs
    becomes very much more complicated,
    and carefully planned experiments
    are very much needed.

REFERENCES

1.   Greidanus, J. H., Van de Vooren,
     A. I., and Bergh, H., "Experimental
     Determination of the Aerodynamic
     Characteristics of an Oscillating
     Wing with Fixed Axis of Rotation,"
     NLL Report F101, 1952, National
     Aerospace Lab., Netherlands.

2.   Ericsson, L. E. and Reding, J. P.,
     "Dynamic Stall of Helicopter
     Blades", J. Am. Helicopter Soc.,
     Vol. 17, 1972, pp 10-19.

3.   Ericsson, L. E. and Reding, J. P.,
     "Dynamic Stall Analysis in Light of
     Recent Numerical and Experimental
     Results", J. Aircraft, Vol. 3,
     1975, pp 248-255.

4.   Ericsson, L. E. and Reding, J. P.,
     "Dynamic Stall at High Frequency
     and Large Amplitude", J. Aircraft,
     Vol. 7, 1980, pp 136-142.

5.   Kline, S. J., "Some New Concepts of
     the Mechanics of Stall in Turbulent
     Boundary Layers", J. Aerospace
     Sci., Vol. 24, 1969, pp 470-471.

6.   Ericsson, L. E., "Transition
     Effects on Airfoil Dynamics and the
     Implication for Subscale Tests",
     AIAA Paper 37-2353-CP, Aug. 1987.

7.   Mabey, D. G., Ashill, P. R. and
     Welsh, B. L., "Aeroelastic
     Oscillations Caused by Transitional
     Boundary Layers and Their
     Attenuation", AIAA Paper 86-0736,
     March 5-7, 1986.

8.   Houvink, R., Kraan, A. N. and
     Zwaan, R. J., "Wind-Tunnel Study of
     the Flutter Characteristics of a
     Supercritical Wing", J. Aircraft,
     Vol. 19, No. 5, May 1982, pp
     400-405.

9.   Ericsson, L. E., "Dynamic Effects
     of Shock-Induced Flow Separation",
     J. Aircraft, Vol. 2, No. 2, Feb.
     1975, pp 86-92.

10. Ericsson, L. E., ERRATA for
     "Dynamic Effects of Shock-Induced
     Flow Separation," J. Aircraft, Vol.
     18, No. 7, July 1981, p. 608.

11. Ericsson, L. E., "Dynamic
     Omnipresence of Moving Wall
     Effects, a Selective Review", AIAA
     Paper 87-0241, Jan. 1987.

12. Swanson, W. M., "The Magnus Effect:
     A Summary of Investigations to
     Date", J. Basic Eng., Vol. 83,
     Sept. 1961, pp 461-470.

13. Carta, F. O., "A Comparison of the
     Pitching and Plunging Response of
     an Oscillating Airfoil", NASA
     CR-3172, Oct. 1979.

14. Ericsson, L. E. and Reding, J. P., "Dynamic Stall Overshoot of Static Airfoil Characteristics," AIAA Paper 85-1773-CP, Aug. 1985.

15. Mabey, D. G., Welsh, B. L., and Cripps, B. E., "Periodic Flows on a Rigid 14% Thick Biconvex Wing at Transonic Speeds," TR 81059, Royal Aircraft Establishment, Farnborough, Hants, May 1981.

16. Ericsson, L. E., "Circular Cylinder Response to Karman Vortex Shedding," AIAA Paper 86-0999-CP, May 1986 (scheduled for J. Aircraft, Nov. 1987.)

17. Ericsson, L. E. and Reding, J. P., "Stall Flutter Analysis," J. Aircraft, Vol. 10, No. 1, Jan. 1973, pp 5-13.

18. Mack, L. M. "Linear Stability Theory and the Problem of Supersonic Boundary-Layer Transition," AIAA Journal, Vol. 13, No. 3, March 1975, pp 278-289.

19. Pate, S. R. "Dominance of Radiated Aerodynamic Noise on Boundary Layer Transition in Supersonic-Hypersonic Wind Tunnels, Theory and Application," AEDC-TR-77-107, March 1978.

20. Bodapati, S., "Compressibility Effects on the Dynamic Stall of Airfoils Undergoing Ramp-Type Motion," Proceedings of Workshop on Unsteady Separated Flow, USAF Academy, July 28-30, 1987.

PROGRESS IN VISUALIZING UNSTEADY SEPARATION

Peter Freymuth, Department of Aerospace Engineering Sciences
University of Colorado, Boulder, Colorado 80309-0429

ABSTRACT

The titanium tetrachloride method of vortex tagging has been extended from visualization of vortex development in accelerated starting flow over airfoils to impulsive flow, to pitching and to plunging airfoils in steady flow, and to three-dimensional configurations. This method finds new vortex interactions, allows global views which were previously unavailable and clarifies the physics of seemingly complex developments. Examples show our progress in visualization.
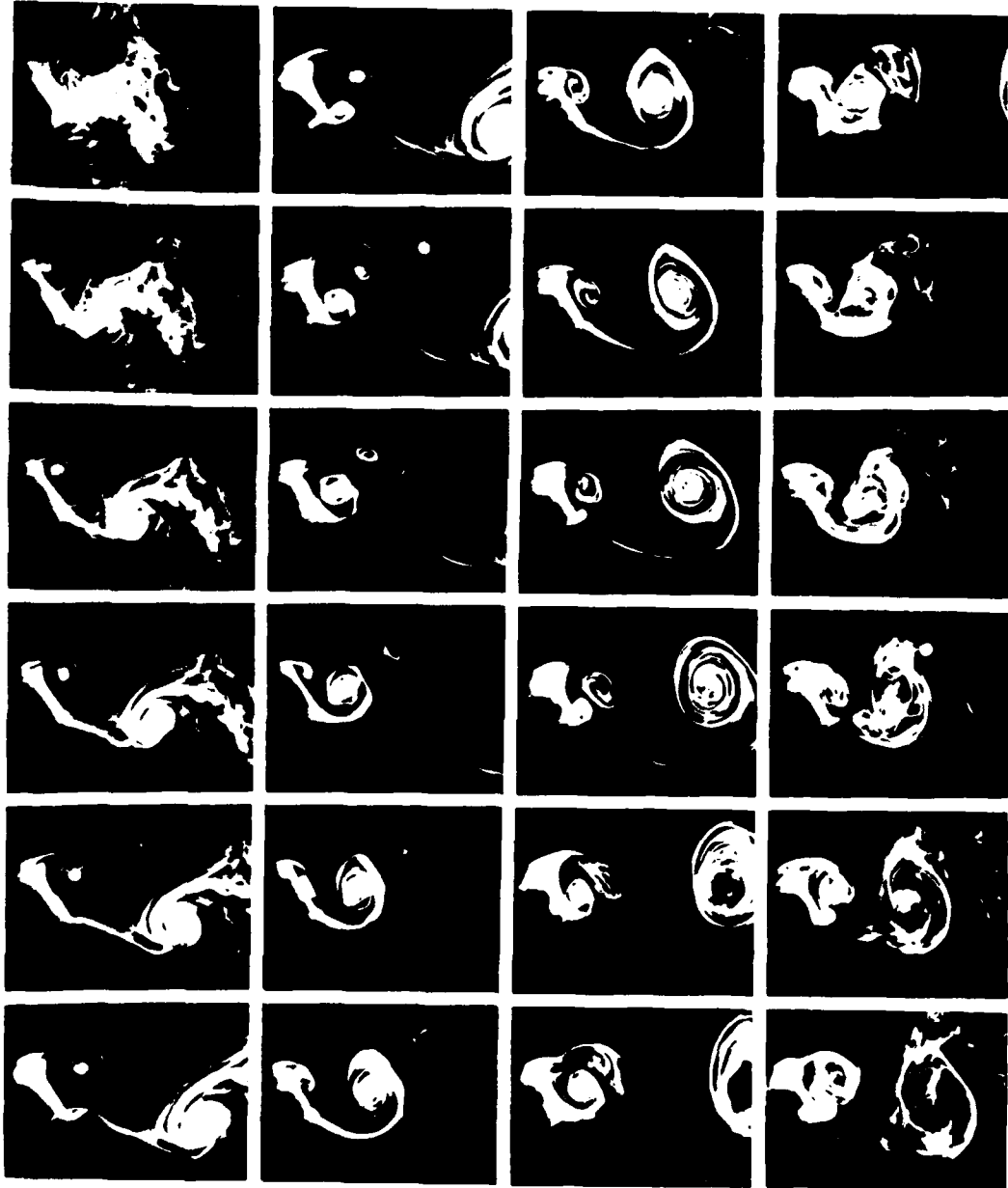
Fig. 1 Impulsive flow over an airfoil, $\alpha = 50^\circ$, c = 5.1 cm, U_c = 37 cm/sec, Re = 1000, time between consecutive frames is Δt = 1/16 sec. From Ref. 13.

INTRODUCTION

At the Workshop on Unsteady Flow at the Air Force Academy four years ago, we presented flow visualization examples of accelerated starting flow around various bodies[1]. By applying smoke producing liquid titanium tetrachloride to vorticity producing body surfaces, vortices were visualized in remarkable detail. In the meantime we have progressed from initial examples of vortex tagging to an extensive parametric study of accelerated starting flow around airfoils and other two-dimensional bodies[2]. In the course of this work many new vortex interactions like splitting[3], shredding[3], squeezing[4], and others were identified by us.

From this basis we progressed to visualizations of vortex developments for pitching and plunging airfoils[5,6]. The visualization of turbulent spots[7] and of the closed three-dimensional vortex systems associated with finite wings[8-12] was also achieved.

In this overview we demonstrate our visualization progress by selected examples. The plan is to commence from two-dimensional examples and to proceed to three-dimensional configurations.

IMPULSIVELY STARTED AIRFOIL

Figure 1 sequences the development of dynamic vortical separation for an NACA 0015 airfoil set impulsively into motion. Movie frames are ordered into columns from top to bottom and from left to right. Flow is from left to right while the airfoil is stationary with respect to the camera. The chord length of the airfoil is $c = 5.1$ cm; speed after start from rest is $U_\infty = 37$ cm/sec at an angle of attack $\alpha = 50°$. The resulting Reynolds number is $Re = U_\infty c/\nu = 1000$, where ν is the kinematic viscosity in air. The sequence is taken from the thesis by Finaish[13] which contains a parametric investigation of this flow configuration. Flow starts with the first frame, which shows random smoke due to smoke introduction on the airfoil by means of a pipette. The next few frames clearly show the development of leading and trailing edge starting vortices. The first trailing edge vortex leaves the airfoil to the right, while the leading edge vortex rolls over the suction surface, inducing creation of a secondary vortex. While the leading edge vortex rolls over the trailing edge, it induces the generation of a second trailing edge vortex. This vortex jumps up the rear section of the airfoil, aided by the leading edge vortex to the right in Column 2. This encourages the secondary vortex to slip down where it gets incorporated into the trailing edge vortex before this reinforced vortex finally moves to the right. The process repeats in Column 3 and gets more turbulent in Column 4. The peculiarities of timing of vortex generation allowed the first leading edge vortex to escape unscathed by the second trailing edge vortex which is reinforced by secondary vortex slipdown. In contrast, an airfoil started at constant acceleration showed splitting of the first leading edge vortex by the second trailing edge vortex and incorporation of the secondary vortex into the

first leading edge vortex, a process which we termed vortex shredding[3]. We conclude that starting flow history can have dramatic and previously unknown effects on dynamic separation.
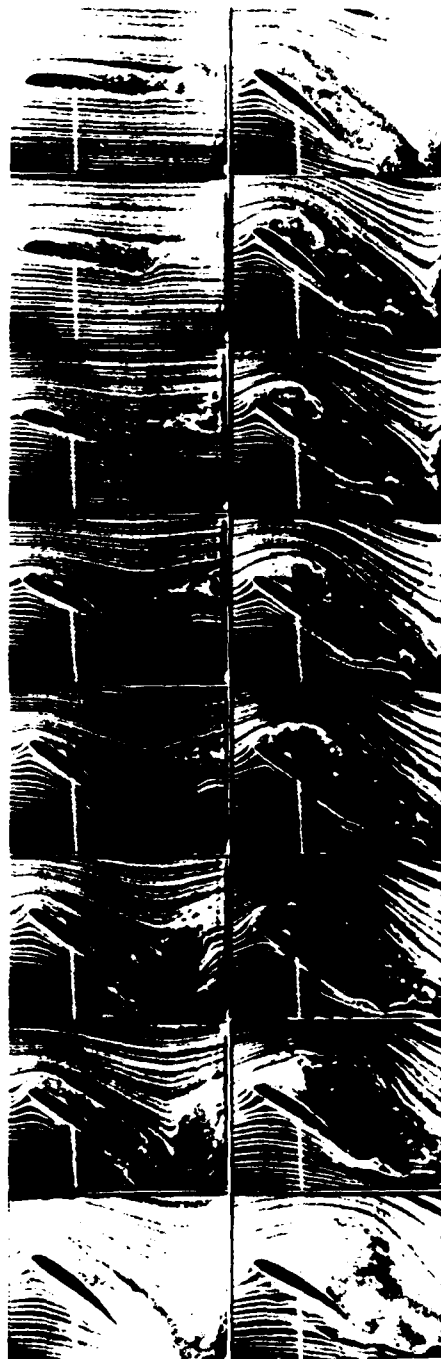

Fig. 2 Large amplitude pitchup of an airfoil in steady wind; from a streakline sequence by Lippisch[14] as reproduced by Bublitz[15].

PITCHING AIRFOIL

A classic smoke rake visualization of an airfoil in pitch up and exposed to steady wind is shown in Fig. 2. It was published by Lippisch[14] over 50 years ago and has been reproduced recently in the definitive historical review by Bublitz[15]. In Fig. 3 we complement this classic with increased vortical detail obtained by our vortex tagging technique in the Reynolds number range best suited for visualization.

This technique also yielded detailed results for airfoils in periodic pitch[5,6]; an example is shown in Fig. 4. Periodic pitching was between angles of attack 20^0 and -20^0 at a frequency f = 1.6 Hz resulting in a reduced frequency k = 2.9, where

$$k = \pi f c / U_o$$
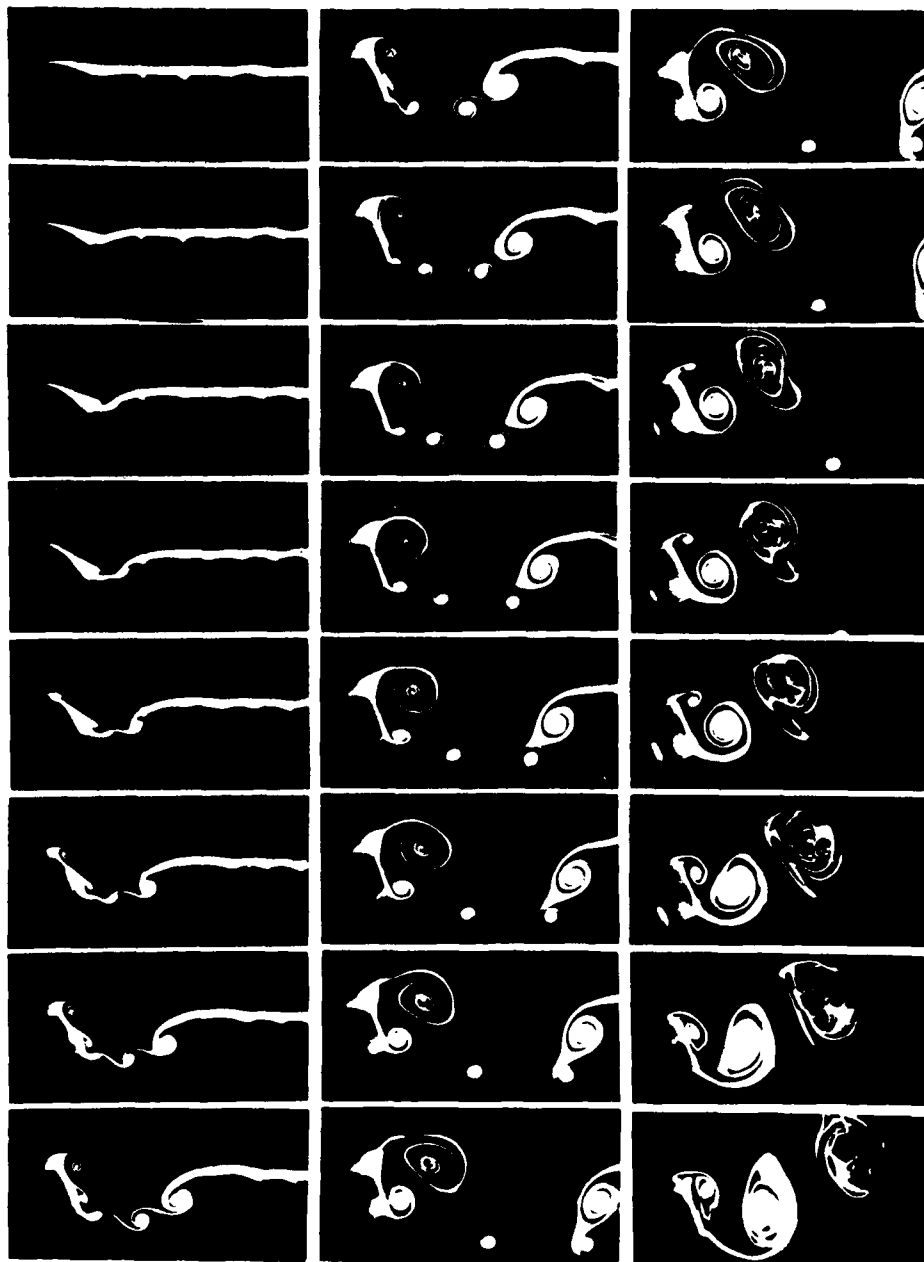

Fig. 3   Large amplitude pitchup of an airfoil in steady wind from 0^0 to 60^0 around the c/4 axis; c = 5.1 cm, U_o = 61 cm/sec, Re = 1700, $\alpha^+ = \dfrac{\alpha c}{U_o} = 0.26$, Δt = 1/32 sec.   From Ref. 5.

199

Alternating vortices are shed from the trailing edge of the airfoil and form a vortex street behind the airfoil. The vortex street has vortices with reverse sense of rotation if compared to the well known drag indicating Karman vortex street in flow behind stationary cylinders. Mutual induction of these vortices is in the downstream direction and the resulting reacting force on the pitching airfoils is therefore in the upstream direction, i.e. the pitching airfoil generates thrust, similar to a pitching fishtail.

PLUNGING AIRFOIL

Pitching and plunging airfoils, as active elements, allow the generation of thrust and this is at the root of sustained animal flight. Obviously, bird and insect flight mechanics can be very complex since pitching, flapping, and other motions are employed in combination and since wings are finite. Almost nothing has been done in
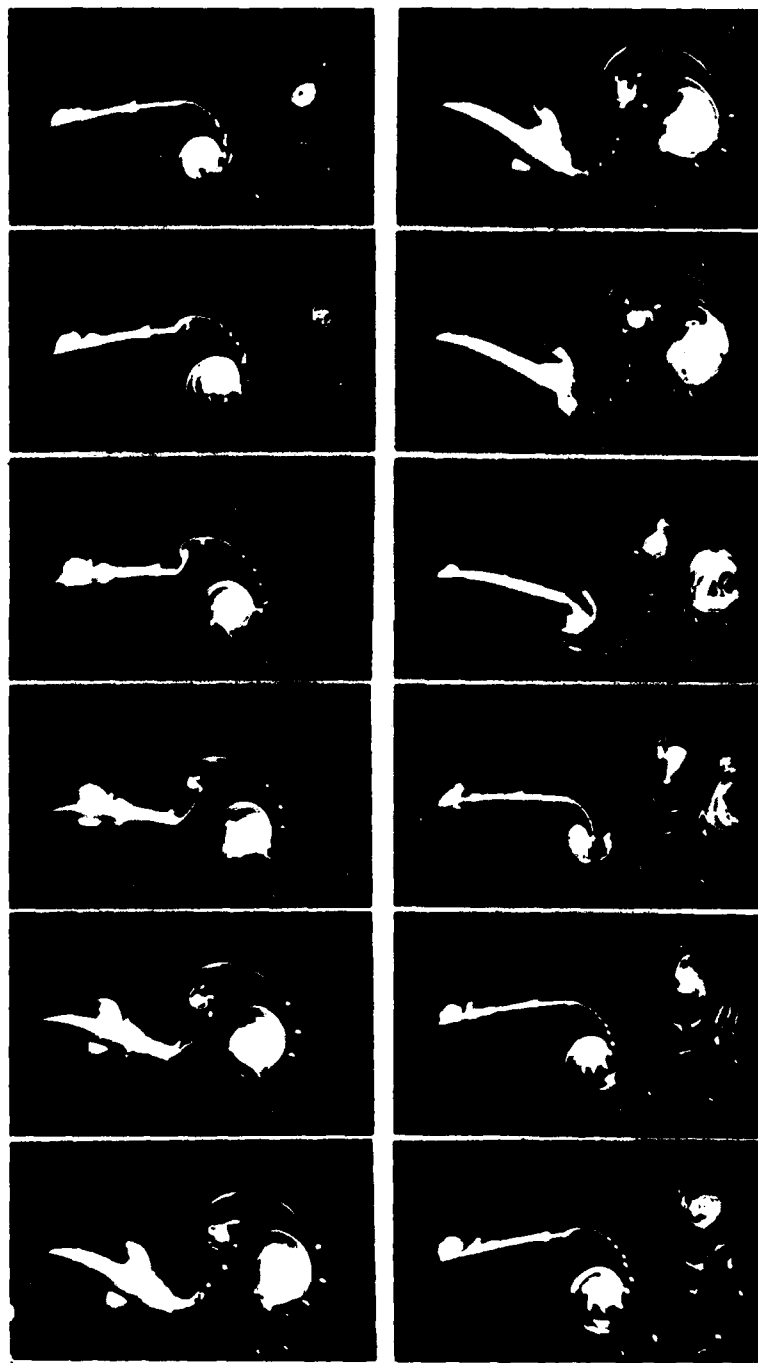
Fig. 4 Airfoil in periodic pitch between -20° and $+20^{\circ}$. c = 35.6 cm, U_o = 61 cm/sec, Re = 12000, f = 1.6 Hz, around the c/4 axis, k = 2.9, Δt = 1/16 sec.

terms of flow visualization to elucidate basic unsteady propulsion mechanisms relevant to bird flight. Simple thrust generation by an airfoil in pure periodic plunging motion and exposed to a steady free stream velocity, $U_0 = 61$ cm/sec, is shown in Fig. 5. We have $c = 15.2$ cm, $\alpha = 5^0$, Re $= 5200$. The plunging frequency is $f = 4$ Hz resulting in a reduced frequency $k = \pi fc/U_0 = 2.7$, the plunging amplitud was $h = 3$ cm. The sequence which should crudely model the flapping of a bird wing, mainly shows the generation of trailing edge alternate vortices which move backward in jet-like fashion, thus generating thrust similar as in Fig. 4. The sequence was taken during a senior design project[16].

Fig. 5 Airfoil in periodic plunge,

$\alpha = 5^0$, $c = 15.2$ cm, $U_0 = 61$ cm/sec, Re $= 5200$, plunge amplitude $h = 3$ cm, $f = 3.5$ Hz, $k = 2.7$, $\Delta t = 1/32$ sec.

An interesting variation of the reverse vortex street was obtained at a higher angle of attack $\alpha = 10^\circ$ as shown in Fig. 6. Here the vortices team up in vortex pairs or jetlets which propel themselves backward and downward, thus thrusting the airfoil forward and upward.

More needs to be done to closely model bird flight, but the basic signatures of thrust generating mechanisms has already been revealed by our simple examples in Figs. 4 to 6.
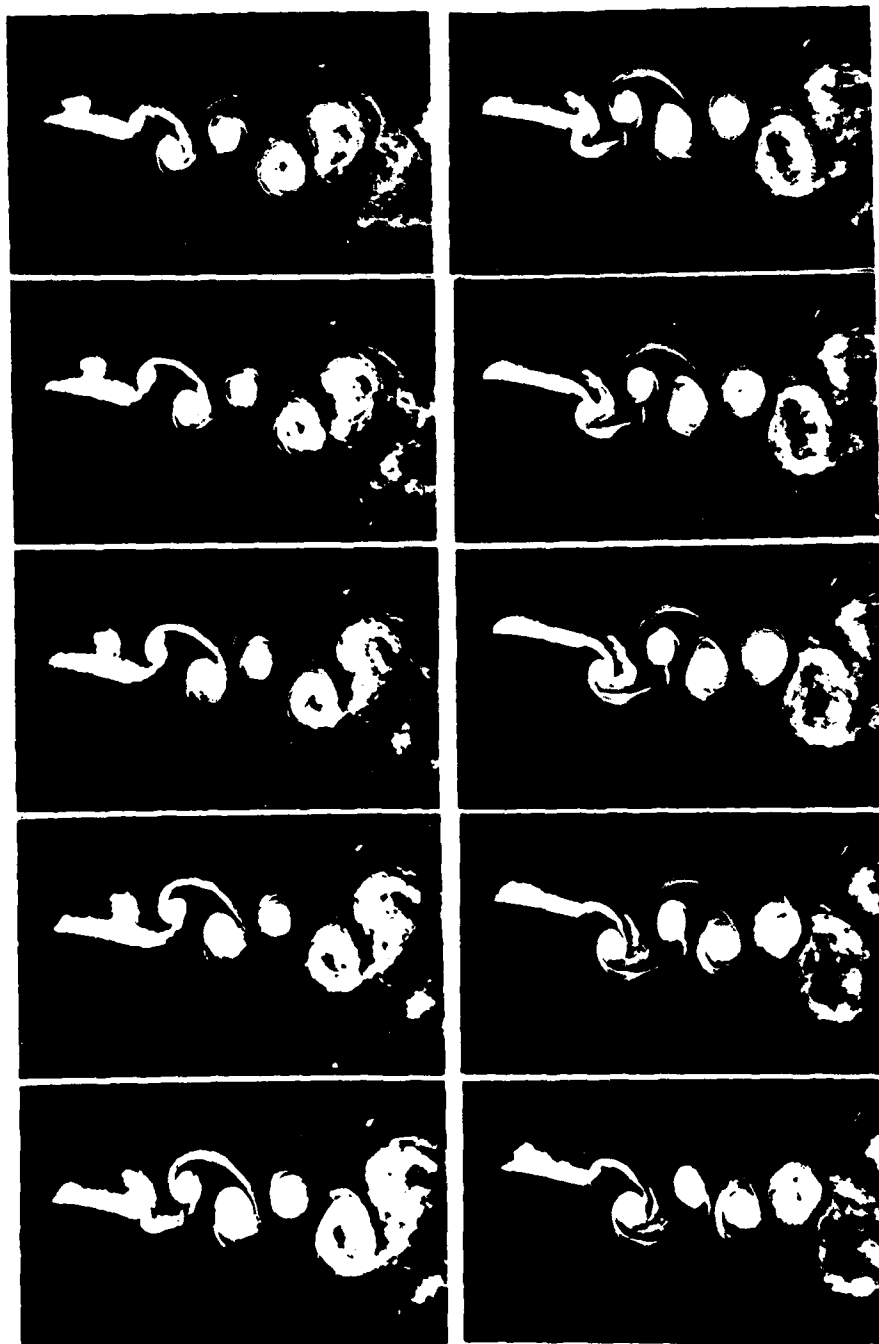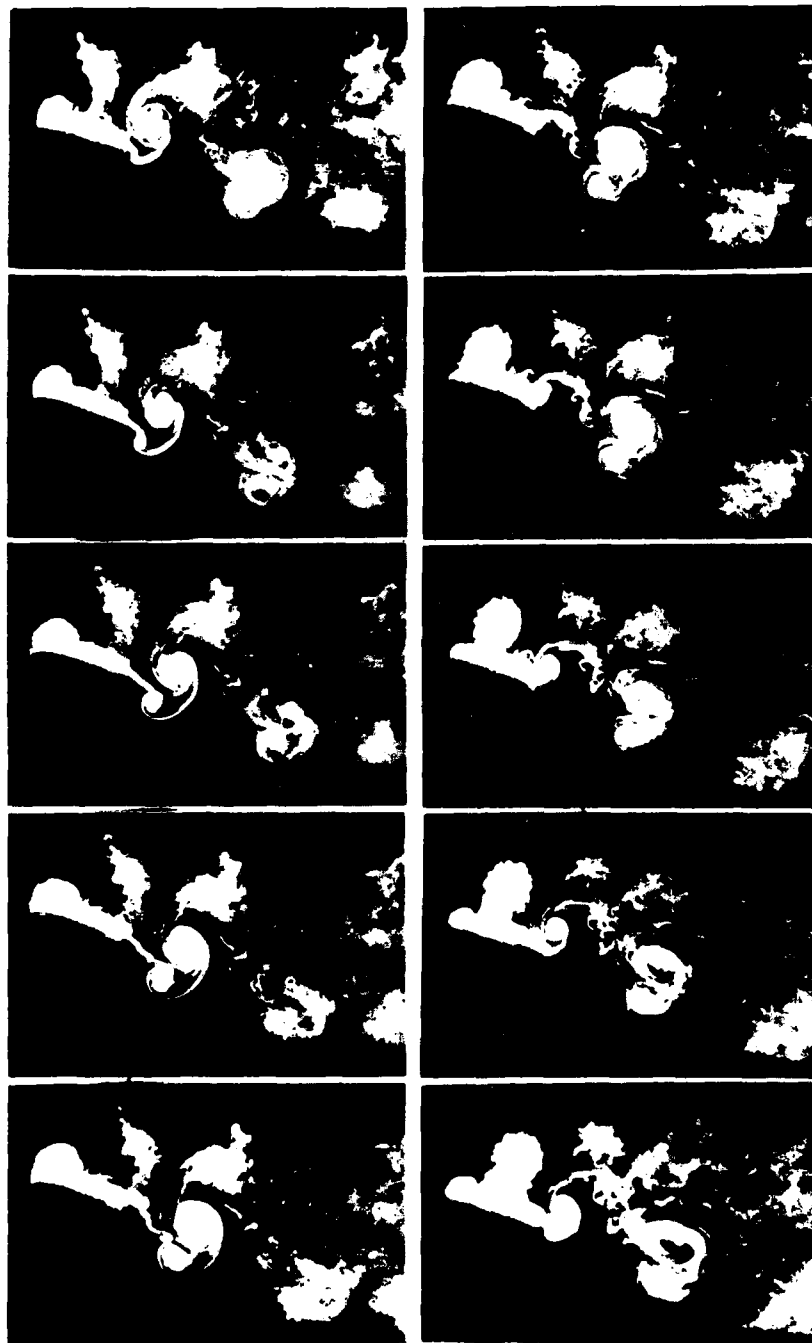

Fig. 6 Airfoil in periodic plunge,

$\alpha = 10^\circ$, c = 15.2 cm, U_o = 61 cm/sec, Re = 5200, h = 2.5 cm, f = 3.5 Hz, ^ok = 2.7, Δt = 1/32 sec.

STALL CONTROL USING AN AIRFOIL WITH ROTATING NOSE

Rotating nose airfoils have been under discussion and experimentation for a long time according to Modi et al[17]. There seems to exist no significant flow visualization of the stall control achieved by this type of device. Furthermore, there is no mention of this device in the context if supermaneuverability.

An airfoil wih rotating nose has been designed by students[18] as a senior design laboratory project and flow reattachment has been successfully visualized for high angles of attack. Their full report is available from the author upon request. Fig. 7, top shows the basic design sketch and the photographic frames below it show the process of reattachment for the airfoil at $\alpha = 40^{\circ}$, at a free stream velocity $U_0 = 91$ cm/sec, c = 12.4 cm, Re = 6000. Circumferential speed of the rotating cylinder was 4.2 times the free stream velocity. The cleanness of the final reattachment is sensational and was achievable at even higher angles of attack.
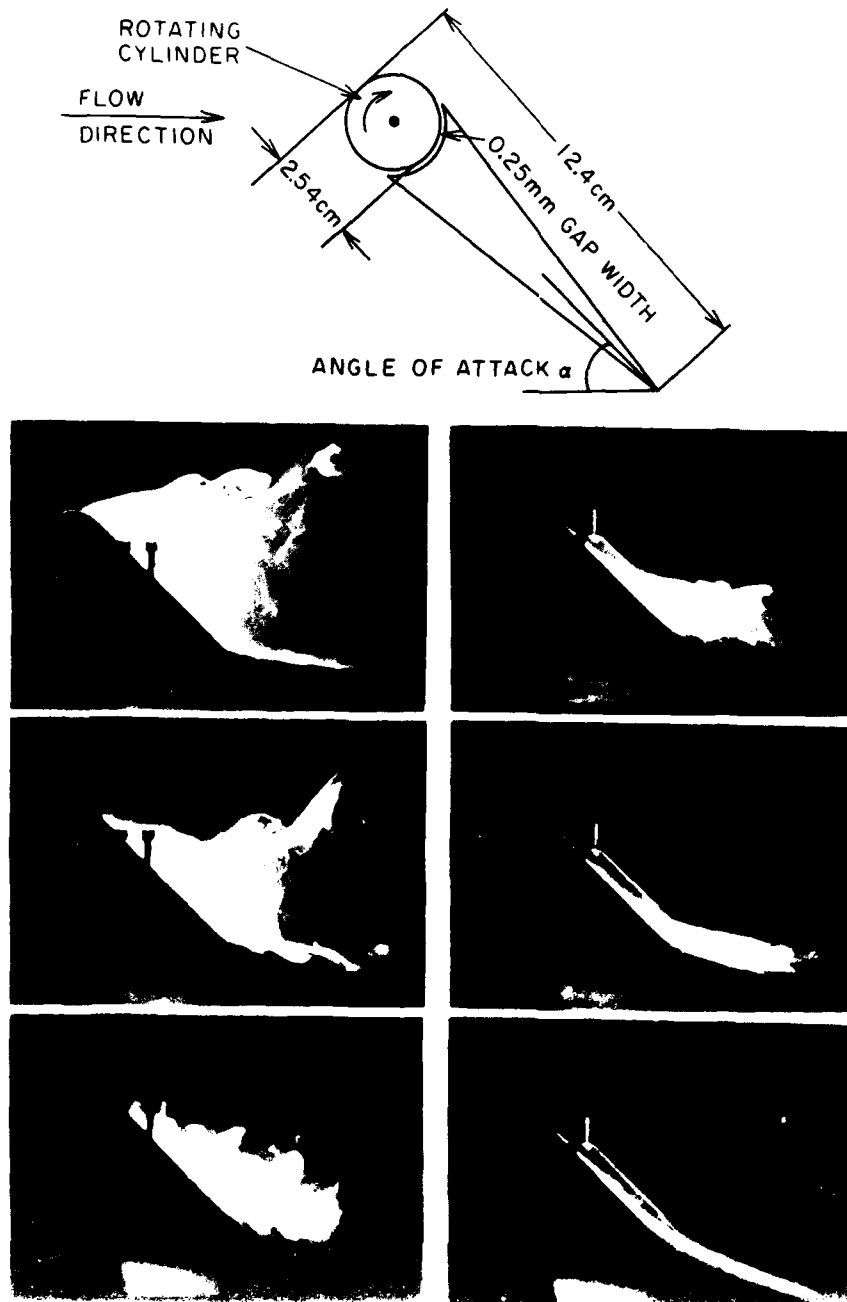
Fig. 7 Rotating nose airfoil. The flow reattachment process is shown after startup of the nose rotation. $\Delta t = 0.5$ sec.

Fig. 7a shows the airfoil with rotating nose in pitch from 0° to 40° in the first 4 frames, then remaining at 40° in the remaining frames. Visualization is by smoke wire with $TiCl_4$ used instead of heated oil. Vortex shedding from the trailing edge is readily apparent during and after pitchup but no leading edge vortex is generated. This new concept of dynamic stall control over the leading edge, while allowing dynamic separation from the trailing edge, may lead to important applications in fast maneuvering aircraft. Fig. 7b shows the same airfoil during pitchup to 40° but without rotation of the nose. Development of the well known dynamic stall vortex behind the leading edge of the airfoil is obvious in this case and is in stunning contrast to the dynamic stall control displayed in Fig. 7a.

Fig. 7a   Rotating nose airfoil pitching from 0° to 40°, Re=4300, α^+ = 0.4, U_o = 61 cm/sec, Δt = 1/8 sec.
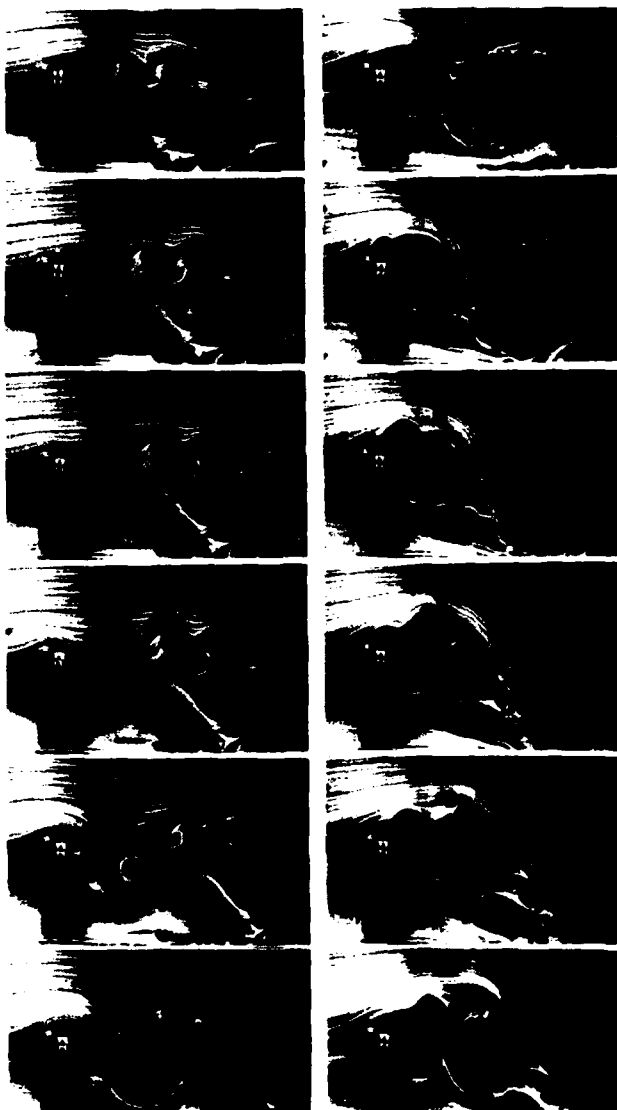
Fig. 7b   Same airfoil in pitch as in Fig. 7a but without rotation of the nose.

204

THREE-DIMENSIONAL VORTEX SYSTEMS OF FINITE WINGS

The vortex strands of a finite three-dimensional vortex system must be connected in accordance with Helmholtz's law. A piercing question is how well flow visualization documents connecting and reconnecting of vortices. Two-dimensional and other cuts of visualization are incapable of addressing the question. Global visualization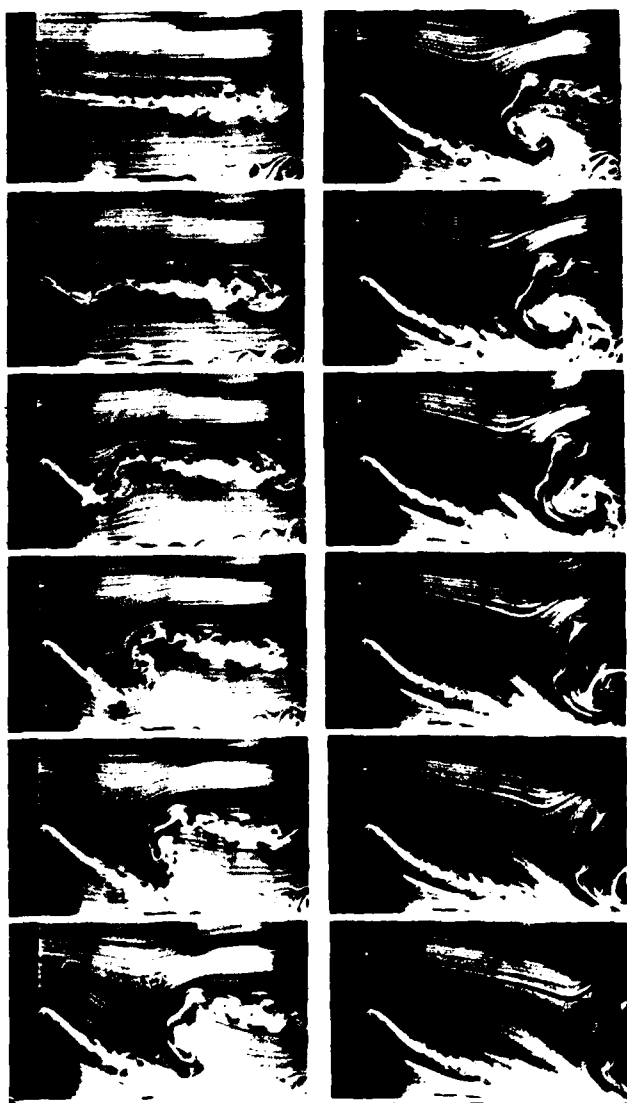s where we introduce the smoke as homogeneously as possible in areas of vorticity production can document connecting and reconnecting of vortices with moderate success as our subsequent examples will show.

Fig. 8 shows the top view or global view of a half wing protruding from the ceiling into the center of the wind tunnel. It is mounted in a turntable which allows periodic and other pitchings. The sequence renders global visualization of vortex development in the tip region of the wing. Pitching is $\pm 5^0$ around a 20^0 mean angle of attack; furthermore, $c = 15.2$ cm, $U_0 = 61$ cm/sec, $f = 0.67$ Hz, $\Delta t = 1/8$ sec. Two counter rotating vortices develop near the tip on the suction side of the wing as Columns 1 and 2 show. Both tip vortices join together at the front corner of the tip and in this way
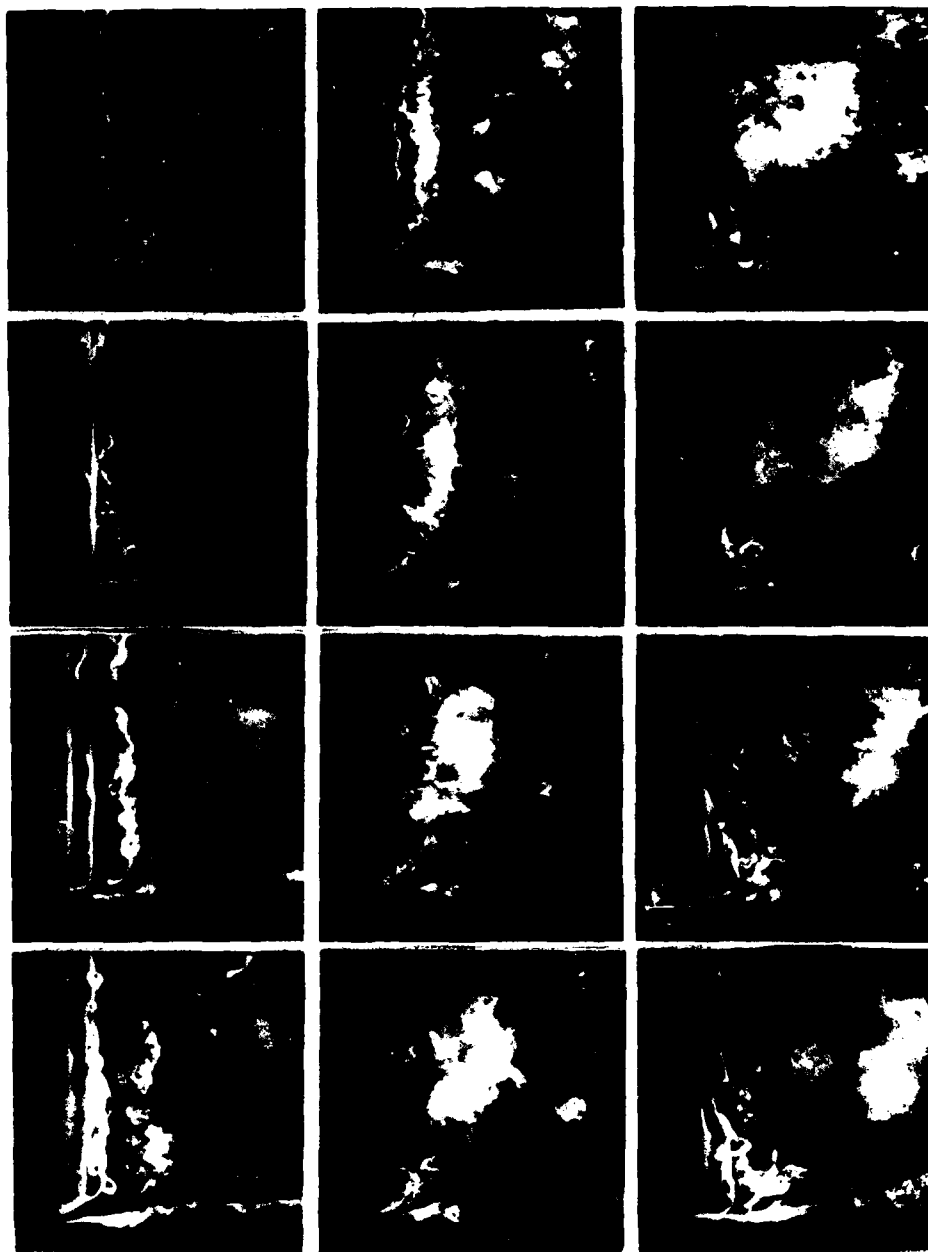
Fig. 8 Rectangular half wing in periodic pitch around the c/2 axis, spanwise or top view,
$\alpha = 20^0$, pitch amplitude $\hat{\alpha} = 5^0$, c = 15.2 cm, $U_0 = 61$ cm/sec, Re = 5200,
k = 0.53, $\Delta t = 1/16$ sec. From Ref. 10.

accommodate the Helmholtz law. The farther inboard vortex also connects to the vortices which separate from the leading edge. In Column 3 both tip vortices move so close together that they may partially annihilate each other by viscous diffusion, thus allowing a growth decay cycle of the tip vortices. Growth and decay of the outer tip vortex has been noticed by Adler and Luttges[19] in their smoke wire visualizations. Vortex tagging thus allowed us to obtain a span-wise or three-dimensional view or global view of tip vortex development. Furthermore, we have been able to learn how the tip vortices accommodate Helmholtz's law and how a growth-decay cycle can be accommodated.

Fig. 9 shows the situation for a pitching delta wing. Periodic pitching is between angles

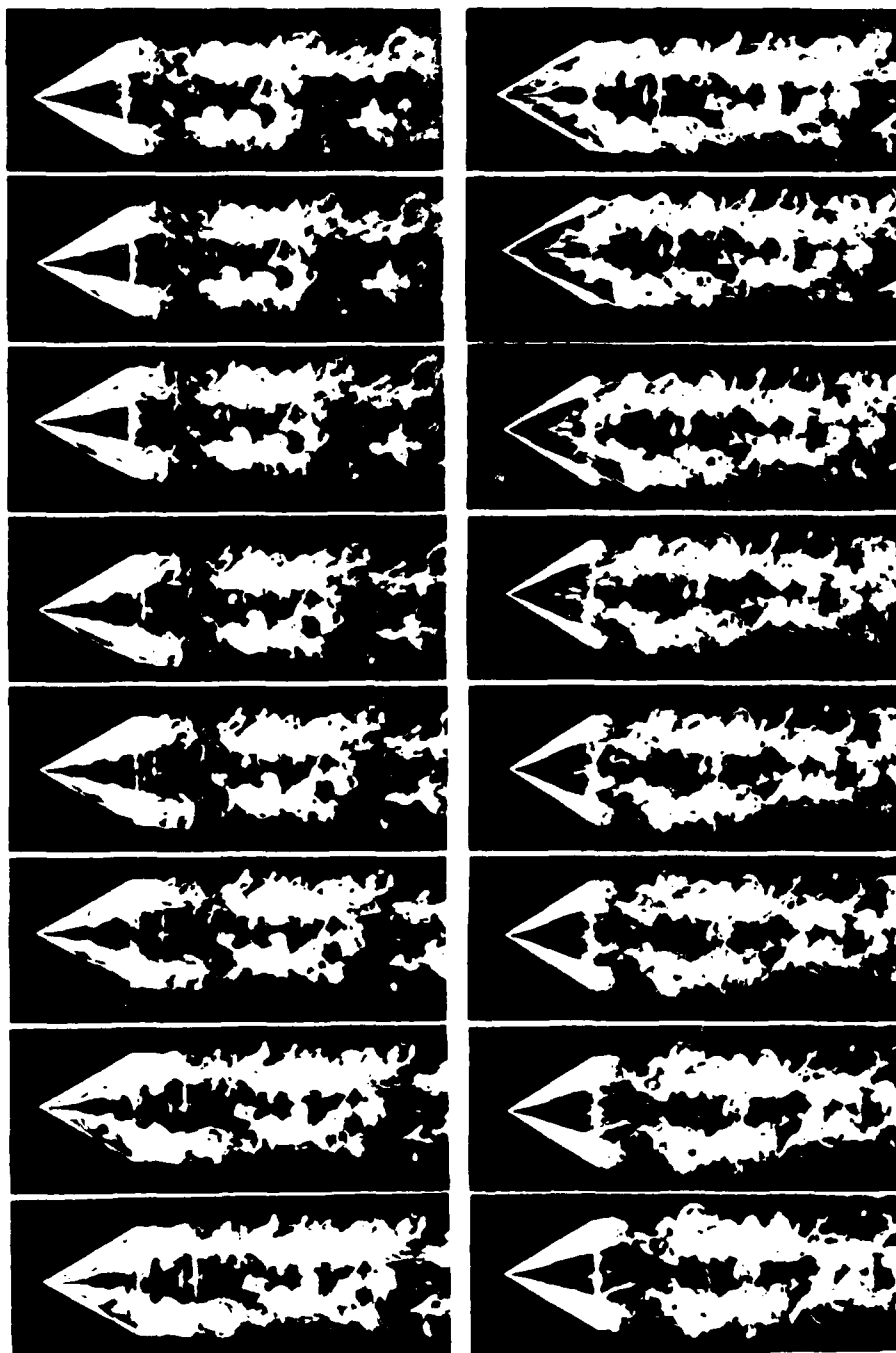Fig. 9 Equilateral delta wing in periodic pitch around the c/4 axis, top view, $\alpha = 15°$, $\hat{\alpha} = 15°$, c = 15.2 cm = side lengths, U_o = 61 cm/sec, Re = 5200, f = 2 Hz, k = 1.6, Δt = 1/64 sec.

of attack 0° and 30° at a reduced frequency k = 1.6. In this case we recognize some growth of the conical leading edge vortices in column 1. They move toward the center line of the delta wing. The parts of the tip vortices close to the front corner keep their laminar and straight appearance. Farther downstream they take on somewhat irregular spiral shapes (double spirals in this case) in the lower frames of column 1. This change in appearance has been observed at constant angle of attack for a long time and is termed vortex break-down or bursting[20,21]. Near the front corner the two tip vortices approach each other so closely that they link up and annihilate above the link in the upper frames of column 2. The linked up or reconnected vortex then convects downstream. Simultaneously, new leading edge vortices start to grow inboard of and close to the leading edges also in column 2 and go through the entire growth-decay cycle. A growth-decay cycle for a pitching delta wing has first been inferred by Gad-el-Hak, Ho and Blackwelder[22] from their two-dimensional cuts of visualization. We now interpret such a cycle by means of three-dimensional vortex principles.

A powerful starting vortex was generated by rapid pitch of a rectangular wing (aspect ratio is 2) from 0° to 60° angle of attack within 0.25 sec. A snapshot of the overall vortex system is shown in Fig. 10. Leading and trailing edge vortices are again linked at the front corners of the wing. The main trailing edge vortex looks very three-dimensional to the eyes which may be captured by holographic techniques in the future.

Further progress can be achieved in the future by applying our global visualization of vortex development to other three-dimensional configurations and pitch histories.

QUEST FOR THREE-DIMENSIONAL DETAILS

While the two examples of the previous section give as good global views of three-dimensional vortex systems additional vortical detail is desirable in areas where smoke is too dense to fully visualize the vortical strands. To obtain finer detail we diluted the titanium tetrachloride to 30% by volume by means of trichloroethylene with the results of less dense smoke production when applied to the wing. We then took closeup movies of areas of interest. An example is shown in Fig. 11 where developments near the upper leading edge of a delta wing at 40° angle of attack are shown in a starting flow of constant acceleration. The development of the tip vortex and of a trailing edge starting vortex are shown in Column 1. In Column 2 a counterrotating secondary vortex develops more close to the leading edge and connects to the tip vortex near the upper back corner of the wing, as does the trailing edge vortex and subsequent trailing edge vortices. In Column 3 even this method gets insufficient to more fully resolve the various vortex strands which become numerous and turbulent. The last few frames of Column 3 show the bursting phenomenon of the main leading edge tip vortex close to the front corner of the airfoil.

Fig. 10 Nikon shot of vortex system of a rectangular wing with aspect ratio 2 after a rapid pitch from 0° to 60°; c = 15.2 cm, U_o = 61 cm/sec.

We previously[9,12] published a global view of this vortex system, which did not produce the fine detail achieved with the dilution method used for Fig. 11. On the other hand using the dilution method in conjunction with a global view produced inferior overall results.

Fig. 12 shows enlargement of a Nikon shot corresponding to frame 2, column 3 of Fig. 11. This frame shows the linkage knots of the secondary and of the trailing edge starting vortices with the leading edge starting vortex quite well although details are still not fully resolved. A peculiar vortex bar exists between the two linkage knots.

Fig. 11 Closeup top view for delta wing in accelerated starting flow at

$\alpha = 40°$, $a = 2.4$ m/sec^2, $\Delta t = 1/64$ sec.

Our examples show that we are making progress in visualizing the connectivity of vortex strands. Complete resolution is an elusive goal and becomes impossible in a strongly turbulent regime.

CONCLUSIONS

We have increased the application range of the titanium tetrachloride method of flow visualization. We have visualized and identified two-dimensional vortical interactions in great detail. Global views of three-dimensional vortex systems have become accessible. The utility of the method in stall control work has been demonstrated.

Future refinements of the method can yield further progress in the quality of visualization. Extending the application range can contribute to the integration and unification of the entire field of unsteady separated flows.

ACKNOWLEDGEMENT

REFERENCES

1. Freymuth, P., Palmer, M., Bank, W. Comparative visualization of accelerating flow around various bodies, starting from rest, Workshop on Unsteady Separated Flow, Aug. 10-11, 1983, Air Force Academy, Colorado Springs, pp. 52-57, 1984.

2. Freymuth, P., The vortex patterns of dynamic separation: a parametric and comparative study. Prog. Aerospace Sci., Vol. 22, pp. 161-208, 1985.

3. Freymuth, P., Bank, W., Palmer, M., Further experimental evidence of vortex splitting, J. Fluid Mech., Vol. 152, pp. 289-299, 1985.

4. Finaish, F., Freymuth, P., Bank, W., Starting flow over spoilers, double steps and cavities, J. Fluid Mech., Vol. 168, pp. 383-392, 1986.

5. Freymuth, P., Vortices. To appear in Handbook of Flow Visualization. Ed. Wen Jei Yang, Hemisphere Publ. Corp, 1988.

Fig. 12 Enlargement of a Nikon shot corresponding to frame 2, column 3 of Fig. 11

6. Freymuth, P., Vortex patterns of dynamic separation: new directions. To appear in Encyclopedia of Fluid Mechanics, Vol. 8, Ed. N.P. Cheremisinoff, Gulf Publishing, 1988.

7. Freymuth, P., Finaish, F., Bank, W., Three-dimensional vortex patterns in a starting flow, J. Fluid Mech., Vol. 161, pp. 239-248, 1985.

8. Freymuth, P., Finaish, F., Bank, W., The wing tip vortex system in a starting flow, Zeitschrift fur Flugwiss. u. Weltraumforschung (ZFW), Vol. 10, pp. 116-118, 1986.

9. Freymuth, P., Visualizing the combined system of wing tip and starting vortices, TSI Flow Lines, Premier Issue, May 1986.

10. Freymuth, P., Finaish, F., Bank, W., Visualization of wing tip vortices in unsteady and steady wind, Paper AIAA-86-1096, also AIAA J. Aircraft, Vol. 23, pp. 730-733, 1986.

11. Freymuth, P., Finaish, F., Bank, W., Parametric exploration of unsteady wing tip vortices. Flow Visualization IV, Hemisphere, pp. 419-424, 1987.

12. Freymuth, P., Finaish, F., Bank, W., Further visualization of combined wing tip and starting vortex systems. AIAA Journal, Vol. 25 pp.1153-1159, 1987.

13. Finaish, F., Experimental study of two-dimensional vortex patterns for impulsively started bodies in comparison with other configurations, Ph.D. Thesis, University of Colorado, May 1987.

14. Lippisch, A., Versuche zur Sichtbarmachung von Stromlinien. Jahrbuch der Vereinigung fur Luftfahrtforschung (VLF), pp. 118-127, 1935.

15. Bublitz, P., History of Aeroelasticity in Germany from the Beginning until 1945, (in German), DFVLR-Mitt. 86-25, 1986.

16. Molloy, M., Lee, M., DePinto, J., Forbes, J., Roberts, B., Somerville, R., Shannon, D., Investigation of a plunging airfoil as a model of natural propulsion. Senior design internal report, U. of Colorado, Dept. Aerospace Eng. Sciences, May 1987 (Available upon request).

17. Modi, V.J., Sun, J.L.C., Akutsu, T. Lake, P. McMillan, K., Swinton, P.G., Mullings, D. Moving-surface boundary-layer control for aircraft operation at high incidence. J. Aircraft, Vol. 18, pp. 963-968, 1981.

18. Bush, R., Freece, T., Hora, K., Jackson, S., Kallemeyn, P., McNall, S., White, T., The effects of a rotating cylinder as a leading edge on boundary layer separation over an airfoil assembly. Senior design internal report, U. of Colorado, Dept. Aerospace Engineering Sciences (Available upon request), May 1987.

19. Adler, J. N., Luttges, M. W., Three-dimensionality in unsteady flow about a wing, Paper AIAA-85-0132, 1985.

20. Payne, F.M., Ng, T.T., Nelson, R.C., Schiff, L.B., Visualization and flow survey of the leading edge vortex structure on delta wing planforms. Paper AIAA-86-0330, 1986.

21. Lugt, H.J., Vortex flow in nature and technology. John Wiley & Sons Inc., 1983.

22. Gad-el-Hak, M., Ho, C.-M., Blackwelder, R.F. A visual study of a delta wing in steady and unsteady motion. Workshop on Unsteady Separated Flow, Aug. 10-11, 1983, Air Force Academy, Colorado Springs, pp. 45-51, 1984.

210

Initiation and Use of Three-Dimensional Unsteady Separated Flows

Marvin W. Luttges
and
Donald A. Kennedy
Aerospace Engineering Sciences
University of Colorado, #429
Boulder, Colorado   80309

ABSTRACT

Throughout the last decade or so much work has been done on unsteady separated flows. The manner in which they are initiated, the development of these flows and the impact of them on lifting surfaces have all received considerable attention. Several major conclusions may be drawn from the research done to date. (1) The unsteady flow initiation and growth support mechanisms are readily controlled such that they can be reproduced from one time to the next. (2) The aerodynamic forces associated with the presence of these flows are demonstrably large yet transient. The flows can be produced repeatedly such that overall time-integrated aerodynamic forces are large compared to forces associated with lifting surfaces in more conventional static test situations. (3) Any rapid angle of attack changes by lifting surfaces, whether achieved aerodynamically or through thrust vectoring, will produce unsteady separation that yields large transient lift forces. (4) The use of unsteady separated flow depends on both the anticipation of flow genesis and force generation as well as the ability to prevent unsteady separated flow generation. This latter control element, although common in the use of other flow regimes, has not been seriously considered for instances in which unsteady flows are likely to be initiated.

The proposed work focuses upon two major questions. (1) What are the separable physical mechanisms that yield unsteady flow separation and development as well as shedding? (2) What are the means through which these physical mechanisms can be controlled to either enhance the effects of these flows or to reduce the effects of them? To achieve these goals we propose to provide systematic quantification of the elements cited in a recent model of physical mechanisms. These quantifications, in turn, will be used for a comprehensive quantitative model of unsteady flow effects on lifting surfaces. The adequacy of the model will be evaluated by experimental tests that are designed to use predicted means for both enhancing unsteady flow effects and reducing them.

The results of the proposed studies will be (1) a comprehensive, testable model of unsteady separated flows and (2) comprehensive schemes for systematic increments or decrements of these flow effects as realized on a variety of lifting surfaces. A new motion device will provide enabling instrumentation. The quantitative anemometry files will provide the basis for achieving the above goals. In addition, these files can be used subsequently for computer simulation models and for corroboration of the fidelity of such models

INTRODUCTION

Unsteady separated flows have been shown to produce large, transient aerodynamic forces. These forces have peak values that are several-fold those values seen in static tests. Despite the vagaries of such transient forces, the magnitudes of these forces have attracted considerable attention in regard to possible applications. If these flows can be sufficiently well understood and controlled, they could become the basis for aerodynamic enhancements used to support higher maneuverability and agility for aircraft.

The following discussion focuses on two major characteristics of unsteady separated flows: reproducibility and physical mechanisms.

In regard to predictability, a number of ordinal scale relations have been empirically determined. Using these ordinal relations flow initiation, development and fate are well-behaved and highly stereotyped. The influences of α_w, $\alpha_{\bar{x}}$, K, α^+, Re and pitching axis are well ordered for both sinusoidal

pitching and matched, large-scale pitching. Whether produced by pitching surfaces, spoilers, air pulses, deforming surfaces or combinations of these, a consistent class of flow perturbations arise. The resulting flow structures (1) are initiated at expected sites and times dependent on *forcing function characteristics,* (2) are likely to develop at reproducible rates to consistent sizes and (3) yield reproducible efforts on the surface from which they arise.

Some basic physical models of unsteady separated flows have been presented recently by Reynolds and Carr (1985). These models employ rather clever interpretations of vorticity accumulation and provide considerable insight into the fluid dynamics underlying unsteady separated flows. Based upon additional laboratory research, another physical model is presented below. It attempts to account for the variations in flow fields observed across a wide range of test parameters employing periodic, repetitive pitching as well as large, scale single pitch motions. Other methods for producing unsteady separated flows are accounted for, as well.

Before discussing a physical understanding of unsteady separated flows, a brief historical perspective is provided for the recent research impetus. Notably, a good deal of the impetus has come from Air Force Office of Scientific Research and was enthusiastically initiated by Mike Francis several years ago.

A BRIEF HISTORY OF UNSTEADY SEPARATED FLOW RESEARCH

In 1975, Mc Croskey brought a good deal of attention to the matter of unsteady flows in fluid mechanics. His Freedman Lecture noted that this was a kind of flow regime that neither obeyed fully laminar nor fully turbulent treatments. Many of his examples resided with those flows encountered in flight regimes that were near high angles of attack, that were encountered as atmospheric perturbances or that were generated as a consequence of mechanical movements displayed by the lifting surfaces in question. Thus, flutter was cited and even the blade slap of helicopter rotors was covered.

The ensuing work by Mc Croskey, Mc Alister and Carr (1978) focused on the flows that were likely to be produced about helicopter rotor blades. To model these conditions, a NACA 0012 airfoil was driven through sinusoidal changes in pitch angles at a variety of different rates. The pitching rates were nondimensionalized with freestream velocity and semi-mean aerodynamic chord to yield a "reduced frequency parameter", K. The K value was taken to be the rotational frequency * chord length divided by 1/2 freestream velocity. Thus, any unsteadiness produced by the pitching would shed from the pitching surface assuming a K=1.0 and that unsteadiness convection rates were approximately 1/2 freestream velocity. The K values examined experimentally by these workers were well below K=1.0. But, the work revealed the generation of unsteady separated flows that produced large, transient lifts on the tested airfoil. Presumably, these lift histories were responsible for much of the rotor fatigue and noise produced by helicopters. A later study by Carr (1979) showed that the use of a leading edge slat could obviate many of the unsteady lift characteristics of the oscillating airfoil.

Partially in response to the studies by the above investigators and in response to flight observations made by Israeli combat pilots using F-4's, the USAFA started to evaluate the kinds of unsteady separated flows that could be produced by rapid pitch up motions of airfoils. Francis and colleagues showed that rapid pitch up motions to 60 deg. angles of attack produced high lift forces (1985) yet a spoiler mounted past mid-chord on an airfoil produced little lift (1982) enhancement. This work has been pursued by Walker, Helin, Robinson and others at the USAFA such that it is now clear that motion history is critical to the amount and time course of the unsteadiness that is produced by the rapidly pitching up airfoil. In any event, it became clear that this particular motion of the airfoil could generate significant periods of brief lift enhancement that might be used for enhanced aircraft maneuverability. The state of the art in experiments using this flow regime was captured in a workshop at the U.S. Air Force Academy in 1983 (Francis and Luttges, 1984).

Early in this revived period of interest in unsteady flows, a number of investigators showed that flow structures produced in the unsteady separated flow regimes were well behaved and highly reproducible. Gad-el-Hak and colleagues had used a delta wing model to show that pitching in sinusoidal fashion led to the periodic growth and decline of relatively stationary vortices on the delta wing upper surface. Carta and colleagues showed that the evolution of a large, poorly defined vortex occurred as the airfoil was pitched beyond the static stall angle characteristic of the NACA 0012 airfoil. The resulting flow field was not observed to be well behaved. Nagib and colleagues had shown that a deployed step would create a significant vortex and that this vortex persevered for several step diameters downstream of initiation. Using a novel means to yield small but high frequency

disturbances, Covert and Lorber showed that unsteadiness with a K=6 had little cohesiveness in terms of the structures resolved in the pressure profiles they collected. Thus, it was believed that high K values might get to a regime in which there were significantly different mechanisms at work. Finally, Luttges and Robinson showed that a variety of test parameters could be used to get cohesive vortex generation and development. Whereas variations in Reynolds numbers and surface geometry had little effect on vortex generation, changes in pitching amplitudes, mean pitching angles and K values did. Further, even changes in pitch axis altered the genesis characteristics of the vortices.

From the above research and additional work cited in the bibliography, several rules of vortex generation became clear. Most reliably, a lifting surface more and more rapidly pitched beyond static stall angles was correlated with ever longer delays in the appearance of a leading edge vortex. This simply means that the lifting surface could attain quite high angles of attack in the absence of the formation of a leading edge vortex. In sinusoidal pitching tests, the lifting surface can be well into the downward pitching portion of the cycle before a leading edge vortex is seen. Another way to state the relation is that motion histories that are rapid enough to occur in the absence of significant freestream passage yield small and delayed vortex structures.

The effect of mean angles of attack (sinusoidal pitching) and final pitch angles (large pitch up motions) are the opposite of those observed for pitch rate variables. Higher angles of attack, however achieved, yield larger vortices and do so earlier in the upward pitching motion history. Here, it seems appropriate to regard this as a matter of the stochastic pitch angle of the lifting surface that is experienced by the passing freestream.

Variables like pitching amplitudes or pitching motions that carries the lifting surfaces well into the areas of attached flow make the genesis of unsteady separation much more difficult to follow. These motion histories carry the lifting surface into flow regimes where vorticity shedding exceeds or matches vorticity production and into areas where considerable flow hysteresis occurs with a sense opposite to that of the predominant flow conditions. In general, these conditions produce different vortex sizes and levels of cohesiveness dependent on the K and mean angle of attack conditions with which they are paired. The convection histories of the major vortex structures are a complex reflection of the above cited variables, as well.

The recent interest in three-dimensionality variables has not been met with extraordinary additional complexity. Whether considering elicitation from three-dimensional surfaces, the three-dimensional aspects of the flow structure or the compound three-dimensionality of the overall test situation, the major facets of the unsteady separated flows have been shown to be relatively unperturbed. In flow character evaluations, finite geometries of the lifting surfaces cause alterations near wing tips. These alterations are limited to areas of the span approximately one chord or less inboard of the tip. The pressure signatures of the passing flows are quite similar to those recorded in two-dimensional tests even within fractions of a chord length of the tips (Robinson et al., 1987). As will be shown later, the spatial character of unsteady flows obviates some of the three-dimensionality that might otherwise complicate the effects realized on the three-dimensional lifting surfaces.

The research conducted in the area of unsteady separated flows has been quite extensive over the last several years. Many useful relations have been observed on both qualitative and quantitative levels. Only recently, however, have investigators begun to put together simple physical models for this rich transitional flow regime. The vorticity model proposed by Reynolds and Carr (1985) provides an excellent overview of unsteady separation support mechanisms. Beginning with some of the salient features of this model we propose herein a working model of the overall genesis of unsteady separated flows as well as a model of the subsequent behavior of these flow structures once they have been produced. The data that are taken into account here are admittedly weighted toward those observations made in the laboratories at the University of Colorado and at the U.S. Air Force Academy. At this time we have limited our physical model to nominal and ordinal scaling observations. We have done so to first identify the major elements of the underlying physics of the flows in question and then to indicate the expected direction and rough magnitude of the influences. Finally, we can use the model to show what measurements are required to systematically anticipate both the initiation and development aspects of these flows in possible applications--- uses dependent on either enhanced or reduced unsteady separated flow effectiveness.

A PHYSICAL MODEL OF UNSTEADY SEPARATED FLOW

Physical Mechanisms Hypothesized in Genesis

a) The initiation of unsteady separation depends upon the local

accumulation of vorticity about the leading edge of the test airfoil surface whether a flat plat or one with thickness and camber distributions. The requirement that the test surface be pitched beyond static angles of attack reflects the nature of both vorticity generation and accumulation mechanisms. It is obvious that higher angles of attack generate larger pressure gradients about the leading edge. Spatially, these large gradients occur over short distances. When the leading edge is rapidly pitched upward these large pressure gradients persist until separation occurs. Below angles of attack that lead to separation in static testing, the generation of vorticity is matched to the shedding of vorticity. This is not the case with a test surface rapidly pitched to angles well beyond static separation. Here, the instantaneous low pressure area near the leading edge and the loss of the boundary layer influences by the freestream couple to lead to a significant decrease in normal amounts of vorticity shedding. The net effect is the production of a vorticity storage area, boundary layer thickening and a flow separation bubble at the leading edge of the airfoil.

Since the amount of vorticity that is produced is dependent on the amount (or length) of passing flow, pitching can be sufficiently rapid to yield little vorticity production. With the passing of time and flow more and more vorticity can be accumulated near the leading edge of the airfoil. The growth of this fluid volume, thickening or bubble can not continue without encountering an increased freestream influence and an increased probability of reverse flow. Slowly pitching test surfaces encounter the same mechanisms but do so under slightly different circumstances. As the slowly pitching surface exceeds static separation angles of attack the amount of passing flow remains comparatively large relative to pitching induced flows. This translates into a comparatively high rate of vorticity production that is distributed more broadly about the leading edge as well as downstream on the test surface. The freestream influences are decreased slowly through increased shadowing as the surface continues to pitch upward. And, these time scales are sufficiently long to allow both vorticity and momentum contributions from reverse flows originating from the trailing edge and traveling upstream over the suction surface to grossly disturb the streamwise flow.

b) The vorticity production mechanisms, as shown above, are intrinsically related to both the accumulation and distribution factors of the vorticity. As will be shown later the distribution of vorticity

accounts for one of two major elements of the overall threshold behavior that trips the flow to produce an unbound vortex. It has been noted repeatedly that low pitch rates yield an elongate vortex that originates at 0.3 or more chords downstream of the leading edge. In contrast, rapid pitch rates yield a well-rounded, smaller vortex clearly visible upstream of 0.2 chord locations. The vorticity produced at low pitch rates accumulates near the leading edge but in response to a somewhat less severe pressure gradient than that of high pitch rates. The overrunning flow is sufficient to generate more vorticity than can be protected in the shadowed area of the upward moving leading edge. The resultant storage or bubble area is subject to some convection in the downstream direction. At the same time, the freestream influence perseveres in encouraging the downstream shedding of vorticity. Only at the time that a vortex is produced does significant rampant reverse flow occur from downstream. Even then, vortex convection and reverse flow move in opposite directions such that the confluence of these flows usually occurs downstream of leading edge vortex initiation sites.

When pitch rates are high, the vorticity accumulates in a volume of test surface shadow that is relatively large yet quite proximal to the leading edge. Most of the vorticity arises from the shear created by pressure gradient between the stagnation pressure site and the immediate adjacent upper surface pressure minima sites. Since the pitching motion is rapid relative to the amount of passing freestream, the total amount of vorticity generated is small and easily contained in this large shadow volume. Accordingly, the occurrence of an unbound vortex must await a sufficient freestream influence interacting with the accumulating storage of vorticity. This often requires that the surface be well into the pitching down portions of the sinusoidal oscillation cycle. Here, the overrunning flow is effectively entrains the vorticity storage volume. Smaller amounts of vorticity are entrained more rapidly than instances of larger vorticity volumes where vorticity is being added at high rates during vortex formation and growth. The ensuing full exposure to the freestream moves the vorticity such that both the overrunning flow and the lifting surface participate in the "spinning-up" of the nascent vortex.

Another way of viewing these vorticity distribution differences is to begin with comparisons to steady tests. Of course, a lifting surface at angles of attack below separation angles will reach a point where it sheds vorticity at the rate at which it is produced. As

the surface approaches separation conditions, it becomes ever more difficult to shed the large amounts of vorticity being produced. Shear layer distortions of the flow testify to the large amounts of vorticity present. The pressure minima near the leading edge compete with the convection influences of the overrunning flow in maintaining a "vorticity balance." The flow finally separates from the trailing edge allowing reverse flow to move upstream adjacent to the suction surface. This creates a localized thickening of the boundary layer and a means for shedding the excess vorticity in the separated regions. In tests of even higher angles of attack full separation occurs and the reverse flow traverses upstream to the leading edge of the upper surface. The vorticity, thus, sheds from the site of production. In a sense, the resulting circulation over the surface of the airfoil is rather like a very flat vortex that is about a chord long in the streamwise direction.

In sinusoidal pitching tests that carry the surface beyond the static separation angle, all of these events can be thought of as occurring within a much restricted streamwise dimension that is bounded temporally by the discrete periodicity of the pitching cycle. The pitching surface defines a region of leading edge pressure minimum that decreases with time as the pitching continues. Deprived of the full freestream influence in the shadow of the surface, the vorticity accumulates until it is of sufficient amount to intercept large freestream influences. If the accumulation is large enough and time-consuming enough, the downstream vorticity ceases shedding and begins to show reverse flow. This means that the reverse flow will return vorticity to the growing leading edge vortex and that this delivery of flow can carry significant momentum flux with it. The reverse flow can, of course, separate the leading edge vortex from the lifting surface before the vortex can convect along the surface to the trailing edge. As will be seen later, the induced reverse flow may be of significant enough momentum to entrain a vortex of the opposite sense from the pressure surface. This second vortex also can be energetic enough to induce large, local pressure fluctuations.

Instances of higher pitching rates yield less overall vorticity but more sharply defined volumes of vorticity. Downstream shedding continues beyond the time that maximum pitch angles are attained since the momentum of the flow to do so persists. The evidence for discrete vorticity accumulations that are given little time for dispersion through freestream diffusion is seen both in the highly cohesive form of the vortices
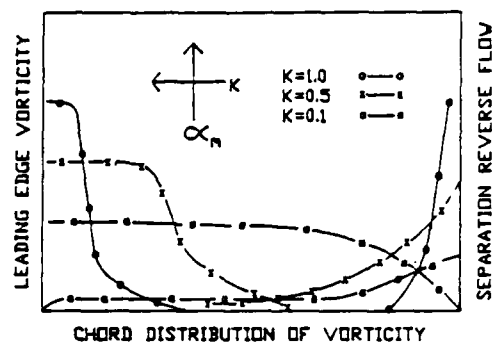

CHORD DISTRIBUTION OF VORTICITY

Fig. 1. Summary of hypothetical vorticity distribution on the chord of a pitching airfoil. High K yields vorticity accumulation proximal to the leading edge. Low K shows more distributed leading edge vorticity as well as vorticity gleaned from reverse flows originating at the airfoil trailing edge. K increments move vorticity accumulations into more restricted volumes. Alpha mean increments lead to larger overall vorticity accumulation values.

that occur and in the likelihood that several chord locales become individual sites for unbound vortices to occur more or less simultaneously. The multiple sites of vorticity accumulation are reflective of the sinusoidal pitching that causes localized velocity increases and decreases about the leading edge before a mean chord length of overrunning flow has passed over the surface chord. The situation becomes more complex as pitch rates yield several full pitch cycles before a mean chord length of flow has passed the surface. The vorticity accumulated in the passing boundary layer forms structures capable of interacting energetically with each other as reflected in both vortex growth and convection speed. Still, the principal factor in these circumstances is that only a fixed amount of vorticity is produced. This vorticity must therefore be shared in the creation and development of these transitional structures.

The final part of the pitching surface test scenario requiring attention is the pressure surface. The pressure surface experiences a uniformly distributed spatial increase and decrease in pressure maxima throughout the pitching cycle. The flow velocities are comparatively uniform over the chord such that major foci of concentrated vorticity production don't occur. The vorticity that is produced in the boundary layer experiences full freestream exposure such that shedding rates are potentially much higher than actually required for full shedding of

vorticity. In this sense, the pressure surface boundary layer is always "starved" for vorticity. As will be seen later, the behavior of the trailing edge vortex reveals the relative vorticity content of the shedding pressure surface boundary layer as compared to that of the suction surface.

c) Vortex growth and development mechanisms are the result of a mixture of vorticity accumulation and freestream mechanisms. The initial size of the vortex reveals the amount of vorticity that was extant when unbound vortex threshold was attained. The resulting vortex, if comparatively small, usually shows high intrinsic rotational velocities and a significant pressure minimum. Translational velocities for these vorticies are high, as well. Larger nacent vortices show comparatively more moderate rotational velocities but may entrain larger amounts of freestream flow. In addition, the larger vortices probably glean much of the flow volume from the assimilation of reverse flow. As the vortex dwells over the surface of the airfoil, it it will bring a fraction of that surrounding flow into the rotational structure. A larger vortex presents
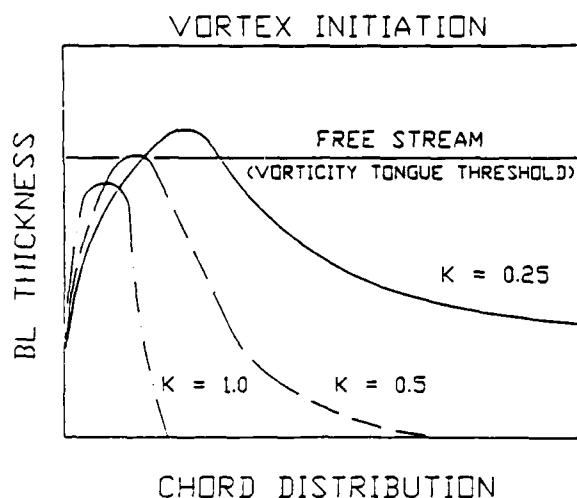
VORTEX INITIATION

CHORD DISTRIBUTION

Fig. 2. Summary of vortex initiation mechanisms. The accumulating vorticity grows in a bubble or storage structure behind the airfoil shadow in the leeward volume. Growth finally exceeds the shadowed volume or the airfoil motion reduced the shadow area. In either event, exposure to free stream is increased. The overrunning freestream "spins up" the vorticity of the bubble generating a nascent vortex. Different K values yield different bubble geometries which, in turn, determine slightly different interactions with the freestream flow.

more surface area to the overrunning flow with two important consequences: "spin-up"is increased and vorticity diffusion is concentrated. As the vortex grows it covers an ever larger percentage of the chord and it readily assimilates the boundary layer into the structure. Lower K values, of course, lead to more boundary layer vorticity. Finally when the structure has exhausted much of the rotational sense to the surrounding flow, it passes into the wake without further growth. If the vortex in question is small and more localized, it generally shares the upper surface (and boundary layer vorticity)with a vortex from a prior cycle of pitching. Thus, most of the surface vorticity is to be found in both of the resident vortices. Also, these conditions are indicative of pitching parameters that force vortex production at comparatively high rates compared to vorticity production and accumulation rates. That is, pitching rates are high and the rates of freestream passage are low.

In summary consideration, the energetic vortex is a place to incorporate surrounding flow. This incorporation process is the same whether considering either freestream (overrunning) flow, reverse flow or flow heavily invested with vorticity. The effects of the incorporation process on the vortex varies dependent on the flow taken in. The momentum of the incorporated flow structure is to be considered as are the laminar/turbulent structure ratios. With laminar overrunning flow the momentum simply determines vortex convection behavior. In the latter case, the flow may deliver fluid elements that are at a lower turbulence level than that of the vortex and thus may provide a working fluid on which the vortex can act. The turbulent fluid, however, already being at a high turbulence level and can absorb little additional input from the vortex. The reluctance of one vortex to accept the turbulence intrinsic to other vortices is seen in the multiple ways that vortices have been observed to interact, one with another (cf., Freymuth).

d) The convection characteristics of the leading edge vortex at first seem enigmatic. The vortices produced by low pitch rates are known to convect relatively slowly, at velocities of 30% V/Voo. Those of the higher pitch rates are seen to have convection velocities of >60% V/Voo. We have shown that a major factor in these convection differences is when a vortex is produced and what exposure to the freestream it experiences. The low pitch rates yield a vortex on the upstroke. The vortex, thereafter, continues to enjoy the increased shadowing from the freestream. The higher pitching rates show vortex

216

initiation delayed until the downstroke. The growing effect of the freestream initiates the vortex and shows a strong convecting influence as well. The rapid pitching motions can create a vortex that experiences varying freestream influences across a full pitching cycle or more. In these instances, the vortex experiences the full freestream influences on the downstroke and then fractional influence on the upstroke, as well. Since the vortex in question often is far enough down the chord to intercept the overrunning flow returned to the surface by the upstream leading edge vortex, the pitch up influences of the freestream can be quite large---- even briefly exceeding Voo.

A major influence on the vortex created by low pitch rates is the reduced convection velocity derived, in part, by the interception of the reverse flow. While this flow can aid in vortex "spin up" it also delivers a considerable amount of momentum to the vortex---momentum that possesses a reverse sense from that of the usual downstream convecting vortex. A large enough reverse flow can evoke full vortex separation from the suction surface. This occurs when the surface pitches so rapidly that little vorticity is trapped until the surface motion stops. Such is the case of the high pitch rate, high angle of attack studies done at the U.S. Air Force Academy. The vorticity accumulated during the rapid pitch up motions is minimal. When the motion stops, the overrunning flow fills the shadowed region behind the surface with energetic vorticity. The accumulation of vorticity comes from the nearby stagnation pressure gradient drivers and the reverse flow that is allowed to develop in the absence of any significant vorticity shedding mechanism. For a brief period, the leading edge vortex does not appear to convect downstream. Then, the convection often moves the vortex off the airfoil suction surface before the vortex reaches the trailing edge. Vast amounts of reverse flow help separate the vortex from the suction surface.

The work done by Helin (1986) using different motion histories best shows in graphical fashion the role of some of these mechanisms from a different test perspective. He pitched airfoils upward to a set angle of attack, allowed time to pass and then continued the pitching to a full 60 deg angle of attack. In some instances variable amounts of time elapsed before the motion history was continued and in other instances, the motion delays occurred at different angles of attack. When the airfoil was moved to the same angle of attack and then allowed different time delays to pass before the motion was continued, the influences of the overrunning freestream could be evaluated alone. When a motion delay equivalent 0.8 chords of freestream
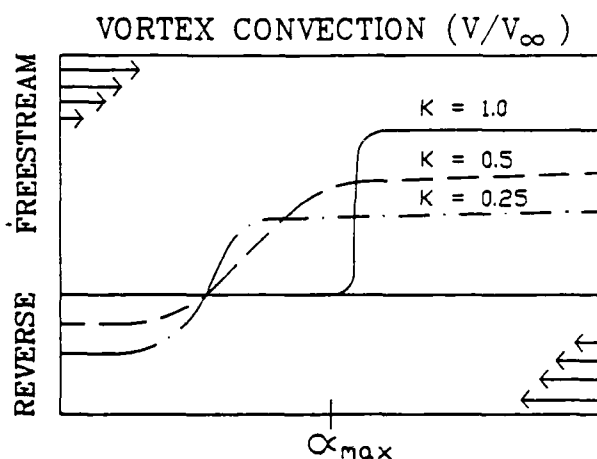

VORTEX CONVECTION (V/V_∞)

Fig. 3. Summary of vortex convection characteristics. Two influences determine the vortex convection velocity: freestream and reverse flows. With low K value motions, the vortex forms in the pitching cycle before Alphamax is attained. The fluid delivered by the reverse flow carries sufficient momentum to slow the downstream movement of the vortex. Also, the vortex is partially shielded from freestream influences. At high K values neither a shielded effect nor a major reverse flow effect is experienced by the vortex, quite high convection rates prevail.

passage occurred at 30 deg, the leading edge vortex grew beyond the size shadowed by the leading edge. The resulting vortex convection velocity was consistent with the vortex growth allowed during the delay. Even when 1.6 chord lengths of fluid were allowed to pass during a longer motion delay at 30 deg, the convection was determined by the size of the leading edge vortex. Thus, all of the observed convection velocities were similar but the times that the vortices formed and began to convect differed.

This relationship was preserved even in the instances of delays occurring at lower angles of attack. Here again, the convection behavior of the vortices depended on when initiation occurred and on the subsequent growth rates of the vortices. The growth and the initiation depended, of course, largely on the time allowed for fluid passage to occur and to deposit vorticity at the leading edge of the airfoil. In these simple pitching up motions, vortex dynamics determined by other factors tend to be constant. The reverse flows are constant for the angles of attack traversed and the amount of time allowed to pass. The shadowed regions behind the airfoil always attain levels

associated with the terminal 60 deg angle of attack attained by the upward pitching airfoil. The time delays and the delays at different angles of attack simply determine when the freestream influence is brought to bear on the formed vortex.

According to the model outlined above for the sinusoidal pitching airfoil, actual vortex initiation must derive from the enhancement of freestream influences associated with increasing volumes of vorticity at or near the leading edge. This was described above as the threshold for vortex formation. In the instances of simple pitching seen above, threshold for vortex formation must derive mostly from the passage of the freestream and from the associated passage of time. Neither the pitch rate nor the angles of attack were varied enough to yield significant differences in either the amounts of vorticity produced per unit time or the distributions of that vorticity over the airfoil chord.

Studies by Helin (1986) show that under the correct circumstances, vorticity can be made to accumulate at specific sites on the surface from which it is produced. A concave leading edge geometry, for example, encouraged such vorticity localization.

There have been instances in which the airfoil surface has been made to yield larger amounts of vorticity and at specific sites than usual. The created vorticity was focused at a specific chord region by the vorticity generation device that was used. Such instances are reported in a paper on the use of a span wise spoiler deployable from the surface of an airfoil at 0.12 chord and on the use of

LEADING EDGE GEOMETRIES
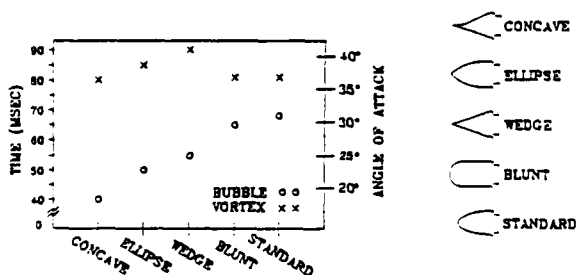(460 °/SEC , V∞ 10 FT/SEC , 0° - 60°)

Fig. 4. Summary of the effects of altered leading edge geometries on vorticity accumulation (bubble) and on vortex production. Clearly, the accumulation mechanisms differ with significant bubble formations occurring in a range of alphas from 20-30 deg during the pitch up motion. The vortex formation, more dependent on shadowing from the freestream, is not as significantly altered by leading edge configurations. (Adapted from Helin, 1986)

suction and blowing administered to the same chord sites (Luttges et al., 1985). This work showed that the control of vorticity production could dictate a variety of unsteady separated flow characteristics. The periodic deployment and retraction of the spoiler produced localized vorticity sites that grew into full vortices immediately downstream of the spoiler. As expected, the more rapidly the spoiler was deployed the less total vorticity produced per cycle. The resulting vortex structures were smaller and occurred only during the time that spoiler retraction increased the exposure to the freestream flow. Interestingly, when the airfoil was at the appropriate angle of attack, usually modestly beyond static stall angles, the retraction of the spoiler caused the flow to accelerate at the nearby leading edge and the resultant vorticity was formed into a second vortex. This second vortex, produced immediately upstream of the other, did not grow significantly after formation at the leading edge. Presumably the downstream vortex was gathering all of the available vorticity to support growth and little "length of fluid" intervened between it and the second leading edge vortex. In all of these instances, the airfoils demonstrated attached flow in angle of attack regimes where static testing would have shown fully separated flows. It was quite clear, however, that the spoiler deployment at the 0.12 chord site yielded less vorticity than would have been the case had it been located closer to the high stagnation pressure region at the leading edge.

When a brief pulse of pressurized air was delivered from the surface of the airfoil, a vortex was produced immediately downstream. An upstream vortex was produced, as well. The character and the apparent perseverance of these structures suggests that each air pulse provides a discrete amount of vorticity. Depending on the angle of attack of the airfoil from which the air pulse was delivered, this vorticity was either (higher angles) accumulated near the leading edge to form a vortex or (lower angles) it was shed as a thickened boundary layer facet into the airfoil wake (without producing a vortex).

When the airfoil was at 15 degrees, the pulsed air produced a vortex sufficiently strong to reattach otherwise separated flow. The reattachment persisted for the period of time elapsing between successive pulses (at K=1). This suggested that the attachment remained for a period consistent with the full development and trailing edge shedding of the vortex, at which time yet another vortex was elicited about the airfoil leading edge. In contrast, the same air pulse delivered from the surface of the airfoil at 20 deg angles elicited a

218

vortex that returned the flow to the surface only very briefly. In this case, attachment occurs transiently beginning shortly after the onset of the air pulse and ending before the air pulse has ceased. These latter conditions are consistent with the creation of a leading edge vortex that returns the flow to the airfoil surface until reverse flow and continued air injection lift it away from that surface. At 20 deg. angles of attack the reverse flow is strong enough to overwhelm the vortex-induced attachment. The continued injection of air dissipated and diluted the rotational energies. With the full freestream exposure characteristic of the lower angles of attack, the air pulse delivered vorticity appears to be carried away in the boundary layer as quickly as it is delivered to it. Clearly, the attached flow at 10 deg. remains attached despite periodic air pulse deliveries. The usual partially separated flow at 12.5 deg. also remained attached when an air pulse was delivered.

The same investigation showed some preliminary results associated with the simultaneous delivery of air pulses with airfoil sinusoidal pitching. The resulting flow structures are larger than those produced by either factor alone. Yet, the convection of the vortex is quite nearly the same as with pitching used alone and the flow attachment is quite similar. One really notable difference in the resulting flow structure is the absence of a counter-rotating trailing edge vortex. The trailing edge vortex interaction with the leading edge vortex occurs far into the airfoil wake. These observations indicate that the air pulse vorticity can be assimilated into the leading edge vortex produced by pitching. And, the assimilation of this vorticity can prevent some of the rapid development of reverse flow that aids in the formation of a trailing edge vortex.

The overall conclusion from these observations is that vorticity can be delivered to any point on the surface of the airfoil to supplement that vorticity being formed at or "diffused" from the surface. The resulting boundary layer distortions can thereafter lead to higher rates of vorticity accumulation localized to the site of boundary layer thickening. The resulting vortex formation is a direct consequence of boundary layer accumulations and distortions related to vorticity and an interacting consequence of the exposure to the overrunning flow that this portion of the boundary layer experiences. If vorticity shedding mechanisms are sufficiently well preserved, a large vortex does not form. But, if vorticity accumulation and localization exceed the shedding rates of the convecting boundary layer, the

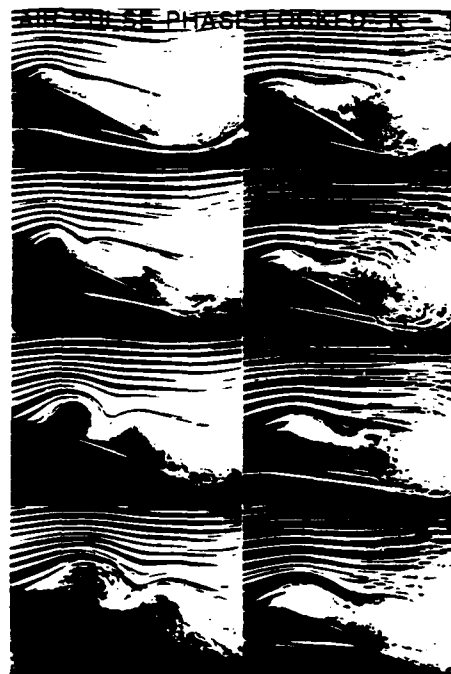freestream influences shape the boundary layer into a localized highly

Fig. 5. Flow visualizations for brief air pulses delivered from a slot at 0.12 chord on an upward pitching airfoil. Note the enhance vortex formation in column one. Simultaneously, both an upstream and downstream vortex are produced. In column two, the air pulse was not delivered coincident with pitch-induced vortex formation. A much smaller, less cohesive vortex is produced. In neither case is a major trailing edge vortex produced.

circumscribed circulation that takes the form of a vortex.

This vortex, in turn, can be viewed as the means that the boundary layer uses for vorticity shedding from the surface of the airfoil. The shedding and accumulation mechanisms change in relative proportions when the airfoil angle of attack is changed. In steady state tests this relation can establish a dynamic equilibrium where the reverse flow helps achieve flow separation from the airfoil surface and thus aids in the shedding of the boundary layer vorticity before the trailing edge is reached. A discrete stall circumstance on the airfoil surface arises from the separation produced by both upstream and downstream delivery of vorticity to the boundary layer at the separation point. Separation point variance along the chord is simply a reflection of the residual tendency of the separating flow to form continuous vortex shedding.

Each vortex enhances vorticity storage and subsequent shedding. The vorticity storage capability of the boundary layer at the separation site increases and decreases accordingly. It is notable that in the air pulse studies secondary vortices form as an indication of the excess vorticity that can not be accommodated in the primary vortices. Such accommodation fails because the primary vortex does not induce transport from distal sites and does not possess sufficient size to simply incorporate the vorticity. Similarly, high K tests often reveal local small sites of vorticity accumulation that upon high exposures to the freestream form into small local vortices. Again, consolidation via transport or direct incorporation fails. But, the threshold of vortex formation is near the boundary layer such that any small perturbances can yield vortices.

The empirical basis for some of the above hypotheses has been provided in a recent paper (Schreck and Luttges, 1988). Using a flat plate in sinusoidal pitching tests across a large range of K and across angles of attack that carried the plate through zero deg, they showed that the initiation of the leading edge vortex was systematically a function of the amount of vorticity produced and the amount of overrunning flow experienced by that vorticity. The subsequent growth of the vortex depended upon the presence or absence of reverse flow originating from the plate surface and extending all along the chord to the trailing edge. Finally, the convection velocity of the leading edge vortex was directly related to the exposure to the freestream and reciprocally related to the amount of momentum delivered in the upstream direction by the reverse flow. The residual vorticity that is not incorporated into the leading edge vortex produces a portion of the trailing edge vortex. That vorticity which remains along the rearward portions of the chord sheds in a manner consistent with the amount of vorticity available: it sheds in a reasonably laminar form if small amounts of vorticity are available and it sheds as a series of vortices if comparatively more vorticity is involved. The difference in these two scenarios is embedded in the pressure gradients produced by the oncoming freestream and produced by the vortices residing at that time on the plate surface.

USE OF UNSTEADY SEPARATED FLOW

The rather comprehensive model of unsteady separated flow presented above, indicates that the fundamental mechanisms supporting these flows are few in number and are readily characterized. Nevertheless, the interactions between these mechanisms

and the lifting surface localization of such interactions threaten to limit the potential utility of unsteady separated flows for aircraft. Several lines of research shed light on the applicability of these flows.

Work on the flight characteristics of dragonflies indicates that these insects employ unsteady separated flows to support highly maneuverable, agile flight. The dragonfly has been shown to generate very high, transient peaks of lift (Somps and Luttges, 1985) and they have been shown to be able to redirect high aerodynamic force generation between lift and thrust vectors (Reavis and Luttges, 1988). Although somewhat complicated, the repetitive wing kinematics used by the dragonfly have been fully modeled and used in a mechanical model in wing tunnel tests (Saharon and Luttges, 1988). It is notable that the dragonfly flight is controlled using very modest nervous system hardware and rather simple sensors (Kliss and Luttges, 1987). As a scaling factor relating dragonfly wing kinematics to common wind tunnel tests of sinusoidal pitching motions, the reduced frequency parameter for dragonfly flight is approximately $K=0.18$. Nevertheless, actual pitch rates occurring at the top and bottom of each wing plunging motion range from 15,000-25,000 degree/sec. Because of finite limits imposed by the operational times of neural tissues and muscles, real time control of dragonfly aerodynamics must be realized in extremely simple fashion. Presumably, some of these control strategies can be used in other flight systems designed to utilize unsteady separated flows.

Several studies have been completed recently using an X-29 reflection model on which the canard has been driven to show sinusoidal pitching (Ashworth et al., 1988). The resulting unsteady separated flow is quite complicated, especially when the model angle of attack is 5 or 10°. The canard (for several combinations of α_{x1}, α_w and K) yields the expected leading edge vortices as well as wing tip vortices. These, in turn, pass over, under and around the trailing forward swept wing. Despite these complex characteristics, the resulting flow field is highly reliable and reproducible; an impression corroborated with partial hotwire anemometric measurements. More recently, researchers at the U.S. Air Force Academy have been testing pitching parameters consistent with the present driving mechanisms actually available on the X-29. The possibility of ensuing flight tests is quite high. Such tests would provide significant information regarding the potential uses of unsteady separated flows.

Again in the domain of insect flight, it is notable that we have used live hawk moth specimens to show aerodynamic
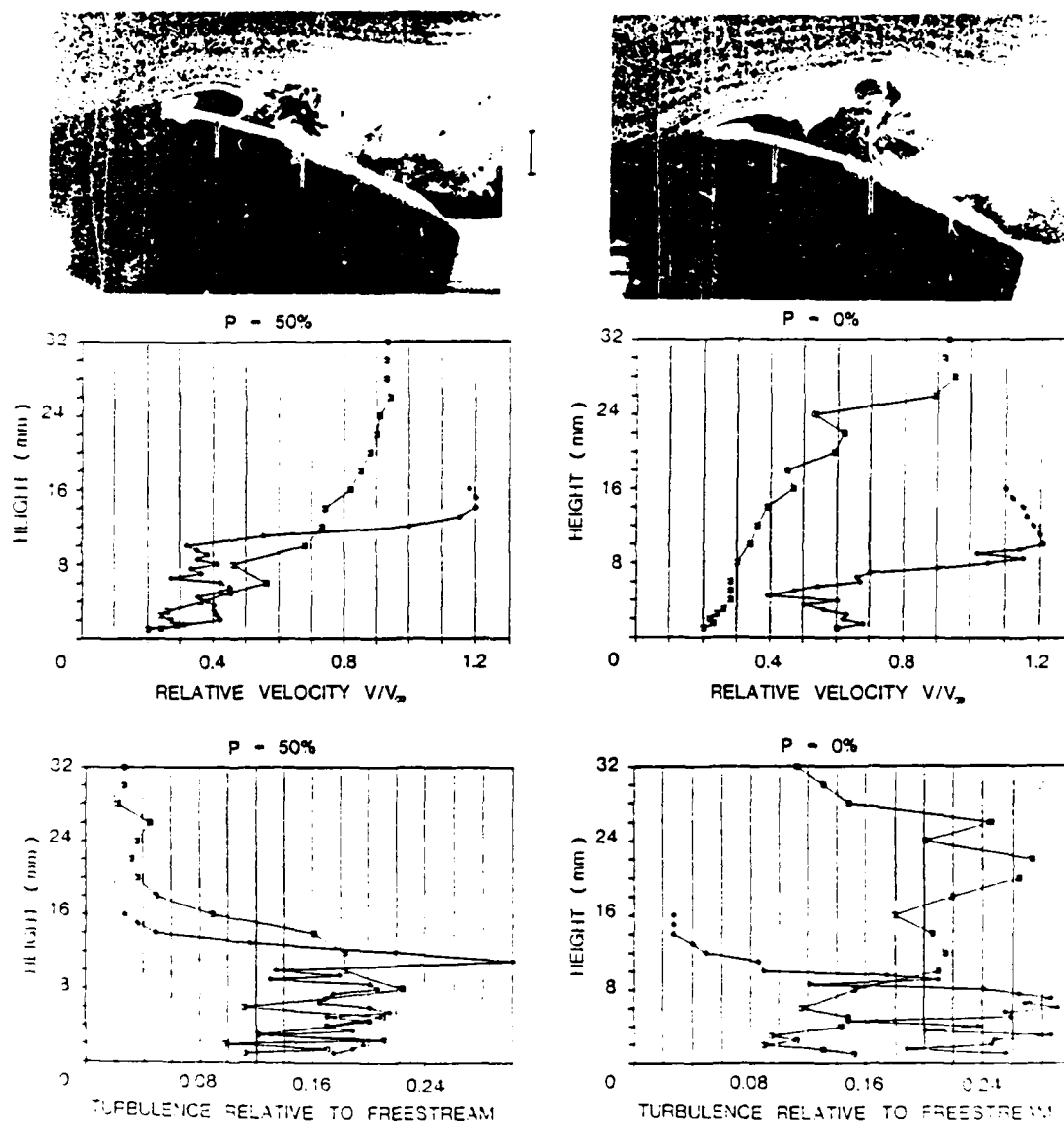
Fig. 6. Typical hot wire (V mean, V variance) data generated for a vortex produced by a deployable longitudinal spoiler at 0.15 chord on a NACA 0015 airfoil. Two chord locations are compared as indicated by the arrows at 0.2 and 0.5 chord. The smooth outer velocity profiles for the vortex disappear into more turbulent flow downstream. In fact, these test conditions show the rapid diffusion of turbulence away from the airfoil at the downstream location.

force generation histories indicative of unsteady flow usage. Unlike the dragonfly, these insects have a low aspect ratio wing surface (latched fore and aft wings) that exhibits radical deformations in surface contour. The surface deformations (in high speed photography) are reminiscent of those exhibited by the giant, ocean-going Manta Rays. When analyzed carefully, these kinematics seem to be an accurate reflection of those kinematics used by the dragonfly. In essence, the fore and aft elements of the wing show an activation phase difference. The vortex created at the rapidly pitching leading edge of the wing appears to convect over the deformed downstream wing surface exerting the aerodynamic forces used by the hawk moth. More detailed analyses are under way. But, this work supports the possibility that unsteady separated flows can be used to support flight despite differences in wing configurations. As in the dragonfly, such flight is accomplished despite limited availability of nervous system and sensors.

CONCLUSIONS

In the present paper we have attempted to summarize some of our experimental efforts in unsteady separated flows. The summary is not intended as a comprehensive review. Rather, we have evolved some ideas about the unsteady separated flow processes based upon our observations. The descriptions have been made as generic as possible to avoid preconceived notions and concepts.

At the end of the paper is a reminder that the goal of using unsteady flows has already been met; albeit by insects. Flow complexity and three-dimensionality have not brought up any extraordinary concerns regarding potential applications. That unsteady flows are highly predictable and reproducible, seems to be the key to alleviating control and related flight mechanics problems. Thus, much remains to be done but the effort appears to be one that will be handsomely rewarded.

LITERATURE CITED

Carr, L.W. (1985) Dynamic Stall Progress In Analysis And Prediction. AIAA Paper 85-1769-CP Snowmass, CO.

Freymuth, P., Finaish, F., and Bank, W. (1986) Visualization Of Wing Tip Vortices In Unsteady And Steady Wing, AIAA-86-1096.

Helin, H.E., and Walker, J.M. (1985) Interrelated Effects Of Pitch Rate And Pivot Point On Airfoil Dynamic Stall. AIAA 23rd Aerospace Sciences Meeting, Reno, Nevada, AIAA Paper 85-0130.

Helin, H.E., Robinson, M.C., and Luttges, M.W. (Aug. 1986) Visualization Of Dynamic Stall Controlled By Large Amplitude Interrupted Pitching Motions. AIAA Atmospheric Flight Mechanics Conference, Williamsburg, VA, Paper No. 86-2281-CPM.

Luttges, M.W., and Huyer, S.A. (June 1987) Unsteady Separated Flows Driven By Periodic Leading Edge Deformation. AIAA 19th Fluid Dynamics, Plasma Dynamics and Laser Conference, Honolulu, HW.

Luttges, M.W., Robinson, M.C., and Helin, H.E. (Aug. 1986) Control Of Wake Structure Behind An Oscillating Airfoil. AIAA-6-2282, AIAA Atmospheric Flight Mechanics Conf., Williamsburg, VA.

Luttges, M.W., Robinson, M.C., and Kennedy, D. (Mar. 1985) Control Of Unsteady Separated Flow Structures On Airfoils AIAA-85-0531, AIAA Shear Flow Conference.

Luttges, M.W. and Schreck, S.J. (Jan. 1988) Unsteady Separated Flow Structure: Extended K Range and Oscillations Through Zero Pitch Angle. AIAA 26th Aerospace Sciences Meeting AIAA-88-0325, Reno, NV.

Reynolds, W.C. and Carr, L.W (May 1985) Review Of Unsteady, Driven Separated Flows. AIAA Shear Flow Control Conference, AIAA Paper 85-0527.

Walker, S.M., Helin, H.E., and Strickland, S.H.(1985) An Experimental Investigation Of An Airfoil Undergoing Large-Amplitude Pitch Motions. AIAA Journal 23: 1141-1142.

Unsteady Surface Pressure Measurements On A Pitching

Rectangular Wing

Michael Robinson[*] and John Walker[**]
Frank J. Seiler Research Laboratory
United States Air Force Academy
Colorado Springs, Co. 80840

John Wissler[***]
Deparment of Aeronautics
United States Air Force Academy
Colorado Springs, Co. 80840

Abstract

Transient pressure measurements collected at three different span locations documented the forced unsteady flow separation from a pitching rectangular wing. The separated flow was dominated by the development of both a leading edge and wingtip vortex. Pressure signatures from the vortex-wing interaction provided an indication of the dynamic vortex behavior along the span. Inboard, away from the wingtip, vortex initiation and development proceeded two-dimensionally, duplicating previous airfoil results.   Near the tip, vortex-vortex interactions prolonged vortex residence times and enhanced the sectional lift coefficient values. The magnitude and duration of these enhancements were directly dependent upon the wing pitch rate. These findings suggest that previous two-dimensional airfoil results should provide a good indication of three-dimensional wing performance.

Nomenclature

c	airfoil chord
C_l	lift coefficient
C_p	pressure coefficient
Re	Reynolds number = $U_\infty c / \nu$
$\bar{t}$	non-dimensional time = $t U_\infty / c$
U_∞	freestream velocity
κ^+	reduced frequency = $\dot{\alpha} c / U_\infty$
ν	kinematic viscosity

Introduction

Utilizing unsteady aerodynamics to extend aircraft performance is being given serious consideration.[1] In two-dimensional test circumstances, such enhancements can be obtained by producing, then exploiting large scale vortices through forced unsteady flow separation. The vortex-airfoil interactions which occur after separation can result in substantial transient lift and moment augmentation.[2,3] Serious questions, however, remain about the applicability of two-dimensional results in three-dimensional enviroments.

Typically, these vortical flow fields are generated through a dynamic separation of the boundary layer from the airfoil surface. Different separation methodologies produce various aerodynamic enhancement effects.[4,5,6,7,8] The most common method which imitates a realizable aircraft motion is a dynamic pitch through the static separation angle of attack. An airfoil driven in pitch beyond normal static stall, either periodically or with a single ramp up motion, will be subject to an unsteady force augmentation from the resulting vortex formation.

A great deal of current research has explored the phenomenology of dynamic stall and vortex-airfoil interactions in two-dimensional test environments.[2,3,4,9,10,11,12,13,14,15,16,17] An airfoil driven rapidly in pitch can maintain dynamic flow attachment to angles of attack well beyond static stall. While in this 'post-stall' attitude, forced unsteady separation of the boundary layer occurs. A large scale vortex initiates from the leading edge and convects over the airfoil surface. The vortex-airfoil interaction both lowers and shifts the local static pressure center during convection producing transient lift, drag and moment coefficients.

Although qualitative assessments of the separation process and subsequent vortex dynamics have been made, descriptive algorithms which predict performance across large parametric changes in airfoil motions have, thus far, evaded researchers. A complete understanding of the fundamental physical processes which drive two-dimensional unsteady separation has yet to be achieved. Successful exploitation of unsteady aerodynamic enhancements will be critically dependent upon the ability to predict vortex-airfoil interaction effects and control vortex dominated flowfields.

When forced unsteady flow separation is invoked from a three-dimensional wing, the resulting flow field is much more complex.[18,19,20,21] The development of a wingtip vortex allows both vortex-airfoil as well as vortex-vortex interactions between orthogonally aligned vortices near the wingtip. Vortex stretching must also be considered as an additional source of vorticity production in the

unsteady separation process. With the added complexity in three-dimensional flows, serious questions arise regarding the applicability of previous two-dimensional test results to actual three-dimensional geometries. Also, understanding the underlying fluid physics which drives the three-dimensional separation process becomes quite formidable.

Although there exists a critical lack of information regarding forced unsteady separation about three-dimensional test geometries (or unsteady three-dimensional test data in general), actual flight demonstrators are being designed and constructed capable of entering flight regimes where enhanced unsteady aerodynamic effects exist. Using various techniques including thrust vectoring to achieve 'super-maneuverability', sufficiently rapid aircraft rotation rates are possible to produce unsteady separation enhancement effects. Both the magnitude and transient nature of these effects are large enough to warrant design and performance consideration.

A series of experiments were conducted to examine the influence of three-dimensionality on the forced unsteady separation process. A rectangular wing was selected as the test model for all experiments. This geometry is a simple three-dimensional extension of previously tested two-dimensional airfoil cross-sections. The wing was instrumented with 15 surface mounted pressure transducers which could be positioned at various locations along the wing span. Transient pressure responses were collected during forced unsteady separation as the wing was pitched with a single constant rate motion pitched from 0 to 60 degrees angle of attack. Three different pitch rates were tested which duplicated the conditions of previous two-dimensional airfoil experiments. This permitted a direct assessment of how three-dimensional influences alter two-dimensional results. Also, measurements at different span locations enabled a span-dependent evaluation of the three-dimensional unsteady separation process to be made.

Forced unsteady separation from a pitching wing has a succession of dependent time scales which affect vorticity production. The temporal dependence on the wing motion, viscous diffusion from the boundary layer, and vorticity convection away from the wing surface all play a role in the vorticity accumulation / vortex formation process.

Methods

Experiments were conducted in the Frank J. Seiler 3'x3' low speed wind tunnel located at the United States Air Force Academy. A 6" chord rectangular wing was constructed from extruded aluminum NACA 0015 airfoil section. The base wing model had a 12" span (semi-aspect ratio of 2.0) and was affixed to a circular splitter plate next to the tunnel wall. The splitter plate was mounted to the wing pitching mechanism and rotated with the model. The pitching axis was centered about the wing quarter chord. The wingtip on the model base was constructed with an adaptive mount so various tip extensions and configurations could be added. Only a flat end
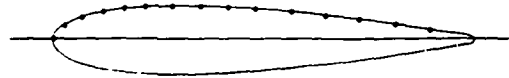
PRESSURE PORT

LOCATION

Figure 1. Pressure port location

wingtip was tested in these experiments.

Fifteen Endevco 8507B-2 pressure transducers were close couple surface mounted in the base model 1.2" (0.2c) from the wingtip. Previous calibration tests indicated a flat frequency response to 200 Khz with this type of installation. The relative spacing of the transducers along the chord is shown in fig. 1. Calibration of all pressure transducers were done in situ by placing the entire wing model in a sealed pressurized tank and measuring the response while slowly bleeding the overpressure. Transducer sensitivities were checked both before and after data collection and were shown to vary less than 1 percent over several calibration runs.

Measuring the pressure responses at span locations other than 0.2c (the fixed position in the base model) required a change in the model configuration (fig. 2). Wingtip extensions of various lengths were added to the base model which changed the relative position of the pressure transducers to the wingtip. Simultaneously, a second splitter plate was located on the base model 12" from the new wingtip position. Thus, a constant semi-aspect ratio of 2.0 was maintained for all span variations. Results from pressure transducer locations at span positions of 0.4c, 1.0c, and 1.8c are reported here. These locations were
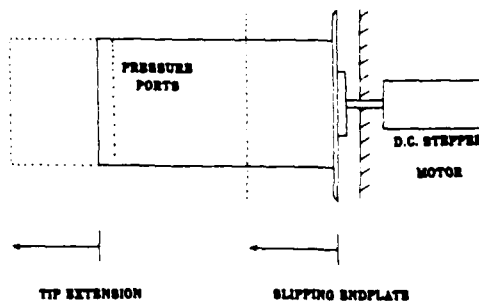
SCHEMATIC OF PRESSURE

MODEL

Figure 2. Wingtip extension geometry

226

selected based upon previous flow visualization results of the same wing geometry at similar test conditions.

The wing motion was controlled by a programmable D.C. stepping motor connected to the model via a 4 to 1 gear reduction. The details of the motion control system are referenced elsewhere.[13,14,16] Although many different motion profiles were possible, only a single constant pitch rate motion from 0 to 60 degrees angle of attack was tested. Three different pitch rates; 286, 573 and 860 degrees/second corresponding to non-dimensional pitch rates of 0.1, 0.2 and 0.3 respectively were tested. Since the wing was symmetrical, pressure data for both the upper and lower wing surfaces was collected by simple changing the direction of pitch. A potentiometer located on the gear reduction provided an instantaneous angle of attack measurement during the pitch motion. The pitching axis was held constant at 0.25c.

Both the pressure transducer and angle of attack output signals were digitized and stored using a Masscomp 5500 data acquisition system. Outputs from the pressure transducers were first amplified (gain 1000) and filtered (1 Khz). Each data set consisted of an ensemble average over 15 consecutively collected pitch sequences. A reference trigger provided by the motion control system synchronized data collection for each pitch motion. The average as well as the running standard deviation were recorded for each data set.

All pressure data were collected at a free stream velocity of 25 ft/sec corresponding to a Reynolds number of 60,000. This low velocity was necessary in order to achieve non-dimensional pitch rates comparable to previous flow visualization results. The upper limit on non-dimensional pitch rate was limited by the pitching capability of the drive mechanism (approximately 900 deg/sec).

Collecting unsteady pressure data at these low flow rates proved to be somewhat of a challenge. Corrections had to be made for errant responses due to vibration of the transducers in the model during pitch as well as temperature drift of the transducers over multiple pitching sequences. Dependent upon test condition, such errors could be 5 to 10 percent of the pressure signal. Both sources of error were minimized through adaptations of the data acquisition software and utilizing a systematic data collection procedure.

For each data set (different span location) the pressure transducers were allowed to temperature stabilize at the free stream velocity. The tunnel velocity was reduced to 0.0 and pressure transducer data were collected for five successive pitching motions under zero flow conditions. This data set was stored as the zero offset condition and contained the bias due to vibrational effects. The tunnel velocity was reset to the test condition (25 ft/sec) and pressure data collection was initiated for 15 consecutive pitch motions. Prior to the first pitch motion event, each of the pressure transducer values were collected and stored. This provided the base line value to adjust for
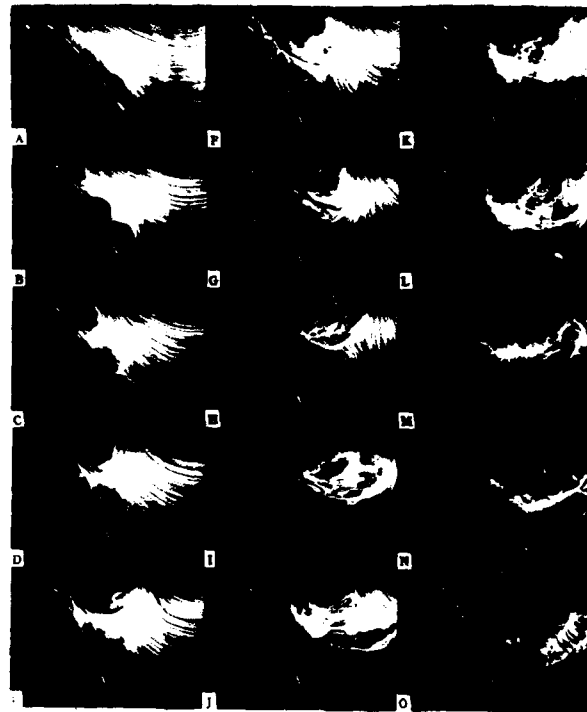

Figure 3. Three-dimensional vortex development on a pitching rectangular wing.

temperature shift over multiple runs. Each pitching motion event was then corrected for temperature drift and vibration effects before being stored in the ensemble average.

Results

Previous flow visualization results of a pitching rectangular wing documented the similarities in flow structure between two and three-dimensional forced unsteady separation. A large leading edge vortex initiated (fig. 3a), developed (fig. 3b-c), and convected (fig. 3d-e) as the wing was pitched to angles of attack beyond static stall. As in previous two-dimensional results, the vortex initiation process was strongly affected by the dynamics of the wing motion. Rapid pitch rates delayed vortex initiation to larger angles of attack and produced vortices with more cohesive structure and greater convecting velocities.

The leading edge vortex development process was also strongly affected by the three-dimensional influence of the wingtip vortex. Fig. 3 shows the leading edge vortex development at a span location of 1.0c inboard from the wingtip. From this side view, what first appeared as a breakdown in the vortex formation (fig. 3f-j), when viewed from a perspective behind the wing, was a convection of the vortex out of the focal plane toward the camera (wingtip). In contrast, a leading edge vortex developed from a pitching airfoil would continue to convect downstream unperturbed and would shed into the wake.

227

VORTEX CONVECTION AT DIFFERENT SPAN LOCATIONS

α^+ 1.0
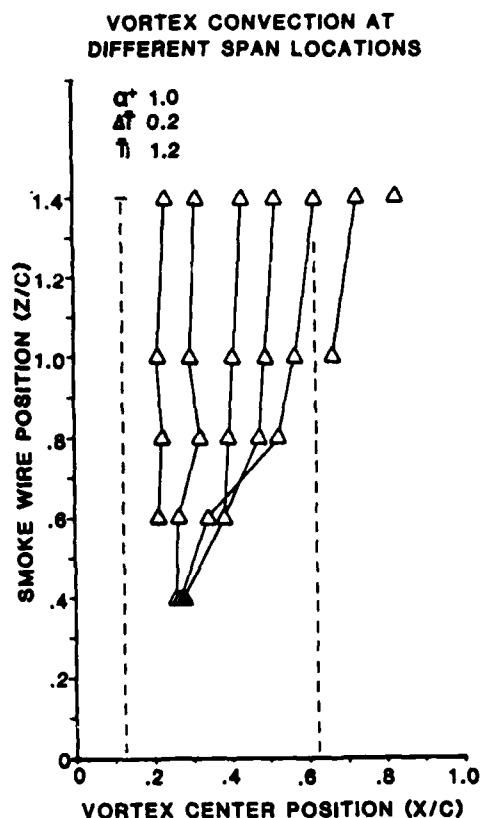$\Delta \bar{t}$ 0.2
$\bar{t}$ 1.2

Figure 4. Vortex convection over a rectangular wing

Three-dimensional influences on the leading edge vortex development from a pitching wing is shown in fig. 4. In this figure, the vortex convection history over the wing was plotted at different span locations. Three distinct regions of vortex development can readily be identified. Span locations greater than 1.4c inboard from the wingtip exhibit two-dimensional vortex convection behavior. Between 0.4c and 1.4c, vortex convection is restrained by the influence of the wingtip vortex. At 0.4c, little downstream convection was observed and the leading edge vortex appeared 'pinned' in place. The region between the wingtip and 0.4c was dominated by the development of the wingtip vortex. Based upon these visualization results, pressure measurements were made at three different span locations to highlight the different facets of the three-dimensional behavior: 1.8c, 1.0c and 0.4c inboard from the wingtip respectively.

Vortex wing interactions

The vortex-wing interactions due to the initiation, development and convection of the leading edge vortex can be expressed in the form of three-dimensional pressure coefficient topologies at different span locations. Fig. 5 shows the transient pressure characteristics on both the upper and lower surfaces of the rectangular wing at a span location 1.8c inboard from the wingtip. Pressure coefficients were plotted along chord with increasing time (non-dimensional) through the pitch cycle. The airfoil pitching motion initiated at $\bar{t}=0.0$ and
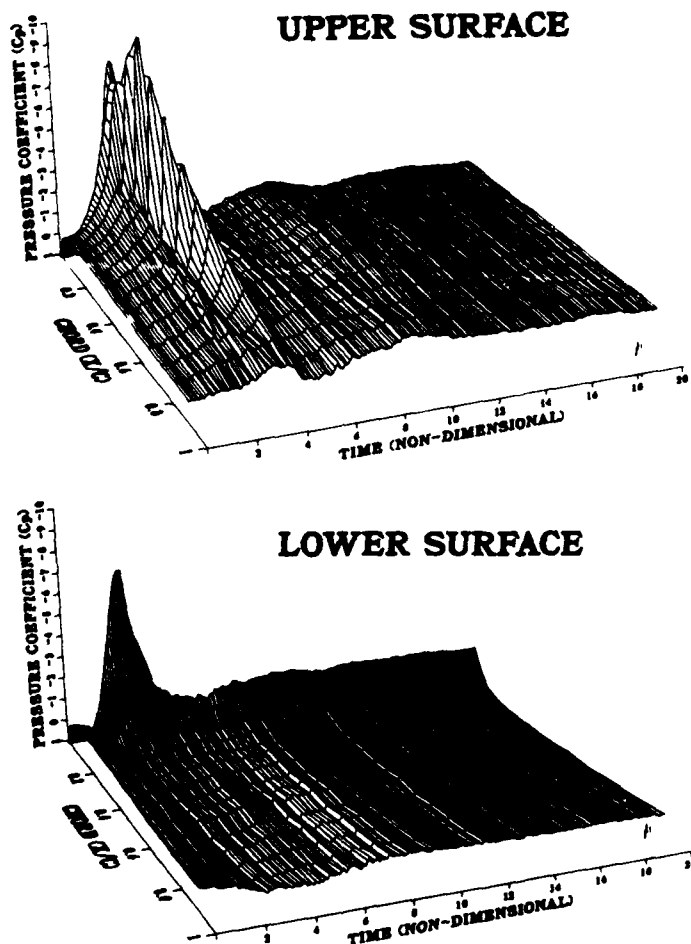

UPPER SURFACE

LOWER SURFACE

Figure 5. Unsteady pressure coefficients produced by vortex initiation and development. α^+ 0.3, span location 1.8c from the wingtip.

ended at different times dependent upon the pitch rate. An instantaneous measure of the corresponding angle of attack at each non-dimensional time can be obtained from fig. 6. Data collection continued well beyond motion cessation until a quasi-steady pressure response was reached ($\bar{t} = 20$).

The dynamics of vortex development can be traced temporally in the pressure signature of fig. 5. As the rectangular wing was pitched toward maximum angle of attack, a rapid pressure decrease (increasing negative C_p) ensued over the leading edge. This sudden decrease culminated in a pressure minimum (C_p -9.7) at approximately 0.2c. From earlier work by these authors and Albertson et al.,[22] this pressure minimum corresponds to the first visible formation of the leading edge dynamic stall vortex over the wing surface. After initiation, vortex convection over the wing can be traced as the pressure ridge line extending from the minimum pressure peak down the chord and off the trailing edge. The vortex interaction with the wing surface is strongest at the initiation point and rapidly attenuates with convection downstream. The
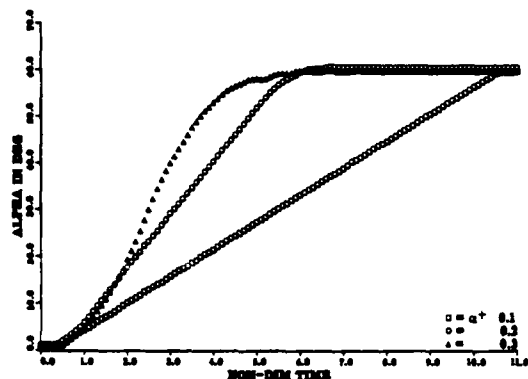
228

ALPHA vs NON-D TIME

Figure 6. Angle of attack vs. non-dimensional time.

significance of this convective behavior on transient loading will be discussed later.

A second vortex formation was also evident in the pressure topology. At $\bar{t} = 10$, the negative C_p rise over the upper surface signals the development of a second leading edge vortex formation. Development of this secondary vortex formation has been reported in previous visualization results by these authors[20] for a rectangular wing and by Helin et al.[16] using two-dimensional geometries. The transient force produced by the secondary vortex formation can be observed in previous unsteady lift data from two-dimensional airfoils reported by Walker et al.[13,14] and Jumper et al.[12]

Pressure transients were observed on the lower wing surface as well, the most dramatic occurring in the first transducer located at the leading edge. Although data from the first transducer is also plotted in the upper wing topology, a more definitive representation of the duration of the separation event is given by the first transducer in the lower surface plot. A rapid increase in pressure occurred over the lower wing surface just prior to vortex initiation. Dependent upon the pitch rate, pressure coefficients on the lower surface could exceed the stagnation condition value of 1.0.[13,14,23] This effect has also been noted previously by researchers conducting two-dimensional tests using both water and wind tunnel facilities.

Effects of pitch rate

The most significant characteristic of the inboard pressure topologies collected at 1.8c is the virtually identical agreement with previous two-dimensional pressure results collected at similar test conditions. Fig. 7 shows the variation in pressure response with changes in non-dimensional pitch rate. At this inboard location (1.8c) both the magnitude and overall shape of the pressure contours agree with previous two-dimensional test results.

Not surprisingly, the effects of non-dimensional pitch rate on vortex development reflect the same general responses observed in previous two-dimensional results. Rapid pitch

motions produced a stronger peak wing-vortex interaction. Also, the duration of the interaction was reduced at higher pitch rates due to the increase in the vortex convection velocity. The decrease in duration with increasing pitch rate was most evident from the leading edge (first) transducer response plotted on the lower surface pressure profile. Although these trends were observed at the inboard span location, the same tendencies apply equally to all span locations.

Effects of span location

Dramatic changes in the pressure distributions occurred at span locations near the wing tip. The pressure signatures created by the vortex-wing interaction directly correlated with the observed vortex motions obtained from previous flow visualization results. Again, three distinct regions of different vortex convective behavior were represented over the wing with span locations closest to the wingtip exhibiting the largest three-dimensional interactions.

These three separate regions can readily be identified by the variation in the pressure topologies of fig. 8. The inboard span location at 1.8c, as noted above, is indicative of two-dimensional vortex initiation and development. These pressure results substantiate the premise of two-dimensional vortex development at inboard span locations derived from previous flow visualization results.

At a span location 1.0c from the wingtip, a very different vortex behavior dominated the wing section. Initially, a rapid pressure decrement ensued with the onset of pitch, culminating in a pressure minimum. This initial topology matched the two-dimensional response at the inboard span location of 1.8c. Immediately following the pressure minimum, the decreasing pressure ridge indicated vortex convection toward the trailing edge. This early convection however, was immediately followed with a resurgence of another pressure minimum which maintained a fixed position over the wing.

Flow visualization results at this span location (figs. 3,4) provide a physical interpretation of this pressure resurgence. At first, the leading edge vortex initiates and convects in a two dimensional fashion. Vortex convection however, is arrested with the onset of three-dimensionality and the vortex remains stationary over the wing. The diffuse appearance of the three-dimensional cross flow toward the wingtip does not impede the magnitude of the local vortex-wing interaction.

Near the wingtip (fig. 8, span location 0.4c), the three-dimensional influence of the wingtip vortex dominated the leading edge vortex development. From visualization results at this span location, the leading edge vortex initiated but failed to convect downstream (fig. 4, 0.4c). The pressure signature indicated the same behavior.

Vortex behavior within the three separate wing regions remained independent of pitch rate over the range of values tested. Fig. 9 shows pressure coefficient topologies at the same span
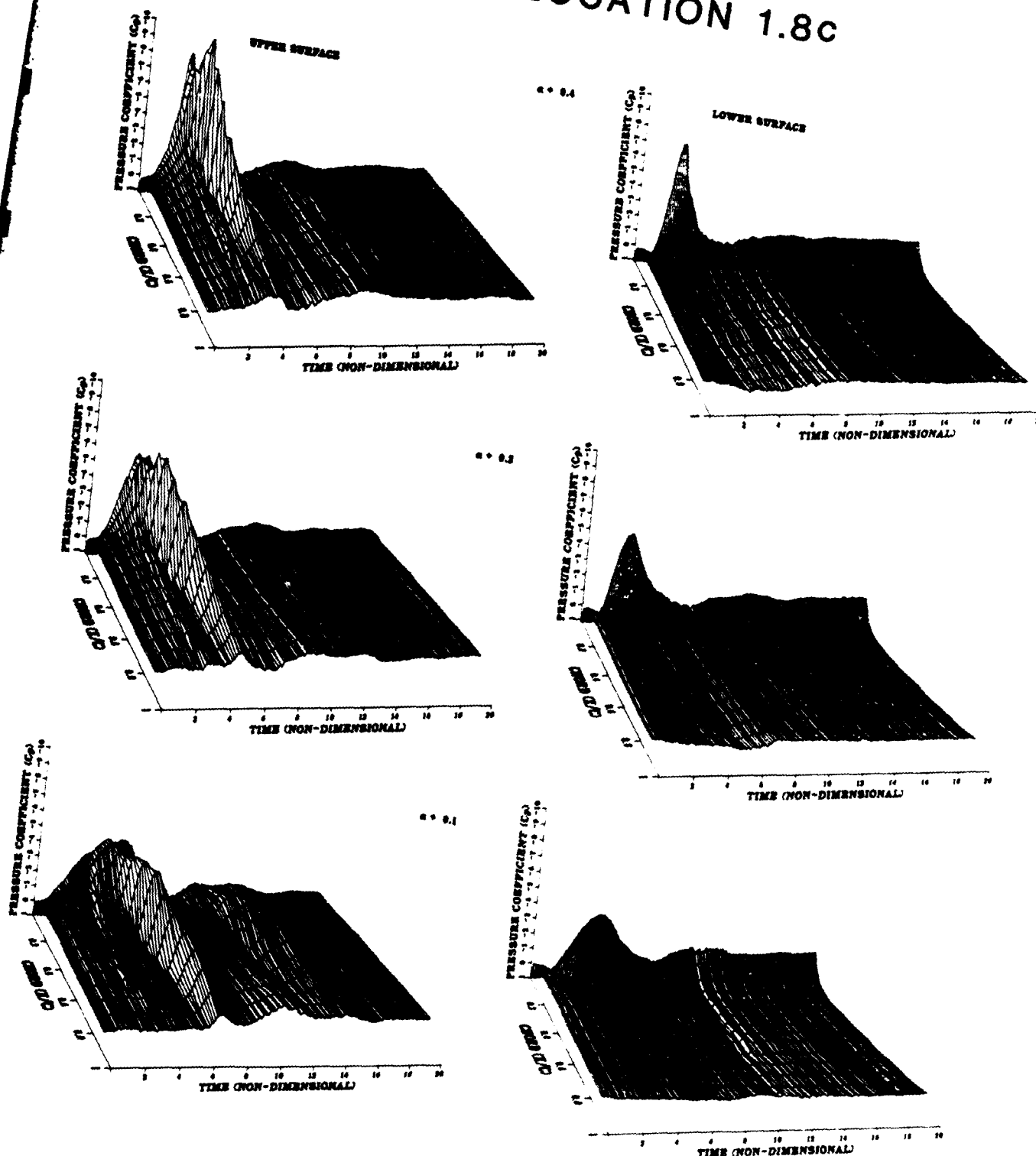
EFFECTS OF PITCH RATE
SPAN LOCATION 1.8c

Figure 7. Influence of non-dimensional pitch rate on vortex development. Span location 1.8c from the wing tip.

EFFECTS OF SPAN LOCATION
α+ 0.3
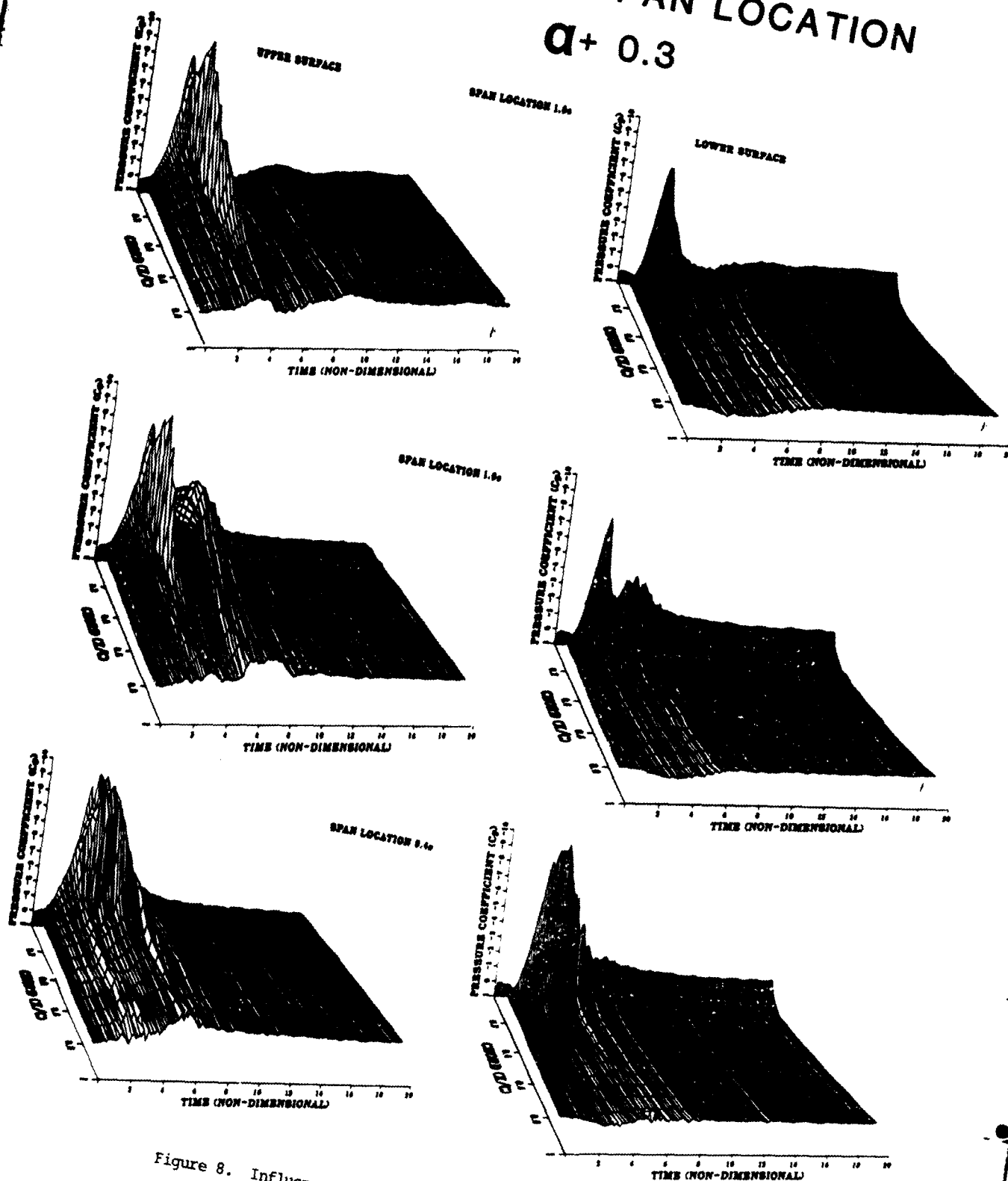

Figure 8. Influence of span location on vortex development. α+ 0.3.
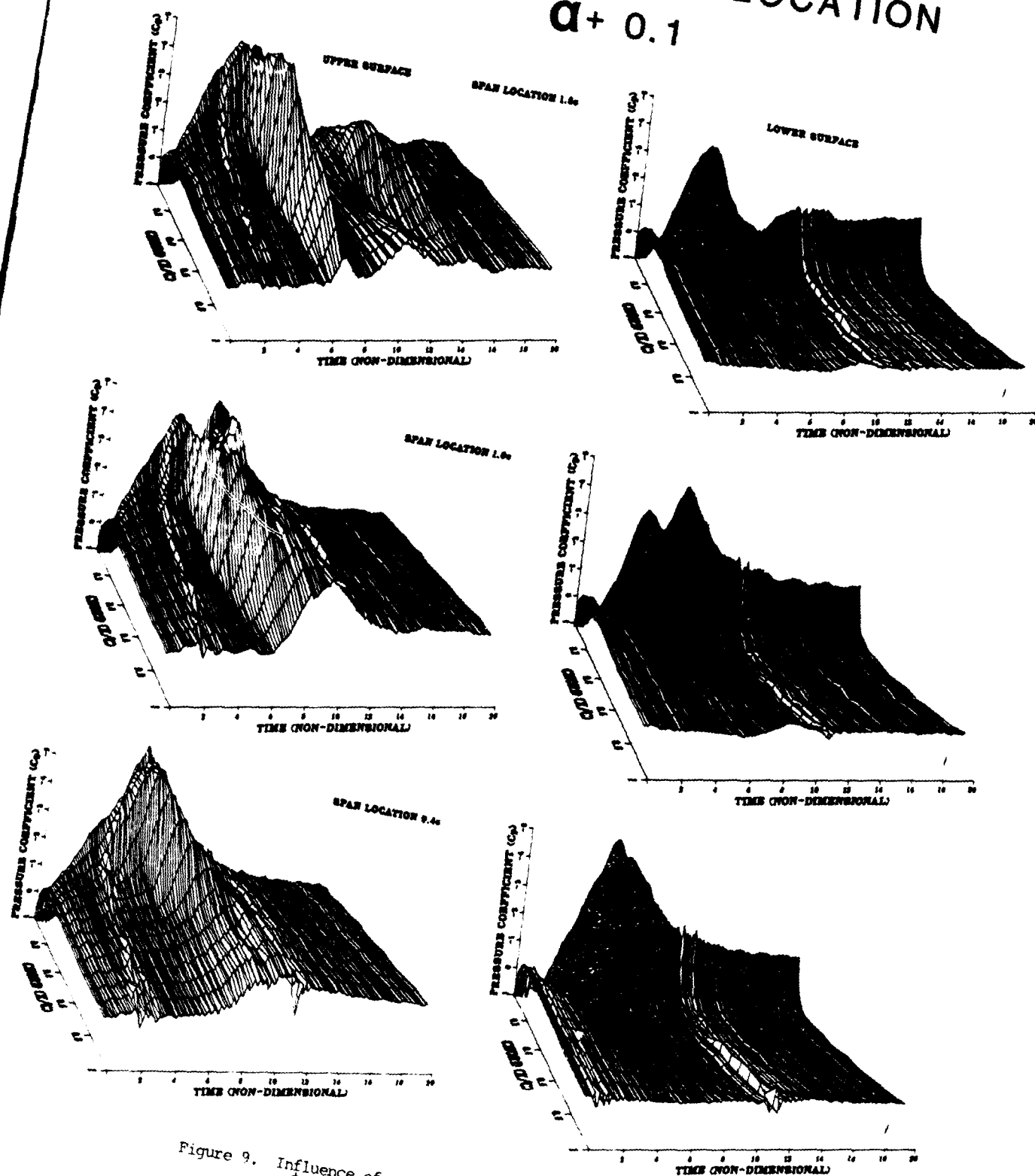
231

EFFECTS OF SPAN LOCATION
$\alpha + 0.1$

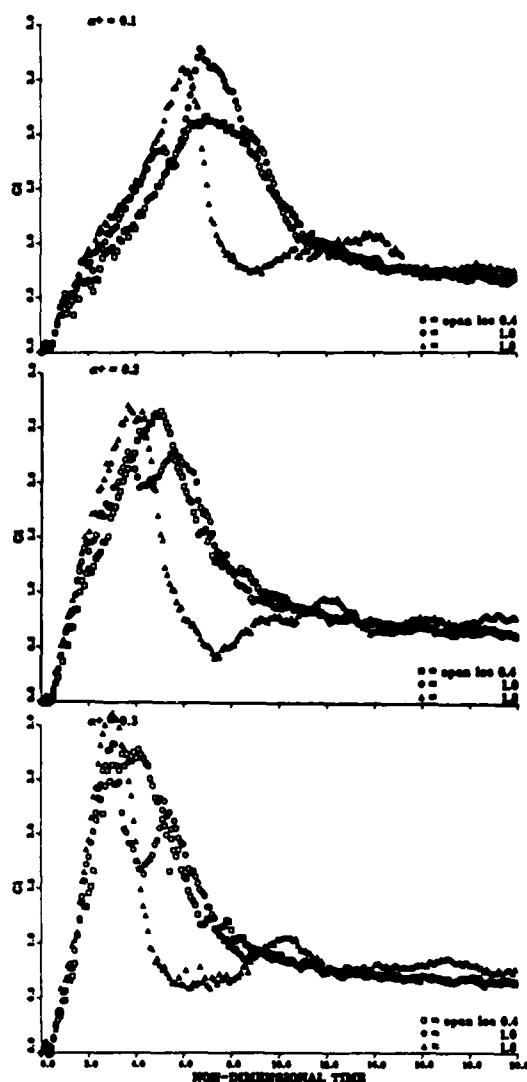Figure 9. Influence of span location on vortex development. $\alpha + 0.1$.

Figure 10. Unsteady lift coefficients produced by a pitching rectangular wing.

independent of the pitching rate. Profile shapes could be directly correlated to the dynamics of vortex development within each region while the magnitude and duration of the vortex-wing interaction appeared to be functions of the wing motion.

The most abrupt lift transients occurred at the inboard span location 1.8c from the wingtip. These profiles were characterized by an initial lift peak elicited by the leading edge vortex initiation. The secondary leading edge vortex formation gave rise to the subsequent peak at later times.

The sectional lift contour at 1.0c was highlighted by a double peak in lift coefficient during vortex development. The first, due to initiation and the second, due to the pressure resurgence associated with convection cessation. No secondary leading edge vortex development was evident in either the pressure distribution or integrated lift profiles.

Near the wing tip (0.4c), a single lift coefficient maximum prevailed over the wing section. The lift peak occurred temporally after the lift peak inboard (1.8c). Once again, no secondary leading edge vortex was evident.

Variations in both the lift contours and peak values possess interesting correlations to the dynamics of the wing motion and vorticity production. A discussion of these relationships will be presented later.

Discussion

A rectangular wing driven in pitch to large angles of attack retained many of the same flow characteristics observed previously with pitching airfoils. A large scale vortex was initiated as the wing pitched beyond the static stall angle. The resulting vortex-wing interactions altered the local surface pressure distribution leaving a descriptive signature of the dynamic development which correlated with visualizations of the vortex motion. However, unlike previous two-dimensional results, three-dimensional vortex development was further complicated by vortex-vortex interactions near the wingtip. These three-dimensional influences were not observed to reduce the magnitude or duration of the transient loads. Both the magnitude and duration of the vortex-wing interaction had strong temporal correlations to the dynamics of wing motion and rate of vorticity production in the boundary layer.

Three-dimensional vortex development

Vortex initiation and development appeared to be driven by two different factions. Initiation along the wing span was primarily a function of pitch rate. The rapid pressure decrease during the pitch motion remained virtually identical at each span location (figs. 8,9) culminating temporally in the same peak minimum value. This pressure distribution profile is indicative of a simultaneous vortex initiation occurring along the wing span over the leading edge. Rapid pitch rates only increased the magnitude (lower pressure) of the vortex-wing interaction. Parallel pressure distributions

locations (1.8c, 1.0c, 0.4c) but at a lower pitch rate (α^+ 0.1). Although the magnitudes of the vortex-wing interactions were reduced, the overall profile shapes remained the same.

Two facets of the pressure profiles in figs. 8 and 9 were unexpected. First, the magnitude of the pressure minimum peak did not vary along the span. And second, the duration of the vortex-wing interaction actually increased at span locations near the wingtip. Both effects directly impacted the transient load characteristics of the pitching wing.

Transient wing loading

Transient load responses from the pitching wing were obtained by integrating the pressure distribution profiles. The unsteady lift coefficients for all test conditions are given in fig. 10. The three regions of vortex development produced similarly shaped unsteady lift profiles

233

along the span indicated that the boundary layer vorticity accumulation, prior to vortex initiation, was largely a two-dimensional process. Subsequent plots of the tangential vorticity flux distributions derived from the pressure distribution profiles also supported this finding.

Inboard, away from the wingtip, the leading edge vortex continued to develop two-dimensionally. The pressure distributions and convection rates matched pitching airfoil results. Even for this low aspect ratio wing (4.0), inboard sectional wing performance could be predicted from previous two-dimensional results.

Three-dimensional influences were localized to within 1.4c of the wingtip. Near the wingtip (0.4c), the leading edge vortex initiated and remained spatially fixed over the wing surface. Between the wingtip and inboard locations (0.4c to 1.4c), the leading edge vortex initiated and started to convect. Convection ceased with the advent of three-dimensionality and also became spatially fixed. Again, increasing the wing pitch rate only affected the magnitude of the vortex-wing interaction with lower pressure signatures. Concurrently, visualization results indicated an extension of the three-dimensional influence region toward the wing root with increasing α^+.

Strong temporal correlations were evident in both the pressure distribution and lift coefficient profiles between span locations. Vortex convection inboard (1.8c) led subsequent vortex events at the wingtip. Peak lift followed by a rapid lift reduction was first achieved inboard (1.8c) and subsequently within the wingtip region(0.4c to 1.4c). Interestingly, the drop off in lift correlated exactly for both the 0.4c and 1.0c locations. Previous visualization results also indicated a temporal correlation between the shedding of the inboard leading edge vortex and the initial separation of the tip vortex from the wing.[20]

A caricature of the vortex development which accounts for the three-dimensional behavior in the tip region is shown in fig. 11. Based upon the classic Helmholtz vorticity relationships, vortex filaments incorporated in the leading edge vortex structure must be contained within the wingtip vortex as well. Hence, the vorticity contained within the wingtip is a continuum of the leading edge vorticity and must reflect any development permutations occurring there. The vortex filament loop is closed (not shown in the figure) by the connection of the vortex filaments in the tip vortex to the vorticity shedding from the wing trailing edge during the pitch motion. Such filaments have been superbly visualized by Freymuth et al. in the wingtip vortex formations trailing both dynamically pitching and accelerating wings.

This model accounts for both the uniformity in vortex initiation along the span and the temporal correlations between the inboard and wingtip vortex shedding phase. During the wing pitch motion, rapidly accumulating and tightly packed vortex filaments separated from the wing surface along a single vortex line. This line
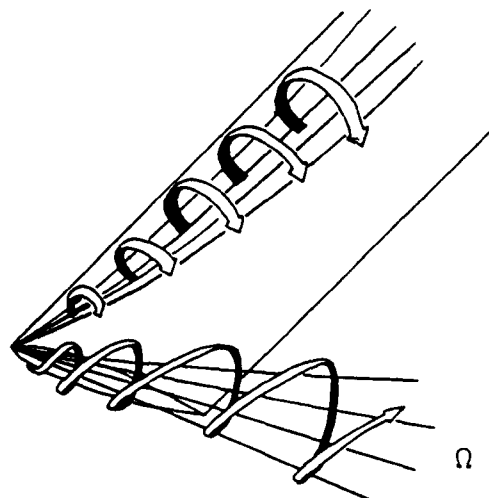

Figure 11. Schematic of vorticity distribution along a pitching rectangular wing.

extended along the wing leading edge, through the wingtip vortex. Inboard (1.8c), the vortex filaments convected and separated, spreading over a larger cross sectional area. Thus, the leading edge vortex appeared to grow in diameter while the locally tangent vortex-wing interaction (pressure signature) was reduced.

In the wingtip region, vortex-vortex interactions between the orthogonal wingtip and leading edge vortices restricted the filament spread. The filaments were focused into a narrow cross section at the leading edge of the wingtip. A vortex union was formed where the wingtip filaments turned 90 degrees in the narrow cross section and passed into the leading edge vortex. The "pinning" of these vortex filaments at the leading edge of the wingtip arrested vortex convection in the wingtip region and prolonged the vortex-wing interaction. The vortex union at the leading edge of the wingtip physically separated from the wing body when the inboard (1.8c) leading edge vortex shed from the wing surface into the wake. This permitted the combined leading edge and wingtip vortex to shed from the wing body as a continuous vortex ring.

Three-dimensional vortex enhancement

Using conventional steady state analysis, loads obtained from two-dimensional results must be altered to account for wingtip downwash effects. Typically, low aspect ratio wings would show significantly reduced sectional lift coefficient values. It was anticipated that similar occurrences would necessitate corrections to account for the differences between two- and three-dimensional transient load results. However, the three-dimensional lift values obtained from the low aspect ratio pitching wing (fig.10) indicated enhanced rather than diminished transient load characteristics.

The nature of this enhancement stems from both the magnitude and duration of the sectional lift coefficients along the wing span. For a three-dimensional wing under steady conditions, the lift coefficient can be derived assuming an elliptic lift distribution profile modified by
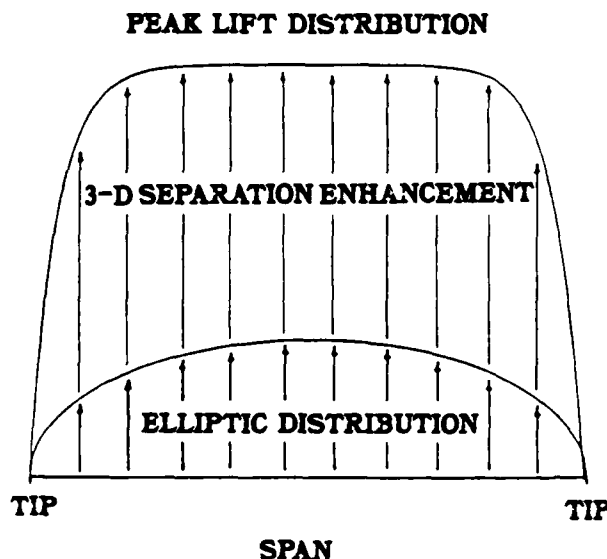
234

PEAK LIFT DISTRIBUTION

Figure 12. Non-elliptic lift distribution from forced unsteady separation.

Figure 13. Time scales of unsteady flow development.

allowances for a non-ideal planform. Fig. 12 contrasts (in schematic form) this ideal elliptic distribution with the sectional distribution obtained from the pitching wing at maximum lift. The shape and magnitude of the C_l distributions for the dynamic pitch case were directly dependent upon the transient character of vortex development described earlier. Simple extensions of classical analysis techniques to account for either the temporal or spatial three-dimensional force anomalies effects are not valid.

Three-dimensional lift enhancement may be assessed based upon the magnitude and duration of the transient vortex-airfoil interaction in the wingtip region. Although the peak pressure magnitudes near the tip were slightly reduced, the prolonged vortex presence due to vortex-vortex interactions sustained the lift event. The difference in area under the C_l curve between the inboard (1.8c) location and wingtip region (0.4c - 1.0c) is a direct reflection of the three-dimensional lift enhancement effect attributable to wingtip interactions.

In general, the transient lift characteristics of forced unsteady flow separation are primarily a function of pitch rate. While larger lift values are attained with greater α^+, the lift duration is reduced due to higher vortex convection velocities. Table 1 gives an indication of this temporal tradeoff. The lift enhancement duration, defined as the interval where C_l exceeds steady state values (0.75 at this Reynolds number), is compared with the time required to pitch the wing from 0 to 60 degrees. An increase in pitch rate reduces the vortex interaction period. The ratio of the two events shows the intermediated pitching value provided a longer interaction period. A more comprehensive and perhaps appropriate index of "maneuver potential" was defined by Francis for two-dimensional separation from pitching airfoils. Using a force integrated impulse, intermediate rather than very rapid pitch rates
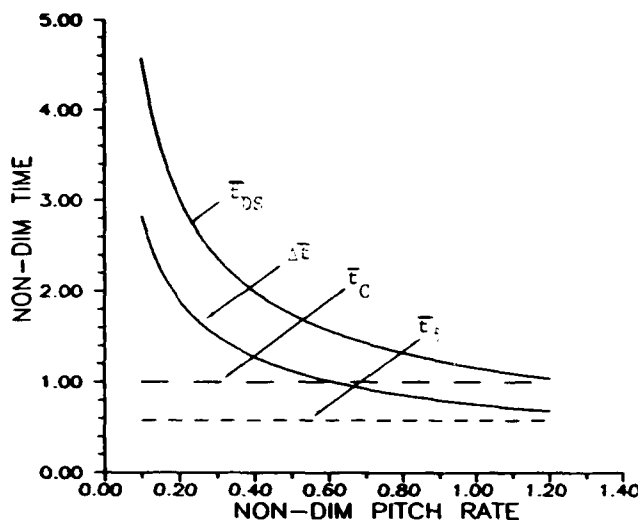
were also found to maximize the maneuver potential with single pitch motions. This same analysis will eventually be utilized for these three-dimensional results after additional data have been collected along the span.

Time Scales

The phenomenology of transient wing loading is intimately interdependent upon the vortex-wing interaction. In turn, production, distribution and convection of vorticity dictate vortex structure and dynamic behavior. Any discussion of vorticity and its development in an unsteady environment must be viewed from the perspective of the dominate temporal scales. Comparisons of these scales help identify the critically dependent parameters influencing the vortex dynamics.

Several time scales are important in the forced unsteady separation process. These scales can be subdivided into temporal measures of the wing dynamics and vorticity accumulation. One of the indices of wing motion is the time required for the wing to pitch from 0 degrees to the vortex initiation angle ($\bar{t}_{DS}$ - dynamic stall). Since three-dimensional separation is governed temporally by the inboard two-dimensional vortex development, the time required to reach dynamic stall was calculated from the empirical relation presented by Strickland et al. using the Gormont model. A plot of the vortex initiation time with increasing α^+ (fig. 13) shows the exponential decrease with rapid pitching motions.

Another critical threshold value is the steady state stall angle (9.7 deg. at this Reynolds number). The wing motion must exceed this angle for vortex initiation to occur. The wing rotation rate will increase the value of the static separation angle due to the relative motion of the leading edge in relation to the free stream velocity vector. The time required to reach the corrected static stall angle ($\bar{t}_{DSS}$) can be obtained by accounting for the induced velocity vector at the leading edge. The time

235

α^+	Motion Time	Enhancement Time	Ratio
0.1	10.5	16.0	1.52
0.2	6.0	14.0	2.33
0.3	5.5	12.0	2.20

(times are non-dimensional)

Table 1. Motion History

difference between the dynamic stall event and corrected static stall threshold ($\Delta t = t_{DS} - t_{DSS}$) is also shown in fig. 13. The rapid pitch rate, as expected, forces a similar exponential decrease in the time difference between events.

The total accumulation of vorticity in the boundary layer is a competitive process between the production terms scaled by diffusion and the convection terms scaled by the free stream velocity. The production rate was appoximated by the time required to diffuse vorticity a distance equivalent to the displacement thickness. A $\bar{t}_\delta$ of 0.58 was obtained based upon a simple flat plate calculation at the quarter chord. In contrast, a convection time ($\bar{t}_c$) of 1.0 is required for the free-stream to travel a single chord length.

Convection and diffusion of the boundary layer vorticity control the nature of vortex development. The wing kinematics determine whether the convection or diffusion processes dominate. At high pitch rates, the time difference between the dynamic and static stall events asymptotically approaches $\bar{t}_\delta$. This behavior suggests that diffusion provides the dominate effect. The vortex filament accumulation and separation process initiates after the wing motion exceeds the corrected static stall angle. The large pressure gradient at the leading edge diffuses vorticity from the boundary at a more rapid rate. The vorticity remains concentrated because the rapid pitch motion limits the vorticity convection potential.

Vorticity convection plays a more dominate role at lower pitch rates. The only source of vorticity, of course, comes from diffusion at the wing surface. At lower pitch rates the pressure gradients near the leading edge are much lower. Hence, the vorticity flux is also reduced. Temporally, vorticity accumulation is subject to reduction from convection. This process can be readily identified from flow visualization results. Vorticity accumulation over a slowly pitching airfoil appears as a "thick" boundary layer. During the pitch motion some of the boundary layer vorticity near the trailing edge convects from the wing into the wake. In contrast, at large pitch rates, all of the boundary layer vorticity becomes entrained into the leading edge vortex without wake shedding.

Conclusions

Forced unsteady flow elicited from a pitching wing was dominated by the same vortical

wake structure observed using pitching airfoils. Dynamic flow separation inboard, away from the tip influence, was characterized by a pressure signature duplicating previous two-dimensional results. In the tip region, vortex-vortex interactions prolonged vortex residence times and enhanced the transient lift effect. Temporal correlations between the leading edge and wingtip vortices indicated that a continuum of vortex filaments could be used to model the vortex-vortex interaction in the tip region.

It is apparent that previous two-dimensional results may provide a good indication of three-dimensional wing performance. Both the magnitude and duration of the transient vortex development were linked to the inboard, two-dimensional, vortex behavior. Physical processes affecting the production, accumulation, distribution and convection of vorticity drive both two- and three-dimensional separation events. Continuing investigations of the net vorticity flux dependence on the dynamic pitching motions should help clarify some of the physical processes involved.

Bibliography

1. Lerner, E.J., "First International X-Plane to Fly," Aerospace America, August 1987.

2. McCroskey, W.J., "Unsteady Airfoils," Annual Review of Fluid Mechanics, 1982, pp. 285-311.

3. Carr, L.W., "Dynamic Stall Progress in Analysis and Prediction", AIAA Paper 85-1769-CP, Snowmass, Co., August 1985, pp. 1-33.

4. Reynolds, W.C. and Carr, L.W., "Review of Unsteady, Driven Separated Flows," AIAA Paper 85-0527, Boulder, Co., May 1985.

5. Luttges, M.W., Robinson, M.C., and Kennedy, D.A., "Control of Unsteady Separated Flow Structures on Airfoils," AIAA Paper 85-0531, Boulder, Co., May, 1985.

6. Francis, M., Keesee, J.E., Lang, J.D., Sparks, G.W. and Sisson, G.E., "Aerodynamic Characteristics of an Unsteady Separated Flow," AIAA Journal, 17, 1979, pp. 1332-1339.

7. Robinson, M.C., and Luttges, M.W., "Vortices Produced by Air Pulse Injection From the Surface of an Oscillating Airfoil," AIAA Paper 86-0118, Reno, NV, January, 1986, pp. 1-13.

8. Koga, D.J., Reisenthal, P. and Nagib, H.M., "Control of Separated Flow Fields Using Forced Unsteadiness," IIT Fluids and Heat Transfer Report R84-1, 1984, pp. 1-252.

9. Carr, L.W., McAlister, K.W., and McCroskey, W.J., "Analysis of the Development of Dynamic Stall Based on Oscillating Airfoil Experiments," NASA TN-8382, January, 1977.

10. McCroskey, W.J., Carr, L.W., and McAlister, K.W., "Dynamic Stall Experiments on Oscillating Airfoils," AIAA Paper No. 75-125, January, 1975.

11. McAlister, K.W., and Carr, L.W., "Water Tunnel Visualizations of Dynamic Stall," J. Fluids Engr., Vol. 101, 1979, pp. 376-380.

12. Jumper, E.J., Shreck, S.J., and Dimmick, R.L., "Lift Curve Characteristics for an Airfoil Pitching at Constant Rate," AIAA Paper 86-0117, Reno, NV, January, 1986, pp. 1-10.

13. Walker, J.M., Helin, H.E., and Strickland, J.H., "An Experimental Investigation of an Airfoil Undergoing Large Amplitude Pitching Motions," AIAA Journal, Vol. 23, August, 1985, pp. 1141-1142.

14. Walker, J.M., Helin, H.E., and Chou, D.C., "Unsteady Surface Pressure Measurments on a Pitching Airfoil," AIAA Paper 85-0532, Boulder, CO, March, 1985, pp. 1-10.

15. Francis, M.S. and Keesee, J.E., "Airfoil Dynamic Stall Performance With Large-Amplitude Motions," AIAA Journal, Vol. 23 November, 1985, pp. 1653-1659.

16. Helin, H.E., Robinson, M.C., and Luttges, M.W., "Visualization of Dynamic Stall Controlled by Large Amplitude Interrupted Pitching Motions," AIAA Paper 86-2281-CP, Williamsburg, VA, August, 1986, pp. 1-18.

17. Lorber, P.F., and Carta, F.O., "Airfoil Dynamic Stall at Constant Pitch and High Reynolds Number," AIAA Paper 87-1329, Honolulu, Hi., June 1987.

18. Adler, J.N., and Luttges, M.W., "Three-Dimensionality in Unsteady Flow About a Wing," AIAA Paper 85-0132, Reno, NV, January, 1985, pp. 1-6.

19. Ashworth, J., Waltrip, M. and Luttges, M.W., "Three-Dimensional Unsteady Flow Fields Elicited by a Pitching Forward Swept Wing," AIAA Paper 86-1104, May, 1986.

20. Robinson, M.C., Helin, H.E., Gilliam, F., Russell, J., and Walker, J., "Visualization of Three-Dimensional Forced Unsteady Separated Flow," AIAA Paper 86-1066, Atlanta, GA, May, 1986.

21. Wissler, J.B., Gilliam, F.T., Robinson, M.C., and Walker, J.M., "Visualization of Three-Dimensional Flow Structures About a Pitching Forward Swept Wing," AIAA Paper 87-1322, Honolulu, Hi., June, 1987, pp. 1-9.

22. Albertson, J.A., Troutt, T.R., Siuru, W.D., and Walker, J.M., "Dynamic Stall Vortex Development and the Surface Pressure Field of a Pitching Airfoil," AIAA Paper 87-1333, Honolulu, Hi., June, 1987.

23. Strickland, J.H., and Graham, G.M., "Dynamic Stall Inception Correlation For Airfoils Undergoing Constant Pitch Rate Motions," AIAA Journal, Vol. 24, April, 1986, pp. 678-680.

Investigation of reactive control of separated flows

with non-stationary separation lines

Mukund Acharya

Fluid Dynamics Research Center

Illinois Institute of Technology, Chicago

The present work is being carried out to examine the feasibility of extending the separated flow control techniques studied at IIT by Koga and Reisenthel, to situations where the separation line is non-stationary. Examples of the latter include gusting flows and the flow over airfoils with rapidly changing angles of attack.

We are investigating boundary-layer flows in which an unsteady separation is introduced using one of two mechanisms: the motion of a spanwise flap into the boundary layer, and the use of a nominally two-dimensional air jet with controllable momentum ratio, which can be directed into the boundary layer from the wall at varying angles. We expect that such 'building-block' experiments will help us assess the feasibility of reactive control and identify signatures of the inception of separation that are both practical and accurate enough for use in a feedback loop to drive the control/management mechanism. The study will also help in identifying the relevant scales for both the formation and collapse of non-steady separated regions.

Fig. 1 is a sequence of photographs showing the formation of separation behind the flap. T was the time in which the flap rose into the boundary layer. The pictures were taken at various times; both during the rise of the flap as well as after it had reached its final position. A time period corresponding to 6 rise times was required in this particular case for the separation to attain steady state conditions. The results of flow visualization experiments such as this will be discussed, together with quantitative measurements using a dual stanton probe in conjunction with a sensitive pressure transducer to detect flow reversal.
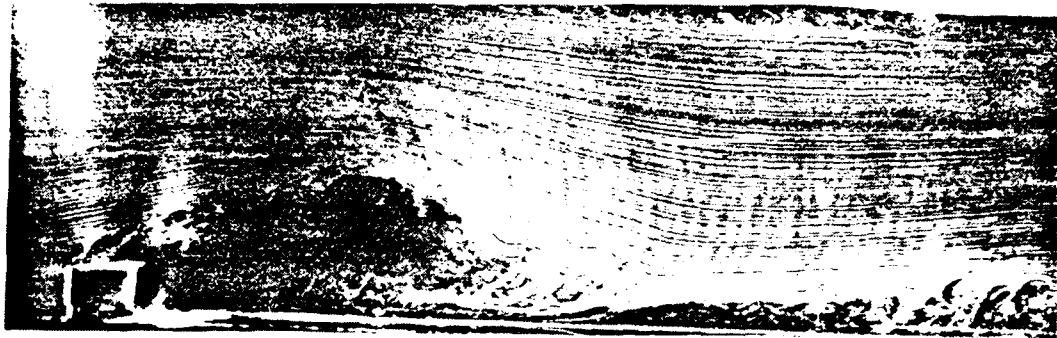
239
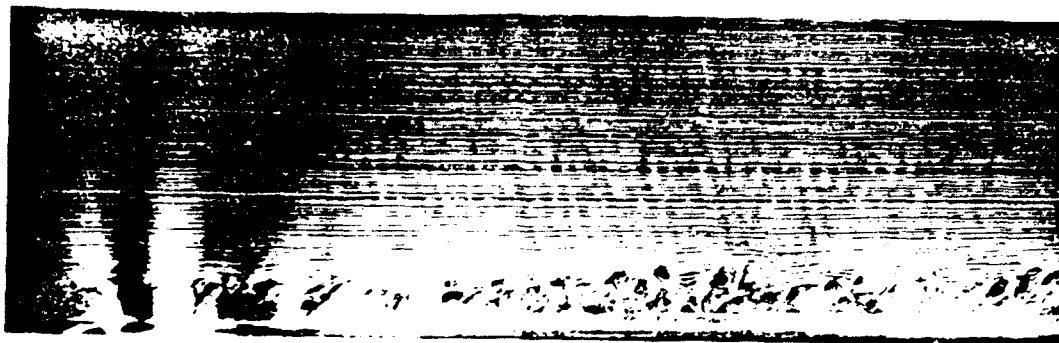
t/T - 0

t/T - 0.5
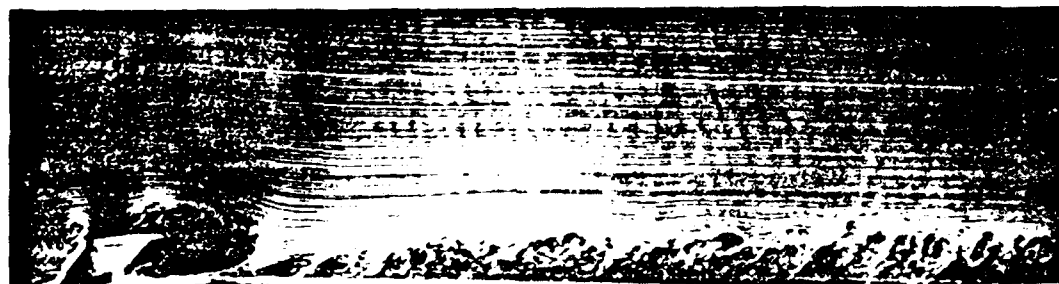
t/T - 0.67

t/T - 1.0

FIG. 1

t/T = 2.0

t/T = 3.0

t/T = 4.0

t/T = 5.0

FIG. 1 (cont.)

241

CONSIDERATIONS FOR ANALYZING SEPARATED FLOWS OVER ARBITRARILY MANEUVERING BODIES

Shan-fu Shen
Sibley School of Mechanical and Aerospace Engineering
Cornell University
Ithaca, New York

Abstract

Bodies moving arbitrarily in a fluid medium experience forces and moments which actually arise from the stresses along the body-fluid interface. A theoretical approach should start from treating the fluid and the body as a coupled system. Unsteady viscous phenomena, including separation, over a moving body are especially poorly understood, attributed by Ericsson as to "moving wall" effects. It is proposed that rational analysis of such problems should start from the common ground of the Navier-Stokes equations in the body-fixed moving axes, as used in typical flight dynamics equations. All the "moving wall" effects are then precisely characterized by the set of generalized Froude number which enter because of the body motion. The boundary layer approximation and two examples are thus analyzed as illustration.

Nomenclature

e	eccentricity of pitching axis
F	magnitude of vector $\underline{F}$
$\underline{F}$	apparent body-force vector, per unit mass
$\underline{g}$	gravitational acceleration vector
O	origin of body-fixed moving axes, usually at c.g. of aircraft
O'	origin of a set of inertial frame coordinates
p	pressure
$\underline{r}$	position vector measured from O
$\underline{r}'$	position vector measured form O'
t	time
u	velocity component in x-direction
$\underline{u}$	velocity vector
$\underline{u}'$	velocity vector in inertial frame
U	velocity component at edge of boundary layer, in x-direction
v	velocity component in y-direction
V	velocity component at edge of boundary layer, in y-direction
w	velocity component in z-direction
x	body-fixed longitudinal coordinates; also, one of the boundary-layer cartesian coordinates on the body surface
x'	one of the cartesian coordinates for inertia frame (x',y',z')
y	body-fixed lateral coordinate; also, one of the boundary-layer cartesian coordinates on the body surface
y'	one of the cartesian coordinates for inertial frame (x',y',z')
z	body-fixed coordinate normal to x- and y-directions; also, the boundary-layer coordinates normal to body surface
z'	one of the cartesian coordinates for inertia frame (x',y',z')
α	angle of attack
δ	value of z indicating edge of boundary layer
θ	angle measured from the fixed leading edge of circular cylinder, positive clockwise
v	kinematic viscosity of fluid
Ω	angular-velocity magnitude
$\underline{\Omega}$	angular velocity vector of body motion

Subscripts

A	aircraft
S	separation
x	x-component
y	y-component

I. Introduction

The subject of unsteady separated flows over bodies which perform rapidly changing motion, possibly in conjunction with distortions of the body geometry, is both fascinating and of increasing practical interest. An example of activities already sustained for a long time is the dynamic stall of an airfoil when the angle of attach rapidly changes. Augmentation of the maximum lift and hysteresis behavior in the oscillatory response are also manifestations of the transient effects on the boundary layer, particularly how it separates and reattaches, and on the vortical wake trailing behind. A current review of such phenomena may be found in the most recent paper, after many going back to 1971, by Ericsson [ref. 1]. He broadly refers to the "moving wall effect" as causing changes of the unsteady separated flow, analogous to that on the rotating cylinder in a uniform stream. There is need for a more rigorous theory. Meanwhile, the concept of super-maneuvering fighter, recently put forward by Herbst [ref. 2], requires the vehicle to execute maneuvers at rates way beyond those customary for conventional aircraft. Design of such vehicles will depend on our knowledge of what individually and together these rates may do to the various forces and moments of concern, but little is known about them at this time. Strictly speaking, the flight dynamic equations governing the aircraft motion as a rigid body, and the fluid dynamic equations governing the aerodynamic reactions to the maneuvering aircraft are coupled. They should in principle be solved simultaneously. In order to follow the aircraft in its six degrees of freedom, logically then, the fluid motion should be described relative to the set of body-fixed

coordinates commonly used in flight dynamics. Ericsson's "moving wall effects", obviously, belong to the domain of these equations. In fact, perhaps the term "moving body" effects is more appropriate.

In specific studies, proper formulation of the Navier-Stokes equations with reference to the relevant moving coordinates of course frequently appear in the literature. General discussions on the different flow behaviors with respect to moving axes resulting from several degrees of freedom, however, seem lacking. This paper represents our initial effort aiming at systematic studies of new flow phenomena relative to the body-fixed axes, as may result from rapid aircraft maneuvering.

In Sec. 2 the Navier-Stokes equations are set down with reference to a set of body-fixed axes with origin at the center of gravity of the aircraft which may be moving arbitrarily in all six degrees of freedom. This choice presumes that one is interested in determining the airloads on the maneuvering aircraft. In other words, the equations of flight dynamics are thus properly coupled to the equations of fluid motion. A set of dimensionless parameters, which may be referred to as generalized Froude numbers, are seen to characterize the moving-body effects. The modified equations being of the same mathematical structure as those in the case of the inertial coordinates, computational codes available or developed for one should work for the other.

In Sec. 3, the boundary-layer approximation for the viscous layer adjacent to the moving body is discussed. Not surprisingly, without separation much of the apparent body-force effects are contained in the relative velocity prevailing at the outer edge of the boundary layer. At high rates, however, the angular motion of the body are expected to introduce unfamiliar effects which deserve future analyses. Sec. 4 contains two examples of systematic study of the initiation of unsteady separation, in particular the role of the location of the pitching axis. The concluding remarks are in Sec. 5.

II. Navier-Stokes Equations for Flow over a Moving Body

The maneuvering aircraft is a special case of a vehicle moving arbitrarily in all its six degrees of freedom as a rigid body. Its motion is governed by the equations of flight dynamics, which contain specifically the aerodynamic forces and moments. Usually the six degrees of freedom refer to the spatial trajectory of the center of gravity and the Euler angles associated with a set of body-fixed axes, with origin at the c.g. (Fig. 1). The geometry of the vehicle is specified with respect to these body axes. If there are other degrees of freedom, such as due to structural flexibility or control devices, they can be added while referring the same axes.

The air load on the aircraft results from the fluid motion stirred up by the moving body. Thus the aircraft and the surrounding air actually form an interacting system. For given initial and boundary conditions, the motion of a viscous and incompressible fluid is completely described by the Navier-Stokes equations, usually written with respect to a set of inertial coordinates. For the airload that acts on specific parts of the moving aircraft, the fluid motion should be now resolved relative to the body axes—i.e. with the observer sitting in the aircraft, making measurements during the flight test.

To recast the Navier-Stokes equations in a set of coordinates moving with the body is accomplished by a reinterpretation of the acceleration of each fluid element, which can be found in, e.g., Batchelor [ref. 3]. All spatial gradients are unaffected. Thus, it can be immediately written, in usual notation,

$$\frac{\partial \underline{u}}{\partial t} + \underline{u} \cdot \nabla \underline{u} = -\frac{1}{\rho} \nabla p + \nu \nabla^2 \underline{u} + \underline{F} + \underline{g} \qquad (1)$$

$$\nabla \cdot \underline{u} = 0 \qquad (2)$$

$$\underline{F} = -[\frac{\partial \underline{u}_A}{\partial t} + 2\underline{\Omega} \times \underline{u} + \underline{\Omega} \times (\underline{\Omega} \times \underline{r}) + \dot{\underline{\Omega}} \qquad (3)$$

where $\underline{u}_A$ = translational velocity of the aircraft,

$\underline{\Omega}$ = angular velocity of the aircraft,

$\underline{r}$ = position vector of the fluid element, measured from the c.g.,

$\underline{g}$ = gravitational acceleration,

$\underline{F}$ = apparent body force, per unit mass, as a result of the body motion.

Note that if we consider compressible fluid, the energy equation and the equation of state are not affected by acceleration, and therefore remain unchanged.

We exhibit above the gravitational acceleration term $\underline{g}$ both to emphasize the kinship between $\underline{g}$ and $\underline{F}$, and to provide a measure for $\underline{F}$. The dimensionless parameter characterizing the importance of gravity effects is the Froude number. Consequently, a generalized Froude number may be introduced, replacing $\underline{g}$ by $\underline{F}$ in the definition. Generally speaking, the moving-body effect should be important whenever by properly redefining a variable $\underline{g}$ in the inertial frame, the ordinary Froude number would become important.

The apparent body force $\underline{F}$ is seen to come from:

1) linear acceleration of the body,
2) Corioli effect between fluid velocity and body rotation,
3) centripetal acceleration,
4) angular acceleration of the body.

As each term is a vector, there are a total of 12 generalized Froude numbers, whose effects need to be assessed and understood, individually and in any combination—for any particular fluid phenomenon of interest, assuming the behavior for $\underline{F} = 0$ to be known. At this time only highly specific investigations exist in the literature. It seems that more systematic studies, preferably of analytic nature, must be relied on to gain insight into an area which may be full of novel surprises.

The present application of Eqs. (1)-(3) is an initial value problem: starting from a certain flight condition and flow, find the unsteady flow following, say, a prescribed maneuver. Thus, 'history effect' is an essential part in the results. As for the boundary conditions at the body surface, the viscous no-slip condition, for instance, is still simply

$$\underline{u} = 0 \quad \text{on the body surface.}$$

If the ambient air is at rest while the body moves through it, we have the asymptotic behavior

$$\underline{u} = -\underline{u}_A + \underline{r} \times \underline{\Omega}, \quad \text{as } r \to \infty.$$

The essence of body-fixed aerodynamics, from a utilitarian viewpoint, is to simplify the statement of the boundary conditions which represents the body surface. This would enable an easier handling of the flow field adjacent to the body. The far-field now is more complex, as seen by an observer riding the aircraft, although in an inertial frame the air is actually at rest. It would seem likely that the solution perhaps should be constructed by a zonal approach: solving the near field around the body using the body-fixed set of equations, constructing a far-field solution separately in the inertial frame, and properly matching the two along some convenient interface. In principle

such a procedure closely resembles the calculation of an interactive boundary layer with the surrounding potential flow. But its feasibility and effectiveness should be examined, at least, by case studies.

III. The Boundary Approximation in Moving Axes

There are, indeed, many boundary-layer problems on a maneuvering aircraft. Although we anticipate unsteady separation to be a central issue, the logical starting point is first to set down the boundary layer approximation for Eqs. (1)-(3). Since they differ from the usual Navier-Stokes equations only in the presence of the body-force $\underline{F}$-term, all the usual arguments used to derive the boundary-layer approximation hold, so long as $\underline{F}$ is on the same order as the 'left-hand side', i.e. the acceleration relative to the moving axes. We consider therefore again a thin layer wrapped around the (appropriate part of the) body surface, and let z denote the distance along the local normal direction to the body surface—so z = 0 coincides with the body surface. The key feature in the usual boundary layer is that the pressure can be taken as constant in the z-direction, hence equal to the inviscid local value at the edge of the boundary layer. It is still valid even if $\partial p/\partial z \sim O(1)$, on account of the small thickness of the boundary layer.

Obviously, except under special conditions, this key feature—that the pressure is unchanged in the z-direction—should generally prevail, as long as we have a thin layer. In this thin boundary-layer the viscous action is mainly to provide a smooth transition between the free stream velocity, nearly parallel to the body surface, and the no-slip condition at the surface. Only the tangential momentum equations and continuity are to be satisfied:

$$\frac{Du}{Dt} = -\frac{1}{\rho}\frac{\partial p}{\partial x} + F_x + g_x + \nu \frac{\partial^2 u}{\partial z^2} \qquad (4)$$

$$\frac{Dv}{Dt} = -\frac{1}{\rho}\frac{\partial p}{\partial x} + F_y + g_y + \nu \frac{\partial^2 v}{\partial z^2} \qquad (5)$$

$$\frac{\partial u}{\partial x} + \frac{\partial v}{\partial y} + \frac{\partial w}{\partial z} = 0 \qquad (6)$$

where (x,y) are the usually boundary-layer cartesian coordinates lying on the body surface, and (u,v,w) are the velocity components in the (x,y,z)-directions, resp.; F_x and F_y are the components of the apparent body force, eq. (3); g_x and g_y are the components of the gravitational acceleration. The boundary conditions are still

$$u = v = 0 \text{ at } z = 0,$$

and u = U(x,y,t), v = V(x,y,t) at the edge of the boundary layer, say z = δ.

It turns out that the momentum equations can be greatly simplified by invoking that U and V at the edge of the boundary layer must satisfy the inviscid version of Eqs. (4) and (5). Since the pressure is taken to be p(x,y,t), independent of z, the following must hold:

$$\frac{\partial U}{\partial t} + U\frac{\partial U}{\partial x} + V_0\frac{\partial U}{\partial y} = -\frac{1}{\rho}\frac{\partial p}{\partial x} + (F_x + g_x)|_{z=\delta} \qquad (7)$$

$$\frac{\partial V}{\partial t} + U_0\frac{\partial V}{\partial x} + V\frac{\partial V}{\partial y} = -\frac{1}{\rho}\frac{\partial p}{\partial x} + (F_y + g_y)|_{z=\delta} \qquad (8)$$

Subtracting Eqs. (7) and (8) from Eqs. (4) and (5), resp., we get

$$\frac{Du}{Dt} = \frac{\partial V}{\partial t} + U\frac{\partial U}{\partial x} + V\frac{\partial U}{\partial x} + F_x' + \nu\frac{\partial^2 u}{\partial z^2} \qquad (9)$$

$$\frac{Dv}{Dt} = \frac{\partial V}{\partial t} + U\frac{\partial V}{\partial x} + V\frac{\partial V}{\partial y} + F_y' + \nu\frac{\partial^2 v}{\partial z^2} \qquad (10)$$

The terms F_x' and F_y' stand for the change of F_x and F_y, resp., from their values at the edge of the boundary layer. Examination of the contributions to $\underline{F}'$ shows that only the Corioli force tangent to the body surface plays a role—thus proportional to the component of the angular velocity in the local z-direction. This is of course well-known in the treatment of boundary layers over steadily rotating bodies; see e.g. Fogarty [ref. 4].

The above amounts to a more careful statement of the practice, typically taken as self-evident, that in cases involving moving axes, the boundary layer can be treated as if in an inertial frame, provided the effective pressure gradient is properly evaluated from the free-stream relative velocity at the edge of the boundary layer. We now see some limitations of its strict validity. The Corioli's force tangent to the stream surfaces of the boundary is surely an extra mechanism worthy of attention. Its influence is similar to that of the earth's rotation on its boundary layer. Note that for two-dimensional airfoils, pitching motion does not produce a Corioli's force along the boundary-layer direction, therefore causing no error when it is simply omitted. On helicopter blades, on the other hand, the chordwise and spanwise boundary layers interact because of the rotation. The same is expected for the boundary layer on a yawing wing.

Insofar as the relative velocity at the edge of the boundary layer is concerned, no advantage is gained by using the moving axes fixed to the body to solve the inviscid flow. Especially for the incompressible case, only the kinematic data along the body contour, assuming a negligible boundary layer thickness, are required to determine the instantaneous velocity field. It therefore points to the construction of the inviscid flow in the familiar inertial frame. By so doing, the boundary-layer problem is to be attacked essentially as if in an inertial frame. Already in Shen and Crimi [ref. 5], where the Oseen approximation was used to solve the two-dimensional oscillating airfoil, a somewhat similar analysis and the same conclusion have been reported.

IV. Illustrative Applications
(1) Ericsson's "leading edge jet" effect

It is beyond the scope of this paper to discuss the various interesting ideas put forth by Ericsson with regard to dynamic stall, oscillating airfoil, "wind-tunnel/free flight equivalence", etc.; see, e.g., his recent article [ref. 1]. We shall focus on his reasoning of the "leading-edge jet effect", which was used to explain why the dynamic stall behavior of an oscillating airfoil in the plunging mode differs form that in the pitching mode. But no quantified statement could be made. Our theory above allows us to study quantitatively the influence on separation, for instance, due to parameters such as the reduced frequency, pitching axis location, etc. If approximations are used to obtain simplified results of limited validity, there will be no muddled picture as to how to make improvements.

We first paraphrase Ericsson's analysis of the separation over an oscillating airfoil, in the plunging or the pitching mode, as follows: It is expected that separation would occur near the leading edge in both cases. At least for low reduced frequencies, the inviscid velocity field may be inferred form the instantaneous effective angle of attack by quasi-steady consideration. In Fig. 2 are shown two airfoils in a uniform stream, one executing a plunging and the other a pitching oscillation. At the same instantaneous effective angle of attack at which separation may be immanent, the plunging airfoil is in downstroke while the pitching airfoil is in upstroke, but the free

stream is approximately the same over both boundary layers. In the leading edge region, shown enlarged in the dotted circle, the opposite wall movements in the two modes are seen by the boundary layer as a moving wall. For the plunging airfoil it de-energizes the flow near the wall and promotes separation. The converse is true over the pitching airfoil. The conclusion is in accordance with experimental findings.

We now translate the above argument into a quantitative approach according to the boundary-layer theory in moving coordinates: The flow over an airfoil moving unsteadily in plunging and plunging degrees of freedom is two-dimensional. At least in the unseparated region, it may be described by the two-dimensional version of the boundary-layer approximation, Eqs. (6), (9) and (10). If the motion starts from zero angle of attack before separation begins, the inviscid flow outside of the boundary layer can be calculated by potential theory alone. To simplify, we limit ourselves further to an artificial airfoil which is a thin ellipse and circulation free. Then the potential flow is quickly given by conformal mapping, with no need to introduce a vortex wake. The time-dependent surface velocity should be used next in conjunction with an unsteady boundary-layer code, and separation for each case would be determined to occur at the instant when the solution turns singular at a certain location.

Ericsson's "moving wall" effect, as a concept, actually relies on the observations of the steady flow over a rotating cylinder. To mimic this basically quasi-steady reasoning, we opted therefore also to calculate as if the boundary layer is steady under the instantaneous surface velocity. Specifically, a Crank-Nicolson scheme marching from the stagnation point was used, and the occurrence of reverse flow signified separation. The Ericsson argument of "moving wall" effect was thus made into a quantitative one, whose predictions could now be systematically examined.

Calculations were carried out for the separation angle-of-attack of our simplified elliptic airfoil, following a pitching motion at constant angular velocity, and its dependence on the location of the pitching axis. Figure 3 shows the definitions of the eccentricity e of the pitching axis, in % chord behind the mid-chord point, and the angular velocity Ω, positive clockwise. Details of the straightforward calculations will be omitted for brevity. For $\Omega = -0.1$, the reuslts in Fig. 4 show how the angle of attack at separation, α_s, changes as the pitching axis moves from mid-chord (e = 0) forward toward the leading edge (e = -1.0). The steady angle of attack at separation, i.e. for $\Omega = 0$, is according to this calculation at $\alpha_s = 6.7$. Curiously enough, the results predict that the pitching motion would rather promote an earlier separation, in this case, when the pitching axis moves ahead of roughly the 1/4-chord point! A closer examination reveals that indeed, as the pitching axis moves forward, the contribution, to the inviscid surface velocity around the leading edge by the pitching motion does change sign. The pitching-axis location where the sign change takes place also depends only on geometry and not on the pitching rate. It should be emphasized that the above example is done mainly to demonstrate how Ericsson's arguments can be quantified. Validity of the key assumptions involved in reducing the complexity of the rigorous boundary layer problem is a different issue and not addressed here.

As for the plunging mode, it clearly may be regarded as the limiting case of the pitching mode with $\Omega = O(1/e)$ as $e \rightarrow \infty$. Instead of a different mode, the results are imbedded in a systematic study in the parametric (Ω,e)-plane.

(2) Unsteady separation over a circular cylinder impulsively started into constant speed translation plus constant speed rotation

We wish next to present a study without simplifying assumptions. The case of impulsively started circular cylinder has been a bench-mark problem of unsteady separation. The instant and location of boundary-layer separation have been established by van Dommelen and Shen [ref. 6], using a Lagrangian description which enables an accurate determination of the boundary-layer *singularity*. Their method of calculation has also been applied successfully to an impulsively started elliptical cylinder of moderate thickness ration and at an angle of attack in Wu [ref. 7]. Thus the example of the ellipse pitching at a constant rate in a uniform stream can be, in principle, accurately solved using the same method. But certain modification of our existing program is necessary.

More conveniently, the unsteady boundary layer of an impulsively started circular cylinder in both translation and pitching can be computed with our program as is. The results of such a study for two values of the angular velocity ($\Omega = -0.1$ and -0.5), and three values of the eccentricity of the pitching axis (e = 0, -0.4 and -0.8) are summarized in Table 1. The symbols are defined in the same manner as in Fig. 3 for the ellipse.

V. Conclusion

Vehicles that move arbitrarily in a fluid medium experience forces and moments resulting from the fluid motion relative to the body-fixed moving axes. Systematic study consequently should start from the Navier-Stokes equation written in terms of the moving axes. What Ericsson [ref. 1] broadly referred to as "moving wall" effects, trying to reason mainly from the conventional inertial framework formulation, would seem to be better named "moving body" effects. The effects are precisely described by analysis of the apparent body-force terms, which may be characterized through a set of generalized Froude numbers. We now have at last a platform to stand on for future research into their effects on complex phenomena such as separating, transition, as well as turbulence.

The properly reduced boundary-layer equations are seen to require, in most cases, only the addition of Coriolis's effects parallel to the body surface, essentially like those used for helicopter blades. Two simple examples have been presented to illustrate their application.

From a computational viewpoint, the moving axes introduce no basic changes of the mathematical structure of the Navier-Stokes equation. Hence, all "codes" developed for the inertial frame are readily adaptable to analyze the moving-body effects. Structural flexibility of the vehicle and unconventional control devices can be accommodated by proper additional degrees of freedom and geometrical specification. Thus, the theory and its further development should yield both short-range and long-range benefits.

Acknowledgement

References

1. Ericsson, L. E., "Dynamic Omnipresence of Moving Wall Effects, A Selective Review", AIAA Paper No. 87-0241, 1987.

2. Herbst, W. B., "Supermaneuverability", in Unsteady Separated Flows, eds. M.S. Francis and M. W. Luttges, 1-x, Univ. of Colorado, 1984.

3. Batchelor, G. K., "An Introduction to Fluid Dynamics", 139-140, Cambridge University Press, 1970.

4. Fogarty, L. E., "The Laminar Boundary Layer over a Rotating Blade", J. Aero. Sci., vol. 18, 247-252, 1951.

5. Shen, S. F., and Crimi, P., "The Theory of an Oscillating Thin Airfoil According to the Oseen Approximation", J. Fluid Mech., vol. 23, 585-609, 1965.

6. Van Dommelen, L. L., and Shen, S. F., "The Boundary Layer in Langrangian Description", J. Comp. Phys., vol. 38, 125-140, 1980.

7. Wu, Tsu-Yin, "Unsteady Incompressible Boundary-Layer Separation Over a Two Dimensional Impulsively Started Elliptic Cylinder Calculated by Lagrangian Method," M.S. Thesis, Cornell University, 1985.

Fig. 2. Ericcson's 'Leading-edge Jet' Effect on Airfoil in Pitching or Plunging Motion.

Table 1. Summary of Computed Unsteady Boundary-Layer Separation for Circular Cylinder Impulsively Started into Forward Motion with Rotation.

Ω	-0.1			-0.5		
e	0	-0.4	-0.8	0	-0.4	-0.8
Separation time t_s						
upper	3.05	3.02	2.96	3.21	2.69	2.21
lower	3.09	3.06	2.99	3.75	2.50	1.98
Separation location θ (clockwise from fixed leading edge)						
upper	99.7°	95.1°	91.7°	50.4°	49.8°	48.1°
lower	238.4°	234.3°	229.8°	185.6°	189.6°	186.8°

Fig. 3. Definitions of eccentricity e and pitching rate Ω.
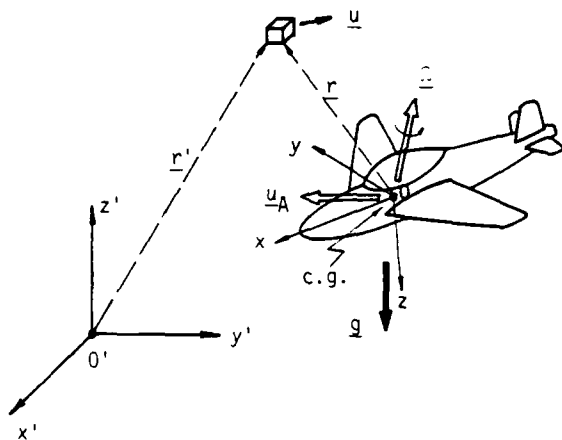
Fig. 1. Body-fixed Moving Axes and Notation.
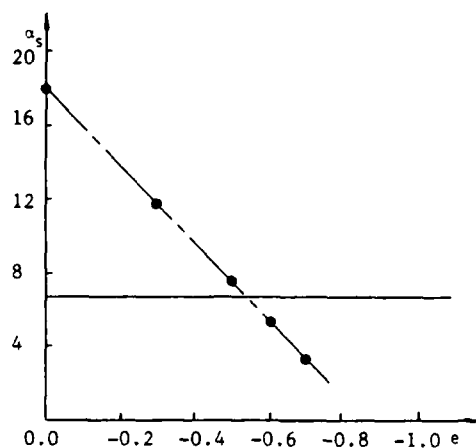
Fig. 4. Quasi-steady Estimates of Dependence of Separation Angle-of-Attack α_s on eccentricity.

UNSTEADY SHEAR LAYERS SEPARATING FORM SMOOTH AND SHARP SURFACES

D. P. Telionis, N. T. Hoang
Department of Engineering Science & Mechanics
Virginia Polytechnic Institute & State University
Blacksburg, VA

D. R. Poling
Boeing Vertol Company
Philadelphia, PA

and

D. S. Mathioulakis
41 Agiou Trifonos
Kifisia, Greece

Abstract

The boundaries of massive separated regions are controlled by free shear layers which in turn emanate from lines of separation. Free shear layers convect large amounts of vorticity which in fact strongly influences their own development. Such layers then roll up into organized vortical structures, dominating global characteristics of lifting surfaces, like lift and drag. Research has been conducted at VPI with flows separating over both sharp and smooth surfaces. For the first case we examined the shear layers emanating form the sharp edge of a pitching airfoil. For the second case we studied steady pulsating flow over curved surfaces. Experimental data were obtained by 2-component Laser-Droppler veloloci-metry in a water tunnel. Measurements were triggered and ensemble-averaged over a period of the oscillatory motion. Moreover, flow visualization of both instantaneous velocity vectors and streak-lines was achieved. It was found that shear layers stretch and roll up tightly and in the process generate almost ideal line vortices.

Introduction

It is well established that the separated regions of lifting surfaces in unsteady motion may contain large amounts of vorticity. In fact, on many occasions, this vorticity is organized in the form of almost ideal point vortices. A typical example is the separated region over an airfoil during unsteady stall. Investigators refer to this unsteady wake as the "unsteady stall vortex", perhaps because indeed the vortical structure resembles strongly the distribution of a single potential vortex.

The detailed structure of the unsteady stall vortex has not been studied yet. Even more important is the mechanism with which vorticity is fed into this structure. Two problems therefore could be studied independently. The first is how vorticity is released from the solid body and the second is how this vorticity interacts with the oncoming flow and eventually organizes itself into discrete and coherent vortical structures.

The authors conducted research, with the support of AFOSR, on these topics. Most of the results have been actually published in one form or another and are listed here in the refer-ences. In the present paper we present a unified picture of our results. More importantly, we offer a new interpretation of our data and we draw conclusions which have not appeared earlier.

1. Vorticity Shedding at Separation

In irrotational flow over rigid bodies, vor-ticity is created at the wall and is released at the point of separation. The flow in the neigh-borhood of the point of separation for a backward facing circular arc was documented for steady and periodic flow[1]. Typical results obtained by pro-cessing LDV data are presented in Fig. 1. In this figure we display vorticity contours for the time-mean and the steady flow.

Upstream of separation vorticity is tightly distributed with a maximum on the wall. This is because the wall is the source of vorticity, as long as the pressure gradient is positive. The station of vanishing pressure gradient coincides with the first appearance of an inflectional velo-city profile, as evidenced by the momentum equa-tion evaluated at the wall

$$\frac{\partial p}{\partial x} + \frac{1}{Re} \frac{\partial^2 u}{\partial y^2}\bigg|_{y=0} = 0$$

From this station on vorticity lines emanate from the wall and in fact slope downstream as Fig. 1 indicates. No more vorticity feeds the viscous layer from the wall. The shear layer continues for a while following the contour of the body. The ridge of the vorticity contours is off the wall. As separation is approached, the vorticity layer turns gently into the flow. At first the space between the wall and the free shear layer is filled with almost stagnant fluid. Further down-stream the space is occupied by recirculating bubbles.

The classical asymptotic theory[2-5] indicates that the shear layer remains thin as long as the Reynolds number is large enough. Concrete experi-mental evidence for this fact for unsteady flow has been provided in Refs. 1 & 6. Velocity vector profiles measured by 2-component laser velocimetry are displayed in Fig. 2. These profiles were obtained by conditionally averaging over many
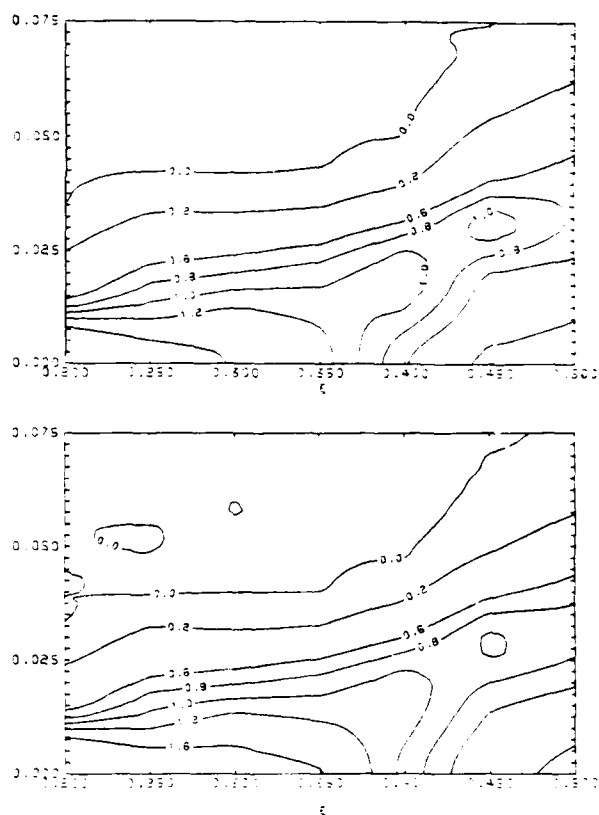
Fig. 1. Vorticity contours in the neighborhood of separation over an alliptical airfoil at an angle of attack. These results were obtained by manipulating 2-component LDV data. Horizontal and vertical scales are dimensionless distances along and perpendicular to the wall, respectively.

realizations. It is now clearly seen that the unsteadiness of the turbulent flow in the space between the free shear layer and the wall averages to a flow which is very slow and consistently moving upstream. The free shear layer fluctuates like a flapping flag. However, and most significantly, it retains its thin character. In other words, vorticity in the free shear layer is not dispersed by the random turbulent motion in the recirculating region or by the unsteadiness imposed externally on the field.

The evidence collected by the authors indicates that the shear layer develops independently of its laminar or turbulent condition. Once the shear layer has separated from the wall, its position and its subsequent rolling up does not depend on the Reynolds number. If this fact is firmly confirmed it will have significant implications for computational methods. It implies that turbulence modeling is not a significant factor in a numerical method. The turbulent character of the attached layer and the corresponding turbulence modeling control, of course, the location of separation and the angle with which vorticity is released but the subsequent fate of the layer is independent of its condition.

2. The Rolling Up of a Free-Shear Layer

The unsteady wake of the body is dominated by the rolling free-shear layers. This is most clearly demonstrated by the development of the unsteady stall vortex on the suction side of a thin airfoil. To isolate the effect of rolling of a free-shear layer, we examined the wake of a pitching airfoil. The airfoil was pitched with an amplitude of 20°. The flow was always attached on the airfoil. Its wake was therefore dominated by the free-shear layer. The vorticity contained in this layer changes sign twice within a period of oscillation. As a result, the free shear layer rolls up into well organized structures of opposite sign, reminiscent of a Karman street but rotating in the opposite sense.

Laser velocimetry data of such a wake were obtained[7] and are displayed in Fig. 3. In this figure phase-averaged velocity profiles are plotted along stations normal to the freestream. A flow visualization is displayed in Fig. 4. In this visualization the velocity field was captured approximately by short particle paths. Dyes emitted for the airfoil surface and eventually released at the trailing edge develop into streaklines which roll around the point vortices.

To expose more clearly the streakline patterns we have also obtained visualization of dyes alone.[8] In such visualizations blue and red dyes were released from the two sides of the airfoil, respectively, to mark the sign of vorticity. It should be emphasized here that streaklines emanating from the surface of a solid body have a special physical significance. They allow the visualization of the displacement of vorticity. This is because the species equation is identical to the equation governing vorticity, except for the numerical factor of the coefficient of the diffusion term. Even so, the diffusion process is almost negligible in the development of free-shear layers. In a nutshell then, such dyes mark the displacement of vorticity in the flow field. Dyes are also visible in Fig. 4 but they are not as clearly exposed, because the conditions are optimum for exposing small particle paths.

Such visual data have been most recently digitized. Input to our program are the slopes of particle paths. With a good approximation, these are the inclinations of the instantaneous velocity vectors. Instantaneous streamlines are then reconstructed. This is accomplished by the classical numerical integration to determine a curve, if its slope is known. In the present case, the slope is estimated at a point by a weighted average of all experimental data within a certain radius from the point of interest. The results corresponding to about 300 discretized data are displayed in Fig. 6. The detailed structure of the vortex is not very clear in this figure but the presence of a closed loop is evident.

Of great importance here is the fact that the vorticity is quickly collected into a core. A careful examination of the numerical data as well as observation of the flow visualizations indicate that the vortices are very nearly ideal point vortices. In the flow visualization of Fig. 4, it can be clearly seen that along the streaklines
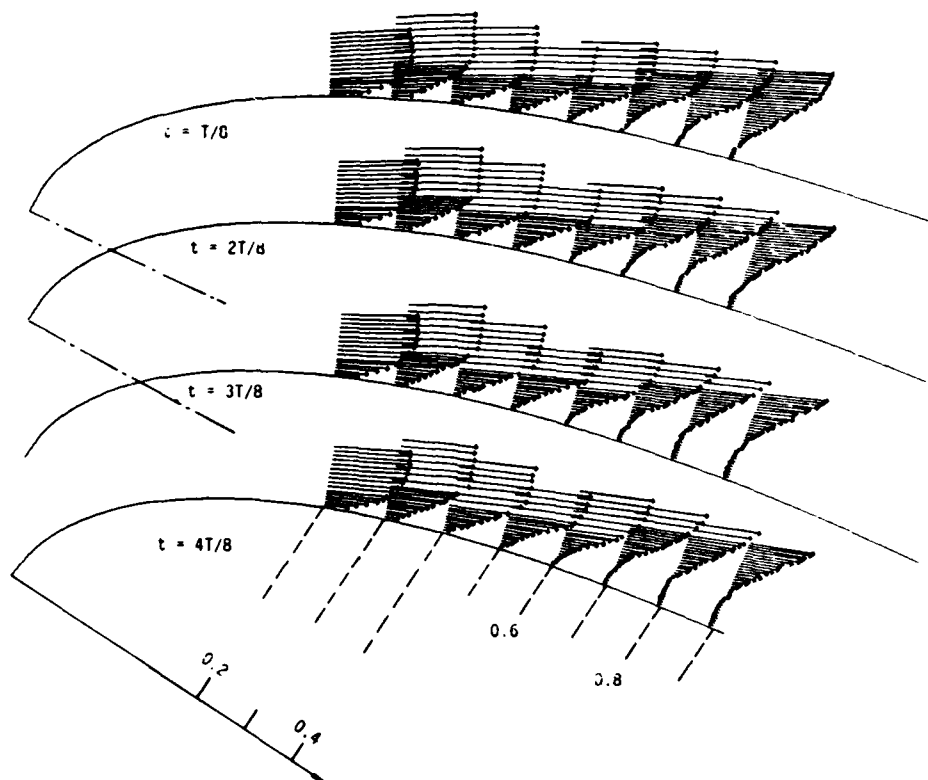
Fig. 2. Phase-averaged velocity vectors in the neighborhood of separation over an elliptical airfoil at an angle of attack. The 4 phases are apart by 1/8 of the period.

that connect the vortex patterns, the velocity field is not at all disturbed. This becomes even more obvious in the digitized information of Fig. 5 where the wavy pattern of the streamlines clearly indicates the presence of point singularities alone. This is evidence that the streak-lines do not contain vorticity anymore.

Since for high Reynolds numbers vorticity diffusion is negligible, the only mechanism possible for depleating the shear layers of their vorticity is stretching. In other words, the vortex sheets are taut and sucked in the core of the organized vortex. Some strong numerical evidence has been recently obtained in favor of this argument.[9]

3. Control of free shear layers

A lot has been written about the control of attached shear layers or layers in which a small separated region is embedded. Extensive work has also been reported on the control of free shear layes separating two uniform streams of different velocities. The reader could trace the most recent contributions in these areas by referring to the relevant contributions of other authors in the present volume. In all these cases a small external disturbance, in tune with a natural hydrodynamic frequency can drastically alter transition to turbulence or can strongly affect the turbulence characteristics. However, in such studies what is controlled is the microstructure of the shear layer, attached or separated.

There is another category of flow control which has not been considered yet in the study of wing aerodynamics. This is the control of large-scale roll up of free shear layers. Natural roll up of free shear layers occurs in many aerodynamic flows as for example in the development of tip vortices, or the unsteady stall vortex. Control of this type of roll up has actually been studied in other disciplines. Flow over single and multiple cylinders display a classical roll-up of shear layers into the well organized Karman vortex street. Studies in flow-induced vibrations have indicated that external disturbances can control the frequency of vortex shedding.

The present group has studied such problems in the past. In particular, the effect of pulsating flow on vortex shedding over bluff bodies has been studied. Of interest is our recent finding that the organization of the free shear layer is not suddenly locked on the driving frequency but rather is attracted to it smoothly. This is displayed in Fig. 6 where the shedding frequency is plotted against the driving frequency for the flow over a circular cylinder.

To control such free shear layers one may generate other shear layers and thus induce inter-action. Alternatively, pulsing the flow may break the roll-up process and generate sequences of such organized structures.
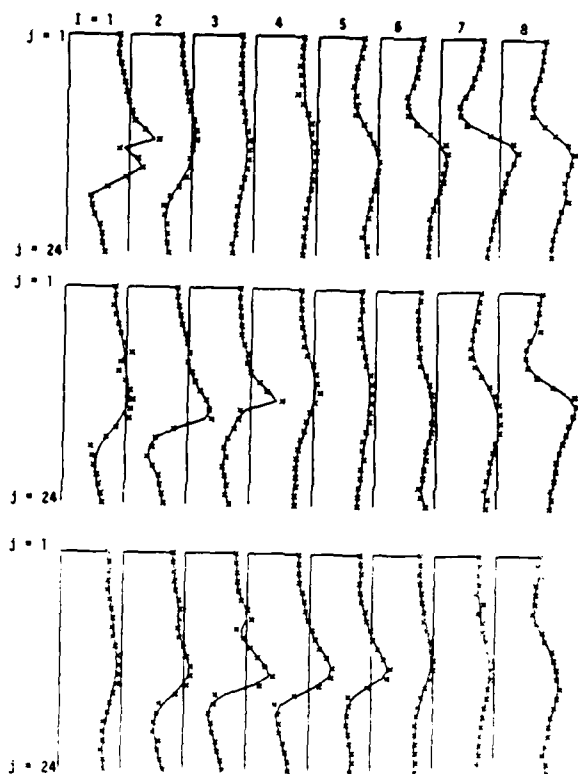
251

Fig. 3 Phase-averaged velocity profiles in the wake of a pitcing airfoil, at 3 instances spaced by 1/8 of the pitching period.
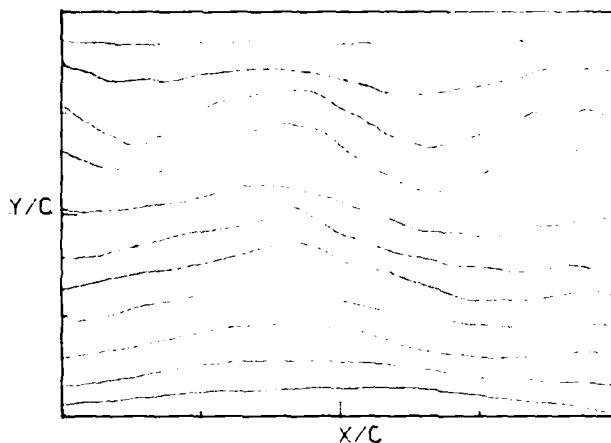

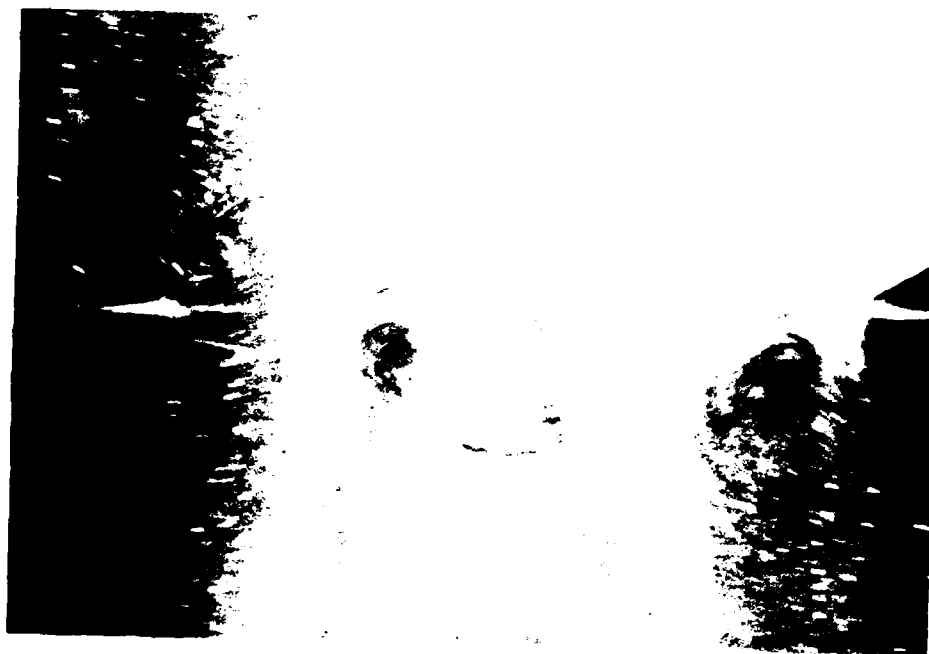Fig. 5 Streamlines obtained by digitizing the data of Fig. 4.

Fig. 4 Flow visualization of the wake of a pitching airfoil. Time film exposure of the paths of bright particles provides approximate information on the instantaneous velocity field. Dyes released at the nailing edge are also visible.
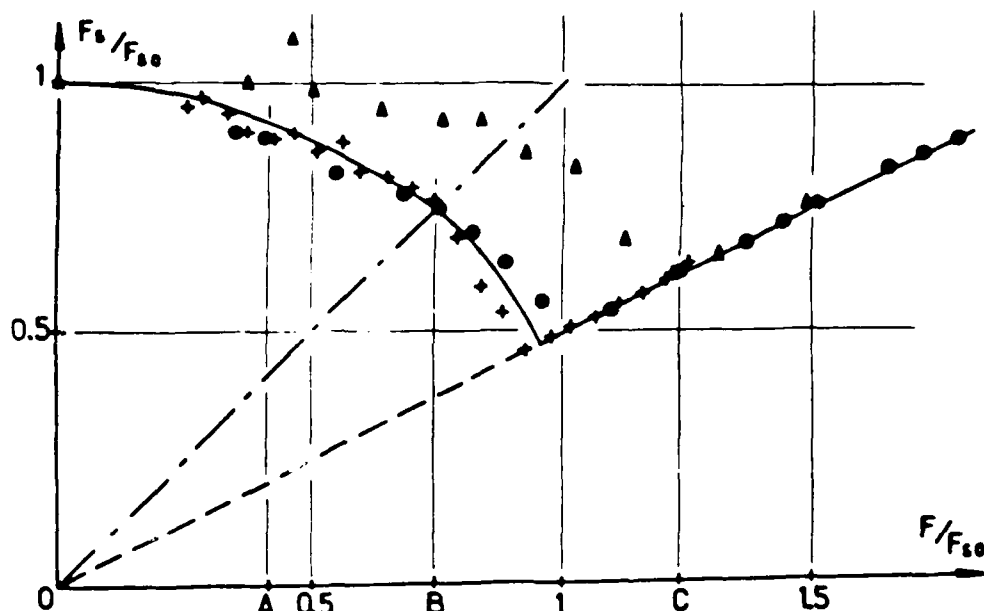
252

Fig. 6 The shedding frequency over a circular cylinder plotted against the driving disturbance frequency. Both are nondimensionalized in terms of the undisturbed shedding frequency.▲, Tanida et al.[11]; for amplitude ratio = 0.14.●,✦Present study for amplitude ratio, 0.30 and 0.40 respectively.

4. Conclusions

It has been demonstrated that free shear layers remain thin as they develop beyond separation. There is also some evidence that this is true even if the flow may break down into turbulence in the scale of the shear layer thickness. Moreover, it was demonstrated that vorticity stretches and tends to accumulate into point vortices.

These findings should have great implications for numerical calculations. Navier-Stokes solvers will encounter great difficulties in capturing very thin layers of very high velocity gradients, fluctuating around the solid body. Apparently numerical diffusion can quickly result in great artificial reductions of the net vorticity. This will require adaptive grids if the flow is to be represented correctly. It may appear that a discrete vortex method may be more reliable, since it preserves the net amount of vorticity contained in the field. This condition of course is only approximately true, but will perhaps give a more realistic representation of the flow.

References

1. Mathioulakis, D. S. and Telionis, D. P., "Velocity and Vorticity Distribution in Periodic Separating Flow," J. Fluid Mech., 184, 303-333, 1987.

2. Sychev, Vik. V., "Asymptotic Theory of Non-stationary Separation," Fluid Dynamics, 14, 829-838, 1979.

3. Smith, F. T., "The Laminar Separation of an Incompressible Fluid Streaming Past a Smooth Surface," Proc. Royal Soc. London, A.356, 433-463, 1977.

4. Smith, F. T., "Laminar Flow of an Incompressible Fluid Past a Bluff Body: The Separation, Reattachment, Eddy Properties and Drag," J. Fluid Mech., 92, 191-205, 1979.

5. Smith, F. T., "A Structure for Laminar Flow Past a Bluff Body at High Reynolds Number," J. Fluid Mech., 155, 175-191, 1985.

6. Mezaris, T. B., Barbi, C., Jones, G. S., and Telionis, D. P., "Separation and Wake of a Pulsating Laminar Flow," Trans. Roy. Soc., in press.

7. Mathioulakis, D. S., Kim, J., Mook, D. T., and Telionis, D. P., "The Near Wake of a Pitching Airfoil," AIAA Paper #85-162.

8. Poling, D. R., "Unsteady Airfoil Interference," VPI&SU Ph.D. Dissertation, August 1985.

9. Mook, D. T., private communication.

253

10. Barbi, C., Farier, D. P., Maresca, C. A., and Telionis, D. P., "Vortex Shedding Locking-on of a Circular Cylinder," J. Fluid Mech., 170, 527-544, 1986.

11. Tanida, Y., Okajima, A. and Watanabe, Y., "Stability of a Circular Cylinder Oscillating in Uniform Flow or in a Wake", J. Fluid Mech., 61, 769-784, 1973.

TOPOLOGICAL STRUCTURE OF

UNSTEADY THREE-DIMENSIONAL SEPARATED FLOWS

W. H. Hui
University of Waterloo
Waterloo, Ontario, Canada
N2L 3G1

Murray Tobak
NASA Ames Research Center
Moffett Field, California, 94035, U.S.A.

SUMMARY

A concise mathematical framework is constructed to study the topology of steady three-dimensional separated flows of an incompressible, or a compressible viscous fluid. Flow separation is defined by the existence of a stream surface which intersects with the body surface. It is shown that the line of separation is itself a skin-friction line. Flow separation is classified as being either regular or singular, depending respectively on whether the line of separation contains only a finite number of singular points or is a singular line of the skin-friction field. The special cases of two-dimensional and axisymmetric flow separation are shown to be of singular type.

In regular separation it is shown that a line of separation originates from a saddle point of separation of the skin-friction field and ends at nodal points of separation. It is also shown that a saddle point of the skin-friction field on the line of separation is simultaneously a half-nodal point of the flow field on the separation stream surface from which emanate all of the streamlines on the separation stream surface. Conversely, a nodal point of the skin-friction field on the line of separation is simultaneously a half-saddle point of the flow field on the separation stream surface.

Unsteady flow separation is defined relative to a coordinate system fixed to the body surface. It is shown that separation of an unsteady three-dimensional incompressible viscous flow at time t, when viewed from such a frame of reference, is topologically the same as that of the fictitious steady flow obtained by freezing the unsteady flow at the instant t.

As an application, the onset of separation for the impulsively started flow past a circular cylinder is studied. In particular, it is found that after a finite time following the start of the flow a separation stream surface begins to appear tangentially to the surface of the cylinder at the rear stagnation point. It rapidly moves into the flow field and becomes non-tangential to the body surface. In a second application, the migration of the separation point on a deforming cylinder in a uniform stream is considered qualitatively. It is found that expansion of the cylinder has the effect of hastening the separation time, whereas contraction tends to delay separation. These agree with the conclusions resulting from the numerical computation of Lin, et. al.

§ 1. INTRODUCTION

Three-dimensional separated flow represents a domain of fluid mechanics of great practical interest that is now just beyond the reach of definitive theoretical analysis or numerical computation. It has been a topic of intensive study over the past three decades. Reliable theoretical analysis and numerical computation and proper interpretation of experimental observations all depend crucially on a correct understanding of the behavior of flow separation.

Steady three-dimensional flow separation has been studied by Maskell (1955), Legendre (1956, 1965, 1972, 1977, 1982), Werlé (1962, 1979), Lighthill (1963), Wang (1972, 1974, 1976), Perry and Fairlie (1974), Hsieh and Wang (1976), Hunt et. al. (1978), Han & Patel (1979), Tobak & Peake (1979, 1980, 1982), Dallmann (1983), Hornung & Perry (1984), and Zhang (1985). Important advances in the understanding of the nature of three-dimensional flow separation have been made which are well summarized in a recent review paper by Chapman (1986). In particular, it is now established (Lighthill, 1963) that the line of separation is itself a skin-friction line onto which adjacent skin-friction lines converge asymptotically, and is not an envelope of skin-friction lines as posed by Maskell (1955). However, issues concerning the origin of three-dimensional flow separation, and especially the existence of Wang's "open" separation, have not been completely resolved.

Unsteady flow separation, on the other hand, is not well understood, particularly in three dimensions. The often-quoted MRS (Moore 1958, Rott 1956, Sears 1956) criterion seems supported by some numerical computations and the analytic solution of Williams and Johnson (1974) to the unsteady boundary layer equations, but is difficult to apply in practice as the movement of the separation point is not known a priori. Virtually all theoretical studies on unsteady flow separation (e.g., Cebeci, 1982) are based on the two-dimensional boundary-layer equations. These cease to be valid at the onset of separation, so that no conclusion about the subsequent behaviour of flow separation can be drawn from them.

It is clear that a correct theory of the onset of flow separation and of the subsequent separated flow must be based on the full Navier-Stokes equations and not the boundary-layer equations. In this respect, it is interesting to note that whilst the solutions to the boundary layer equations may possess singularities (e.g. the Goldstein singularity on the line

255

of separation), solutions of the Navier-Stokes equations are analytic everywhere. Therefore, it is not only more desirable but actually conceptually simpler to base our study of flow separation on the properties of solutions to the full Navier-Stokes equations rather than their boundary-layer approximation.

In this paper we shall restrict the scope of our investigation to the topological aspects of unsteady three-dimensional separated flows. In this regard, we observe that all results concerning the topology of steady three-dimensional separated flows that have been reported to date are obtainable solely on the basis of the following properties of the velocity field $\vec{V}$, namely

$$(i) \quad \vec{V} \text{ is analytic} \tag{1}$$

$$(ii) \quad \vec{V} = 0 \quad \text{on the body surface} \tag{2}$$

$$(iii) \quad \nabla \cdot \vec{V} = 0 \tag{3}$$

Equation (2) expresses the no-slip boundary condition of the viscous fluid at the wall, whereas equation (3) is the continuity equation of an incompressible flow. We further point out that a critical analysis (Hui & Tobak, 1987) reveals that only (3) on the body surface is needed for deriving all the topological properties. Consequently, the topological properties of steady compressible separated flows are identical to those of incompressible flows, as they have the same continuity equation on the body surface. On the other hand, as pointed out earlier, the analyticity condition (1) of $\vec{V}$ is a property of any solution to the Navier-Stokes equations; $\vec{V}$ would be singular (e.g. the Goldstein singularity at the line of separation) if the flow were governed by the boundary-layer equations. These properties (1) - (3) are shared, of course, by all solutions of the Navier-Stokes equations. On the other hand, separation properties that result from them are shared by classes of solutions.

It is the existence of properties that are shared by classes of solutions that suggests the adoption of a topological description of the flow, since topological properties also are shared by classes of solutions. By restricting our attention to topological properties only, we are able to avoid invoking the momentum equation which would be needed if we were to ask for the solution corresponding to specific boundary conditions. Nevertheless, the literature cited has shown that a fairly complete (albeit non-specific) topological description of separation in steady three-dimensional flow can be drawn based on Eqs (1) - (3) alone. In sections 2 and 3 we shall construct a mathematical framework for steady three-dimensional flow separation of compressible or incompressible fluid, ending up with a precise description of the class of flow separation we consider. The same framework will permit us, in section 4, to draw an analogous description of unsteady incompressible three-dimensional separated flow of the same class.

We note that the analysis given in this paper based on the postulates (1) - (3) is actually more generally applicable than to the Navier-Stokes equations alone. In particular, the analysis will be applicable to whatever modeled equations are used to represent steady or unsteady turbulent flow.

§ 2. CLASSIFICATION OF STEADY FLOW SEPARATION

Consider a steady flow of a compressible or incompressible viscous fluid over a body whose surface is B. Let $\xi\eta\varsigma$ be a local orthogonal curvilinear coordinate system such that $\varsigma = 0$ coincides with the body surface and the η-axis is along the line of separation (to be defined more precisely in § 2.2). Denote the corresponding unit vectors by $\hat{e}_1$, $\hat{e}_2$ and $\hat{e}_3$, and let $\vec{V} = u\hat{e}_1 + v\hat{e}_2 + w\hat{e}_3$.

2.1 Properties of a Vector Field

Let $\vec{U}(\xi,\eta,\varsigma)$ be a vector field in the three-dimensional space $\xi\eta\varsigma$, where $\vec{U}$ is analytic jointly in ξ, η and ς. A field line of $\vec{U}$ is a curve whose tangent is everywhere parallel to $\vec{U}$, whereas a field surface is one whose normal is everywhere perpendicular to $\vec{U}$. When the vector field is the flow velocity $\vec{V}$, its field lines are called streamlines and its field surfaces are called stream surfaces.

By the theorems of existence and uniqueness of solutions of ordinary differential equations, it is shown that: (a) the field lines and field surfaces are determined solely by the direction, and not the magnitude, of the vector field; (b) if two field lines intersect with or are tangent to each other the point of intersection or of tangency must be a singular point where $\vec{U} = 0$; (c) if two field surfaces intersect with each other, the line of intersection must be a field line; (d) if two field surfaces are tangent to each other, the line of tangency must be a singular field line.

By use of the continuity equation (3) on the body surface and Eqs (1) and (2) it is easily shown that the body surface B is a limiting stream surface of $\vec{V}$ as $\varsigma \rightarrow 0$. It can also be shown that limiting streamlines coincide with skin-friction lines, the latter being the field lines of $\vec{\epsilon} \equiv \left(\dfrac{\partial \vec{V}}{\partial \varsigma} \right)_{\varsigma=0}$.

2.2 Classification of Flow Separation

In what follows we shall define flow separation in a way that will exclude consideration of what Wang (1974) has called "open" separation. This is not to deny the existence of such a category of flow but simply to affirm that it escapes our classification. A flow is said to separate from the body surface B if there exists a stream surface S that intersects B on the line Γ and if streamlines on S in the vicinity of Γ all originate from Γ and are directed away from Γ. We call S a separation stream surface and Γ a line of separation; the latter will be taken to be the η-axis. Flow attachment differs from flow separation merely in having an opposite flow direction, but otherwise has identical topological properties. For simplicity we shall refer, wherever no confusion may arise, only to flow separation with the understanding that whatever we say can be made to apply to flow attachment as well by a suitable reversal of flow directions.

Within our classification, there exist two and only two types of flow separation of an incompressible or compressible viscous fluid:

(a) Regular separation, where the line of separation is itself a regular skin-friction line (containing, possibly, a finite number of singular points), from which the separation stream surface leaves the body surface at a non-zero angle.

(b) Singular separation, where the line of separation is a singular skin-friction line, from which the separation stream surface leaves the body surface either at a non-zero angle or tangentially along the line of separation.

Regular separation is the common type of flow separation in genuinely three-dimensional flow (Peake & Tobak, 1980) and will be studied in the next section. By contrast, two-dimensional and axisymmetric flow separation must be of singular type due to flow symmetry. If there exists a singular point of the skin-friction field from which a streamline leaves the body surface, symmetry requires that the singular point must lie on a singular line and the streamline must lie on a stream surface which leaves the body surface, rendering the separation singular.

§ 3. REGULAR SEPARATION

The mathematical properties of regular flow separation are as follows (Hui & Tobak, 1987).

(a) The line of separation Γ is itself a skin-friction line. Consequently, when it is chosen as the η-axis of a curvilinear orthogonal coordinates $\xi \eta \varsigma$ it is necessary (but not sufficient) that

$$\left(\frac{\partial u}{\partial \varsigma}\right)_{\xi=\varsigma=0} = 0 \qquad (4)$$

Also

$$\left(\frac{\partial^2 u}{\partial \xi \partial \varsigma}\right)_{\xi=\varsigma=0} < 0 \quad \text{for flow separation} \qquad (5a)$$

$$\left(\frac{\partial^2 u}{\partial \xi \partial \varsigma}\right)_{\xi=\varsigma=0} > 0 \quad \text{for flow attachment} \qquad (5b)$$

(b) The line of separation must originate from a saddle point of the skin-friction field. It must end at a nodal point of separation if it is a closed curve or at a pair of nodal points of separation if it is an open curve.

(c) A saddle point of the skin-friction field on the line of separation is simultaneously a half-nodal point of the flow field on the separation stream surface (cf. Fig. 1). A nodal point of separation of the skin-friction field on the line of separation is simultaneously a half-saddle point of the flow field on the separation stream surface (cf. Figs. 2a,b).

§ 4. UNSTEADY THREE-DIMENSIONAL FLOW SEPARATION

By unsteady flow separation we mean time-dependent flow separation relative to an observer on the body surface. An unsteady flow is said to separate from the body surface B at time t if there exists a stream surface S at t that intersects B on the line Γ and if the streamlines on S at time t in the vicinity of Γ all originate from Γ and are directed away from it. The stream surface S is called the instantaneous separation stream surface at the instant t, and Γ the instantaneous line of separation. Flow attachment at time t is defined analogously with flow directions reversed.

To describe unsteady flow separation relative to an observer on the body surface, it is imperative that we use a frame of reference that is fixed to the body surface. The body in question may be a rigid body performing a given motion, or it may be a deformable body.

Now for an unsteady **incompressible** flow viewed in a frame of reference fixed to the body surface, the continuity equation at any instant of time remains the same as that of steady flow, i.e.

$$\nabla \cdot \vec{V}(\vec{x};t) = 0 \qquad (6)$$

Furthermore,

$$\vec{V}(\vec{x};t) \quad \text{is analytic in the spatial variables } \vec{x} \qquad (7)$$

being a consequence of the Navier-Stokes equations. With our choice of the frame of reference, the boundary condition that there be no slip at the body surface remains

$$\vec{V}(\vec{x};t) = 0 \quad \text{on the body surface} \qquad (8)$$

even though the flow above the surface may be unsteady.

We note that the time variable t appears only as a parameter in Eqs. (6) - (8) which are otherwise identical to Eqs. (1) - (3). Of course, the time t appears as a genuine independent variable through the term $\frac{\partial \vec{V}}{\partial t}$ in the momentum equation. The time-history effects of the unsteady motion of the fluid are thus introduced only through the momentum equation, which now contains an inertia force term F_i arising from the motion, or deformation, of the body in addition to any external force. For instance,

$$\vec{F}_i = -\left[\frac{d\vec{V}_c}{dt} + 2\vec{\Omega}\times\vec{V} + \vec{\Omega}\times(\vec{\Omega}\times\vec{V}) + \frac{d\vec{\Omega}}{dt}\times\vec{x}\right] \qquad (9)$$

for a rigid body where $\vec{V}_c$ is the velocity of the center of mass of the body and $\vec{\Omega}$ is its angular velocity.

As we have noted in § 1, the momentum equation for steady flow, which would be needed to determine the separated flow field uniquely, could be by-passed if we asked only for a topological description of the flow near the body surface. Analogously, we can avoid invoking the unsteady momentum equation by again asking only for a topological description of unsteady flow separation, this time based on Eqs

257

(6) - (8) instead of Eqs. (1) - (3). By comparing the two sets of equations, we conclude that separation of an unsteady incompressible viscous flow at time t, when viewed from a frame of reference fixed to the body surface, is topologically the same as that of the fictitious steady flow obtained by freezing the unsteady flow at the instant t. In other words, the topological properties of unsteady flow separation at time t, as recorded by, say, a snapshot of the flow, are governed by the same rules that govern separation in steady flow. In this sense, all results in §§ 2 and 3 for steady separation apply to unsteady incompressible flow separation instantaneously.

We further remark that the MRS criterion of unsteady flow separation aims at answering the question of "massive" flow separation which is determined by the momentum equation with an inertia force term, whereas our theory based on equations (6) - (8) and ignoring the momentum equation describes only the local behavior of flow separation near the body surface. Of course, the behavior of flow separation as described in this paper must always be present locally in any "massively" separated flow field.

§ 5. APPLICATIONS

This section is devoted to a preliminary, qualitative discussion of some aspects of unsteady flow separation.

5.1 Onset of Separation for Impulsively Started Flow past a Circular Cylinder

As an example, consider the two-dimensional impulsive incompressible flow U_∞ past a stationary circular cylinder of radius a. For high Reynolds number flow, $R_e = \dfrac{U_\infty a}{\nu} \gg 1$, C.Y. Wang (1967) used the method of matched asymptotic expansions to obtain a uniformly valid solution to the third order in $\epsilon = 1/R_e$ that is valid for small time. His solution for the stream function near the body surface in polar coordinates (r,θ) simplifies to (Hui & Tobak, 1987)

$$\psi = 4\epsilon\sqrt{t}\sin\theta\,\eta^2 S \qquad (10)$$

where

$$S = \frac{1}{\sqrt{\pi}}\left[\left\{1+\sqrt{\epsilon T}\left(\frac{\sqrt{\pi}}{2}-\frac{4\eta}{3}\right)\right\}+2T\left(1+\frac{4}{3\pi}-\frac{2\eta}{3}\right)\cos\theta\right]$$

$$+0(\eta^2) \qquad (11)$$

where all the lengths are measured in units of a, velocity components in units of U_∞. Hence ψ is measured in units of $U_\infty a$ and we choose to measure time t in units of $\epsilon a/U_\infty$. The variable η is related to r by $\eta = (r-1)/(2\epsilon\sqrt{t})$ and $T = \epsilon t$.

From (11) we observe

(a) Only after a finite time can it happen that $S = 0$.

(b) The time T when the surface $S = 0$ intersects with the body surface $\eta = 0$ is given by

$$2 + \sqrt{\epsilon\pi T} + 4(1+\frac{4}{3\pi})T\cos\theta = 0 \qquad (12)$$

It is clear from (11) that the surface $S = 0$ will first intersect with the body surface at $\theta = \pi$, i.e. at the rear stagnation point.

(c) The separation time T_s, defined as the time when the surface $S = 0$ first intersects with the body surface, is given by

$$T_s = \left[\frac{\sqrt{32(1+\frac{4}{3\pi})+\epsilon\pi}+\sqrt{\epsilon\pi}}{8(1+\frac{4}{3\pi})}\right]^2 = 0.35 + 0(\sqrt{\epsilon}) \qquad (13)$$

We note that the separation time T_s calculated above as the time when the separation surface first appears is identical to Wang's estimate of the time when the surface shear stress first becomes zero.

(d) From (11) it can be shown that at the separation time T_s, whence $\theta = \pi$, the separation surface $S = 0$ leaves the body surface tangentially, i.e., initial separation is a tangent singular separation. However, at any later time $T > T_s$ it is a non-tangential singular separation. In Fig 3 are shown the stream surfaces, including $S = 0$, at three different times $T = 0$, $T = T_s$ and $T = 1 > T_s$, all cases for $R_e = 100$. It is seen that the surface $S = 0$ emerges from inside the cylinder; as soon as it moves into the flow field, the flow becomes separated.

5.2 Effects of Expansion of a Circular Cylinder on Flow Separation

An interesting numerical study has just been made by Lin, Mekala, Chapman and Tobak (1986) on the migration of the separation point on a deforming cylinder. The qualitative aspects of the effects of deformation of the cylinder on the onset of flow separation can now be discussed from a frame of reference fixed to the body surface. From this frame of reference the effect of acceleration and of deformation of the cylinder surface is equivalent to adding appropriate inertia forces.

To consider the effect of surface deformation alone on flow separation, let $a(t)$ be the radius of the cylinder and r the distance of a fluid particle from the surface of the cylinder (Fig. 4). Let $\hat{r}$ and $\hat{\theta}$ be unit vectors in the ratial and azimuthal directions respectively. The absolute acceleration of the fluid particle is

$$\vec{A} = \left[\left\{\ddot{r}-(a+r)\dot{\theta}^2\right\}\hat{r}+\left\{(a+r)\ddot{\theta}+2\dot{r}\dot{\theta}\right\}\hat{\theta}\right]+\left[\ddot{a}\hat{r}+2\dot{a}\dot{\theta}\hat{\theta}\right]$$

$$\equiv \vec{A}_0 + \vec{A}_D \qquad (14)$$

where $\vec{A}_0$, the quantity in large brackets, is the acceleration of the particle that would be present

alone if there were no deformation of the cylinder, and A_D is the additional acceleration arising from the deformation. Relative to the cylinder surface at time t the inertia force $\vec{F_i}$ of a particle of unit mass is thus

$$\vec{F_i} = -\vec{A_D} = -\ddot{a}\hat{r} - 2\dot{a}\dot{\theta}\hat{\theta} \qquad (15)$$

In the case of a flow U past a circular cylinder whose surface is expanding at constant rate (Fig. 4) $\dot{a} > 0$, $\ddot{a} = 0$, the inertia force acting on the particle is equal to $-2\dot{a}\dot{\theta}\hat{\theta}$. This force acts in the direction just opposite to the motion ($\dot{\theta} > 0$) of the particles near the body surface, and, like an adverse pressure, has the effect of hastening the separation time. In the case of constant-rate contraction of the body surface, the inertia force is $2|\dot{a}|\dot{\theta}\hat{\theta}$ which acts in the same direction of motion as the particles near the body surface, and therefore has the effect of delaying the separation time. These qualitative conclusions agree with those resulting from the numerical computation of Lin, et. al. for an impulsively starting flow past a cylinder deforming at constant rate.

§ 6. CONCLUDING REMARKS

(a) A concise mathematical framework has been constructed to study the topology of steady and unsteady three-dimensional separated flow of a viscous fluid.

(b) It is shown to be advantageous to define unsteady flow separation as time-dependent flow separation relative to the body surface.

(c) The topology of unsteady incompressible flow separation, as viewed from a frame of reference fixed to the body surface is shown to be identical to that of the fictitious steady flow obtained by freezing the unsteady flow at instant t.

(d) The effects of compressibility of fluid on the topological structure of unsteady separated flows remain to be investigated.

ACKNOWLEDGEMENTS

REFERENCES

Cebeci, T. (ed.), 1982. "Numerical and Physical Aspects of Aerodynamic Flows, Part 3, Singularities and Unsteady Boundary Layers." Springer-Verlag.

Chapman, G.T., 1986. "Topological Classification of Flow Separation on Three-Dimensional Bodies", AIAA Paper 86-0485.

Dallmann, U., 1983. "Topological Structures of Three-Dimensional Vortex Flow Separation," AIAA Paper 83-1935.

Han, T. and Patel, V.C., 1979. "Flow Separation on a Spheroid at Incidence," Journal of Fluid Mechanics, Vol. 92, pp. 643-657.

Hornung, H.G. and Perry, A.E., 1984. "Some Aspect of Three-Dimensional Separation. Part I: Streamsurface Bifurcations," Z. Flugwiss, Weltraumforsch, No. 8, pp. 77-87. Also Perry, A.E. and Hornung, H.G., "Part II: Vortex Skeletons," pp 155-160.

Hsieh, T. and Wang, K.C., 1976. "Concentrated Vortices on the Nose of an Inclined Body of Revolution," AIAA Journal, Vol. 14, No. 5, pp. 698-700.

Hui, W.H. and Tobak, Murray, 1987. "Topology of Unsteady Three-Dimensional Separated Flows", to be published.

Hunt, J.C.R., Abell, C.J., Peterka, J.A., and Woo, H., 1978. "Kinematical Studies of the Flows Around Free or Surface-Mounted Obstacles: Applying Topology to Flow Visualization," Journal of Fluid Mechanics, Vol. 86, pp. 643-657.

Legendre, R., 1956. "Séparation de l'Ecoulement Laminaire Tridimensionnel," La Recherche Aéronautique no. 54, pp. 3-8.

Legendre, R., 1965. "Lignes de Courant d'un Ecoulement Continu," Recherche Aérospatiale, Vol. 105, pp. 3-9.

Legendre, R., 1972. "La Condition de Joukowski en Ecoulement Tridimensionnel," Recherche Aérospatiale, Vol. 5, pp. 241-248.

Legendre, R., 1977. "Lignes de Courant d'un Ecoulement Permanent: Décollement et Séparation," Recherche Aérospatiale, Vol. 6, pp. 327-355.

Legendre, R., 1982. "Regular or Catastrophic Evolution of Steady Flows Depending on Parameters," Recherche Aérospatiale, Vol. 4, pp. 41-49.

Lighthill, M.J., 1963. "Attachment and Separation in Three-Dimensional Flow," Laminar Boundary Layers, edited by L. Rosenhead II, 2.6:72-82, Oxford University Press.

Lin, S.P., Mekala, D., Chapman, G.T., and Tobak, M., 1986. "Migration of the Separation Point on a Deforming Cylinder," AIAA J., Vol. 24, pp. 1783-1790.

Maskell, E.C., 1955. "Flow Separation in Three Dimensions," RAE Aero. Rept. 2565.

Moore, F.K., 1958. In "Boundary Layer Research," ed. Görtler, H. Springer, pp. 296-311.

Peake, D.J. and Tobak, M., 1980. "Three-Dimensional Interactions and Vortical Flows with Emphasis on High Speeds," AGARDograph No. 252.

Perry, A.E. and Fairlie, B.D.. 1974. "Critical Points in Flow Patterns," Advances in Geophysics. 18B:299-315, Academic Press, New York.

Rott, N., 1956. Q.J. Applied Maths, Vol. 13, pp. 444-451.

Sears, W.R., 1956. J. Aero. Sci., Vol. 23, pp. 490-499.

Tobak, M. and Peake, D.J., 1979. "Topology of Two-Dimensional and Three-Dimensional Separated Flows," AIAA Paper 79-1480.

Tobak, M. and Peake, D.J., 1982. "Topology of Three-Dimensional Separated Flows," Annual Review of Fluid Mechanics, Vol. 14, pp. 61-85.

Wang, C.Y., 1967. "The Flow past a Circular Cylinder Which is Started Impulsively from Rest," J. Maths and Phys., Vol. 46, pp. 195-202.

Wang, K.C., 1972. "Separation Patterns of Boundary Layer Over an Inclined Body," AIAA Journal, Vol. 10, No. 8. pp. 1044-1050.

Wang, K.C.. 1974. "Boundary Layer over a Blunt Body at High Incidence with an Open Type of Separation," Proceedings of the Royal Society of London. Series A, Vol. 340, pp. 33-35.

Wang, K.C., 1976. "Separation of Three-Dimensional Flow," Reviews in Viscous Flow, Proceedings of Lockheed-Georgia Co. Symposium LG 77ER0044, pp. 341-414.

Werlé. H.. 1962. "Separation on Axisymmetrical Bodies at Low Speeds." Recherche Aéronautique, no. 90, pp. 3-14.

Werlé. H., 1979. "Tourbillons de Corps Fuselés aux Incidences Elevées," L'Aero. L'Astro, no. 79.

William. J.C. and Johnson. W.D.. 1974. AIAA J. Vol. 12. pp. 1388-93.

Zhang, H.X., 1985. "The Separation Criteria and Flow Behavior for Three Dimensional Steady Separated Flow." Acta Aerodynamica Sinica, pp. 1-12.
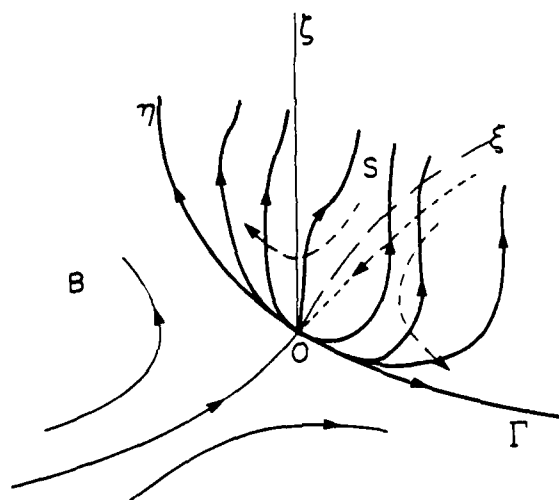
Fig 1. Flow near a saddle point of separation 0 of the skin-friction field on the line of separation Γ. With flow directions reversed this figure also represents the flow near a saddle point of attachment.
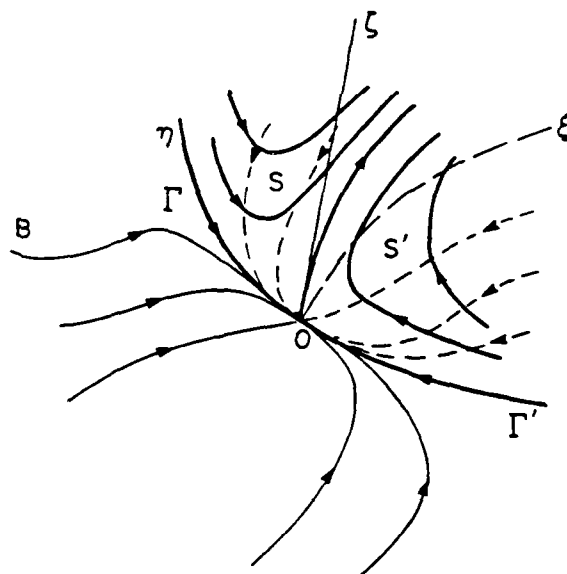
Fig 2a. Flow near a regular node of separation 0 of the skin-friction field on the lines of separation Γ and Γ'. With flow direction reversed this figure also represents the flow near a node of attachment.
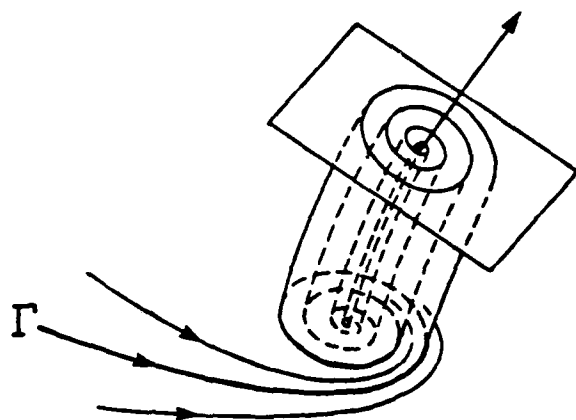
Fig 2b. Flow near a focus of separation of the skin-friction field.
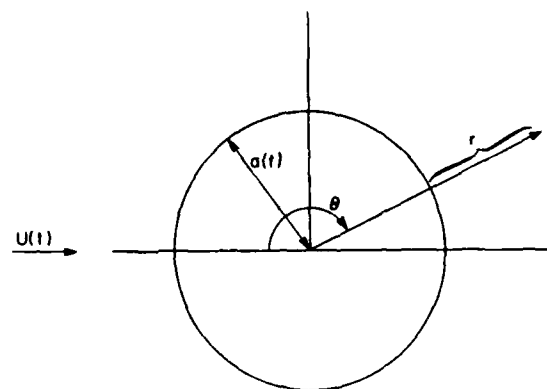
Fig 4. Uniform flow past a deforming circular cylinder showing notation.
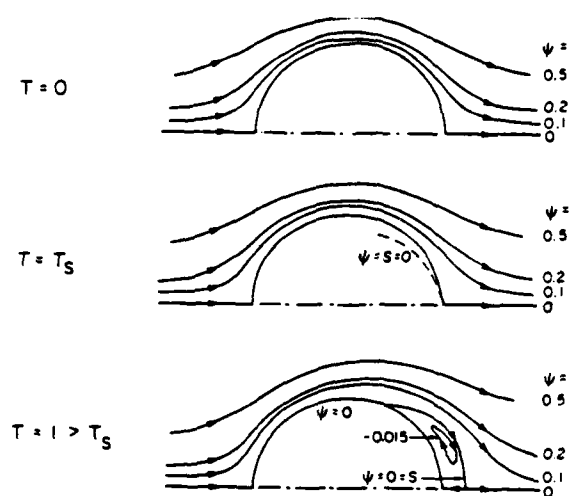
Fig 3. Impulsive flow past a stationary cylinder. $R_e = 100$.

HARMONIC ANALYSIS OF FORCE AND PRESSURE
DATA RESULTS FOR AN OSCILLATING STRAKED WING
AT HIGH ANGLES*

Atlee M. Cunningham, Jr.**
General Dynamics Fort Worth Division
and Ruud G. den Boer***
National Aerospace Laboratory (NLR)
Amsterdam, The Netherlands

ABSTRACT

A low speed wind tunnel test was performed during 1986 in a cooperative program between General Dynamics and the National Aerospace Laboratory (NLR) of The Netherlands. This test was funded by the Air Force Wright Aeronautical Laboratories. The test conditions were based on a matrix developed for mean angles ranging from $-10°$ to $54°$, amplitudes of pitch oscillation from $\pm2°$ to $\pm18°$ and frequencies from 0 Hz to 16 Hz. The model had a straked delta wing planform and was instrumented with an array of in situ pressure transducers and accelerometers as well as a six-component force balance. In addition to force and pressure measurements, vortex flow visualization data were recorded from smoke flow illuminated by a laser light sheet. All data were taken for both steady and unsteady flows. This paper presents data from the test that are ameanable to harmonic analysis which limits the amplitudes to about $\pm4°$ or $\pm6°$ but does not limit mean angles or frequencies. Those results are applicable to flutter and dynamic response problems as well as stability and control characteristics at high incidences. Force, pressure and flow visualization data are used to describe the perceived flow phenomena and how they interact with the model to produce the aerodynamic forces.

NOMENCLATURE

b	Local model span, m
c	Local model chord, m
C_r	Model root chord
C_m	Pitching moment coefficient
C_{m_α}	Slope of C_m w.r.t. α
C_n	Normal force coefficient
C_{n_α}	Slope of C_n w.r.t. α
C_p	Pressure coefficient

C_p'	Real (in phase) part of the unsteady pressure coefficient normalized by $\Delta\alpha$
C_p''	Imaginary (out of phase) part of the unsteady pressure coefficient normalized by $\Delta\alpha$
$C_{p_{harm}}$	1st harmonic unsteady pressure coefficient
f	Model oscillation frequency, Hz
Imag ( )	Out of phase component
k	Reduced frequency, $k = 2\pi f C_r/2U$
M	Free stream Mach number
Real ( )	In phase component
U	Free stream velocity
x,y,z	Cartesian coordinates
α	Angle of attack, deg
α_m	Mean angle of attack, deg
$\Delta\alpha$	Oscillatory amplitude, deg
ϕ	Phase angle, deg

INTRODUCTION

Recent interest in flying at very high angles of attack beyond the static stall conditions has been kindled by proposals to exploit this flow regime to improve fighter aircraft maneuverability [1,2]. Herbst's concept to fly into the post-stall regime to achieve quicker turns [1] and the use of unsteady aerodynamics at high incidence discussed by Lang and Francis [2] open a Pandora's box of new aerodynamic problems. Since these ideas require flying at incidences as high as $90°$ or beyond, a single maneuver could cover attached flows, vortex and burst vortex flows as well as to totally separated flows. In addition, the more highly separated flows are increasingly sensitive to unsteady and time history effects, hence maneuver dynamics become very important under such conditions. The understanding of these flow fields and dynamic effects is needed in order to design aircraft to exploit the concepts, however this represents several quantum jumps over current aerodynamic technology.

Aerodynamic loads experienced by flexible maneuvering aircraft may be classified into three distinct catagories: (1) Quasi-steady cruise and maneuvering loads due to rigid body aircraft motions with static aeroelastic effects; (2) Structural dynamic loads due to aircraft vibration as a result of gust response and flutter; and (3) Buffet loads due to separated flow fields. In terms of aircraft motions, the first category involves large aircraft attitude excursions, for example as in a pitch up maneuver starting at an incidence of 5° and ending at 35°. The development of these loads can become very non-linear, particularly where several flow regimes are traversed during a single continuous maneuver [3]. This development is also sensitive to the maneuver time history such as the starting and stopping points and angular rates. The second category of structural dynamic loads involves small surface motion, nominally less than 3° or 4° incidence change, and high frequencies typical of aircraft natural modes of vibration. These loads are usually linear because of small perturbations, however, the mean flow condition will directly control how the incremental loads develop for a given surface motion. As an example, aerodynamic loads due to a wing bending mode oscillating at a fixed amplitude are greatly reduced for completely separated flows as compared with attached flows. Finally, the third category of buffet loads does not require aircraft or surface motion to produce the loads, however, they are influenced by such motions as has been discussed by Cunningham [4].

In order to better understand the development of aerodynamic loads for fighter aircraft maneuvering beyond stall, a low speed (M ≈ 0.2) wind tunnel test was performed during August-September 1986 in a cooperative program between General Dynamics and the National Aerospace Laboratory (NLR) of The Netherlands [5]. This effort was funded by the Flight Dynamics Laboratory of the Air Force Wright Aeronautical Laboratories. The model was designed and built at NLR with funds provided by General Dynamics and NLR. The test conditions, described in more detail in Ref. 5, were based on a matrix of conditions for mean angles ranging from -10° to 54°, amplitudes of pitch oscillation from ±2° to ±18° and frequencies from 0 Hz to 16 Hz. The model, as shown in Fig. 1, had a straked delta planform and was instrumented with an array of in situ pressure transducers and accelerometers in addition to a six-component force balance. Force and pressure results were recorded in the form of time history and harmonic component data. Vortex flow-visualization data from smoke flow illuminated by a chopped laser light sheet were also recorded with a still photo camera and a video camera. With over 1200 test points and 3600 flow-visualization photos, the data base generated by this test is quite extensive.
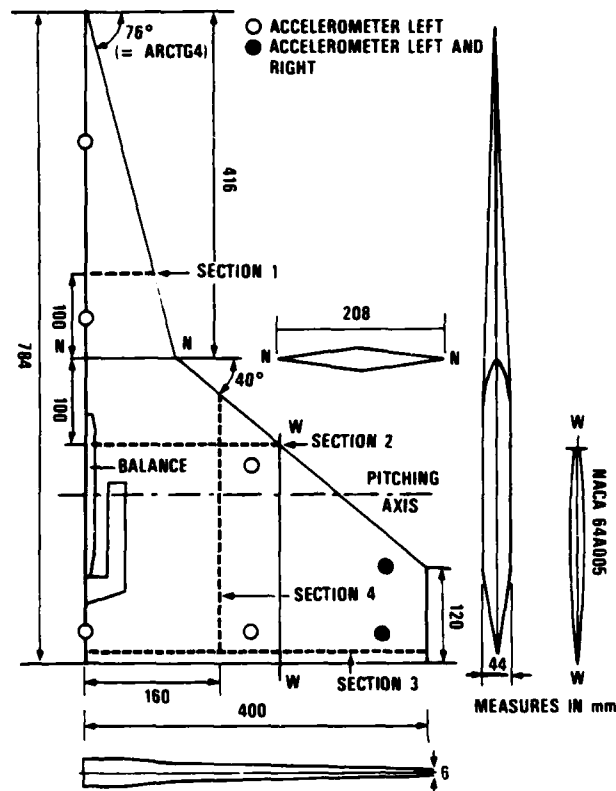
Fig. 1 Wing model and instrumentation.

The current paper will present some results and discussions for data from the above test that are ameanable to harmonic analysis. This limits the maximum amplitudes to about ±4° or ±6° but does not limit mean angle or frequency. These results pertain to the second category described above for structural dynamic loads and are thus applicable to flutter and dynamic response problems. The results are also meaningful for high incidence stability and control but are restricted to small excursions in aircraft attitude about the mean. The steady and unsteady characteristics will first be discussed to provide a general understanding of the flow fields and related forces and pressures. Next the first harmonic force data will be more fully analyzed to show the effects of mean angle, frequency and amplitude. A similar analysis will then be presented for the first harmonic pressure data. Finally, flow-visualization photos will be presented to illustrate the harmonic vortex motion during pitch oscillations and to provide further insight into the flow field characteristics.

STEADY AERODYNAMIC CHARACTERISTICS

The key to understanding the unsteady aerodynamics is to first understand the steady aerodynamics. The combination of force, pressure and flow-visualization data available from this test makes it possible to break down the angle of attack range of $-10°$ to $54°$ into definable flow regimes separated by smaller transition regimes.

The variations of steady normal force, C_n, and pitching moment, C_m, with angle of attack, α, are shown in Fig. 2. Important flow field characteristics and transitions are also denoted where the "sections" referred to in those notations are the pressure transducer rows shown in Fig. 1. Corresponding steady pressure data for all four sections are shown in Fig. 3 for $\alpha = 10°$, $19°$, $22.4°$, $36°$ and $42.3°$. The pressure data where chosen to highlight various flow regimes and transitions.

The "Linear" range of aerodynamic force development is clearly evident in Fig. 2 in both the C_n and C_m data from $-8°$ to $8°$. Beyond $8°$, the curves show an upward change in slope that is indicative of the development of vortex flows over both the wing and strake. This is illustrated by the pressure data in Fig. 3 at $\alpha = 10°$ for section 2. The small peak at $2y/b = 0.45$ is produced by the strake vortex and the stronger peak at $2y/b = 0.8$ by the wing vortex. The vortex structure is also illustrated by the accompanying sketch in Fig. 3.
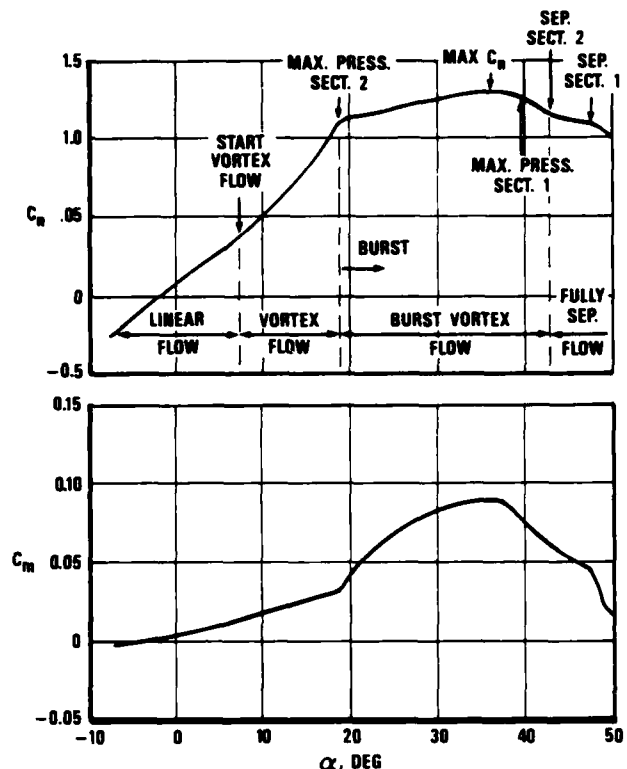
Fig. 2 Steady force data vs α.
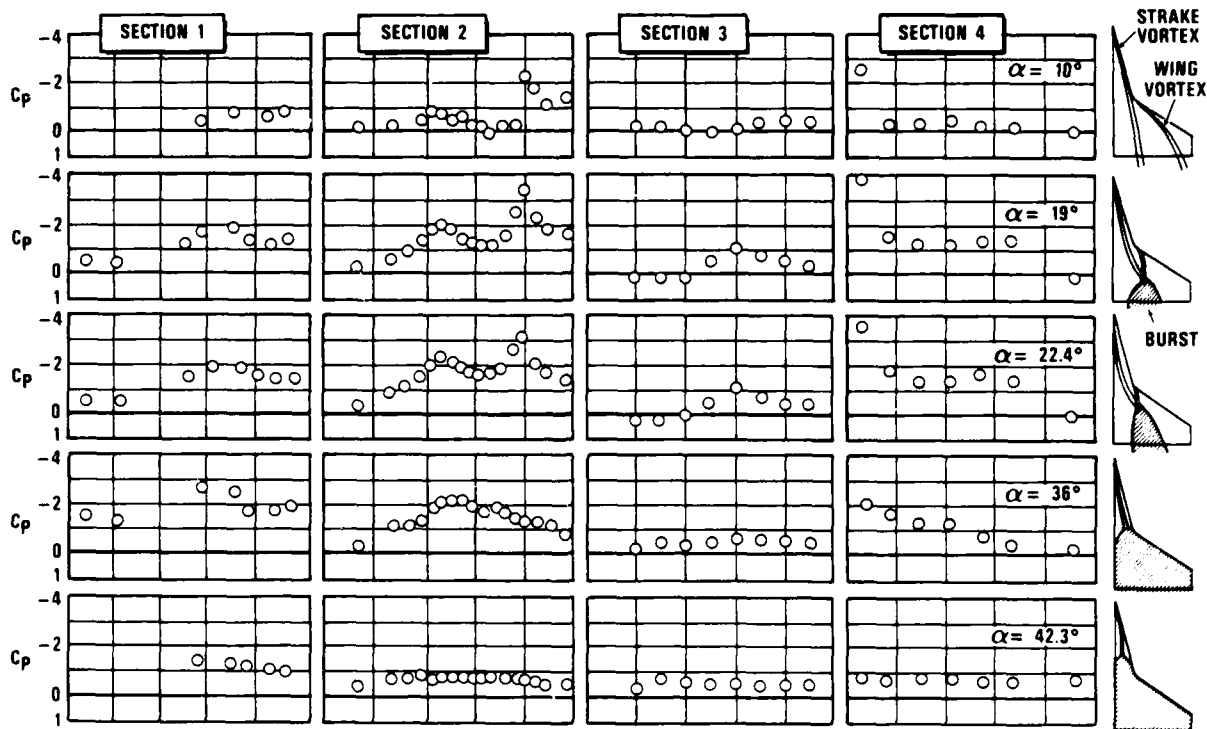
Fig. 3 Steady pressure variation with α.

The vortex flow range continues to develop until $\alpha \approx 18^\circ$-19° where a distinct break occurs in both the C_n and C_m data. This break signals the onset of vortex burst which represents the limit of vortex strength that can be maintained by the flow fields. The burst tends to occur simultaneously for the wing and strake vortices when the two merge as will be illustrated later with the flow-visualization results. The pressure data for $\alpha = 19^\circ$ in Fig. 3 show well developed vortices at both the forward sections (1 and 2) but a deterioration of pressure recovery on the outboard half of the trailing edge section (3). The burst vortex structure is also illustrated in the sketch for $\alpha = 19^\circ$ in Fig. 3.

For increasing α in the burst vortex regime, the strake vortex strength increases but the burst point continues to move forward. These opposing trends result in a much lower slope in the C_n curve as shown in Fig. 2, however, the slope is almost constant from $\alpha = 19^\circ$ to about 34°. The gain in lift forward due to strake vortex strength increase and the loss in lift aft due to vortex burst forward movement produces a pitch-up in the C_m curve as shown in Fig. 2. The pressure data in Fig. 3 for $\alpha = 19^\circ$, 22.4° and 36° show the deterioration of the wing vortex strength at section 2 and the continued increase of the strake vortex strength up to 36° at section 1. These characteristics are illustrated in the sketches for $\alpha = 19^\circ$, 22.4° and 36°.

Beyond the maximum value of C_n at $\alpha = 36^\circ$ the flow over the entire wing and strake rapidly collapses to completely separated or flat plate flow. Under these conditions for increasing α the normal force is falling off and the center of pressure is moving toward the geometric centroid of the planform as indicated by a rapid decrease in the C_m curve. The pressure data at $\alpha = 42.3^\circ$ in Fig. 3 show that the pressure distributions are nearly flat at about the same level for all sections except section 1 on the strake. At this angle, the strake vortex burst has progressed forward of section 1 as shown in the sketch for $\alpha = 42.3^\circ$.

Another view of how pressure data are related to force data can be obtained by considering only the suction peaks at pressure section 2 associated with the wing and strake vortices plotted vs α as shown Fig. 4. The wing vortex peak reaches its maximum strength at about $\alpha = 18^\circ$ at which point vortex bursting first appears over the wing as denoted in Fig. 2. The pitch-up in the C_m data corresponds to the loss in lift at the trailing edge as indicated by the rapid drop in the wing vortex suction peak. Note also that while the wing peak is falling in Fig. 4, the strake vortex suction peak is rising and continues to do so until about $\alpha = 32^\circ$. However,

slope of the strake vortex peak begins to diminish starting at $\alpha = 20^\circ$ which correlates with reduction of the C_m curve slope in Fig. 2 from $\alpha = 22^\circ$ to $\alpha = 36^\circ$ near the maximum value of C_n. The wing vortex suction peak shows a flat characteristic from about 31° to 36° which indicates that its burst passed the pressure section 2 at $\alpha = 31^\circ$. The rapid fall of the strake vortex suction peak starts at about 36° which corresponds to well known characteristics of delta wings where burst appears at the trailing edge of a 76° delta wing at about 35° to 38°.[6] Maximum C_n occurs at about 36° after which all flows begin to deteriorate rapidly to flat plate type flows. The strake vortex is still formed but burst is quickly moving forward as indicated by the strake vortex suction peak. Fully separated flow at the section 2 pressure row appears to be reached at about 42° to 44° where both suction peaks merge.
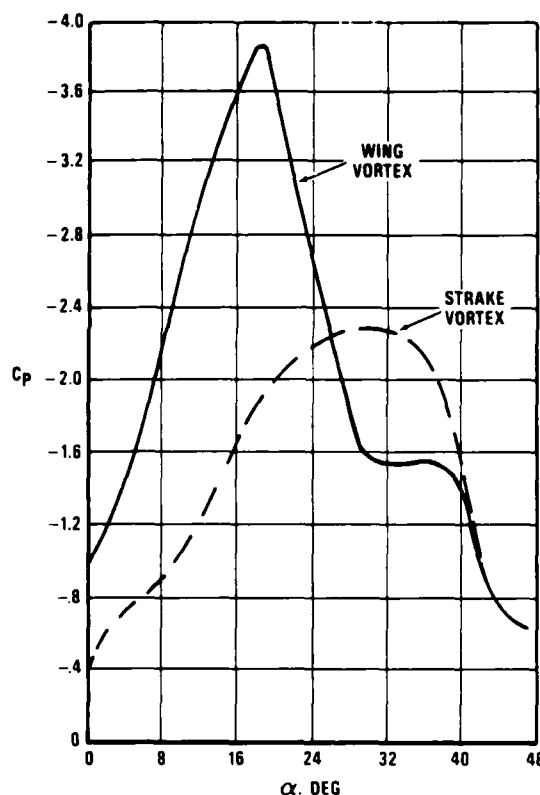

Fig. 4 Vortex suction peak as a function of angle of attack.

In addition to the force and pressure data discussed above, flow-visualization data provided valuable insight for interpreting the source of changes in the forces and pressures. This was evidenced by the sketches shown in Fig. 3. It was also possible, however, to identify the mechanism that caused the wing and strake vortex bursting. Fig. 5a shows sketches of how the strake vortex appeared at low angles

266

and at pre-burst conditions just before burst as viewed from the top. The occurrence of the "S" shaped strake vortex just before burst took place as a final step in a very rapid transition from the straight low angle path to the burst condition shown in Fig. 3 for $\alpha = 19°$. When viewed from the aft laser light sheet position (corresponding to pressure section 3, Fig. 1) in Fig. 5b, the same transition showed that the strake vortex was wrapping around the wing vortex and bursting as it was lifted away from the wing surface by the wing vortex. Thus vortex burst for this straked-wing configuration was attributed to the sudden combining of the wing and strake vortices to produce the unstable flow that immediately led to burst vortex flow.

UNSTEADY AERODYNAMIC CHARACTERISTICS

With a better understanding of the various flow regimes for steady flow, the unsteady characteristics will be more easily developed, especially for small amplitude oscillations. An example of some of the unsteady force data is shown in Fig. 6. These data are the harmonic components of C_{n_α} and C_{m_α} (slopes of C_n and C_m) measured at the model oscillation frequency. The real part is that component which is in phase with model motion, ie the value at model maximum angle. The imaginary part is that component which is out of phase with model motion, ie the value at the model mean angle of attack with positive pitch rate.

As shown in Fig. 6, the changes in slope closely track the steady data shown in Fig. 2 over most of the incidence range. This is understandable since the amplitude is only $\pm 3.5°$ and the frequency is fairly low at 3 Hz (k = 0.09). Dominance of the real part at angles up to vortex burst is also expected because the flow fields are well organized. Beyond vortex bursting, however, the imaginary part becomes increasingly important and actually crosses over at about $36°$ at the occurrence of the maximum value of C_n. Therefore, increase of the imaginary part relative to the real part simply reflects the increasing lag introduced by developing separated flow fields as the mean incidence is increased.

The first harmonic components as shown in Fig. 6 are not the only terms to be considered. Because the separated flows are highly non-linear, higher harmonic components are introduced at multiples of the first harmonic frequency. The higher harmonics become increasingly important as the amplitude is increased or as the flow becomes more dominated by separated flows. This effect is illustrated in Figs. 7 and 8 with power spectral density (PSD) plots

(a) TOP VIEW

(b) AFT LASER LIGHT SHEET POSITION
(LOOKING FORWARD)

Fig. 5 Sketches of vortex characteristics near burst observed in flow-visualization.
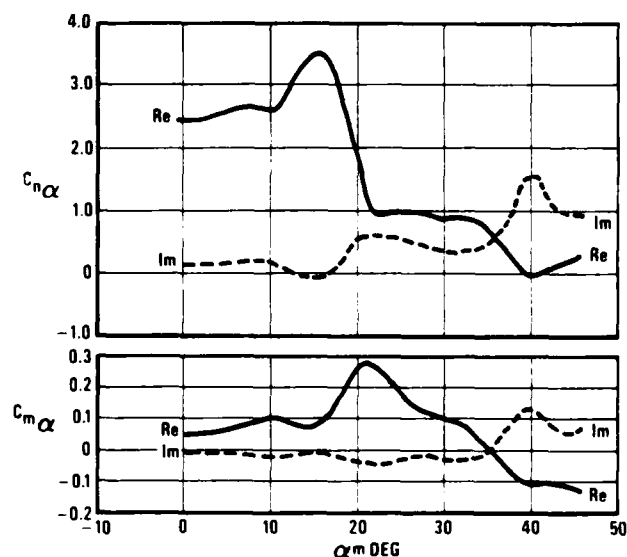
Fig. 6 Unsteady C_{n_α} and C_{m_α} vs α_m at M=0.22 for $\Delta\alpha=3.5°$, f=3Hz, k=0.09.

of pitching moment and normal force balance output for several conditions. Fig. 7 shows the influence of amplitude on pitching moment for a mean incidence of 22° and a frequency of 2 Hz. As can be seen, for an amplitude of $\pm 1.75^\circ$ the spectrum is clearly dominated by a peak at 2 Hz. (The peaks around 40 to 48 Hz are due to model motion on the balance and the 50 Hz peak is due to electrical noise.) Increasing the amplitude to $\pm 18^\circ$ still produces a dominant peak at 2 Hz but also at least four strong higher harmonics at 4, 6, 8 and 10 Hz.
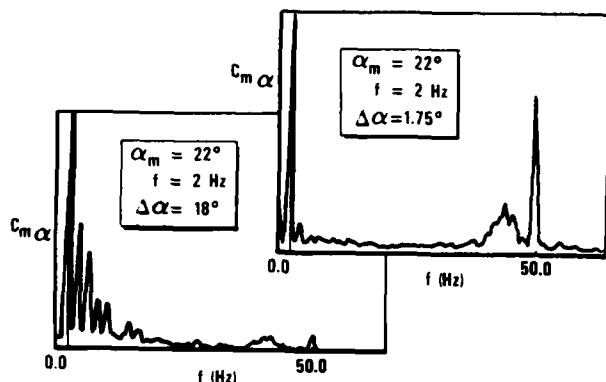
Fig. 7   Power spectral density plots for unsteady moment data to show influence of amplitude at a lower mean angle of 22°.
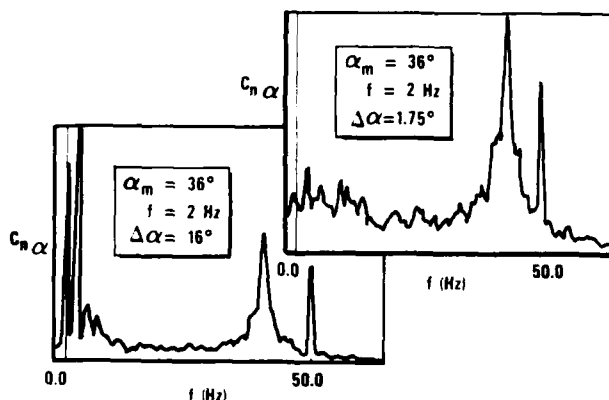
Fig. 8   Power spectral density plots for unsteady force data to show influence of amplitude at a higher mean angle of 36°.

The PSD's shown in Fig. 8 are for normal force output at a mean angle of 36°, the low amplitude motion of $\pm 1.75^\circ$ is almost lost in the natural mean flow turbulence. The symbols on the plot indicate higher harmonics, and as can be seen, they show little correlation with the spectral peaks. Increasing the amplitude to $\pm 16^\circ$ produces a strong peak

at 2 Hz, however, the second harmonic at 4 Hz is dominant. Smaller peaks also show up at 6 Hz and 8 Hz but are not significant. It is also interesting to compare the relative size of the model response peak at about 42 Hz with the fundamental peak at 2 Hz for the two amplitudes.

The PSD's discussed above may be used to point out the limitations of harmonic analysis for these highly non-linear flows. At $\alpha_m = 22^\circ$, as shown by extensive PSD analyses, the influence of amplitude at 2 Hz produces a second harmonic of about 12% of the first harmonic for $\Delta\alpha = \pm 3.5^\circ$, a third harmonic of about 15% for $\Delta\alpha = \pm 5.25^\circ$ and a third harmonic of about 30% for $\Delta\alpha = \pm 7^\circ$. Compared with The PSD's in Fig. 7, the limit of applicability of linear harmonic analysis would be an amplitude of about $\pm 3.5^\circ$ or possibly $\pm 5.25^\circ$. At $\alpha = 36^\circ$, an amplitude of $\pm 3.5^\circ$ at 2 Hz produces a second harmonic that is about 80% of the first harmonic. As shown in Fig. 8, the first harmonic for $\Delta\alpha = 1.75^\circ$ at 2 Hz is almost lost in the natural turbulence at this high angle. Thus, in order to obtain a meaningful signal at angles close to and beyond maximum C_n, a compromise is necessary on purity of the harmonic components. Using an amplitude of $\pm 3.5^\circ$ for the higher angles will be necessary because of signal to noise requirements, however, the presence of higher harmonics must be kept clearly in mind. For this amplitude, the higher harmonics are not a problem for mean angles of 34° or less. This discussion also has an impact on the higher mean angle data shown in Fig. 6.

FORCE DATA ANALYSIS

Although limitations have just been discussed on the validity of first harmonic components for describing the forces resulting from pitch oscillations, harmonic analysis of amplitudes of $\pm 4^\circ$ or less still makes sense. Since these are the types of forces that would be experienced for natural modes of vibration at their natural frequencies, such an analysis of the first harmonic is well justified. As shown in Fig. 6, the variation of C_{n_α} and C_{m_α} with mean angle is quite pronounced and would greatly impact any dynamic aeroelastic analysis.

Results are shown in Figs. 9 and 10 for the variation of C_{n_α} and C_{m_α} respectively with α_m and frequency. Included are the data shown in Fig. 6 for the lowest frequency of 3 Hz (k = 0.09). The real and imaginary parts are plotted separately so as to highlight the frequency effects. All data, with exception of those for 12 Hz, were obtained with an amplitude of $\pm 3.5^\circ$. The high frequency data at 12 Hz were obtained with a lower amplitude of 1.75° as required by the high frequency inertial load limits.
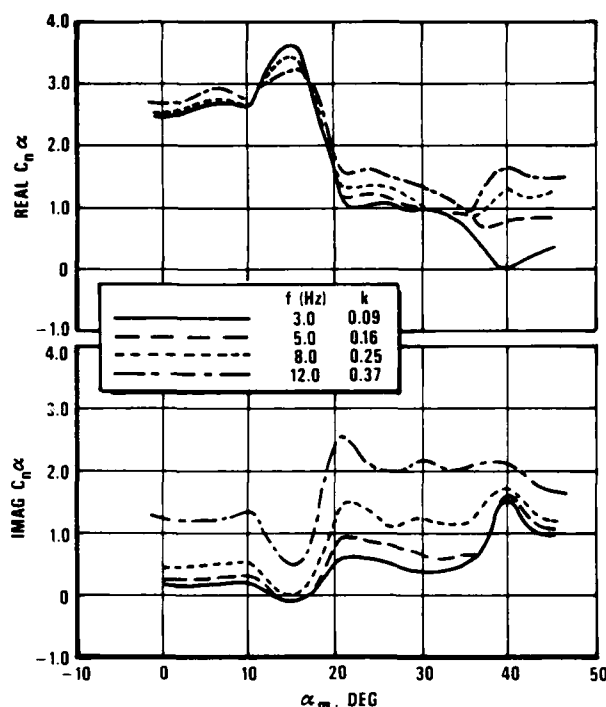
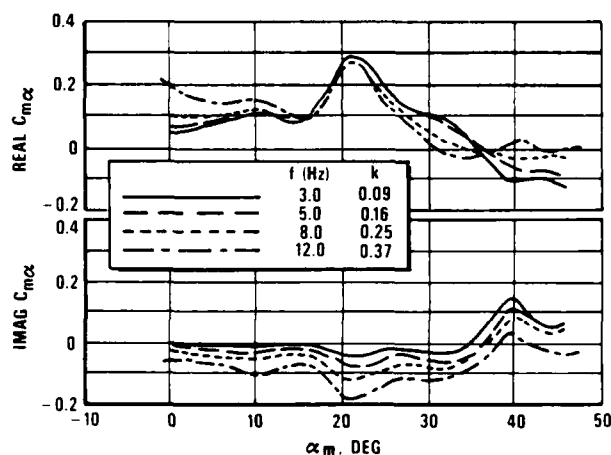Fig. 9 Influence of mean angle and frequency on unsteady C_{n_α} for M=0.22 and $\Delta\alpha$=1.75° to 3.5°.

Fig. 10 Influence of mean angle and frequency on unsteady C_{m_α} for M=0.22 and $\Delta\alpha$=1.75° to 3.5°.

response of separated flowfields. Beyond 36°, the trend reverses with a decreasing lag due to small changes in the imaginary part relative to the larger percentage changes in the real part.

In order to highlight the effect of frequency and α_m on lag, a plot of real part vs imaginary part for C_{n_α} is shown in Fig. 11. Increasing time is shown as a counter clockwise rotation of the C_n vector, thus increasing lag would result in a counter clockwise rotation of the vector whereas a decreasing lag would produce a clockwise rotation. For the α_m = 0°, the flow is attached and the vector rotation for increasing frequency is counter clockwise as would be expected. At the peak of vortex flow, α_m = 16°, the rotation is still counter clockwise. After vortex burst at α_m = 22°, the vector is significantly changed due to a large reduction in the real part, however, the rotation is again counter clockwise. Characteristics for angles greater than 22° do not essentially change until about maximum C_n, at α_m = 36°. After this point, a trend develops where the rotation becomes clockwise as shown for α_m = 40°. Thus, in fully separated flows the oscillatory forces show an opposite trend compared to lower angles by exhibiting a decreasing lag for increasing frequency. It must be kept in mind that significant higher harmonics are present at α_m = 40° and this trend may not tell the whole story; certainly, further analysis is needed on this phenomenon.
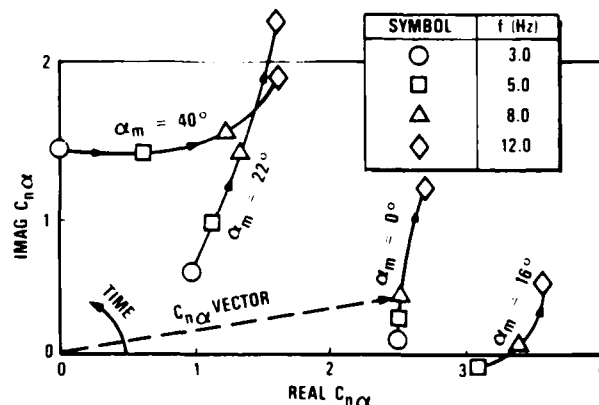
Fig. 11 Real vs imag part of C_{n_α} for various frequencies and mean angles.

The most striking feature of the C_{n_α} data is a tendency of the imaginary data to mirror image the real data. This effect is intensified with frequency, especially beyond vortex burst. The dip for vortex flow between 10° and 18° for the imaginary part indicates that the increased velocities associated with well developed vortex flows have a significant effect in reducing phase lag of the aerodynamic response to wing motion. An increase in imaginary part from 20° to 36° likewise indicates an increase in phase lag as a result of the slower

Similar to the C_{n_α} data, the C_{m_α} data shown in Fig. 10 exhibit identifiable trends in the same flow regimes, ie. attached, vortex, vortex burst and totally separated flows. For the C_{m_α} data, a plot of real part vs imaginary part in Fig. 12 reveals a decreasing lag with increasing frequency by virtue of all vectors rotating clockwise. This is due to an inherent tendency of a pitching mode to lead as a result of the vertical surface motion which produces the natural pitch damping. This damping is stabilizing if the

imaginary part of C_{m_α} is negative so that it opposes wing motion at maximum velocity. If the imaginary part of C_{m_α} is positive, it provides a kick to wing pitching at maximum velocity in the direction of the motion and hence drives the wing to increasing amplitudes of oscillation until it either structurally fails or reaches a limit amplitude. The regions of positive imaginary C_{m_α} in Fig. 10 are thus regions of unstable aerodynamic forces for pitch oscillations. As can be seen, the stability boundary varies with both frequency and mean angle, where higher frequencies tend to reduce the unstable region. It would appear that extrapolating from 12 Hz, a stable imaginary curve would be produced at about 16 Hz (or k = 0.5).
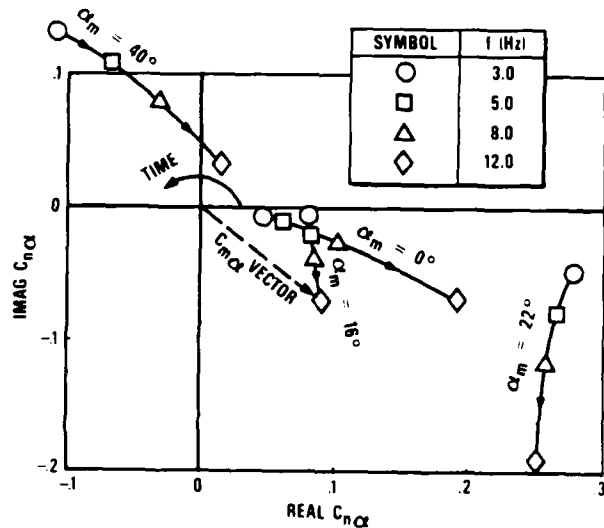
Fig. 12 Real vs imag part of C_{m_λ} for various frequencies and mean angles.

The influence of amplitude on the first harmonic of C_{n_α} is shown for several α_m values in Fig. 13 for 3 Hz (k = 0.09) and in Fig. 14 for 8 Hz (k = 0.25). These results indicate that amplitude has a fairly small impact on all components with exception of the imaginary part at α_m = 19° and 36° for both frequencies. This is not surprising since both angles represent major transition points, ie. α_m = 19° is vortex burst and α_m = 36° is maximum C_n. In both cases, an increase in amplitude increases the mixture of flow field extremes within a given cycle. More importantly, separation transition points are very sensitive to pitch rate such that a positive pitch rate tends to delay separation and a negative pitch rate tends to delay re-attachment. Since pitch rate leads wing pitch angle by 90°, the imaginary part is more affected by this phenomenon. Under these conditions, the higher harmonics are more significant which reflects the highly non-linear nature of these regions.
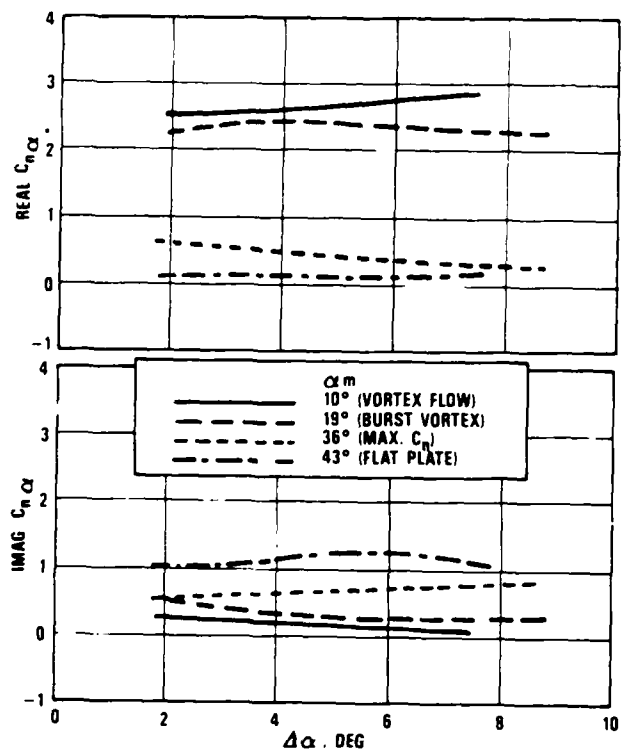
Fig. 13 Influence of oscillation amplitude on unsteady C_{n_λ} for M=0.22 and f=3Hz (k=0.09).
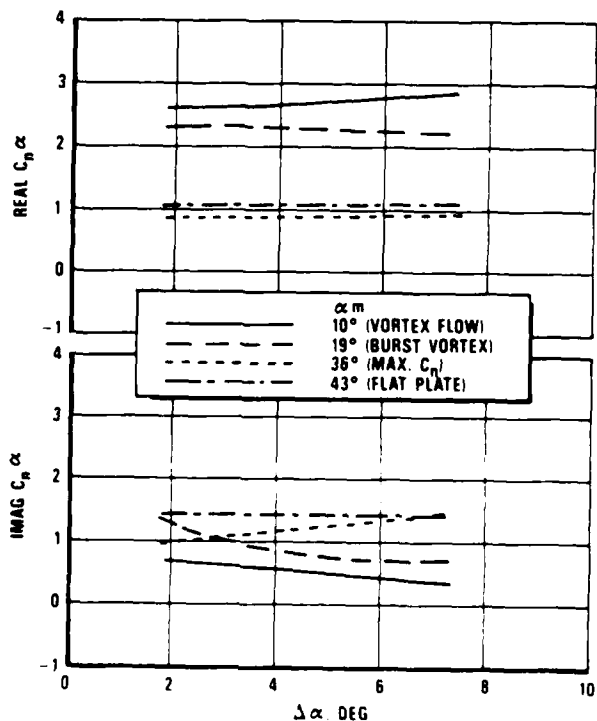
Fig. 14 Influence of oscillation amplitude on unsteady C_{n_λ} for M=0.22 and f=8Hz (k=0.25)

PRESSURE DATA ANALYSIS

Pressure data from the low speed test were also analyzed on a harmonic basis. The arguments set forth previously on the presence of higher harmonics in force data are also valid for pressure data. The pressures to be discussed in this paper were measured at the four sections as shown in Fig. 1 with in situ mounted pressure transducers which provided both steady and unsteady data. The format presents the steady mean distributions and the unsteady first harmonic distributions at the same locations. The unsteady data are shown in derivative form for real (in phase) and imaginary (out of phase) parts defined as

$$C_p' = \text{Real } (C_{pharm}/\Delta\alpha), \text{ per rad.}$$
$$C_p'' = \text{Imag } (C_{pharm}/\Delta\alpha), \text{ per rad.}$$

(Since the C_p' and C_p'' results are on a per radian basis, the amplitudes will be quite high.)

The influence of mean angle on the unsteady pressures is shown in Figs. 15-19 for $\alpha_m = 10°$, $19°$, $22.4°$, $36°$ and $42.3°$ for an amplitude of $\pm 3.5°$ and a frequency of 8 Hz (k = 0.25). The general trend shown by these results is an increasing lag with increasing angle in agreement with the force data. This is evidenced by the growing importance of the imaginary part, C_p'' with increasing α_m. The pressures at spanwise section 1 on the strake provide the clearest example of this effect since they are affected only by the strake vortex.

The pressures at spanwise section 2 are more complicated as they cover both the wing and strake vortices. At $\alpha_m = 10°$, the unsteady real pressures, C_p', reflect the same shape as the steady pressures while C_p'' values are almost zero. At $\alpha_m = 19°$ near vortex burst, the C_p' results are strong for the inboard part of the row associated with the strake vortex and C_p'' are almost zero. The outboard part is very weak for C_p' but C_p'' is about the same level, all indicating breakdown of the wing vortex. Well into burst at $\alpha_m = 22.4°$, the trend noted at $19°$ is further developed where the C_p' pressures associated with the wing vortex are showing a large negative lift and the C_p'' are quite significant. At maximum C_n, $\alpha_m = 36°$, both wing and strake vortices have burst at section 2 as indicated by the negative C_p' values and significant positive C_p'' values. Finally at $\alpha_m = 40°$, the imaginary part, C_p'', is dominant as expected for totally separated flows.

At the trailing edge, spanwise section 3 is even more complicated because of the dominance of trailing edge separation at all angles with exception of $\alpha_m = 10°$. The large amplitudes at $\alpha_m = 19°$ and $22.4°$ during vortex burst produce high local loadings but tend to integrate out to much smaller levels. Such loading could contribute significantly to the fatigue life of trailing edge control surfaces and actuators.

The chordwise row at section 4 shows a streamwise cut through the region of interaction between the wing and strake vortices. This flow field is also quite complicated particularly during vortex bursting at $\alpha_m = 19°$ and $22.4°$ as was discussed in reference to Fig. 5. The distortion of the strake vortex into an "S" shape and consequent bursting of the combined wing and strake vortices is highly non-linear. As a result, higher harmonics are expected to be very important for this flow regime. For the more fully separated flows at $\alpha_m = 36°$ and $42.4°$, the flows are highly turbulent but less complicated due to their non-transient nature. It is interesting to note that the distributions at $\alpha_m = 22.4°$ and $36°$ are almost mirror images of each other for the real parts.

The influence of frequency on the pressures at section 2 are shown in Fig. 20 for $\alpha_m = 22.4°$. The frequencies are 3 Hz, 5 Hz, 8 Hz and 12 Hz (k = 0.09, 0.16, 0.25 and 0.37) and seem to have little effect on the mean pressures or the real part, C_p'. The influence on the imaginary part, C_p'', however, is far more noticeable and tends to exhibit a nearly linear increase with frequency. This is in agreement with the force data results shown in Figs. 9 and 10 for the imaginary parts.

Summarizing the overall effects of pressures, it is now evident why the C_n curve slope changes occurred and how. At vortex burst, the increasing lift due to the strake vortex was partially negated by the loss due to the wing vortex as shown in Figs. 16 and 17. This was also pointed out in the discussions associated with Fig. 4. The maximum value of C_n was reached when the continued building of lift by the strake vortex could no longer overcome the loss due to the wing vortex break-down. Finally, for totally separated flow at $\alpha_m = 42.4°$, the dominance of imaginary pressures likewise produced a dominance of imaginary forces. This occurrence is a natural result of the influence of pitch rate which tends to delay separation for nose-up pitch rate and delay re-attachment for a nose-down pitch rate. Since max pitch rate occurs at the mean angle, the unsteady pressures tend to lag the instantaneous angle by $90°$ phase angle.

FLOW-VISUALIZATION DATA ANALYSIS

Flow-visualization data were recorded from smoke flow illuminated by a chopped laser light sheet with both a still photo camera and a video camera as
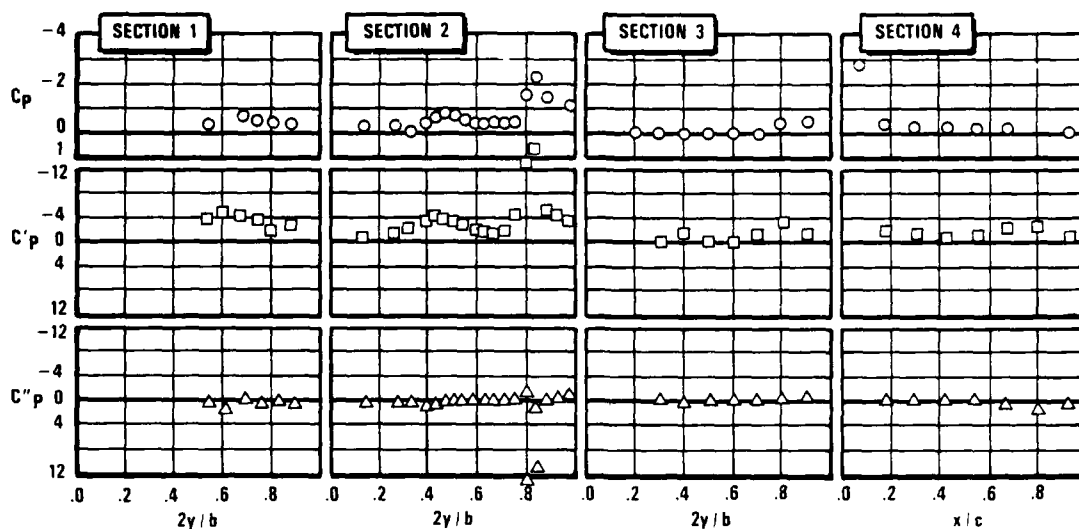
Fig. 15 Influence of mean angle on unsteady pressures at $\alpha_m=10.01°$ for M=0.22, $\Delta\alpha=3.64°$ and f=8Hz (k=0.25).
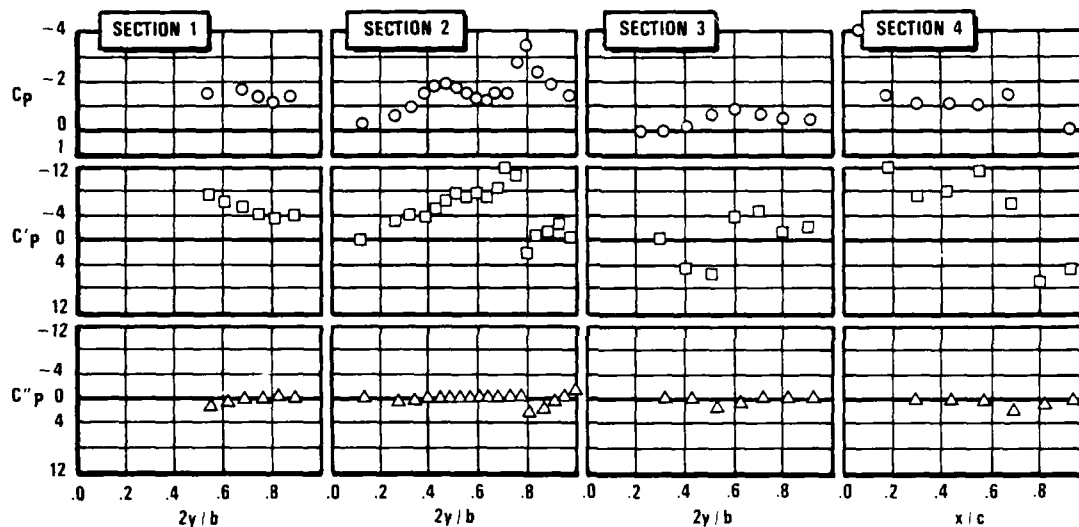

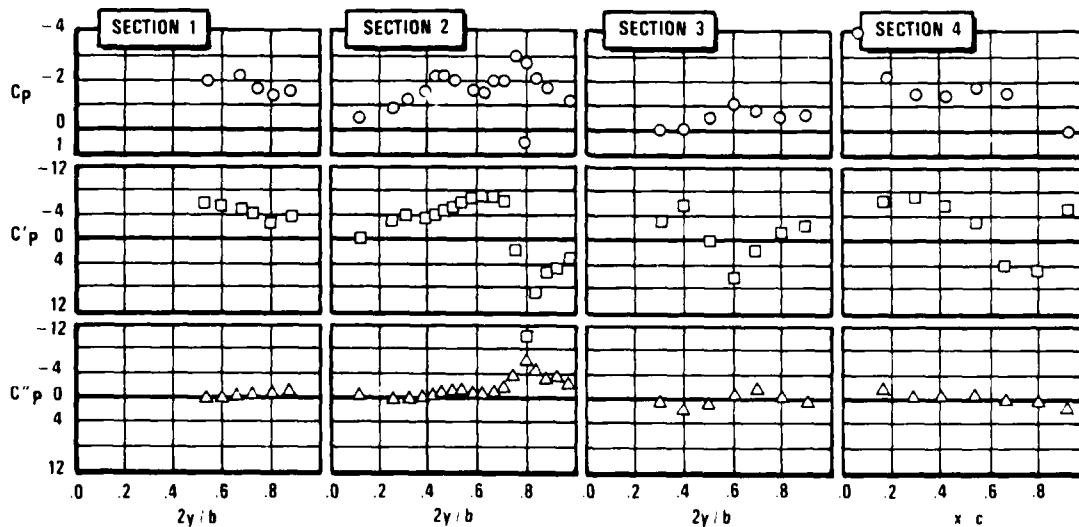Fig. 16 Influence of mean angle of unsteady pressures at $\alpha_m=18.96°$ for M=0.22, $\Delta\alpha=3.47°$ and f=8 Hz (k=0.25).

Fig. 17 Influence of mean angle on unsteady pressures at $\alpha_m=22.44°$ for M=0.22, $\Delta\alpha=3.45°$ and f=8.0 Hz (k=0.25).
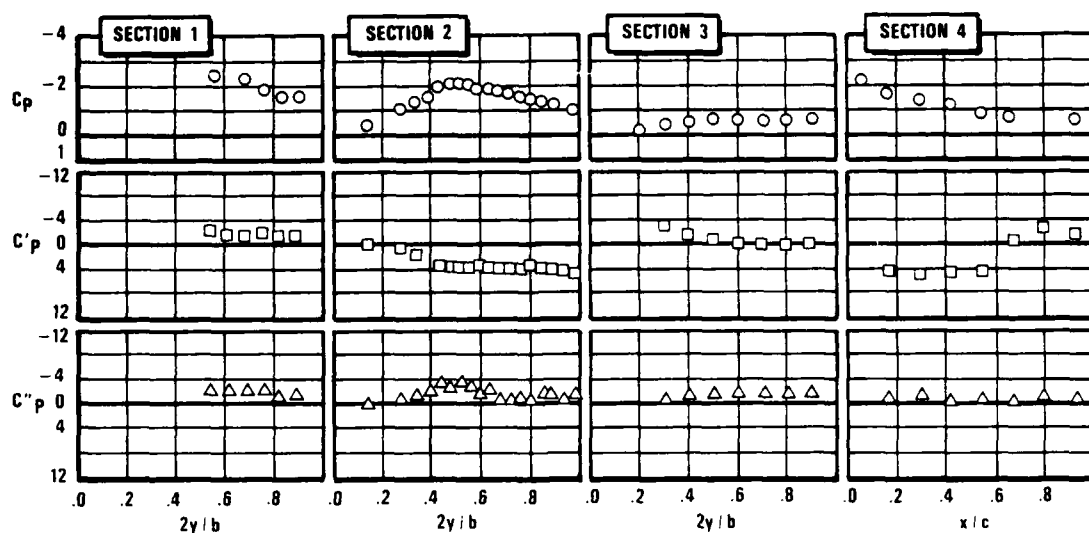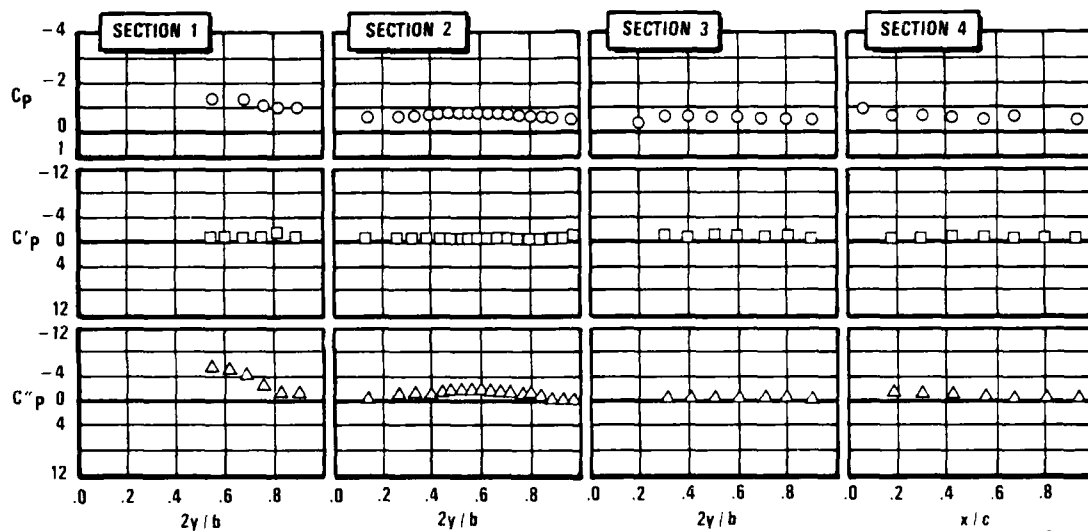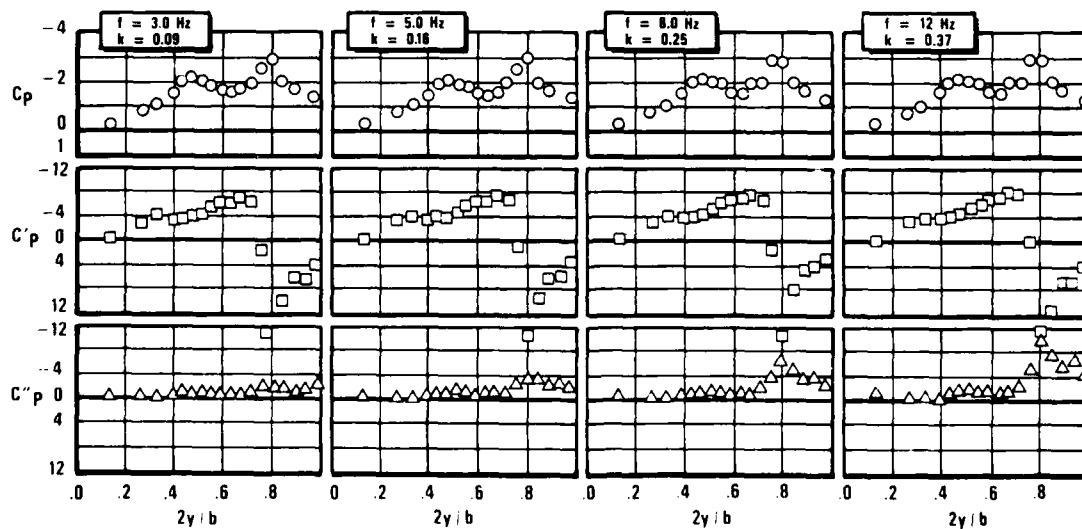
272

Fig. 18   Influence of mean angle on unsteady pressures at $\alpha_m=35.84^{\circ}$
for M=0.22, $\Delta\alpha=3.38^{\circ}$ and f=8 Hz (k=0.25).

Fig. 19   Influence of mean angle on unsteady pressures at $\alpha_m=42.29^{\circ}$
for M=0.22, $\Delta\alpha=3.54^{\circ}$ and f=8 Hz (k=0.25).

Fig. 20   Influence of frequency on the unsteady pressures at
Section 2 for $\alpha_m=22.4^{\circ}$, M=0.22 and $\Delta\alpha=1.75^{\circ}$ to 3.5°.

273

more fully described by den Boer and Cunningham[5]. The laser light pulse was controlled by a device that permitted a fixed phase angle to be maintained with respect to model oscillatory motion. By varying this phase angle it was possible to obtain a "continuous" illumination of a vortex flow field cross-section for a fixed model angle and pitch rate at different points during the cycle. The still photo camera lens was opened for a sufficient time to obtain adequate exposure, hence the photos represented multiple exposures obtained from several cycles. The video camera had sufficient sensitivity, however, to register each cycle as it was illuminated.

An example of a set of still photos taken at pressure section 2 is shown in Fig. 21. These data were taken for the condition $\alpha_m = 22.45°$, $\Delta\alpha = 3.79°$, 30m/sec, $f = 1.13$ Hz ($k = 0.09$). (The velocity was 80m/sec for force and pressure testing. Hence, the frequencies were adjusted to maintain the same values of k for all testing.) The photos show various phase angles during the cycle at 45° spacing. Hence the phase angles, ϕ, and corresponding instantaneous angles of attack, $\alpha(\phi)$, for Fig. 21 were:

ϕ	$\alpha(\phi) = 22.45°$ $+ 3.79°\sin\phi$
0°	22.45°
45°	25.13°
90°	26.24°
135°	25.13°
180°	22.45°
225°	19.77
270°	18.66
315°	19.77
360°	22.45°

At 0°, the model was at the mean position with positive pitch rate and at 180°, it was also at the mean position but with a negative pitch rate. A+ 90° and 270°, the model was at the maximum and minimum angles respectively.

These photos, taken with the laser sheet located perpendicular to the model $\alpha_m = 22.45°$ at pressure section 2 (65.88% of the root chord), show the positions of both wing and strake vortices on both sides of the model. The strake vortex pair is most noticeable as the larger white areas each with a small black center which is the vortex core. The wing vortex pair is more difficult to see in most photos but is quite clear at $\phi = 180°$. The bright line is the intersection of the laser sheet with model surface on the left side and thus provides a reference for the left vortices. The right side was shaded by the model center "bump", hence no "reference" line was available. The "bump" also cut off the bottom of the right vortices.
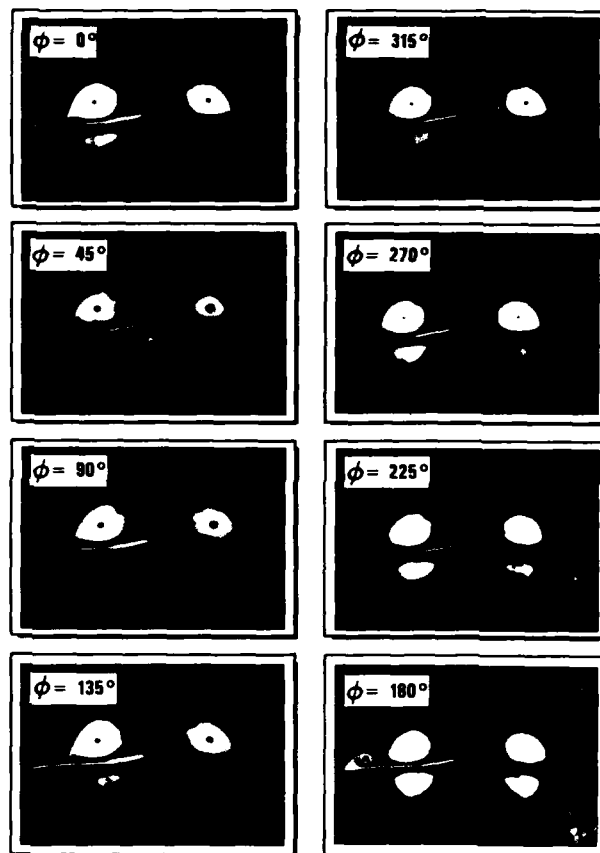

Fig. 21   Unsteady vortex flow visualization at Section 2 for $\alpha_m = 22.45°$.

It was possible to measure the vortex positions relative to the wing during the oscillation from these photos. Results obtained from measuring Fig. 21 are shown in Fig. 22 for all four vortices. The spanwise location is shown as a local semi-span fraction and the vertical position is also shown normalized by the local semi-span. The mean vortex core locations on the right side agree very well with the steady mean pressure peak positions shown in Fig. 20 for $k = 0.09$. The locations are 0.46 and 0.80 for the strake and wing vortices respectively in both Figs. 20 and 22.

Also shown in Fig. 22 are the directions of core motions as denoted by both the arrows and phase angle. The right vortices show a counter clockwise rotation and the left show the expected clockwise motion for the strake vortex but counter clockwise for the wing vortex. The principle motion for all vortices, however, is vertical.

Two very important conclusions can be drawn from these results. First, it is clear from Fig. 21 that neither the wing or strake vortices burst during the oscillation at $\alpha_m = 22.45°$. Thus, the loss in lift shown by the wing vortex in Figs. 17 and 20 is not due to bursting at

pressure section 2. Second, it appears that the loss in lift from the wing vortex is instead due to the motion of that vortex away from the wing. Since the suction force produced by a vortex is inversely proportional to the square of the distance perpendicular to the vortex core, a greater separation between the wing and vortex will result in lower surface suction on the wing. As shown in Fig. 22, the wing vortex vertical position varies from 0.12 to 0.17, which, for a constant vortex strength, produces a relative variation of surface suction from 1.0 at the minimum position (ϕ = 270°) to about 0.5 at the maximum position (ϕ = 90°). This extreme is not shown by the strake vortex whose vertical position varies only from 0.22 to 0.25 during the cycle.
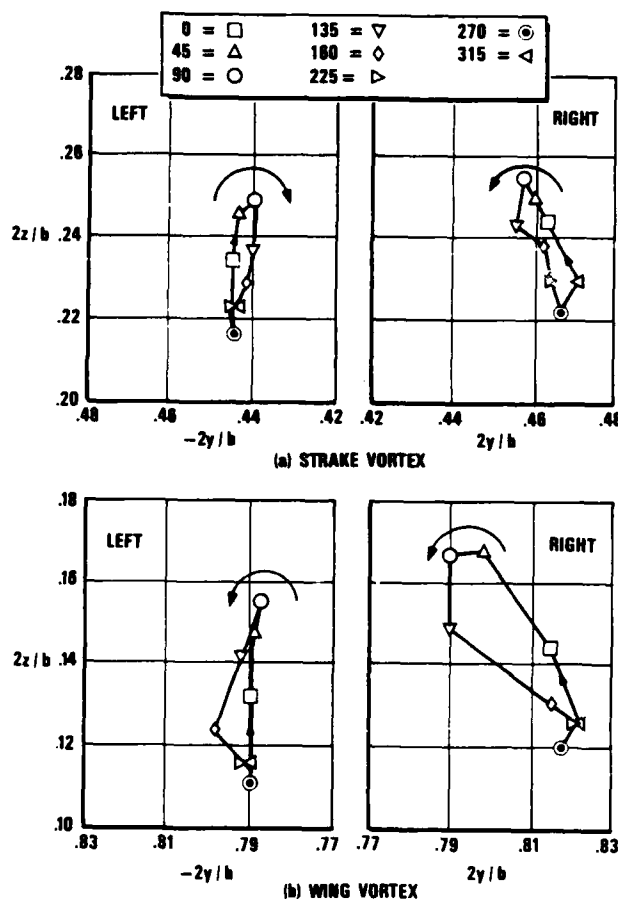
Fig. 22 Unsteady vortex positions at Section 2 for α_m=22.45° , $\Delta\alpha$=3.79° and f=1.18 Hz (k=0.09) (measured from Fig. 21).

Flow visualization data similar to those shown in Figs. 21 and 22 are available from this test for other mean angles, amplitudes and frequencies. As demonstrated by the above analysis, these data provide valuable insight when combined with both pressure and force data, to the phenomena involved in the flow fields and how they react with the model to produce the aerodynamic forces.

CONCLUSIONS

A discussion has been presented on the steady and unsteady aerodynamic forces that are developed on a straked wing model oscillating in pitch. The mean angle of attack ranged from -10° to 50° with amplitudes up to ±18° and frequencies up to 12 Hz. The data analyzed included forces, pressures and flow-visualization results for the steady mean values and the first harmonic unsteady values.

The important flow regimes were identified as linear, vortex, burst vortex and totally separated flows. The unsteady harmonic normal force data tracked the steady force data for the real (in phase) part and the imaginary part exhibited an increasing lag tendency at higher angles and frequencies. The unsteady harmonic pitching moment data also showed similar characteristics with an unstable region defined above maximum C_n that diminished with increasing frequencies.

The influence of mean angle on unsteady data was found to be very significant. Besides influencing the phase angle (or lag), amplitude changes ranged up to about a 60% reduction in $C_{n\alpha}$ when compared with values at the low angle attached flow data. Thus, aeroelastic analyses concerned with flutter and dynamic response would be greatly impacted when considering the high angle separated flow regimes.

Harmonic analysis of the pressure data was used to improve the understanding of how the trends in force data occurred. It was possible to separate the impact of wing vortex bursting and strake vortex bursting on developing normal force with increasing angle up to and beyond the maximum value of C_n. Beyond this point, the almost purely imaginary values of C_n were shown to be a result of the dominance of imaginary pressures and very small real pressure levels. This dominance was due to the tendency of fully separated flows to be more sensitive to pitch rate rather than incidence change.

Flow visualization data analysis provided further information on the flow structure during vortex bursting at α_m = 22.45°. It was shown that pressure changes produced at section 2 were not a result of wing vortex bursting at that point but were probably due to vortex vertical displacement caused by downstream bursting.

Finally, it must be concluded that this paper has demonstrated the value of combining force, pressure and flow visualization results as an approach to understanding the highly complicated flow fields incurred during this test.

REFERENCES

1. Herbst, W. B.: "Dynamics of Air Combat", Journal of Aircraft, Vol. 20, July 1983, pp. 594-598.

2. Lang, J. and Francis, M. S.: "Unsteady Aerodynamics and Dynamic Aircraft Maneuverability", Paper No. 29, presented at the AGARD Symposium on Unsteady Aerodynamics - Fundamentals and Applications to Aircraft Dynamics, Gottingen, Germany, May 6-9, 1985.

3. Cunningham, A. M., Jr., "Vortex Flow Hysteresis", Paper No. 11, NASA CP 2416, Vol. I, 1986.

4. Cunningham, A. M., Jr. and Benepe, D. B., Sr.: "Prediction of Transonic Aircraft Buffet Response", Paper No. 3, AGARD-CP-226, 1977.

5. Den Boer, R.G. and Cunningham, A. M., Jr.: "A Wind Tunnel Investigation at Low Speed of the Flow About a Straked Delta Wing Oscillating in Pitch", AIAA Paper No. 87-2493, presented at the AIAA Atmospheric Flight Mechanics Conference, Monterrey, CA., August 17-19, 1987.

6. Malcolm, G. N.: "Impact of High-Alpha Aerodynamics on Dynamic Stability Parameters of Aircraft and Missiles", Paper No. 2, AGARD-LS-114, 1981.

VORTEX DYNAMICS FOR TRANSIENT FLIGHT CONDITIONS

G. A. Reynolds* and A. A. Abtahi**
Lockheed-Georgia Company

Abstract

The unsteady response of leading-edge vortex flows over a delta wing is described for high angle-of-attack conditions. This description focuses on the response of vortex development and breakdown due to large-amplitude transient pitching motions of a sharp-edged delta wing. Flow visualizations of this unsteady process were obtained in a low-speed water-channel facility. These visualizations were used to establish response time scales and to describe the underlying physical mechanisms. The test results show that at high angles of attack the flow-field response is an order-of-magnitude slower than the low angle-of-attack response. This behavior at high alpha is described in terms of both the vortex development and the propagation of breakdown waves in the vortex core. Several important advantages are cited for carrying out such unsteady testing at low speed in water.

Nomenclature

C – Root chord length, meters
K – Dimensionless pitch rate, $\dot{\alpha}\tau/2$
M – Mach Number
R_c– Reynolds number based on the root chord
T – Dimensionless time t/τ
U_∞ – Freestream velocity, meters/second
α – Angle of attack, degrees
$\dot{\alpha}$ – Pitch rate, rad/sec
Λ – Wing sweep, degrees
τ – Convective time scale C/U_∞, seconds

Introduction

The high angle-of-attack maneuverability of fighter aircraft is limited by the interaction and breakdown of forebody and leading-edge vortex flows. To overcome this limitation, the ability to predict and control the behavior of these separated vortical flows must be developed. This objective is complicated by the highly transient nature of high-alpha maneuvers. Under these maneuvering conditions, time-dependent effects are expected to become more significant. The results presented in this paper describe the nature of some of these time-dependent effects in terms of the leading-edge vortex development and breakdown dynamics.

The experimental results presented in this paper correspond to unsteady pitching motions of a simple delta wing. Previous investigators described various aspects of the associated leading-edge vortex flows and their response to unsteady pitching motions. Woodgate[1] considered harmonic pitching motions of one-degree amplitude, with the objective of defining the influence of vortex breakdown on the pitching moment derivatives. For this type of motion it was found that the mean position of vortex breakdown was the same as for steady conditions. The amplitude and phase of the breakdown motion, however, varied with the frequency of oscillation and mean angle of attack. Due to this dependency, Woodgate[1] found that the occurrence of breakdown significantly influenced the pitching moment derivatives. At high angles of attack, the unsteady aerodynamics are therefore strongly influenced by the response of the vortex breakdown process.

The response of these leading-edge vortex flows to large amplitude motions is of interest in the context of high angle-of-attack maneuverability. For relatively low angles of attack, without breakdown, Lambourne et al.[2] considered the leading-edge vortex development during large-amplitude constant rate plunging motions. Based on the visualizations of the time-dependent vortex core position, Lambourne concluded that the vortex development is completed in the time it takes the freestream to convect the distance of one model chord. Hence, the vortex development was considered to be a convective process.

At high angles-of-attack, the dynamics of leading-edge vortex breakdown are of fundamental importance. In a recent investigation, Wolffelt[3] described some of these dynamics for both harmonic and transient large-amplitude pitching and plunging motions. For harmonic pitching motions, significant hysterisis effects in the breakdown position were observed. In contrast to the low-amplitude behavior[1], Wolffelt[3] observed a significant shift in the mean breakdown position during these harmonic motions. The breakdown response to transient pitching motions also demonstrated a marked departure from the steady state breakdown positions. These transient pitching results were presented in terms of the instantaneous angle-of-attack which unfortunately resulted in a loss of the response history after the motion's end. Nevertheless, the highly nonlinear character of the leading-edge vortex flow-field response is evident. These significant departures from steady state behavior suggest the need to consider the breakdown response to transient motions in more detail.

The results to be presented in this paper focus on the time history of leading-edge vortex development and breakdown corresponding to large-amplitude transient pitching motions. The character of both the short-term and long-term flow-field response are described. This description is based on detailed visualizations of the leading-edge vortex structure and breakdown location throughout the recovery to steady-state conditions. Although the wing motions here differ from that of Lambourne et al.[2], it appears that the convective response of the vortex development is retained for the high-alpha pitching motions. The response of vortex breakdown, however, adds a second slower time scale to the flow-field response.

These longer time scales have been interpreted in terms of the breakdown propagation speeds associated with the transient pitching motions.

---

* Scientist, Advanced Research Organization
** Associate Scientist, Advanced Research Organization

Further interpretation of the results has been facilitated through a series of experiments conducted to determine the disturbance propagation characteristics in a steady leading-edge vortex. Comparisons of the wave propagation for steady versus unsteady conditions confirm the role of vortex development in the early breakdown response. These comparisons also demonstrate the wave speed dependence on the disturbance amplitude.

Although aerodynamic loads have not been measured here, consideration of the breakdown response trajectories suggests some aerodynamic consequences which are important for high-alpha maneuvering. The occurrence of two distinct aerodynamic time scales may be inferred from the observed response, and some conclusions concerning dynamic vortex lift may be made.

Experimental Facilities

The characterization of leading-edge vortex dynamics described here was obtained in a series of low-speed experiments in water. These experiments were conduced in the Lockheed-Georgia Low Turbulence Water Channel facility. This open-surface facility has test section dimensions of: 0.8m wide, 0.4m deep, and 4.0m long. Flow speeds were in the range 0.08m/sec to 0.2m/sec.

A simple delta planform wing was used to generate the leading-edge vortex flow of interest. This was a flat-plate delta wing with a leading-edge sweep of 75°. As shown in Figure 1, the leading-edges of the wing are beveled to a sharp edge on the pressure surface of the wing. Dye ports are imbedded in the wing for injection of dye at several locations along the leading edge. For this

aspect-ratio-one wing the critical angle of attack where breakdown first occurs over the wing is approximately $\alpha = 33°$. The chord Reynolds number for these experiments was between $R_C = 19,300$ and $R_C = 64,900$.

The pitching motions were executed by a stepping-motor driven pitching strut, also in Figure 1. Rotation of the wing was about an axis at the 1/2 chord and 15 mm beneath the wing. The pitching motions were specified and controlled via the data-acquisition system such that any harmonic or transient pitching function could be executed.

Experimental Procedures

Various types of flow-field visualizations were used to define the time dependence of the leading-edge vortex structure and breakdown position. The hydrogen bubble wire technique was found to be the most valuable for these purposes. Through careful placement of the bubble wire along the leading edge of the wing, it was possible to visualize both the outer vortex structure and the inner core region. In Figure 2 the free shear-layer roll-up into the vortex is evident and the path of the vortex core is emphasized by the radially inward migration of the hydrogen bubbles. Figure 3 corresponds to a highe. angle of attack and the breakdown can be easily seen in the vortex core region at approximately the three-quarters chord point.

Fig. 2. Hydrogen bubble-wire visualization of leading edge vortex flow for conditions below the critical angle of attack.
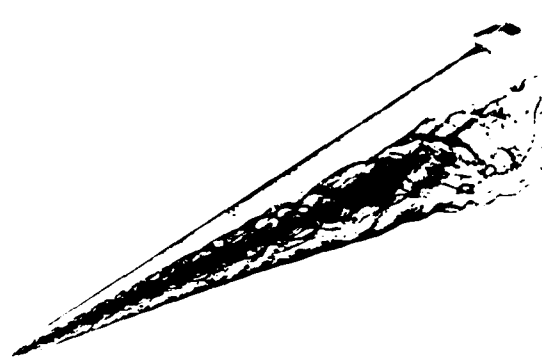

Fig. 3. Hydrogen bubble-wire visualization of leading-edge vortex flow for conditions above the critical angle of attack.

Fig. 1. Schematic of delta wing and pitching mechanism.

The transient response of vortex breakdown was evaluated based on the measured chordwise breakdown position versus elapsed time. This information was collected on video tape, including the appropriate timing and instantaneous angle-of-attack information. A number of constant-rate pitching motions were considered for an angle-of-attack range of 30° to 50°. For the aspect-ratio-one wing, this angle-of-attack range corresponds to chordwise breakdown locations between the trailing edge and the apex. Two dimensionless pitch rates, K = 0.06 and K = 0.12, were used.

A comparison of transient breakdown response to wave propagation in a steady leading-edge vortex was made through the introduction of controlled disturbances. Disturbance waves were generated in the leading-edge vortex by passing a solid rod through the core region near the wing apex. Through variation in the probe-rod diameter the initial wave amplitude could be consistently controlled. Down-stream propagation of these waves under steady conditions is compared with the unsteady breakdown response to a pitch-down motion. The steady condition was chosen to coincide with the final condition of the unsteady motion.

Research Results

Detailed descriptions of the unsteady breakdown response have been obtained in these low-speed water channel experiments. An accurate determination of vortex breakdown position was possible due to the quality of visualization possible in water. For dynamic testing, however, the most distinct advantage was the low freestream convection speed. At these low speeds, the unsteady flow-field development could be observed in much greater detail than possible in higher speed wind tunnel facilities. Hence, the longer response time scales relaxed the need for high dimensional pitch rates and allowed relatively long response times to be observed. For realistic pitching motions, there is no limitation on pitch rates due to mechanical inertia effects.

Dimensional Scaling

The typical breakdown response to a large amplitude transient pitching motion is shown in Figure 4. These results represent a time history of the breakdown position due to a constant-rate increase in angle of attack from 30 to 51 degrees. The wing motions were executed at the same reduced pitch rate, K = .06, but at four flow speeds corresponding to the convective times shown. At the initial angle, breakdown does not occur over the wing. After initiation of the pitch-up motion, breakdown first appears at the trailing edge of the wing, at X/C = 1. Breakdown then proceeds toward its steady-state position near the apex, at approximately X/C = 0.15. The long dimensional response times were typical in these low speed tests, indicating the ease with which the vortex dynamics were tracked.

Since there is evidence that the leading-edge vortex development occurs on a convective time scale[2], it is natural to express the time response relative to this scale. Such a scaling of the data in Figure 4 results in a reasonable collapsing of the data, as shown in Figure 5. For the remaining discussion, the time response results will therefore be scaled with the appropriate convective time, τ.
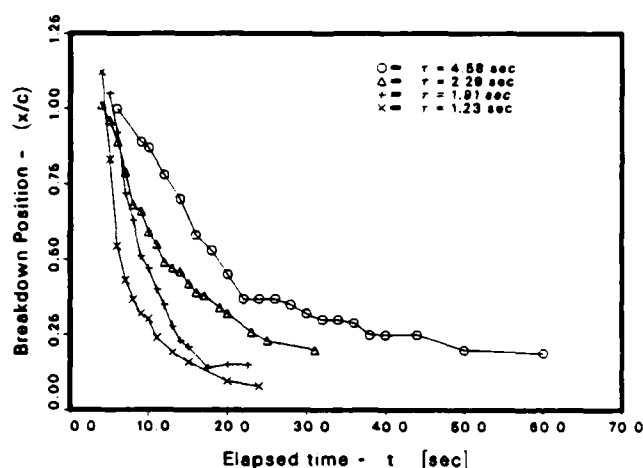

Fig. 4. Effect of convection speed on breakdown response for pitch-up motions between α = 30° and α = 51°. The reduced pitch rate is constant at K = .06.
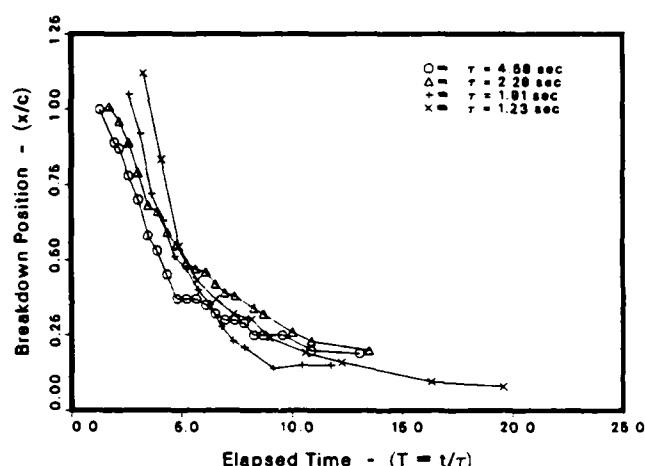

Fig. 5. Response of Figure 4 scaled with the convective time, τ.

Hysteresis Effects

Considerable hysteresis effects might be expected for pitch-up versus pitch-down response in this separated flow regime. In Figure 6, the breakdown approach to steady state conditions is shown for both pitch-up and pitch-down motions at two pitch rates. For convenience, the breakdown position shown in this figure has been measured from the trailing edge. In addition to the pitch rate dependence indicated, it is evident that the two motions result in distinctive behavior. Due to the spanwise variation of the wing chord for a delta wing, it is clear that the local angle of attack varies strongly along the leading edge during a pitching motion. Depending on pitch rate, this effect appears to result in the early onset of breakdown near the trailing edge during pitch up. Conversly, breakdown may remain near the apex for some time during pitch-down motions. This may explain the significant difference in the initial slope of the response curves for these two motions.
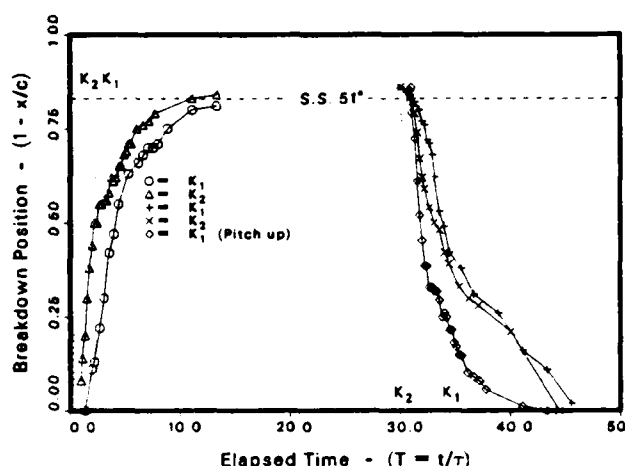
Fig. 6. Pitch-up and pitch-down response between $\alpha = 30°$ and $\alpha = 51°$ compared for two reduced pitch rates $K_1 = 0.06$ and $K_2 = 0.12$. Diamonds designate the inverted pitch-up characteristic, for comparison.

Breakdown Response Regimes

It is evident from the data presented thus far that breakdown may significantly increase aerodynamic response times relative to low angle of attack behavior. The range of expected response times is indicated in Figure 7 for a series of pitch-down motions. All these motions begin at the same initial angle and end over a range of final conditions. For these motions, the response times observed range from one to over thirty convective times after the motion is completed.

The response times observed may be classified into two groups, corresponding to the cases where the final breakdown location is either over the wing or off the wing. When the steady state breakdown location is over the wing, breakdown approaches this location asymptotically. For these cases, we may expect response times, $T > 10$, especially when the final angle of attack is near the critical angle. In contrast to this, when the final position is below the critical angle, the behavior approaches a convective response, such that, $1 < T < 10$.
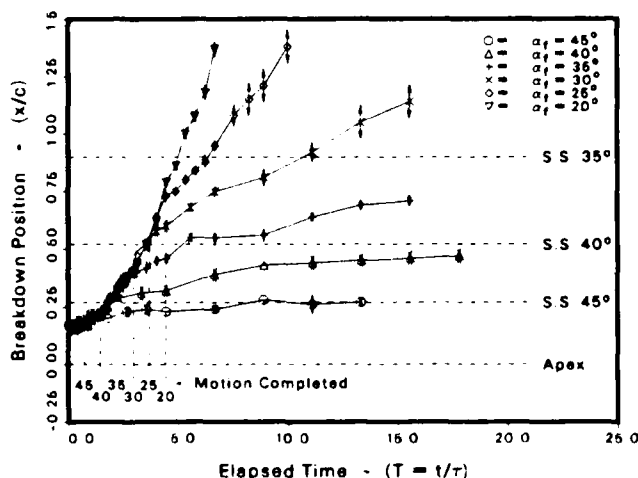
Fig. 7. A range of pitch-down response for initial $\alpha = 51°$. The vertical dashed lines designate the motion's end. K = 0.06.

Breakdown Propagation Speed

Each of the response curves shown in Figure 7 also appear to follow a similar time history during and after the pitching motion. This is shown more clearly in Figure 8, where the breakdown propagation speeds have been derived from Figure 7. For each motion, a distinct change in the propagation speed is observed within one convective time after the motion ends. Based on the previous results of Lambourne et al.[2], this marked change in the breakdown response appears to coincide with the establishment of a steady vortex flow.
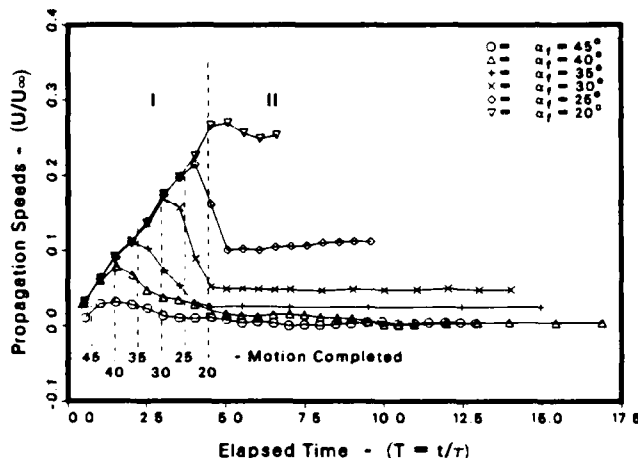

Fig. 8. Breakdown propagation speeds derived from the data of Figure 8. K = 0.06.

Two regimes of breakdown behavior are therefore evident. The first of these, noted in Figure 8 by region I, contains breakdown behavior which is dependent on the initial angle of attack and the pitch rate. This is followed after completion of the motion by region II. In region II, the propagation is determined in some way by the motion history and by the final condition. This behavior suggests that breakdown response is not limited by a delayed development in the vortex core region, but by the inherent propagation speed of the breakdown.

For an interpretation of this dynamic breakdown behavior, it is helpful to relate the observed breakdown motion to wave propagation in these longitudinal vortex flows. The ability of such vortex flows to support the propagation of infinitesimal dispersive waves has been recognized for some time[4,5]. Using a technique similar to that of Maxworthy[6], disturbances were introduced into the steady leading-edge vortex near the apex of the wing. These disturbances quickly evolved into isolated waves which propagated downstream in the leading-edge vortex core. By matching the steady flow-field condition with the final condition of a pitch-down motion the steady and unsteady behavior was compared.

In Figure 9, the breakdown propagation speed is plotted for two different pitch rates and compared to wave propagation in a steady vortex. The difference in the two dynamic response curves during the pitching motion demonstrates again that the developing vortex flow plays a major role in determining the early breakdown response. Hence, this early response is very pitch rate dependent. During the second phase of the response the

280

breakdown wave speeds compare well with the wave propagation for steady conditions. This becomes increasingly so for increasing disturbance amplitude as the probe-rod diameter is increased. The propagation of these waves is therefore inherently nonlinear, and this is especially the case for vortex breakdown.
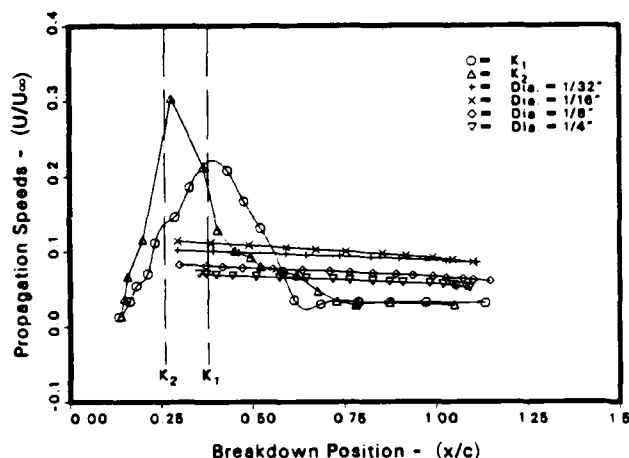

Fig. 9. Steady wave propagation compared to dynamic breakdown response at two reduced pitch rates, $K_1 = 0.06$ and $K_2 = .12$. Under steady conditions, disturbance amplitudes are established using the probe diameters shown.

Conclusions

Evaluation of leading-edge vortex response to large-amplitude transient pitching motions has demonstrated the occurrence of a long time-scale response associated with vortex breakdown. Depending on the pitching motion, this breakdown response to a steady state can be more than twenty to thirty convective times after the motion is completed. While the vortex flow-field development appears to be convective, the slower breakdown response was found to be wave speed limited. During the pitch-down response for example, vortex breakdown is not convected downstream, but propagates downstream with a speed often less than one-tenth the convective speed.

This breakdown behavior is descriptive of the fundamental mechanisms which control the vortex breakdown process. The dynamic response of vortex breakdown was shown to be characteristic of wave propagation in the vortex core. A functional dependence between the wave amplitude and the wave speed was also demonstrated, reinforcing the view that breakdown is analogous to surface waves and the related hydraulic jump.

Some important inferences may also be made concerning the aerodynamics at high alpha as well as for the development and interpretation of relevant aerodynamic testing methods. The occurrence of two response time scales suggests that the high alpha aerodynamics will include significant motion history effects. Assuming this behavior scales with the convective time, the aerodynamic memory may be from 0.5sec to 2.0sec for typical maneuvering flight conditions of $U = 140m/sec$ and $M = 0.4$. Aerodynamic testing methods which are based on oscillatory motions will clearly not capture these large deviations from linearized aerodynamic behavior. Depending on the driving amplitude and frequency employed, such testing may be more sensitive to only one of the two time scales involved.

These results have been obtained through the exclusive use of qualitative flow visualization techniques. For for the characterization of important flow-field dynamics and for establishing direction of further quantitative investigations, these techniques have proven both powerful and efficient. Further investigations must now focus on the mechanisms controlling wave propagation in three-dimensional leading-edge vortex flows for steady and unsteady conditions.

Acknowledgement

References

1. Woodgate, L. "Measurements of the Oscillatory Pitching Moment Derivatives on a Slender Sharp Edged Delta Wing in Incompressible Flow," ARC R&M 3628, Part 3, 1968.

2. Lambourne, N.C. and Bryer, D.W. and Maybrey, J.F.M. "The Behavior of the Leading Edge Vortices over a Delta Wing Following a Sudden Change of Incidence," NPL Aero. R&M 3645, 1969.

3. Wolffelt, K.W. "Investigation of the Movement of Vortex Burst Position with Dynamically Changing Angle of Attack for a Schematic Delta Wing in a Water Tunnel with Correlation to Similar Studies in Wind Tunnel," AGARD CPP-413, 1986.

4. Squire, H.B. "Analysis of the Vortex Breakdown Phenomenon. Part 1." Imperial College, London, Report 102, 1960.

5. Benjamin, T. B. "Theory of the Vortex Breakdown Phenomenon," J. Fluid Mech., vol. 14, 1962, pp. 593-629.

6. Maxworthy, T., Hopfinger, E.J. and Redekopp, L.G. "Wave Motions on Vortex Cores," J. Fluid Mech., vol 151, 1985, pp. 141-165.

Unsteady Vortex Flows Over Delta Wings

G.R. Spedding, T. Maxworthy & E. Rignot
Department of Aerospace Engineering.
University of Southern California.
Los Angeles, CA 90089-1191

1. ABSTRACT

Quantitative flow visualisation techniques were used to measure the circulation enhancement of the attached, leading edge vortices on a delta wing with a leading-edge flap. At low angles of attack ($\alpha \approx 10°$), the separation vortex doubled in strength for a flap with a fixed including angle of $70°$. At moderate reduced frequencies ($\Omega \approx 0.4$) this factor increased to 2.7 for continuous sinusoidal flap oscillation. The relevance of these results to the problem of generating high instantaneous forces on the wings of super-manoeuvrable aircraft is discussed.

2. INTRODUCTION

The generation of unsteady leading edge separation vortices with high circulation has been known for some time to occur in both insect flight[1,2,3], and in some geometries of turbomachinery[4]. In both cases, it has been observed that the efficiency of these processes (specifically, lift or thrust generation) may be significantly enhanced by the interaction of the lifting surface with the unsteady separation vortex or vortices. This study is concerned with the application of some of these ideas to aerofoils in steady flow, where the unsteadiness is due to the operation of a flap in time.

In order to stabilise the vortex behind a leading edge flap (and also over an insect wing), the flow must have a strong three-dimensional component, such as an axial flow along the vortex core which removes excess vorticity from the core, transporting it into the wake. The leading edge flap concept is not new, and neither is the axial flow stabilising mechanism which has been used in both experimental[5] and theoretical[6] investigations before. Here, the 3d characteristics of the naturally occuring flow over a moderately-swept, conically-symmetric delta wing allow the generation of large, stable vortices over the wing in both unforced and unsteady configurations.

With the current interest in super-manoeuvrable aircraft, the objective of this study is to determine the extent to which high lift forces may be rapidly developed due to enhanced circulation of the leading edge vortex on a delta wing with a leading edge flap. The circulation increment is produced by the unsteady operation of the flap.

3. APPARATUS

The delta wing geometry is shown schematically in Fig. 1. The half delta wing and leading edge flap assembly was mounted on a flat base plate and could be rotated about the three pivot points marked by dark blobs. The angles α, β and γ, the angle of attack, the flap angle, and the sweep angle, respectively, could thus be varied continuously. In practice, γ was fixed at $16.7°$, α was varied from $0°$ to $15°$, and the flap was oscillated through $70°$ from $0°$. x, y and z are streamwise, spanwise and normal coordinate axes attached to the wing with origin at the apex. The ratio of flap span/delta wing semispan was 0.45.
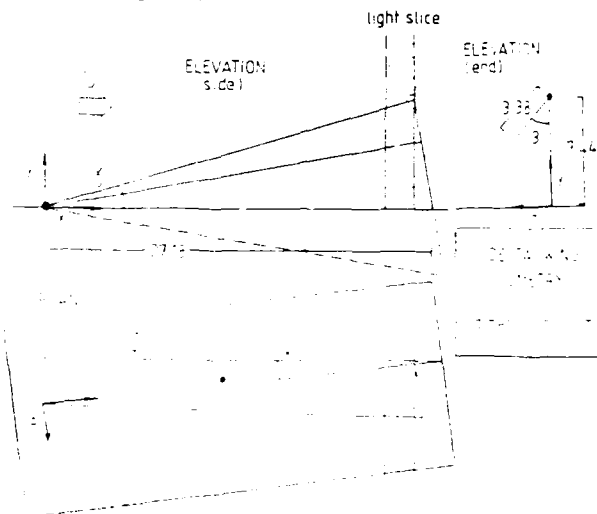

Figure 1: Schematic of the half-delta wing geometry

The delta wing assembly was mounted immediately in front of, and at the same level as a flat plate spanning the working section (92 cm x 25 cm) of a low-turbulence water channel (Fig. 2). The beam of a 5W argon laser was brought to the water channel via a fibre optic cable, where it was spread into a sheet by two cylindrical lenses (l_2, l_3) and deflected into the flow off an inclined mirror (m_1). The optical rail base at the channel end of the fibre optic was movable so that a number of cross-stream and/or streamwise locations for the light slice could be selected with minimum fuss. A second inclined mirror (m_2) was placed two wing centreline chord lengths downstream of the wing trailing edge for photographing cross-stream sections through the flow field. Before passing through the lenses, the unexpanded laser beam was chopped by a rotating disk. The indexer controlling the rotation of this disk, and the camera shutter were triggered on the same switch, which could be be operated manually, or by computer. The freestream velocity in the water channel was measured at $10.4\ cm\,s^{-1}$, to give a Reynolds number based on centreline chord $Re_c = 2.7 \times 10^4$.
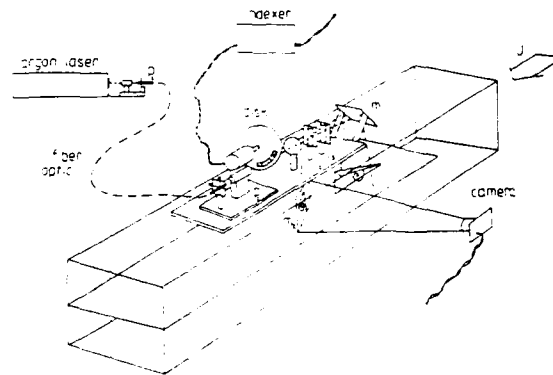

Figure 2: Water channel test section. The delta wing projects upwards from a flat plate boundary. Not to scale

4. TECHNIQUES

4.1 Flow visualisation

Qualitative descriptions of the flow field were obtained by photographing fluorescein dye lines with 35mm and video cameras. The dye was injected via flexible tubing which ran out to small diameter cylindrical nozzles protruding from the base plate. Most frequently, dye was introduced at the apex, though occasionally it was also released at the leading edge of the wing and/or at the trailing edge of the flap.

Small (650-850 μ diameter), spherical, polystyrene beads were used to trace the flow field in all of the quantitative measurements. The particles were coated with rodamine dye and heated very gently to lower their sinking speed in water to $1-3\ mm\,s^{-1}$. If introduced into the water channel in the settling chamber, just after the final screen, the particles could be arranged to arrive at, or close to, the delta wing apex some distance downstream in the test section. Time-exposure photographs were taken of the beads as they passed through the light slice. The time of exposure and level of illumination were governed by a chopper disk with a slit covered with semi-transparent material of two different levels of opacity so that each particle streak on the 35 mm negative was composed of one bright spot, a grey central section, a second bright spot, and finally, a grey tail section. The thickness of streamwise light slices was 3 mm, while cross-stream sections had a thickness of around 15 mm or 0.06 times the centreline chord length.

4.2 Image processing

The coded particle streaks were digitised using automated video image processing techniques suggested by the work of Gharib et al. Streak photographs were imaged by a video camera and digitised at 512 x 480 pixel x 8 bit resolution. Each digital image was treated with some simple global, and then local thresholding and all streaks composed of two and only two, bright spots and a tail were retained. Multiple passes with varying local detection criteria were implemented in an effort to extract as

many streaks as possible from each single frame. The magnitude of each
velocity vector was determined by the length of the curved line segment
between bright spots, its direction was given by the tail location, and the
location was assigned to a point half way along the curved central line
segment. This line segment was approximated by a series of small straight
line segments, the number depending on the average curvature along its
length.

In the cross-stream sections, it was rare to retrieve a sufficient
number of particle streaks from a single frame, in which case streaks from
several frames were combined to produce a phase-averaged velocity field.

4.3 Grid interpolation and error analysis

Many different interpolation schemes have been tested to reduce this
irregularly-spaced data to a regular rectangular grid. There are a number of
aspects to this problem, some of which have been discussed in the context
of fluid mechanics[8], and also in the fields of meteorology and computer
graphics[9]. Just a few points will be briefly mentioned here. The total error
in the interpolated grid velocity fields (and their spatial derivatives) depends
on the quality of the original data and on the particular interpolating
scheme. Fig. 3 shows an example of data from an artificial velocity field (a)
which was marked with randomly scattered pseudo-streaks and then
reconstructed by simple convolution with an adaptive gaussian window
(AGW)[8] (b) and by a spline-thin-shell (STS) method[10], (c). In this instance,
where the errors in the original data are very small, the root mean square
error (r.m.s.e.) in the interpolated vorticity field is always smaller in the STS
interpolation, which exactly reconstructs the original data. Computation
times are long however, and wher the raw data field is composed of a large
number of particles averaged from a number of frames, the simplicity and
implicit smoothing of the AGW technique make it the preferred option. In
real data, when some error is present in the original streaks (from diverse
sources, such as optical misalignments anywhere along the photographic
path, film shrinkage, non-uniform bead densities, finite light slice
thicknesses, superimposition of multiple phase-averaged data fields) the ω
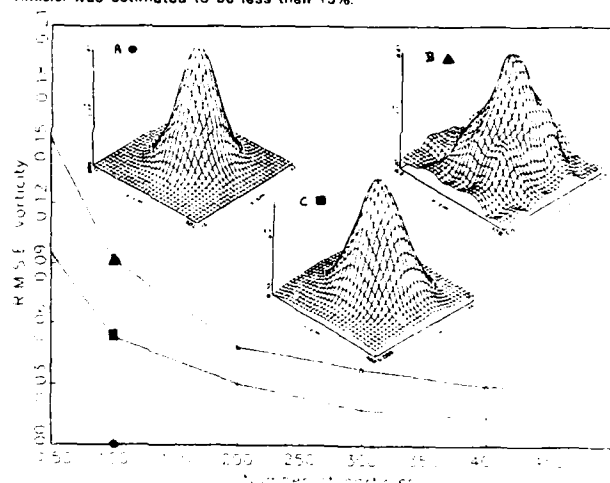r.m.s.e. was estimated to be less than 15%.

Figure 3:   In general, the root mean square error in estimating
the vorticity field on a grid depends on the ratio of
number of particles/integral length scale of the flow,
and on the interpolation algorithm employed. The error
in reconstructing a Burgers Vortex (a), is shown for
the AGW (b) and STS (c) schemes. The insets show the
vortex reconstructions from 100 particles.

The circulation, (Γ), around cross sections through the vortex was
estimated on the interpolated grid by following numerical particles around
instantaneous streamlines (Fig. 4a,b). Due to the finite size of each
timestep, these numerical particles tend to be forced away from centres of
rotation as each short pathline is tangential to the local velocity. The effect
is rather like a centrifugal force acting on each particle which has some
small mass. A correction was applied (Fig. 4b) which could be used, not
only to counteract this tendency, but also to force certain integration paths
in the flow field. The paths could also be forced to respect various
impermeable boundary conditions. Being an integration, the estimation of Γ
was quite robust in the presence of noise. Provided the integration path
lies outside the core of a vortex, the calculated value of Γ was always
within 5% of its true value in artificial velocity field simulations. In
experimental data, successive estimates of Γ from different paths around a
vortex in a single interpolated velocity field, and from phase-averaged
ensembles of more than one data field, yielded Γ values with standard
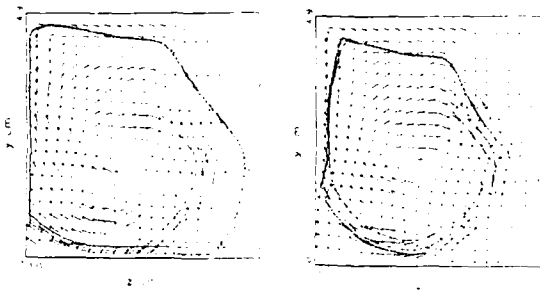deviations of less than 10%.

Figure 4:   (A) computation of the circulation around a vortex
from experimental data by following a particle path
around a closed loop, and (B) application of constant
bias to force different particle trajectories.

Finally, a technique termed 'bootstrapping' has been implemented and
tested, following the work of Garcia & Jimenez[8]. The general method for a
data field composed of N velocity measurements, interpolated on to a grid,
is to successively resample the original N samples and construct new data
sets composed of N samples selected at random from the original N
samples. Some data are thus repeated while others are omitted.
Cumulatively averaging the differences at grid points from the re-
interpolated velocity fields results in an error estimate which converges
after a number of iterations. The errors in interpolating a grid may therefore
be estimated, even when the true velocity field is not known (and is, of
course, not knowable). The correspondence of this method with known
errors in artificial velocity fields was verified, and together with the AGW
interpolation, bootstrapping was routinely used to detect and check for
serious errors in the automated velocity grid reconstructions.

5. RESULTS

5.1 Qualitative

Fluorescein dye lines were photographed and video taped to identify
the general flow regimes in the three configurations: delta wing without flap
($\beta = 0°$), wing + flap at fixed β and wing with sinusoidal flap oscillation. In
the latter, β varied from $0° - 70°$. Conditions were noted for optimum lift
enhancement, associated with increased separation vortex circulation, or
alternatively, with the increased camber and effective thickness of the wing
and its attached vortices. The apparent increase in strength of the
separation vortices on flap deployment is most noticeable at low α, typical
of cruise conditions. At $\alpha > 15°-20°$, the vortices are already large, and
relative increase in strength is reduced. In this regime, vortex breakdown
was delayed by the order of one flow transit time. In the absence of the
flap, the vortex breakdown location varied in a fashion consistent with
previously-reported delta wing experiments (see ref 11 for a recent
example). Some care was taken to operate in a parameter domain where
the breakdown location lies downstream of the trailing edge of the aerofoil
in the wake. When the inclined mirror was placed behind the trailing edge
the adverse pressure gradient and diverging flow around the obstacle
caused the breakdown location to move upstream, towards wing, effectively
contracting this breakdown-free window in parameter space.

5.2 Circulation and vorticity distribution

The quantitative flow visualisation techniques described in the
previous section were used to map out the distribution of streamwise
vorticity and to measure the strength of the leading edge vortex, or vortices.
Here we will summarise the results pertaining to the effects of steady-state
and unsteady flap deployment on the growth and strength of the separation
vortex.

Fig. 5 is an example of the streamwise vorticity distribution $\omega(y,z)$ at
four downstream locations, shown schematically in the centre of the figure.
The wing and flap were fixed at $\alpha = 0°$ and $\beta = 68°$, respectively. At all
four x/l stations, the vorticity appears to be concentrated in a single,
identifiable core region, which increases in size and ω_{max} from sections 4 -
1. From a similar series of measurements. Fig. 6 shows the circulation
measured at the same x/l stations for a fixed flap angle $\beta = 70°$. The error
bars represent standard deviations of the Γ estimates from different
integration paths in the same velocity field. Γ increases linearly with x/l
even as far as x/l = 0.92, where one might have expected to detect an
upstream influence from the trailing edge. It proved difficult to measure Γ
with any degree of confidence further upstream than x/l = 0.5 due to the
relatively small scales involved. this is reflected in the larger error bar for Γ
at x/l = 0.52. Note that this configuration is a steady state one and that the
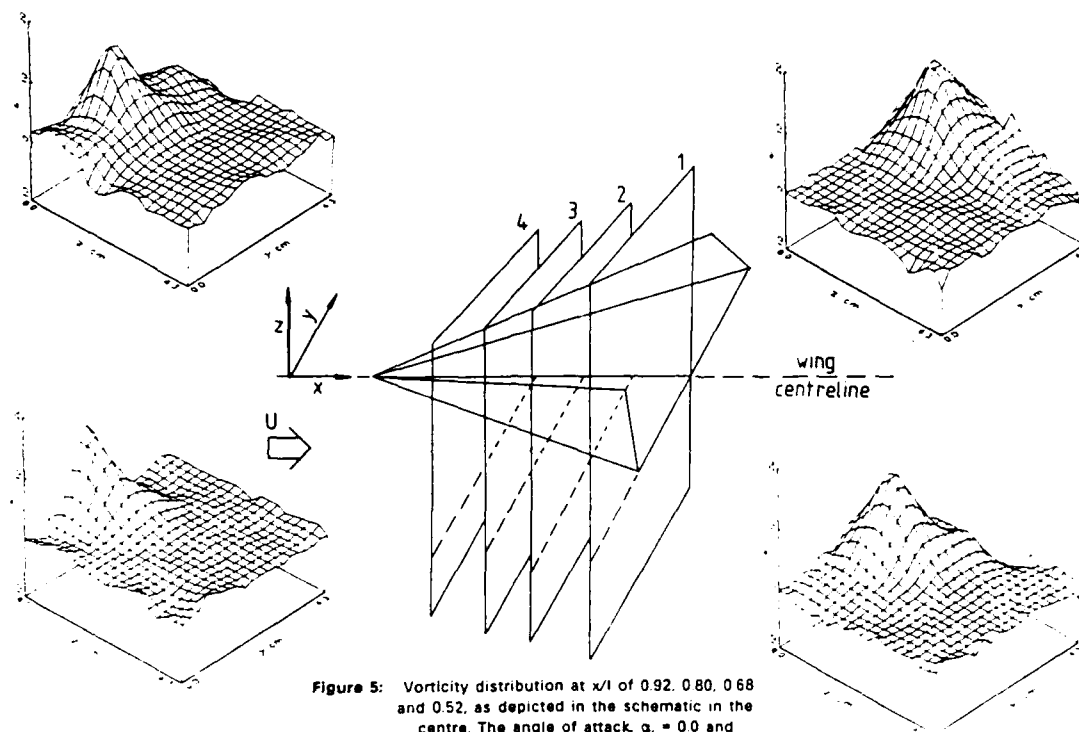trapped vortex is quite stable.

Figure 5: Vorticity distribution at x/l of 0.92, 0.80, 0.68 and 0.52, as depicted in the schematic in the centre. The angle of attack, α, = 0.0 and the flap angle, β, = 68°.
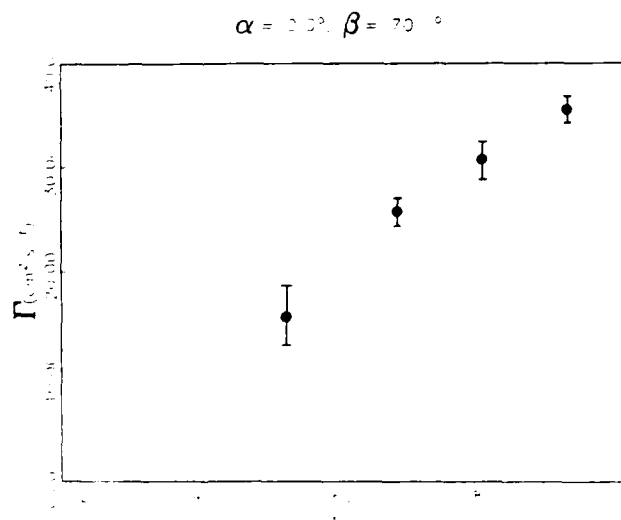

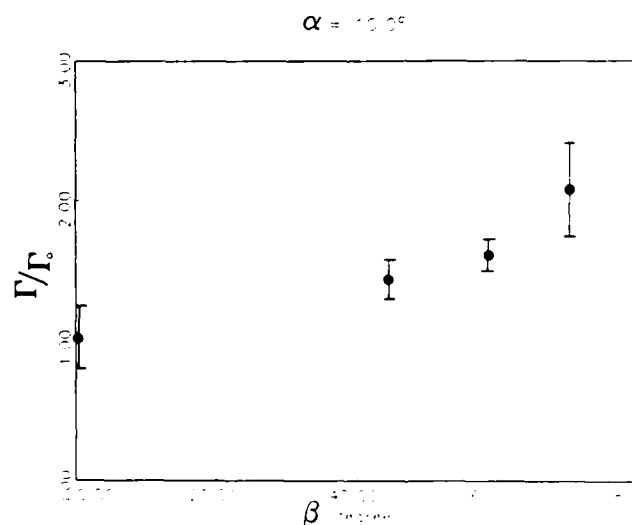**Figure 6:** The variation in separation vortex circulation with downstream distance for constant flap angle β

Figure 7: The change in normalised vortex circulation with steady state flap angle

The relative increase in Γ for different flap opening angles may be expressed as $\Gamma^* = \Gamma/\Gamma_0$, where Γ_0 is the separation vortex strength in the absence of a flap (or $\beta = 0°$). Γ^* appeared to increase linearly with β up to $\beta = 70°$ for a moderate angle of attack ($\alpha = 10°$) (Fig 7). At $\beta = 70°$ the separation vortex circulation is approximately twice the unforced value. The circulation around the whole wing was not measured so this result would translate into a doubling of the lift due to the separation vortex.

In investigating the unsteady performance of the wing/flap system the flap was opened and closed in a continuous sinusoidal motion. Frames of data could be phase-averaged by synchronising with the circular drive wheel at various points round its circumference. The data in Figs 8 & 4

were taken from frames phase-averaged at $\beta_{max} = 70°$. The delta wing was at a moderate angle of attack ($\alpha = 13°$) and the separation vortex circulation in Fig 8 has again been normalised by the value for the same configuration without a flap. The reduced frequency $\Omega = \omega c/U$ is defined based on the radian frequency, ω (units of radians sec⁻¹) and the mean flap width c, equivalent to its value at x/l = 0.5. This definition of the reduced frequency takes into account the flap oscillation amplitude through the radian frequency ω, and is not the same as a definition based on $2\pi f$ which does not. In Fig 8. Γ^* increases with Ω up until $\Omega = 0.42$ when $\Gamma^* = 2.7$. This represents a substantial enhancement of the separation vortex circulation over the case without any flap, and a 35% increase over the equivalent steady state flap configuration.
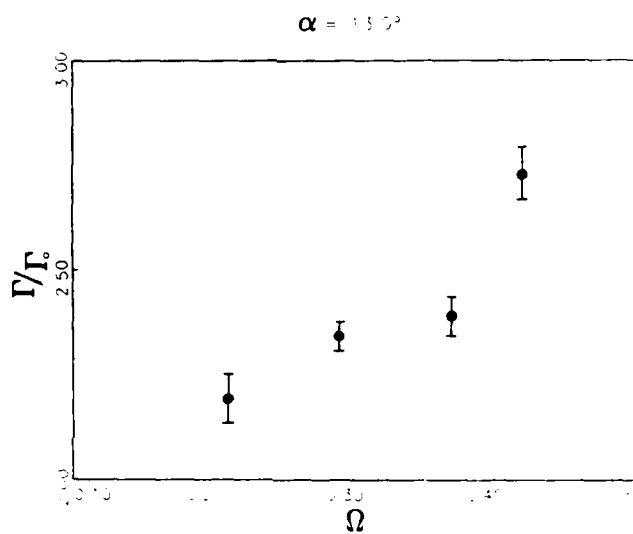
285

Figure 8: The change in normalised circulation with reduced frequency for a flap in continuous sinusoidal oscillation. The measurements were taken at the maximum flap opening angle, $\delta_{max} \approx 70°$.
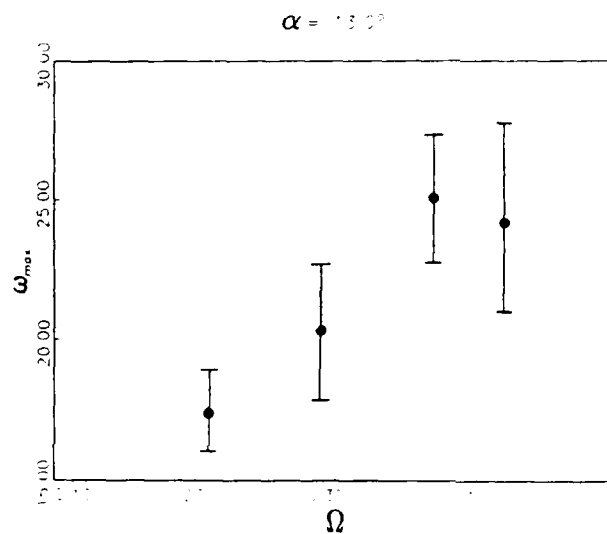
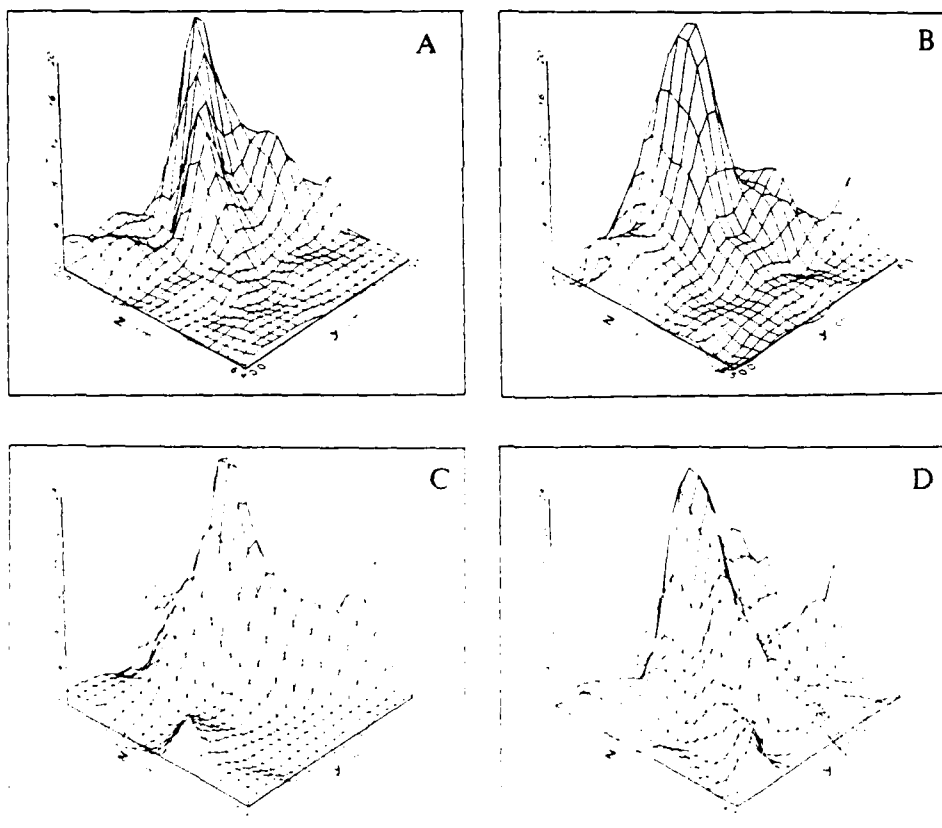Figure 9: The change in peak vorticity with reduced frequency Conditions as Fig. 8.

Figure 10: $\omega(y,z)$ for reduced frequencies (Ω) corresponding to the data points in Figs 8 & 9

From the same phase-averaged data, the peak vorticity, ω_{max} is plotted against reduced frequency Ω in Fig. 9. The uncertainty in the measurements is rather high (the error bars represent the standard deviation in phase-averaged frames; the number of contributing frames ranged from 3 to 6), but there are indications that ω_{max} does not continue to rise with increasing Ω. A plot of four isometric surfaces of the $\omega(y,z)$ distribution corresponding to single instances of the four points of Fig. 9 is shown in Fig. 10. As Ω increases from A - D, the vortex at first simply increases in size and strength, but at the highest value of Ω in D, the vortex core appears considerably disorganised and hard to define, so while the total amount of vorticity generated must increase with reduced frequency, it no longer continues to accumulate in a compact, well-defined core region.

6. CONCLUDING REMARKS

The circulation of the leading edge separation vortex on a delta wing at moderate angles of attack was increased significantly by deployment of a leading edge flap. The pitching moment characteristics of this geometry are known to be quite favourable[12] and the unsteady operation of this flap configuration should enable rapid changes in the instantaneous lift force on the wing to be realised.

The $\omega_{max}(\Omega)$ curve implies that an optimum reduced frequency may exist for maintaining a coherent or compact vortex core structure along the wing leading edge. This might be expected to have important implications for the stability and control of such separated flows. If, on the other hand, this result is simply a consequence of the vortex breakdown point moving upstream on to the wing trailing edge, the location of the inclined mirror downstream in the flow must be taken into account; this point therefore *requires confirmation.*

Finally, a number of questions naturally emerge from this work. Although the measured circulation enhancements have been quite large, the ratio of flap span to wing semispan (0.45) was also large and it remains to be seen how the performance and power requirement depend on this ratio. The effect of varying sweep angle has yet to be *investigated,* as has variation in flap opening time history; various non-continuous and non-sinusoidal motions are likely to be of practical relevance. C_p measurements from wind tunnel experiments enable the total force, location of the vortex centreline and aerofoil centre of pressure to be estimated as a function of time. These quantities are currently being analysed. The wing surface pressures depend on both the position and the strength of the separation vortex, for which data are available from the water channel experiments. It is hoped that the correlation between the two sets of measurements will help to identify any Reynolds number-dependant features in the flow.

7. ACKNOWLEDGEMENTS

8. REFERENCES

1 Lighthill, M.J. (1973) *J. Fluid Mech.* **60**, 1-17.

2 Maxworthy, T. (1979). *J. Fluid Mech.* **93**, 47-63.

3 Spedding, G.R. & Maxworthy, T (1986). *J. Fluid Mech.* **165**, 247-272.

4 Furber, S.B. & Ffowcs Williams, J.E. (1979). *J. Fluid Mech.* **94**, 519-540

5 Malcolm, G. & Skow, A. (1986). *AGARD-CPP-413*

6 Rossow, V.J (1978). *J. Aircraft* **15**, 618-625.

7 Gharib, M, Dyne, B, Thomas, O & Yap, C (1986). *AGARD-CPP-413*, No. 22

8 Garcia, J.C.A & Jimenez, J (1987). Submitted to *J. Fluid Mech.*

9 Lancaster, P & Salkauskas, K (1986) *Curve and surface fitting.* Academic Press, London

10 Sommeria, J (1987) *J. Fluid Mech.* In press.

11 Payne, F.M., Ng, T.T & Nelson, R.C (1987). *AIAA-87-1231*

12 Grantz, A.C & Marchman, J.F (1983). *J. Aircraft* **20**, 165-169

VORTEX DOMINATED AERODYNAMIC FLOWS AS

NUMERICAL EXPERIMENT WITH A POINT VORTEX METHOD

H.K. Cheng and Z.X. Jia
Department of Aerospace Engineering
University of Southern California
Los Angeles, California 90089-1191

ABSTRACT

Computational simulations of vortex shedding and interaction, with the objective of identifying features/concepts applicable to vortex-lift control, are studied. In providing a simple framework where a meaningful comparison with concurrent laboratory experiments can be made, a numerical model based on a point-vortex method has been applied to two major problem categories: (i) unsteady flow about a flat plate at a fixed angle of attack, with and without a leading-edge vortex flap, (ii) transient, vortical cross flow produced by a slender delta wing. Evolution of the patterns of vortex traces, streamlines, surface pressure and forces are studied. Flow features based on data obtained by different point-vortex shedding rates and different integration time steps are found to be consistent on length and time scales comparable to as well as considerably smaller than those of the global flow. The paper summarizes the progress made and the results obtained in these two categories; the topic areas, where research direction is to be taken, are indicated.

1. INTRODUCTION

Separation vortex from a sharp edge is a common feature dominating many important unsteady, nonlinear problems in aerodynamics. Underlying the quest of vortex lift enhancement,[1-9] dynamic stall control,[10] as well as understanding the lift hysteresis,[11,12] are the mechanism of free-vortex production and interaction. This work presents a computational simulation of the vortex dynamics in aero-/hydrodynamic flows, in which production of free vortices represents an aspect as important as the interaction among the free vortices themselves. An inviscid flow is assumed and the numerical procedure employs a point-vortex method.[13-16] The latter is implemented by an algorithm adopted from the model of a discrete separation vortex[17-19] which is allowed to grow but remains force free.

Just like the well known limitation of a Euler CFD solver which cannot resolve the free-vortex sheet location to great accuracy without introducing a surface of discontinuity, the point-vortex approach must also fail in this respect, strictly speaking. Depending on the specific problems considered and the particular version used, the approach is also known for its computational instability,[20-23] although successful schemes for delaying the computational breakdown are available. Setting aside the difficult question of whether a tightly rolled up vortex sheet may represent the fluid physics any better than a discrete vortex with or without a viscous core, it remains unclear if a sense of convergence of the point-vortex method can be established by shedding more and more vortices. The answer may seem less certain in the face of recent sentiment about chaos in vortex motions.[24a,b] From the viewpoint of aerodynamic applications, and with the computer resources becoming more accessible, one should, perhaps, be more concerned with the grim prospect that the evolving flow features/properties from a point-vortex computation could be ruined by the chaos engendered by an ever increasing population of the point vortices. The concern is by no means trivial, inasmuch as increasing the point-vortex shedding rate is found to improve the description of the free vortex sheet at least in the vicinity of the sharp edge. Thus, the degree to which the point-vortex approach may succeed/fail in the context of aerodynamic analysis will be one major aspect to be ascertained from the study.

To accomplish the dual purpose of assessing the point-vortex approach and developing a viable framework for vortex-lift study, attention is focused on generic examples of two problem categories: I. the flat-plate airfoils impulsively accelerated to uniform speed, with and without a leading-edge (vortex) flap, II. the transient cross flow about a flat slender delta wing. The following section (§2) will briefly discuss the theoretical and algorithmic essentials. Results in categories I and II are summarized and discussed in Sections 3 and 4. Earlier results on the 2-D vortex flap was discussed in a related work by Cheng, Edwards & Jia.[26] Solution details and additional examples are documented in a 1987 dissertation of Z.X. Jia.[31]

2. THEORETICAL AND ALGORITHMIC ESSENTIALS

We consider an inviscid incompressible plane flow. The initial state and the far field are assumed to be uniform and the basic flow excluding the vortex sheets, is therefore irrotational. The velocity and pressure fields are governed by the Laplace equation for the velocity potential and the Bernoulli equations, respectively. Of pri-

mary importance for the present study are the conditions expressing pressure and normal-velocity continuity across the free vortex sheet, which is assumed to have a vanishingly small thickness. The Kutta condition which disallows infinite velocity and infinite pressure at a sharp edge will be stipulated; this is consistent with the identification of the sharp edge as the location where the vortex sheet emerges.

Free Vortex Sheet

In terms of the velocity potential ϕ, the pressure and normal velocity continuity requirement mentioned can be expressed with the help of the Bernoulli relation

$$\left(\frac{\partial}{\partial t} + <\frac{\partial \phi}{\partial s}> \frac{\partial}{\partial s}\right) [\phi] = 0 \qquad (2.1)$$

$$[\nabla \phi] \cdot \nabla S = 0 \qquad (2.2)$$

on a free vortex sheet $S(x,y,t) = 0$, where $\partial \phi/\partial s$ represents a tangential derivative along the sheet, $[\ ]$ and $<\ >$ denote the jump (difference) and the arithematical mean across the sheet, respectively. Equation (2.1) signifies the invariance of the circulation of a Lagrangian element $\delta s'$ on the sheet $\delta \Gamma = -\delta [\phi] = -[\partial \phi/\partial s'] \delta s'$ which is advected with the tangential velocity $<\partial \phi/\partial s'>$ on the sheet. This is the theoretical basis for the advecting an individual discrete free vortex at the "vortex velocity", i.e. the finite velocity which would exist after excluding the individual vortex in question, as is well known.[27,28] It also supports the equation of Birkhoff[29] and Rott,[30] which employs the principal value of a line integral to evaluate the self induced velocity at a curved, free-vortex sheet.

A Force-Free Separation Vortex

In applying the point-vortex method to the problem of vortex shedding from a salient edge, the method must be implemented with an algorithm for the production of new vortices to be released as free vortices. Since the instant release of a discrete vortex of a small but nonvanishing strength would imply a violation of the Kutta condition between shedding, the vortex in question must be allowed to grow in strength from a near-zero value at some point next to the edge (but away from the edge and the wing/body surface) until its strength becomes large enough to meet the purpose of discretization. In the meantime, the Kutta condition must be met during the incubation period of this nascent vortex.

As indicated earlier, in the present analysis, an equation governing the growth and excursion of a discrete separation vortex representing the centroid of the free vortex sheet near the salient edge is adopted.[23-25] Denoting the total strength (circulation) of the shed vortex sheet by Γ_c, the complex coordinates of the centroid of the shed vortex and the edge by z_c and z_a, the equation governing growth rate $d\Gamma_c/dt$ and the centroid excursion rate dz_c/dt is

$$\left(z_c - z_a\right) \frac{d}{dt}\Gamma_c = \left(\overline{W}^\tau_c - \frac{d}{dt}z_c\right)\Gamma_c \qquad (2.3)$$

where $\overline{W}^\tau_c$ is the complex conjugate velocity at $z = z_c$ which is evaluated in the same manner as for the classical "vortex velocity" but no longer signifies the drift velocity of a free vortex. This equation is a form extended from Edwards'[17] original work by Cheng[18] and used in Edwards & Cheng[25] in their study of the Weis-Fogh lift mechanism. The equation had been applied by Rott[19] and Brown & Micheal[29] in flow with conical symmetry. It was also recovered by Graham[30] in a paper on simulating vortex shedding from a sharp edge.

Equation (2.3) signifies the balance of the force due to a nonvanishing unsteady potential jump across the diaphragm (feeder sheet) and the Joukowskii force determined by the circulation around the centroid, as noted in Refs. [17, 19, 29, 30]. As such, it must represent a discretized form of the pressure continuity requirement (2.1). Expanding an argument indicated in Edwards' original paper, it can indeed be shown on the basis of (2.1) and (2.2) that the equation relating the rates of centroid excursion and the circulation increase of a nascent vortex is no more or less than (2.3), provided that the segment of the sheet represented by the centroid is sufficiently close to the edge (Appendix Ref. [31]).

With an explicit knowledge of the velocity field in terms of Γ_c, z_c and the wing/body geometry, (2.3) and the Kutta condition suffice for the determination of Γ_c and z_c as functions of time t.

Growth and Excursion of Nascent Vortices

In the present analysis, this procedure is applied to determine the growth and excursion for the nascent vortex of each of the K edges where shedding is allowed, using Euler/Runge-Kutta scheme for time integration. After a period of growth $\Delta_1 t$ which is identified also with the vortex-shedding interval, the growth is terminated and the nascent vortex is released as a free vortex, advected according to

$$\frac{d}{dt}z_{jk} = \overline{W}^\tau_{jk}, \quad \frac{d}{dt}\Gamma_{jk} = 0 \qquad (2.4)$$

where the subscript jk refers to the j-th free vortex shed from the kth edge. The solution is determined by the integration time step Δt and the shedding interval $\Delta_1 t$ which controls the number of point vortices in the field and has been taken to be 5-20 times of Δt.

To illustrate the distinct nature of the present version of the point-vortex method, we show in Fig. 1 the trajectories of nascent vortices from a sharp edge and their subsequent paths as free vortices. As indicated earlier, the nascent vortex (system) based on (2.3) is force-free --- being quite unlike the treatment in Refs. [31-33] where the nascent vortex is held at a fixed position prior to its release.

Remarks on Procedures

The complex potential is computed as

$$W = W_1 + \frac{i}{2\pi} \sum_{k,j=1}^{K,N} \frac{\Gamma_{jk}}{(z-z_{jk})} + W_2 \qquad (2.5)$$

and W_1 is an acyclic solution in the absence of shed vortices and W_2 is that corresponding to the system of image vortices. The problem is solved in a transformed plane. At each time level t (with $N\Delta_1 t < t < (N+1)\Delta_1 t$), the positions and strength of the K nascent vortices and $(N+1)K$ free vortices are needed for computing the induced velocity at each of the KN vortices. Taking the work in computing the velocity induced by the (k,j) vortex at another vortex (k',j') to be one unit, the work required at each time level is proportional to N^2 (assuming a finite number of edges K); the total work performed up to the time with N vortices in the field is seen to be proportional to N^3 (the constant of proportionality is a large number depending on the ratio $\Delta_1 t/\Delta t$).

A variety of schemes have shown promise in saving computer work as well as delaying small-scale chaos for the point-vortex methods; notably among them are the vortex in cell method,[15] as well as the amalgamation and consolidation treatments.[32,35] These variants for work saving have not been attempted in this study. Nevertheless, the present method employing the force-free procedure for nascent-vortex generation should afford the use of stronger, hence fewer, free vortices than other existing models and procedures.

3. IMPULSIVELY STARTED MOTION OF A FLAT PLATE WITH AND WITHOUT VORTEX FLAP

In the following we discuss the problem of simulating the flow about an inclined flat plate, with and without a leading-edge spoiler deployed as a vortex flap, which is generated by an impulsive acceleration of the plate. The study with the point-vortex method in this case was motivated by an earlier investigation reported in [26] on the influence and stability of a stationary free vortex over the wing, in which exceptionally high lifts associated with solution multiplicity are admissible at certain incidence and flap angles to the inviscid steady-state description, and that some of the high-lift solutions are found to be dynamically stable (on the basis of an Edwards-type separation vortex model). It was felt that this type of model cannot describe the crucial details of vortex interaction near the sharp edge which may affect the fate of the captured eddy, hence its global stability. A point-vortex method capable of simulating the vortex-sheet dynamics in the wing vicinity should provide a more solid analysis. The example, for which much computational effort were directed, was chosen to have an angle of attack $\lambda = 8.5°$, and an (acute) leading-edge flap angle $\beta = 45°$; the ratio of the flap width to the wing chord is

$L_1/L_0 = 1/3$. The choice of $\alpha = 8.5°$ was influenced by the critical nature of the vortex-lift development occurring at $\alpha = 8.25°$ found with the Edwards model for the single vortex, which we hope to recover or assess.

The problem was solved in the transformed unit-circle plane for which the acyclic part of W is simply that of the flow past a circular cylinder. Explicit analytic form of the transformation $z = z (\zeta;\beta,L_1/L_0)$ is needed and can be obtained, which greatly facilitates the formulation and computation in the ζ-plane.

Vortex Traces and Streamlines

Results of extensive computation for the evolving patterns of point-vortex traces (instantaneous locations), instantaneous streamlines and forces are obtained and studied at successive sequences from the impulsive start until the wing has travelled more than eight (8) chord lengths whence the field is inundated by 1200 point vortices shed. During an earlier period when the wing has travelled no more than one chord length, the traces appear to be simple and regular enough to allow the shape of the rolled up vortex sheets to be unambiguously identified. Subsequently, the sheet pattern is more difficult to recognize as more and more vortices are fed slowly into the pool of eddies which form and break up in turn over the wing. On the other hand, a rather well organized array of vortex clusters resulting from merging of individual vortices of the same polarity are found along the main trail, the latter is recognizable as a partly rolled up vortex sheet. These sequential trace pictures have been shown earlier in Ref. 26 and in fuller detail in Ref. 31, where the effects of using different combinations of the shedding interval $\Delta_1 t$ and integration time step Δt were also examined for this specific case. A sense of convergence has been established from the test with $\Delta_1 t$ and Δt in that well organized features, with scales (even) considerably smaller than the wing chord or flap width, can be consistently identified. We shall not elaborate the resulting details except to show a set of typical results in Fig. 2 on the traces and streamlines at t = 25 corresponding to a travel distance of 6.8 chord length. Notice that the abscissa scale in the trace pattern and the streamline pattern are not the same and that the streamline pattern shown on the lower plot pertains to that observed in a frame fixed to the undisturbed fluid at rest. While the small-scale flow characteristic is uncertain from the trace pattern, the corresponding streamline patterns indicate far greater regularity, revealing well organized eddy structure on the larger scales.

The sequential patterns obtained (not shown) reveal in addition the emergence of a clockwise rotating eddy from the leading-edge flap and counter rotating eddy next to the wing trailing edge, also their interactions leading to their disintegration and departure with the appear-

ance of new eddies.

Resulting Aerodynamic Forces

The history of the normal and tangential force coefficients C_y and C_x resulting from this development is presented as solid curves in Fig. 3, which was computed by a generalized Blasius formula indentical to that given by Graham[30] and accounts for the shed vortices and their locations. The data scatter has been treated neither by filtering nor averaging, yet the cyclic behavior is clearly evident. Also included are C_y values computed from the unsteady surface pressure (in filled circles) which compare reasonably well with those based on the generalized Blasius formula. The difference represents the error in the overall y-momentum balance.

The data shown in Figs. 2 and 3 from an earlier computation in which the vortex separation from leading-edge/apex was assummed not to occur for expediency. Surprisingly, this stipulation is justified a posteriori for the special example under study, since the forward stagnation points are seen to occur at locations consistently close to the apex according to all streamline patterns examined, of which the plot at the center of Fig. 2 is typical.

Comments on Time Averaged Lift

Whereas, a special effort has not been made to identify the best combination of the flap angle and flap size for maximum lift at each angle of attack, Fig. 3 for the example $\beta = 45°$, $L_1/L_0 = 1/3$ at $\alpha = 8.5°$ indicates a peak value of the normal force coefficient C_y to be 3 with an averaged value about 1.75. A time-averaged lift coefficient C_L may also be inferred from C_x and C_y of Fig. 3 to give

$$\bar{C}_L = 1.55$$

which is considerably higher than the theoretical value $C_L = 0.929$ for a symmetric airfoil at the same incidence, allowing no boundary-layer separation. (The laboratory determined C_L value for a symmetrical airfoil depends on Reynolds number and shape, it is about 0.90 for NACA0012 at $Re > 10^6$, and well below 0.90 for a flat plate at all Re.) Even if one were to compute $\bar{C}_L$ based on an increased wing chord by including the width of the vortex flap in the reference wing chord, the coefficient is reduced to $\bar{C}_L = 1.16$, a figure still higher than that of a symmetrical airfoil below stall by nearly 30%.

While the goal of capturing a stationary vortex is far from being reached, the unsteady lift found here has a high enough time-averaged value to warrant a more critical search for a vortex lift development featuring shallower peaks and valleys.

Flat Plate At Moderate Incidence: Counter Rotating Eddy Pairs

The flow about an inclined flat plate provides not only an opportunity to test the present version of the point-vortex method, for which Sarpkaya[31] reported difficulty with incidences below 30°, but brought out certain unique features not found at the larger angle of attack. In this study, an angle of attack $\alpha = 40°$ is chosen in the belief that the inviscid vortex dynamics of the flow will not be seriously affected by boundary-layer breaking away at locations other than the two edges. We study once again the impulsively started motion for this case with the point-vortex method, using a shedding interval of $\Delta_1 t = 0.10$ (corresponding to a distance travelled at 0.25% chord) and an integration time step $\Delta t = \Delta_1 t/20 = 0.005$. The computation extending to beyond 80 corresponding to a twenty chord-length travel, shows a quasi-periodic flow structure in the wing's vicinity reminiscent of the description in the preceding example.

The development of leading-and trailing- edge eddies, their interaction and aerodynamic history are not too different from those observed in the case of a vortex flap, except for a considerably longer period (corresponding to a 7.5 chord travel as compared to 2.75 found in the preceding study) and for the cyclic emergence of distinct pairs of oppositely rotating eddies. The vortex traces (instantaneous positions) displayed in Fig. 4 for $t = 88.5$ show a representative pattern in which two eddy pairs of this kind formed earlier have travelled far out into the field and a third has begun its departure. Consistent with the quasi-periodic flow structure in the wing vicinity not to be detailed here is the history of force components normal and tangential to the plate. The results computed from the generalized Blasius formula[30,31] shown in Fig. 5, from which three peaks and valleys in the normal-force coefficients, spacing roughly 30 t-units (7.5 chord travel) apart, can be discerned. Examination of Fig. 5 with trace and streamline patterns confirms that the eddy pair begins to form shortly after a normal-force maximum. Whereas, the untreated data fluctuate considerably towards the end of the computer run, the nonvanishing tangential component scattered about the axis $C_x = 0$ measuring the error in an overall x-momentum balance is encouragingly small.

Similarity to "Vortex Couple" and Comments

Owing to the large circulation in each of the counter-rotating eddies and the relatively short distance between them, the self-induced velocity of the pair is high enough to become comparable in magnitude with the forward speed of the plate, leading to a path angle signigicantly different from the free-stream flow angle. The behavior of the eddy pair may be described by the classical vortex- pair kinematics as well as by a dipole/

doublet on a global scale. Their occurrence, uncommon among well documented results on vortical wakes behind bluff bodies and plates at normal and large incidence, could be attributed to the shortening of the distance between the upper and lower vortex street, made possible by the reduced angle of attack; this allows an opportunity for the interaction among vortices across opposite rows (streets). Whereas, it is unclear if these eddy pairs are primarily a product of a purely 2-D inviscid analysis, whose existence could very well be affected by 3-D and viscous effects, the omnipresence of strikingly similar features are observed by Couder and Basdevant[36a] and others[36b] in 2-D experiments with soap film. Couder & Basdevant propose the term "vortex couple" with the specific idea that the pair's structure approaches a vorticity distribution within a circular boundary found in Lamb.[37] Apparently the eddy pairs observed here are still far from this proposed form, inasmuch as the two eddies remain at a distinct distance apart. The trajectories as well as the orientation of the pair reported in Ref. [36] are in general accord with data documented in Ref. [31].

In passing, we note from Fig. 5 that the lift coefficient averaged over a long enough period may be inferred to be $\bar{C}_L = 1.32$ in this case, which is far less than the ideal value $2\pi\sin\alpha = 2.15$ for a thin symmetricl airfoil with a fully attached boundary layer, yet is substantially higher than the typical measured value $C_L = 0.7$-0.9 for a symmetrical airfoil or flat plate at $\alpha = 20°$ beyond stall. Whether the latter discrepancy is accountable through the absence of small-scale, 3-D streamwise vorticities and viscous/diffusion effects disallowed in the present analysis remains an interesting aspect for subsequent investigations.

4. APPLICATION TO SLENDER DELTA WINGS

The analysis of the flow next to a pointed slender wing can be reduced to that of an unsteady 2-D motion in the cross-flow plane as is well known;[38] its validity has been stipulated in the earlier works on vortex separations from leading and side-edges of low aspect ratio wings.[17,18,29,39] Numerical simulation of vortex-dominated (steady) flow about delta wings by 3-D full-potential and Euler solvers have received wide attention recently.[40-42] In spite of the lack of upstream influence and other limitations, the slender-wing approach is meritorious for its simplicity which may have great promise to conceptual-design and separation-vortex control applications. Taking into consideration the ad hoc nature of full-potential and Euler codes in their vortex-capturing capability, a successful comparison of these codes with the present approach should lend credence to both. In passing, we pointed out that the validity of the slender-wing theory has never been formally established to allow free-vortex sheets in the cross flow and for a nonvanishing (unit-order) angle of attack. An extension covering both aspects can be formally made.[31]

From the viewpoint of the separation-vortex control, vortex flaps are expected to be more successfully applied to a pointed slender wing than to the preceding 2-D examples, inasmuch as the shed vortices will not drift far away from the expanding wing/body cross section.

Conical Symmetry

As an example for assessing the adequacy of the point-vortex algorithm, a triangular flat plate at incidence is considered. Let y and z be the spanwise and transverse Cartesian variables, the x-y plane be that of the plate and ε be the half-apex angle of the planform. The inviscid slender-wing theory predicts a conical symmetry in which the cross-flow velocity components are invariant along the conical rays $y/x\tan\varepsilon$ and $z/x\tan\varepsilon$ corresponding to $y/U_\infty t\cdot\tan\varepsilon$ and $z/U_\infty t\cdot\tan\varepsilon$ in the transient 2-D problem. On the other hand, the dissipative nature of the numerical errors from the time integration in the point-vortex method may lead to the departure from this symmetry. Thus, the degree to which the conical symmetry can be recovered/captured represents a crucial test of the method.

The formulation indicates a similitude controlled by

$$\frac{\tan\varepsilon}{\tan\alpha}$$

which measures the expansion rate of the width of the flat plate. In the computation, nascent vortices are formed next to the leading edges of the linearly expanding plate during the interval $\Delta_1 t$ and are shed as free vortices at the interval end.

In Figs. 6-8, we examine the instantaneous vortex traces, cross-flow streamlines and the corresponding surface pressure at successive time levels corresponding to different x-stations on the wing. Conical variables based on the half-width of the expandingg plate are used so that the approach to conical symmetry can be readily identified. The particular data set shown were generated for an angle of attack $\alpha = 20°$ and a sweep angle 70°, i.e. $\varepsilon = 20°$. The four graphs in Figs. 6,7 describes the cross flow at four successive time levels corresponding to x-stations 50,100,150 and 200, with N = 50,100,150 and 200 shed vortices respectively from each edge. In the computation, the shedding did not begin precisely at the apex but started at a station where the span is 1/ 200 of the span at x = 200. In spite of this, and the other uncertainties mentioned, conical symmetry is approached closely after N = x = 50, as is clearly evident from Figs. 24,25. The conical symmetry is recovered well on a scale comparable to the local half-span characterizing the cross flow, but becomes ambiguous for features with a scale much smaller than 10% span. This is brought out more clearly in the cross-flow streamlines (Fig. 25), for which contour plots employing a uniform 61x81 mesh were used. It must be pointed out that the difference of the stream function between neighboring streamlines assigned to the plots

are different for different stations, since the original computations were not performed in the conical variables; this will not affect, however, the streamlines reaching the plate, for which the stream function is taken to be zero. The agreement among the contours in the four stations pertaining to this particular streamline is surprisingly good. Spanwise surface pressure distributions at eleven stations between x = 50 and x = 200, computed from velocity potential data are correlated in Fig. 8. The very encouraging correlations in this and the preceding figures, as well as similar correlation/comparison of computed results for other apex angle and angle of attack (not shown) establish also a degree of convergence of the method with regards to the number of shed vortices, in agreement with the conclusion made earlier in §3.

Comparison

Comparisons can be made with corresponding data obtained by Hoeijmaker & Rizzi[42a,b] who succeeded in producing shed vortices from delta wings using 3-D steady Euler and fullo-potential codes. The data of Refs. [42a,b] show very strong upstream influence of the trailing edge, causing significant departure from the conical symmetry. At a station sufficiently far upstream on the wing, however, the slender-wing theory should apply and the conical symmetry prevails. Figure 8 presents the comparison of the surface-pressure coefficient from the slender-wing, point-vortex method (in dots) and the corresponding results from a Euler solver (in heavy solid curves) and a full-potential solver (in light solid curves) taken from the most upstream station (30% root chord) given in Hoeijmaker's[42b] for a delta wing with $\varepsilon = \alpha = 20°$. Considering the uncertainties in the Euler and full potential code indicated earlier, the comparison must be regarded as being rather encouraging. The slight pressure rise on the upper surface towards the leading edge revealed by the dotted curves are well converged results of the point-vortex method, and the absence of such features in the Euler/full-potential data could very well result from the lack of resolution therein.

For a delta planform with a straight trailing edge, the slender-wing approach is obviously inadequate for its failure to account for the upstream influence. However, smoothing out the sharp corners of the triangular planform at the trailing edge, i.e. fairing the wing tips as in the Concorde, should render a much smoother load transition at the tail, hence a lesser upstream influence. Interestingly, in a recent experiment with a slender conical wing made up of two right triangles (cf. Figs. 1,7 of Ref. [44]), Spedding et al. found the growth of the leading-edge separation vortex to remain linear up to the 92% root chord. Their result supports the contention that a relatively minor planform alteration near the trailing edge may favorably reduce the upstream influence, hence the error in the slender-wing analysis.

5. CONCLUDING REMARKS

Two types of generic, vortex-dominated, unsteady flows of aerodynamic interest have been studied with a point-vortex method: I. flat plates at moderate incidence, with and without a vortex flap, II. the cross-flow and vortex-lift development on a slender delta wing. The method requires a means of generating free vortices which is provided by an algorithm of growing nascent vortices near a salient edge based on a force-free model. Whereas fascinating orders and chaos in the vortex traces abound when examined on extremely small scales, our solutions with the free-vortex population ranging from a hundred to a thousand bring out consistently the well organized evolving structure on the global spatial and time scales, as well as considerably small scales with which emergence and growth of small eddies/ blobs and their interactions can be unambiguously discerned. Thus, the study has demonstrated the merits and limitations of an approach to numerically simulating two-dimensional aerodynamic flows, which is computationally intensive but theoretically and algorithmically simplistic; the study promises a more rational alternative to existing vortex methods in the treatment of vortex shedding from sharp edges.

To fully attain the objective of enhancing and controlling the vortex lift, additional studies within, as well as beyond, the present framework are needed; the specific aspects requiring additional analyses are apparent from the foregoing presentation and Refs. [26,31]. We cite, in particular, that the results on the unsteady lift on a flat plate at 8.5° incidence and 45° flap with a seemingly high $\bar{C}_L = 1.55$ calls for an improvement for its excessively large peak amplitude of variation, and that the significance of the "eddy couple" noted in §3 requires a closer scrunity for the 3-D and viscous effects. Whereas, the potential of the slender-wing approach to the steady and unsteady vortex flap problem is apparent from §4, the lack of upstream influence represents a major weakness in the slender-wing approach and must be investigated to determine if the planform contouring near the trailing edge may reduce the influence in question.

REFERENCES

1. Cox, J., Soaring 37, 20 (1973).

2. Walton, D., Soaring 38, 26 (1974).

3. Saffman, P.G. & Saffield, J.S., Studies in Appl. Math. 57, 107 (1977).

4. Saffman, P.G., J. Fluid Mech. 63, 225 (1974).

5. Saffman, P.G. & Tanveer, S., J. Fluid Mech. 154, 351 (1984).

6. Rossow, V.J., J. Aircraft 15, 618 (1978).

7. Huang, M.K. & Chow, C.Y., AIAA J. 20, 292 (1982).

8. Chow, C.Y., Huang, M.K. & Yan, C.Z., AIAA J. 23, 657 (1985).

9. Lamar, J.E. & Campbell, J.F., Aerospace America, Jan. 1984.

10. McCrosky, W.J., Annual Rev. Fluid Mech. 14, 285, (1982).

11. Meuller, T.J., "Low Reynolds Number Vehicles", AGARDograph 288 (1985).

12. Cheng, H.K. & Lee, C.J., "On Massive Laminar Separation and Lift Anomalies in Subcritical Re-Range", Proc. International Conf. Aerodynamics at Low Reynolds Numbers, Royal Aero. Soc., London, Oct. 16,17 (1986).

13a. Saffman, P.G. & Baker, G.R., Annual Rev. Fluid Mech. 17, 95 (1985).

13b. Anderson, C. & Greengard, C. SIAM J. Numerical Analysis 22, 413 (1985).

14. Christiansen, J.D., J. Comp. Physics 13, 363 (1973).

15. Fink, P.T. & Soh, W.K., Proc. R. Soc. London, Ser. A 362, 195 (1978).

16. Kuwahara, K. & Takami, H. Turbulence and Chaotic Phenomena in Fluids (ed. T. Tatsumi), Elsevier Sci. Pub. (North-Holland), 377 (1984).

17. Edwards, R.H., J. Aero. Sci. 21, 134 (1954).

18. Cheng, H.K., J. Aero. Sci. 21, 212 (1954).

19. Rott, N., J. Fluid Mech. 1, 111 (1980).

20. Leonard, A., J. Comp. Phys. 37, 289 (1980).

21. Moore, D.W., SIAM J. Sci. Statics Comp. 2, 65 (1981).

22. Aref, H. & Siggia, E.D., J. Fluid Mech. 109, 435 (1981).

23. Krasny, R., J. Fluid Mech. 167, 65 (1986).

24a. Aref, H., J Fluid Mech. 143, 1 (1984).

24b. Aref, H., J. Fluid Mech. 173, 15 (1986).

25. Edwards, R.H. & Cheng, H.K., J. Fluid Mech. 120, 143 (1982).

26. Cheng, H.K., Edwards, R.H. & Jia, Z.X., Studies in Vortex Dominated Flows, (ed. M.Y. Hussaini & M.D. Salas) 195, Springer-Verlag (1985).

27. Milne-Thompson, L.M., Theoretical Hydrodynamics, MacMillan (1967).

28. Batchelor, K.G., An Introduction to Fluid Dynamics, Cambridge Univ. Press (1980).

29. Brown, C.E. & Michael, W.H., J. Aero. Sci. 21, 690 (1954).

30. Graham, C.E. & Michael, W.H., J. Aero. Sci. 21, 690 (1954).

31. Jia, Z.X., Simulation of Vortex Dominated Aerodynamic Flows by a Point-Vortex Method, Univ. So. Calif. Sch. of Engineering Dissertation (1987).

32. Sarpkaya, T., J. Fluid Mech. 68, 109 (1975).

33. Wu, J.C. & Hu-Chen, H., AIAA paper 2184 (1984).

34. Chow, C.Y. & Sheen, Q.Y., Proc. AFOSR Workshop II Unsteady Separated Flow, U.S. Air Force Academy (July 28-30, 1987).

35. Moore, D.W., Mathematica 23, 35 (1976).

36a Couder, Y. & Basedevant, C. J. Fluid Mech. 173, 225 (1986).

36b Lesieur, M., Comte, P., Chollet, J.P. & Roy, P.L., Proc. NATO Workshop Conf. on Math. Modeling in Combustion & Related topics, NATO-ASI Series, Martinus Nijhoff Pub. (1987).

37. Lamb, H., Hydrodynamics, Cambridge Univ. Press (1932).

38. Jones, R.T., NACA TR 835 (1946).

39. Mangler, K.W. & Smith, J.H.B. Proc. Roy. Soc. A251, 200 (1959).

40. Rizzi, A. & Eriksson, L., J. Fluid Mech. 153, 275 (1985).

41. Murman, E.M. & Powell, K.G. Studies of Vortex Dominated Flows (ed. M.Y. Hussaini & M.D. Salas) 270, Springer-Verlag (1985).

42. Hoeijmakers, H.W.M. Studies of Vortex Dominated Flows (ed. M.Y. Hussaini & M.D. Salas) 223, Springer-Verlag (1985).

43. Kandil, O.A. & Yates, E.C., AIAA J. 24, No. 11, 1729 (1986).

44. Spedding, G.R., Maxworthy, T. & Rignot, E., Proc. AFOSR Workshop II Unsteady Separated Flow, U.S. Air Force Academy (July 28-30, 1987).

FIGURE CAPTIONS

Fig. 1. Illustration of trajectories of nascient and free vortices, representing a vortex sheet from a salient edge.

Fig. 2.   Instantaneous positions of point
           vortices and corresponding stream-
           lines observed at t = 25 in two
           reference frames for a plate at
           8.5° angle of attack with the
           vortex flap deflected at 45°.
           The chord ratio of the flap and
           plate is 1/3. The motion is gen-
           erated by in impulsive accelera-
           tion to uniform speed.

Fig. 3.   Histories of normal and tangential
           force components on the inclined
           plate with a vortex flap after an
           impulsive start. Conditions are
           the same as in the preceding fig-
           ure.

Fig. 4.   Pattern of instantaneous point-vortex
           positions at t = 85.70 after an
           impulsive start of a flat plate
           at 20° angle of attack. Note:
           eddy pairs are far above the
           plate.

Fig. 5.   The history of the normal and
           tangential force components of
           the flat plate after the impul-
           sive start. Conditions same as
           in preceding figure.

Fig. 6.   Patterns of point-vortex distri-
           bution in the cross-flow plane
           of a flat delta wing with a ratio
           $\tan\epsilon/\tan\alpha = 1$ at stations 50, 100,
           150 and 200. Data are presented
           presented in the plane of $y/x \tan\epsilon$
           $z/x \tan\epsilon$.

Fig. 8.   Correlation of surface-pressure
           coefficients on the delta wing at
           eleven successive stations. Con-
           ditions same as in preceding fig-
           ure.

Fig. 9.   A comparison of the slender-
           wing, point-vortex method
           (in dots) with Euler solver
           (in heavy solid curves) and
           full-potential solver (in
           thin solid curves) in surface
           pressure for a delta wing with
           half-apex angle 20° and angle of
           attack 20°.

                    CORRIGENDA

Page 5, right column, 5th line from
bottom: replace "Fig. 25" by "Fig. 7".

Page 7, right column, Ref. 30 should
be corrected to read: "Graham, J.M.R.,
J. Fluid Mech., 97, 133 (1980).

Page 8, Caption for Fig. 7 should be
added to read: "Fig. 7. Cross-flow
streamline patterns for the flat delta
wing at stations 50,100,150 and 200.
Conditions same as in preceding figure.

Fig. 1

REY NO. = INFINITY
T = 25.00
GM1 = 19.45910
GM2 = -13.82915
DTO(DT) = 0.05(.010)
RANGE(X)= (0.0, 8.0)
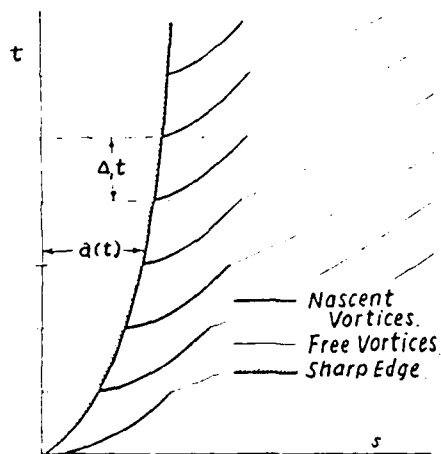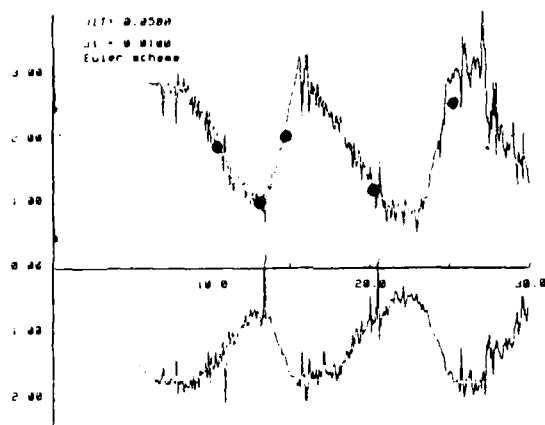
T = 25.00
ALPH = 8.50

Fig. 2

Fig. 3

Ang of At 20.00
T = 85.70
Gm1 = 66.95643
Gm2 = -67.26337
d(O(dt) =0.10(0.005)
RANGE(X)= (-1.0,20.0)

Fig. 4

Fig. 5

297
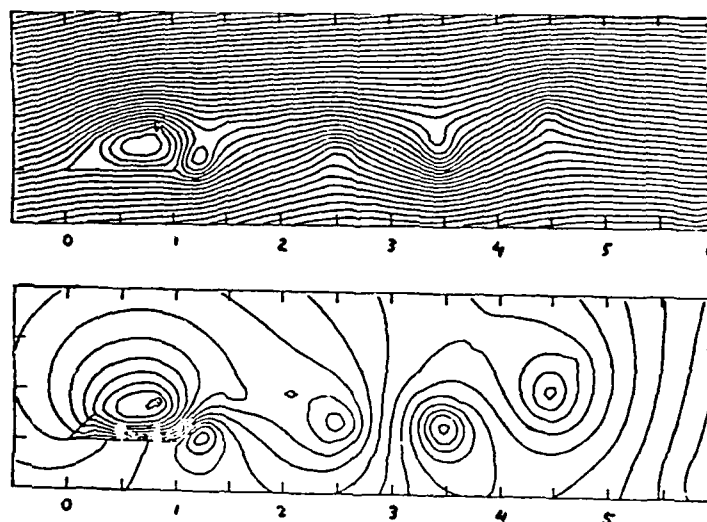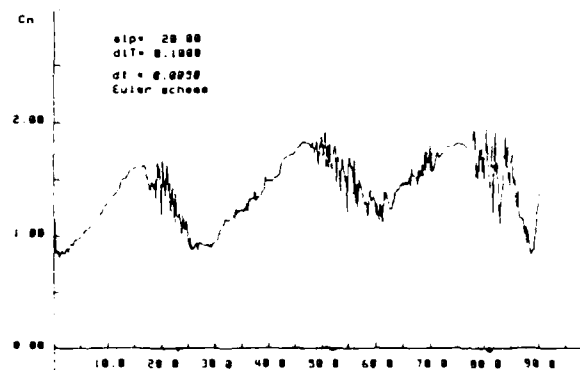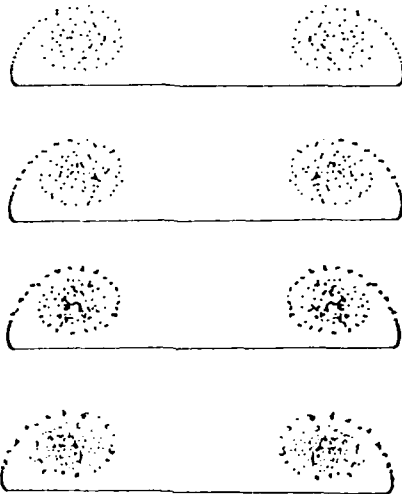
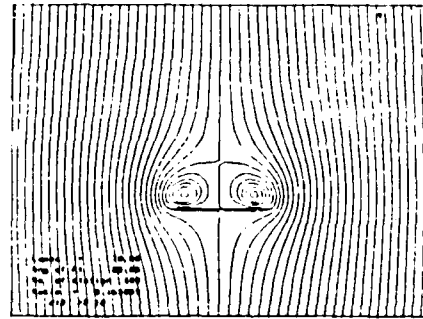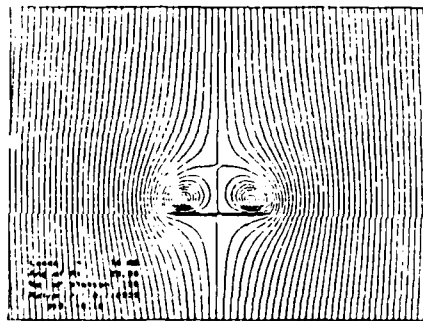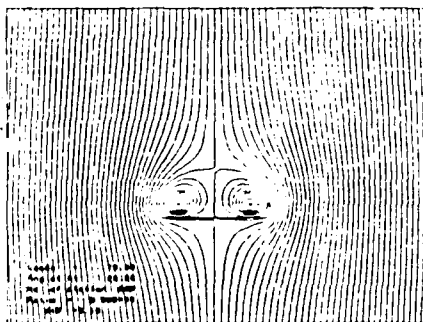Fig. 6
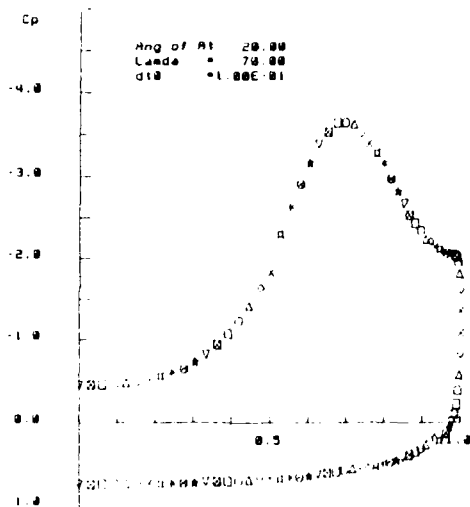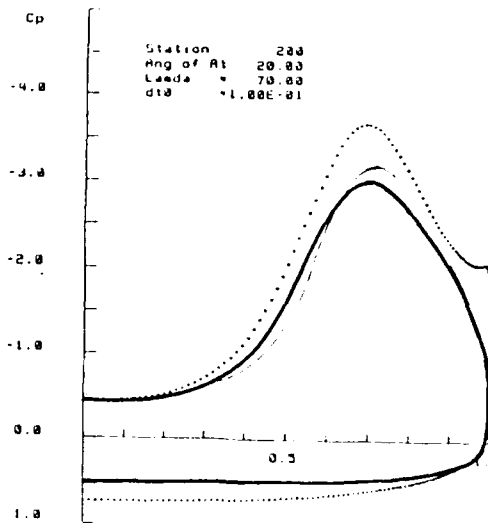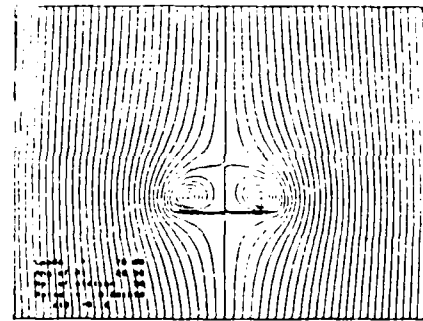
Station 50

Station 100

Station 150

Station 200

Fig. 8

Fig. 9

Fig. 7

298

ON UNSTEADY FLOW STRUCTURE FROM SWEPT EDGES SUBJECTED TO CONTROLLED MOTION*

D. Rockwell, R. Atta, C.-H. Kuo, C. Hefele,
C. Magness and T. Utsch
Department of Mechanical Engineering and Mechanics
354 Packard Laboratory #19
Lehigh University
Bethlehem, Pennsylvania 18015

ABSTRACT

This investigation addresses active control of the leading-edge vortices formed from delta wings and wing segments. A variety of modifications of the flow structure are characterized with quantitative, global flow visualization in conjunction with LDA techniques.

INTRODUCTION

The structure of flow past a stationary delta wing has been studied extensively over the past few decades. Early investigations established that flow separation from the leading-edge of the wing gives rise to a spiral-vortex sheet on the upper surface of the wing; the consequence of this vortex pattern is an increase in lift, above that which would occur without leading-edge separation (e.g., Lee[1]; Ornberg[2]; Elle[3]). The study of Kuechemann[4], which involves a nonlinear lifting-surface theory, describes this effect. More recent studies (Kuechemann[5]; Hoeijmakers[6]; Rizzi et al[7]; Woodson and DeJarnette[8]) delineate details of the primary-secondary vortex system adjacent to the leading-edge and the corresponding separation and reattachment lines.

The unsteady flow structure on a delta wing subjected to controlled motion has received less attention. The investigation of Lambourne et al[9] demonstrated the concept of phase shift between development of the vortex pattern and the stepwise motion of the wing in the plunging mode. For the case of simple harmonic motion in the pitching mode, Gad-el-Hak and Ho[10] observed an analogous phase shift of the growth-decay cycle of the leading-edge vortices. This phase shift, or hysteresis, during the course of the wing oscillation cycle was characterized in terms of height or thickness of the dye blob marking the vortex; the degree of hysteresis was found to be a strong function of reduced frequency. Further aspects of the unsteady three-dimensional structure on various wings are addressed in the subsequent investigations of Gad-el-Hak and Ho[11,12]. They emphasize the importance of mutual induction between leading- and trailing-edge vortices in determining the overall flow structure.

Central to the unsteady structure of the leading-edge vortices is the time-dependent development of the vortex core along its streamwise extent and its eventual breakdown. This breakdown is characterized by abrupt transition from a jet-like to a wake-like core of the vortex, accompanied by a substantial increase in turbulence activity. Such vortex breakdown has been investigated for flow past a variety of stationary wing configurations, as reviewed by Wedemeyer[13]. For nonstationary (sinusoidal) wing motion, Atta and Rockwell[14] observed: occurrence of the maximum breakdown position of the core near the maximum angle of attack, rather than near the minimum value; substantial overshoot of the core breakdown length relative to its steady counterpart; and existence of the vortex core only over a fraction of the oscillation cycle. There have been extensive and insightful studies of vortex breakdown in various types of axisymmetric tube arrangements as, for example, described by Garg and Leibovich[15], Escudier[16] and Sarpkaya[17]. These, as well as other experimental studies and a wide range of theoretical approaches beyond the scope of this introduction are incisively assessed by Leibovich[18,19]. In essence, the investigations of vortex breakdown addressed therein focussed on steady inflow conditions. Exceptions include the investigations of Lambourne[20] and Sarpkaya[21] who reveal interesting aspects of transient vortex development and overshoot of the vortex breakdown position.

There are a number of unexplored features of unsteady vortex flows on oscillating delta wing and flap arrangements. These issues include: flow structure of the vortex development and breakdown; evolution of the mean and unsteady velocity fields of the vortex in the pre- and post-breakdown regions, including alteration of the velocity eigenfunctions and spectral energy transfer; and the effects of mutual interference between flap/wing combinations. Particularly helpful for investigating these aspects are quantitative flow visualization techniques which, when employed in conjunction with laser-Doppler and pressure measurement techniques, can provide both local and global views of the evolving flow structure.

EXPERIMENTAL SYSTEM AND TECHNIQUES

All experiments were carried out in one of the three water channel systems custom-designed for unsteady, separated flows. The cross-sectional areas of the test sections of these channels ranged from 1.5 ft^2 to 6 ft^2. In order to allow observation of the flow from an arbitrary

---

perspective, all channels of the test section were made entirely of glass or Plexiglas. Furthermore, in the case of the largest channel, the entire system upstream and downstream of the test section is made of PVC and bronze, in order to preclude problems with corrosion. The chord C length of the delta wings ranged from $C \approx 50.8$ mm to $C \approx 508$ mm and the corresponding Reynolds number range extended over $5.8 \times 10^3 \leq U_\infty C/\nu \leq 3.9 \times 10^4$. Values of Re up to Re $\approx 4.5 \times 10^5$ are attainable in the large-scale water facility, while still allowing reasonably low absolute frequencies (~ 0.5 Hz) to be employed to attain high values of reduced frequency. This concept simplifies the mechanical forcing of the wing, as well as data acquisition. In all cases, the viewing surface was the flat machined surface of the wing; the opposite side of the wing was machined at an angle of $\alpha = 10^\circ$ to 20°, depending upon the wing under consideration. All wings were of Plexiglas. For the technique of illumination by laser-induced reflection, the wing surface was machined to a one micron finish. In cases where diffuse stroboscopic lighting was employed, the wing was spray-painted flat black for employment of the hydrogen bubble technique and flat white for use of the dye injection method of visualization.

The experimental objectives require employment of laser-Doppler anemometry techniques in conjunction with quantitative flow visualization in order to characterize flow structure. Eventual measurements of the unsteady surface pressure will allow establishment of a direct relationship between the instantaneous loading and the instantaneous flow structure. The first stage of laser-Doppler measurements described herein were made with a single channel two watt Argon-ion system with a beam expander to optimize signal to noise ratio. Quantitative flow visualization involved tracking of hydrogen bubble markers. The intention of these tracking techniques is to circumvent the many fallacies associated with interpretation of traditional dye and smoke injection techniques (Lusseyran et al[22]; Hama[23]). Preliminary pressure measurements have been carried out with a high sensitivity Kulite transducer coated with a Paralene film to inhibit corrosion; alternately, a PCB transducer operating on the piezo electric principle was also employed. Further details of these techniques are described by Rockwell et al[24,25].

A primary objective of this program is to develop an integrated active control system that allows forcing of wings and wing segments with arbitrary functions and simultaneously accommodates acquisition of instantaneous quantitative flow visualization, laser-Doppler, and pressure information. The first version of this system has been completed. Forcing is provided by Superior Electric stepping motors with appropriate gear reduction; or with Compumotors running at ten to twenty thousand steps per revolution. These motors are interfaced with a Zenith-241 computer. Also interfaced with the computer are: the output of the LDA system; the marker pulse generator and switch system for producing grids of visualization marker at a desired phase of the wing motion; and the microprocessor linked to the servomotor drive system that will eventually translate the laser scanning system (in the direction of the flow) in order to allow three-dimensional sweeps of the

flow structure.

Illumination of the flow structure is achieved by a two-watt Argon-ion laser (with a multi-line mirror holder) impinging upon a system of mirrors. This system allows a rotating mirror to sweep the laser at an arbitrary angle with respect to the freestream while the entire optical train is translated in the freestream direction. Alternately, diffuse illumination can be employed; it involves stroboscopic lights having a power of 90 watts, a flash duration of ten microseconds, and a repetition frequency of 120 Hertz. Or, a higher powered strobe having an intensity of 8.3 Joules at 120 cycles per second was employed. Recording of the visualization images was achieved with either one or two video cameras having a zoom lens capability. Each of the two video cameras could be connected to the mainframe of the video system and the corresponding images displayed simultaneously using the split-screen capability of the mainframe.

Figures 1a and 1b show simplified overviews of the two basic types of image acquisition: a dual-view method (Figure 1a); and a single-view method (Figure 1b). In concept, each of these techniques provides the capability for tracking visualization markers in three-dimensional space.

For the dual image method of Figure 1a, stroboscopic lighting is employed. The lights are angled with respect to the surface of the bubble markers in order to provide optimum reflection when viewed through the cameras. Mirror arrangements located external to the test section, as well as sufficiently far downstream of the region of interest so as to preclude interference, were employed to facilitate viewing the flow structure from various perspectives. Various locations and orientations of 25 micron platinum wires allow generation of hydrogen bubbles. In the arrangement shown in Figure 1a, the wire flies at the same velocity as the apex of the wing; this is accomplished by mounting the wire between two probe supports that are rigidly attached to the pitching axis of the wing. The orientation of the wire is adjusted to allow examination of either: the core flow, by ensuring continuous injection of marker at or near the apex of the wing; or, the exterior flow, by injecting markers from a wire in the plane of the wing at the apex (Rockwell et al[24,25]).

For the single image method of Figure 1b, the principle is to employ the localized injection of bubble markers of defined width and length in conjunction with a laser sheet (or sheets) of finite thickness in order to determine the velocity field. As opposed to the previous technique, only a single video camera is employed with various mirror arrangements in order to obtain the desired cross-sectional view of the flow image. This image is produced by laser-induced reflection from the hydrogen bubble markers. By use of an optically transparent wing, it is possible to view both sides of the wing simultaneously. Bubble markers are generated upstream of the wing from a single segmented wire, arrangements of them, or a wire grid as schematically portrayed in Figure 1b. The basic concept of this technique is that by generating bubble markers of defined frequency and duration and employing a laser sheet of finite thickness, estimates of the velocity field can be made from a single view.
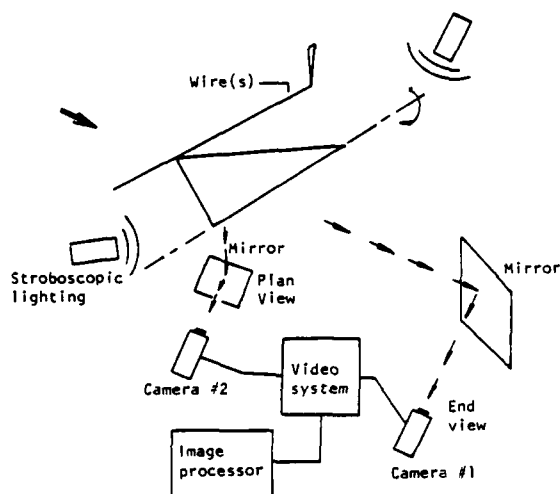
Figure 1a: Dual image technique for tracking three-dimensional flow structure.
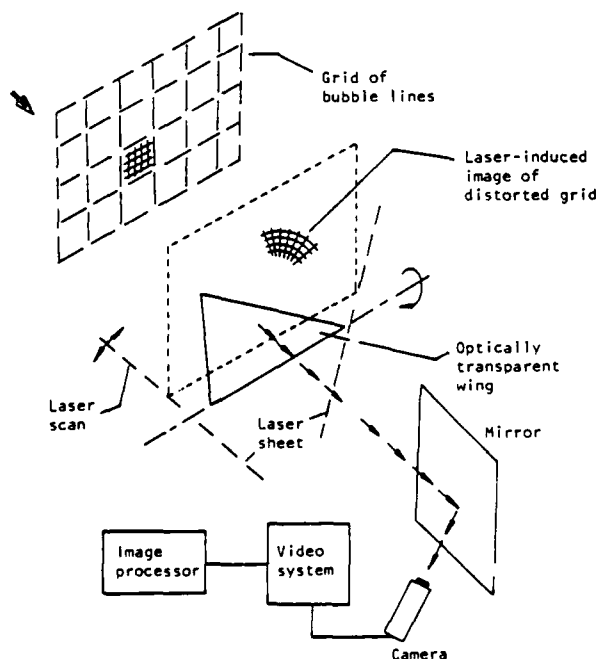

Figure 1b: Single image technique for determining two- and three-dimensional flow structure.

In order to facilitate quantitative interpretation of flow visualization images, a variety of image processing techniques have been developed. For overviews of these, the reader is referred to Rockwell et al[24,25] and Smith[26]. In short, quantitative techniques for characterizing the unsteady process of bursting in a turbulent boundary layer (Lu and Smith[27]) and vorticity in an unstable wake flow (Lusseyran and Rockwell[28]) have been employed. In addition, efforts have been focussed on the following techniques: reconstruction of three-dimensional flow structure using a phase-reference technique (Ongoren et al[29]); ensemble-averaging between images and correlation within or between images (Kerstens and Rockwell[30]); and Fourier discriptor techniques for pattern recognition (Gumas and Rockwell[31]).

QUANTITATIVE FLOW VISUALIZATION

Flow past a stationary delta wing having a sweep angle $\lambda = 45^o$ and inclined at an angle of attack $\alpha = 15^o$ with respect to the freestream produces the flow structure given in Figure 2a; the photos show only a portion of the flow field. In this case, the wing is made of brass, requiring modification of the single image technique of Figure 1b; use of an appropriate mirror arrangement allowed simultaneous views of the upper and lower sides of the wing. Bubbles were generated continuously from the grid located upstream of the wing, and the laser was translated to various distances x from the apex in order to provide the desired images. It should be emphasized here, and in subsequent photos of this type, that the thickness of the bubble sheets forming the grid pattern is of the order of 25 microns. Use of high gain on the video system, for purposes of illustration, greatly exaggerates the actual thickness. In this sequence of photos, the direction of circulation about the wing is readily apparent. Moreover, it clearly increases in the streamwise direction.

By tracking each of these nodes of the bubble grid in three-dimensional space, and making use of photos in addition to those of Figure 2a, it is possible to determine the three-dimensional streamline pattern of the flow. This is accomplished by digitizing the node locations, then using CROSS THREE-D of the Unigraphics CAD software system. The three-dimensional pattern is displayed on a McAuto D-100 C color terminal allowing rotation of the three-dimensional image in real time. Figures 2b through 2d show selected results. In Figure 2b, an end view of the streamline pattern is illustrated. Figure 2c shows an end view of stream surfaces, formed by connecting streamlines whose upstream positions are located in defined vertical planes prior to encounter with the wing. Figure 2d shows the same stream surfaces from a different perspective. Various combinations of horizontal surfaces, not shown here, were also constructed. With this type of streamline information, it is possible, in concept, to proceed with calculation of the corresponding velocity field and circulation. Occurrence of flow separation along the upper surface of the wing (see photo corresponding to x/C ≈ 0.8 in Figure 2a) produces inaccuracies of the streamline pattern in and immediately around that region. Moreover, there is inadequate spatial resolution there that
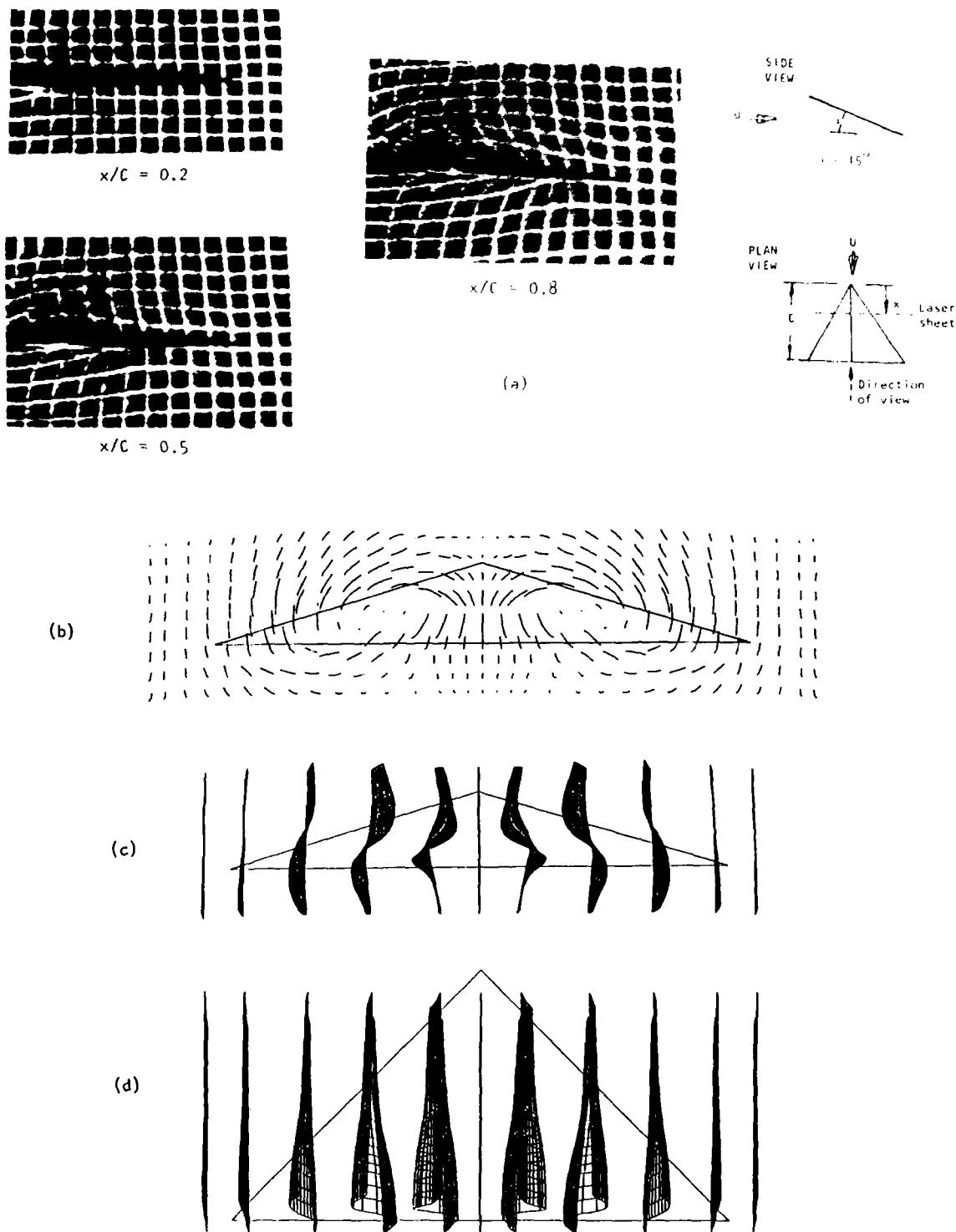
301

Figure 2: (a) End view of distorted grid of hydrogen bubble lines (actual thickness of 25 microns greatly exaggerated by high video gain); (b) end view of streamline pattern obtained by tracking nodes of distorted grid in three-dimensional space and connecting them with CROSS-3-D CAD technique; (c) end view of stream surfaces obtained from connecting streamlines in initially vertical plane before encounter with the wing; and (d) an additional view of (c) from an elevated perspective.

precludes calculation of the velocity and vorticity distributions. This technique for determining the flow structure exterior to the vortex core is currently being extended to unsteady flows past oscillating delta wings.

In order to determine the streamline pattern and velocity field of the vortex core, it is most effective to generate markers locally from a single wire or an arrangement of wires located within the core itself. The photo of Figure 3a shows representative markers from a single, segmented bubble wire located in the core of a vortex on a delta wing having a sweep angle $\lambda = 75°$, an angle of attack $\alpha = 20°$, and at a streamwise location x/C = 0.87. In the case of steady flow, translation of the laser sheet in the streamwise direction provides a family of marker locations in three-dimensional space which, in turn, can be connected to give the streamline pattern of the flow. Note the distortion in the marker pattern on the left-side of the photo as well as to the right of the apparent center of the vortex. These distortions are caused by the shear layer that originally separated from the edge of the wing. Averaging provides the streamline pattern shown in Figures 3b through 3d. In Figure 3b, the view is in the upstream direction along the axis of the center of the vortex. Figures 3c and 3d show this streamline pattern at different orientations; in both of these cases, both the streamlines and lines corresponding to constant streamwise coordinate are displayed.

(a)
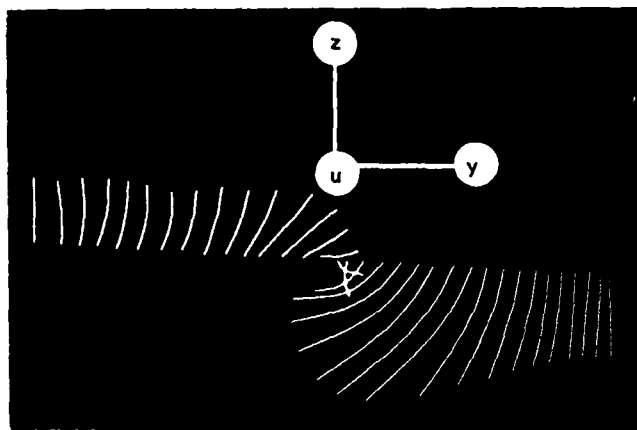
(b)
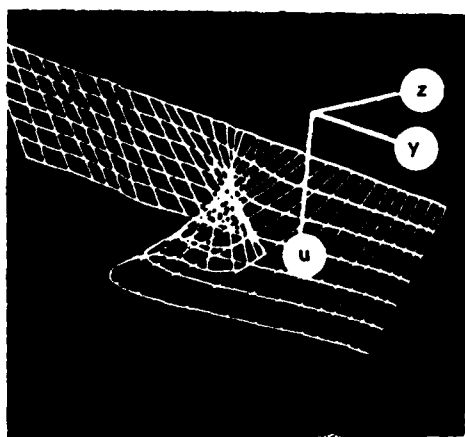
(c)
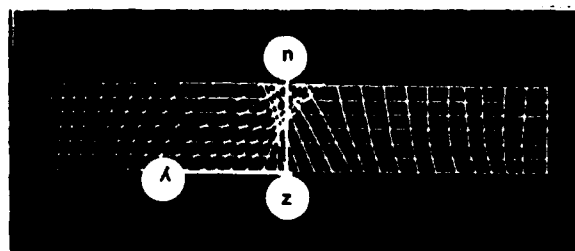
(d)

Figure 3: (a) Elements of bubbles generated from two different segmented wires located in vortex core; (b) end view of streamlines obtained by translating laser sheet in streamwise direction and tracking bubble elements in three-dimensional space; (c) pattern of (b) from another perspective including lines representing constant values of streamwise coordinate; and (d) view of (c) from another perspective.

303
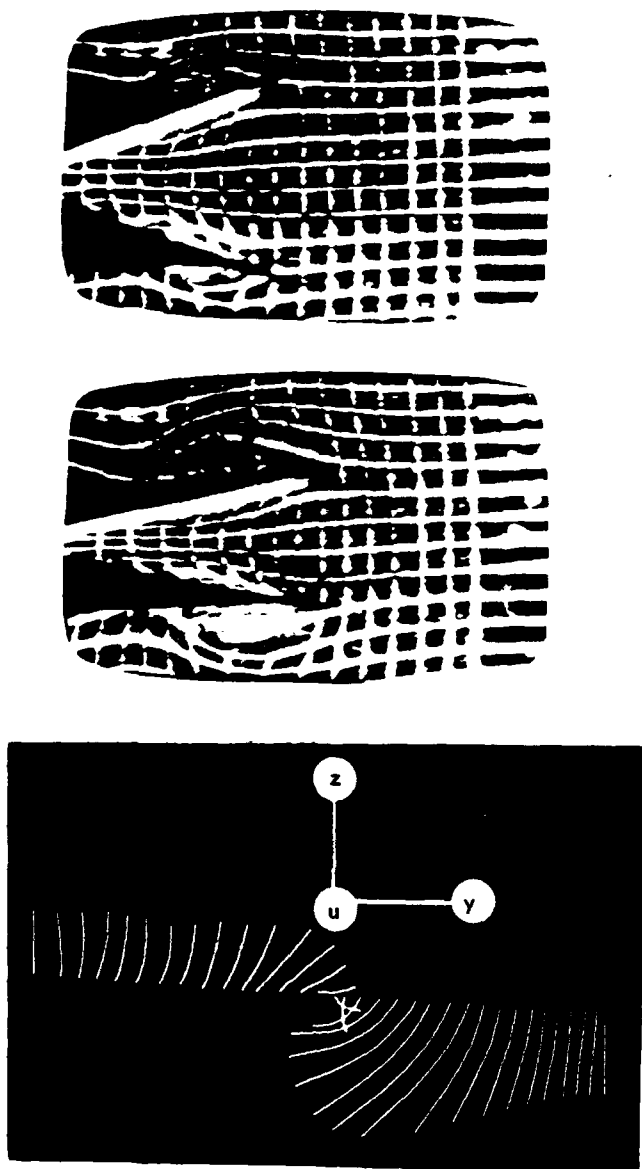
(b)

Figure 4: (a) End view of delta wing segments oscillating about a common axis in harmonic version of clap and fling maneuver, with top photo taken at x/C = 0.7 and bottom photo x/C = 0.8 and a time delay between photos corresponding to the transit time of the freestream between two stations (bubble sheets have a thickness of 25 microns, greatly exaggerated here due to video gain); (b) excerpt of upper half of velocity field.

Using the general types of techniques shown in conjunction with Figures 2 and 3, it is possible to determine directly the velocity field by pulsing the voltage applied to the bubble wires, such that discrete markers are generated. Such methods can be applied to both steady and unsteady flows, and efforts are continuing in this direction in our laboratory. In fact, distributions of axial and swirl velocity components obtained for the conditions described in conjunction with Figure 3a show a reasonable approximation to the expected distributions.

Determination of the instantaneous velocity field in the cross-stream plane is of obvious importance in determining the circulation for various wing-flap or flap-flap arrangements. The photos in Figure 4a correspond to a simple harmonic version of the clap and fling motion of two delta wing segments (or "flaps") oscillating about a common axis, corresponding to the center of the corresponding stationary delta wing. The top photo was taken at x/C = 0.7 and the bottom one at x/C = 0.8. The wing segments are in the process of closing, and the time shift between the two photos was calculated to correspond to the time required for a defined bubble segment to travel between x/C = 0.7 to 0.8 in the freestream region. The axial velocity component at any location in the cross-section can be estimated by pulsing the front of the bubble grid and calculating the "glow time" corresponding to passage of this pulsed front of bubbles through the laser sheet of finite thickness. Outside the vortex core, the axial velocity deviates relatively little from the freestream value, simplifying the tracking process. For the present purposes, it is the circulation about the vortex core that is of primary interest. The velocity field corresponding to the upper half of the flow is shown in Figure 4b. It was obtained by averaging the node displacements about the plane of symmetry of the wing segments, then carrying out a linear interpolation. Circulation calculated using two different circuits differed by less than 3%, thereby suggesting that the circuit for determining the circulation was exterior to the vortex core. The dimensionless circulation corresponding to the pattern of Figure 4a is about one-half that generated in a ramp-type fling of a two-dimensional wing system (Spedding and Maxworthy[32]) with no mean flow in the axial direction.

PHASE SHIFT AND HYSTERESIS OF VORTEX CORE DEVELOPMENT AND BREAKDOWN

When a delta wing is pitched about its trailing-edge in sinusoidal motion, examination of the flow structure over the range of reduced frequency $0.025 \leq K \leq 1.7$, and mean angle of attack $5^\circ \leq \alpha \leq 20$ shows that there are two fundamental types of vortex development during the course of an oscillation cycle. At low reduced frequencies, the core development is of the form shown in the left column of photos of Figure 5, while at higher reduced frequency, the form is as shown in the right column. Considering first the case of low reduced frequency at $\alpha = 9^\circ\uparrow$, the dye has been swept from the mid-portion of the wing to a region along its leading-edge. At $\alpha = 15^\circ\uparrow$, onset of vortex core development is evident in the right portion of the photo, and at $\alpha = 18^\circ\uparrow$ and $19^\circ\uparrow$, this core development progresses in the upstream direction towards the apex.

304

On the other hand, at higher reduced frequency, as shown in the right column of Figure 5, the scenario is as follows. At $\alpha = 15°\!\uparrow$, the dye still flows along the mid-portion of the wing. At $\alpha = 18°\!\uparrow$, it has been abruptly swept to the leading-edge and at $\alpha = 19.5°\!\uparrow$, there is onset of vortex core formation characterized by ejection of the leading-edge of the dye marker from the pocket of dye. At $\alpha = 20°$, this ejected leading-edge of the core has moved to the right-edge of the photo. There are many additional features of this vortex core development and breakdown, which have been visualized using various dye marker and flying wire (see Figure 1a) techniques. They will be
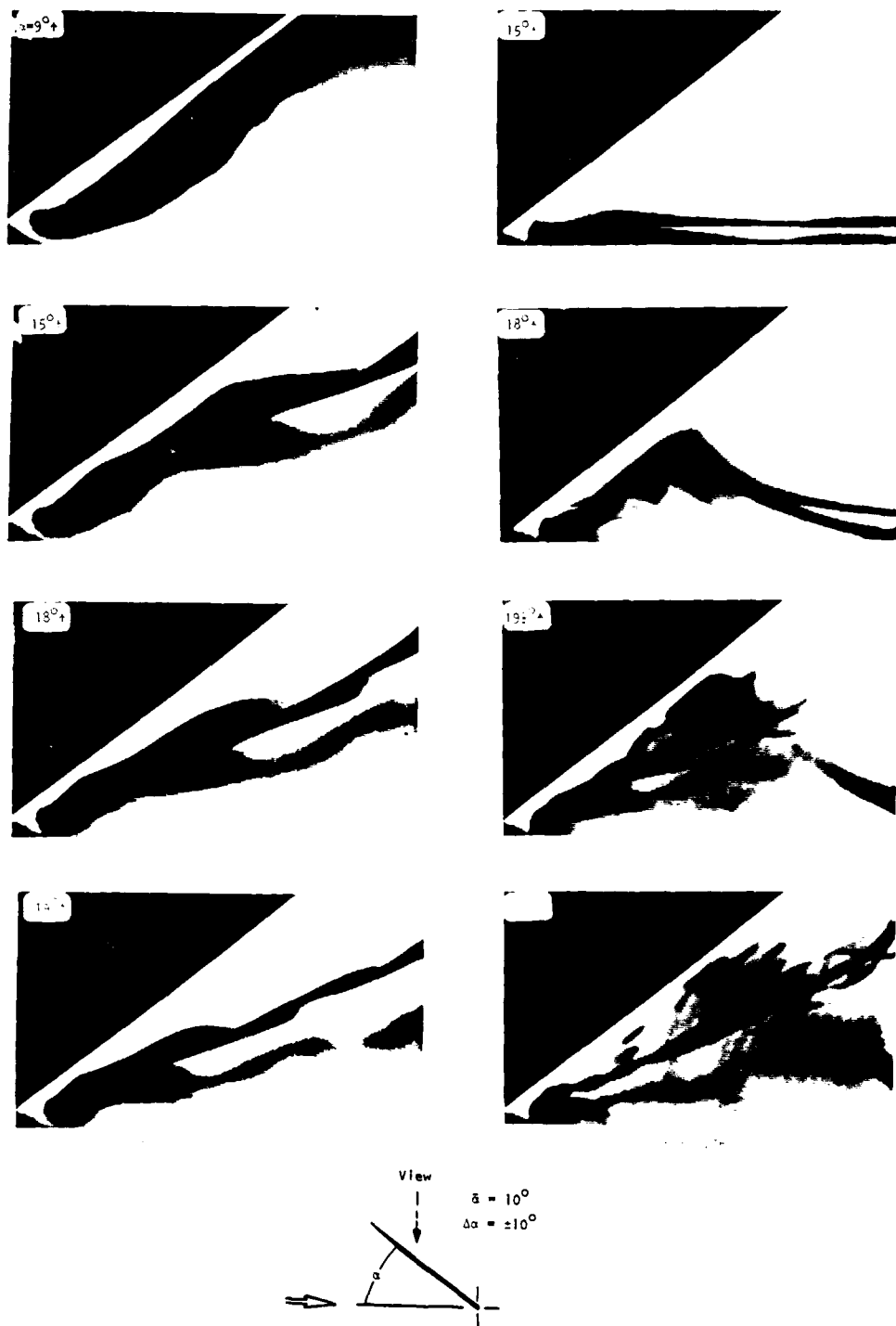
Figure 5: Comparison of development of vortex core on an oscillating delta wing. Left column of photos shows development representative of low frequencies of wing oscillation and right column that of higher frequencies.

305

delineated in forthcoming writeups. Among them is the fact that the process of vortex breakdown shows new types of structure beyond that of the traditional spiral mode observed on stationary wings. These breakdown mechanisms include abrupt onset of a very large-scale spiral mode; or a column-type instability that can supercede the classical, small-scale spiral mode.

It is evident from the photos of Figure 5 that there is substantial phase shift between the process of vortex development and the instantaneous position of the wing. For the stationary wing, the vortex core is completely broken down at the apex for $\alpha = 20°$. In contrast, the photo of Figure 5 shows that at the maximum instantaneous angles of attack shown therein, the core maintains its integrity well downstream of the immediate vicinity of the apex. A particular dramatic illustration of this phase shift occurs at a mean angle of attack $\bar{\alpha} = 20°$ for K = 0.13 (not shown here). In this case, the maximum streamwise length of the vortex core occurs at $\alpha = 29°†$. The issue arises as to whether this sort of drastic phase shift can be effectively employed in phased motions of control surfaces during a typical maneuver.

These phase shifts are manifested in hysteresis loops when the instantaneous position of the vortex breakdown x_b is plotted as a function
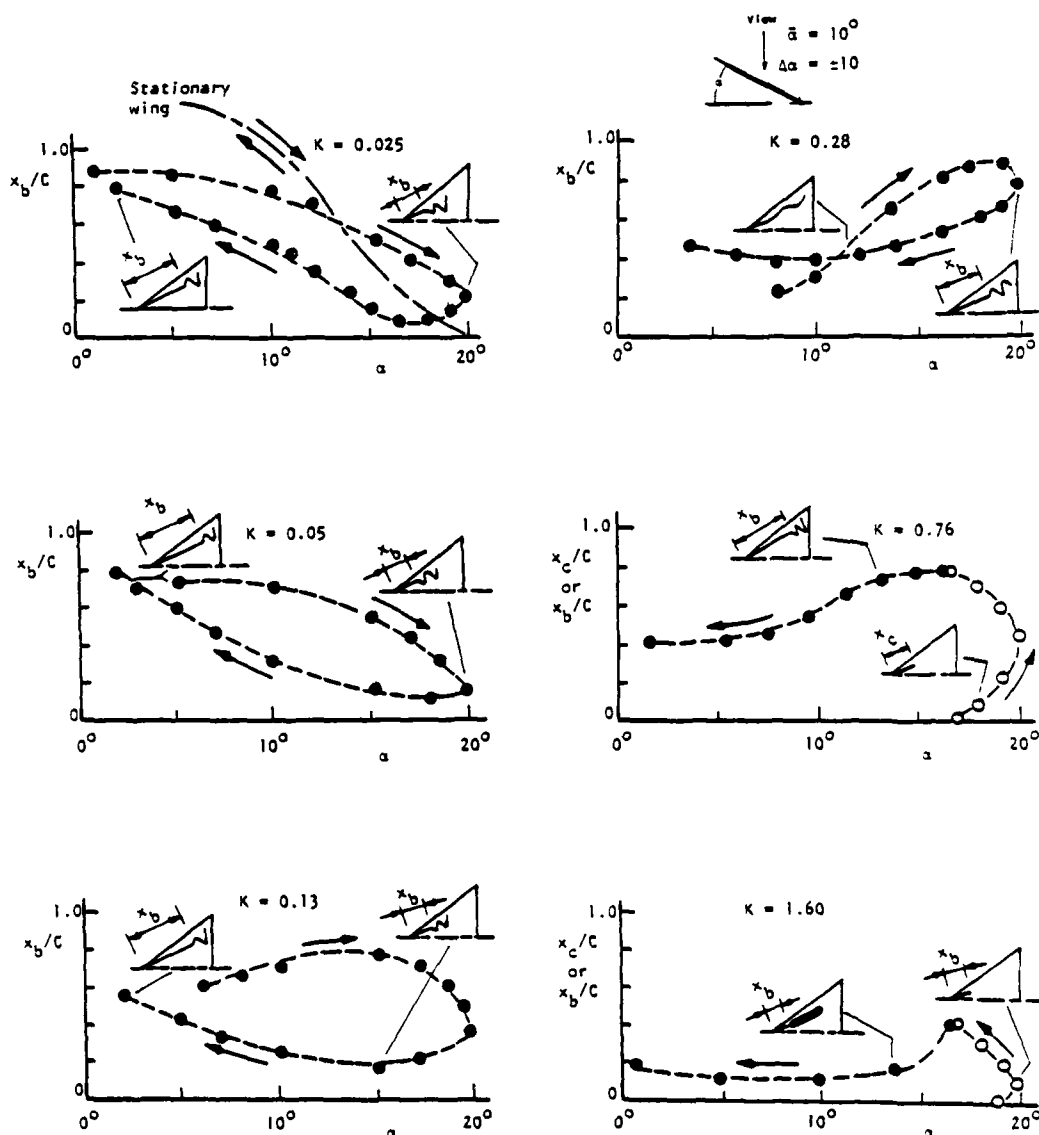
Figure 6: Hysteresis loops characterizing instantaneous position of vortex core and vortex breakdown as a function of instantaneous angle of attack.

306

of instantaneous angle of attack α. It is essential to verify the character of such loops by considering various types of dye injection and hydrogen bubble flying wire methods in order to preclude fallacious interpretation. Figure 6 shows that even at a reduced frequency as low as K = 0.025, there is substantial hysteresis relative to the characteristic of the stationary wing. The form and sense of the hysteresis loop is generally the same for higher values of K until K = 0.28 is attained. At K = 0.28, the form of the hysteresis loop takes on a figure eight form, and at K = 0.76 and higher values of K, the form and the sense of the hysteresis loop change drastically. Whereas the hysteresis loops corresponding to lower values of K are in the clockwise direction, the sense of higher frequency loops is in the counterclockwise direction. These differences in form and sense of the hysteresis loops are directly related to the manner in which the vortex core develops, as discussed in conjunction with Figure 5. At K = 0.025, it is of the low frequency type, at K = 0.76 of the high frequency type, and at K = 1.28 there is transition between these two extremes.

In addition to the primary vortex described in the foregoing, there also exists an unsteady secondary (counterrotating) vortex between the primary vortex and the leading-edge of the wing. Typical hysteresis loops of the secondary vortex, in relation to their primary counterparts, are given in Figure 7. Over the range of reduced frequencies considered, the following t.~nds, exemplified in Figure 7, are evident for the secondary vortex: the same form (shape) of hysteresis loop as for the primary vortex; a smaller value of maximum breakdown length than that of the primary vortex; and a phase shift with respect to the primary vortex, i.e. lag of breakdown of the primary vortex relative to that of the secondary vortex.

To characterize the time-dependent evolution of the vortex core, characteristic axial and swirl velocities are required. Figure 8 shows the variation of the axial velocity component u_c along the core centerline as a function of distance x from the apex. For reference, the case K = 0 is

also shown. Remarkable is the essentially constant value of u_c during the initial stage of the core development followed by an abrupt decrease to zero, corresponding to the instantaneous stagnation condition at the onset of vortex breakdown. Not shown here are normalized velocity variations within the deceleration region over a range of mean angle of attack $\bar{\alpha}$ and reduced frequency K. Such normalization suggests a universal velocity variation for the unsteady core that is essentially coincident with that corresponding to the stationary wing.

Under current consideration is a comparison of various functional forms of the wing forcing, e.g., sinusoidal vs. ramp forcing. This comparison will allow further insight into the mechanisms of phase shift of vortex development and breakdown with respect to the wing history.

PERTURBATIONS OF VORTEX CORE

Perturbations applied to a swept leading-edge can provide further insight into the possibility of vortex control by various means of alteration of boundary conditions at the leading-edge in the form of very small flaps, pulsed blowing, etc. In determining the appropriate excitation frequency f_e, consideration should be given to: the frequency of vortex breakdown (Leibovich[18]); and the inherent instability frequency of the shear layer separating from the edge (Pierce[34]; Payne and Nelson[35]; Gad-el-Hak and Blackwelder[36]). Here, the case of a delta wing having a sweep angle $\lambda = 75^\circ$, at an angle of attack $\alpha = 35^\circ \pm 10^\circ$, will be addressed. Oscillations were in the pitching mode about the trailing-edge; the amplitude of the apex motion was 0.0175 C and the dimensionless frequency of oscillation was $f_e r_c / u_c = 0.027$, which corresponds to the natural breakdown frequency of the core on the stationary wing. These parameters apply to Figures 9 through 14. In Figures 9 through 13, data was acquired at x/C = 0.38, upstream of vortex breakdown. In Figure 14, the station x/C = 0.883 was considered.
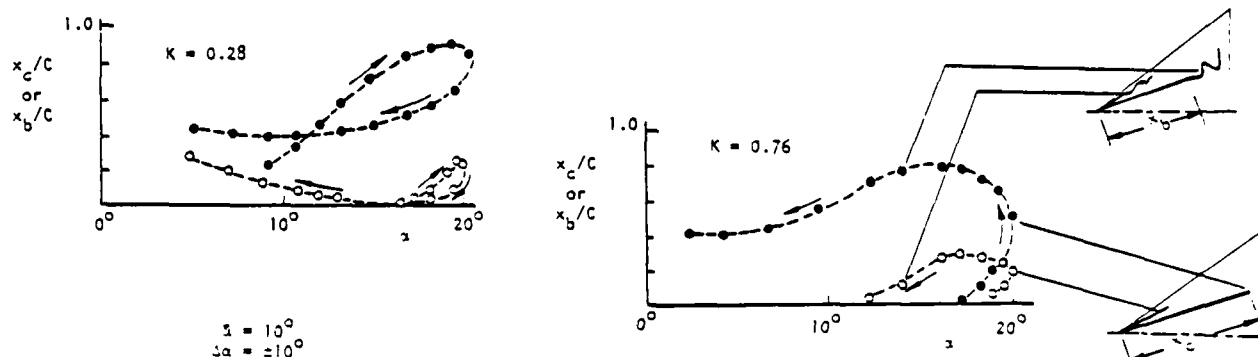
The mean distributions of the axial and swirl

Figure 7: Representative hysteresis loops of secondary (counter-rotating) vortex in comparison with its corresponding primary vortex.

307

velocity, designated by $\bar{u}$ and $\bar{w}$ are given in Figure 9. The forms of these distributions are similar to those corresponding to the stationary wing ($f_e = 0$). Particularly important is the asymmetry of these velocity distributions with respect to the center of the vortex core. Asymmetry arises from mutual induction by the vortices from both of the leading-edges of the wing, as well as from distortion of the unsteady shear layer shed from the edges of the wing. Clearly, theoretical formulations that assume symmetry of the velocity and vorticity field of the vortex core must be interpreted with care. Calculation of criticality conditions and instability criteria for the vortex core should account for the nonaxisymmetric mean vorticity field. Further studies of the mean velocity field

K	
■	0.00
●	0.28
▽	0.50
▲	0.76
○	1.15
◐	1.60
□	1.94

$\bar{\alpha} = 10^{\circ}$
$\Delta\alpha = \pm 1^{\circ}$
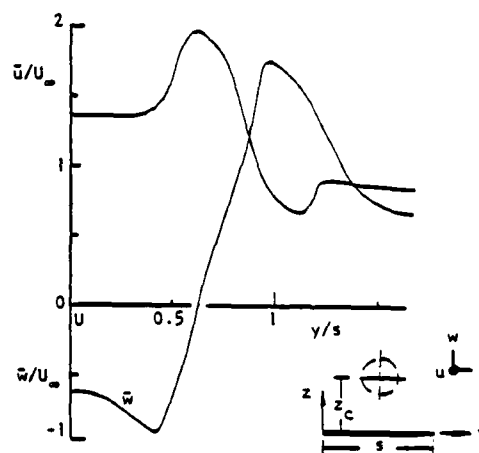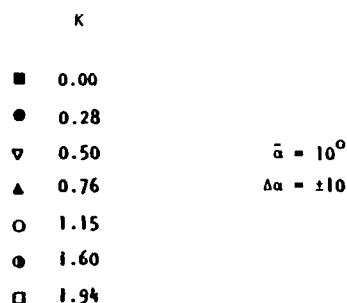
Figure 9: Mean axial and swirl velocity components on a delta wing (sweep angle $\lambda = 75^{\circ}$) at a mean angle of attack $\bar{\alpha} = 35^{\circ}$ undergoing oscillations of magnitude $\Delta\alpha = 1^{\circ}$ at a frequency $f_e r_c/u_c = 0.027$. Velocities determined at $x/\bar{c} = 0.38$.
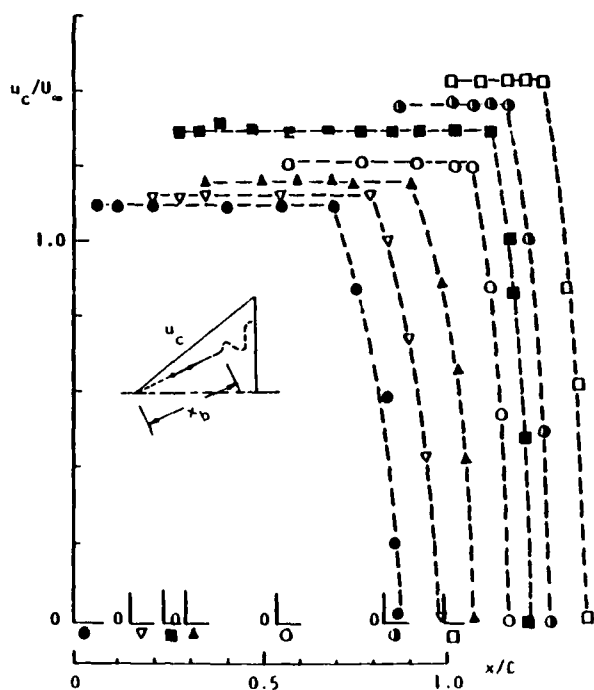
are focussing on determination of the $\bar{u}$ and $\bar{w}$ distributions for forcing at fundamental, as well as sub- and superharmonics of the inherent instability of the shear layer separating from the edge and the vortex breakdown frequency.

Rigorously speaking, one should consider the entire cross-section of the flow, and not simply the velocity distribution through the center of the vortex core, as suggested in Figure 9. As illustrated in Figures 10 and 10b, the distribution of the axial velocity component $\bar{u}$ across the flow shows further features of the asymmetry. These three-dimensional plots extend over elevations from the wall of $z/s = 0.1$ to $z/s = 1.1$, in which z is normal to the wing surface and s is the local semi-span.

The amplitude and phase distributions of the axial fluctuation component $\tilde{u}$ at the forcing frequency f_e are given in Figure 11. These distributions were taken at the same elevation $z = z_c$ as for the mean velocities of Figure 9. The distributions of amplitude and phase at a spanwise location near the edge of the wing are characteristic of those observed in unstable shear flows: two adjacent peaks of unequal amplitude with a phase shift of about π across them. Further inboard, near the apparent center of the vortex, there occur two additional peaks with a gradual phase shift of about π across them. These amplitude and phase distributions extending across the vortex through the separating shear layer form what might be termed a composite eigenfunction; it embodies both the eigenfunction of the separating shear layer as well as that of the integrated history of the vortex of the core. A clear picture of this composite eigenfunction requires similar
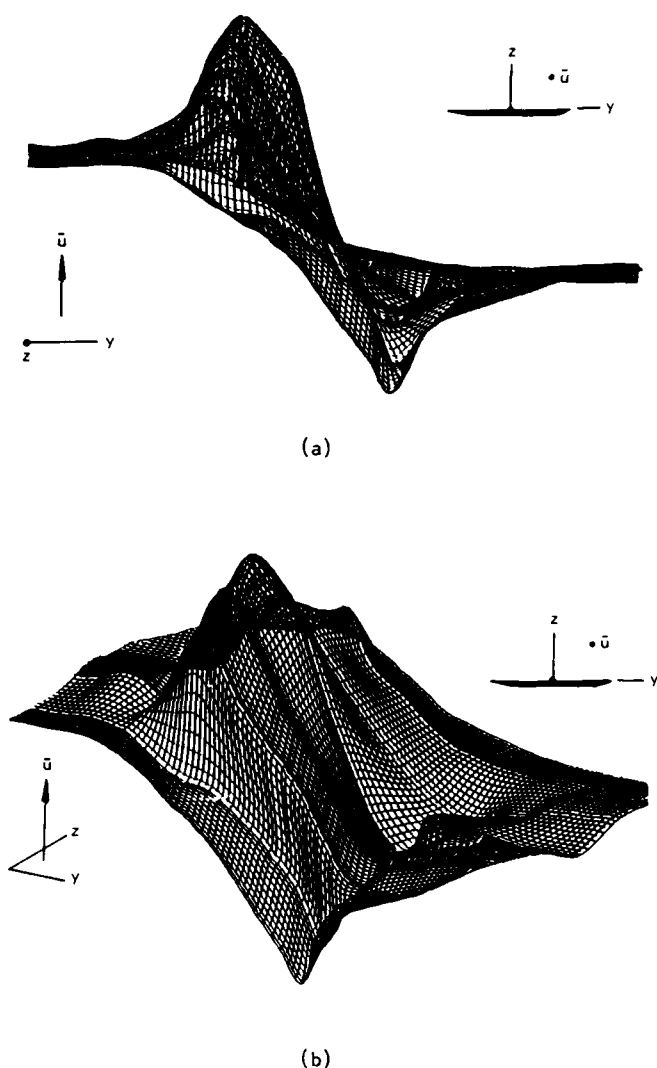
Figure 8: Variation of instantaneous axial velocity along centerline of vortex core as a function of distance from the apex of wing for a range of reduced frequency.

308

(a)

(b)

Figure 10: (a) Three-dimensional representation of the distribution of the mean velocity component $\bar{u}$ over the cross-section of the flow. (b) Same as (a) but viewed from different perspective.

information for the swirl component of velocity; it is currently being acquired.

Contours of constant magnitude of the fluctuating velocity $\bar{u}$ over the flow cross-section are given in Figure 12. The location of the star ☆ corresponds approximately to the apparent center of the mean vortex. The region of high intensity near the wall just inboard of the edge is tentatively attributed to the secondary (counter-rotating) vortex in that region. Above the edge, the elongated regions of high intensity are clearly due to the separated shear layer. As the shear layer evolves in the direction of the mean swirl, there is a region of large fluctuation amplitude, located above the vortex center, whose leading portion is distorted in the direction of the swirl. Just below the apparent center of the
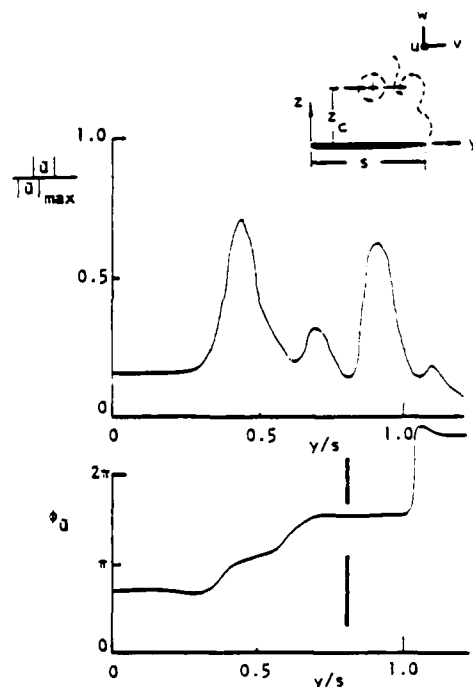
Figure 11: Distribution of axial component of fluctuating velocity $\bar{u}$ and its phase $\phi_{\bar{u}}$ through the center of the mean vortex.

vortex, there is yet another peak of $\bar{u}$. The structure suggested by the contours of Figure 12, namely that of an unstable three-dimensional shear layer, continuously feeding into the inner portion of the vortex, is in accord with flow visualization (not shown here).

Up to this point we have addressed amplitude and phase variations only at the excitation component f_e. However, due to nonlinearity of the flow structure, other spectral components will be present. Detailed spectra have been acquired for a range of excitation conditions, and representative ones are shown in Figure 12. In Figure 13a, the spectra were taken at the location of the large amplitude peak at $y/s = 0.90$ in Figure 11 and in Figure 13b at the location of the peak at $y/s = 0.45$. As evidenced in Figures 13a,b and in other spectra not shown here, the organized, multiple-peaked spectral content persists across the entire extent of the vortex core including the separating shear layer. Remarkable is the highly ordered nature of these spectra showing as many as nine well-defined peaks over the frequency range. Each of these peaks corresponds to a multiple of the fundamental spectral component, representing the forcing frequency f_e. The possible interpretation of these ordered spectra in terms of concepts of nonlinear interaction is underway. There are, of course, many issues related to the spectral evolution of the flow in the streamwise direction.
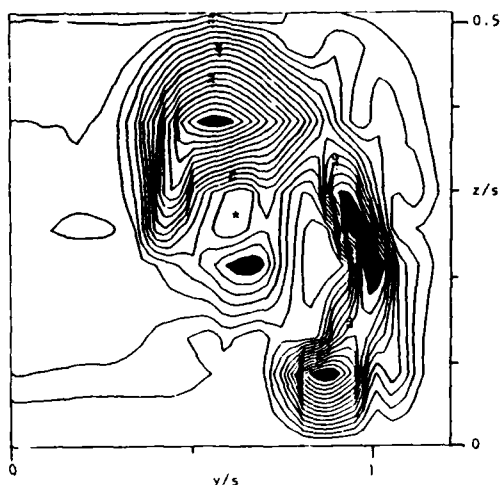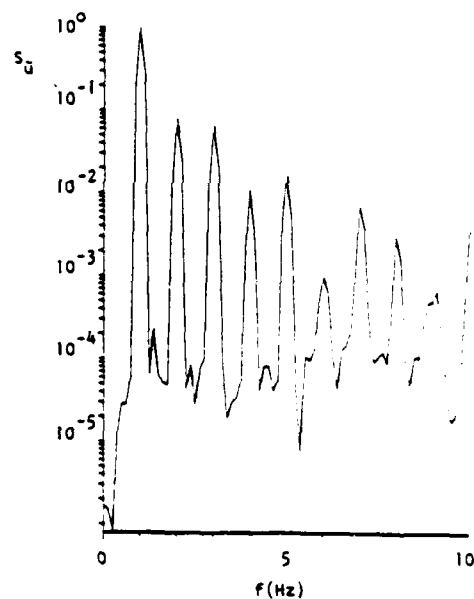
309

Figure 12: Contours of constant magnitude of $\bar{u}$ over the flow cross-section.

(a)

(b)

Figure 13: Representative spectra of the velocity fluctuation $\bar{u}$.

In particular, the nature of the spectral energy transfer as the vortex enters and passes through the breakdown region is of particular importance.
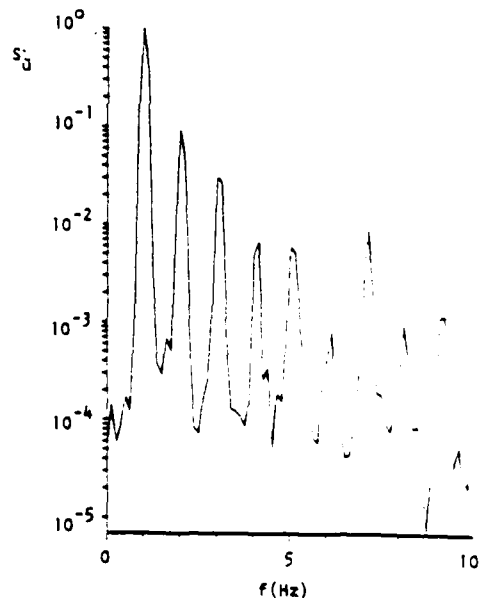
External forcing can alter the mean flow character and thereby the vortex breakdown location in several interesting fashions, as will be addressed in forthcoming writeups. We address here one such observation. The vortex on the opposite side of the wing (relative to the one under consideration) is stabilized such that its break-down occurs beyond the trailing-edge. For excitation at frequency f_e equal to that of the natural breakdown frequency f_o^*, Figure 14 compares representative mean and fluctuating velocity distributions without and with forcing at the same streamwise location $x/C = 0.883$. Without forcing, there is clearly vortex breakdown: the mean velocity distribution $\bar{u}$ shows a wake-like profile and the velocity goes through zero to a negative value as the vortex centerline is approached. The $\bar{u}$ distribution of the organized component at the breakdown frequency f_o^* is also illustrated. On the other hand, in the case of forcing at the natural frequency of vortex breakdown, i.e. at $f_e = f_o^*$, vortex breakdown does not occur. The distance that the breakdown of the forced vortex is delayed, relative to the unforced vortex, corresponds to about twenty percent of the chord C. The mean velocity $\bar{u}$ of the forced vortex shows the same general form as that of Figure 9. The magnitudes of the spectral components $\bar{u}(f_e)$ and $\bar{u}(2f_e)$ are comparable. Determination of the possibility of a simultaneous or intermittent presence of symmetric and spiral modes of instability requires corresponding phase distributions; this issue is currently under consideration.

CONCLUDING REMARKS

Active control of the flow structure of leading-edge vortices on a delta wing and delta wing segments through both small and large (displacement) amplitude pitching motion is attainable if the excitation frequency is properly selected. Such excitation should consider the following characteristic frequencies: the fundamental frequency (or its subharmonics) of the unstable shear layer separating from the edge of the wing; the frequency of vortex breakdown; and
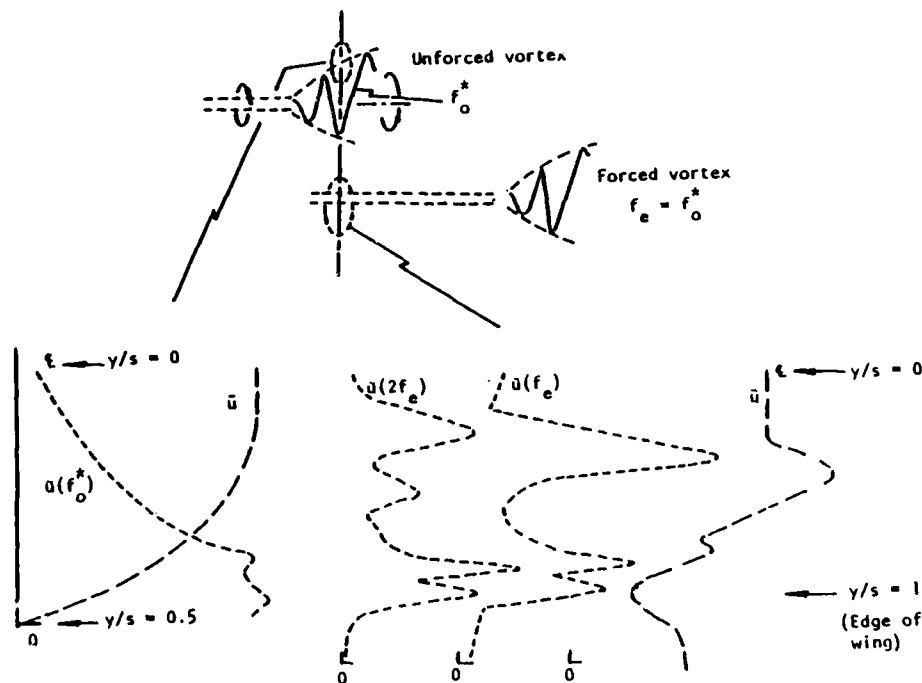
310

Figure 14: Comparison of representative mean and fluctuating velocity distributions of the unforced and forced vortices at the same streamwise location x/C = 0.883.

the characteristic frequency of the separation zone downstream of the onset of vortex breakdown. Depending upon the frequency selected, there can occur a variety of interesting modifications of the leading-edge vortices. Among them are alteration of: the mean velocity field of the vortex; the mechanism of vortex breakdown; and the phase shift of the instantaneous vortex breakdown position relative to the instantaneous angle of attack.

Development of an integrated active control and quantitative measurement system is aimed towards relating the instantaneous flow structure to the instantaneous wing motion. Both global and local characterization, exterior to and within the vortex core, are insightful and constitute the thrust of further efforts in this direction.

REFERENCES

1. Lee, G. H., "Note on the Flow Past Delta Wing with Sharp Leading-Edges", Aeronautical Research Council, Report & Memorandum 3070, September.

2. Ornberg, H., "A Note on the Flow Around Delta Wings", Swedish Technical Note K. T. H. Aero. T. N. 38, 1954.

3. Elle, B. J., "An Investigation at Low Speed of the Flow Near the Apex of Delta Wings with Sharp Leading-Edges", Aeronautical Research Council, Report & Memorandum 3176, 1958.

4. Kuechemann, D., "On Nonlinear Lifting-Surface Theory for Wings of Small Aspect Ratio with Separation", Aeronautical Research Council, Reprt 17769, April, 1959.

5. Kuechemann, D., "The Aerodynamic Design of Aircraft - An Introduction. Part V", RAE Tech. Memo. Aero. 1622, 1975.

6. Hoeijmakers, H. W. M., "Computational Vortex Flow Aerodynamics", Aerodynamics of Vortical Type Flows in Three Dimensions, AGARD Conference Proceedings No. 342, 1983, pp. 18-1 to 18-35.

7. Rizzi, A., Eriksson, L.-E., Schmidt, W., and Hitzel, S., "Numerical Solutions of the Euler Equations Simulating Vortex Flows Around Wings", Aerodynamics of Vortical Type Flows in Three Dimensions, AGARD Conference Proceedings No. 342, 1983, pp. 21-1 to 21-14.

311

8. Woodson, S. H. and DeJarnette, S. R., "A Direct and Inverse Boundary Layer Method for Subsonic Flow Over Delta Wings", Vortex Flow Aero-dynamics, NASA Conference Publication 2416, Vol. 1 (edited by J. F. Campbell, R. S. Osborn and J. T. Foughner), 1986, pp. 115-133.

9. Lambourne, N. C., Bryer, D. W., and Maybrey, J. F. N., "The Behavior of the Leading-Edge Vortices Over a Delta Wing Following Sudden Change of Incidence", Aeronautical Research Council Technical Report, Report & Memorandum 3645, 1969.

10. Gad-el-Hak, M. and Ho, C.-M., "The Pitching Delta Wing", AIAA Journal, Vol. 23, No. 11, 1985, pp. 1660-1665.

11. Gad-el-Hak, M. and Ho, C.-M., "Three-Dimensional Effects on a Pitching Lifting Surface", AIAA Paper No. 85-0041 presented at AIAA 23rd Aerospace Sciences Meeting, January 14-17, 1985, Reno, Nevada.

12. Gad-el-Hak, M. and Ho, C.-M., "Unsteady Vortical Flow Around Three-Dimensional Lifting Surfaces", AIAA Journal, Vol. 24, No. 5, May, 1986, pp. 713-721.

13. Wedemeyer, E., "Vortex Breakdown", AGARD Lecture Series No. 121, High Angle of Attack Aerodynamics, December, 1982, pp. 9-1 to 9-17.

14. Atta, R. and Rockwell, D., "Hysteresis of Vortex Development and Breakdown on an Oscillating Delta Wing", AIAA Journal (in press), 1987.

15. Garg, A. K. and Leibovich, S., "Spectral Characteristics of Vortex Breakdown Flow Fields", Physics of Fluids, Vol. 22, No. 11, 1979, pp. 2053-2064.

16. Escudier, N. P., "Confined Vortices in Flow Machinery", Annual Review of Fluid Mechanics, Vol. 19, 1987, pp. 27-52.

17. Sarpkaya, T., "Effect of Adverse Pressure Gradient on Vortex Breakdown", AIAA Journal, Vol. 12, No. 5, 1974, pp. 602-607.

18. Leibovich, S., "Vortex Stability and Breakdown: Survey and Extension", AIAA Journal, Vol. 22, No. 9, 1984, pp. 1192-1206.

19. Leibovich, S., "Structure of Vortex Breakdown", Annual Review of Fluid Mechanics, Vol. 10, 1978, pp. 221-246.

20. Lambourne, N. C., "The Breakdown of Certain Types of Vortex", Aeronautical Research Council Current Paper No. 915, 1965.

21. Sarpkaya, T., "On Stationary and Travelling Vortex Breakdown", Journal of Fluid Mechanics, Vol. 45, Part 3, 1971, pp. 549-559.

22. Lusseyran, D., Rockwell, D., and Gursul, I., "On Interpretation of Flow Visualization of Unsteady Shear Flows", in preparation for publication, 1987.

23. Hama, S. R., "Streaklines in a Perturbed Shear Flow", Physics of Fluids, Vol. 5,

No. 6, June, 1962, pp. 644-650.

24. Rockwell, D., Atta, R., Kramer, L., Lawson, R., Lusseyran, D., Magness, C., Sohn, D., and Staubli, T., "Structure of Unsteady Flows at Leading- and Trailing-Edges: Flow Visualization and Its Interpretation", Aerodynamic and Related Hydrodynamic Studies Using Water Facilities, AGARD Conference Preprint No. 413 based on Symposium of the Fluid Dynamics Panel, Monterey, California, 20-25 October, 1986.

25. Rockwell, D., Gumas, C., Kerstens, P., Backenstose, J., Ongoren, A., Chen, J., and Lusseyran, D., "Computer-Aided Flow Visualization", Proceedings of Sixteenth Symposium on Naval Hydordynamics (ed. W. C. Webster), National Academy Press, 1986.

26. Smith, C. R.,"Computer-Aided Flow Visualiza-tion", Handbook of Flow Visualization (ed. W. J. Yang), Hemisphere Publishing Corporation, New York, 1987.

27. Lu, L. J. and Smith, C. R. "Image Processing of Hydrogen Bubble FLow Visualization for Determination of Turbulence Statistics and Bursting Characteristics", Experiments in Fluids, Vol. 3, 1985, pp. 349-356.

28. Lusseyran, D. and Rockwell, D., "Estimation of Velocity Eigenfunction and Vorticity Distributions from the Timeline Visualiza-tion Technique", Experiments in Fluids, Vol. 6, 1988 (in press).

29. Ongoren, A., Chen, J., and Rockwell, D., "Multiple Time-Surface Characteristics of Time-Dependent, Three-Dimensional Flows", Experiments in Fluids, Vol. 5, 1987, pp. 418-422.

30. Kerstens, P. and Rockwell, D., "Ensemble-Averaging and Correlation Techniques for Flow Visualization Images", Experiments in Fluids, 1988 (in press).

31. Gumas, C. and Rockwell, D., "The Fourier Descriptor Technique: Means of Pattern Description and Recognition in Fluid Mechanics", in preparation for publication, 1988.

32. Spedding, G. R. and Maxworthy, T., "The Generation of Circulation and Lift in a Rigid Two-Dimensional Fling", Journal of Fluid Mechanics, Vol. 165, 1986, pp. 247-272.

33. Pierce, D., "Photographic Evidence of the Formation and Growth of Vorticity Behind Plates Accelerated from Rest in Still Air", Journal of Fluid Mechanics, Vol. 11, 1961, pp. 460-464.

34. Payne, S. M. and Nelson, R. C., "An Experimental Investigation of Vortex Break-down on a Delta Wing", Vortex Flow Aero-dynamics, Vol. 1, NASA Conference Publication 2416, 1985, pp. 135-162.

35. Gad-el-Hak, M. and Blackwelder, R., "The Discrete Vortices from a Delta Wing", AIAA Journal, Vol. 23, June, 1985, pp. 961-962.

LOW SPEED WIND TUNNEL TEST PROGRAM FOR DELTA WINGS OSCILLATING IN PITCH TO ALL ANGLE OF ATTACK

by
M.A. Jarrah
STANFORD UNIVERSITY
June 1987

313

Abstract.

The high angles of attack aerodynamics is a subject of very extensive research. The problem is complex and requires a clear understanding of the flow structure and evolution as the angle of attack approaches ninety degrees. The change of the flow structure as the angle of attack increases makes current methods of predicting aerodynamic loading have some serious drawbacks limiting their use for practical design of super maneuverable aircraft. The least understood regime is the one involving the vortex breakdown of the vortices above the wings. The mechanism underlying the breakdown is not clear.

There are a very limited number of experimental results for wings at high angle of attack and no experiments studying the unsteady effects of the breakdown. It was noticed in some experiments that the response of the vortex breakdown position to an increase in the swirling is to move downstream, then move upstream to a new equilibrium position. This observation was reversed in the opposite case. This character can be expected in the case of delta wings also,since the effective angle of attack is changed by the sudden pitch. This change is due to the change in wind direction as seen by an observer riding on the wing.

The summary of the objectives of this experiment are:

1. To determine the aerodynamic forces and moments on several sharp edge flat delta wings with a time dependent angle of attack according to :

$$\alpha = A\left(1 - \cos\Omega t\right).$$

The measurements of the side forces will be emphasized. These forces are generated due to the asymmetry of the flow field caused by the nature of vortex breakdown.

2. To study the structure of the flow field throughout the range of the angle of attack up to 90 degrees. This study will be performed using flow visualization techniques. Under this objective fall many items,some of which are as follows:

   a) To examine the leading edge vortices as a function of the flow parameters such as the Reynolds number,angle of attack,reduced frequency,etc.

   b) To isolate the modes of the flow field and their frequency. This is related to the fact that one can observe various flow modes when vortex breakdown dominates the upper surface of the wing.

   c) To study the asymmetry of the flow field,and how it can be affected by the unsteadiness.

314

3. To study the stability of the leading edge vortices by perturbing the sheer layer at the leading edge.

The testing plan was divided into three separate tests according to the above stated objectives. These tests are listed and described according to their priority and the order of their tunnel entries.

1.Measurement of Steady and Unsteady Aerodynamic Loads:

This experiment was planned to start on Apr 24 1987.Due to Ames 7' - 10' the experiment was postponed until May 28 and last until June 22. Using the guides of "pseudomanuevers" analyzed by Prof.Holt Ashley,scaled α time histories will be applied to each model.The models involved in this test are sharp leading edge flat delta wings of aspect ratio 1.1.5,and 2.The steady aerodynamic loads will be measured for these wings for all angles of attack.The unsteady aerodynamic loads will be measured for a range of reduced frequency between 0.1 and 0.01. Suitably nondimensionalized,the results will form a standard for comparison for theoretical results.

It is expected as stated earlier,that high pitch rate can delay the onset of vortex breakdown to much higher angles of attack than in the steady case during the pitch up,and it will have the opposite effect in the reverse mode.

2.Flow Field Visualization and Study.

This test will use the flow visualization model with aspect ratio of one.The smoke will be introduced through the model and injected through the leading edges. The flow visualization experiment will be divided into two separate experiments.These are as follows:

a) Unsteady Flow Visualization:This experiment will use the same model support to enforce a specific angle of attack time dependent motion.It is important in this experiment to inject the smoke through the leading edge.The use of a laser light sheet will be made to record the time development of the various cross sections of the flow field on the upper surface of the wing.By this method one can determine what the effects are of the reduced frequency,Reynolds number and the other parameters. This experiment will reexamine the discrete vortical structure with higher Reynolds numbers ,wider range of reduced frequencies,and much larger amplitude of oscillations.By means of this experiment,the origin of the side forces will be examined by studying the asymmetry of the vortices. It is possible that the modes of vibration will have some influence on the asymmetry of the vortex breakdown. This influence stems from the asymmetry

315

of the boundary conditions at both ends of the support mechanism.Therefore some of the mode shapes are asymmetric,particularly the fundamental one.By taking a real time movie, the vortex core and breakdown positions above the wing surface,and along the chord respectively,will be examined as a function of time dependent angle of attack.The possibility of exciting certain vortical modes by choosing appropriate value for the reduced frequency will be examined.

b) Stationary and Perturbed Flow Visualization: The stability of the vortex sheet will be studied.The basic idea of this test is to take the delta wing,the smoke generator,laser light sheet,and a movie camera,and then perform static wind tunnel tests.By taking a real time movie,the vortex core position above the wing surface,the breakdown location,and the modes of the vortex breakdown will be determined.With this information,the wing will be fixed at an angle of attack close to to where the breakdown occurs.The circulation shed at the leading edge can then be perturbed by cyclically or impulsively changing the blowing rate from the leading edge.If the vortex breakdown is initiated by a sheet instability this will then cause the leading edge vortex to burst. Oil flow visualization is planned here.Oil flow will enable the study of separation and attachment lines and other important details.

THE CONTROL OF VORTICAL FLOWS
OVER A DELTA WING

L. Roberts*, L. Hesselink*
I. Kroo* and N. J. Wood**
Stanford University
Stanford, Ca 94305

ABSTRACT

A research program to examine active control of vortical flows over delta wings at high angles of attack has been initiated. A thin tangential wall jet, exiting at the rounded leading edge of a delta wing, is used to control the primary separation of the cross flow and hence to control the equilibrium of the lee-side vortices. Initial experimental results using a high speed ramp change in the blowing momentum of the jet suggest that this technique will be suitable for development as an active control. Initial results from a simple analysis have also served as an aid in the interpretation of the experimental results. The present paper is in part a report of the progress in establishing an unsteady vortex control experiment and a parallel control system analysis.

NOMENCLATURE

b	wing semi-span
C_N	wing normal force coefficient
C_p	pressure coefficient
$C\mu$	blowing momentum coefficient
y,z	spanwise, normal coordinates
α	angle of attack
δy	position of displaced separation relative to leading edge
δz	position of displaced separation relative to wing chord plane

INTRODUCTION

Advanced aircraft configurations of delta wing planform, even at moderate angles of attack, experience significant asymmetries in the vortical flow over the wing upper surface, including the so-called vortex bursting, due to asymmetries in forebody geometry or slight yaw. At high angles of attack the vortex flow ceases to be steady and well organized and is replaced by unsteady shedding with a consequent significant loss of lift. In light of these problems there is a strong interest both in understanding vortical flows associated with aerodynamic lift and in devising an approach to regulate or actively control them. This paper describes a method to directly affect the vortex flow field over a delta wing by controlling the boundary layer separation near the leading edge of the wing using a wall jet.

Although this research leading to the active control of wing vortex aerodynamics is only in its initial stages, sufficient progress has been made to point the way toward an approach to vortex control that should eliminate unwanted flow asymmetries at low angles of attack and create

steady, organized flow at high angles of attack. Further work is required to demonstrate the feasibility of active control for various specific applications such as the control of wing rock or post-stall maneuvering and research in this direction will be undertaken as part of the future program.

Description of the Flow

The flow considered is that over a delta wing at angle of attack. Separation occurs in the vicinity of the leading edge forming vortex sheets which feed a pair of vortices lying above the wing. For a rounded leading edge (in contrast with a sharp leading edge) the location of separation is determined by the adverse pressure gradient near the leading edge on the upper surface. Figure 1 gives a simplified description in the cross-flow plane illustrating the vortex and its feeding sheet, reattachment and the secondary structure formed by the confluent boundary layer starting from the lower and upper stagnation lines.

Inasmuch as the equilibrium of the entire flow field is determined by the primary boundary layer separation it should be possible to control the flow field (i.e. the location and strength of the vortex and its feeding sheet) by controlling the location of that separation; moreover, it is expected that such an approach would be very effective in that a relatively small momentum change in the boundary layer will have a large influence on the strength and position of the resulting vortex.

In the present work this momentum change is accomplished through the use of a thin wall jet placed along the leading edge and blowing tangentially inward. The jet energizes the boundary layer as it flows around the leading edge and across the upper surface of the wing, figure 2. The wall jet is more robust than the original boundary layer and remains attached to the rounded leading edge by the Coanda effect. This causes a delay in separation which in turn influences the entire flow field. The vortex and its feeding sheet must relocate and the vortex strength is modified such that equilibrium is maintained.

By measuring changes in the pressure distribution on the wing surface and using this information to regulate the blowing strength (i.e. the momentum coefficient) of the wall jet, it should be possible to control the location of the vortices and thereby control any asymmetries. Rolling moments may be produced or the lift modified, independent of angle of attack.

The analysis and experiments described in the following sections represent the first attempts to understand more completely this approach to vortical flow control, to provide some basic information that will lead to the formulation of control laws, and to assess the effectiveness of this approach to aerodynamic control at high angles of attack.

---

*   Professor, Dept of Aero/Astro
**   Research Associate, Dept of Aero/Astro

ANALYSIS

The methods used here to analyze the flow over the delta wing are approximate and have been chosen over more accurate but more complex methods in order to identify the parameters of primary importance and enhance the interpretation of the experimental results. The initial analysis assumes that the inviscid flow will respond instantaneously to the change of location of the vortex sheet due to the momentum of the wall jet. This analysis will be improved subsequently to incorporate unsteady effects with wall jet blowing using a modified vortex-lattice method.

For the present, the analytical approach used to represent the flow is that first used by Brown and Michael[1] modified to allow for a rounded leading edge and an arbitrary placement of the vortex separation line as shown in figure 3. A pair of planar vortex sheets is assumed, whose strengths increase linearly with distance downstream, consistent with conical symmetry, and which feed a concentrated vortex pair in the flow above the surface.

This configuration is analyzed in the cross-flow plane using conformal mapping methods to solve a two-dimensional problem, while taking into account the three dimensional nature of the flow by applying a force free condition on the vortex system. From this analysis the pressure distribution (and the forces and moments) on the wing are determined when the location of the separation lines are assumed. This pressure distribution is used in the calculation of the turbulent boundary layers on the upper and lower wing surfaces starting from the stagnation points of the cross-flow and continuing to the separation points (a viscous analysis which accounts for the three dimensional nature of the boundary layers is used). The fact that the pressure at these points is assumed to be equal (implying that the secondary flow is weak) provides a condition which is used to correct the location of the vortex feeding sheet separation that was previously assumed. This gives a unique solution for flow over the wing in the absence of blowing into the boundary layer.

The influence of blowing is represented by replacing the boundary layer near the leading edge by a wall jet whose strength is characterized by a momentum coefficient. The wall jet separation is governed by a similar condition to that of the turbulent boundary layer but requires a much larger pressure gradient at separation. Thus the vortex sheet is displaced inboard and the entire inviscid flowfield is modified. The vortex displacement is determined by again equating the surface pressures at the cross-flow separation points (for the wall jet and upper surface boundary layer) and in this way relationships between the blowing momentum coefficient and the inviscid flow field parameters (vortex position, vortex strength etc.) are established. In general it is found that tangential leading edge blowing will reduce the magnitude of the vortex-induced lift but increases that due to leading edge suction.

$$\frac{\text{Vortex Lift}}{\text{Unblown Vortex Lift}} = (1 - (\delta y/b)^{0.5})^n$$

where $n \approx 3$ for a flat plate, ≈ 2.6 for a 10% ellipse.

These observations are based on a very simple theoretical model which may not be sufficiently accurate to be used as a basis for control laws; however the results reflect the physical mechanism by which the wall jet provides separation control in a qualitative way and give insight into the experimental results. Improved methods of calculating the flow field with sufficient accuracy including the effects of the trailing edge are currently under development.

The purpose of the improved method of analysis is to provide a simulation of the unsteady aerodynamics of a wing, including the effects of blowing in a typical maneuver. The method must be computationally fast and efficient inasmuch as the results will be used to provide the logic for the control algorithm.

The basic aerodynamic model is a low order vortex-lattice method. The wing is represented by panels having concentrated vorticity around the perimeter, figure 4. The flow separates from both the leading and trailing edges and the separated sheets are modelled as vortex rings that evolve in a time accurate way under the influence of the flow computed at a previous time step and the motion of the wing. The separation lines are taken to be at the leading edge in the absence of blowing.

In the presence of blowing two effects must be taken into account in this model, namely:

a) movement of the separation line inboard from the leading edge

and

b) additional suction near the leading edge due to the centrifugal action of the wall jet.

These effects will be reflected as changes in the amount of vorticity shed into the free sheets and will ultimately influence the forces and moments on the wing.

The work will first consider the range of angle of attack below that corresponding to the point of maximum normal force for which the flow is generally well organized. It is hoped that with strong blowing, which helps retain organized flow to higher angles of attack, this model may still give reasonable results.

EXPERIMENT

Previous Work

The concept of tangential leading edge blowing (TLEB) has previously been examined for the case of steady blowing only. Details of the experimental configuration are contained in reference 2 and, together with reference 3, describe some of the more interesting observations of the effects of TLEB on the vortical flow over a delta wing at high angle of attack. A brief summary of some of the basic performance characteristics is now presented.

The model under test, figure 5, was a semi-span delta wing with 60 degree leading edge sweep; the blowing slot extended over approximately 70% of the leading edge. The model was designed to be as near conical as possible and consequently the slot gap and the wing thickness increased linearly from the apex of the wing. The normal force results were obtained from integration of surface pressure measurements over the chordwise extent of the jet. The Reynolds number based on the root

318

chord was approximately 7×10^5. Figure 6 shows the effects of TLEB on the overall wing normal force as a function of angle of attack. Two different regimes can be observed. The first, at angles of attack below the point of maximum normal force, (referred to as low angle of attack) indicates that the blowing has little or no effect on normal force. The second, at angles of attack beyond the point of maximum normal force, (referred to as high angle of attack) indicates that a significant amount of force augmentation is produced. Note that the increment in normal force is 10 to 20 times the increment in blowing momentum, where the momentum represents the gain in normal force if the jet were used as a pure thrusting device. Further information regarding the similarity of these two regimes can be obtained from examination of the spanwise pressure distributions for both low and high angles of attack.

Figure 7 illustrates the effect of TLEB on the spanwise pressure distribution for the low angle of attack condition. It is obvious that the condition of nearly constant normal force arises from a cancellation of two opposite effects. As the blowing momentum is increased, the point of cross-flow separation moves around the leading edge and a region of high suction is created under the attached wall flow. At the same time, the influence of the vortex appears to diminish and the location of the peak vortex-induced suction relocates inboard. It is simple to demonstrate experimentally that in the limit, the crossflow separation point can be relocated all the way to the wing root thereby eliminating any vortical flow. For that case the pressure distribution conforms to that expected from the 'R.T. Jones' or 'attached flow' cases. It is important to note that the primary effect of TLEB at low angles of attack is to reduce the strength of the vortical flow and relocate the vortex inboard while maintaining nearly constant wing normal force.

Figure 8 shows the effects of TLEB on the spanwise pressure distribution at high angles of attack. Observe, that initially with no blowing, no vortical flow is apparent from the pressure distribution. The flat distribution on the upper surface suggests a separated flow over the entire span of the wing. For the smallest increment in blowing momentum illustrated, the first effect of TLEB at high angles of attack is to recreate the vortical flow over the wing upper surface. This causes a corresponding large increase in the normal force. Flow visualization studies have also indicated a strong stabilization of the flow. As the blowing momentum is increased the augmentation of the vortical flow and the normal force reaches a maximum beyond which a lateral movement of the vortex, coupled with a decrease in the vortex strength, is observed. This corresponds exactly to those effects observed at low angles of attack. Recognizing that for any geometrical angle of attack, in the absence of blowing, there exists a unique vortex strength and location. Then the concept of an 'effective' angle of attack of a vortical flow may be proposed. The effect of TLEB may be thought of as reducing the 'effective' angle of attack that the vortical flow represents. In the limit the fully attached flow case for a given geometrical angle of attack represents a vortical flow with an effective zero angle of attack.

Objectives of the Present Program

The experimental objective is to determine the effectiveness of TLEB in providing active control of a vortical flow over a range of angles of attack. To obtain the information necessary for the eventual development of control laws for TLEB it was required to determine the time constants associated with the restructuring of the vortical flow. Sensor types and locations to act as feedback or feedforward inputs to the control system also had to be determined. There were 3 inter-related capabilities that needed to be developed in order to achieve the objectives. Those capabilities were: a fast optical scanning laser light sheet system, an unsteady blowing control mechanism, and an unsteady surface pressure measurement system.

Laser Light Sheet System In order to obtain visual perception of the transient effects of TLEB, a fast scanning image processing system has been developed. This consists of scanning a laser light sheet through the flow of interest, the laser being pulsed at rates which effectively freeze the flow structure. The images produced can be recorded on a high speed camera which is synchronized with the light pulses. The recorded images may then be digitized, processed and assembled to provide a three-dimensional image of the vortex structure. This information should clearly show how the jet flow affects the trajectory and strength of the feeding sheets and the vortex core. Since the pulse width of the laser is small (30nS), an extremely high powered laser is required to provide sufficient illumination of the flow. A Copper Vapor laser has been acquired for this purpose and is presently undergoing installation into the wind tunnel area. A suitable optical arrangement for scanning the sheet down the axis of the vortex has been developed and is also being installed.

Unsteady Blowing Control To provide the transient blowing, a pneumatic control system had to be developed. It was decided that a simple ramp change of internal pressure was the most practical form of control, both from pneumodynamic and time constant derivation considerations. It was anticipated that multiple time scales would be present, some of which could be related to the downstream convection of the wing wake. Sinusoidal or other periodic variations of pressure would tend to obscure these effects. A simple rotary solenoid system has been fabricated with a custom built switching power supply which enables operation of the solenoid at rates of 9000 degrees/second. It was found that the optimum configuration of the solenoid in the supply line was as close to the model plenum as possible, figure 9. The solenoid controlled a bleed flow that corresponds to the change in pressure required in the plenum. In addition, an upstream air bleed was included, which, when coupled with a simple manual flow control valve, provided sufficient control over both the initial and final pressure levels in the model plenum. A ramp time of the order of 4 milliseconds has been achieved with little or no overshoot in the pressure.

Surface Pressure Measurement To correlate the flow visualization and the transient loads on the wing it was required to measure the unsteady surface static pressures. A data acquisition

319

system has been assembled which is capable of operating the blowing control system and sampling a maximum of 16 channels of analog information with an aggregate sampling rate of 160 Khz. Kulite miniature pressure transducers will be mounted in the surface of the new model and will provide real time records of the changes in the vortex influence on the wing surface. Each channel will be simultaneously sampled at 10 Khz over a total time of 6 seconds. These results should provide accurate measurements of the time constants and phase relationships involved in TLEB.

Wind Tunnel Model The original model that was used to determine the feasibility of TLEB was designed to be geometrically conical. This proved to be an unnecessary complication and for the present effort a new semi-span model has been produced, figure 10. A semi-span configuration has again been chosen for simplicity of construction and relative scale in the test section. The wing is of constant thickness and has a 50 degree leading edge sweep. The trailing edge is closed to a point by the inclusion of a simple dual flap system which may be later used to determine the improved effectiveness of mechanical flap devices in the presence of TLEB. The leading edge slot extends over most of the leading edge and the slot gap can be varied by replacement of the leading edge cylinder. The model can be configured for either unsteady or steady pressure measurement or a combination of both. Model fabrication has been successfully completed.

Experimental Program
The assembly and validation of all the components of this program should be completed on schedule by the end of the first year of the program. Initial steady state testing of the new semi-span wing (October 87) will include measurement of the blown/unblown vortex influence and flow visualization using an existing CW laser light sheet system and video camera. Having confirmed the operation of the model and support systems, initial scanning light sheet images will be obtained for a selection of predetermined conditions. These conditions will also be examined in some detail using the unsteady surface pressure measuring system and the correlation of the results will provide initial information on the time scales associated with TLEB. This information will provide the initial input for the formulation of control laws for the active control of vortical flows.

CONCLUDING REMARKS

An ambitious research program to determine the effectiveness of tangential leading edge blowing in providing active control of vortical flows has been initiated. Simple analytical techniques have been used to gain insight into the interpretation of previous steady state experimental results. Analysis of the time dependent problem is being pursued using a vortex lattice technique. All the required experimental systems have been assembled and are awaiting initial testing. A new wind tunnel model has been designed and fabricated and is capable of providing both steady and unsteady surface pressure measurements in the presence of

transient blowing momentum. In the coming year, initial results for the time scaling of the response of the vortical flow to changes in blowing momentum will be obtained and this will provide input for the initial formulation of control laws.

REFERENCES

1. Brown,C.E. and Michael,W.H. 'On Slender Delta Wings with Leading Edge Separation' Journal of Aeronatical Sciences, Vol 21, 1954.

2. Wood,N.J. and Roberts,L. 'The Control of Vortical Lift on Delta Wings by Tangential Leading Edge Blowing' AIAA paper 87-0158, Jan 1987.

3. Wood,N.J., Roberts,L. and Lee,K.T. 'The Control of Vortical Flow on a Delta WIng at High Angles of Attack' AIAA paper 87-2278, Aug 1987.
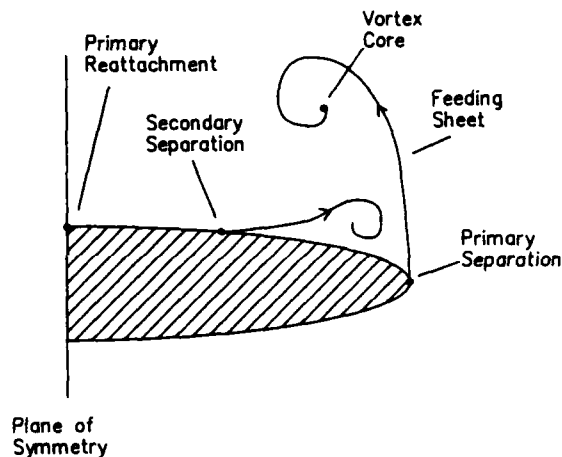
Figure 1: Flow in the Cross—Flow Plane of a Delta Wing at Angle of Attack.
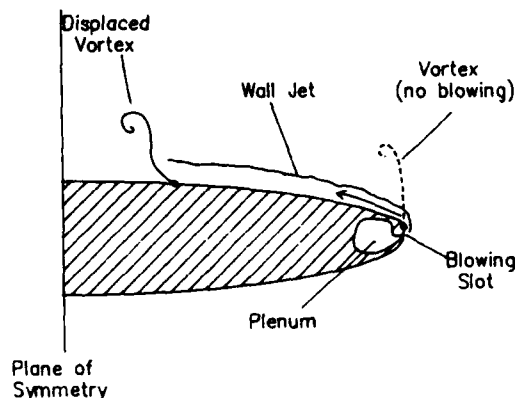

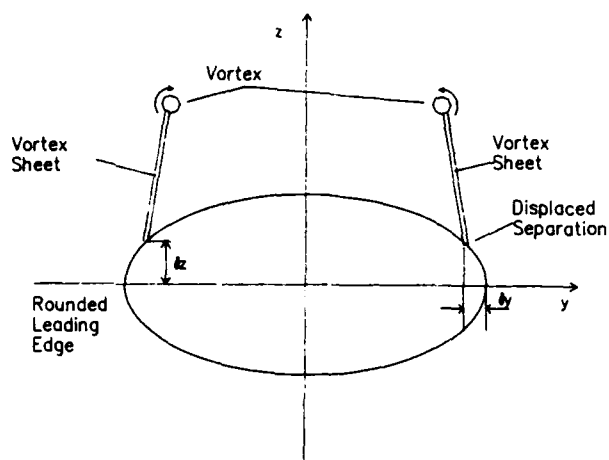Figure 2: Tangential Leading Edge Blowing Configuration.
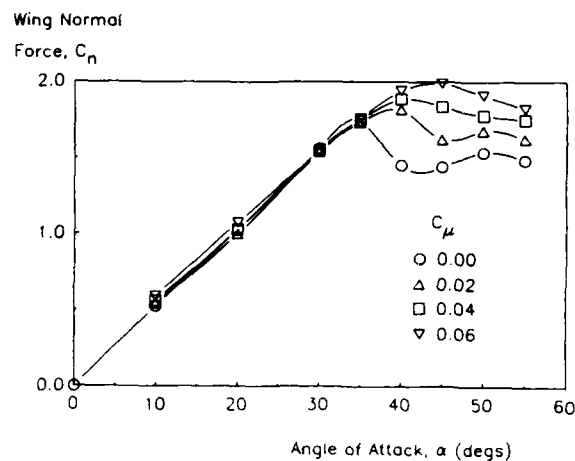
Figure 3: The Modified Brown and Michael Model.

Root Chord = 27.9 cm, L.Edge Sweep = 60 degs

Figure 4: The Vortex–Lattice Method.

Figure 5: Original Wind Tunnel Model

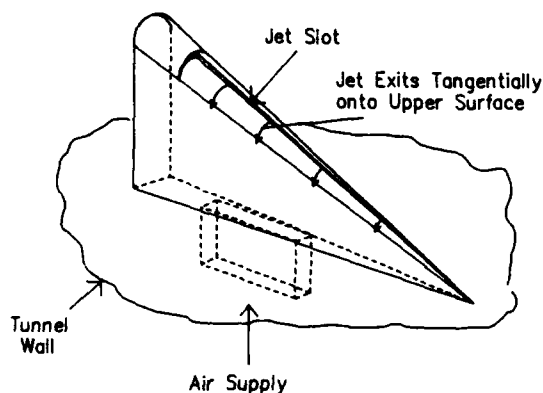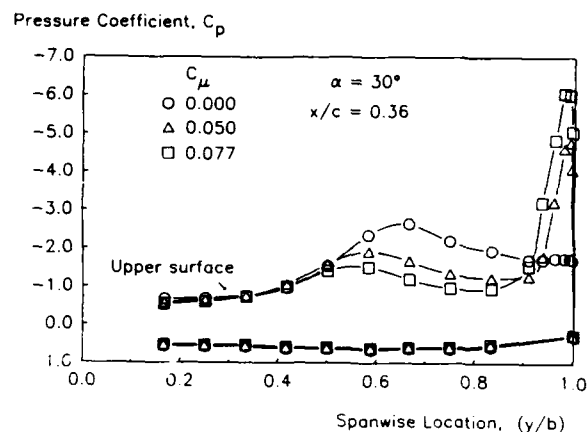Figure 6: Effect of TLEB on Wing Normal Force.

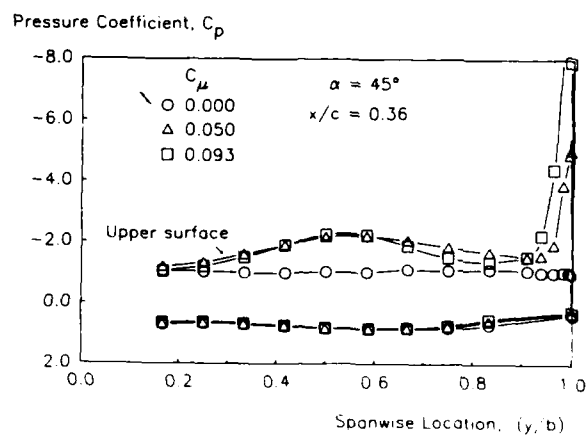

Figure 7: Spanwise Pressure Distributions for the Low Angle of Attack Case.

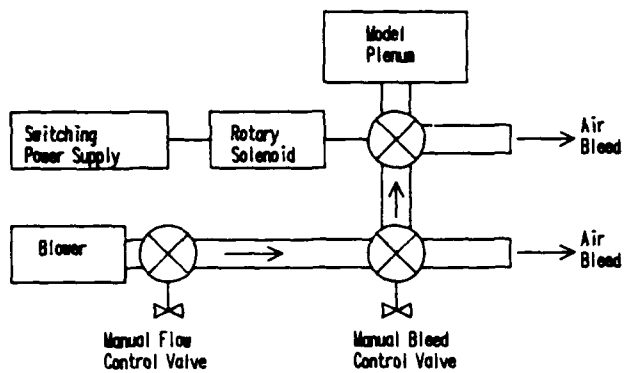Figure 8: Spanwise Pressure Distributions for the High Angle of Attack Case.

321
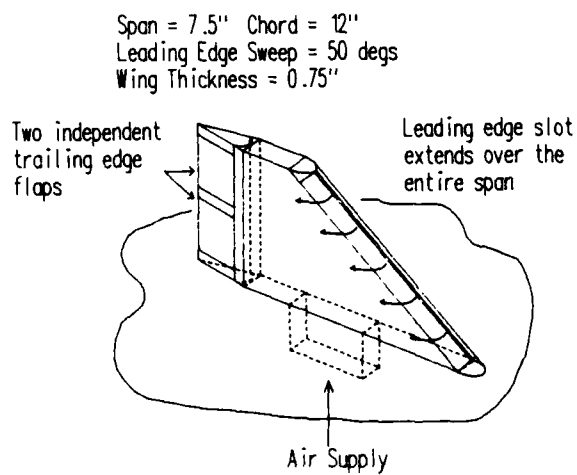
Figure 9: Unsteady Blowing Control System.

Span = 7.5"   Chord = 12"
Leading Edge Sweep = 50 degs
Wing Thickness = 0.75"

Figure 10: New Wind Tunnel Model.

Automatic Control of

Acoustically Excited Air Jets

C. R. Koch, J. D. Powell, W. C. Reynolds
Department of Mechanical Engineering
Stanford University, Stanford, CA 94305

Introduction

The subject of research to be discussed is: Automatic Control of Acoustically Excited Air Jets. The purpose of the research is to try and understand the automatic control problems as they pertain to a complex fluid dynamical system. This is a relatively new field called flow control, which is a combination of control theory and fluid mechanics. A brief background on the fluid mechanics and control systems, as well as a discussion of the current research, and future work will be undertaken

Background

Fluid Mechanics

The fluid mechanics of an axially excited jet is quite complex, yet it is fairly well understood, making this flow field an ideal candidate for an attempt at closed loop control. A brief qualitative description of the flow will be given next.

Equipment

The experimental apparatus for studying the excited jet is shown in figure 1 which shows how the air travels through the plenum and out the nozzle[1]. The speakers in the axial and transverse direction are driven by properly phased sine wave signals. This provides dual mode - axial and transverse - excitation to the air jet. From a control theory perspective, the speakers are the actuators by which one can control the plant (the flow field downstream of the nozzle exit).
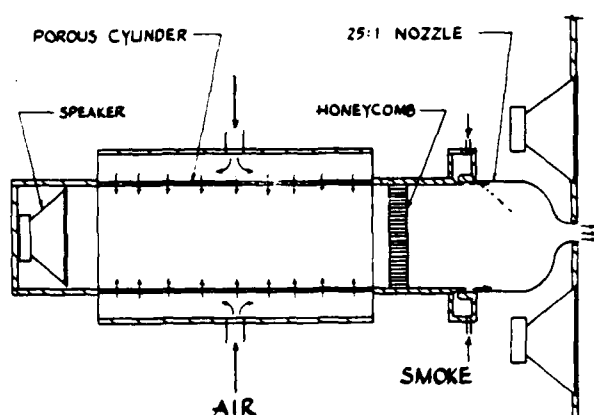
Figure 1 - Experimental Apparatus
from [1] by permission

Vortex Rings

Large changes in the flow field from the natural or

unexcited jet can be obtained using relatively little excitation with the speakers. A schematic of several remarkable excited flow states is shown in figure 2.
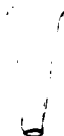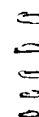
Figure 2 - Jet Schematic

The rings shown in figure 2 are vortex rings, and they are the key to understanding the flow field. A vortex ring is formed by the shear layer between the fast moving jet air and the relatively slow moving room air. That is, the viscosity of the fluid, air in this case, causes a shear stress on the fluid in the region of relative motion which in turn cause the fluid to roll up in a circular ring, a vortex ring.

Natural Jet

In a natural jet, one with no acoustical excitation, the formation of vortex rings is irregular with time. This results in some vortex rings, which start at the nozzle exit close together, to coalesce. Other vortex rings which are sufficiently far apart do not coalesce. The result is a turbulent jet with time varying small turbulent structures and time varying large structures (vortex rings in this case)[1].

Axial Acoustic Excitation

In an axially excited jet, the acoustical excitation comes from the axial speaker only. Methods other than speakers such as resonating cavities can be used to axially excite a jet. A relatively small acoustical excitation causes the vortex rings to be formed at the acoustical excitation frequency. The axial excitation triggers a uniform (in time) spaced train of vortex rings to be formed at the nozzle exit.

Dual Mode Acoustic Excitation

In the dual mode excited jet, both the axial and orbital acoustical excitation are used. A small perturbation[2] (15% and 4% of the jet exit velocity for the axial and orbital direction respectively) causes a large change in the flow field. Vortex ring interaction is the key to understanding how the flow field changes from the natural state, to the dual mode excited state. The idea of the acoustical excitation is this: 1) the axial excitation forces a regularly spaced train of vortex rings and concentrates the vorticity in these rings, the rings are formed at the frequency of the axial speaker; 2) the orbital excitation

perturbs the vortex ring at the nozzle exit, which interacts with the other vortex rings further downstream according to the Biot Savard law for thin filament vortices[3]. The vortex rings tilt each other.

Important Parameters

When R, the ratio of axial to transverse frequency is two for example, odd numbered vortices are perturbed one way (perpendicular to the jet axis) while even numbered vortices are perturbed the other way. This causes a bifurcating jet (the jet splits into two branches) if the jet is in the proper region in a Strouhal Number phase plane plot - more on this later. When R is equal to 3 the jet trifurcates or splits into three branches. Non-integer values of R from 1.7 to 3.5 cause the vortex rings to go in all directions. This is called a blooming jet because the vortex rings look like a flower blooming. The fluid dynamical model of the jet using vortex ring interaction model has been verified both experimentally and by computer simulation[2,3].

The jet will only go into the excited or high mixing state if the the parameter R (axial to transverse frequencies) and the axial Strouhal number is in an experimentally determined range[2] (Axial Strouhal Number - STax=Fax*D/U is the non-dimensionalized axial frequency, by jet exit velocity and jet exit diameter). The excited region is shown in an axial vs transverse phase plan plot in figure 3. One would expect the Strouhal number to be important because it is measure on how far apart successive vortex rings are. When the axial Strouhal number is high, above approximately 0.7 the vortex rings are close together so they get tangled up rather than tilting each other. When the axial Strouhal number is low the vortex rings are relatively far apart and since the induced velocity of one ring on another follows the Biot Savard Law which falls off as an inverse square of distance, the tilting of the rings is small[3].
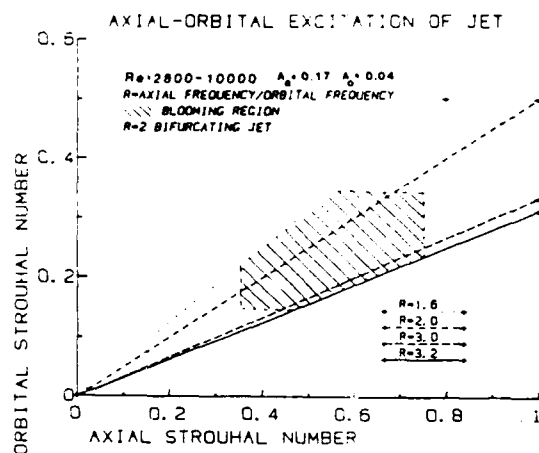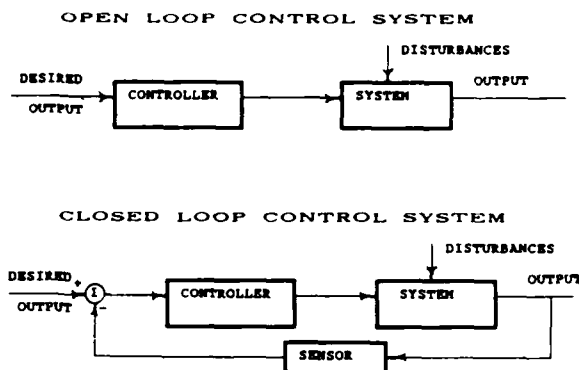
Figure 3 - Phase Plane Plot

from [3] by permission

Controls

General

Now turning to some general concepts in the area of controls. The two types of control systems that will be discussed are open and closed loop control. A schematic of open versus closed loop control is shown in figure 4.

Figure 4 - Open vs Closed Loop Control

In this case the jet flow field is the system, the controller is the logic determining the speaker frequency, amplitude and phase, the actuators are the speakers, and the disturbances are the jet exit velocity and velocity disturbances to the jet flow field.

Closed loop control systems have many advantages over open loop control systems. Three major advantages of closed loop control are: 1)Less sensitive to changes in the system or plant; 2)less sensitive to disturbances; 3)speed of response/stability can be improved. Closed loop control requires sensors to provide a feedback signal.

Sensors

The sensor(s) in a closed loop control system (figure 4) must be such that they allow the controller to characterize (observe) the system. That is, the modes of the system that are of interest must be observable and non-observable modes should be stable. For example, placing a position sensor at the node of a vibrating beam yields no information about that particular vibrating mode making that mode unobservable with that particular sensor. Placement of sensors in the flow field of the acoustically excited jet for closed loop control is one of the more difficult aspects of the current investigation.

Current work

General Objectives

The first stage of the research is to implement an open loop control system. That is, for changing flow speeds hold the jet at a particular point in the Strouhal number phase plane (Figure 3) by changing the frequencies in the axial and transverse direction.

The aim of the open loop control is : 1) to gain an understanding of some of the problems that will be encountered - such as equipment, and software; 2) to automate (computerize) the inputs and outputs of the system so a high speed closed loop controller can be implemented.

Original Apparatus

The original jet apparatus required complete manual adjustment at each steady operating point. Note - the jet is open loop stable and very robust to disturbances so it is possible to manually dial up the desired operating point.

Existing Apparatus

The first stage of open loop control was to add a sensor to measure the jet exit velocity or flow speed. To determine the flow speed, the stagnation pressure in the plenum is measured and the jet exit velocity is deduced. An Omega piezo-resistive 0 - 10 in. of H2O pressure transducer is used. The range of flow velocities that obtainable with the current experimental rig are 3 - 30 m/s. The system was automated using an IBM AT computer and a data translation DT2821-F digital and analog I/O board. The frequencies and amplitude of the sine wave signals that actuate the speakers can be controlled using function generators (HP 61014A) set on a nominal value and using the VCO - voltage controlled oscillator, and by the AM - amplitude modulation inputs. This was in fact done for the frequency only and not for the amplitude because the effect of amplitude on the jet has not yet been completely investigated . The resulting system was built and resulted in a system in which the jet flow rate could be changed and the open loop control program would schedule the frequencies to hold the jet at a given R and STax. Two problems were encountered. One, the pressure transducer needed to sampled for several cycles of axial frequency in order to yield a satisfactory average of jet velocity. This problem can be easily solved by a low pass filter. The second problem was that the phase shift circuit that is used to give the 90 degree phase shift between successive transverse speakers is frequency dependent. This requires manual adjustment of the phase shift electronics when there are large changes in jet flow rate and in excitation frequency. The phasing problem is more difficult to solve and a phase locked loop (PLL) was designed. The pull in frequency range (how far the unlocked frequency can be from the reference frequency and still lock into the reference) was found to be unacceptable in the PLL circuit.

The apparatus is now being modified to be completely open loop controlable. To do this the electronics are completely automated. The electronics have been changed by changing how the sine wave signals which drive the speakers are generated. The sine waves are going to be generated by a ROM look up table external to the IBM control computer to avoid the overhead of servicing this function. Instead the IBM will interface to the external sine wave generator resulting in much less computation overhead.

In addition, a shroud has been added for several reasons. One, a shrouded jet is a interesting problem with practical applications to jet ejectors and thrust augmenters. Two, there is a simple performance parameter that can be measured - entrained air - which can be maximized in an optimal control algorithm. In order to measure entrained air a flat surface is desirable which is one reason why the speakers were enclosed. The other reason for enclosing the speakers is to concentrate the speaker energy at the nozzle exit where it is the most effective. The third and final reason for adding a shroud is that it provides a convenient platform on which to mount sensors in the flow, that will be used in the next stage of the investigation to provide a feedback signal.

Work Remaining

The work in the immediate future is to complete construction of the shrouded apparatus. This apparatus will be used as a vehicle to test out control algorithms which are developed by theoretical considerations and experimental system identification techniques. Eventually a control algorithm will be developed. At this stage, the utility of closed loop control for this system is unclear because the jet is open loop stable and robust to disturbances. Perhaps one objective of closed loop control is for a burning jet. To date, in a burning (methane), the acoustical excitation seems to have no effect on the jet. That is, the excited state of the jet can not be obtained using a manual open loop control scheme. Perhaps closed loop control would provide a means to hold the burning jet in an excited state. However a burning jet is a very difficult control problem because even the fluid mechanics is not well understood. A more realistic approach would be to use closed loop control to filter out simulated disturbances. The simulated disturbances could model the combustion process, with the disturbance model becoming more and more complex (and realistic) as an understanding of the control problems is gained.

Summary

Substantial progress has been made. The control electronics have been updated from completely manual to partially automated with a completely automated configuration in the design / construction phase. A shrouded configuration for the jet was decided on and is being constructed. The redesign was done from both a fluid mechanical and a control theory perspective which will allow for substantial advances in the next year.

Acknowledgments

References

1. Parekh, D. E., W. C. Reynolds, and W. G. Mungal, " Bifurcation of Round Air Jets by Dual- Mode Acoustic Excitation," AIAA paper 87-0164 (1987), January 12-15, 1987.

2. Lee, Mario, and W. C. Reynolds, "Bifurcating and Blooming Jets," Fifth Symposium on Turbulent Shear Flows, pp. 1.7-1.12 (1985).

3. Parekh, D. E., A. Leonard, and W. C. Reynolds, "A Vortex-Filament Simulation of a Bifurcating Jet," Bulletin of the Amer. Phys. Soc., vol. 28, no. 9, p. 1353 (1983).

Experiments on an Unsteady, Three-Dimensional

Laminar Separation

R.W. Henk,* W.C. Reynolds,+ and H.L. Reed++
Stanford University, Stanford, California

An experimental program in unsteady, three-dimensional, pressure-driven laminar separation is investigating the structure and scaling of these flows; of particular interest is the development, washout, and control of flow separation. Flow visualization of the three-dimensional separation has revealed its complex, unsteady, vortical structure which depends on the frequency, amplitude, and waveform of the driving pressure gradient.

Unsteady, three-dimensional separations can occur in a variety of technical situations, including turbomachinery and low-speed aircraft. An experimental study of these flows has begun at Stanford to provide basic information about the development, washout and control of such separations. This paper will describe the experimental facility, the means of controlling the separation, and an interpretation of the flow visualization results.

Experimental Facility and Operating Conditions

The experimental facility is a closed-circuit water tunnel, figure 1, in which water flows from an overhead tank through the test section and then to a sump tank. Turbulence attenuation by honeycomb, screens, and acceleration through a nozzle provides a low turbulence freestream to the test section. A fresh boundary layer then develops under a zero pressure gradient until it reaches the unsteady portion of the test section. At this point, the boundary layer encounters either (1) a steady, zero or adverse pressure gradient, or (2) a computer-controlled, time-varying pressure gradient, as determined by the valves draining flow through the wall opposite the test surface. The water is continually pumped from the sump to the overhead tank to close the circuit.

This tunnel has been extensively rebuilt to provide flexibility in control of the freestream flow and improved optical access for diagnostics. The new test section measures 3.66 m along the streamwise direction, 0.36 m across the span, and 0.13 m from the test surface to the opposite wall. Glass on the top and plexiglas on the sides and at the end of the test section permit optical access for flow visualization and measurement. Side-wall bleeds, spaced every 0.45 m, remove the sluggish portion of the side-wall boundary layers.
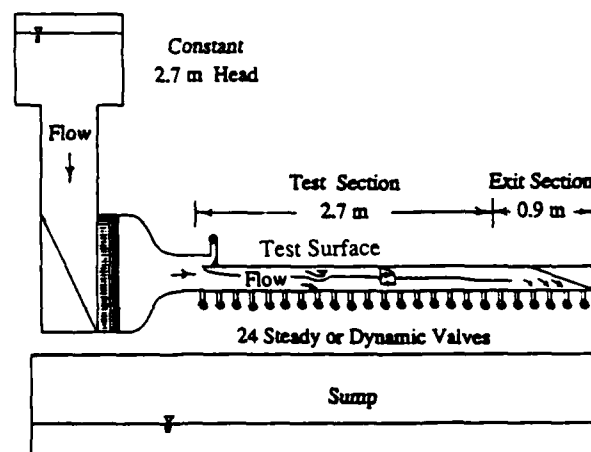

Figure 1.   Unsteady Boundary-Layer Water Tunnel

A test boundary layer grows on the test surface, a flat plate 2.7 meters long, which is the top wall of the test section. An half ellipse, figure 2, forms the leading edge of the test surface; the ratio of major to minor axis for this half ellipse is 16:1. The precise location of the flow stagnation point, for genesis of the test boundary layer, is set by adjusting a bank of bypass valves. These bypass valves direct to the sump all water passing over the upper surface of the leading edge. On the lower surface of the leading edge, a fresh boundary layer grows.

The freestream flow is controlled by a bank of manual and computer-controlled valves located on the wall opposite the test surface. When all valves but those at the end of the test section are trimmed down, the flow sees a zero pressure gradient. Alternatively, some upstream valves may be opened to create an adverse pressure gradient. The flowrate drained through each valve, and hence the imposed freestream flow, can be steady or unsteady. Printed-circuit motors driven by a custom computer interface control eight specially-designed valves. Computer control allows any waveform to be used; sinusoids, square waves, and triangular waves are pre-programmed. For these experiments one upstream valve and one downstream valve are commanded to operate 180 degrees out of phase, producing a steady flow in the upstream portion

*   Graduate Student, Department of Mechanical Engineering, Stanford University.
+   Professor, Department of Mechanical Engineering, Stanford University.
++   Associate Professor, Department of Aeronautical and Mechanical Engineering, Arizona State University.

of the test section while the flow is unsteady downstream; leading-edge vorticity is thereby kept constant. In other experiments, w; can oscillate the entire flow so that the influence of leading-edge vorticity fluctuations can be investigated.
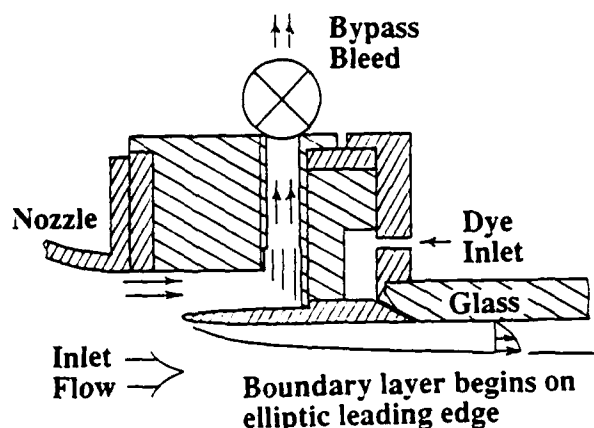

Figure 2. Schematic of inlet flow to test section.

Figure 3. Sample Data from Brereton and Reynolds (1987). Variation of U_{∞} with phase angle of driven unsteadiness.

Laminar and turbulent boundary-layer experiments alike are performed in this tunnel: laminar studies take place in the first meter; when a trip is installed, turbulent studies occupy the latter 1.7 meters. The range of available chord Reynolds numbers is 2×10^4 through 1.9×10^6, however, for the separation experiments only chord Reynolds numbers from 5×10^4 through 3×10^5 will be investigated. The freestream velocity through the test section can be maintained within the range of 0.1 to 0.7 m/s. The turbulence intensity in the free stream has been measured at less than $u'/U = 0.5\%$, however, an analysis of the disturbance-eigenfunction, ie. u'/U vs. y, in the laminar section has indicated that the freestream turbulence may be even lower.

Two laser doppler anemometer (LDA) systems measure the flowrate through the water tunnel. At the entrance to the test section, a single-component Helium-Neon LDA monitors the inlet flow. Downstream, the second LDA measures the velocity of the separated flow. This two-component Argon-Ion LDA is mounted on a traverse that permits movement of the measuring volume in all spatial directions. Motion normal to the test surface is automated for velocity surveys, which can continue for days without intervention.

Special features of the previous facility which assured reliable, repeatable experiments have been retained in the new tunnel. A refrigeration system maintains the water temperature within a fraction of a degree. Also, air is removed from the water by a continuously operating system to prevent microbubbles from contaminating the LDA measurements. Previous results from this facility are documented by Jayaraman, Parikh, and Reynolds (1982) and by Brereton and Reynolds (1987). Each of these research efforts resulted in extensive data sets against which turbulence modelers may test their computer codes. Brereton, for example, has indicated which elements of the Reynolds Stress tensor are most significant in unsteady, turbulent boundary layers. A sample of Brereton's data has been included, figure 3.
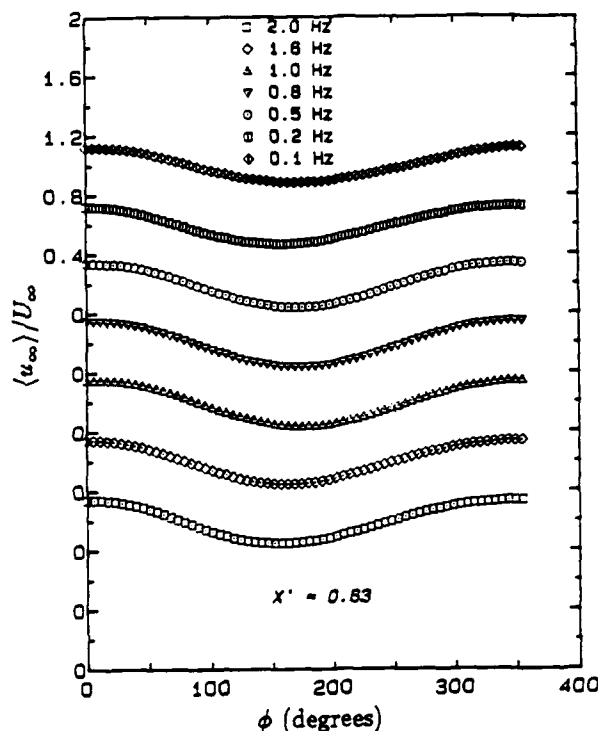
Control of Pressure Gradients and Generation of the Three-Dimensional Separation

Streamwise and spanwise pressure gradients throughout the tunnel are controlled to influence the development of the test boundary layer. The control of these gradients by opposite wall suction enables us to generate a three-dimensional separation on a flat plate. While side wall bleeds remove the sluggish portion of the side-wall boundary layers to help the layers remain attached, they do little to alter the spanwise gradient. Greater control of pressure gradients arises from the opposite wall suction. By tailoring the location and the magnitude of the opposite wall suction, the desired pressure gradient is obtained.

Two types of interchangeable valves, spaced every six inches, are located under the opposite wall to control the strength of the suction. Manual gate valves, stationed at 16 of the 24 locations, provide a zero pressure gradient during steady operation of the tunnel. Elsewhere computer-controlled, gate-type valves, custom designed for this project, provide dynamic variation of the flow removed from the tunnel. This gate-type valve incorporates a perforated disc revolving atop a flat bearing which has a matching hole pattern; henceforth it will be labelled a Revolving-Disc Valve. Since a single revolving-disc valve can remove up to 40% of the maximum volume flowrate through the tunnel, substantial adverse gradients can be imposed if desired. The revolving-disc valve is fast-acting; in tests it has followed a 40 Hz square wave at full amplitude without distortion, ensuring repeatable control of imposed unsteadiness.

328

A selected pattern of holes in the opposite wall sets the location of suction. For example, an uniform array of holes across the span draws a two-dimensional response from the test boundary layer; in contrast, a singular hole draws a three-dimensional response. Figure 4 schematically shows a three-dimensional separation generated in the manner just described.
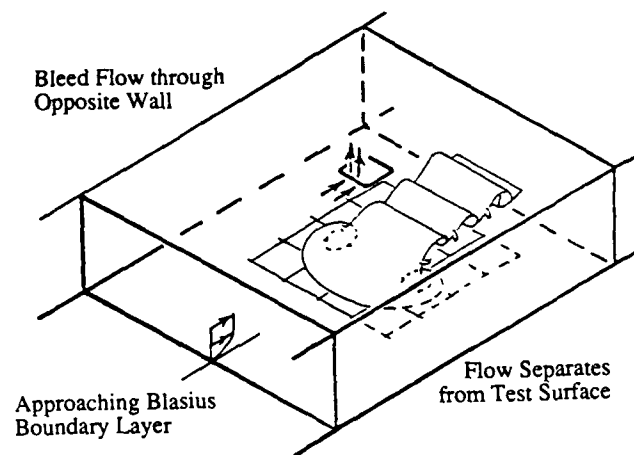

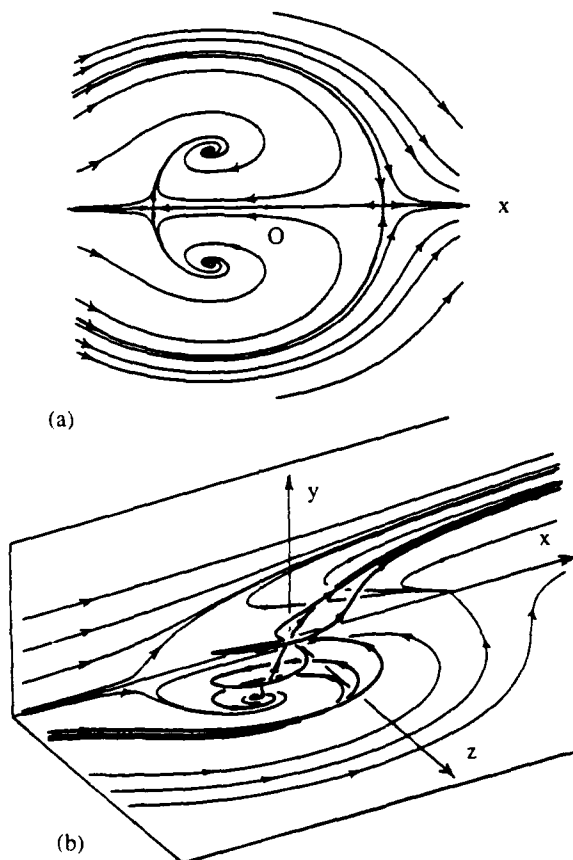Figure 4. Basic method for inducing a three-dimensional separation.

(a)

(b)

Figure 5. Mean structure of a symmetric Owl Face of the First Kind from Perry (1987): (a) Surface flow pattern; (b) Oblique View with some trajectories.

Flow Visualization

In our experiment, flow visualization with food dye has revealed a three-dimensional separation known as an Owl Face of the first kind, figure 5 (Perry and Chong, 1987). A variety of three-dimensional separations have been observed and reported in the literature. These are categorized according to the time-averaged pattern observed on a surface oil flow in wind tunnel tests. Owl Face separations have been observed on stalled airfoils.

To visualize our separation, steady conditions were set throughout the tunnel: upstream, there was a zero pressure gradient; downstream, at a chord Reynolds number of 10^5, a localized adverse pressure gradient caused the boundary layer to separate, figure 4. Dye was then released into the inner portion of the boundary layer via a slot in the test surface.

Upon encountering the separation, the dye lifted from the wall and formed a localized free shear layer. A sketch of an instantaneous streaksheet formed by the dye is shown in figure 6. The plan view, figure 7, revealed the separation to be an Owl Face of the First Kind. From a side view, that is across the span of the tunnel, the separation appeared like a flat pancake with the upstream end forming a thin wedge. At the downstream and thicker end of the pancake, the free shear layer rolled up and transitioned to turbulence, as is typical of free shear layers.
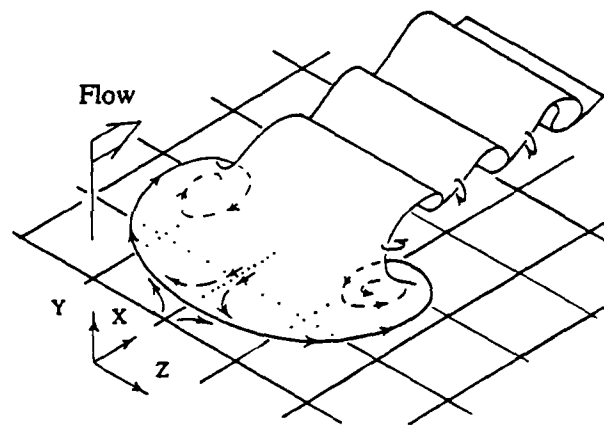

Figure 6. 'Streaksheet' Structure of Separation: Owl Face of the First Kind

The differences between our streaksheet structure and the mean structure given by Perry and Hornung (1983) are due to unsteadiness in the separation. The time-averaged flows which guided their analysis could not reveal the rolling up of the trailing portion of the free shear layer. They did note, however, that the symmetric structure they modeled is itself topologically unstable. The instability suggests additional unsteadiness about the mean structure. Indeed, an unsteady analysis of the Owl Face by Perry and Chong (1987) indicated that one of the eyes of the Owl Face could occasionally disappear. We verified this behavior in our separation which, although encouched in steady boundary conditions, was prone to wander about the mean structure and 'wink' such that one eye was no longer visible.

Though the separation generated under steady freestream conditions is intriguing ('steady' separation), our capability and interest is in the behavior of the three-dimensional separation when the pressure gradient is driven in a controlled, unsteady manner. Thus, we left further study of the steady separation until an opportune time and proceeded to visualize the driven separation. The local pressure gradient

was oscillated between a zero pressure gradient and an adverse gradient. Two waveforms were selected, sinusoidal and square wave, for the oscillation. Three frequencies, listed in Table 1, were chosen for study. The middle of these three frequencies, 1/2 Hz, roughly corresponds to the frequency of vortex roll-up in the free shear layer. The other two frequencies bracket this value.
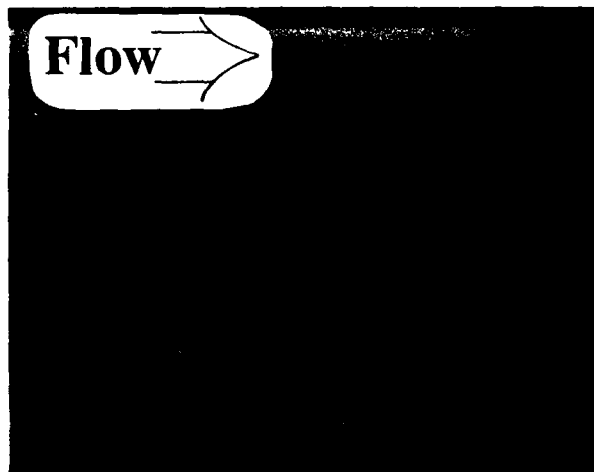

Figure 7. View of Separation through Test Surface. Notice bleed hole in opposite wall. It is actually centered with respect to separation.

Table 1. Flow Visualization Parameters	
U_o	0.217 m/s
X_{chord}	0.41 m
Re_x	10^5
L_s = Length of steady separation	0.1 m
f	0, 1/16, 1/2, 2 Hz
$\dfrac{\pi f L_s}{U_o}$	0, 0.09, 0.72, 2.9
$\dfrac{dp/dx \, L_s}{1/2 \rho U_o^2}$	0.29

The first observation made regarding the driven, unsteady separations is that they appeared to be bilaterally symmetric about the central streamwise axis. This symmetry contrasts with the wandering of the steady separation. We will investigate this behavior more thoroughly in the future.

Our second observation is that the Owl Face separation evolves with the frequency, amplitude, and waveform of the driven, three-dimensional pressure gradient. For example, forcing at the low frequency would allow the separation to be

completely washed out before the next cycle started: square wave forcing brought dramatic development of the separation as well as its sudden washout; sinusoidal forcing at the same amplitude barely caused separation before it washed out again. At the middle and high frequencies, the Owl Face persisted throughout the cycle for both waveforms. Now, the size of the mean structure would vary, decreasing as the frequency increased. The instantaneous size of the unsteady separation modulated with the phase of the cycle. We did not vary the amplitude for our recorded visualization and have not yet investigated conditions for incipient separation.

Summary and Future Work

An experimental study of unsteady, three-dimensional separations has begun at Stanford to provide basic information about the development, washout and control of such separations. The water tunnel used for this investigation has excellent optical access and flexible control of the freestream flow. Tailored streamwise and spanwise pressure gradients, controlled by a set of custom, computer-controlled valves, can cause a steady or an unsteady separation in a laminar boundary layer.

Flow visualization has provided the first results of our investigation. The separation was visualized both under universally steady conditions and under locally unsteady conditions. Flow visualization revealed the separation we generated in all cases to be an Owl Face of the first kind (Perry and Hornung, 1984). The Owl Face separation evolved with the frequency, amplitude, and waveform of the oscillating, three-dimensional pressure gradient.

Future work will include extensive visualization of a larger variety of imposed frequencies and amplitudes. The chord Reynolds number at which the separation is generated will also be varied. Furthermore, phase-averaged velocity profiles of the separation will be collected via a two-component LDA. As our investigation continues, the theoretical analysis of evolution of three-dimensional separation by R. Legendre (1982), will assist our understanding. In addition to the experimental study described herein, a computational simulation of the same flow is being done by Laura Pauley. Thankfully, the parallel efforts are beginning to bear fruit in the understanding and prediction of these important flows.

References

Brereton, G.B. and Reynolds, W.C. 1987. 'An Experimental Study of the Fluid Mechanics of Unsteady Turbulent Boundary Layers.' Doctoral thesis, Stanford University.

Jayaraman, R., Parikh, P. and Reynolds, W.C. 1982. 'An Experimental Study of the Dynamics of an Unsteady Turbulent Boundary Layer.' Doctoral thesis, Stanford University.

Legendre, R. 1982. 'Regular or Catastrophic Evolution of Steady Flows Depending on Parameters.' La Recherche Aérospatiale, 1982-4, pp. 41-49.

Perry, A.E. and Chong, M.S. 1987. 'A Series Expansion Study of the Navier-Stokes Equations with Applications to Three-dimensional Separation Patterns.' Journal of Fluid Mechanics 173: 207-224.

Perry, A.E and Hornung, H. 1983. 'Some Aspects of Three-dimensional Separation, Part II: Vortex Skeletons.' Zeitschrift für Flugwissenschaften und Weltraumforschung 8, pp. 155-160.

Tobak, M. and Peake, D.J. 1982. 'Topology of three-dimensional Separated Flows.' Annual Review of Fluid Mechanics 14: 61-85.

THE USE OF A VIBRATING RIBBON TO DELAY SEPARATION ON TWO-DIMENSIONAL AIRFOILS:

SOME PRELIMINARY OBSERVATIONS*

D. Neuburger and I. Wygnanski[†]
Faculty of Engineering, Tel-Aviv University, Ramat-Aviv 69978, Israel

1. INTRODUCTION

The phenomenon of "dynamic stall" occurs during pitch-up maneuvers of fixed-wing airplanes, on helicopter rotors, and on vertical-blade, wind-driven, power generators. The maximum lift coefficient attained dynamically may exceed, by a factor of 5, the maximum lift coefficient attainable in steady flight. A large hysteresis loop characterizes the oscillating wing in pitch. The time during which supercirculation is maintained depends mostly on the rate of pitch, $\dot{\alpha}$, the chord of the airfoil, c, and the velocity of the free-stream, U, combined into a dimensionless parameter, $\alpha^+ = \dot{\alpha} c/U$, or a dimensionless frequency for the oscillating airfoil, $f^+ = f c/U$. The effects of the shape of the airfoil, the Reynolds number, and the Mach number are all considered to be of secondary importance, although the evidence substantiating these considerations is scant. The effects of compressibility were recently examined by Fung and Carr[1] in view of the very low pressure sustained near the leading edges of oscillating airfoils. The computations of Fung and Carr suggest that the flow may become locally supersonic at Mach numbers as low as 0.3.

Visualization experiments on NACA-0015 airfoils during pitch-up maneuvers, at $0.1 < \alpha^+ < 0.2$ and at moderately low Reynolds numbers, revealed few characteristic flow patterns. These observations were correlated with the measured angle of attack and, therefore, lift coefficient during an upward-pitching motion of an airfoil:[2]

1. $0° < \alpha < 25°$. The boundary layer on the upper surface of the airfoil thickens with increasing α; however, it remains fully attached to the surface, in spite of the growing adverse pressure gradient. Large coherent structures, similar to the ones observed in a free mixing layer, appear to straddle the entire width of the boundary layer when $\alpha > 10°$. The lift coefficient at this part of the motion increases almost linearly with α and attains a value of 2 at $\alpha \simeq 25°$.[2] One should recall that the maximum C_L attainable from this airfoil under static conditions at comparable Reynolds numbers is approximately 0.8.

2. $25° < \alpha < 30°$ at $\alpha^+ = 0.1$ or $25° < \alpha < 40°$ at $\alpha^+ = 0.2$. In this range of angles of attack, the boundary layer separates near the leading edge of the airfoil, enclosing a large-scale bubble whose length is commensurate with the chord. The lift coefficient continues to increase and, in some instances, even the slope of the lift curve, $dC_L/d\alpha$, increases due to the growth of the bubble which effectively changes the camber and the thickness of the airfoil. The maximum C_L attainable appears to increase with the increase of α^+ [for $\alpha^+ = 0.1$, $(C_L)_{max} = 2.4$, while for $\alpha^+ = 0.2$, $(C_L)_{max} = 3$].

3. $35° < \alpha < 45°$. In this range of angles of attack, the separated shear layer fails to reattach to the surface, thus forming a large vortex, which is referred to in the literature as the "dynamic stall vortex." The direction of the flow over the airfoil surface is reversed, and this reverse flow is entrained into the core of the vortex, which increases in size with increasing α.

4. $\alpha > 45°$. The dynamic vortex separates from the leading edge of the airfoil and is convected downstream at approximately 1/3 of the free-stream velocity while another vortex of opposing sign is being generated at the trailing edge. The lift coefficient decreases as the dynamic vortex is shed.

The shear layer existing in stages 2 to 4 is inviscidly unstable and generates its own eddies, whose scale is commensurate with the local characteristic thickness of the boundary layer at separation. Thus, the "dynamic stall vortex" is surrounded by an array of Kelvin-Helmholtz eddies spiraling inward, into its core, from the peripheries. The most clear photographs of a similar phenomenon (i.e., the separation of an accelerating flow around an airfoil at a high angle of attack) were taken by Freymuth,[3] an example of which is shown in Fig. 1. The "dynamic stall vortex" may therefore be viewed as a spiraling shear layer. The radius of curvature of the spiral depends on the acceleration of the flow (either linear, dU/dt, or angular, dα/dt) and represents the time elapsed from the initiation of the separation of the boundary layer to the shedding of the "dynamic stall vortex." The size of the eddies surrounding the spiral depends on the thickness of the boundary layer at separation. Consequently, two characteristic length scales may be required to represent the phenomenon of dynamic stall. The radius of curvature of the spiral becomes infinite when the acceleration vanishes and the entire stall phenomenon may be considered as static. The shear layer, in this case, remains parallel to the undisturbed flow, and the corresponding lift coefficient is considerably lower than $(C_L)_{max}$.

One may view a deep stall as a sudden change in the inclination angle of the shear layer relative to the free stream (i.e., the shear layer

which is approximately inclined to the free stream at the angle of incidence of the airfoil while the flow is attached becomes parallel to the free stream when the airfoil stalls). It seemed plausible that one could delay the detachment of the shear layer to higher angles of attack by increasing its characteristic width or the scale of the eddies generated by the Kelvin-Helmoltz instability. The change in the size of these eddies implies a change in the rate of entrainment into the separated shear layer. When the entrained fluid comes from the limited reservoir bounded by the separated shear layer and the solid upper surface of the airfoil, the pressure in this reservoir is reduced, causing the separated shear layer to bend toward the surface to provide the required balance between the curvature of the flow and the pressure gradient in the direction perpendicular to the streamlines. Thus, by controlling the rate of spread of the shear layer, taking advantage of the inherent instability of this flow, one may produce an equivalent of a Coanda effect and increase the maximum lift attainable.

The experiments described in the present report are aimed at proving this hypothesis. An extension of the concept may provide the means of controlling, at least partially, the dynamic stall, since the ratio between the two length scales of the problem is affected by the enhanced entrainment into the separated shear layer. The initial flow visualization experiments were carried out on a thin, uncambered airfoil having a sharp leading edge. The approximate Reynolds number based on the airfoil chord was 5×10^4. The rate of spread of the shear layer was controlled by the harmonic motion of a small ribbon hinged to the surface of the airfoil near its leading edge. Quantitative data were generated on a NACA-0015 airfoil and on a Wortmann FX63-137 airfoil at Reynolds numbers ranging from 10^5 to 4×10^5. The vibrating ribbons, in these experiments, were situated upstream of the anticipated static separation point corresponding to the onset of a deep stall. The airfoils were mounted on turntables which spanned the tunnel test section. The lift coefficient was determined by integrating the pressure distribution on the surface, while the drag coefficient was measured by traversing the wake. The tests were carried out in a 3 foot-by-2 foot test section. The airfoils had a 1-foot chord and a 2-foot span, and therefore standard, wind tunnel wall corrections had to be applied to the data.

2. RESULTS AND DISCUSSION

2.1 Flow Visualization

The flow over the sharp leading-edge airfoil shown in Fig. 2 is fully separated at $\alpha = 19°$ when the ribbon, seen near the leading edge, is inactive. The smoke filaments visible above the upper surface of the airfoil are flowing in the direction of the undisturbed stream (i.e., they are not deflected downward), indicating that the airfoil does not impart any appreciable downward momentum to the fluid and thus generates little or no lift. The tufts placed on the upper surface provide, by oscillating vigorously in random directions, an additional indication that the flow is fully separated. When harmonic forcing is

applied to the ribbon, the same tufts become attached to the surface, with the exception of the tuft adjacent to the trailing edge of the ribbon. Although the thickness of the mixing layer increases dramatically as a result of the excitation, the free stream above the airfoil is deflected downward at an average angle of 16°, which differs by approximately 3° from the angle of incidence on the airfoil itself (Fig. 3). The structure of the large eddies visible above the airfoil resembles the coherent structures observed in a plane mixing layer, generated by two parallel streams of different velocities, in the absence of a pressure gradient and in the absence of a solid surface. The level of turbulence in the attached mixing layer ought to be high, as may be deduced from the diffused smoke in the core of the large eddies.

Similar observations were also made on the NACA-0015 airfoil at an angle of incidence $\alpha = 16°$ and at Re $\approx 5 \times 10^4$ and are shown in Fig. 4.

2.2 The Lift and Drag Characteristics of the NACA-0015 Airfoil

The dependence of the lift coefficient on the angle of incidence, for Re $= 4 \times 10^5$ and U $= 20$ m/sec, is shown in Fig. 5. The slope $dC_L/d\alpha$ is almost a constant for $\alpha < 10°$, regardless of whether the ribbon was oscillating or not. In the absence of external excitation, the airfoil stalled at $11° < \alpha < 12°$, giving a maximum value of $C_L = 1.04$. Oscillating the ribbon at an amplitude of 1 mm at a reduced frequency $f^+ = 0.9$ delayed the stall to $15° < \alpha < 16°$ and enabled the airfoil to generate a $(C_L)_{max} = 1.33$. The dependence of C_L on α remained virtually linear between $\alpha \approx 10°$ and 15°.

The pressure distributions measured at $\alpha = 12°$ for the above-mentioned forced and unforced situations were almost identical (Fig. 6). At $\alpha = 15°$, however, the airfoil stalls in the absence of excitation, as may be deduced from the constant pressure coefficient observed on the upper surface. The low pressure coefficients and the adverse pressure gradient on the upper surface are recovered by forcing the ribbon to oscillate. At $\alpha = 18°$, the forced oscillations at a displacement amplitude of 1 mm and $f^+ = 0.9$ cannot prevent a leading-edge bubble, which extends from $x/c \approx 0.1$ to $x/c \approx 0.25$. Thereafter, the flow reattaches to the surface as a result of the amplification of the oscillations in the free shear layer which enabled it to negotiate the large adverse pressure gradient farther downstream. The local separation and reattachment resulted in a loss of lift equivalent to 15% of $(C_L)_{max}$.

The measured drag coefficient, shown in Fig. 7, is independent of the excitation provided $\alpha < 7°$. For $8° < \alpha < 12°$, the drag of this airfoil in the absence of forcing is somewhat lower than it is with the ribbon operational; this may be attributed to a higher level of turbulence caused by the imposed oscillations, which presumably results in an earlier transition of the boundary layer. The drag coefficient measured between $\alpha = 10°$ and $\alpha = 18°$, with the ribbon oscillating, is always smaller than the drag coefficient measured with the ribbon stationary; the largest difference

occurs at $\alpha = 15°$, which amounts to a 33% reduction in the C_D as a result of the excitation. At this angle of attack, the flow is fully attached in one case and completely separated in another. There are no significant differences at $\alpha > 18°$ since the flow is separated irrespective of the oscillations of the ribbon.

An attempt was made to explore the dependence of C_L on f^+ and on the displacement amplitude of the ribbon. The displacement of the ribbon was chosen to be maintained at a constant value because of the ease at which it was observed. Stroboscopic illumination which was phase locked to the motion of the ribbon was sufficient to monitor the amplitude and the spanwise uniformity of the oscillation. Since the ribbon oscillated in a harmonic motion described by

$$Y_r = A \sin(\omega t) ,$$

it was believed that the velocity perturbation imparted to the flow is linearly related to the velocity at the trailing edge of the ribbon and may be described by

$$V_r = \kappa A \omega \cos(\omega t) ,$$

where κ is a proportionality constant to be determined experimentally. The proof of the fallacy of this simplification will be discussed.

The dependence of C_L on α and f^+ is shown in Fig. 8. The Reynolds number and the displacement amplitude of the ribbon, A, was maintained constant throughout these experiments. The data shown in Fig. 8a correspond to a displacement A = 1 mm, while the data shown in Fig. 8b represent A = 0.5 mm. The triangular symbols in both figures correspond to the C_L obtained with the ribbon being stationary. For $\alpha < 11°$, the value of C_L was not affected by the ribbon, regardless of the frequency and the amplitude of the oscillation. In both instances, the maximum value of C_L increased with increasing f^+. Since the oscillators used in the experiment were too weak to maintain the prescribed amplitude at higher frequencies, the eventual reduction in $(C_L)_{max}$ was not observed. The angle of incidence beyond which the airfoil stalled increased with f^+, while A was maintained constant. For example, for A = 1mm (Fig. 8a),

f^+	α Corresponding to $(C_L)_{max}$
0.00	11°-12°
0.36	12°-13°
0.45	15°
0.90	15°-16°

The value of α at which C_L was maximum hardly changed in this case provided $f^+ > 0.45$. Similar deductions can be made for A = 0.5 mm. As shown in Fig. 8b, increasing the frequency of the oscillations while decreasing their amplitude generated similar values of $(C_L)_{max}$. Plotting the maximum value of the lift coefficient attained versus the Strouhal number comprising $A \omega/U$ suggested that the relationship between these parameters is by no means simple (Fig. 9a), thus the sinusoidal velocity perturbations, rather than the

displacement amplitude of the flap, will be maintained constant in future experiments.

A better empirical correlation collapsing the two sets of data is shown in Fig. 9b. The dependent parameter considered is the product of lift coefficient at a given large angle of incidence and the Strouhal number $A\omega/U$, while the independent parameter is this particular Strouhal number. The angle α considered for comparison should be higher than the angle of stall in the absence of the forced oscillations. The data collected at $\alpha = 15°$ are plotted in Fig. 9b, and the collapse onto a single curve is fairly good. Linear dependence may be fitted to the data provided St > 0.5×10^{-3}. The validity for such a correlation for different geometries, Re, St, etc., will have to be explored further.

2.3 The Lift and Drag Characteristics of the Wortmann FX63-137 Airfoil

The Wortmann FX63-137 airfoil was especially developed for high-performance gliders, and its characteristics at Re lower than 5×10^5 are well documented. It is also considered one of the best airfoil sections available for low-speed applications as its combination of camber and thickness enables a laminar separation bubble to reattach over a fairly broad range of angles of attack. The lift coefficient on this airfoil, however, exhibits a strong hysteresis in its recovery from stall, resulting in severe control problems. For example, if a typical inception of a stall at a prescribed Re occurs at $\alpha = 18°$, the recovery from stall may occur at $\alpha = 10°$. The difference between the two angles may depend on the smoothness of the surface, the Reynolds number, the noise level and its predominant frequency band, as well as the turbulence level in the free stream.[4] The $(C_L)_{max}$ attained is approximately 1.6, dropping to $C_L = 1$ after the inception of a stall.

The observations presented in the report were made at Re = 2×10^5 with a small ribbon whose chord was less than 2% of the airfoil chord mounted on the upper surface at x/c = 0.10. The ribbon was placed at this x/c because a laminar separation bubble originated at this location on the clean airfoil (i.e., in the absence of the ribbon) at $\alpha = 15°$. The inactive ribbon, whose trailing edge was held at a distance of 0.5 mm above the upper surface of the airfoil, in order to permit symmetrical oscillations about this neutral location, acted as a two-dimensional tripping device, changing somewhat the characteristics of the airfoil. The unforced data presented in Fig. 10 refer to this configuration and, therefore, the stall hysteresis loop is significantly narrower in terms of $\Delta\alpha$ than for the clean airfoil. By vibrating the ribbon at A = 1 mm at $f^+ = 0.9$, the maximum lift coefficient increased from 1.6 to 1.75 and the angle of stall was delayed by approximately 3° (Fig. 10).

The width of the hysteresis loop was narrowed when the frequency of the excitation was increased while the displacement amplitude of the vibrating ribbon was maintained at 1 mm (Fig. 11). At $f^+ = 1.8$, the hysteresis loop was entirely eliminated, enabling the airfoil to stall and to recover from stall at an identical angle of

attack ($17° < \alpha_{stall} < 18°$). Although the value of $(C_L)_{max}$ measured at $f^+ = 1.8$ was almost identical to the value measured in the absence of forcing, the range of angles at which the lift coefficient remained close to $(C_L)_{max}$ doubled when compared with the unforced case.

The pressure distribution corresponding to $\alpha = 17°$ is shown in Fig. 12. In the absence of forcing, the airfoil is on the verge of a deep stall, having a constant pressure coefficient over 80% of its chord. The pressure distribution does not show any indication of recovery when the angle of incidence is reduced from α corresponding to a deep stall to $\alpha = 17°$. By activating the ribbon at $f^+ = 1.2$, the hysteresis loop is narrower and the pressure distribution shows signs of recovery at $\alpha = 17°$. Nevertheless, the imposed oscillations could not reestablish the steep pressure gradient near the leading edge of the airfoil. The pressure distributions corresponding to $\alpha = 17°$ and $f^+ = 1.8$ are identical whether or not the angle of incidence was decreasing or increasing, even though the measurements were not made on the fly (i.e., α remained constant throughout the process of data acquistion).

3. CONCLUDING REMARKS

Periodic, two-dimensional perturbations which are self-amplified by the shear layer enhance the entrainment capacity of the shear layer, resulting in a delay of separation. The maximum lift measured under these conditions is increased, and the drag at an angle of attack corresponding to the maximum lift is decreased. The enhancement of $(C_L)_{max}$ between 10% and 40% was achieved depending on the geometry of the airfoil, the Reynolds number, the location of the vibrating ribbon, and the frequency and amplitude of the imposed oscillations. The parameter space is far from being explored at this time, but there are indications that a more complex excitation using a combination of frequencies emanating from a single element or a combination of vibrating elements enhances the overall result. The possible elimination of the hysteresis loops from the characteristic behavior of high-lift laminar airfoils and the concomitant broadening of the C_L versus α curves near $C_L = (C_L)_{max}$ may serve in the future as an important consideration in choosing a particular form of an airfoil section.

REFERENCES

1. Fung, K. Y. and Carr, L. W., "An Analytical Study of Compressibility Effects on Dynamic Stall," presented at the Workshop on Unsteady Separated Flow, Air Force Academy, July 1987.

2. Walker, J. M. and Seiler, F. J., "Forced Unsteady Vortex Flows Driven by Pitching Airfoils, AIAA Paper No. AIAA-87-1331, 1987.

3. Freymuth, P., "Vortex Patterns of Dynamic Separation; A Parametric and Comparative Study," Progress in Aerospace Sciences, Vol. 22, Pergamon Press, London, 1985, pp. 161-208.

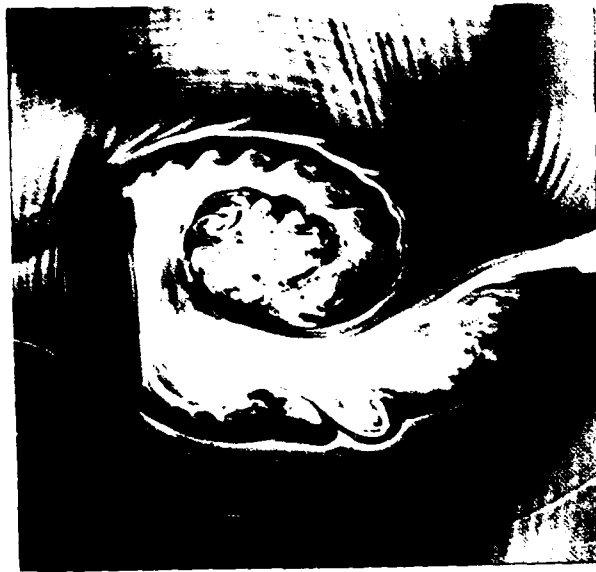4. Marchman, J. F., "Aerodynamic Testing at Low Reynolds Numbers," J. of Aircraft, Vol. 24, No. 2, 1987, pp. 107-114.

Fig. 1 Accelerating flow over a NACA-0015 airfoil at $\alpha = 80°$ (courtesy of Prof. P. Freymuth).

Fig. 2 The flow over a stalled airfoil at $\alpha = 19°$ (stationary ribbon is seen near the leading edge).
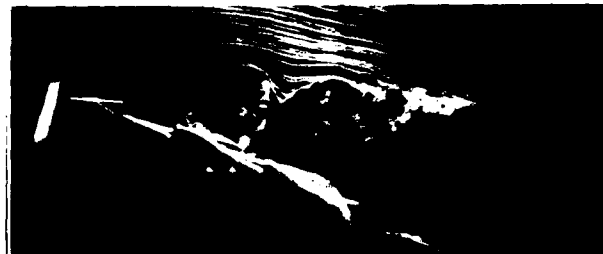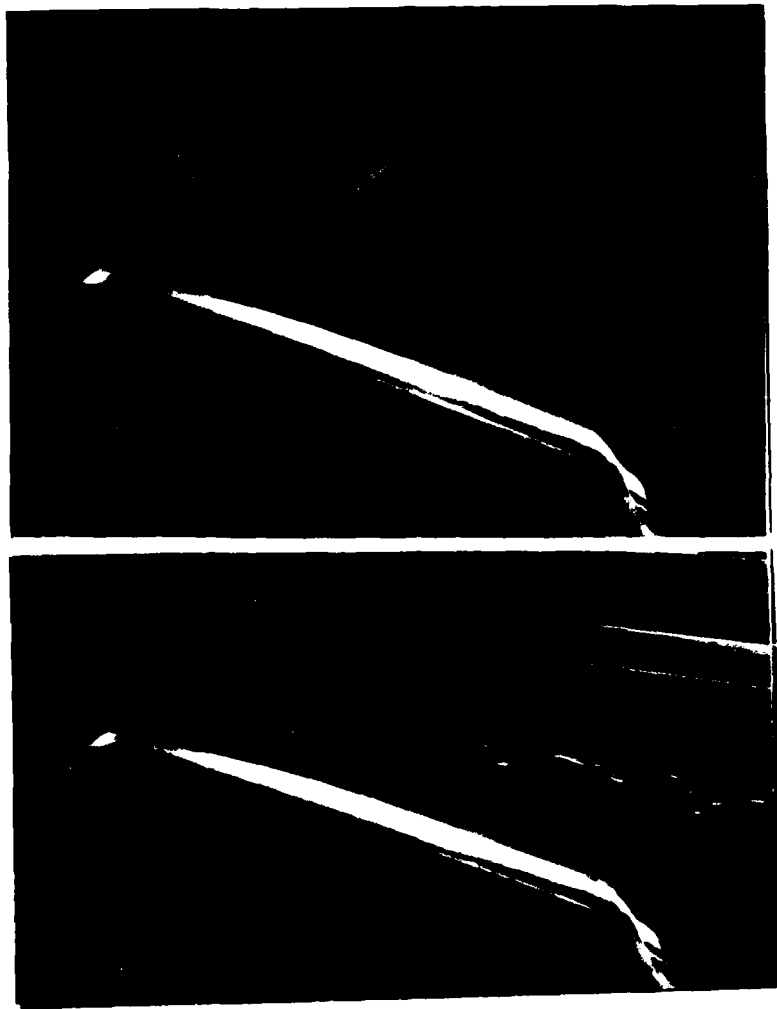

Fig. 3 The effect of the vibrating ribbon on the flow.

Fig. 4   The effect of ribbon oscillations on the flow around
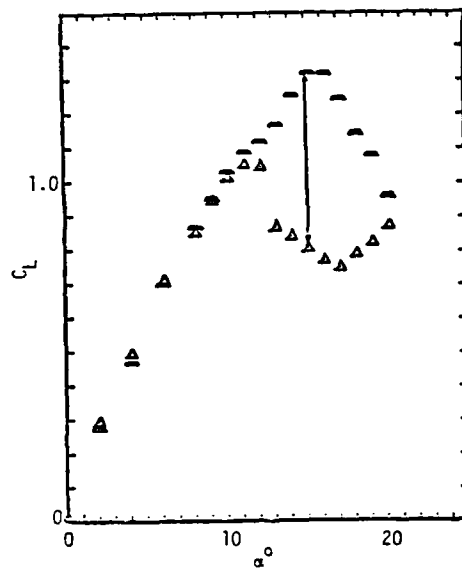the NACA-0015 airfoil at $\alpha = 16°$.

Fig. 5   The variation of C_L with α for the NACA-0015 airfoil
with and without the oscillations of the ribbon; Re = 4
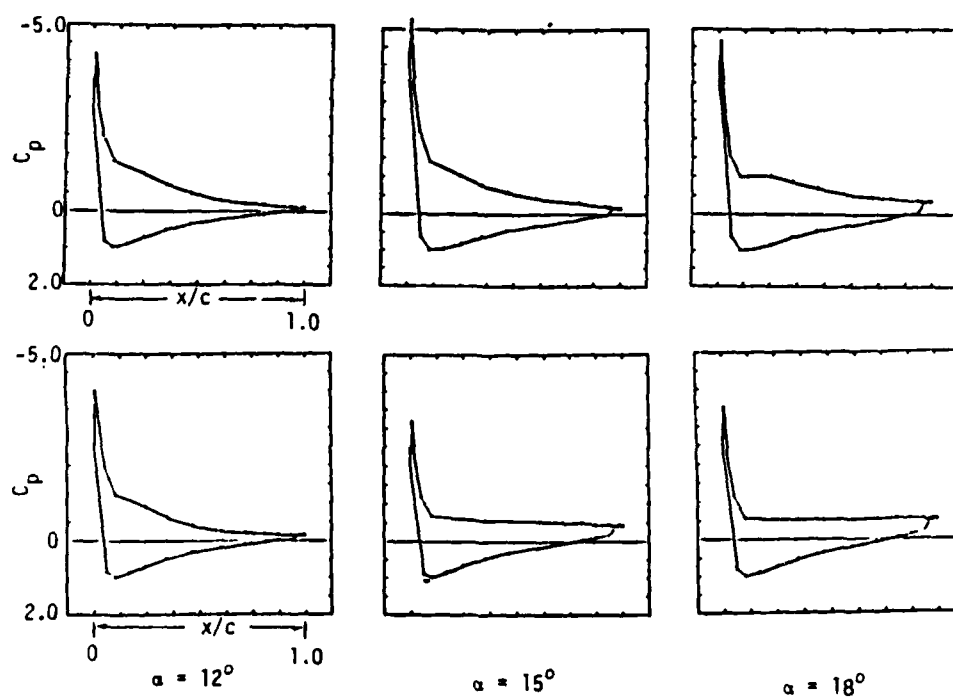× 10⁵; Δ - no oscillation; ◁ - ribbon oscillated at f^+
= 0.9; St = fA/U = 2.95 × 10⁻³.

337

Fig. 6   A comparison of the pressure distributions over the NACA-0015 airfoil with and without the oscillations of the ribbon; $\alpha \simeq 12°$, $15°$, $18°$; $f^+ = 0.9$; $St = 2.95 \times 10^{-3}$.
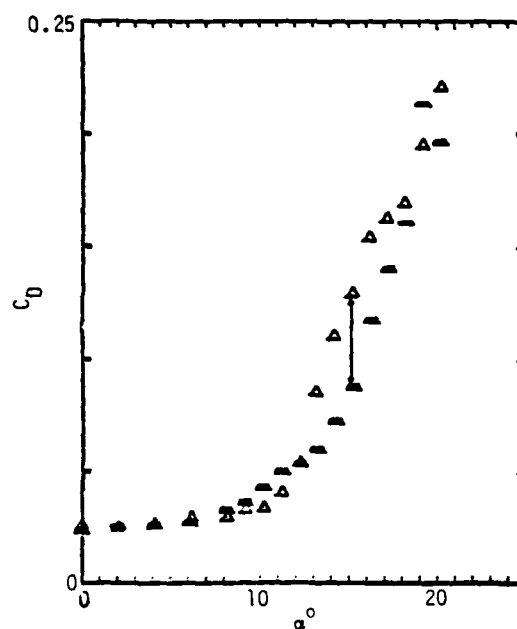
Fig. 7   The variation of C_D with α for the NACA-0015 airfoil with conditions identical to those shown in Fig. 5.
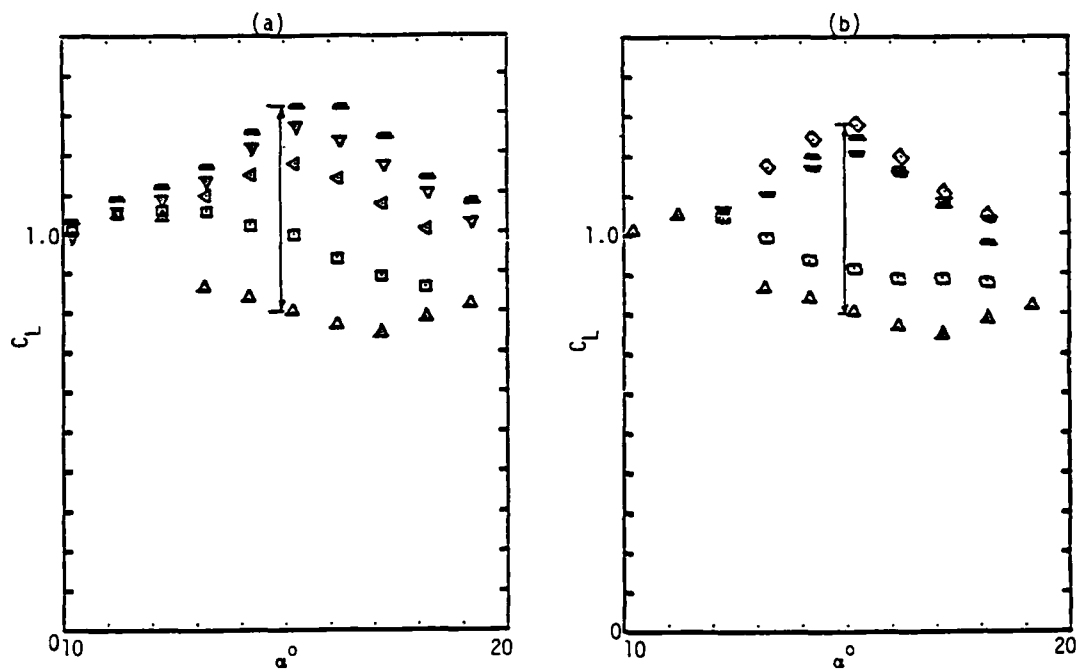
Fig. 8   The dependence of C_L on α for different frequencies of forcing on the NACA-0015 airfoil at Re = 4 × 10⁵:

(a)

		f^+	$St \times 10^3$
A = 1 mm	△	0	--
	□	0.36	1.19
	◁	0.45	1.75
	▽	0.63	2.67
	▱	0.90	3.92

(b)

		f^+	$St \times 10^3$
A = 0.5 mm	△	0	--
	□	0.3	0.50
	▱	0.6	1.00
	▱	0.9	1.50
	◇	1.2	1.95

Fig. 9   Attempts at correlating the amplitude and frequency of the ribbon with the measure C_L on the NACA-0015 airfoil:

(a) A plot of $(C_L)_{max}$ versus $St = Af/U$.   (b) A plot of $(C_L)_{\alpha=15°} \times St$ versus St.

339
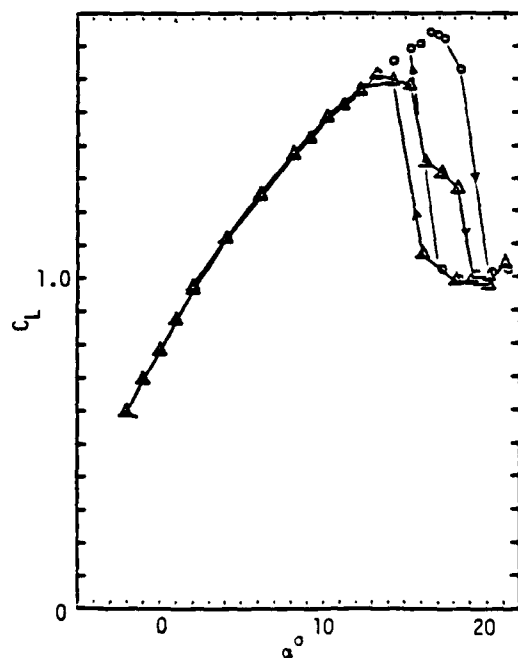
Fig. 10 The dependence of C_L on α for the FX63-137 airfoil at Re = 2 $\times 10^5$.

$\triangle$ - ribbon stationary   o - f$^+$ = 0.9, St = 3 $\times$ 10^{-3}
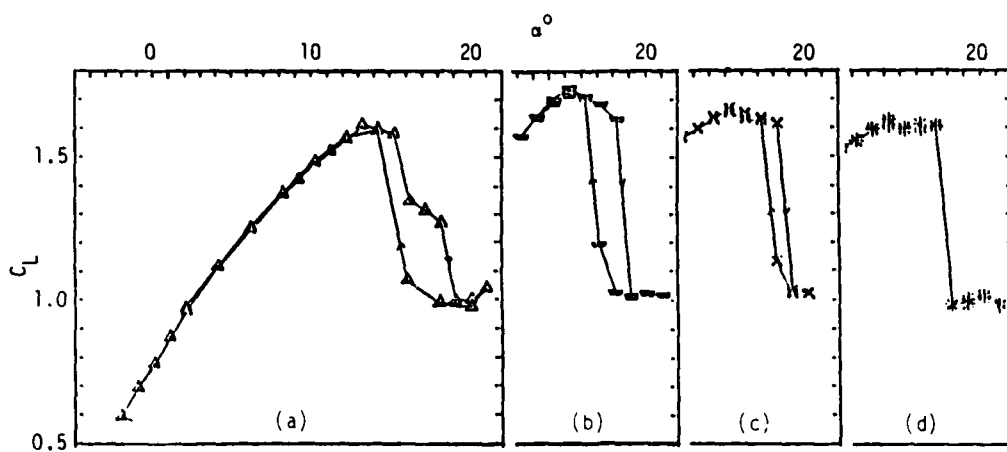
Fig. 11. The variation of C_L with α for the FX63-137 airfoil at Re = 2 $\times$ 10^5 showing stall hysteresis.

(a) f$^+$ = 0   (b) f$^+$ = 1.2   (c) f$^+$ = 1.5   (d) f$^+$ = 1.8

340
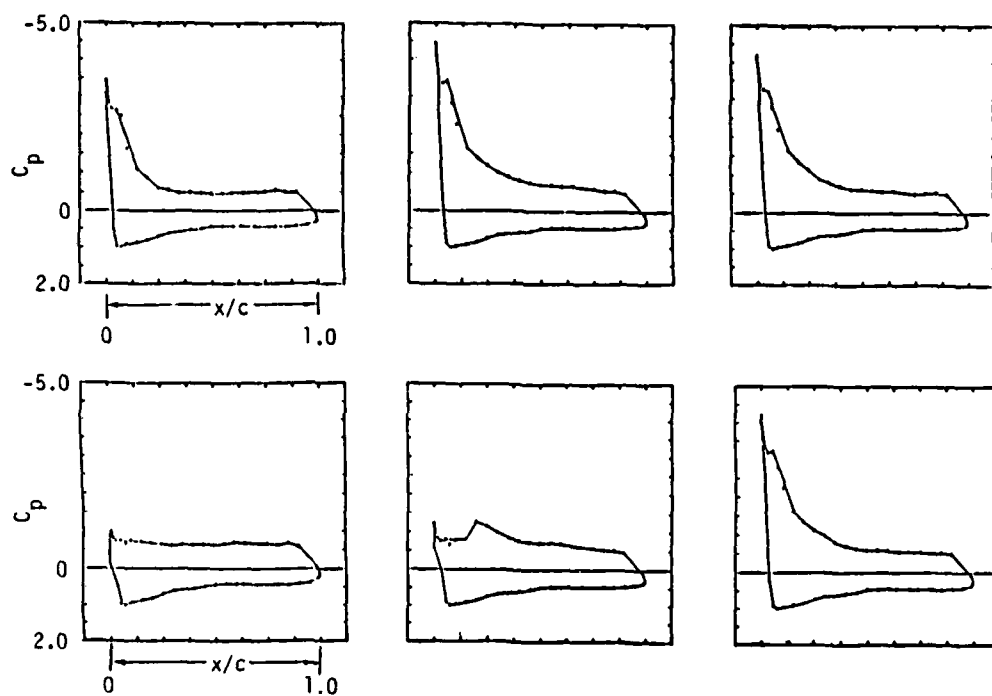
Fig. 12   The pressure distribution on the FX63-137 airfoil at $\alpha = 17°$ and $f^+ = 0$, 1.2, and 1.8; top row corresponds to stall inception, bottom to stall recovery.

A New Program for Active Control of Unsteady, Separated Flow Structures

D.J. Koga*, C.F. Nelson+, and J.K. Eaton++
Mechanical Engineering Department
Stanford University, Stanford, California

A new three-part research program has been initiated to establish active flow control of a simulated dynamic stall vortex flowfield, which is generated using a two-dimensional, motion-controlled flap. The first part of the program consists of mapping the two-dimensional vorticity field, using laser Doppler anemometry and phase-conditioned processing, to document the vorticity transport mechanisms of the formation, growth and shedding of the unsteady vortex, either naturally developing or subject to various additional control vortex generators. Current results show that the vortex vorticity profiles maintain their distribution in phase for at least the first five vortex diameters downstream, while the peak vorticity decreases as x^{-1}. These characteristics will be utilized in the second part of the program to aid in the development of appropriate sensors for the early detection and state estimation of the separated flow vortex. Finally, this information along with optimized vortex control methods, will be used in the third part of the program to establish an active flow control loop of an unsteady, separated flow vortex.

I. Introduction

In the past few years, new research goals have focused on the possibilities for post-stall flight and aircraft supermaneuverability. The tactical advantages of this increased performance have been well established by Herbst (1983), and additional safety advantages are quite apparent for aircraft with a reasonable degree of post-stall maneuvering capabilities. Current research efforts directed towards achieving such goals of post-stall flow control encompass a wide range of programs from experiments that study the characteristics of the unsteadiness associated with flow separation to the latest experiments that attempt to enhance the advantageous effects of the unsteady, separated flowfield.

The solution to the problem of post-stall and super-maneuverability involves the control of flow in the two quite different regimes of steady and unsteady flow separation. As an aircraft initially exceeds the static-stall angle, the phenomenon of dynamic stall becomes important, particularly in fast-accelerating aircraft motions. At this point, the airfoil can exceed its maximum steady-lift coefficient by more than a factor of two, due to the temporary presence of a large, spanwise, leading-edge vortex. However, for sustained post-stall maneuverability, flow control on the airfoil upper surface must be maintained as the dynamic-stall vortex sheds off the surface and the flow adjusts to the "steady" separated-flow regime. Additionally, it will be necessary in most cases to modify the steady, separated flowfield in order to maintain adequate lift.

Historically, the unsteady and separated-flow processes have often been investigated in oscillating airfoil experiments on dynamic stall. McCroskey et al. (1975) documented the time-history development of the unsteady, high-lift characteristics of the leading-edge vortex before the catastrophic flow-separation process, and Carr et al. (1977) identified various types of mechanisms leading to dynamic stall. The identification of these mechanisms, which include trailing-edge stall and boundary-layer flow reversal, bursting of the leading-edge separation bubble, and separation of the turbulent boundary layer, will be vital for the eventual consideration of dynamic-stall control.

* Senior Research Associate

+ Research Assistant

++ Associate Professor

Recently, several experiments have sought to modify or manipulate a flowfield through the use of moving-surface-generated flow unsteadiness. Francis et al. (1979) provided vorticity characteristics of an unsteady flowfield generated with a spoiler motion normal to the surface. Viets (1981) showed the usefulness of such artificially generated vortical structures in controlling diffuser separation with an upstream, rotating-cam mechanism.

More recently, experiments utilizing unsteady boundary conditions, generated by controlled surface motions, have established that a static stall or steady, separated flow can be prematurely reattached by use of forced unsteadiness. Koga (1983) and Reisenthel (1984) have demonstrated that generated unsteadiness on the scale of the separation height is capable of causing significant premature flow reattachment.

In this short review of the various studies on flow unsteadiness and separation control, the common effect that is shared by all is the control or controlled generation of vortical structure introduced into the flowfields, as summarized by the Reynolds and Carr (1985) review. Important questions on the mechanisms of this vortical generation have arisen from the reduced frequency scaling and its apparent optimum for control near a value of 0.06 to 0.08. In addition, the phase relationships in the generation of the controlling vorticity and their interaction with the natural, separated flowfield structure will be an important factor in flow control.

II. Research Program Description

The present research program has as an overall objective the true active control, both with and without feedback, of typical large-scale vortical structures that are likely to be encountered in post-stall maneuvering. Such structures may be either two- or three-dimensional, depending on the physical geometry and the maneuver involved. The present program will focus on primary flow structures which are basically two-dimensional in nature, although both two- and three-dimensional disturbance structures will be introduced for control purposes.

In order to meet this general overall objective, the program is divided into three distinct phases, each with its own set of objectives and experimentation plan. The first phase involves the investigation of several control techniques for dynamic stall flow scenarios. The second phase, which overlaps with sections of phase one, will focus on the rapid detection and recognition of pertinent separated flow

structures. The third phase will combine the results of the first two phases in an attempt of true, active flow control with real-time sensing. The experimental plans for each phase are discussed below.

Phase I. Investigation of Flow Control Mechanisms

The objectives of the first phase of the program are to examine the effectiveness of several control mechanisms and strategies on unsteady separated flowfields. A wide range of control strategies is possible in which two- or three-dimensional flow disturbances are introduced by devices mounted either on the surfaces or in the shear layer, and located upstream, downstream, or at the separation zone.

A number of these configurations have already been examined for the steady-flow separation problem. Koga (1983) and Reisenthel (1984) have studied the case of control induced by a surface-mounted flap introducing concentrated spanwise vorticity into the separated-flow region. Westphal et al. (1984) injected longitudinal vortices into the boundary layer upstream of separation, thereby increasing the entrainment in the separated shear layer. Roos and Kegelman (1985) introduced small, two-dimensional disturbances at the separation point by moving the corner of a backward-facing step which organized the naturally occurring vortical structures and augmented early shear-layer entrainment. The results of these experiments have led to significant decreases in the flow-reattachment lengths, with the largest improvement being over a 50% reduction in the Koga and Reisenthel experiments.

The problem of direct flow control of the initial dynamic-stall vortex has not yet been widely investigated, due mostly to the complicated, fast and transient nature of the experiment itself. However, recent enhancements in VLSI computer speeds and capabilities along with advanced processing and modelling techniques should now provide the tools for adequate data acquisition and flow-structure recognition necessary in this type of investigation. Similarly, it is this new computer capability which will also provide the fast sensing and response-formulation capacity for the currently proposed research efforts into true active flow control.

The dynamic stall experiments of phase I of this program will employ a computer-controlled, spanwise-flap motion to model the flow development in a typical unsteady, separated flow environment, such as that found on a pitching airfoil. This flowfield embodies most of the important features of dynamic stall, including the roll-up and shedding of a large, spanwise vortex and the eventual relaxation to a steady, separated flowfield. The lifting-flap configuration has the instrumentation advantage in that probes and flow-visualization hardware can remain fixed rather than moving along with a pitching airfoil. The rising flap motion will be produced by a servo-controlled printed-circuit motor which allows the capability of specifying the precise flap motion under computer control. The goals of this part of the research phase will be to develop flow-control techniques to retain the large, spanwise vortex and its attendant enhanced lift for the longest possible time and, when it can no longer be retained, to cause it to be shed in an orderly and controlled fashion.

The physics of control mechanisms for dynamic stall are somewhat more difficult to understand, making selection of an appropriated control strategy quite complicated. Following the suggestion of Reynolds and Carr (1985), it is instructive to examine the transport of vorticity in unsteady, separated flows. As dynamic stall is initiated, spanwise vorticity is convected into the separated flow region, yet only a small fraction is convected out. The vorticity accumulates as a large, spanwise vortex which is eventually shed, carrying the accumulated vorticity downstream. A control method must therefore prevent or delay the shedding of this large vortex, which requires that the control device must create a path to drain spanwise vorticity from the separated-flow region to balance the inflow from the upstream boundary layer.

Spanwise vortices injected by a smaller upstream flap may provide an appropriate path to drain such vorticity. The upstream flap would be oscillated at relatively high frequencies

to produce small, spanwise vortices. If these small vortices are simply entrained by the main spanwise vortex, this technique will not stabilize the main vortex. However, the spanwise vortices may produce sufficient shear stresses that they will be swept downstream by the freestream flow, thereby serving to stabilize the main vortex. This configuration offers the additional advantage that the main vortex could probably be forced to shed on command by introducing a very large perturbation with the upstream control flap.

The injection of longitudinal vortices upstream of separation is the second technique to be investigated for the control of dynamic stall. Westphal et al. (1984) have already demonstrated the success of this technique at reducing the reattachment length in steady, separated flows. In addition, it is a well-known technique for delaying separation in moderate, adverse-pressure-gradient flows and for suppressing trailing-edge flow reversal on airfoil surfaces. The key to the success of this method for dynamic stall control lies in the vortex stretching term of the mean transport equation for spanwise vorticity. This term allows intercomponent transfer of vorticity, and in particular, the transfer of spanwise vorticity to the longitudinal component can appear as a sink term. An example of this is the formation region of a horseshoe vortex near the leading edge of an obstacle protruding from a surface. The upstream boundary layer provides a continuous inflow of spanwise vorticity which is passed via the vortex-stretching term to longitudinal vorticity. This continuous sinking of spanwise vorticity allows the formation of a steady, spanwise vortex ahead of the leading edge. Mehta (1985) has shown that a longitudinal vortex embedded in the upstream boundary layer will cause a kinking of the separation line and thus the development of a secondary longitudinal vortex. Such a secondary vortex may provide the path to drain sufficient vorticity from the main spanwise vortex, thereby stabilizing the dynamic stall.

Phase II. Detection and Identification Algorithm

The objective of the second phase of the research program will be to establish valid sensing criteria and techniques for identifying both when an optimized flow-control reaction is necessary (initial sensing) and how the control performance is progressing (feedback loop). These sensing and evaluation techniques must necessarily be rapid and must also respond to a wide variety of flow conditions, yet accurately isolate prespecified characteristics of a targeted flow structure.

The first work of this phase will overlap and interact significantly with the Phase I experiments, using selective filtering and pattern-recognition techniques to reduce the large amount of data to a few "structure" criteria. These criteria must be simplified into the most common, uniquely detectable, structure-identifying signatures, which most probably will result in the need for multi-parameter sensing instrumentation for proper detection. The data reduction work will investigate the flow-structure-signature sensitivity to a number of parameters, which include the flow-structure strength, size, frequency content, trajectory, and transient time signature.

The concentration of phase II analyses will be directed toward the development of state-estimation techniques for the dynamic stall flowfield. In addition, this state-estimator must be efficiently implemented into a real-time flowfield model which will most likely involve vorticity field estimation of the developing spanwise vortex structures associated with the dynamic-stall flowfield. This model must accurately correlate and predict the vortex structure strength, location, and subsequent transient time-signature, factors which will be necessary for the subsequent active vortex-control experiments of Phase III.

Phase III. Active Flow-Control Performance Experiments

The last phase of this research program has as its objective the establishment of an active flow-control-loop experiment. This will involve closing the loop between the

detection methods of Phase II and the generation of the flow-control mechanisms optimized in Phase I. The active flow-control experiments will be designed to utilize either a sensor reactor control scheme (open-loop) or an upstream feedback-loop arrangement (closed-loop), depending on whether the detection sensors are located upstream or downstream of the control surface, respectively. Although the open-loop control schemes are much easier to generate from a control-system point of view, the closed-loop system could be of greater advantage, particularly in controlling the initial vortex in a dynamic-stall situation. However, to do so adequately, the closed-loop-feedback system response must be free of dynamic instabilities which will be quite complex in the non-linear combined fluid-mechanical system.

III. Present Data and Results

Phase I and II of the research program are currently underway. Two-dimensional phase-averaged velocity and vorticity field maps have been obtained for three different reduced frequency cases, k = 0.025, 0.04 and 0.06, where k = fH/U, using f = flap oscillation frequency, H = flap height (2.5 cm) and U = freestream velocity. A strong, well-organized spanwise vortex dominates the k = 0.06 case and will be the topic of the present report.

The experiments were performed in the Stanford University, Mechanical Engineering Department HMT-1 blower wind tunnel (15 cm x 45 cm x 3.5 m test sction) with a freestream velocity of 5 m/sec. The approach flow was tripped to obtain a turbulent boundary layer on the test wall, and the side wall boundary layers were removed to maintain a two-dimensional approach flow.

Phase-averaged LDA velocity measurements

The two-dimensional, phase-averaged velocity field data was obtained using a rotatable, single-component laser Doppler anemometer, operating in forward-scatter mode. A TSI counter processor was used to process the Doppler signal and the velocity data was read through the TSI parallel-data output port into a Masscomp MC-5500 computer system. The data was acquired with a simultaneous A/D flap phase-position indication for phase-bin referencing. A minimum of 30,000 LDA velocity samples were obtained at each spatial location for each velocity component. The large amount of data was necessary to obtain adequate convergence in each of the 36 phase bins (10 degrees wide) of the flap cycle. This typically represented averaging over 500 flap cycles, with the velocity sampling uniformly distributed between phase bins within a ±10% range, as shown in Figure 1a. This produces uniform statistical accuracy for each phase-bin and minimizes LDA velocity bias errors in the overall velocity calculations.

Once the velocity component data was phase-bin sorted at each spatial location, the mean and rms velocity signatures were processed as functions of phase, with typical velocity traces shown in Figure 1b, for the flap phase-bin of 120-130 degrees (where the flap has just begun to move downward). This procedure was continued over a 76 point spatial grid to obtain the two-dimensional velocity field vector map shown in Figure 2. Note that 36 such mean and rms velocity vector maps are available to describe the cyclic process, due to the 10 degree resolution in the phase-bins. From this sequence of velocity maps, it is possible to observe and track the convected vortex as it moves downstream, correlating its presence with other parameters such as surface pressure and surface shear stresses.

Vorticity field estimation and development

In order to calculate the vorticity field distribution as a function of the phase, the velocity data was splined in both directions and differentiated onto a finer grid to obtain the vorticity contours of Figure 3. Again 36 such contour plots are available per flap cycle, so that the spatial distribution and evolution of the vorticity field can be examined. The 120-130

degree phase case shown in Figure 3 clearly identifies the strong vortical structure centered at x/H = 2.0 and y/H =1.0, with indications of forming opposite-signed vorticity nearer the test surface due to viscous interaction effects of the vortex near the wall. The solid contours in the figure represent equally-spaced vorticity increments of the main vortex structure, while the dashed contours signify the zero-vorticity line and equally-spaced levels opposite in sign to the main vortex vorticity.

The results in Figure 4 show the phase (or time) signatures of the integrated spanwise vorticity as a function of phase, developing over the first six flap heights in downstream distance. The significant feature of this plot is that though the peak and total vorticity levels are clearly decreasing, the phase distribution of vorticity remains relatively the same, except for a little low level phase-broadening distortion at small vorticity values. This indicates that the convecting unsteady vortex is well-behaved in phase, and thus time, so that reasonably simple models for flowfield prediction may be possible. In fact, if the downstream development of the integrated vortex strength is plotted from the vortex formation point (between x/H from 0.0 to about 2.0) to a downstream location of x/H = 6.0, it is seen in Figure 5 that as long as the vortex remains relatively coherent, the vorticity decreases as x^{-1} for both the k = 0.04 and 0.06 flap oscillation cases. These observations and similar results from further examination of the vortex under natural and control conditions will be essential for the development of flowfield state estimation and prediction models.
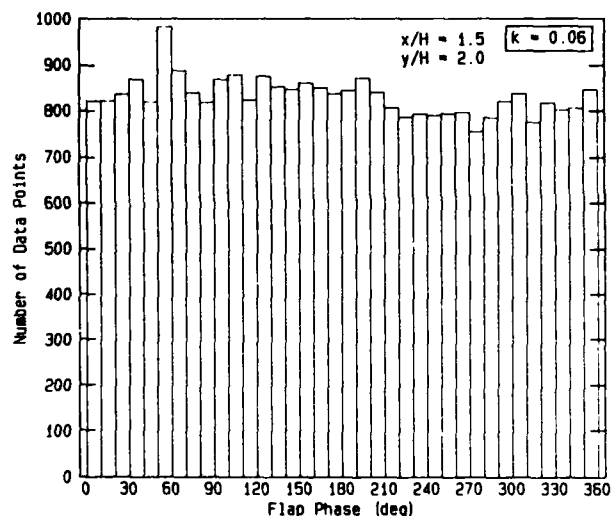
(a) Typical Phase-bin Distribution of Velocity Data
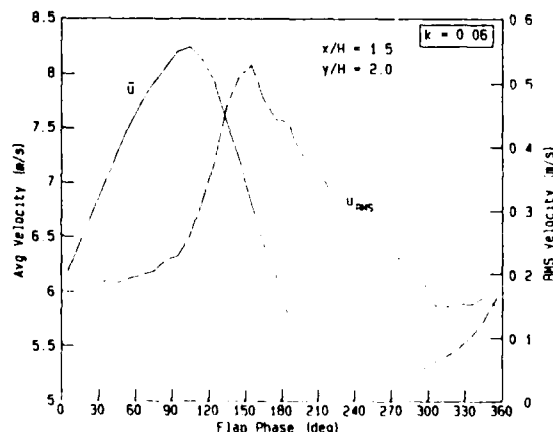
(b) Typical Mean and RMS Velocity Signatures

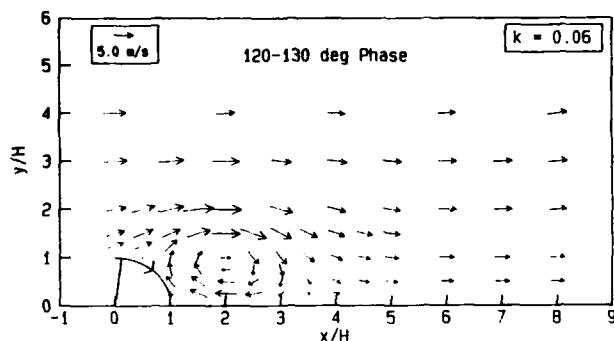Figure 1. Phase-averaged Velocity Measurement Process

345

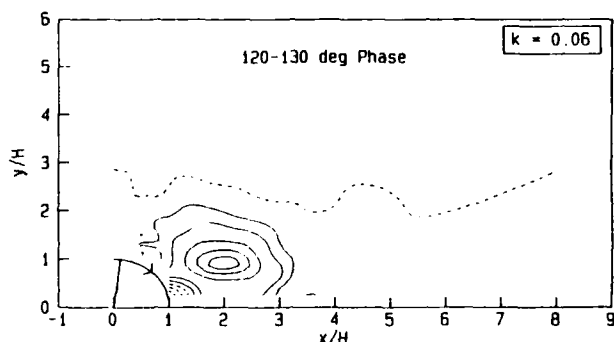Figure 2. Typical Measured Mean Velocity Field Map

Figure 5. Downstream Development of Vortex Strength

Figure 3. Typical Calculated Vorticity Contour Map
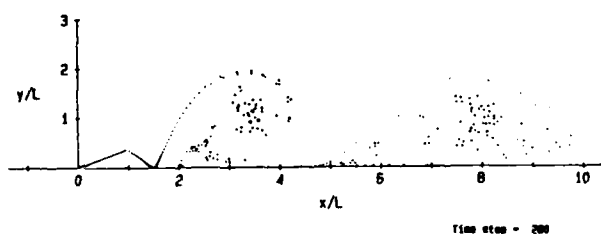

Figure 6. Discrete Vortex State-estimator Model

State Estimation and Flow Modelling

The current results of the phase II investigations have been concentrated on a fast-response discrete vortex model of the oscillating flap flowfield. The calculations were originally performed using 120 discrete vorticity-lumps being shed from the flap tip at equal phase increments of the sinusoidal flap oscillation cycle. The resulting computed flowfield, as seen in Figure 6, shows promise as a vorticity field state estimator for the behavior of the primary spanwise vortex.

In an effort to improve this state estimator model of the vortex, several refinement experiments are currently underway. The first is the determination, from wind tunnel LDA experiment measurements, of a more accurate distribution of the shed vorticity-lump values as a function of flap phase. In the present model, the magnitude of the shed vorticity-lumps was approximated using a sinusoidal vorticity variation for the shedding process, with the shed vorticity peak corresponding to the maximum flap height location. Measurements of actual vorticity shed from the flap, determined from spatial circulation field integrations and vorticity budget balances, will provide insight into the cyclic phase distribution of the vorticity shed from the flap tip. This will also serve to identify the contributions of the two vorticity sources, namely the approach flow boundary layer vorticity and the unsteady generation of the flap tip vortex source.

Once the correct vorticity-lump introduction is established, the vorticity field state estimator model will be optimized for speed. Preliminary experiments have shown that reducing the phase stepping in the model from 120 to 60 phase increments per cycle does not significantly alter the resulting vorticity field results. Also, exact modelling of a no-flow-

Figure 4. Vorticity-phase Distribution of Convecting Vortex

through condition at the moving flap boundary does not significantly affect the downstream-convecting vortex flow model in terms of significant parameters such as vortex size, strength, convection speeds and surface pressure distributions. Further numerical experiments will be continued in an effort to streamline this discrete-vortex state estimator model so that it can be implemented as a real-time model for flow control implementation.

IV. Concluding Remarks

The present results indicate that the behavior of the developing vorticity field for the modelled unsteady flow vortex might be estimable, as a first attempt, with a few relatively simple parameters if an adequate state-estimator is determined. However even though the naturally convecting vortex structure might be estimable with linear parameters, the results of the addition of interacting vortical-control flow structures will undoubtedly lead to much more complicated, non-linear interactions. It is these physical mechanisms of the interacting vortex structures which must be ascertained in order to establish a functional model for active control loop implementation. Important questions as to the effects of turbulent stresses in the boundary and shear layers, and the significance of three-dimensional vortex stretching must be clarified in the next step of the program which will involve the study of various forms of vortex control effects.

The vortex control effectiveness experiments are planned in a recently completed 90 cm x 60 cm x 4 m test section closed-return, blower wind tunnel. The large test section, 25 m/sec maximum speed tunnel facility will allow larger scale vortex interaction experiments without the contamination of opposite wall boundary effects. Initial experiments on the interaction of control vortices with the primary unsteady spanwise vortex structure are planned for both spanwise and longitudinal control vortices acting on either a cyclic or a one-shot generated dynamic stall vortex model. In addition, phase response experiments utilizing two computer-controlled, variable-phase-coupled flap motions will be performed to see if non-linear vorticity component transfer mechanisms can be stimulated and controlled for the dynamic stall flow model.

The results presented and forthcoming from the described experiments will result in the completion of both phases I and II of the research program and should provide a sound data base for the formulation of the final state estimation techniques and flow predictor model needed for a stable

control loop in the final phase of the program. In conclusion, from the progress and results thus far in the research program, it is quite hopeful that the modelled unsteady, separated flow vortex is a realizable candidate for the proposed active flow control.

References

Carr, L. W., McAlister, K. W., and McCroskey, W. J. (1977), "Analysis of the Development of Dynamic Stall Based on Oscillating Airfoil Experiments," NASA TN-8382, January.

Francis, M. S., Keesee, J. E., Lang, J. D., Sparks, G. W., and Sisson, G. E. (1979), "Aerodynamic Characteristics of an Unsteady Separated Flow," AIAA Journal, 17: 1332-1339.

Herbst, W. B. (1981), "Supermaneuverability," Joint Automatic Control Conference, Munich, Germany, June 17-19.

Koga, D. J. (1983), "Control of Separated Flowfields Using Forced Unsteadiness," Ph.D. thesis, Illinois Inst. of Technology.

McCroskey, W. J., and Philippe, J. J. (1975), "Unsteady Viscous Flow on Oscillating Airfoils," AAIA Journal, 13: 71-79.

Mehta, R. D. (1985), "Effect of Longitudinal Vortex on a Separated Turbulent Boundary Layer," AIAA-85-0530, presented at AIAA Shear-Flow Control Conference, Boulder, CO, March 12-14.

Reisenthel, P. H. (1984), "Reattachment Control Behind a Rearward-Facing Step Using Forced Unsteadiness," M. S. thesis, Illinois Inst. of Technology.

Reynolds, W. C., and Carr, L. W. (1985), "Review of Unsteady, Driven, Separated Flows," AIAA-85-0527, presented at AIAA Shear-Flow Control Conference, Boulder, CO, March 12-14.

Roos, F. W., and Kegelman, J. T. (1985), "Control of Coherent Structures in Reattaching Laminar and Turbulent Shear Layers," AIAA-85-0554, presented at AIAA Shear-Flow Control Conference, Boulder, CO, March 12-14.

Viets, H., Piatt, M., and Ball, M. (1981), "Forced Vortices Near a Wall," AIAA 19th Aerospace Sciences Meeting, St. Louis, MO, Jan. 12-15.

Westphal, R. V., Johnston, J. P., and Eaton, J. K. (1984), "Experimental Study of Flow Reattachment in a Single-Sided Expansion," NASA Report CR-3765.

A Study of Stall on an Airfoil
Using a Subproblem Technique

David Nixon and Mohammad Farshchi
Nielsen Engineering & Research, Inc.

Introduction

The aerodynamic behaviors of a maneuvering aircraft has certain essential features. The actual airflow depends on the maneuver being executed and consists of its response to the pitch, roll, yaw, and deceleration or acceleration of the aircraft. The flow will be transient and may be separated. Some form of three-dimensional dynamic stall may also be present. If the aircraft is a fighter, it will have a low aspect ratio wing and, hence, will experience considerable three-dimensional effects. The motion will not be periodic, and the "reduced frequency" of the maneuver is such that phase lag effects will be important. Transonic flows may be present due to the high angles of attack even at low flight Mach numbers. Under the influence of these phenomena the controllability of the aircraft could suffer severely.

The effect of yaw is essentially to change the oncoming flow angle and speed relative to the airfoil; however, the rate of yaw should be small enough to make this problem relatively unimportant. Roll, however, is an important parameter. A simple calculation shows that a modern fighter can roll very quickly, and at maneuver speeds the effective angle of attack at the wing tip due to roll rate can be the same order of magnitude as that due to the pitch angle. Furthermore, there is an exceptionally strong gradient in the effective roll angle of attack along the span. For example, if the wing root is one-fifth the distance of the tip from the roll axis, then the effective roll angle of attack varies by a factor of five along the span. It is implicitly assumed that pitch should be studied, and, hence, the two main features that should be examined are pitch and roll. In addition, the effects of aircraft deceleration may be included; it is not known at present how significant a factor this may be. That the flow is transient must be considered, especially the phase lag effects which may be used to some advantage in control. The problem is not periodic so any experiment or analysis cannot be simplified using periodic motions.

In summary, the basic problem consists of a low aspect ratio wing in a transient motion of both pitch and roll. The aim of a study of this flow must be to identify and understand the fluid mechanics phenomena that occur and to devise means of controlling such flows. The most obvious way of examining the maneuver flow is by experiment, but such experiments should be able to measure and thus quantify the phenomena. Flow visualization alone is not sufficient. Experiments on maneuver flows can be complex, and the resulting data difficult to interpret. A further disadvantage of a purely experimental study of supermaneuver flows is that it is a "passive" process in which data around a specified configuration is obtained. Beyond providing data it does not, in itself, give any guidelines for flow control. This is equally true of a standard computational study where, again, the solution (data) is for a fixed configuration. The object of the present work is to develop a more "active" process in which some possible flow control mechanisms are suggested, as well as data gathered.

The concept introduced in this report is that of using "subproblems" to examine interesting phenomena of a given flow and to determine the parameters which control this flow. The basic principle of the technique is that in any subdomain of the flow the only factors that can affect the flow phenomena are represented by the boundary conditions of a calculation. The number of boundary conditions is limited by the mathematics of the flow model. By changing these mathematical boundary conditions all possible control devices can be simulated. Once a certain combination of boundary conditions has been found to enhance a favorable flow phenomena, attention can be directed to determining the physical analog of these conditions. The technique allows an exploration of the causes of isolated flow phenomena that would be impossible in an experimental context.

In the present study the control of the flow over a stalled airfoil is investigated. The flow around the airfoil is computed using a standard Navier-Stokes solver. In this initial study it is found that the subproblem techniques will give known mechanisms for controlling the lift of the airfoil.

The Subproblem Technique

The problem that is considered in the present work is the control of a stalled airfoil. It is assumed that the qualitative features of a stalled airfoil can be modeled by the Reynolds averaged Navier-Stokes equations with a turbulence model. In the present case a simple eddy viscosity model, the Baldwin-Lomax model, is used. The subproblem technique is described below.

A calculation of the entire airfoil flowfield (the global calculation) is performed using the Navier-Stokes equations; this gives a numerical approximation of the stalled airfoil. To study the separation region, for example, a subdomain that encompasses the separation zone is specified, and the complete solution on the boundary of the domain is recorded. Subdomain II in Figure 1 sketches a typical region that would be used. Given the domain and boundary information, the simulation of the separation can be repeated without recomputing the global flowfield. This isolated phenomenon, called the subproblem, can then be studied.

If the subproblem is recomputed using the recorded boundary data and a computational grid taken from the global grid, then the subproblem solution will match exactly that portion of the global calculation. However, specifying all boundary conditions makes the problem overdetermined, and, if the subproblem is recomputed using slightly different boundary data, then the subproblem solution may differ significantly from that in the global solution. This is because it is mathematically improper to specify all variables as boundary conditions for the Navier-Stokes equations. What is needed is a subset of the complete boundary data that forms mathematically correct boundary conditions for the subproblem. The mathematical conditions correspond to physical phenomena on the boundary. The determination of the correct boundary conditions is crucial because it is the key to understanding controlling mechanisms of the flow within the subdomain. The means for determining correct boundary conditions is discussed later.

By numerically perturbing the boundary conditions of the subproblem, further insight into the fluid mechanics is achieved, and, especially important, mechanisms for controlling the flow can be deduced. The key research problems are the identification of the consistent boundary conditions and the physical interpretation of these conditions. The subproblem procedure is described below.

(a) First compute a global solution and ensure that this computation qualitatively represents all the flow features of importance that are corroborated by experiment. This means that the reverse flow region must also be captured in the calculation.

(b) Construct a subproblem for the separated flow zone.

(c) Using the information on the subproblem boundaries that can be obtained from the global solution, compute a solution of the subproblem using the corresponding subdomain of the global grid. The key problem is to isolate, from the complete flow data available from the global solution, the necessary and sufficient boundary conditions to reproduce the subproblem.

(d) Compute a fine grid solution of the subproblem using the correct set of boundary conditions. This is a very cost effective way of examining flow details because of the greatly reduced computer time.

(e) Make a preliminary examination of the effect of changes in the magnitude of the boundary conditions to determine ways of advantageously controlling the phenomena. In other words, ascertain if the stall can be controlled by certain choices of the boundary conditions. Examine the meaning of the boundary conditions to identify the physical parameters that are necessary to sustain the subproblem and, thus, learn about the physics of the subproblem. For a stalled airfoil this

may mean restrictions on the mass flux of vorticity through the boundary or some minimum value of turbulence.

Numerical Techniques

The Reynolds averaged Navier-Stokes equations are solved in the conservative form using the ARC2D code developed by Pulliam and Steger (Ref. 1). The turbulence model is the Baldwin-Lomax algebraic eddy viscosity model (Ref. 2). This model is not really suitable for separated flows but is used here for convenience. It is assumed that this model will represent qualitatively, if not quantitatively, the physical mechanisms of stall.

All of the examples computed in the study are flows around a NACA 0012 airfoil at a freestream Mach number of 0.3. The flow in all cases is subcritical. In order to validate the code a series of calculations was performed.

It was felt that beginning with a laminar flow case might be wise since, if it was successful, the inaccuracies due to the turbulence model could be avoided. Consequently, a case at five degrees angle of attack was run. The lift distribution with time is shown in Figure 2. This calculation used a grid of 81 x 27; the periodic lift distribution was confirmed by Pulliam (Ref. 3) who used a finer grid and a much longer run time. This result is interesting because it indicates that unsteady results are possible for rigid airfoils, although the unsteadiness may be due to subtle differences in the formulation of the equations rather than in the physical phenomena. Because of the unsteadiness it was decided not to proceed further with laminar flow studies. However, the example should act as a warning that computational results may not be physically realizable.

A series of calculations for turbulent flow around the NACA 0012 airfoil at various angles of attack and a Reynolds number of 6×10^8 were performed. The variations of the lift coefficient with angle of attack are given in Table I. For comparison the data of Abbot and Van Doenhoff (Ref. 4) is also shown in Figure 3. It can be seen that the computational results are in qualitative agreement with the experimental data. Grid refinements were performed for five degrees angle of attack on grid sizes of 81 x 27 and 149 x 39 and for 16 degrees angle of attack on grid sizes 85 x 36 and 149 x 39. The changes in lift and drag coefficients are shown in Table II. It is observed that a grid independent solution is not obtained; however, a grid of 85 x 36 is the maximum practical limit for multiple calculations on the VAX 11/750 computer. The calculations are continued until the residual has fallen by three orders of magnitude.

In summary, the ARC2D code with the Baldwin-Lomax turbulence model is capable of predicting qualitively the flow around a stalled airfoil; however, it should be remembered that a grid independent solution is not obtained for practical grid sizes.

Tests of the Subproblem Technique

The subproblem technique is tested on the NACA 0012 airfoil at 16 degrees angle of attack. The Reynolds number is 6 x 10^6 and the grid used in the calculations is 85 x 36. The flow is subcritical so no shock waves appear. In the formulation of ARC2D the freestream pressure is given by $P_{\infty} = 1/\gamma = 0.714$. The pressure distribution, streamlines, and velocity vectors are shown in Figures 4a, 4b, and 4c respectively. It may be seen that there is a considerable region of reverse flow. It is the object of the present exercise to reduce or remove this reversed flow region using the subproblem technique. A sequence of calculations in which various boundary conditions are used on the subdomain boundaries is given below. Each of the different boundary conditions adds to the knowledge of the technique; some of this knowledge is positive, some negative.

The first step in the subproblem technique is to identify a subdomain and to reproduce the features of the global solution in this subproblem. As an initial step the subdomain is taken to be the region from the separation point to one grid point upstream of the trailing edge. The "normal" coordinate extends to the boundary of the global computational grid. The global grid and the subdomain are shown in Figures 5a and 5b.

The boundary conditions used in the ARC2D code are derived from one-dimensional characteristics theory. In general, if there are m outgoing characteristics and n ingoing characteristics at a boundary, then the number of variables that can be specified at the boundary is n. It should be noted that the Navier-Stokes equations are multidimensional and elliptic in space rather than the one-dimensional hyperbolic equations used in the boundary condition analyses, which may invalidate the use of idealized characteristics boundary conditions in certain cases. However, because of time constraints, boundary conditions based on the one-dimensional characteristic analysis are used in the present work.

As a first attempt the boundary conditions specified for the subproblem were an inflow condition of U, V, and ρ specified and pressure extrapolated from the subdomain. At the downstream boundary the two velocity components and density are extrapolated, and the pressure is specified. On the airfoil surface U and V are put equal to zero and the density and pressure are extrapolated using zeroth order extrapolation. The calculation using these boundary conditions diverged. The precise cause is not clear but a probable reason is that the "downstream" boundary of the subdomain is in a reversed flow region, and the direction of the flow is, therefore, into the subdomain, invalidiating the use of an outflow boundary condition. This result demonstrates that an incorrect choice of boundary conditions can lead to a divergent computation which reduces the chances of obtaining a converged but erroneous solution. Consequently, a boundary condition at the "downstream" boundary which specifies the streamwise velocity component and the pressure is

used. These values are obtained from the global solution; the V component of the velocity and the density are extrapolated. The pressure distribution and the streamline contours are shown in Figures 6a and 6b respectively. These results should be compared to the data from the global calculation shown in Figures 7a and 7b. It may be seen that the subproblem calculation agrees with the global calculation indicating that an appropriate choice of boundary conditions has been made.

Since one of the critical parameters in a separated flow is the streamwise pressure gradient, the outflow boundary condition of extrapolated velocity components and the density with a specified pressure gradient was applied. The pressure coefficient and stream function contours are shown in Figures 8a and 8b, respectively. The flow in the subdomain is attached. The reason is that an outflow boundary condition, that is U, V, and ρ extrapolated, has been applied, thus, eliminating the possibility of a reverse flow. The fact that the computation with extrapolated ρ, U, and V with pressure specified diverges, whereas that with streamwise pressure gradient specified converges, raises some questions about the validity of boundary conditions derived from one-dimensional characteristics theory. In the subdomain the flow through the downstream boundary condition is not one dimensional since a normal pressure gradient is necessary to balance the centrifugal acceleration. The imposition of a constant streamwise pressure gradient allows a floating normal pressure gradient to balance the floating ρ, U, and V from the extrapolated boundary conditions. The real lesson is that a more detailed study of the proper conditions is necessary. A consequence of this result is that any control device that can reverse the direction of the flow at the "downstream" boundary will reattach the flow in the subdomain. An example of such a control could be a trailing edge flap which would increase the camber and, hence, the velocity over the upper surface of the airfoil; this velocity increase may be sufficient to counter the reverse flow mechanism.

It is well known that suction will inhibit boundary layer separation, and, consequently, the subproblem technique was used to simulate suction. In this example the boundary conditions at the downstream boundary are U and p fixed with V and ρ extrapolated where p is the pressure. The values of U and p are the values obtained from the global solution. On the airfoil surface the normal velocity, V, is given by

$$V = -k \, Q_{\infty} \cos \alpha$$

where Q_{∞} is the freestream velocity and α is the angle of attack. The constant k is taken to be between -0.001 and -0.2. For values of k above -0.2 a convergent solution was not obtained. The location of the separation point for various values of k is shown in Figure 9 and, as expected, the separation point moves downstream with increasing suction. Since the boundary condition at the downstream boundary requires a separated flow,

separation must occur somewhere on the airfoil for a converged solution. The pressure distribution and the stream function contours for a value of k of -0.02 are shown in Figures 10a and 10b, respectively. To investigate whether the subproblem result applies to the complete airfoil, a global solution was obtained. This is shown in Figures 11a and 11b; comparison with Figures 10a and 10b indicates that the behavior identified in the subproblem is applicable to the complete airfoil.

The difficulty with the subproblem described above is that the downstream boundary condition specifies whether separated flow exists. In other words the boundary condition enforces either some separation or zero separation. To allow more flexibility the downstream boundary condition is given as an outflow, if the skin friction coefficient, C_f, is greater than 0.1 anywhere in the subdomain. The physical implication is that if C_f is large in the subdomain, the chance of attached flow is high and the downstream boundary condition should be an outflow condition. Thus, pressure is specified (from the global solution), and the velocity components and density are extrapolated. Application of this boundary condition reattaches the flow in the subproblem as can be seen in Figure 12 where the streamline contours are shown. When the suction used in this calculation is applied to the airfoil problem, the flow in the subdomain is attached but there is a separation bubble upstream of the subdomain. This example illustrates the fact that alterations to the subdomain boundary can significantly affect the flow exterior to the subdomain, reinforcing the need to perform global computations in conjunction with the subproblem computations.

Concluding Remarks

The examples given above indicate that the subproblem technique is capable of providing insight into flow control. There are several topics that need to be investigated before the technique is fully developed. Most important is a more detailed study of boundary conditions for the subdomain; the existing form of the boundary conditions can reduce the flexibility of the method significantly. A second topic that should be addressed is the realism of the Navier-Stokes computations since the laminar flow example in the present study differs considerably from the turbulent flow examples; this difference may or may not be physically realizable.

References

1. Pulliam, T. H. and Steger, J. L.: Implicit Finite-Difference Simulations of Three-Dimensional Compressible Flow, AIAA J. 18 (1980), p. 159.

2. Baldwin, B. S., and Lomax, H.: Thin Layer Approximation and Algebraic Model for Separated Turbulent Flows, AIAA Paper No. 78-257 (1978).

3. Pulliam, T. H., Private Communication, Oct. 1986.

4. Abbott, I. H. and Van Doenhoff, A. E.: Theory of Wing Sections, 1949, Dover Publications, Inc. New York.

α	C_L	C_d	C_m	Separation	Grid Size
5	0.55	0.0175	0.0065	NO	81x27
8	0.89	0.0208	0.0014	NO	81x27
11	1.20	0.0294	0.0064	NO	81x27
13	1.31	0.0403	0.0200	YES	81x27
15	1.40	0.0674	0.0183	YES	85x36
16	1.43	0.0823	0.0144	YES	85x36

Table 1: Predicted results for a NACA0012 airfoil with $R_e = 6 \times 10^6$.

α	C_L	C_d	C_m	Grid Size
5	0.55	0.0175	0.0065	81x27
5	0.56	0.0139	0.0029	149x39
16	1.43	0.0823	0.0144	85x36
16	1.54	0.0653	0.0236	149x39

Table 2: Grid refinement tests for a NACA0012 airfoil with $R_e = 6 \times 10^6$.
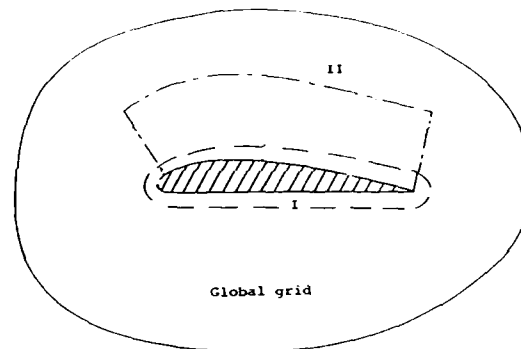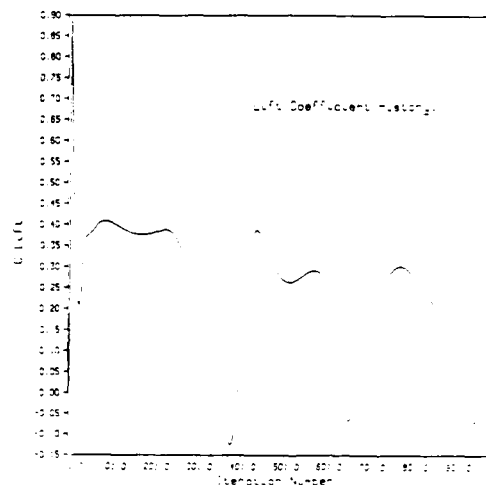

Figure 1.- Subproblem schmetic.

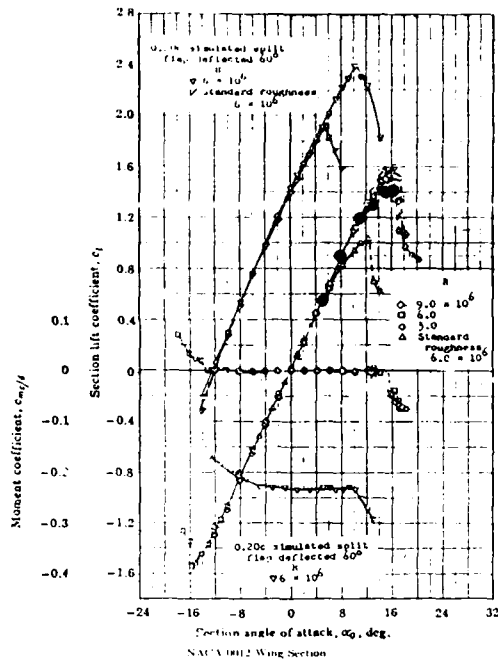Figure 2.- Lift coefficient history for 5° angle of attack laminar flow case, NACA 0012 airfoil.

352

Figure 3.- Comparison of predicted lift coefficient with experimental results of Abbott and Von Doenhoff (large circles indicate predicted results).
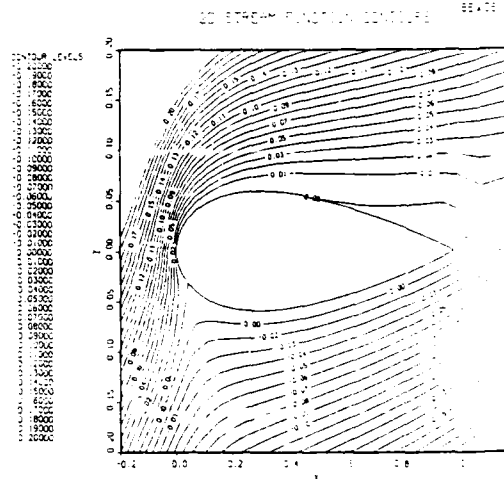

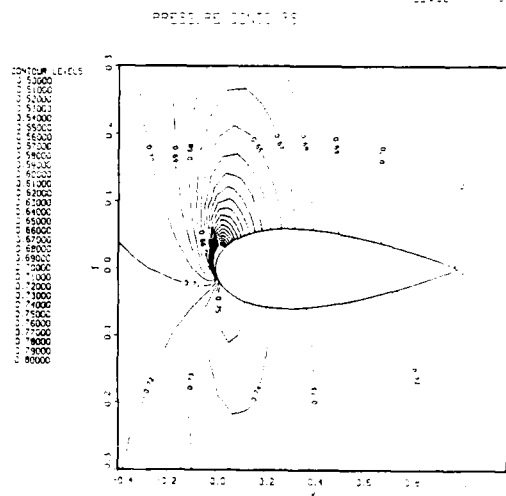Figure 4b.- Streamlines around a NACA 0012 airfoil at 16 degrees angle of attack.

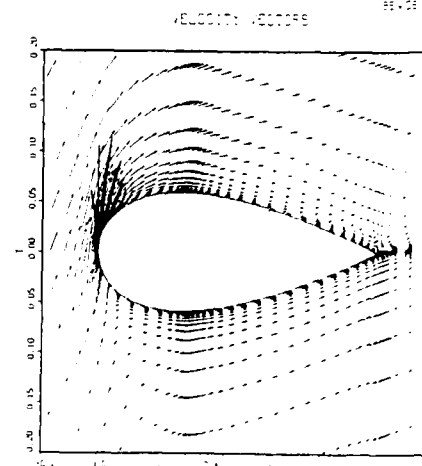Figure 4a.- Pressure distribution around NACA 0012 at 16 degrees angle of attack.

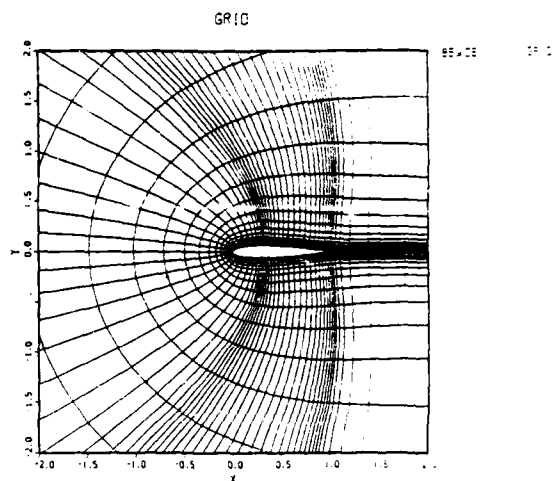Figure 4c.- Velocity vectors around a NACA 0012 airfoil at 16 degrees angle of attack.
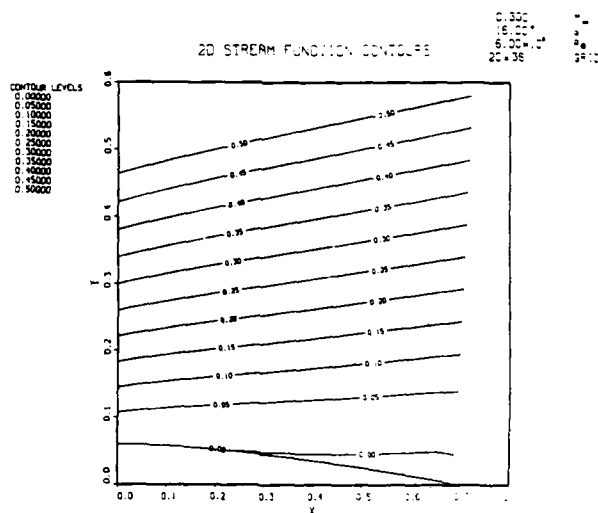
Figure 5a.- The global C-mesh for NACA 0012 airfoil.

Figure 5b.- Subdomain grid.

Figure 6a.- Pressure distribution from subproblem solution with inflow downstream boundary conditions.

Figure 6b.- Streamlines from subproblem solution with inflow downstream boundary conditions.

Figure 7a.- Pressure distribution obtained from the complete airfoil solution.
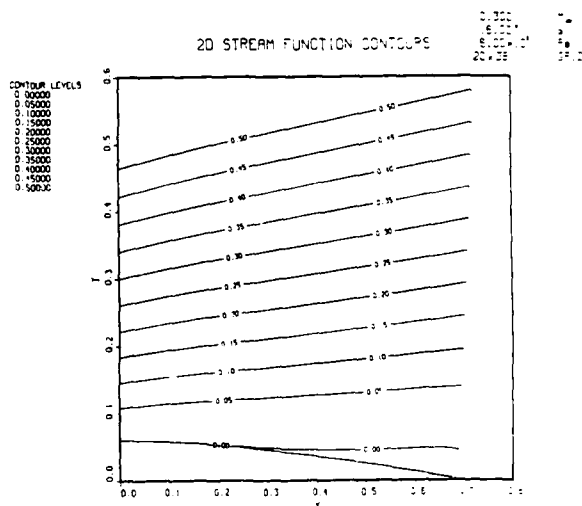
Figure 7b.- Subdomain streamlines obtained from the complete airfoil solution.

354

PRESSURE CONTOURS

CONTOUR LEVELS
0.53000
0.53500
0.54000
0.54500
0.55000
0.55500
0.56000
0.56500
0.57000
0.57500
0.58000
0.58500
0.59000
0.59500
0.60000

K = -0.001
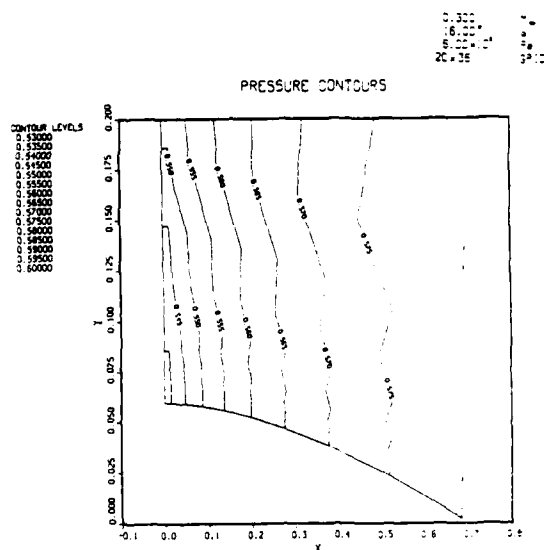
Figure 8a.- Subdomain pressure distribution with constant pressure-gradient outflow boundary condition.

K = -0.005

20 STREAM FUNCTION CONTOURS

CONTOUR LEVELS
0.00000
0.05000
0.10000
0.15000
0.20000
0.25000
0.30000
0.35000
0.40000
0.45000
0.50000

K = -0.02

Figure 9.- *Effect of suction on the subproblem separation point.*

Figure 8b.- Subdomain streamlines with constant pressure-gradient outflow boundary condition.

PRESSURE CONTOURS

Figure 10a.- Pressure distribution for a subproblem with suction constant, k = -0.02.

Figure 11a.- Pressure distribution obtained from the complete airfoil solution with subdomain suction constant, k = - 0.02.

2D STREAM FUNCTION CONTOURS

Figure 10b.- Streamlines for a subproblem with suction constant, k = -0.02.

2D STREAM FUNCTION CONTOURS

Figure 11b.- Streamlines obtained from the complete airfoil solution with subdomain suction constant, K = - 0.02.

Figure 12.- Streamlines for a subproblem with k = -0.06 and modified outflow boundary conditions.

UNSTEADY AND SEPARATED FLOWS

P. E. Dimotakis, A. Leonard, A. Roshko, C. H. K. Williamson
California Institute of Technology
M. Gharib, University of California at San Diego

This research addresses the three broad areas outlined below.

1. **Experiments on Unsteady and Separated Flows.**

   The objective is to learn about the interactions between accelerating simple bodies and the vortical structures which they generate. Typical bodies are cylinders and flat plates at angles of attack; motions include unsteady linear, pitching or plunging trajectories. Facilities include wind tunnels and a water towing tank. Forced vortices are produced during acceleration phases of the motion; in addition, instability vortices may develop in free shear layers and wakes if the flow is separated.

   Figure 1 shows a tow-tank picture of a circular cylinder on a sinusoidal path with short wave length, relative to natural Strouhal wavelength. The small, forced vortices form an unstable configuration which regroups into a large vortex street. Figure 2 shows a suddenly accelerated flat plate at fixed angle of attack, forcing a starting vortex, which interacts with an upper flap. The first picture is taken just after start of motion and the second one after approximately one chord length of travel. For certain flap settings the forced vortex may evolve into a "trapped" vortex when steady state conditions are reached. It is of interest to see whether the flap can prolong or enhance transient or steady lift.

2. **Adaptive Feedback Control of Separated Flows.**

   Our objectives in this part of the work are to study and attempt to modify the dynamics of unsteady/separated flows via feedback control techniques. We have begun our investigations by exploring the generic possibilities on the separated flow generated by a cylinder executing rotary oscillations. Our intent is to first study the response of this system to open loop excitation, in particular sinusoidal rotary oscillations at a (normalized) frequency f/f_s, where f_s is the natural (non-oscillating cylinder) vortex shedding frequency. Sample flow visualization pictures for $f/f_s = 0$ (no forcing), 0.4, 2.2 and 10.7 derived from these preliminary investigations are depicted in Figure 3. It can be seen that the system is rather sensitive to this kind of excitation. In particular, the cylinder wake can be made either wider or narrower, depending on the value of f/f_s in a rather complicated manner. The ratio of the peak circumferential velocity of the cylinder to the free stream velocity was kept constant ($=2.4$) for the oscillating cylinder flows in these data ($Re_d = 3,300$). We are using system identification methods to investigate whether the cylinder/wake flow system can be described parametrically, for short times, as a low order system. Contingent on the outcome of that investigation, we will subsequently design and implement a feedback control strategy that depends on the continuously updated system identification parameters and study the resulting closed loop flow response and dynamics.

3. Vortex Methods for Flow Calculation.

The objective is to perform three-dimensional numerical simulations of the dynamics of large-scale separated vortices in the wake of a bluff body and to study the mutual interactions between the vortex structures and the body during transient motions. These computational studies will be performed using vortex methods and they should complement the experimental investigations described above. Lagrangian vortex elements are used to represent the vorticity in the wake and a panel method is used to satisfy the inviscid boundary condition at a solid surface. In addition the mechanics of a separating boundary layer must be represented.

We have tested several types of Lagrangian elements on a flow that features a strong interaction between vortex structures - the merging of two vortex rings. Figure 4 shows the merging as computed by a vortex filament method while in Figure 5 a vortex stick method was used. In the filament method, tubes of vorticity are defined by a sequence of material points that move with the local velocity. This is an efficient representation for short times but has difficulties once the viscous reconnection of vortex lines becomes important. In the vortex stick method, vector elements of vorticity are used that move with the local velocity and are stretched and rotated according to the local strain field. This method appears to have the flexibility to handle vortex merger in three dimensions.
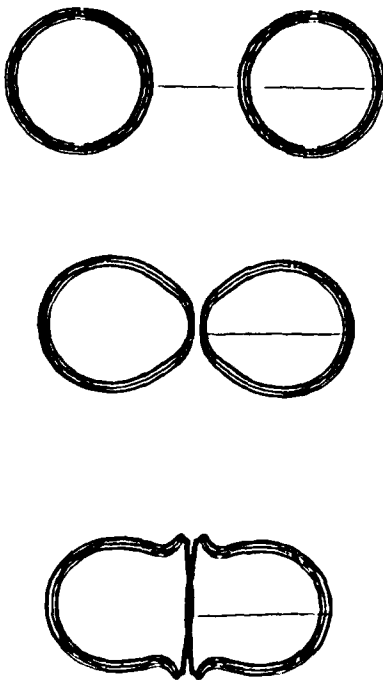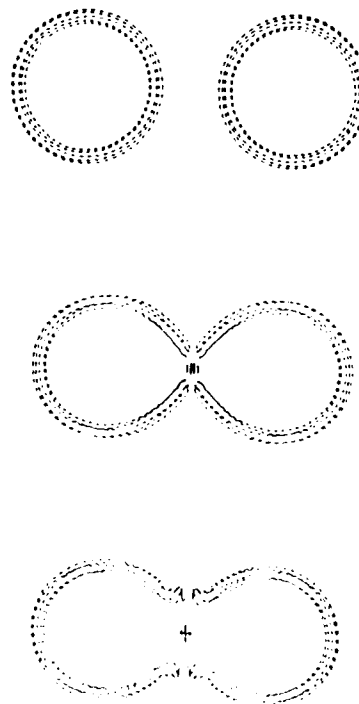

Figure 4

Figure 5

Figure 1

Figure 2

- 4 -

$f/f_s = 0.4$

$f/f_s = 10.7$

$f/f_s = 0.0$

$f/f_s = 2.2$

FIGURE 3. Cylinder wake response to rotary oscillations. Top left: unforced wake. $Re_d = 3,300$. $\alpha_{max} = 2.4$ (see text).

Formation, Evolution and Control of

Vortices Separating from Inclined Bodies of Revolution

by

David R. Williams, Robert Montividas and Hassan Nagib

Fluid Dynamics Research Center

Illinois Institute of Technology

Separation and development of vortices on inclined bodies of revolution involve many interacting complex flow modules which lead to several flow regimes. Changes in the flow parameters lead to transition from one flow regime to another with additional complications arising in the process of separation and development of these vortices. Therefore, flow unsteadiness (such as in angle of inclination), even at low reduced frequencies, can introduce such interactions along with the dynamic effects of unsteadiness. The changes in the flow modules include the development of non-symmetric conditions and the change from a partly-attached/partly-detached system of streamwise vortices to one with vortex shedding.

Using a slender cylinder with various nose configurations that can be held stationary or oscillated about adjustable mean angles of attack, the flow field is investigated using flow visualization, two-component LDV and scanning LDV measurements. The objectives of our work are to document the main features of these flow modules, particularly those involving separating vortices and explore the vortex control by unsteady forcing with pulsed jets. A parametric examination of active control arrangements should lead not only to development of an effective means for flow management, but also to improved understanding of the mechanisms governing these flow modules and their interaction.

In conjunction with the forced cylinder studies, we are developing a

scanning laser anemometer capable of measuring one component of velocity over a plane parallel to the optical axis. Most of our measurements have been made by scanning along the optical axis, but the system also works well when scanning perpendicular to the optical axis. The combination of the two scanning directions gives the planar scanning technique. Since the data acquired by the planar scanning system are functions of two positions and time, one can obtain quasi-instantaneous velocity profiles, spatial correlations and maps of the velocity field from the system. The data can be displayed three dimensionally (velocity, and two spatial coordinates) at a rate close to real-time on a Masscomp computer graphics terminal. The high-speed data display allows us to make changes to the flow field and immediately evaluate its response. Furthermore, transient flow phenomena which do not repeat on a periodic basis can easily be recorded by the scanning LDV system.

AUTHORS